3   Ambient Hydrology KTI – Hydraulic Properties

Account Number: **20-5708-861**
Collaborators: **Jim Winterle, Gordon Wittmeyer**
Directories: **$HOME2/AmbientKTI/3Ddata and as noted**

Objective: Perform detailed analysis of the spatial distribution of hydraulic properties at Yucca Mountain (YM) and their effects on flow. Topics include investigation of USGS-measured properties and analyses, as well as predictions of their impact on flow.

Some of the work was documented in the notebook chapter entitled "Ambient Hydrology KTI – Infiltration." This chapter was created on October 10, 1997, immediately following the October 8, 1997, printout of the scientific notebook. Relevant prior entries in the other chapter were moved to this chapter upon creation of the chapter, in order to improve clarity of presentation in both chapters.

8/29/96 Revisiting PTn modelling ideas.

Further discussions with English and Sitakanta suggest that examining the behavior of the PTn layer may be of the most direct use to PA. For example, the appropriateness of the various models for flow in the subsurface can be examined (i.e., ECM versus dual-permeability versus weeps) by examining the time behavior of pulses reaching the top of the PTn layer. If extremely long time scales at the bottom of the PTn are observed, the ECM model may be in order. If extremely short time scales are observed, the weeps model is in order. Intermediate cases presumably would require the dual-permeability model).

A second question that can be examined is the issue of the spatial distribution of fluxes leaving the PTn layer. There are direct implications for the distribution of fluxes at the drift scale, since the TSw units are relatively homogeneous from the PTn to the repository. My conceptual model of drift-scale processes under ambient conditions has high relative humidity at all flow packages and relatively few packages contact a dripping fracture (i.e., dripping fractures are widely spaced). In this case, the drips are a strong focussing mechanism, shielding most surrounding packages. Studying the behavior of the PTn layer may shed some light on the relative spacing of dripping fractures.

9/21/96 Setting up 1D PTn modelling.

Two detailed sources of information are available for unsaturated-zone tuff properties, Rautman et al. (1995) and Flint et al. (1996). The Rautman et al. (1995) data set is finely resolved in both the lateral and vertical directions, but only covers part of the PTn layer and does not provide van Genuchten properties for the samples. The Flint et al. (1996) data set consists of 8 transects, covering the full range of layers in less detail. The Flint et al. (1996) data set does provide several measurements of van Genuchten properties, however.

The Flint et al. (1996) data set will be used to test the behavior of wetting pulses, since it provides a much longer vertical transect (the Solitario Canyon transect, in particular) and some van Genuchten information. Two approaches are immediately obvious: (i) use average layer thicknesses and properties, based on Tables 2, 5, and I-1; and (ii) use Table I-1 for fullest spatial resolution but supplement properties as necessary. The idea would be to assume fracture flow with the wetting pulses translated undamped from surface conditions as a top boundary condition, with the top boundary at the top of the shardy base of the Tiva Canyon Tuff, and use gravity drainage bottom conditions in fractures to correspond to the Topopah Spring Tuff vitric caprock and lower layers. There are between 20 and 25 measured K_{sat} values within the roughly 35 m section of the transect of interest, with perhaps 35 additional core samples that do not have K_{sat} values. It is not clear whether the reported transect distance is vertical distance, horizontal distance, or along-ground distance, but assuming that the slope is roughly 30 degrees in this region, the vertical section of nonwelded tuff is about 20 m, about twice the thickness considered by Rautman et al. (1995).

As a first cut, the detailed stratigraphy implied by Table I-1 of Flint et al. (1996) will be assembled into detailed layering. For points where K_{sat} and van Genuchten properties are missing, the regressions provided by Tables 3 and 6 will be used. Between each data reading, K_{sat} and van Genuchten α will be loglinearly interpolated and van Genuchten n will be linearly interpolated. Initial conditions will be provided by using the steady-state vertical ODE approach discussed in the PA Research and Ambient Hydrology projects.

The regression equation for K_{sat} as a function of porosity for the welded and nonwelded portions of the Solitario Canyon transect in Table 3 of Flint et al. (1996), based on 36 samples and with an r^2 value of 0.90, is:

$$K_{sat} = -13.9 + 33.1\varepsilon - 30.8\varepsilon^2, \tag{3-1}$$

where K_{sat} is in m/s. Based on Figure 11, it appears that the regressed equation is actually for $\log_{10}(K_{sat})$, which makes much more sense.

From Table 6 of Flint et al. (1996), based on 10 samples and with r^2 values of 0.01 and 0.44 for van Genuchten α and n, respectively, the regression relationships are:

$$\alpha = 0.49 + 0.31\varepsilon, \tag{3-2}$$

$$n = 0.95 + 1.94\varepsilon, \tag{3-3}$$

where α is in units of MPa^{-1}.

Parenthetical note:

My suspicion is that the van Genuchten regression relationships could be significantly improved by solving for all samples simultaneously, since there is considerable latitude in changing the α and n parameters without greatly affecting the fit between data and formula. The simultaneous-solution procedure minimizes the least-squares sum of squares,

$$Y = \sum_{i=1}^{N}[\theta_i - \hat{\theta}(P_i)]^2, \tag{3-4}$$

where θ_i is a measured saturation value and $\hat{\theta}$ is the corresponding predicted saturation value for measured pressure P_i. The prediction formula is

$$\hat{\theta} = \hat{\theta}(\alpha, n, \theta_{res}, P), \tag{3-5}$$

$$\alpha = C_0 + C_1\varepsilon, \tag{3-6}$$

$$n = C_2 + C_3\varepsilon, \tag{3-7}$$

$$\theta_{res} = C_4 + C_5\varepsilon. \tag{3-8}$$

The minimization takes place when the gradients of Y are zero, or

$$F = \frac{dY}{dC_j} = -2\sum_{i=1}^{N}[\theta_i - \hat{\theta}(P_i)]\frac{d\hat{\theta}_i}{dC_j} = 0. \tag{3-9}$$

Newton's method is convenient for this minimization, which simply states that for each iteration k,

$$J(\mathbf{x}_k)s_k = -F(\mathbf{x}_k), \tag{3-10}$$

$$\mathbf{x}_{k+1} = \mathbf{x}_k + s_k, \tag{3-11}$$

where $J(\mathbf{x}_k)$ is the Jacobian and $\mathbf{x}$ is the vector of unknowns C_j. It shouldn't be too difficult to check this out on the data presented by Flint et al. (1996).

9/24/96 First results from 1D PTn modelling.   SAS

After a good deal of putting together *Matlab* code and some *breath* debugging, the first set of PTn simulations were run using the base-case infiltration traces for 2-cm and 5-cm colluvium over a fracture continuum. The 2-cm case has weekly outputs of flux, while the 5-cm case has daily flux outputs; both cases have fluxes that are higher than almost any pixel value would show, so the simulations are probably more extreme than will be observed in future work.

All work is done in */home2/sierra/stothoff/Matlab/PTnCheck*. The input files for *breath* are created using **fix_FFRI_dat.m**, which in turn uses **extract_qw.m**, **pre_ydot_setup.m**, and **ydot_setup.m**. The built-in *Matlab* ODE solver ode23s is used to create initial conditions for the temporal average of the input flux, using **ydot_setup.m**. Output is examined using **show_stuff.m** and **new_show_seq('t', 'nf\1;col\co;plot\pl;nseq\1;last\10')**.

Several cases were tried, varying (i) the assumption for the continuum underlying the PTn layer and (ii) the input flux case. The 2-cm input-flux case was run using 2 m of fracture continuum, 2 m of TS58 material, and 20 m of TS58 material. The last material case was also run using the 5-cm input-flux case. All cases use 5-cm nodal spacing.

Several observations were made:

- The fracture continuum below the PTn causes time steps on the order of 3 seconds, while simulations using the matrix below complete in minutes of CPU time.

- The steady-state moisture profile is very different for fractures underlying the matrix and for tuff underlying; the fractures cause the PTn to be essentially saturated in locations, while the tuff allows much drier profiles *even with the same flux.*

- The flux distribution is very peaky. Over the period of a day, fluxes can jump by 4 orders of magnitude, then decay exponentially.

- The flux pulse propagates essentially instantaneously (less than a day) through the PTn layer, but the pulse magnitude decreases exponentially with depth.

- The moisture content responds by a few percent in the same timeframe.

- The gravity drainage condition 2 m below the bottom dampens the peakiness significantly relative to the 20-m depth.

- There are roughly 2 pulses a year, although the pulses are clumped. As the colluvium depth increases further, the number of pulses will decrease.

There are several implications to the work:

- Capturing flux pulses with moisture-content readings may be a hopeless endeavor.

- Steady-state assumptions may be appropriate for calculating moisture contents.

- Using the gravity-drainage assumption with moisture contents must be examined carefully, since structural features and heterogeneity can modify moisture contents without modifying fluxes.

- It may not be that bad to use the ECM assumptions below the PTn, as there is indeed strong damping in the input signal.

The current *breath* approach must be augmented to provide more realistic simulations. In particular, it is still not possible to check the ECM assumptions since there is no possibility for more than one continuum below the PTn. Also, the saturation profile in the PTn is strongly impacted by the lower-layer assumptions. An approach that may bear fruit is to allow several continua to dangle off the bottom of the PTn, each independent except that the same pressure exists in each one at the bottom of the PTn. One continuum might be the matrix, with the rest being fracture sets. Occasional lower cross-links between the fracture continua might okay.

The augmented approach would allow the investigation of which fracture set(s) kick in, if any. In addition, the saturation in each set may be able to be translated into an equivalent wetted length, which can than be used to intersect with the drifts.

It may be considerably more difficult to construct a steady-state solver for this case, since there are multiple threads of flux joining at a middle node. Shooting may be necessary.

3/23/97 Data from DOE. $\boxed{\mathcal{SAS}}$

A CD-ROM disk was received from L. Flint about two weeks ago that contains the entire set of matrix-property core-sample measurements from 31 boreholes, including 23 neutron-probe boreholes and 8 deeper boreholes. A total of nearly 5000 samples have properties reported. The CD-ROM disk is entitled "Matrix Properties" and is dated 3/2/97. The CD-ROM disk has one

file, entitled **database.wk4**, which is a file in Lotus 1-2-3 version 4.0 format. The CNWRA does not have software current enough to be capable of reading this format; however, the Net Force contractors to the CNWRA were able to convert the file to Lotus 1-2-3 version 3.0 format, which is capable of being read. E. Pearcy was able to pull this into Excel and output it in tab-delimited ASCII form. I stored both the Lotus 1-2-3 version 3.0 file, entitled **database.wk4**, and the tab-delimited ASCII form, entitled **usgs_borehole_db.asc**, in *$HOME2/AmbientKTI/3Ddata*. The original CD-ROM will be delivered to B. Mabrito and stored in the QA vault.

A second set of data was obtained from the NRC, which consists of a 8-mm tape that copies a CD-ROM with numerous ARC-VIEW coverages stored as 99 themes. The themes range from base-map information (e.g., Nellis Air Force Range boundaries, roads) through contour maps, borehole locations, ecological study plots, a digitized version of the Scott and Bonk stratigraphy, and various other information. The files take up roughly 31 Mb. The original CD-ROM resides at the NRC offices. The CD-ROM was accompanied by a user's guide dated May 1, 1996, with 18 pages plus 3 appendices. I am maintaining the tape in my office until the information can be transferred to disk in an accessible location.

8/31/97 Investigation of USGS UZ properties.

Files for the following investigations can be found in *$HOME2/AmbientKTI/3Ddata*.

On 8/28, Amit Armstrong requested that I provide estimates of the layer properties for the TPA sensitivity exercises. The idea is to use the microstratigraphy property information (including porosity, particle density, and K_{sat}) provided by Flint (1996), in conjunction with the layer microstratigraphy thicknesses extracted from the recently obtained DOE Earthvision model, to estimate the equivalent thicknesses of the TPA subareas. Amit provided layer thicknesses and a mapping of the sublayers into the TPA layers.

In Table 7 of the Flint (1996) report, K_{sat} for the individual sublayers is reported as a mean and a standard deviation. The K_{sat} mean statistics are reported for three cases: (i) geometric mean of raw K_{sat} values, (ii) power-law mean of raw K_{sat} values, and (iii) geometric mean of K_{sat} values derived from regression equations applied to all measured porosities. In each case, the standard deviation is reported on the raw values. The combination of log-10 mean and base-10 standard deviation renders these statistics unsuitable for coming up with a distribution.

This spring, Lorrie Flint sent me the database used in the Flint (1996) report. The database includes UZ core properties from 31 boreholes. I have not had a chance to examine the database in

detail, but this represents a good opportunity to digest it. I created two *Matlab* routines (extract_k.m and show_pdk.m) to extract information from the database and to show results. A total of 589 K_{sat} measurements were made, of which 188 were less than 5×10^{-12} m/s (0.16 mm/yr). At first blush, the raw K_{sat} statistics would be best to use for estimating layer properties; however, as the numerous low-K_{sat} measurements are not considered in the statistics for the raw values, second thought suggests that it may be appropriate to use the far more numerous porosity samples to estimate properties.

There have been a number of UZ formation classification schemes at YM. In Table 1 by Flint (1996), correspondences between the classification scheme of Buesch et al. (1996), Scott and Bonk (1984), and Montazer and Wilson (1984) are shown. For the most part, correspondences are clearly denoted, although based on comparing Figure 12 by Flint (1996) and a direct plot, it appears that there may be discrepancies in the assignment of units:

- Although apparently assigned to the TC hydrogeologic unit in Table 1, all of the Tptrn unit with porosity less than a cutoff value (perhaps 9 percent?) seemed to have been assigned to the TR hydrogeologic unit in Figure 12.

- There are two high-porosity, low-K_{sat} outliers not shown in Figure 12 (from the BT2 and BT4 units, respectively).

Flint (1996) provides regression relationships between porosity and the remaining hydraulic properties, as porosity is far easier to measure than most other properties. Three categories are identified: (i) microfractured, (ii) altered, and vitric/crystallized.

The microfractured category has samples from vitrophyres assigned to it (i.e., Tptrv1 and Tptrv3 from the Topopah Spring Tuff). The microfractured category reportedly includes the TC and PV3 hydrogeologic units. In addition, one sample each from the crystallized and welded Tptrn, Tptpul, and Tptpln units is assigned to the microfractured category due to visible microfractures.

The altered category includes all lithostratigraphic units below the vitric/zeolitic boundary (BT1, CHZ, BT, PP4, PP3, PP2, PP1, BF3, and BF2) plus the CMW (an altered portion at the base of the Tiva Canyon formation). As Flint (1996) notes, there are crystallized and vitric units within the "altered" category, but the assignment was done for simplicity in developing predictive equations.

The vitric/crystallized category includes everything left over after the other categories are considered.

Although one can wish that the hydrogeologic layers would be relatively homogeneous within each layer, unfortunately the properties are not necessarily homogeneous. As can be seen in the section of borehole SD7 displayed in Figure 10 by Flint (1996), zeolites occur in samples from the CHV, CHZ, BT, PP4, PP2, and PP1 hydrogeologic layers, while zeolites are missing from samples in the BT1, CHV, PP3, PP2, and BF3 hydrogeologic layers. Flint (1996) suggest that the presence of alteration can be estimated by a significant change in porosity after drying at elevated temperatures. Two porosity measurements were obtained for each sample: (i) dried at a temperature of 60 °C and a relative humidity of 65 percent, and (ii) dried at 105 °C and an ambient relative humidity ($<$ 20 percent). Flint (1996) suggests that if the two porosity measurements differ by 0.05, the sample is altered. Areas in SD7 with the 5-percent differential porosity but not having zeolites (in the form of clinoptilolite) are reported to have vapor-phase minerals tridymite and cristobalite, although elevated cristobalite without tridymite does not exhibit the differential porosity.

Other areas with the 5-percent differential are pointed out as occurring at the base of the Tiva Canyon Tuff, and are attributed to alteration to clay (such as smectite). It is pointed out that the extent of alteration appears to be related to the topographic location of the borehole. Boreholes in narrow upwash channels may receive more frequent runoff, hence infiltration maintains higher water contents. Flint (1996) implies that alteration to clay is due to wet conditions. Despite the presence of the differential, these altered high-porosity samples tend to also have high K_{sat}.

A method for discriminating between alteration to zeolites and alteration to clays is offered by Flint (1996) using measurements of particle density obtained in two ways: (i) calculated from bulk density and porosity, and (ii) directly measuring the volume of the solid particles using helium pycnometry. Approximately 180 samples from UZ16 (judging from Figure 11 by Flint (1996)) were analyzed using the two techniques. For zeolitic samples, the calculated particle density almost invariably was greater than the measured density, by an average of about 0.07 g/cm^3 (my estimate), and the measured particle density was always less than 2.5 g/cm^3. For nonwelded vitric samples, the calculated particle density was less than the measured density when the calculated density was less than 2.35 g/cm^3 and gradually switches above that value; however, the zeolitic samples tend to have a larger differential. The nonwelded vitric samples tend to have somewhat larger particle densities than the zeolitic.

The welded crystallized samples had calculated particle densities uniformly greater than 2.45 g/cm^3, while the densely welded vitric samples had calculated particle densities uniformly less than 2.45 g/cm^3. Three classes could be distinguished from these samples: (i) welded/crystallized, (ii) nonwelded vitric, and (iii) nonwelded zeolitic or densely welded vitric. Despite the usefulness of the technique, helium-pycnometric measurements did not appear to be made on the majority of
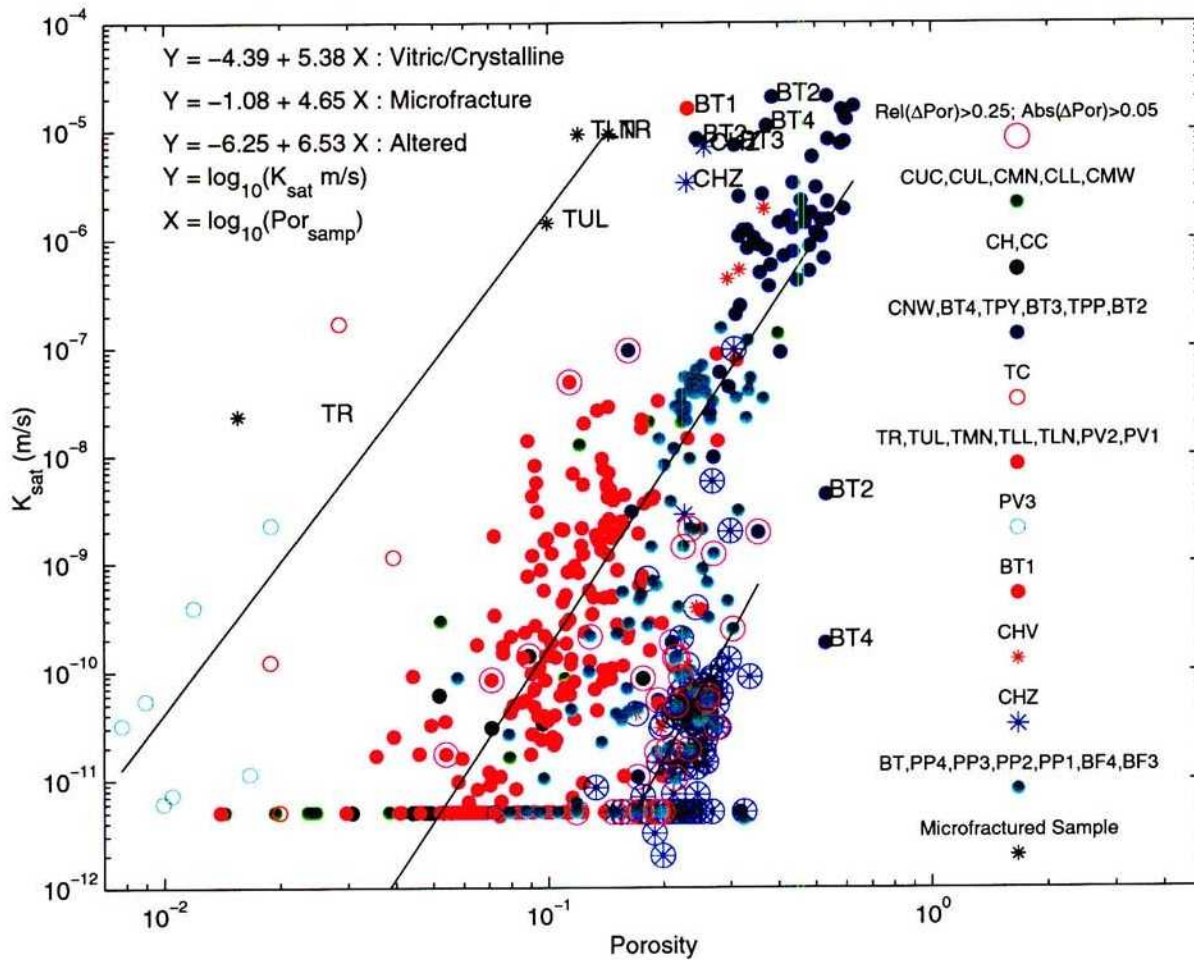
Figure 3-1: 8/31/97. The complete set of measured K_{sat} values in the USGS database.

YM samples.

The complete set of measured K_{sat} values in the database reported on by Flint (1996) are shown in Figure 3-1. The database reports three microstratigraphic classifications for each sample, corresponding to the Buesch et al. (1996) nomenclature: (i) formation (e.g., Tpc, Tpt); (ii) zone, where applicable (e.g., pul, rn); and (ii) subzone, where applicable (e.g., pv2, rv2). Where the formation has no subzones, the database repeats the zone identification for the subzone. The generating routine is *Matlab* show_pdk.m.arch091097.

In Figure 3-1, the microstratigraphic zones are grouped into the nomenclature of Montazer

and Wilson (1984) according to Table 1 of Flint (1996).

The samples considered microfractured are the TC and PV3 units (denoted with small circles), and obviously microfractured samples (denoted with black asterisks). For consistency with Figure 12 of Flint (1996), the TC unit consists of only the Tptrvl subzone in Figure 3-1, even though the Tptrn subzone appears to be classified as TC in Table 1 of Flint (1996).

The remaining samples are color-coded, broadly by formation. Outlying samples are labeled according to unit. Classification into the BT1a and BT1 hydrogeologic units is not clear from Table 1 by Flint (1996); the one Tpbt1 sample was placed into the BT1 hydrogeologic unit. As alteration is a key component of the property-classification scheme proposed by Flint (1996), any sample meeting the 5-percent porosity-change criterion is circled.

Based on Figure 3-1, it can be argued that five general categories exist for the samples:

- Microfractured, low (< 0.05) porosity

- Microfractured, high (> 0.05) porosity

- Zeolitic

- Vitric/crystallized

- Inexplicably high (> 0.5) porosity, low-permeability

Flint (1996) lumps the first two categories, and never presents data in the last category. It is not clear where the high-porosity microfractured category turns into the vitric/crystallized category; some of the high-permeability bedded-tuff samples may fall into the microfractured category due to handling difficulties. It is also not clear where the zeolitic and the vitric/crystallized categories turn into each other; many of the "altered" samples in Figure 12 by Flint (1996) appear to fall squarely into the vitric/crystallized category.

9/9/97 Further investigation of USGS UZ properties.

It is my feeling that a successful use of matrix properties to predict matrix K_{sat} should have one formula for all cases (except, perhaps, for the microfractured cases). Accordingly, I played with various forms of a predictive relationship and have come up with a set of formulae that better match the non-microfractured data than the estimates in the database provided by L. Flint. I

used a least-squares measure to make quantitative evaluations of the fit of the prediction to the measured data:

$$\log_{10}(M) = \left[\sum_{i=1}^{N} (Y_i - Y_{mi})^2 \right]^{1/2}, \tag{3-12}$$

where M is the performance measure, Y_i is the ith predicted value of $\log_{10}(K_{sat})$, and Y_{mi} is the ith measured value of $\log_{10}(K_{sat})$.

There are a number of properties measured for each core sample, including:

- Bulk density (at 65 and 105 °C)

- Porosity (at 65 and 105 °C)

- Particle density (at 65 and 105 °C)

- Volumetric water content (at 65 and 105 °C)

- Saturation (at 65 and 105 °C)

- Tuff unit, zone, and subzone

In addition, some of the core samples have subsamples for which porosity and K_{sat} are measured.

I systematically tested all sets of 1-, 2-, 3-, and 4-parameter regression equations. The linear and loglinear predictions for each of the parameters were tested, as well as calculated absolute and relative change in particle density, bulk density, and porosity. In order to systematically test regression equations, I created a *Matlab* routine (test_usgs_regr.m) that ran through all possible combinations using all vitric/crystalline and altered samples with measured K_{sat} above the measurement limit (5×10^{-12} m/s) and porosity greater than 0.05. The samples denoted microfractured were not used, although I think that some of the samples retained could be classified microfractured.

For reference, performance measure M is 15.7 when using the estimated K_{sat} values in the database and is 19.1 when using a linear regression on subsample porosity (23.9 for $\log_{10}$ regression). The estimated K_{sat} values are thus off by a mean value of more than an order of magnitude (i.e., a factor of 16 for the USGS regression). The USGS regression also has 6 coefficients: two for the altered, three for the unaltered, and an exponent in the unaltered equation.

The best single regression fit (13.1) occurs, rather surprisingly, for $\log_{10}$ saturation at 65 °C. Saturation provides the single best predictor; all 4 values of M, for the 65 and 105 °C pairs (i.e.,

---

linear and $\log_{10}$), are better than the USGS estimate, which is based on classifying samples into bins and using two regression equations). Even better, only 2 coefficients are used.

A significant improvement occurs with one more variable, porosity. In this case, the best match occurs with saturation at 65 °C and the subsample porosity, with M dropping to 8.22. Considering three variables, the best match occurs with $\log_{10}$ of the subsample porosity, porosity at 65 °C, and volumetric water content at 105 °C, yielding an M value of 7.62. The case with four variables yields the same set as the 3-variable case, with the saturation at 65 °C added, and M drops to 7.46. Clearly the parsimonious selection would use two variables, a saturation and a porosity, with a total of 3 coefficients. Note that there is not a tremendous difference between predictions using different types of porosity measurement or water content measurement. Also note that the difference between the USGS estimate and the 2-parameter estimate in log space is $1.196 - 0.914 = 0.28$, which is a significant but not outstanding improvement.

The estimated K_{sat} using the best-fit 1-, 2-, and 3-parameter equations, as well as the USGS-estimated K_{sat}, are plotted as a function of the measured K_{sat} in Figure 3-2. The closer a point lies to the diagonal line, the better the fit. The *Matlab* routine generating the plots is archived as test_usgs_regr.m.arch091097 in *$HOME2/AmbientKTI/3Ddata*.
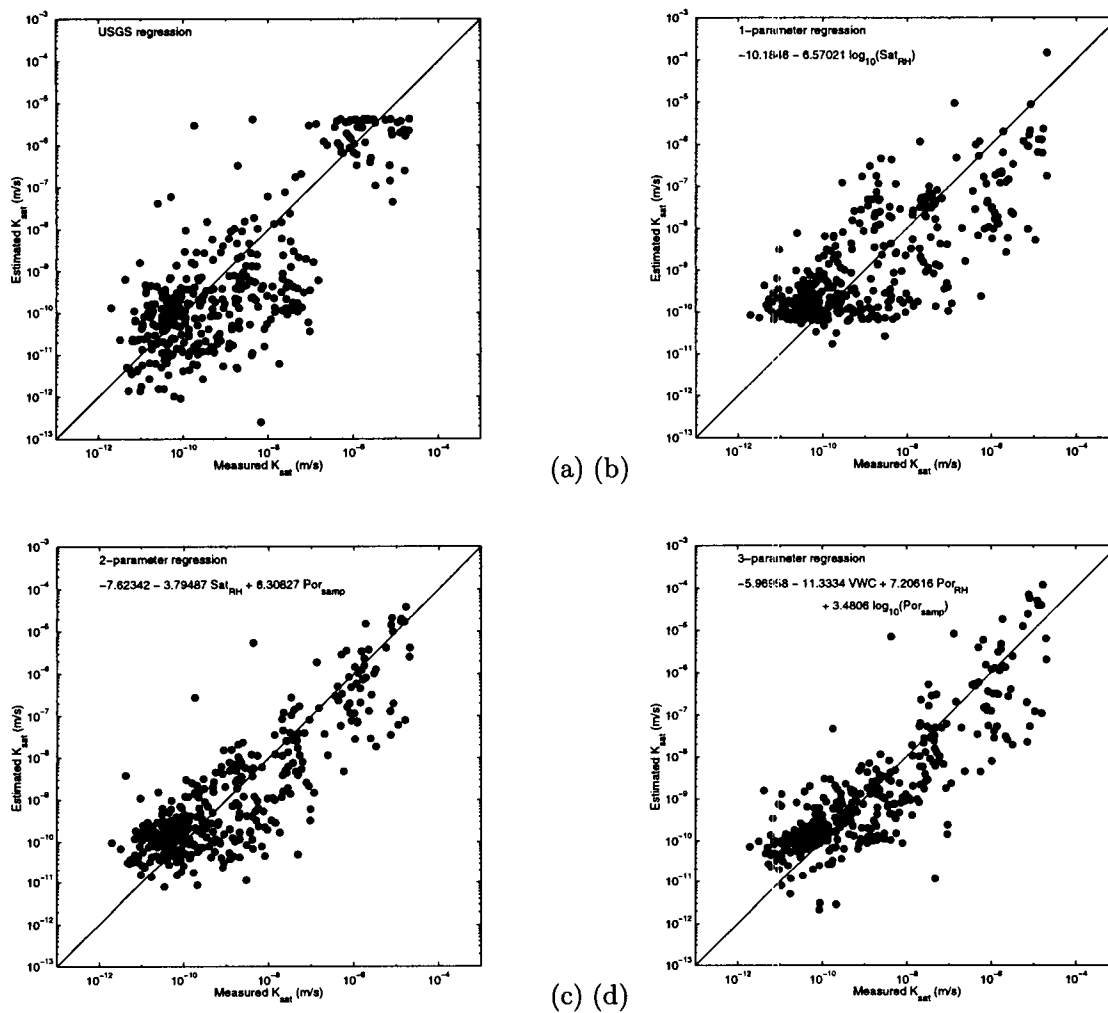
Figure 3-2: 9/9/97. Comparison of best-estimate K_{sat} and measured K_{sat} using (a) the USGS database, (b) the best 1-parameter regression, (c) the best 2-parameter regression, and (d) the best 3-parameter regression.

The best-fit regression equations are:

$$\log_{10}(K) = -10.1846 - 6.57021 \log 10(\theta_{65}), \tag{3-13}$$

$$= -7.62342 - 3.79487\theta_{65} + 6.30827\varepsilon_{sample}, \tag{3-14}$$

$$= -5.96958 - 11.3334 VWC_{105} + 7.20616\varepsilon_{65} + 3.4806 \log_{10}(\varepsilon_{sample}), \tag{3-15}$$

where a subscript of 65 denotes the measurement at 65 °C, a subscript of 105 denotes the measurement at 105 °C, a subscript of *sample* denotes the subsample measurement, θ is saturation, ε is porosity, and VWC is volumetric water content.

In the following plots, important components of the regression equations are shown graphically for each borehole. Components include: (i) porosity at 65 °C (shown both as a bar height and a color); (ii) saturation at 65 °C; (iii) particle-density difference (absolute density by bar height, relative density by color); (iv) measured K_{sat} where available (blue dots); (v) estimated K_{sat} (USGS are green dots, best 2-parameter regression are red dots); (vi) formation identification. The *Matlab* routine generating the plots is archived as show_usgs_db.m.arch091797 in *$HOME2/-AmbientKTI/3Ddata*. The *Matlab* routine converting the ASCII database into a *Matlab* binary (".mat") file is archived as make_flint_db_to_mat.m.arch091797, and the resulting file is archived as usgs_bhdb.mat.arch091797.
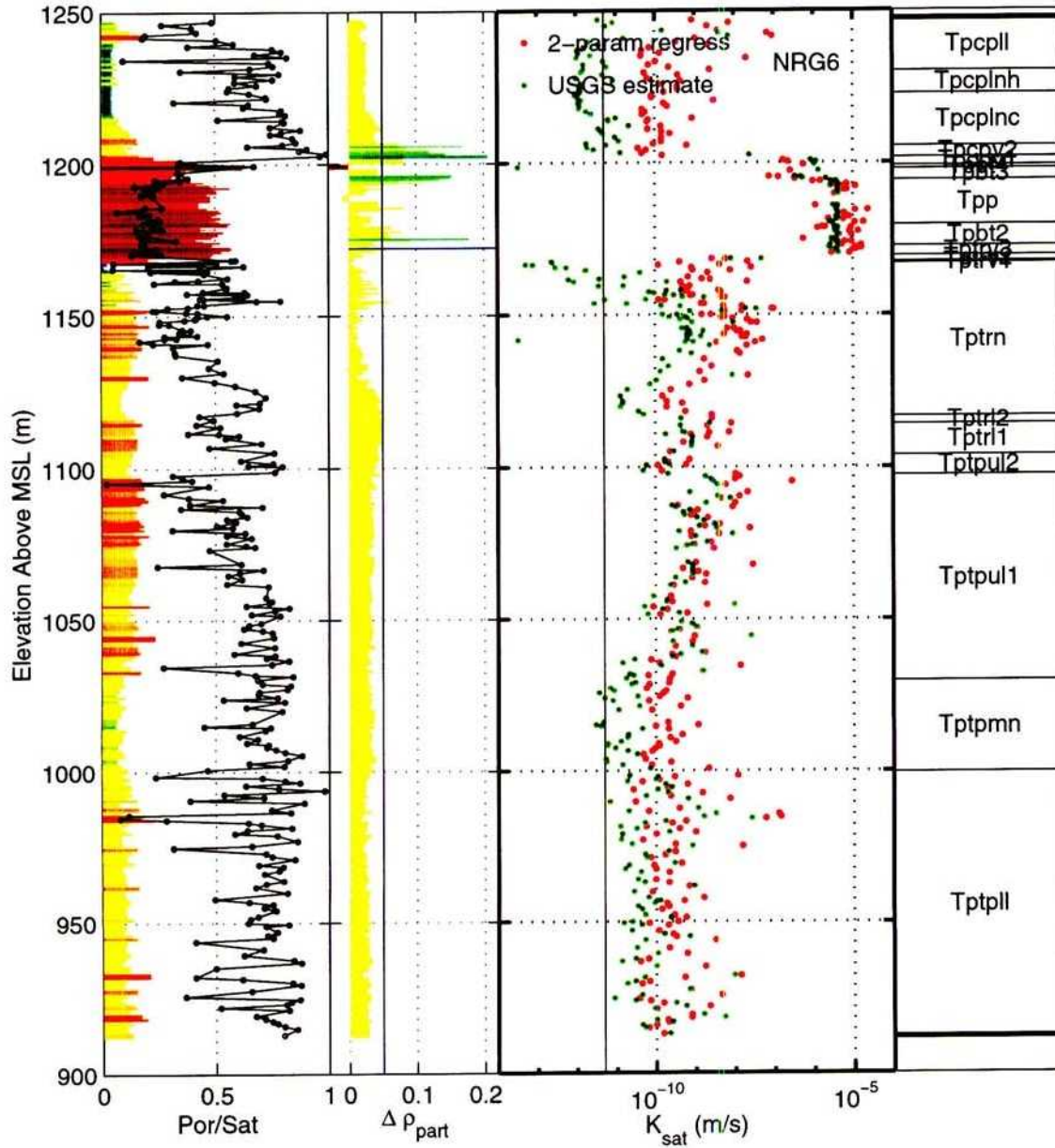
Figure 3-3: 9/9/97. **BHprofile_NRG6_c.eps**. Porosity, saturation, change in particle density, and measured and estimated values for K_{sat} in borehole NRG6.
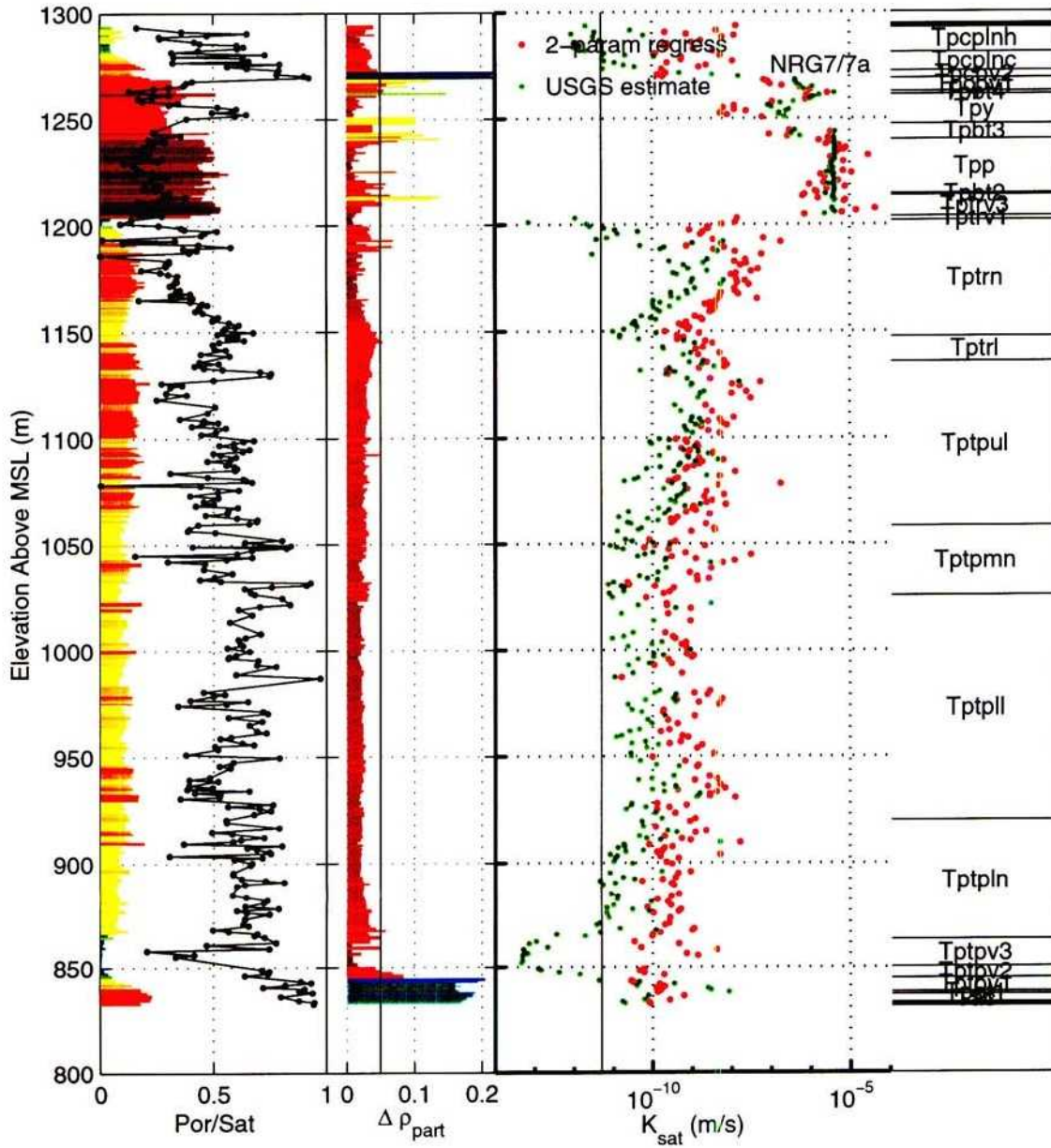
Figure 3-4: 9/9/97. **BHprofile_NRG77a_c.eps**. Porosity, saturation, change in particle density, and measured and estimated values for K_{sat} in borehole NRG7/7a.
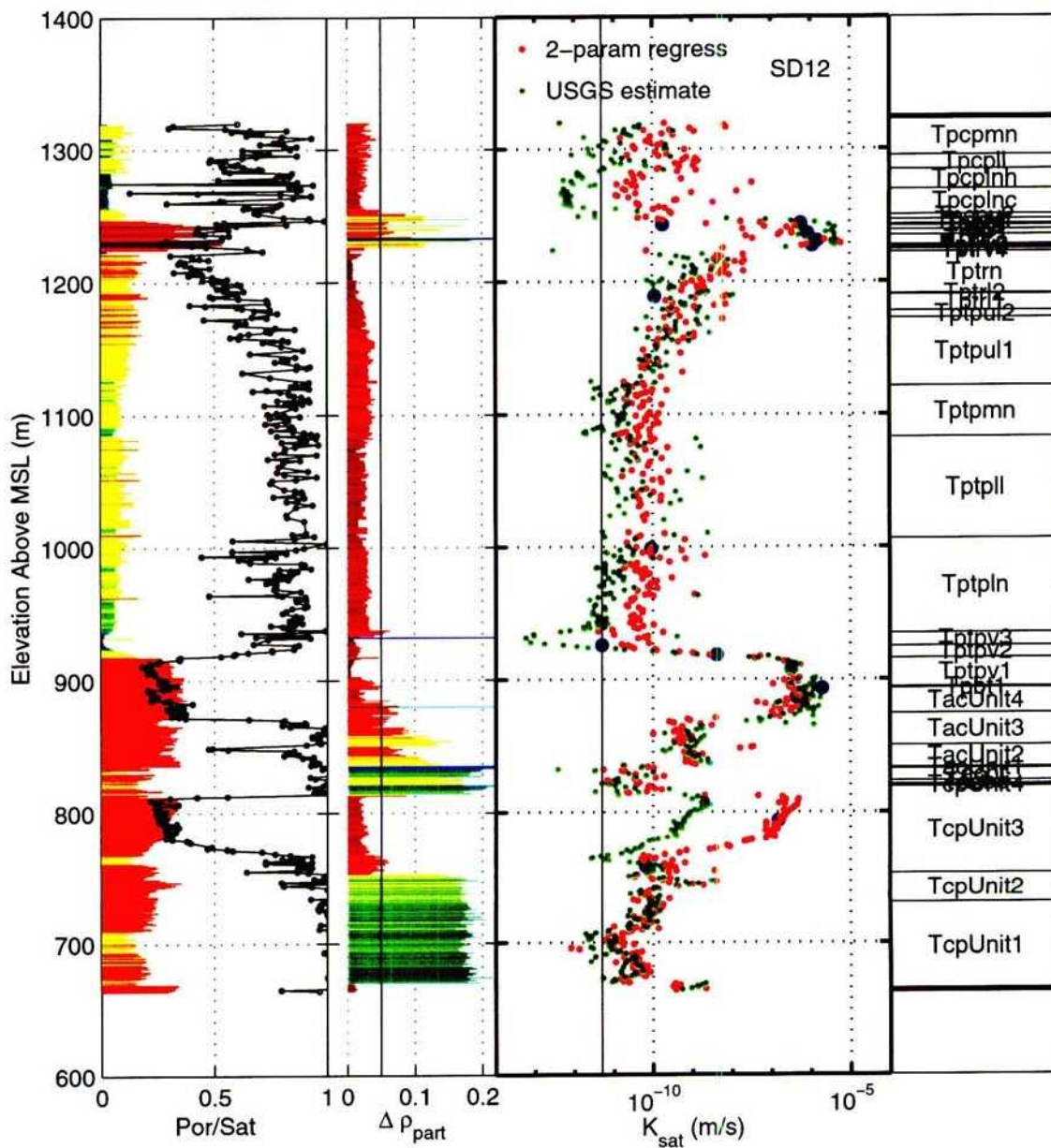
Figure 3-5: 9/9/97. **BHprofile_SD12_c.eps**. Porosity, saturation, change in particle density, and measured and estimated values for K_{sat} in borehole SD-12.
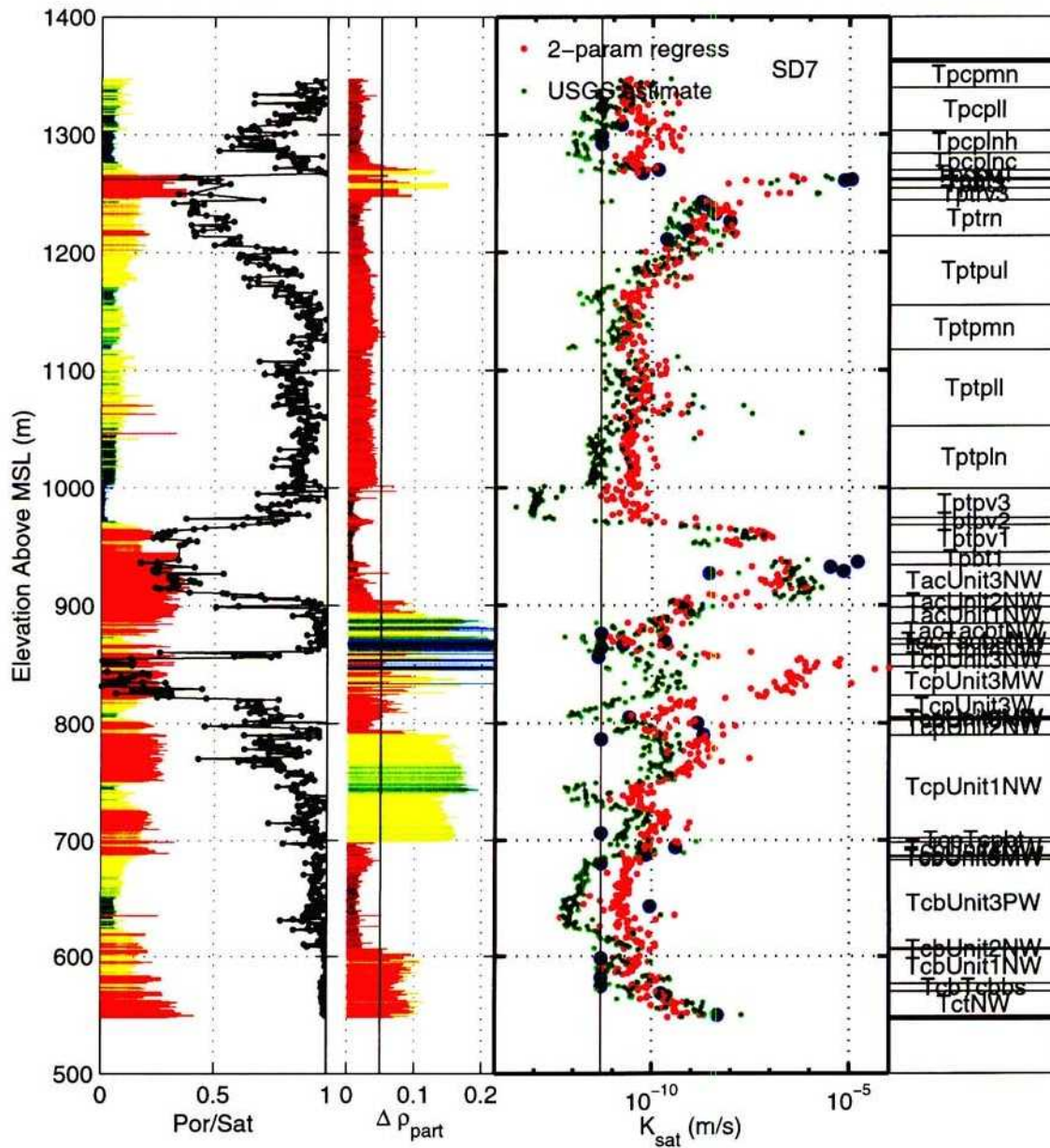
Figure 3-6: 9/9/97. **BHprofile_SD7_c.eps**. Porosity, saturation, change in particle density, and measured and estimated values for K_{sat} in borehole SD-7.

Figure 3-7: 9/9/97. **BHprofile_SD9_c.eps**. Porosity, saturation, change in particle density, and measured and estimated values for K_{sat} in borehole SD-9.
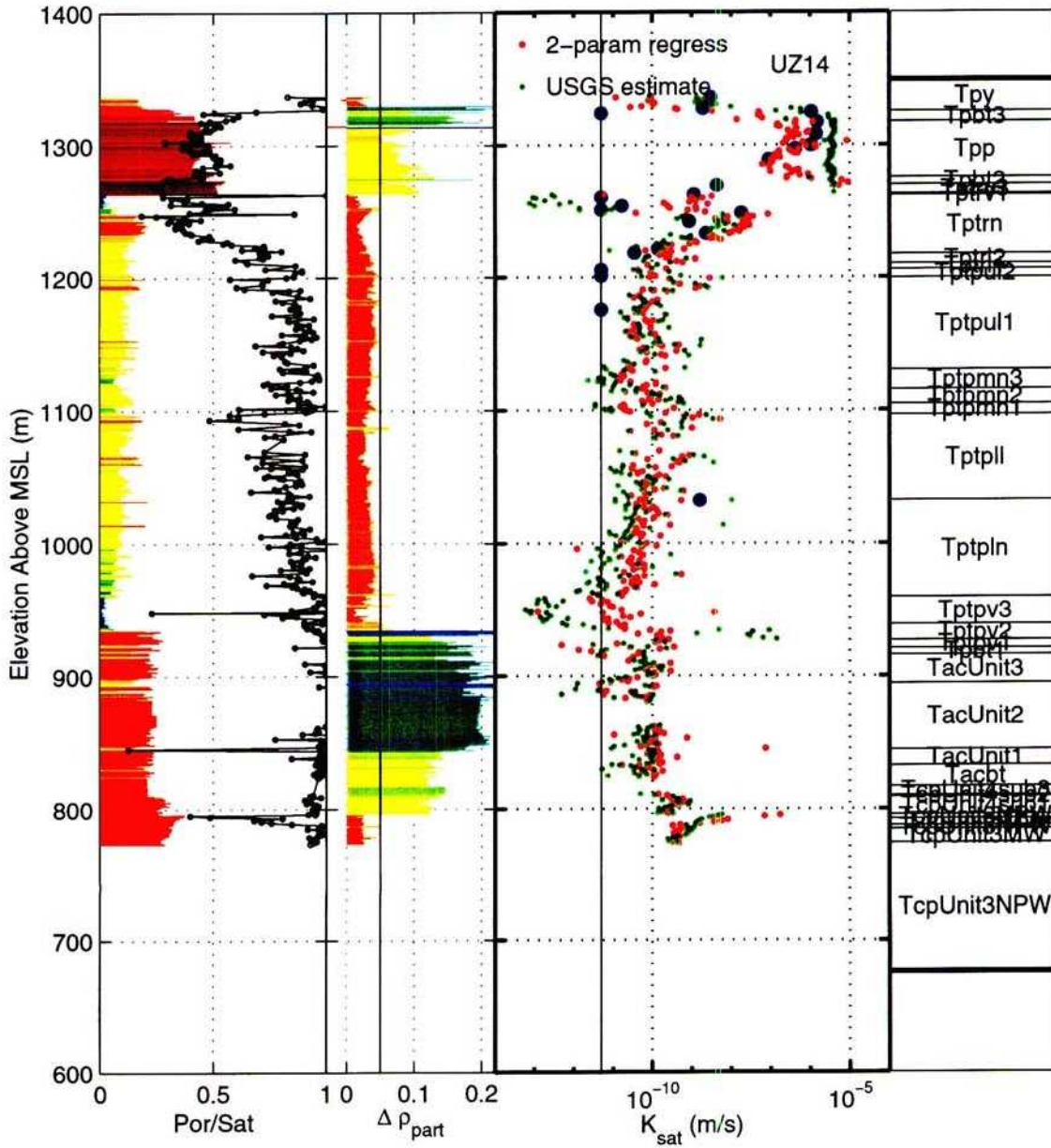
Figure 3-8: 9/9/97. **BHprofile_UZ14_c.eps**. Porosity, saturation, change in particle density, and measured and estimated values for K_{sat} in borehole UZ-14.

Figure 3-9: 9/9/97. **BHprofile_UZ16_c.eps**. Porosity, saturation, change in particle density, and measured and estimated values for K_{sat} in borehole UZ-16.

Figure 3-10: 9/9/97. **BHprofile_UZ7a_c.eps**. Porosity, saturation, change in particle density, and measured and estimated values for K_{sat} in borehole UZ-7a.

Figure 3-11: 9/9/97. **BHprofile_UZN11_c.eps**. Porosity, saturation, change in particle density, and measured and estimated values for K_{sat} in borehole N11.
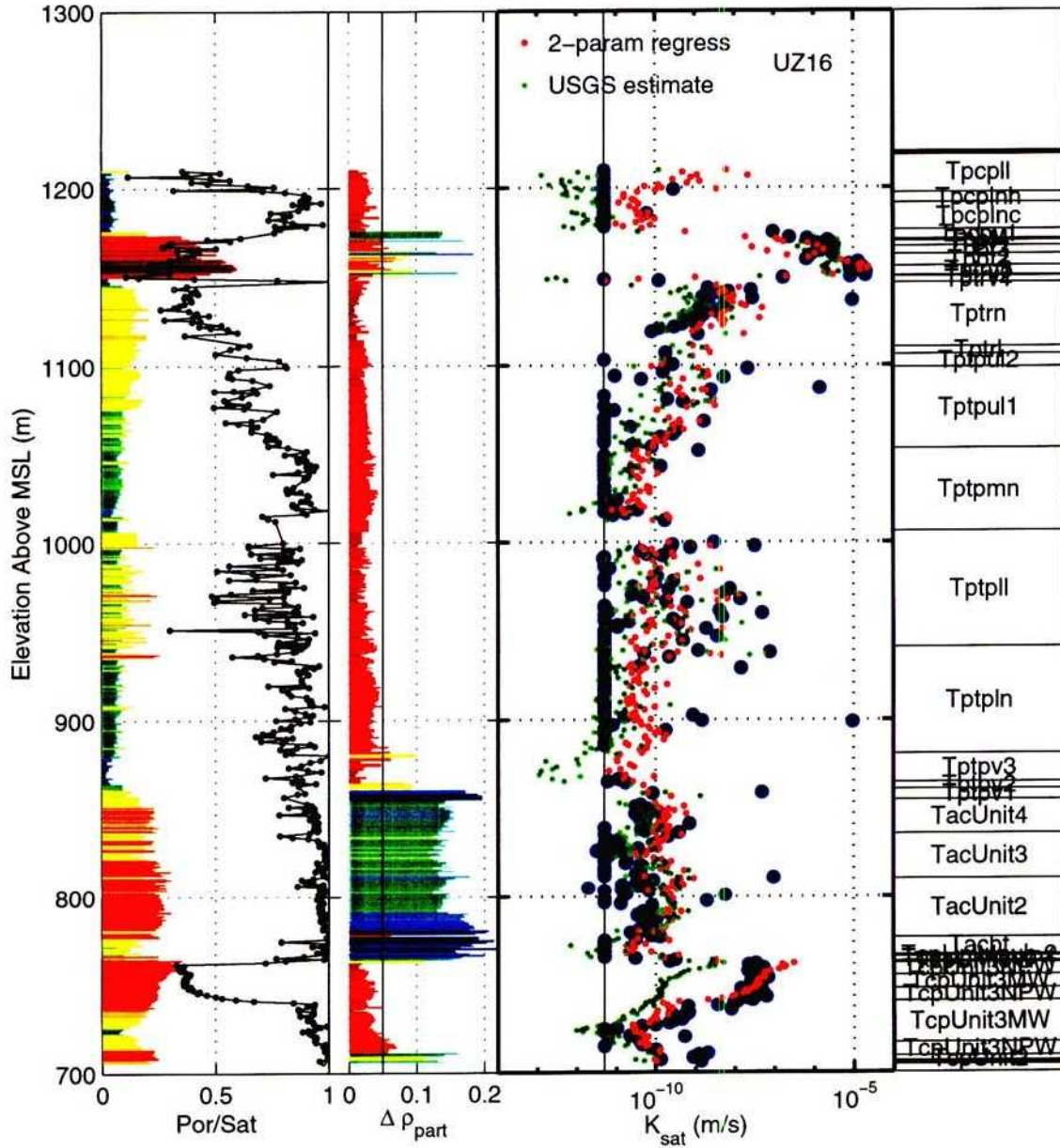
Figure 3-12: 9/9/97. **BHprofile_UZN15_c.eps**. Porosity, saturation, change in particle density, and measured and estimated values for K_{sat} in borehole N15.

Figure 3-13: 9/9/97. **BHprofile_UZN16_c.eps**. Porosity, saturation, change in particle density, and measured and estimated values for K_{sat} in borehole N16.
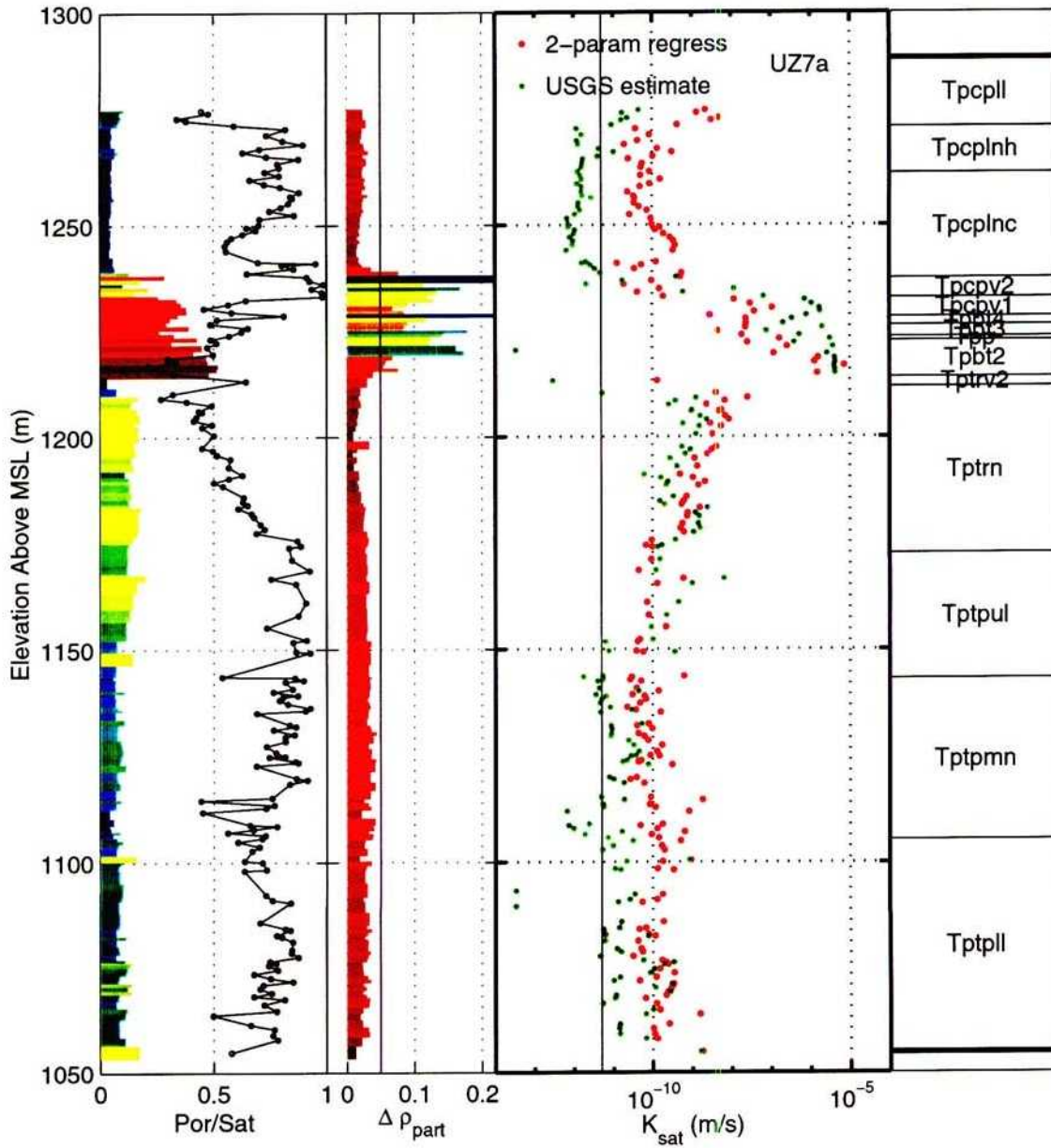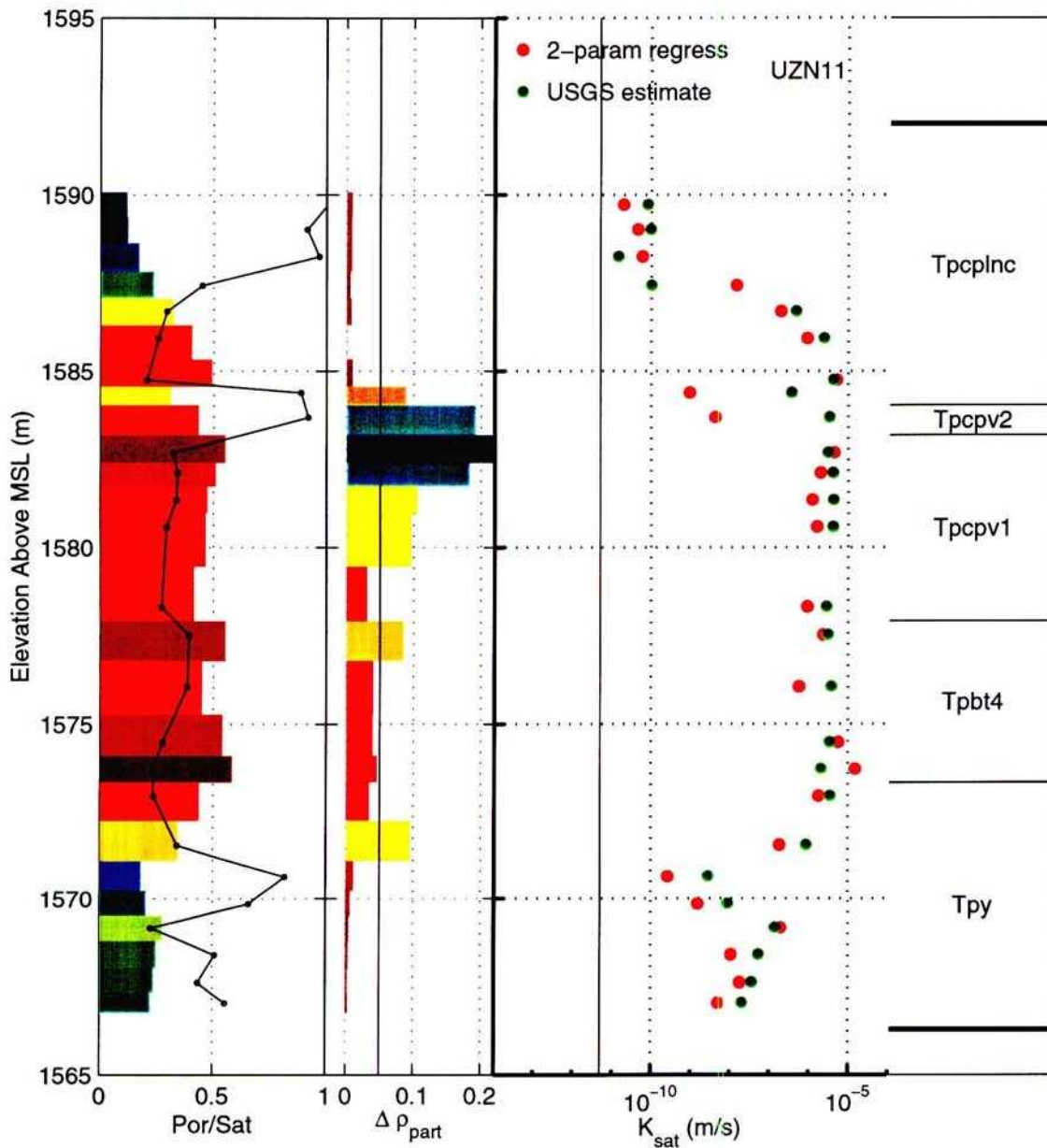
Figure 3-14: 9/9/97. **BHprofile_UZN17_c.eps**. Porosity, saturation, change in particle density, and measured and estimated values for K_{sat} in borehole N17.

Figure 3-15: 9/9/97. **BHprofile_UZN27_c.eps**. Porosity, saturation, change in particle density, and measured and estimated values for K_{sat} in borehole N27.
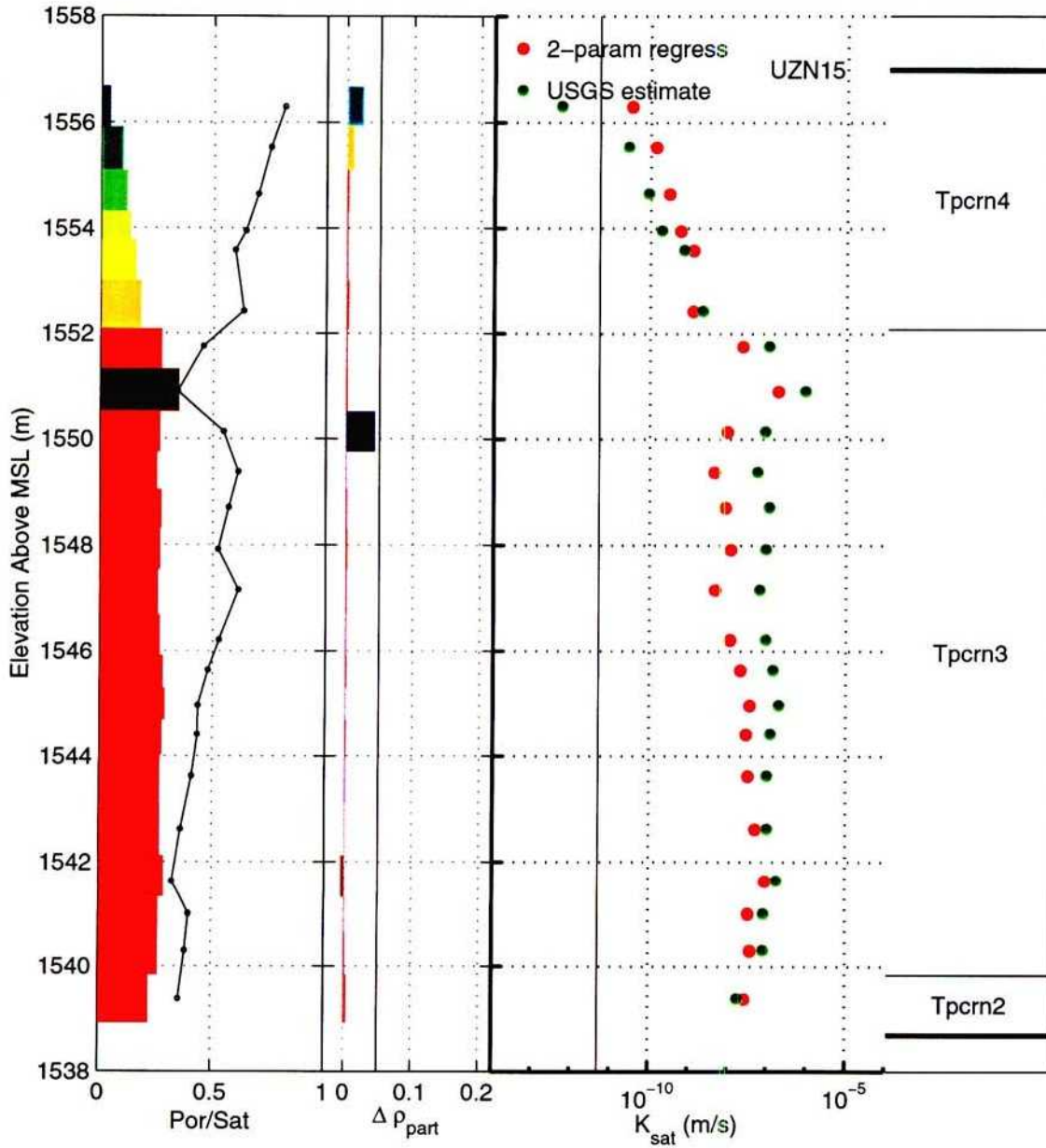
Figure 3-16: 9/9/97. **BHprofile_UZN31_c.eps**. Porosity, saturation, change in particle density, and measured and estimated values for K_{sat} in borehole N31.

Figure 3-17: 9/9/97. **BHprofile_UZN32_c.eps**. Porosity, saturation, change in particle density, and measured and estimated values for K_{sat} in borehole N32.
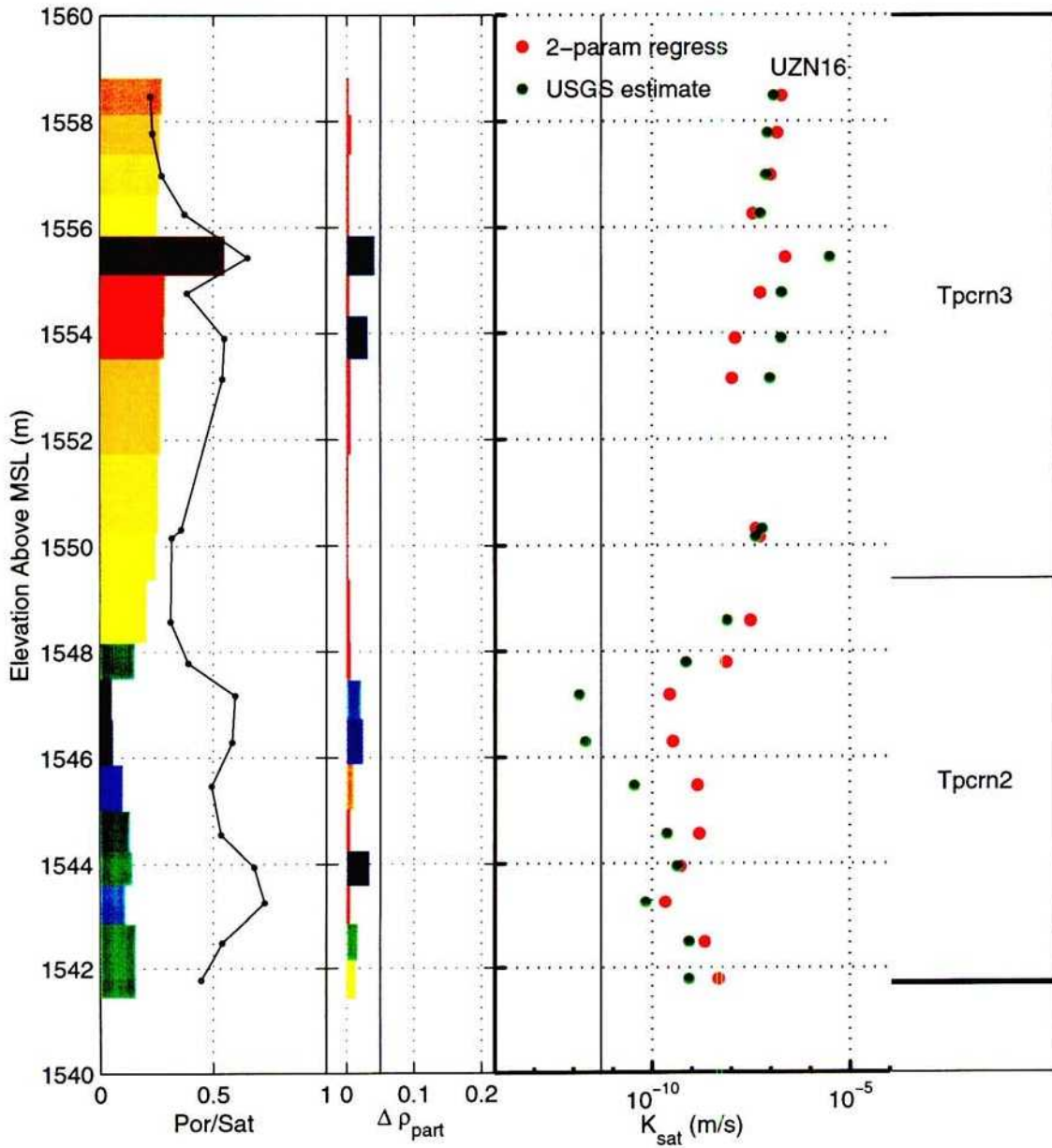
Figure 3-18: 9/9/97. **BHprofile_UZN33_c.eps**. Porosity, saturation, change in particle density, and measured and estimated values for K_{sat} in borehole N33.

Figure 3-19: 9/9/97. **BHprofile_UZN34_c.eps**. Porosity, saturation, change in particle density, and measured and estimated values for K_{sat} in borehole N34.

Figure 3-20: 9/9/97. **BHprofile_UZN35_c.eps**. Porosity, saturation, change in particle density, and measured and estimated values for K_{sat} in borehole N35.

Figure 3-21: 9/9/97. **BHprofile_UZN36_c.eps**. Porosity, saturation, change in particle density, and measured and estimated values for K_{sat} in borehole N36.
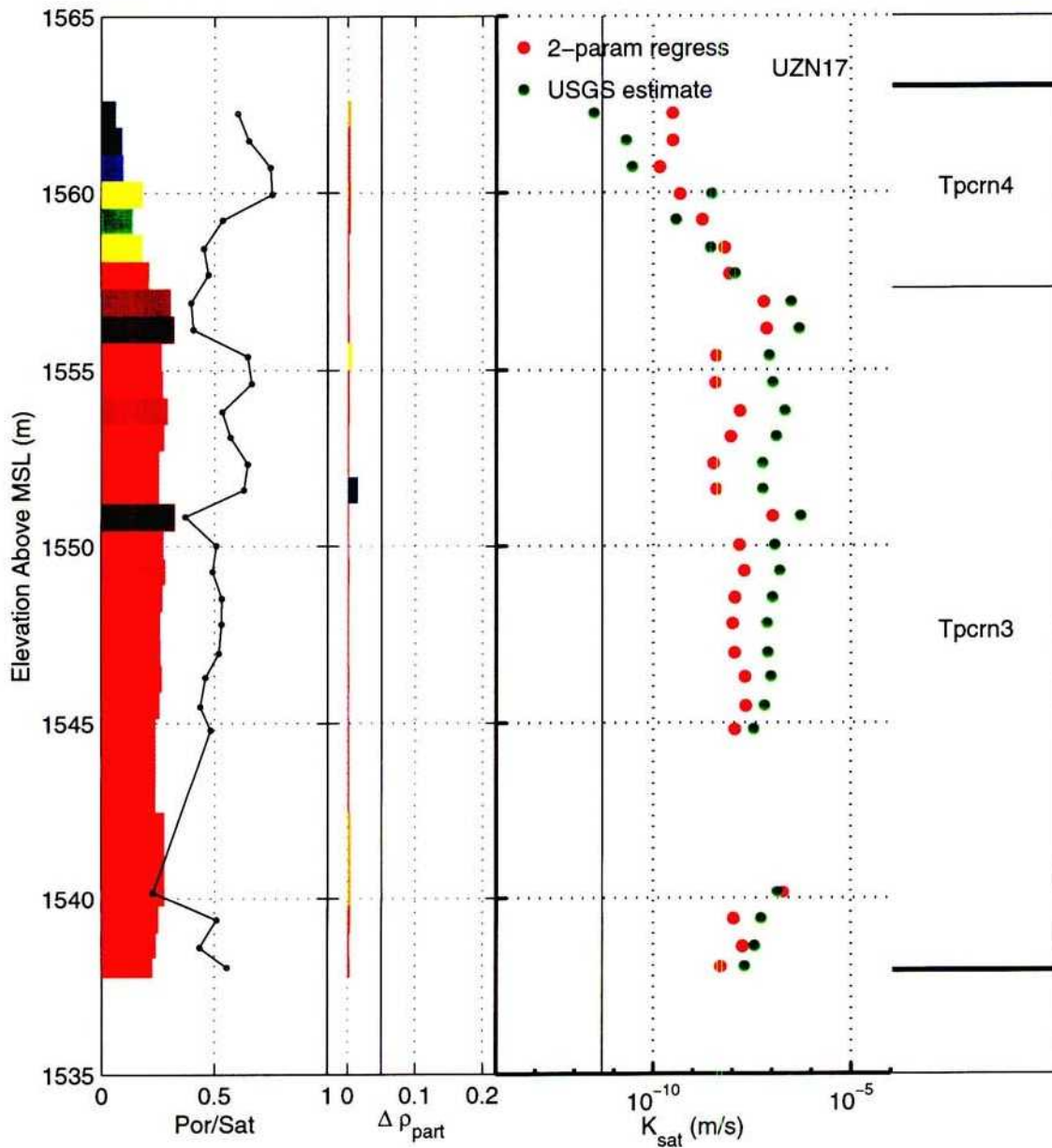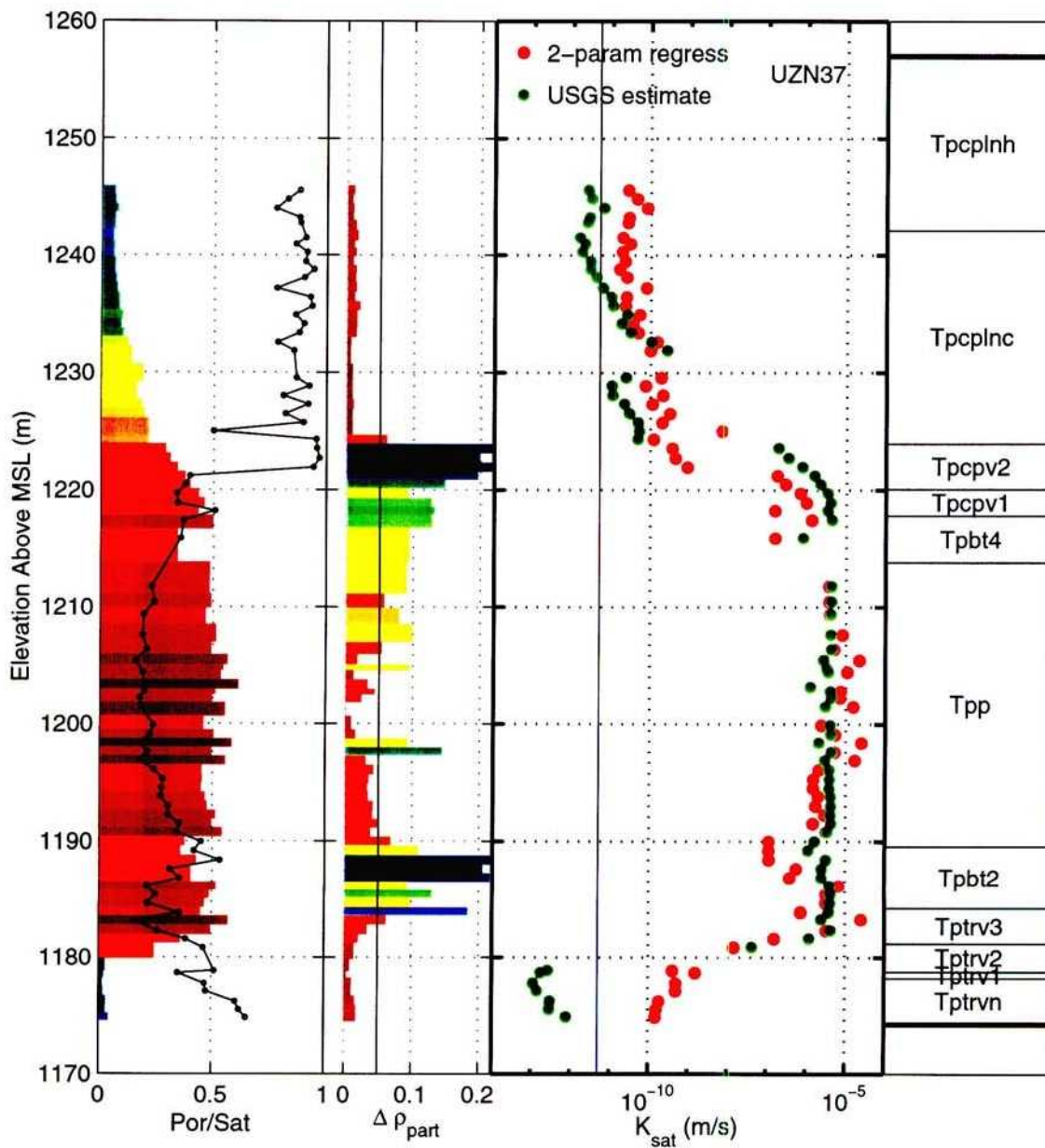
Figure 3-22: 9/9/97. **BHprofile_UZN37_c.eps**. Porosity, saturation, change in particle density, and measured and estimated values for K_{sat} in borehole N37.
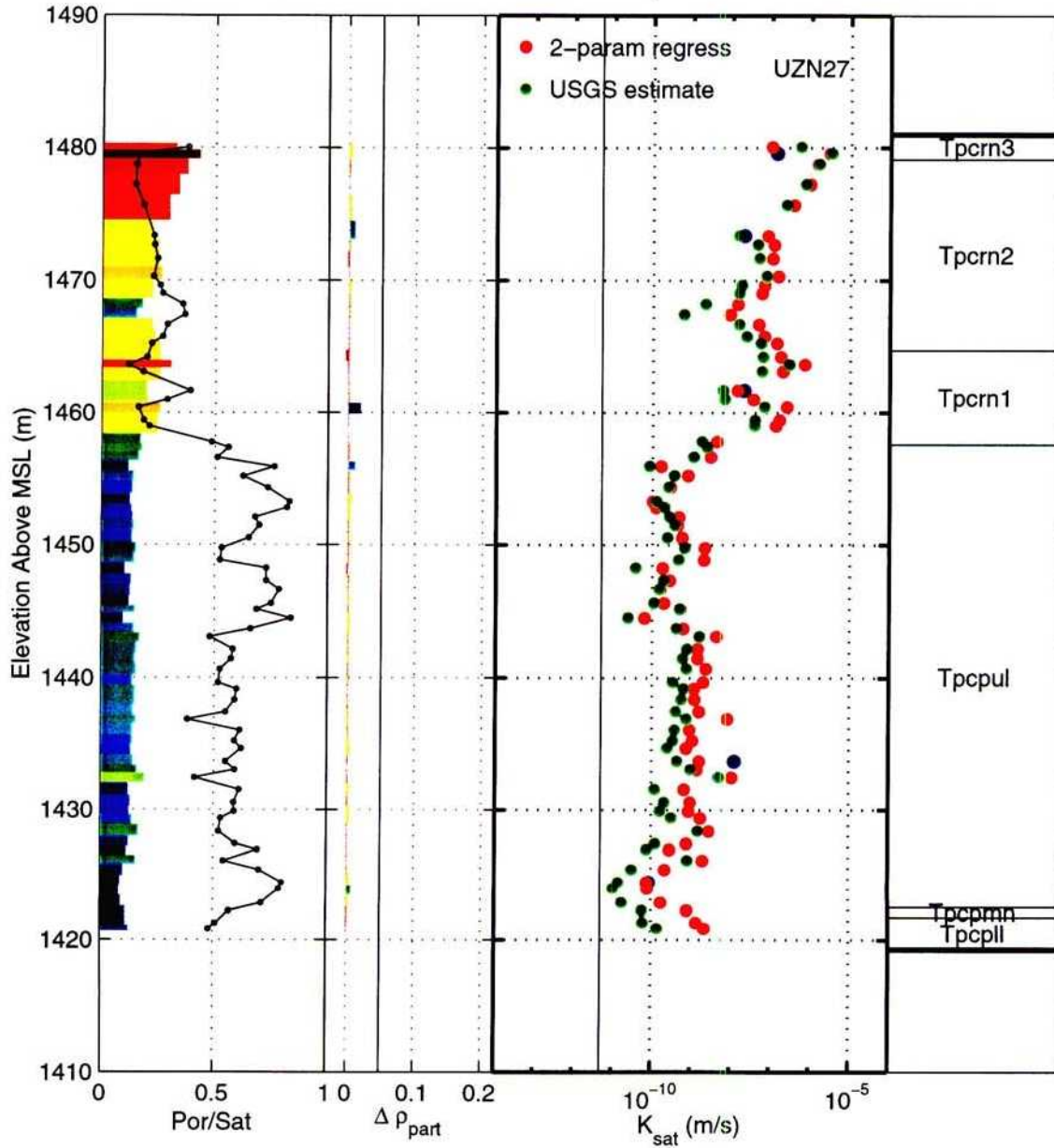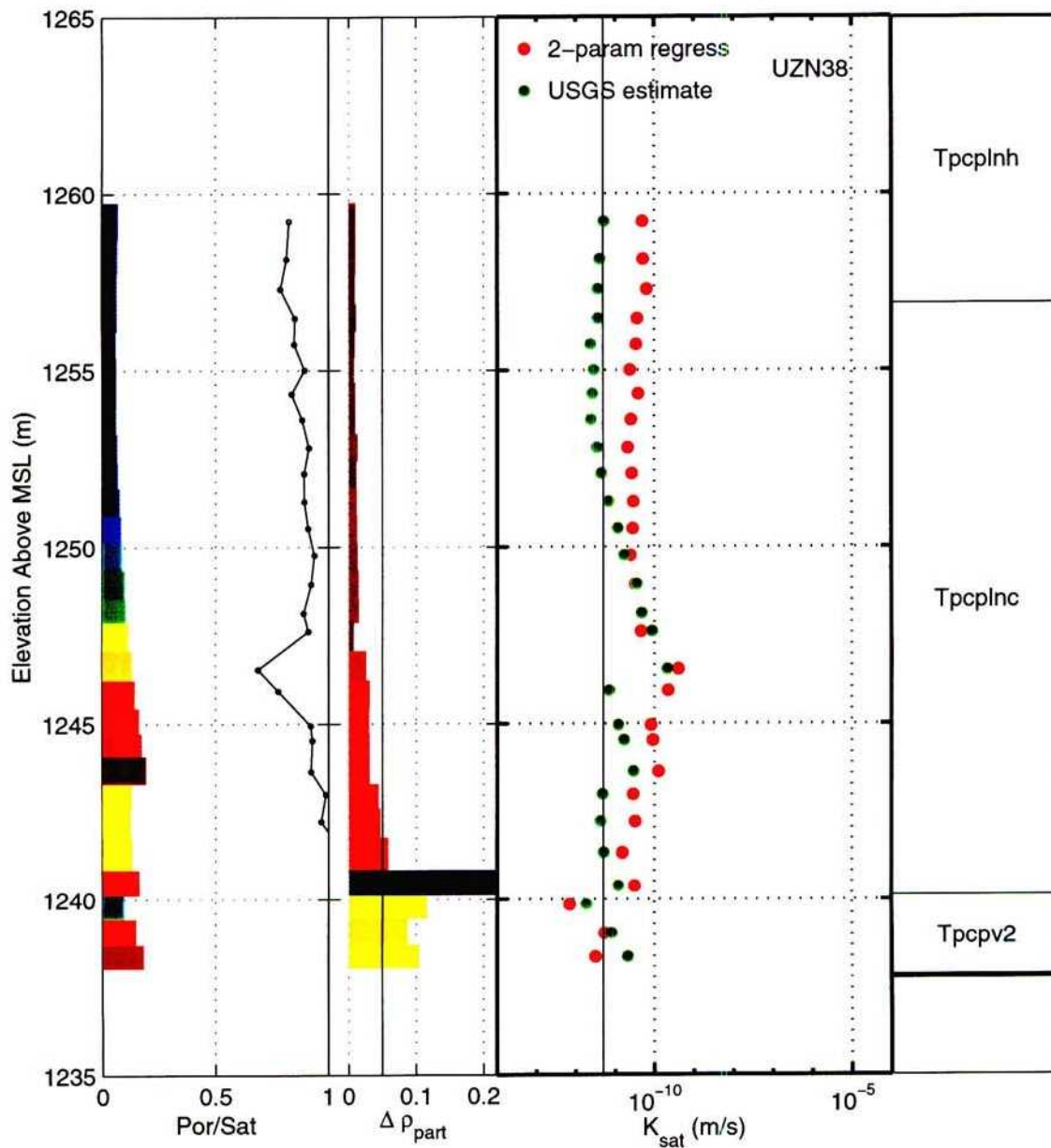
Figure 3-23: 9/9/97. **BHprofile_UZN38_c.eps.** Porosity, saturation, change in particle density, and measured and estimated values for K_{sat} in borehole N38.
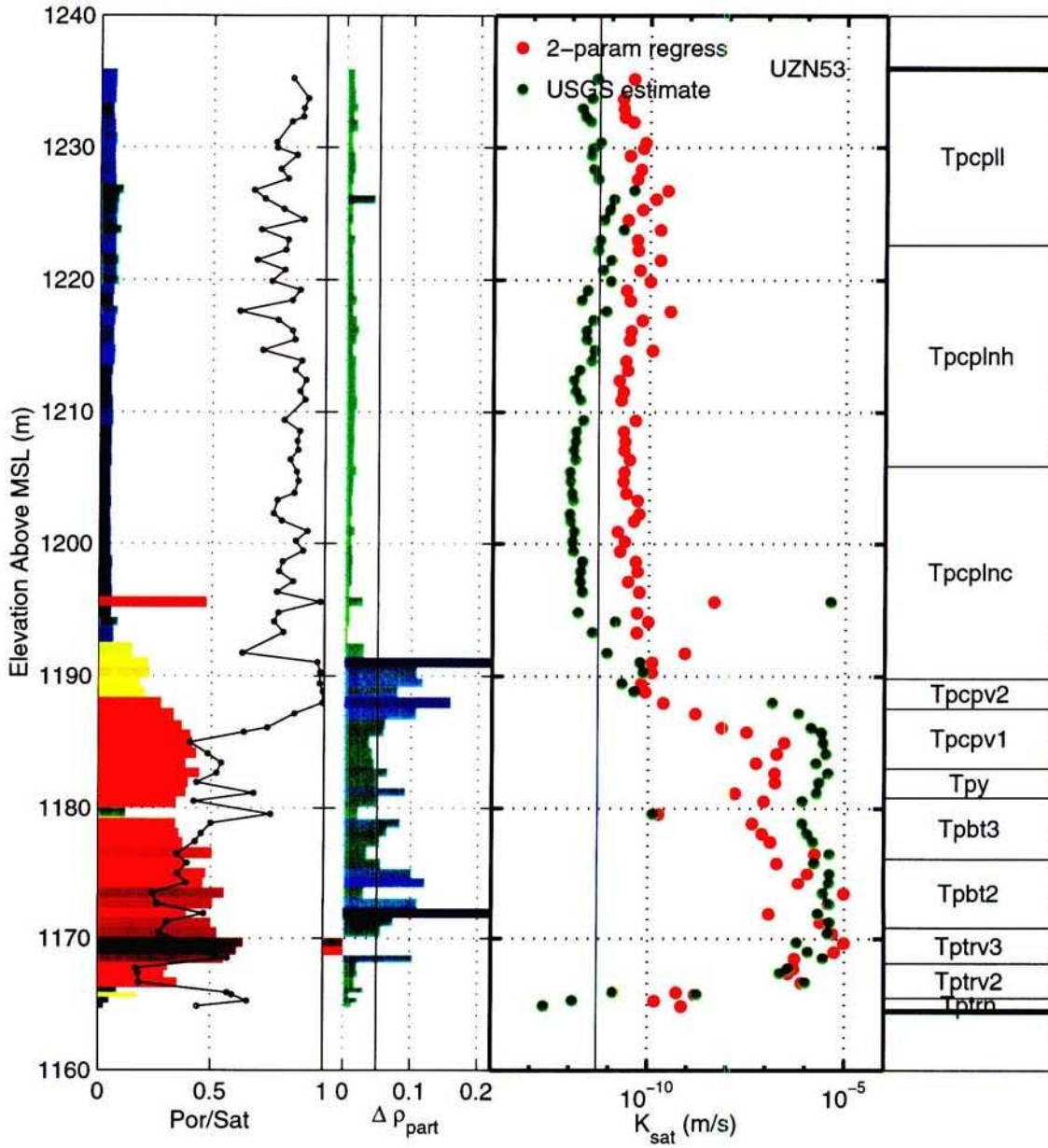
Figure 3-24: 9/9/97. **BHprofile_UZN53_c.eps**. Porosity, saturation, change in particle density, and measured and estimated values for K_{sat} in borehole N53.
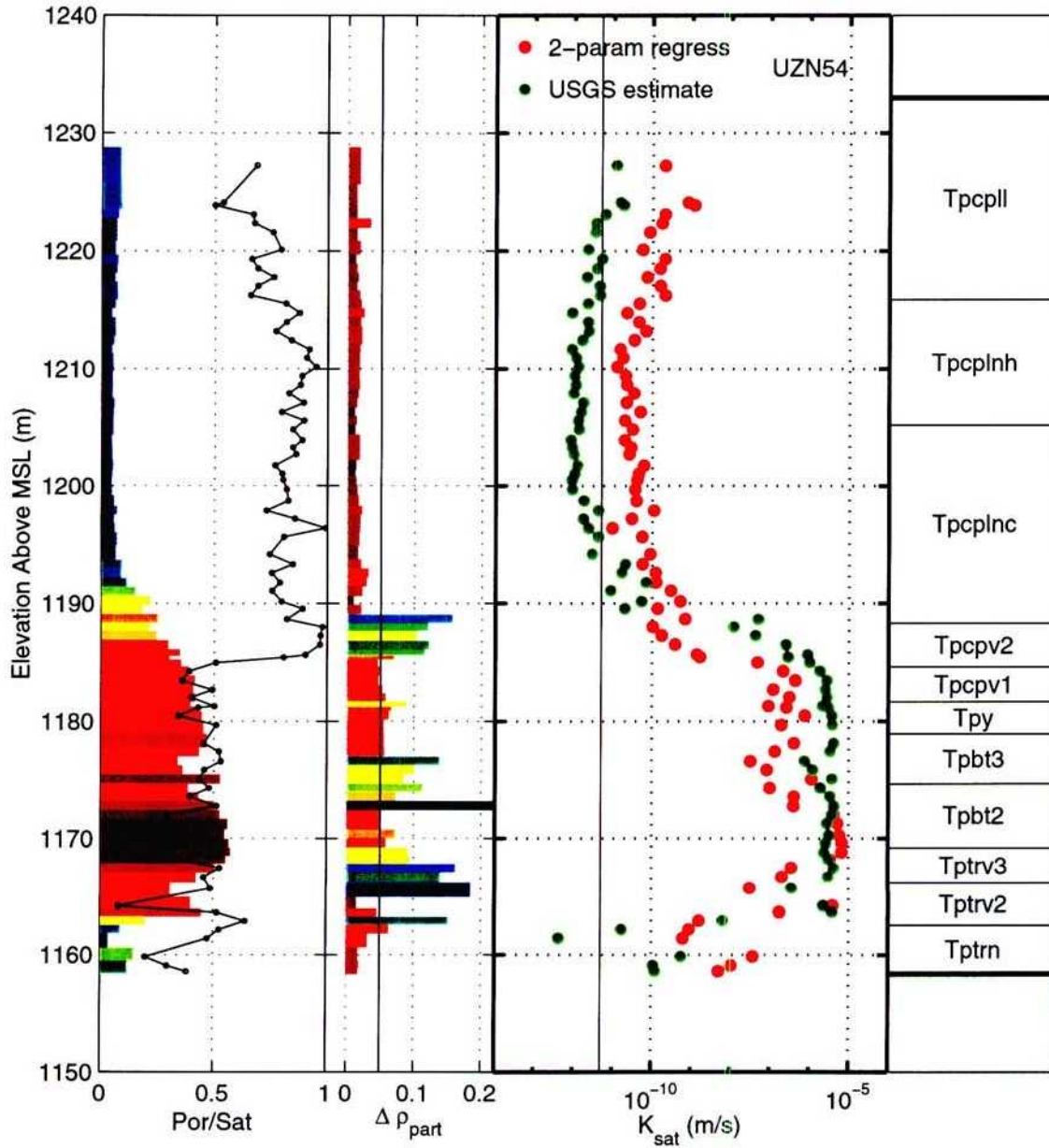
Figure 3-25: 9/9/97. **BHprofile_UZN54_c.eps**. Porosity, saturation, change in particle density, and measured and estimated values for K_{sat} in borehole N54.
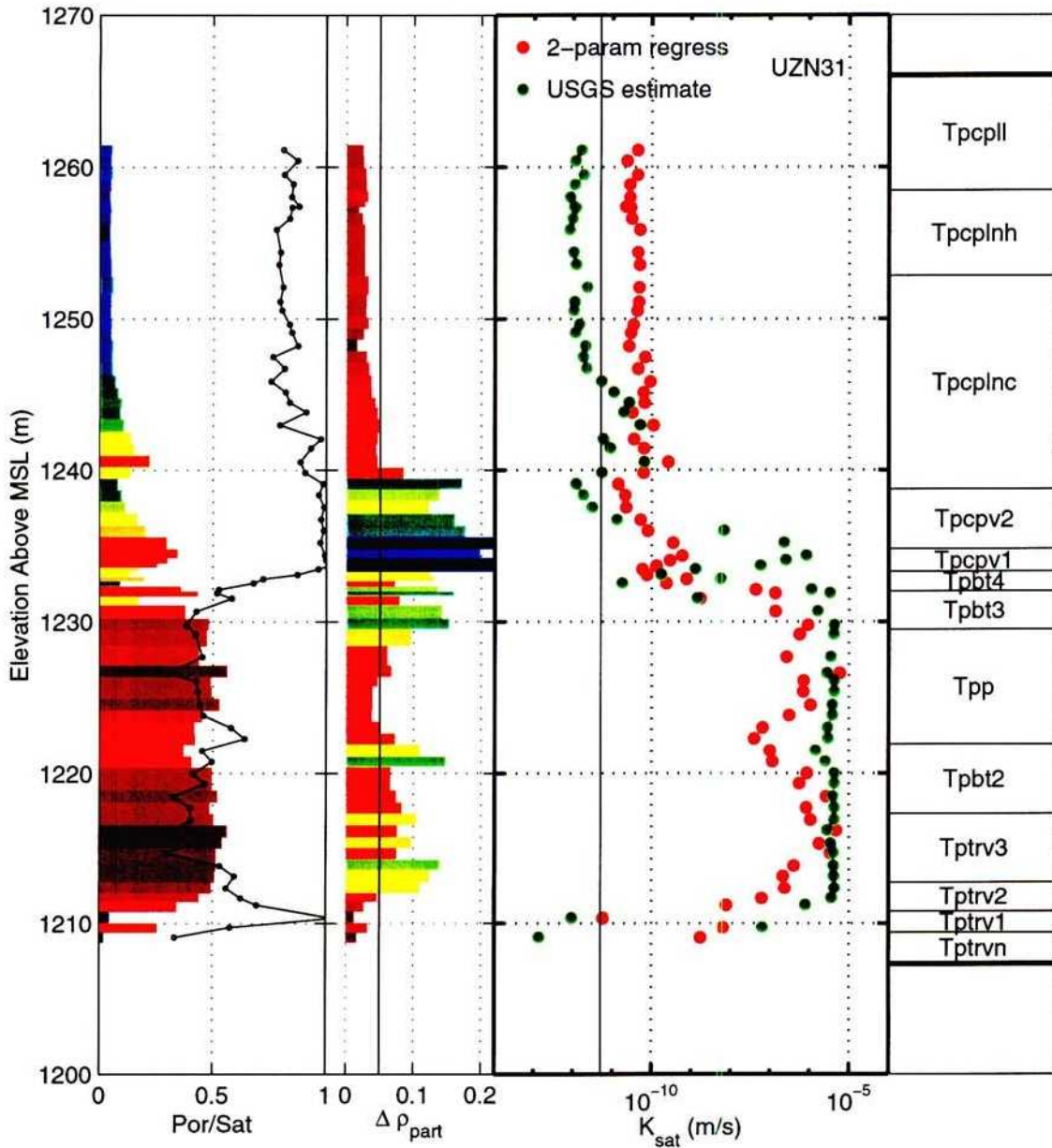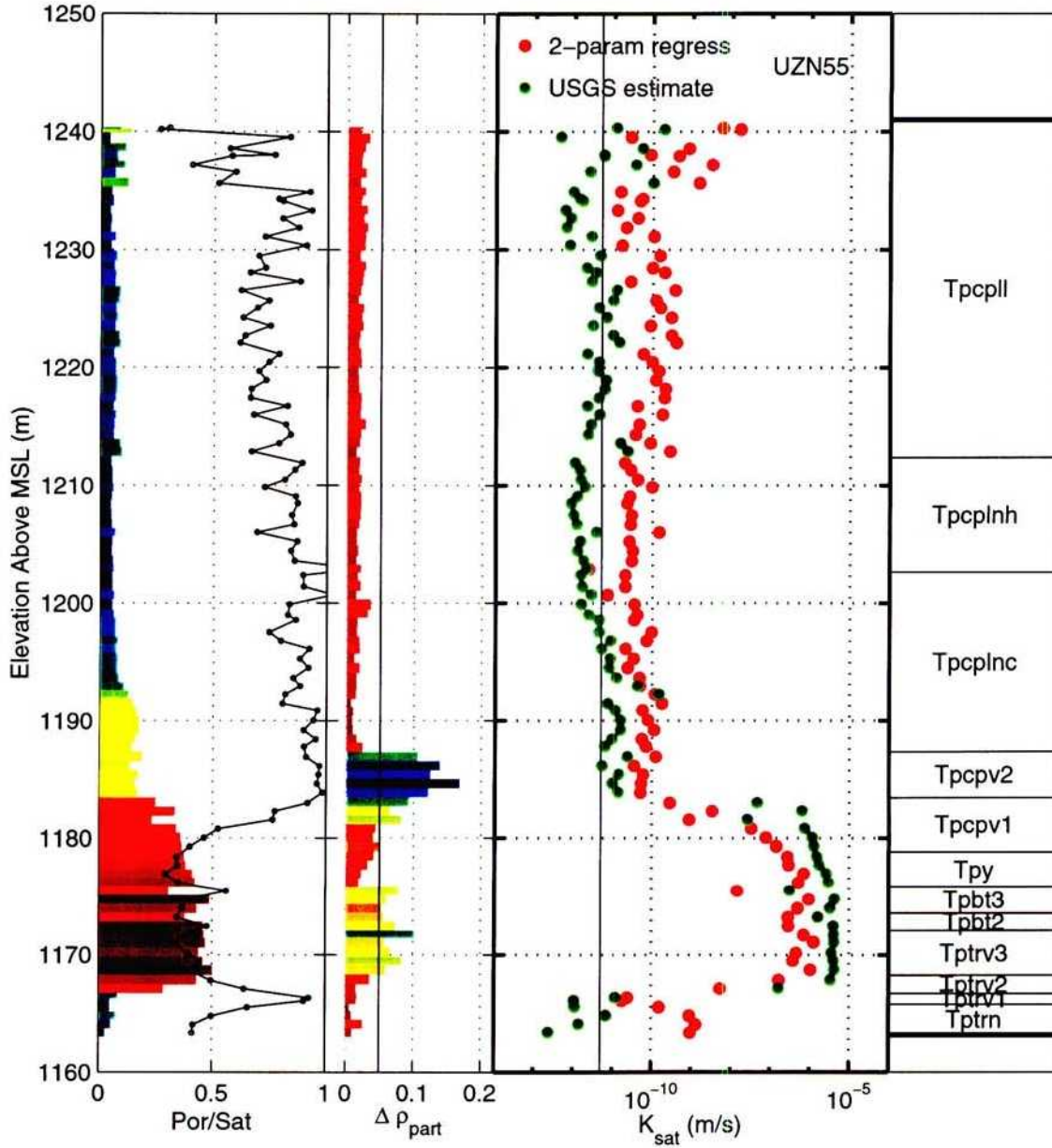
Figure 3-26: 9/9/97. **BHprofile_UZN55_c.eps**. Porosity, saturation, change in particle density, and measured and estimated values for K_{sat} in borehole N55.
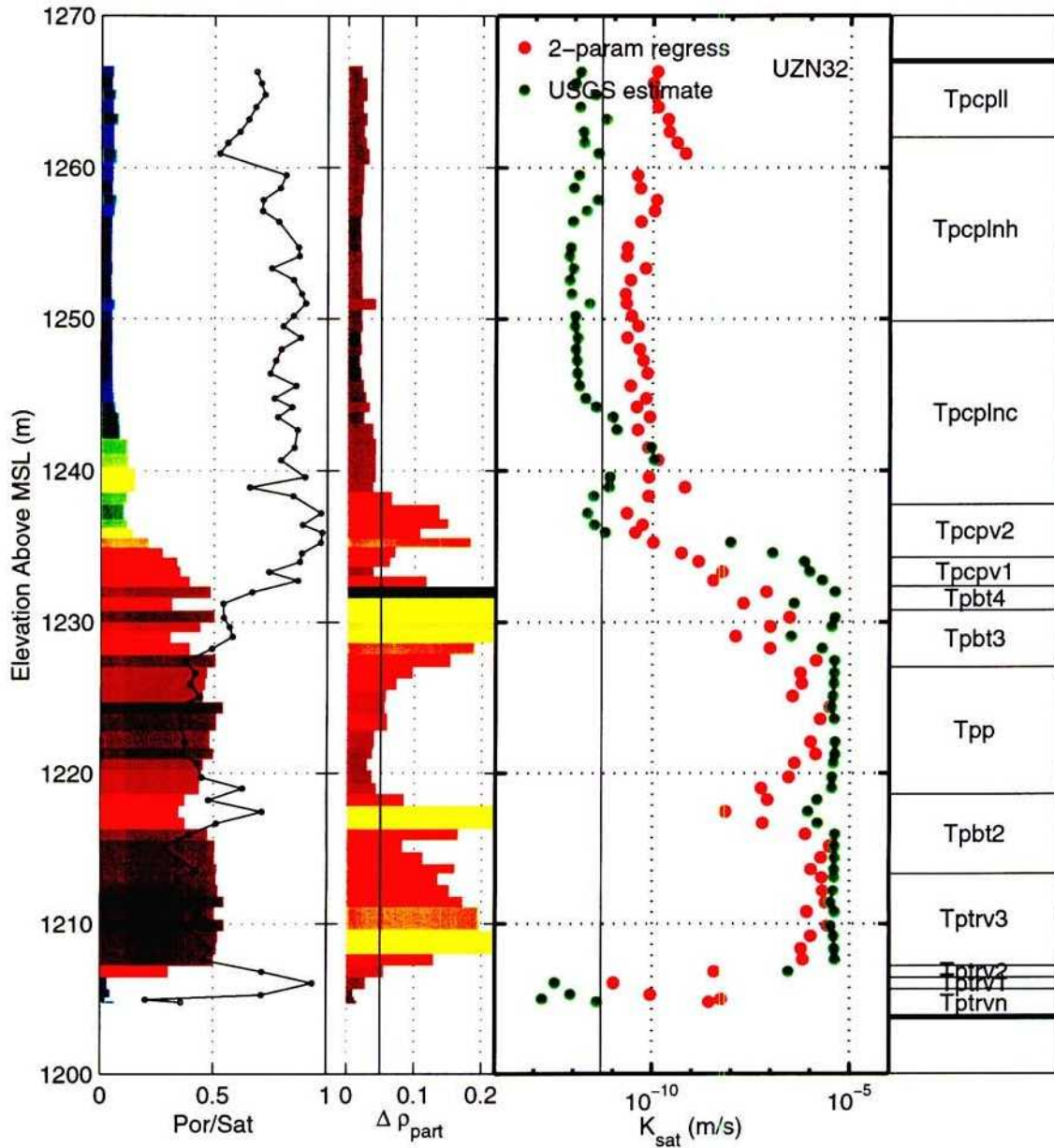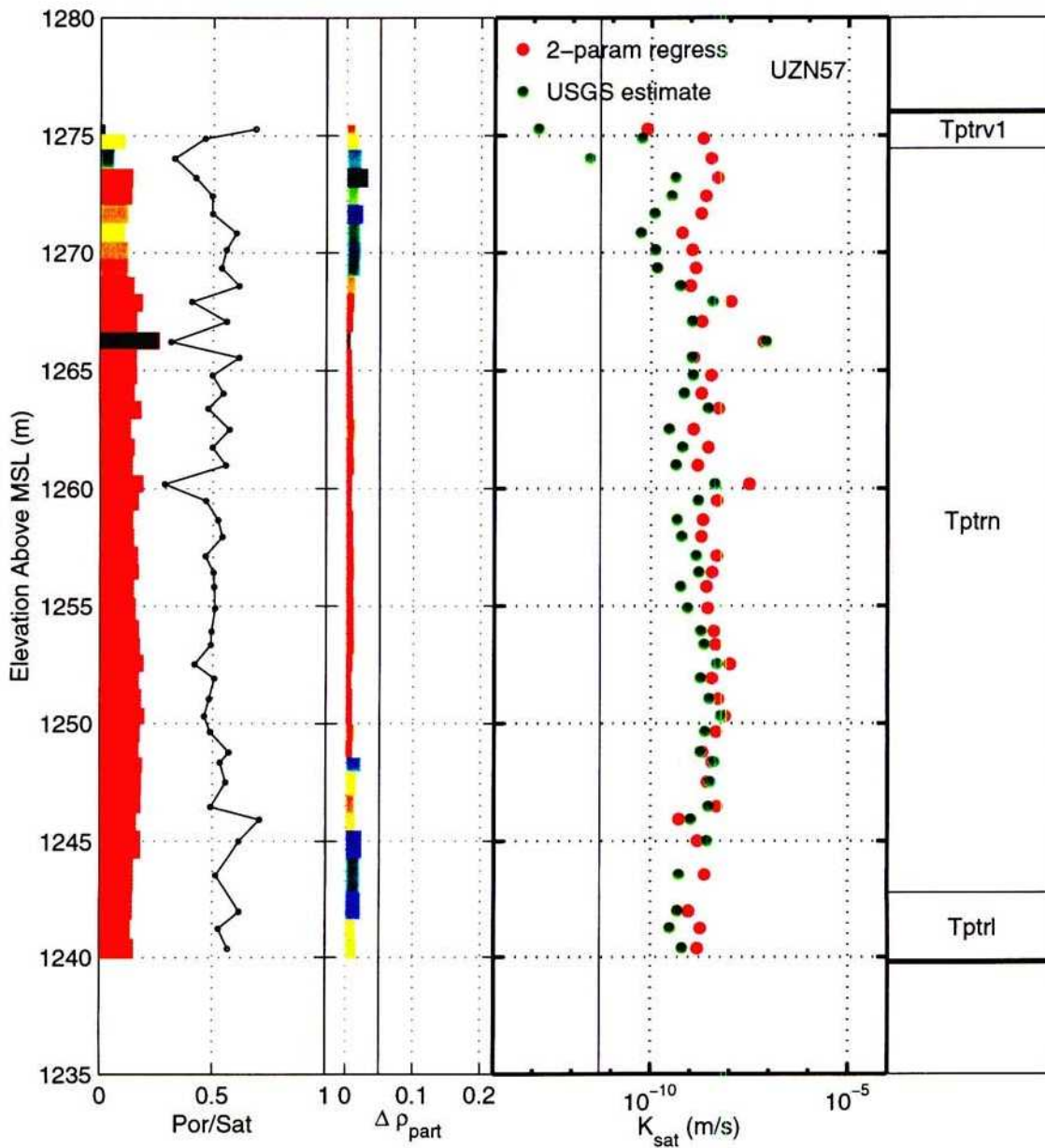
Figure 3-27: 9/9/97. **BHprofile_UZN57_c.eps**. Porosity, saturation, change in particle density, and measured and estimated values for K_{sat} in borehole N57.
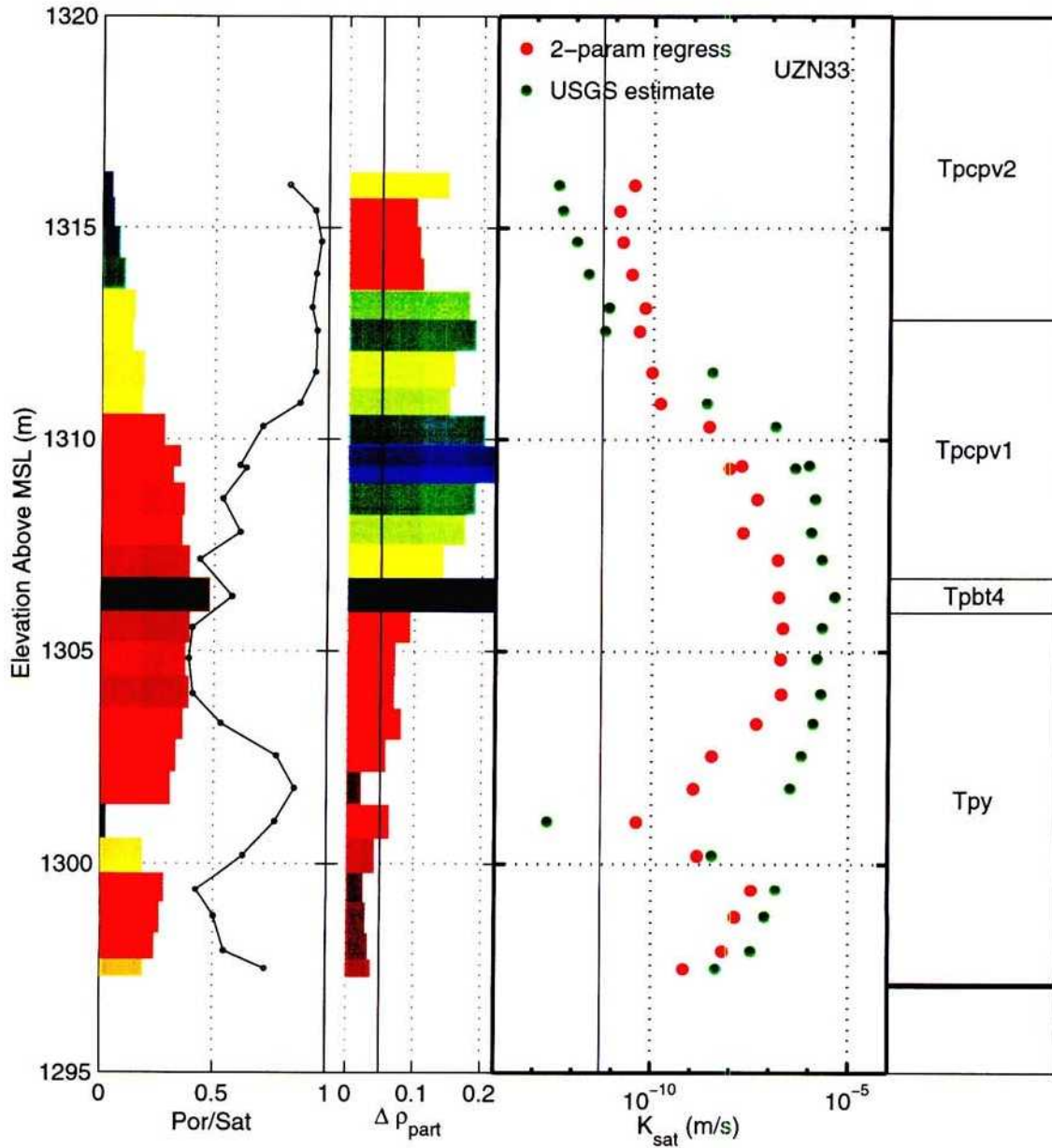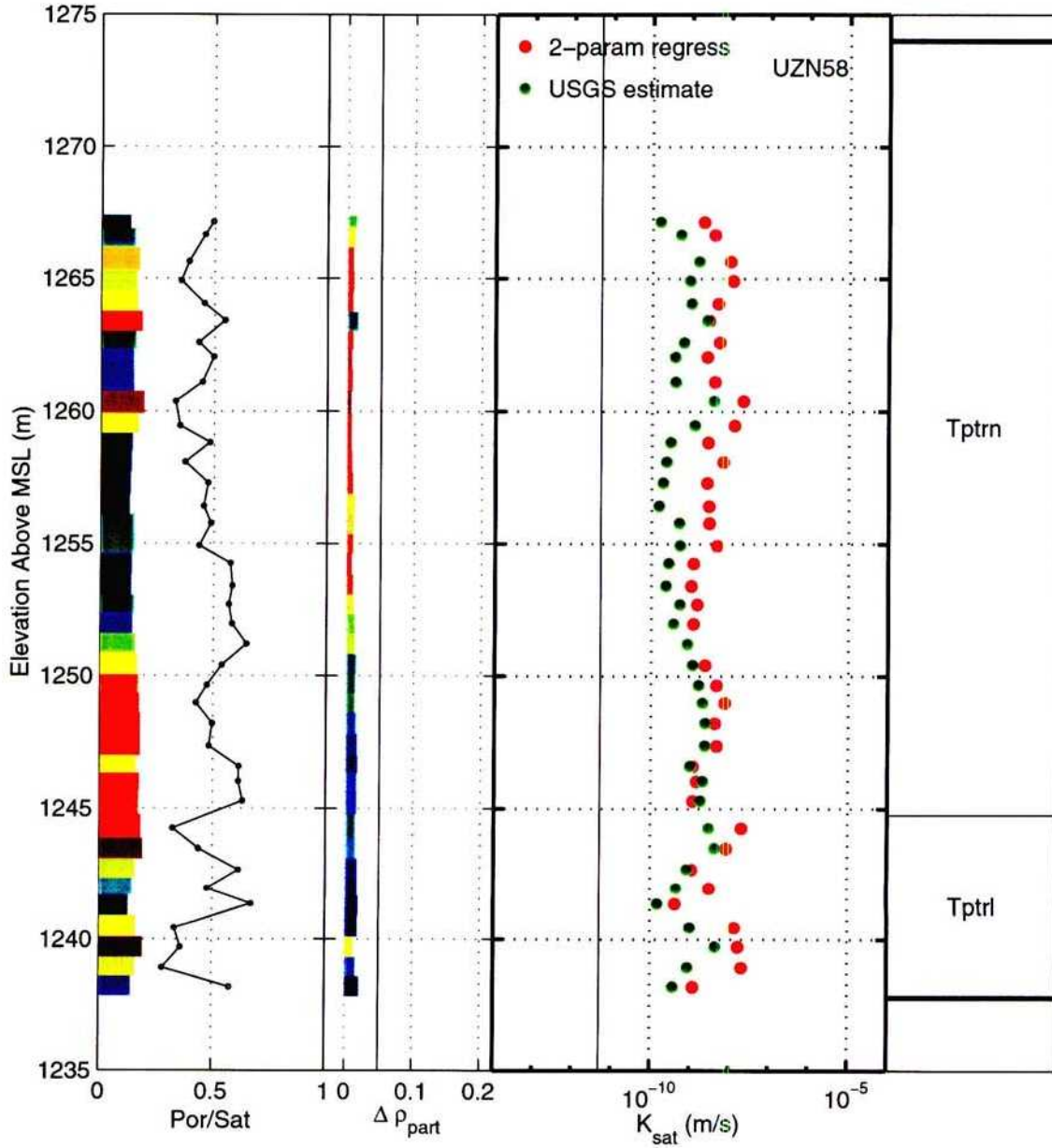
Figure 3-28: 9/9/97. **BHprofile_UZN58_c.eps**. Porosity, saturation, change in particle density, and measured and estimated values for K_{sat} in borehole N58.
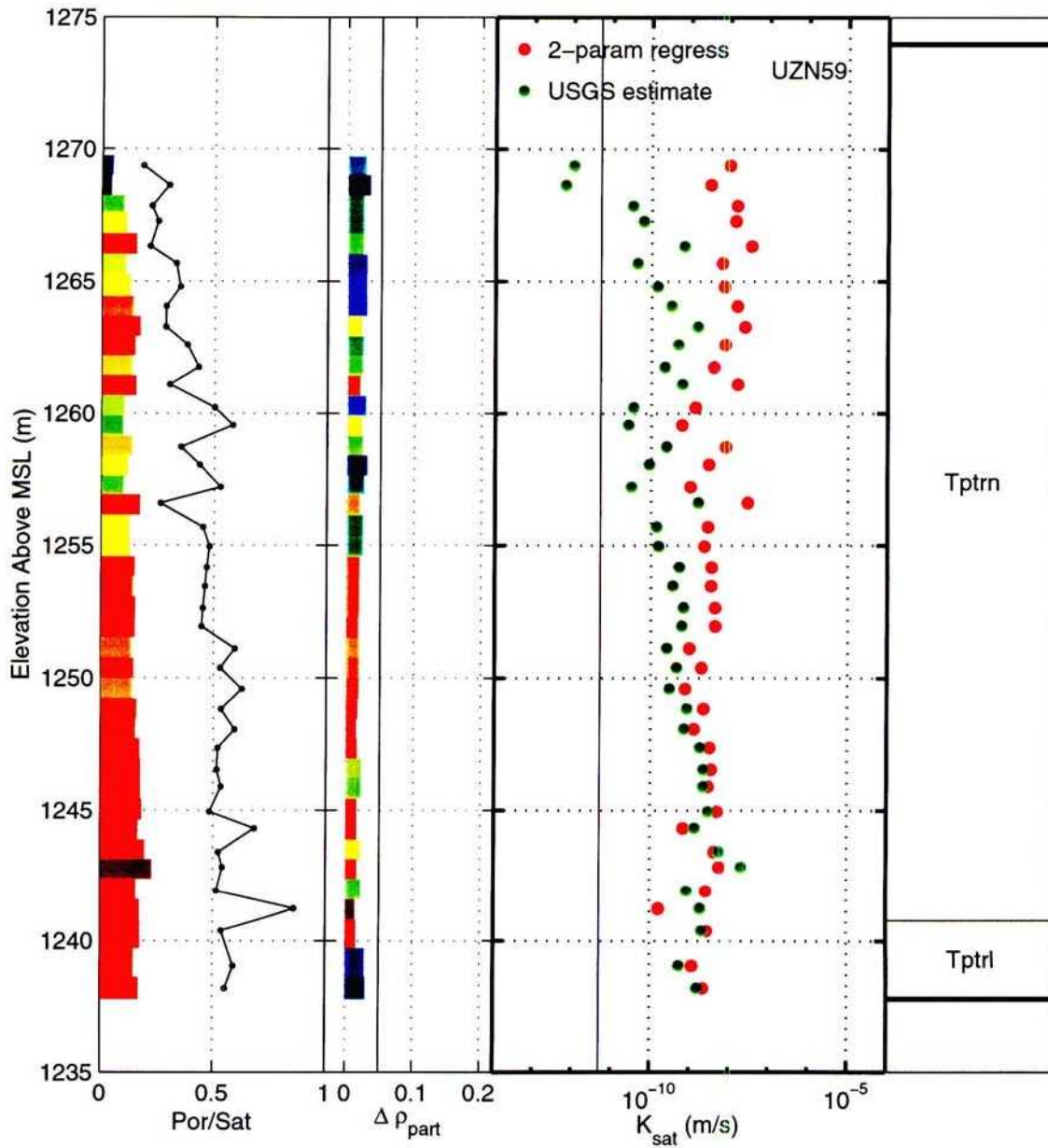
Figure 3-29: 9/9/97. **BHprofile_UZN59_c.eps**. Porosity, saturation, change in particle density, and measured and estimated values for K_{sat} in borehole N59.
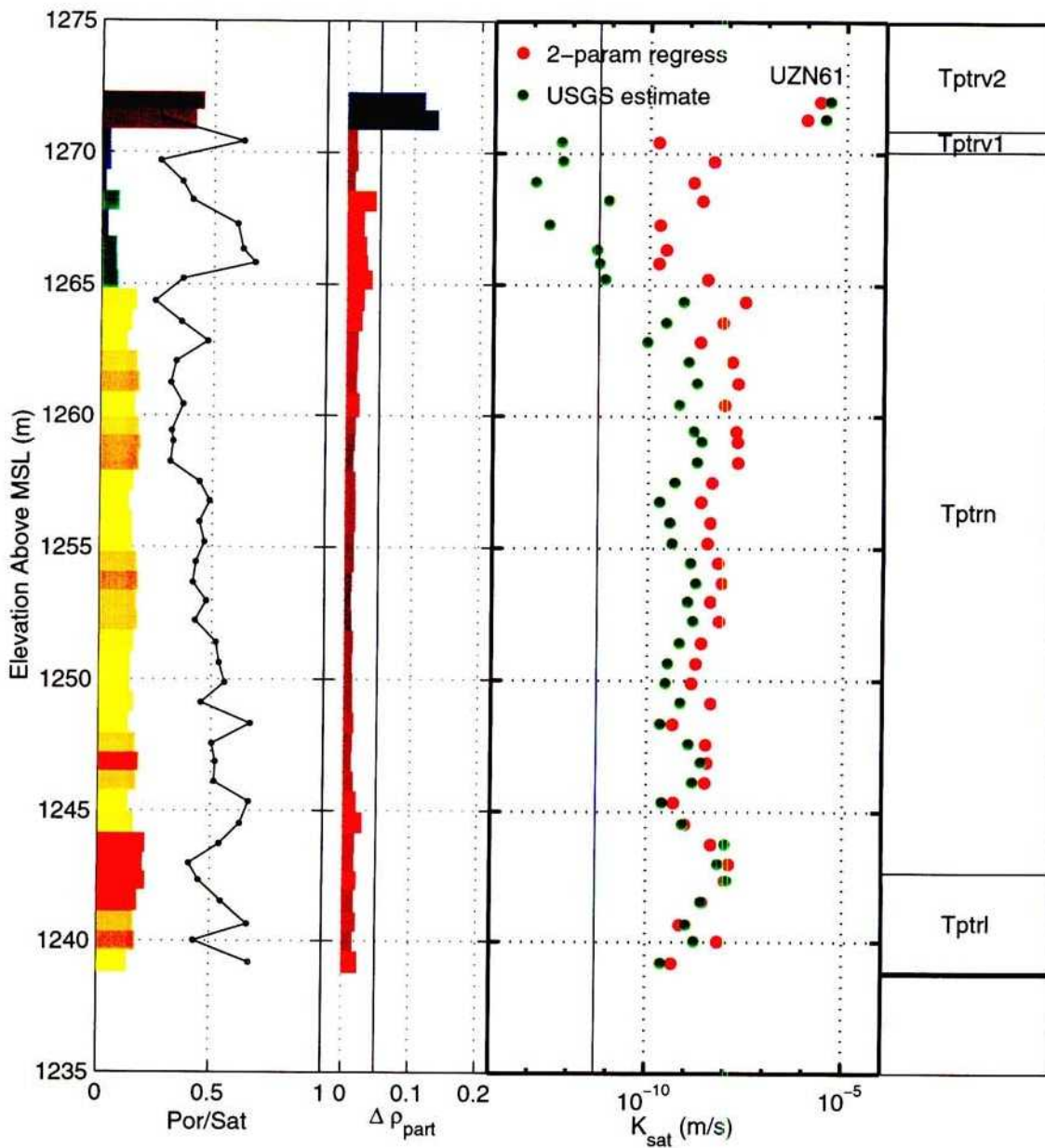
Figure 3-30: 9/9/97. **BHprofile_UZN61_c.eps**. Porosity, saturation, change in particle density, and measured and estimated values for K_{sat} in borehole N61.
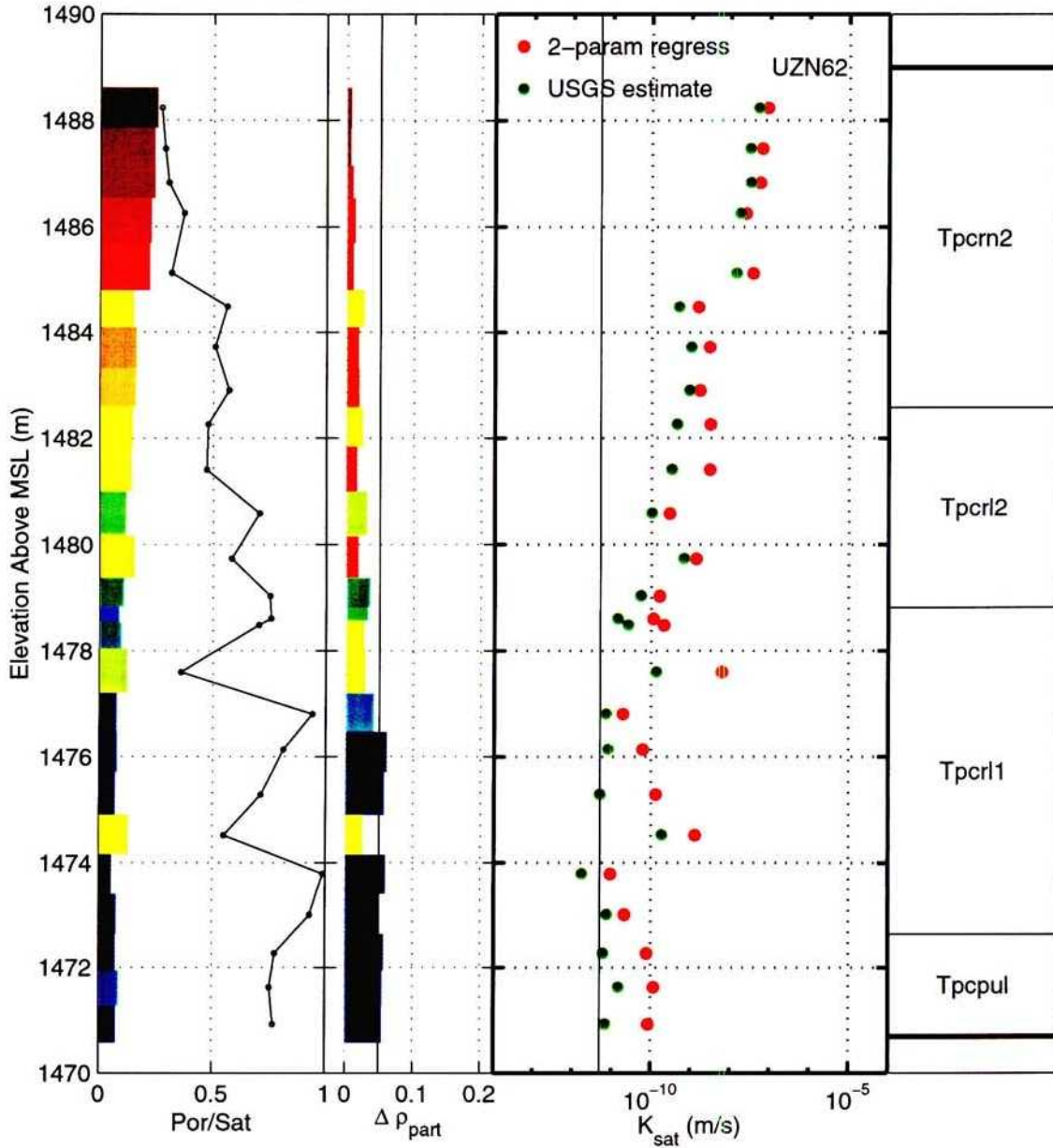
Figure 3-31: 9/9/97. **BHprofile_UZN62_c.eps**. Porosity, saturation, change in particle density, and measured and estimated values for K_{sat} in borehole N62.
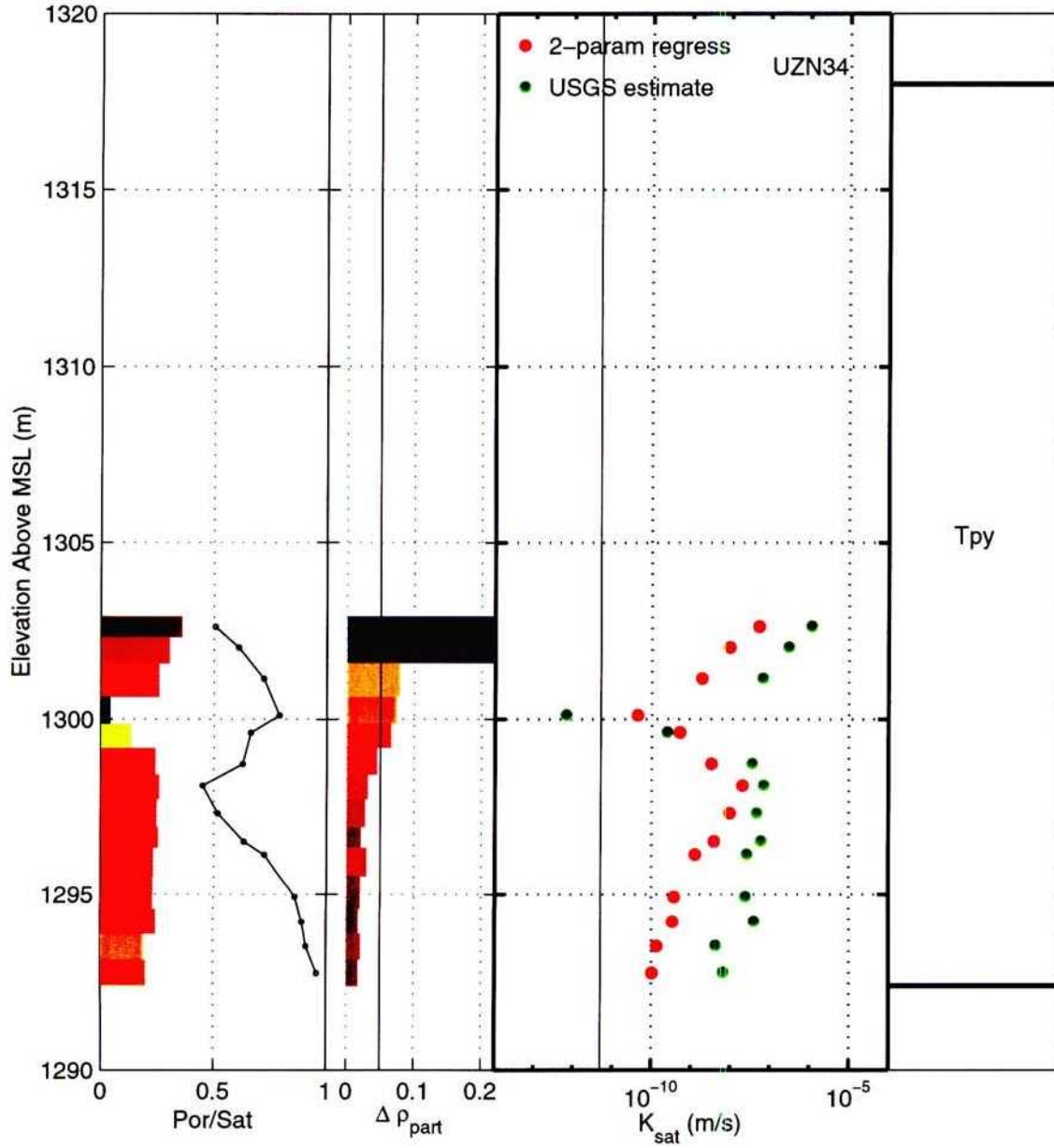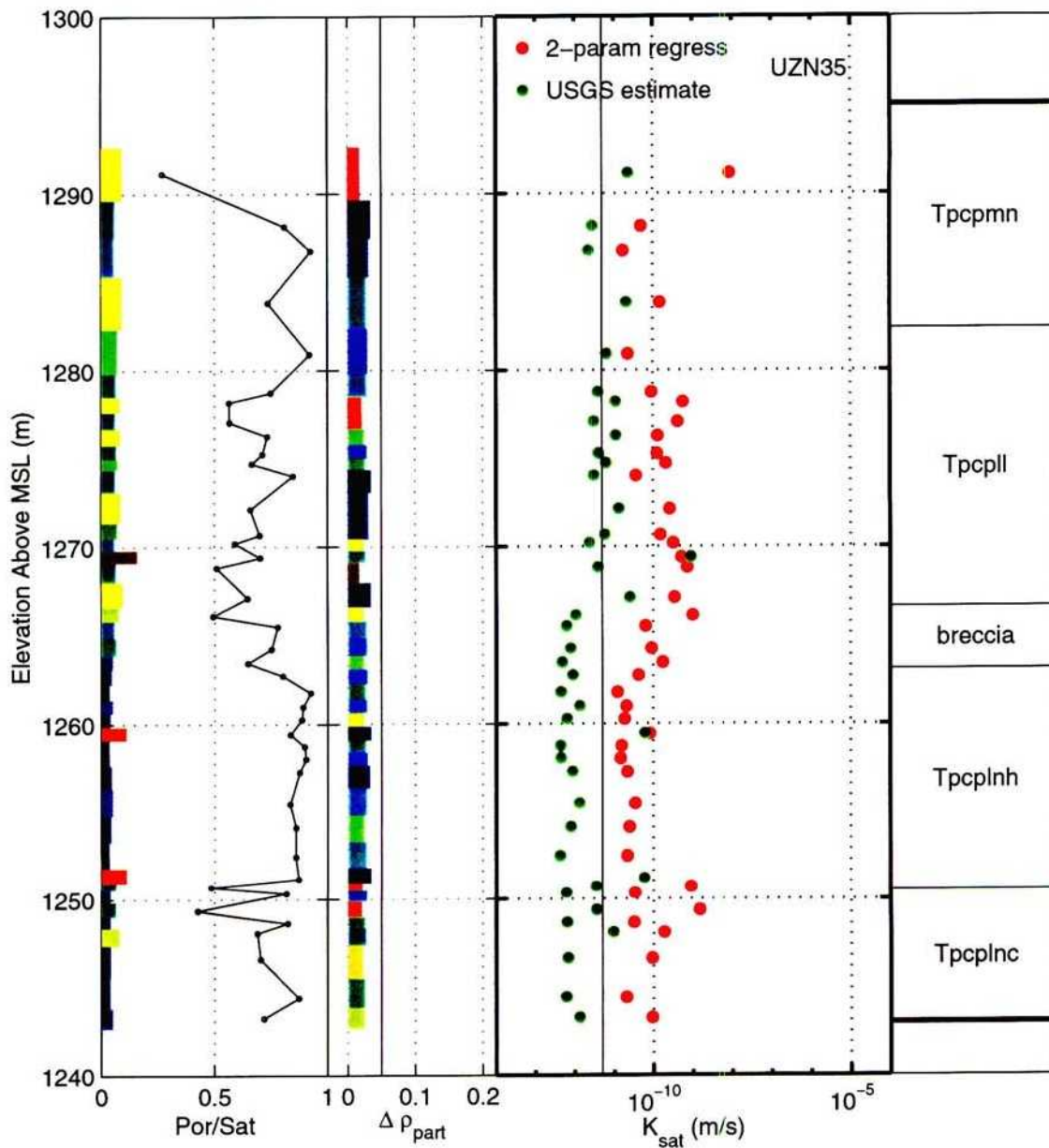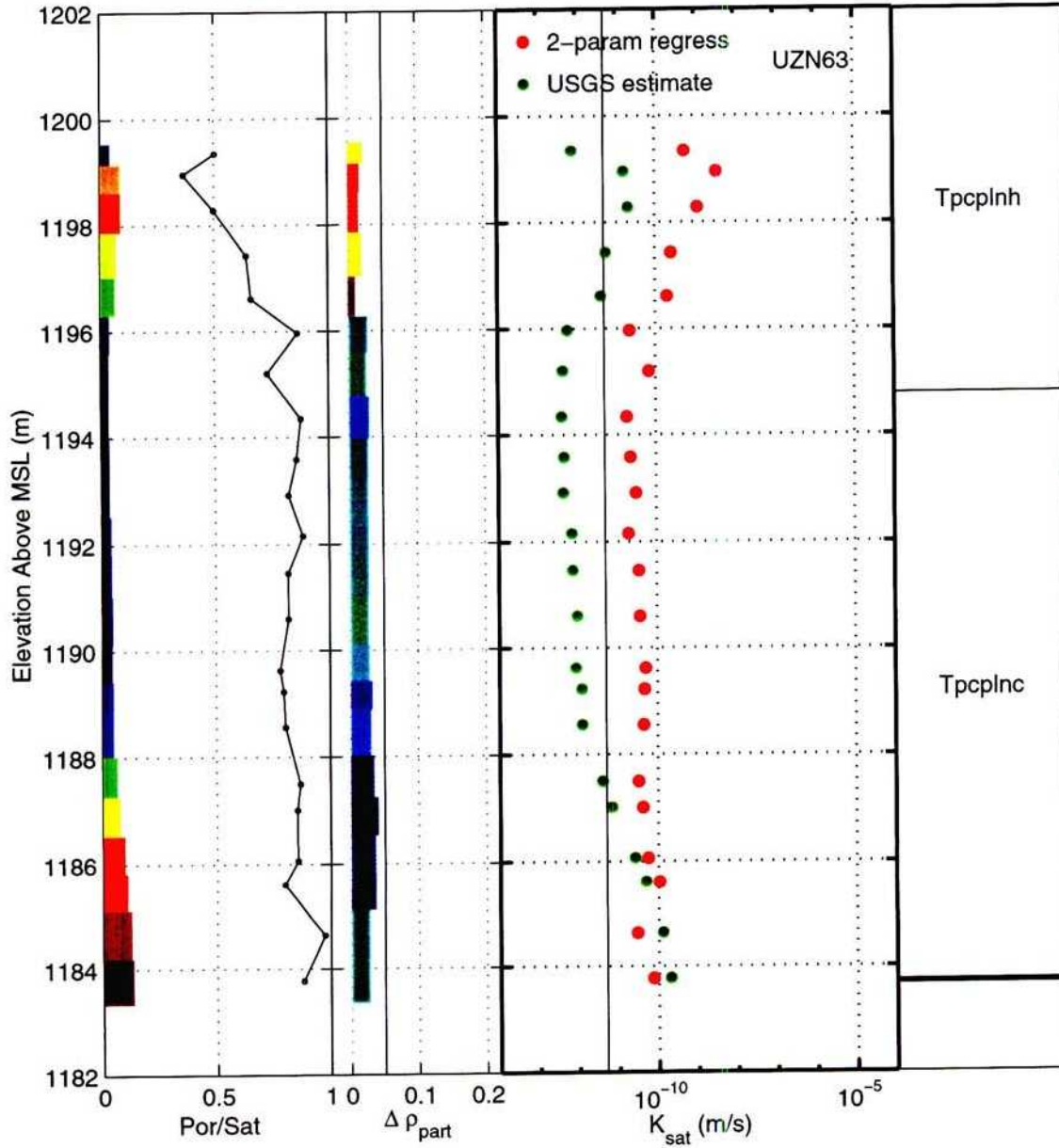
Figure 3-32: 9/9/97. **BHprofile_UZN63_c.eps**. Porosity, saturation, change in particle density, and measured and estimated values for K_{sat} in borehole N63.
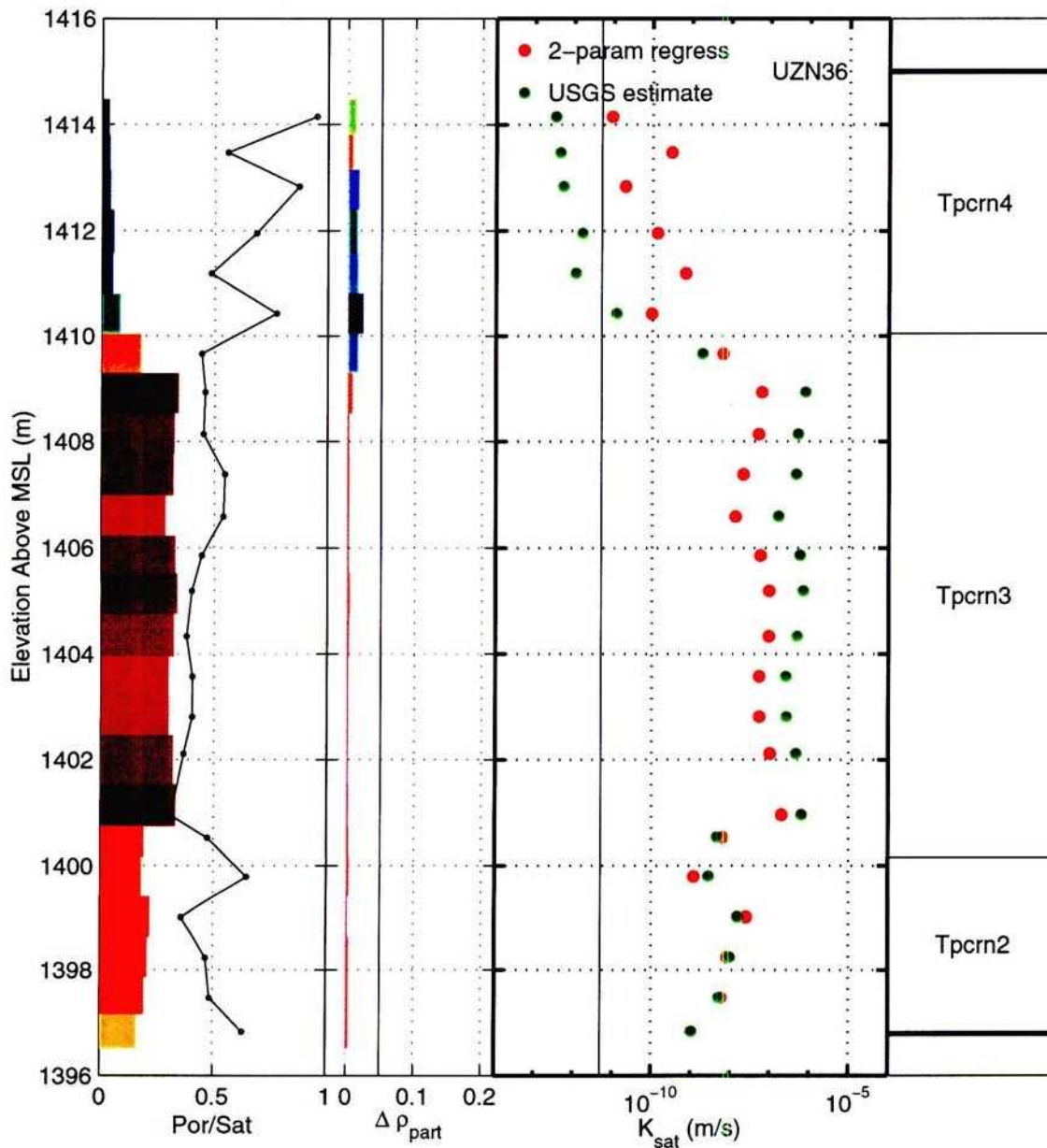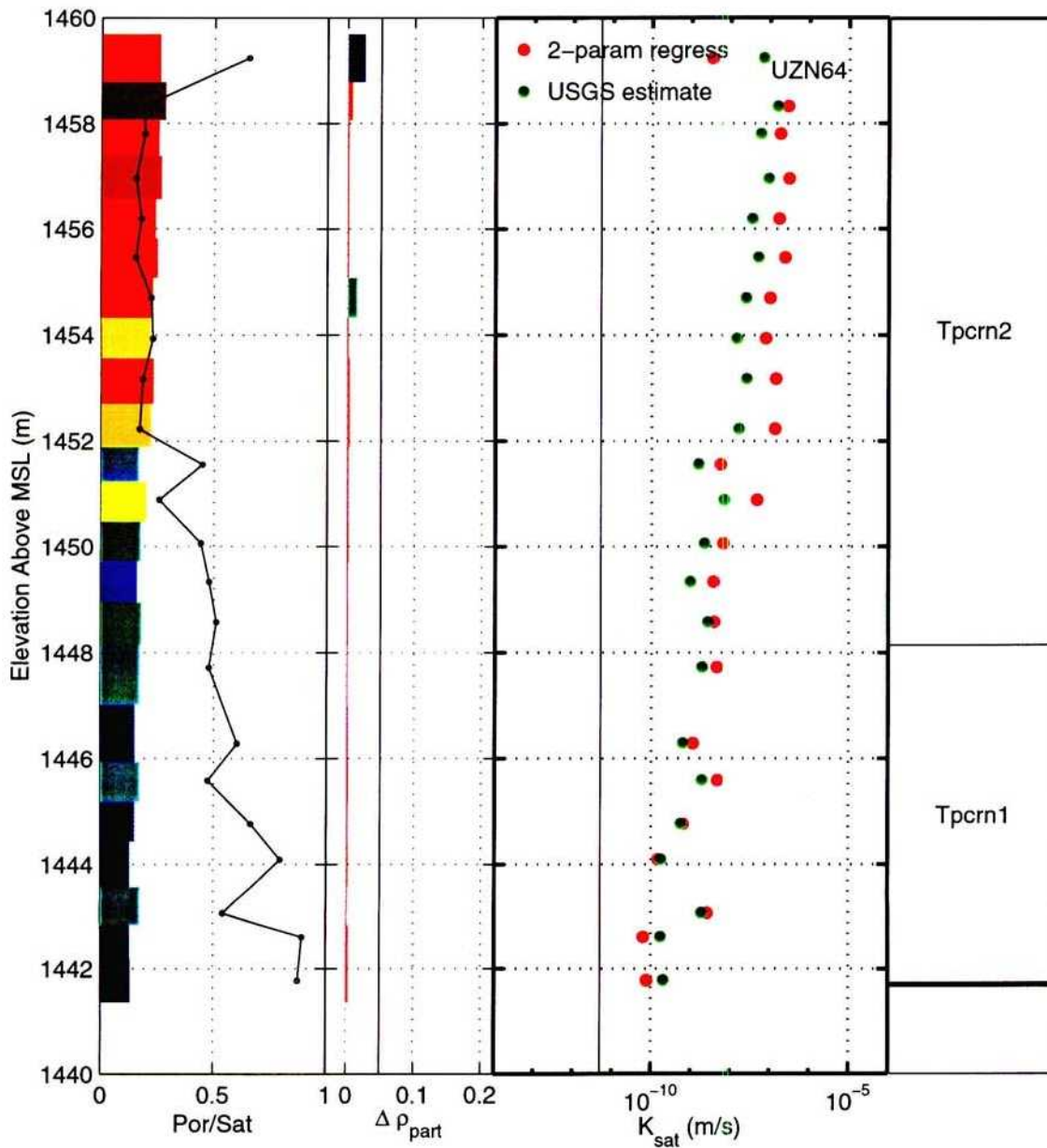
Figure 3-33: 9/9/97. **BHprofile_UZN64_c.eps**. Porosity, saturation, change in particle density, and measured and estimated values for K_{sat} in borehole N64.

9/17/97 Further investigation of USGS UZ properties.

In *$HOME2/AmbientKTI/3Ddata*, I created a *Matlab* routine, show_usgs_db_ksat.m, that plots the K_{sat} values for each formation using all boreholes having K_{sat} values for the formation, either measured or estimated using my regression. A small location map, idealized formation map, and statistical information are part of each plot. The creating routine is saved with a .arch091697 appended.

The plots are shown in the following pages. The statistical descriptions are summarized in the tables following the plots.
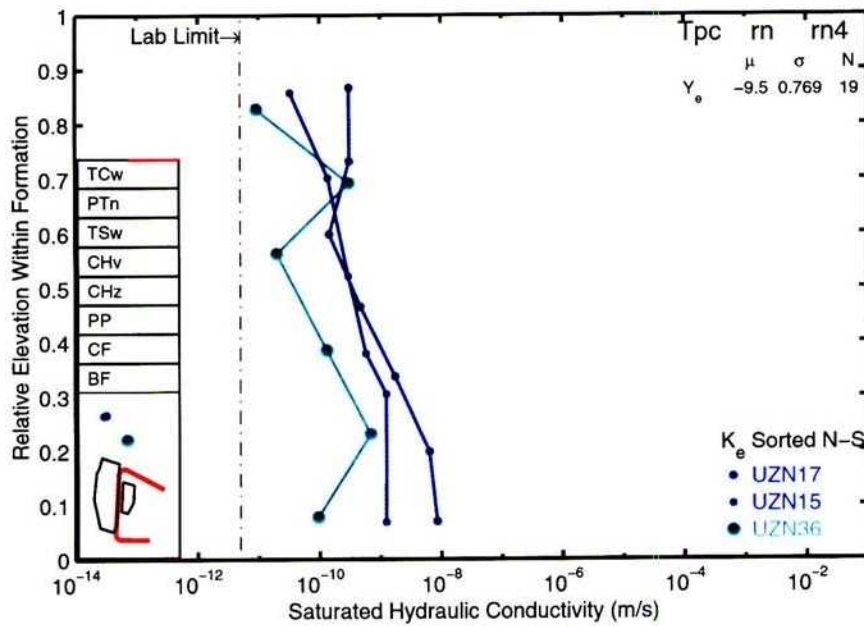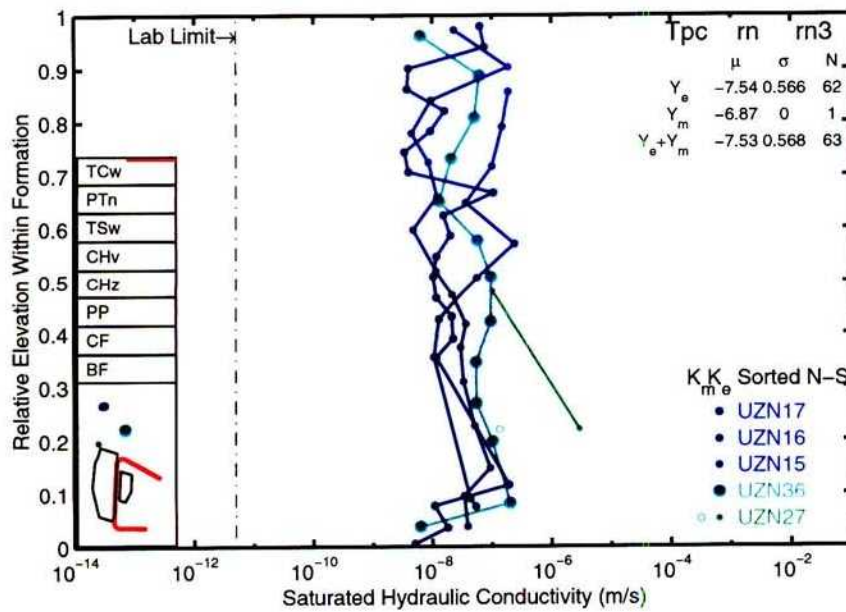
Figure 3-34: 9/17/97. All CNWRA-estimated and USGS-measured K_{sat} values in formation: (a) Tpcrn4 (**FormK_Tpcrn4_c.eps**), and (b) Tpcrn3 (**FormK_Tpcrn3_c.eps**).
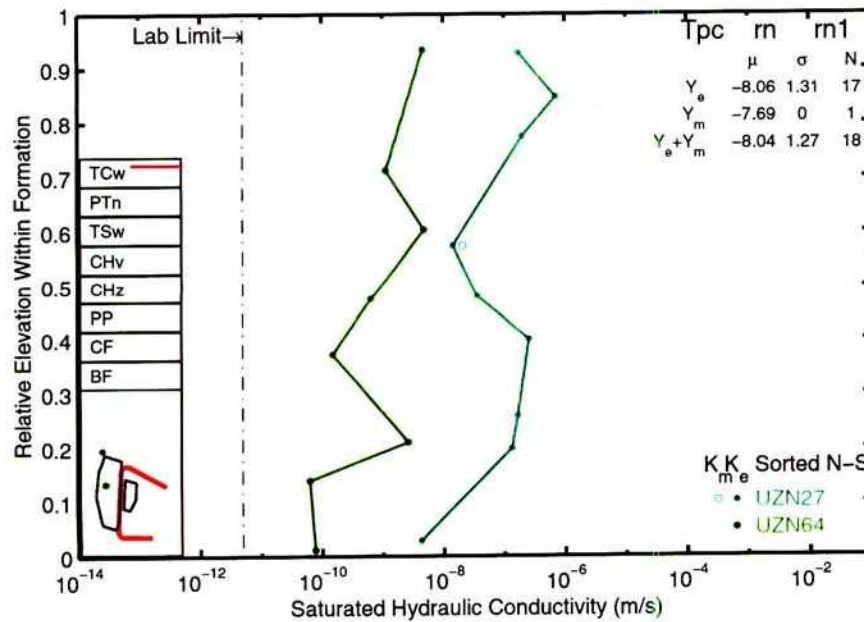
Figure 3-35: 9/17/97. All CNWRA-estimated and USGS-measured K_{sat} values in formation: (a) Tpcrn2 (**FormK_Tpcrn2_c.eps**), and (b) Tpcrn1 (**FormK_Tpcrn1_c.eps**).
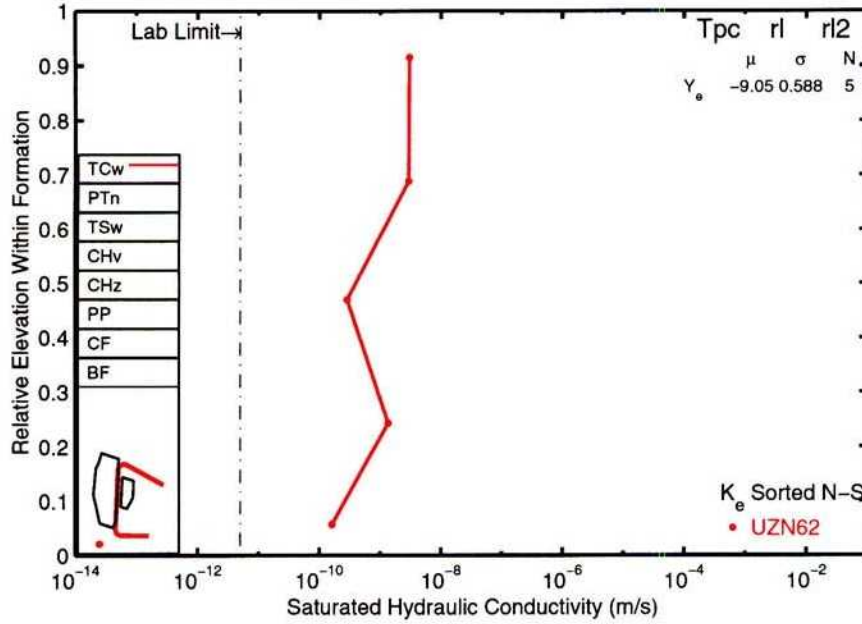
(a)
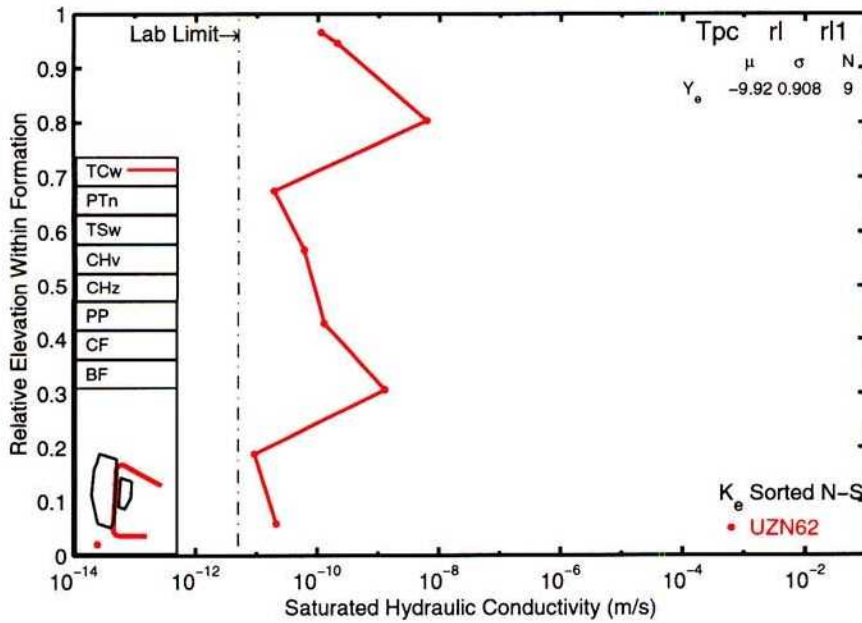
(b)

Figure 3-36: 9/17/97. All CNWRA-estimated and USGS-measured K_{sat} values in formation: (a) Tpcrl2 (**FormK_Tpcrl2_c.eps**), and (b) Tpcrl1 (**FormK_Tpcrl1_c.eps**).
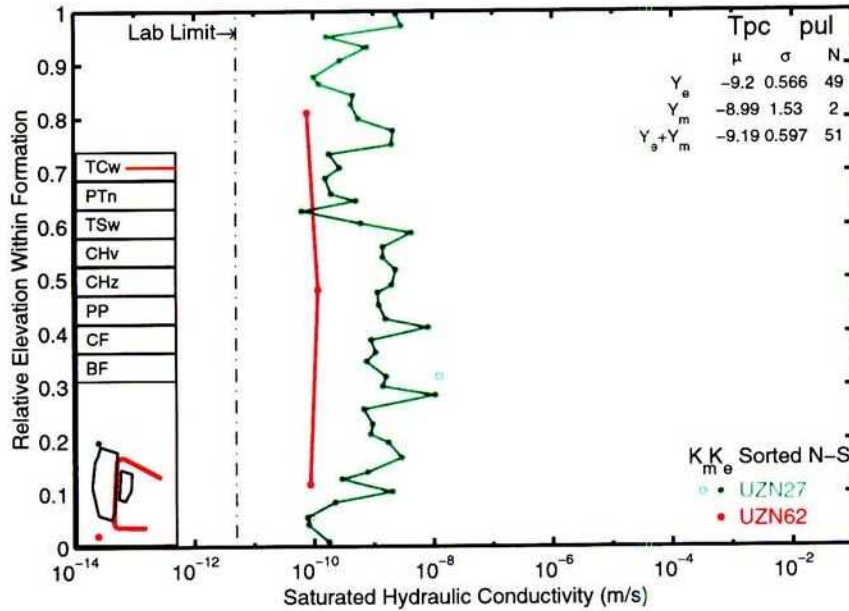
(a)
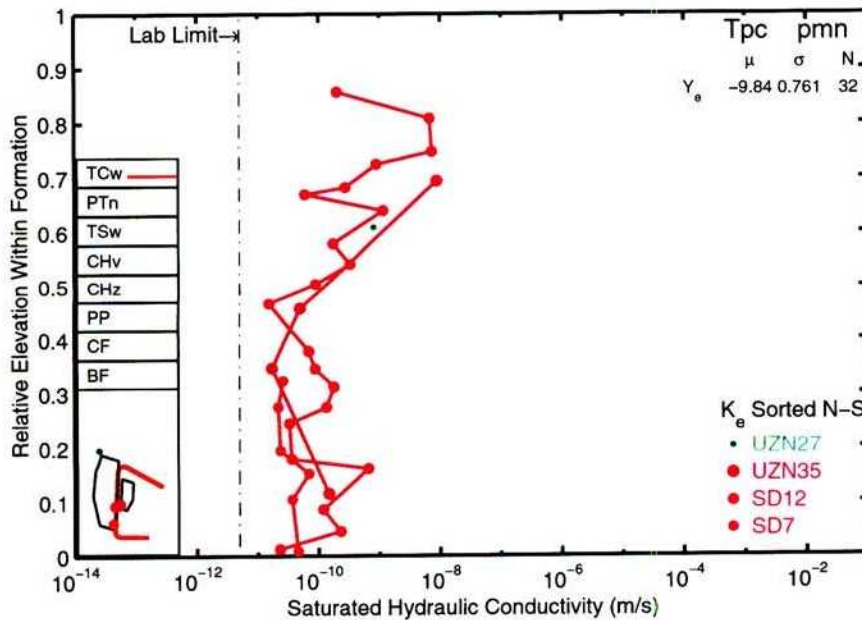
(b)

Figure 3-37: 9/17/97. All CNWRA-estimated and USGS-measured K_{sat} values in formation: (a) Tpcpul (**FormK_Tpcpul_c.eps**), and (b) Tpcpmn (**FormK_Tpcpmn_c.eps**).
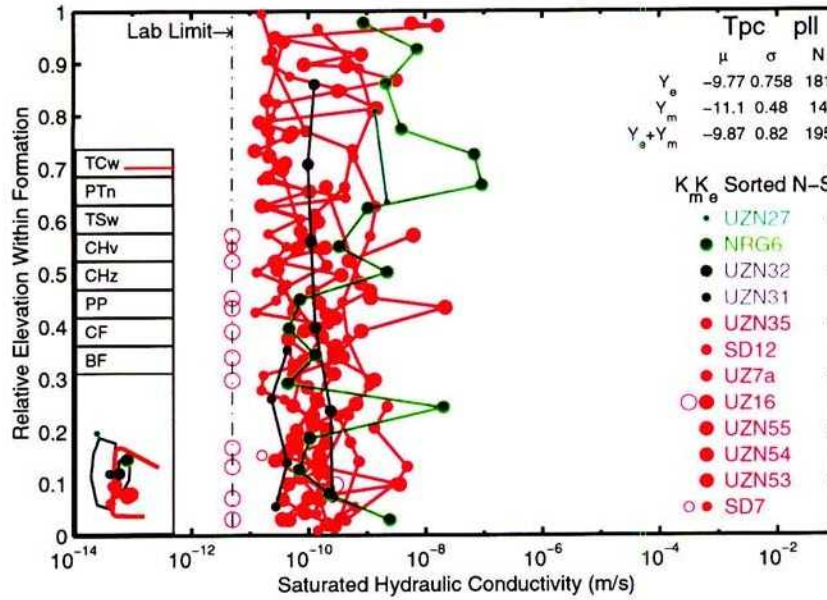
(a)
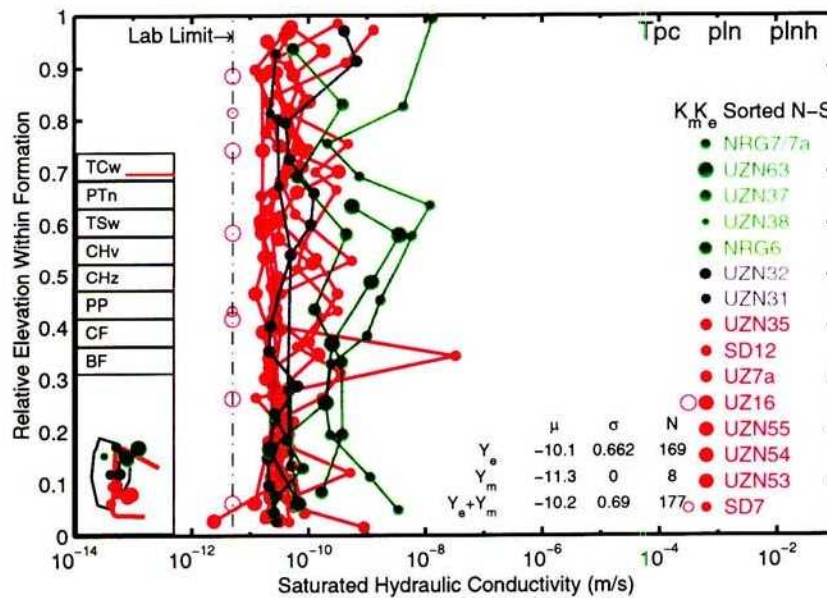
(b)

Figure 3-38: 9/17/97. All CNWRA-estimated and USGS-measured K_{sat} values in formation: (a) Tpcpll (**FormK_Tpcpll_c.eps**), and (b) Tpcplnh (**FormK_Tpcplnh_c.eps**).
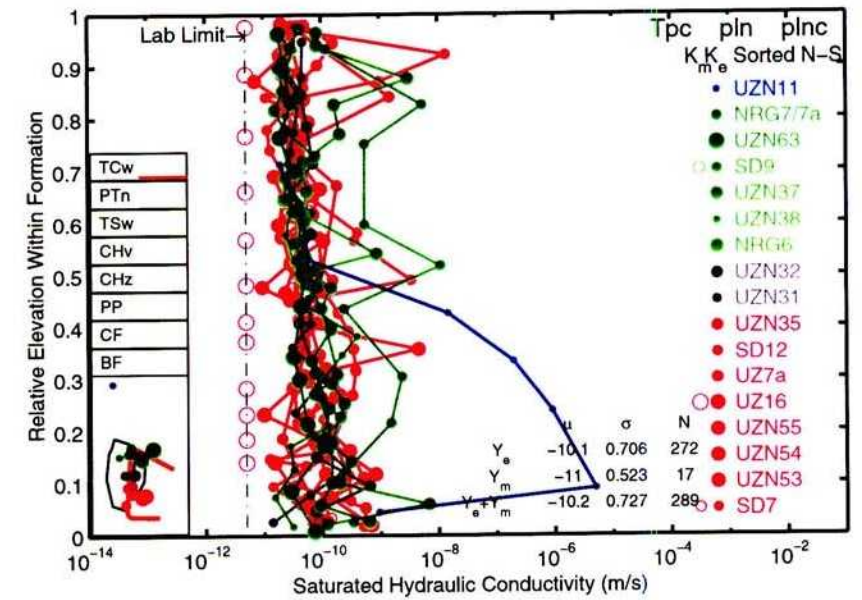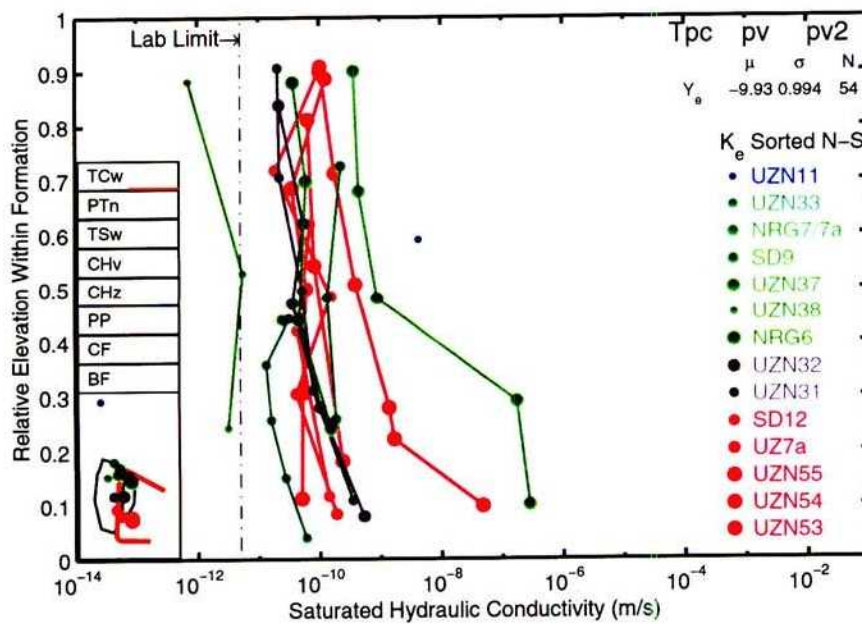
Figure 3-39: 9/17/97. All CNWRA-estimated and USGS-measured K_{sat} values in formation: (a) Tpcplnc (**FormK_Tpcplnc_c.eps**), and (b) Tpcpv2 (**FormK_Tpcpv2_c.eps**).
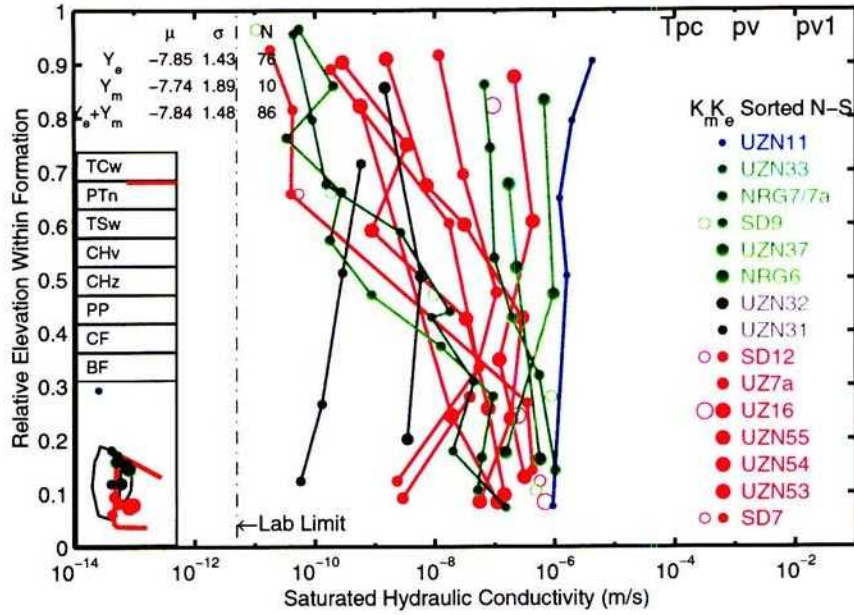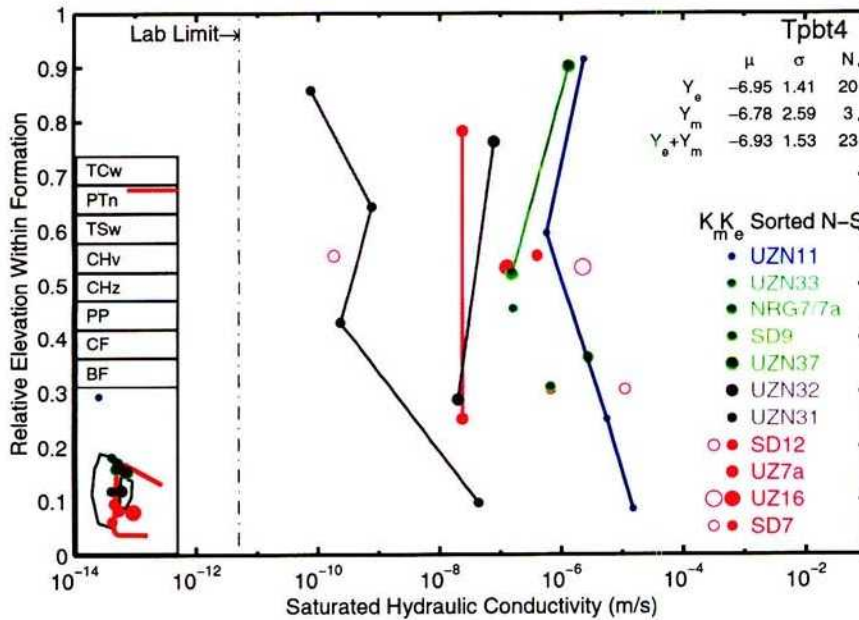
Figure 3-40: 9/17/97. All CNWRA-estimated and USGS-measured K_{sat} values in formation: (a) Tpcpv1 (**FormK_Tpcpv1_c.eps**), and (b) Tpbt4 (**FormK_Tpbt4_c.eps**).
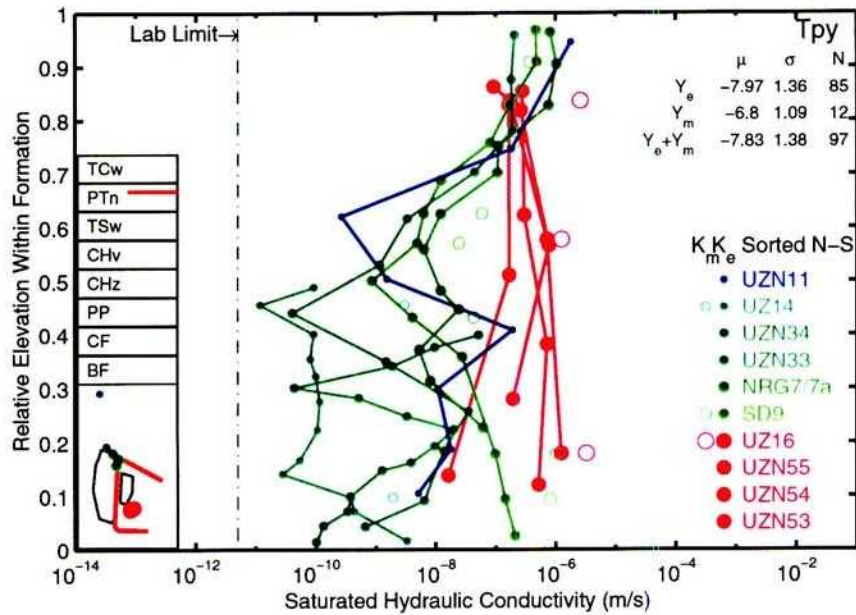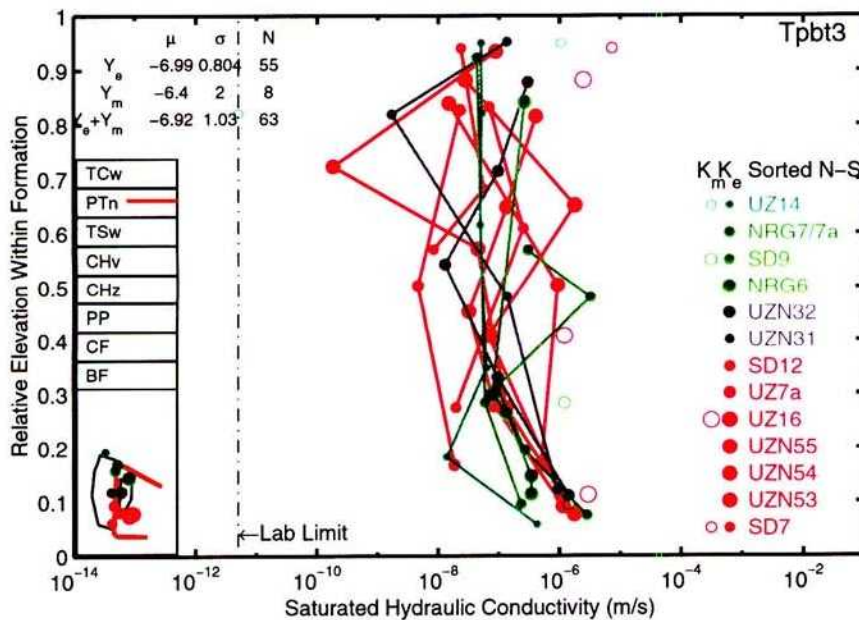
Figure 3-41: 9/17/97. All CNWRA-estimated and USGS-measured K_{sat} values in formation: (a) Tpy (**FormK_Tpy_c.eps**), and (b) Tpbt3 (**FormK_Tpbt3_c.eps**).
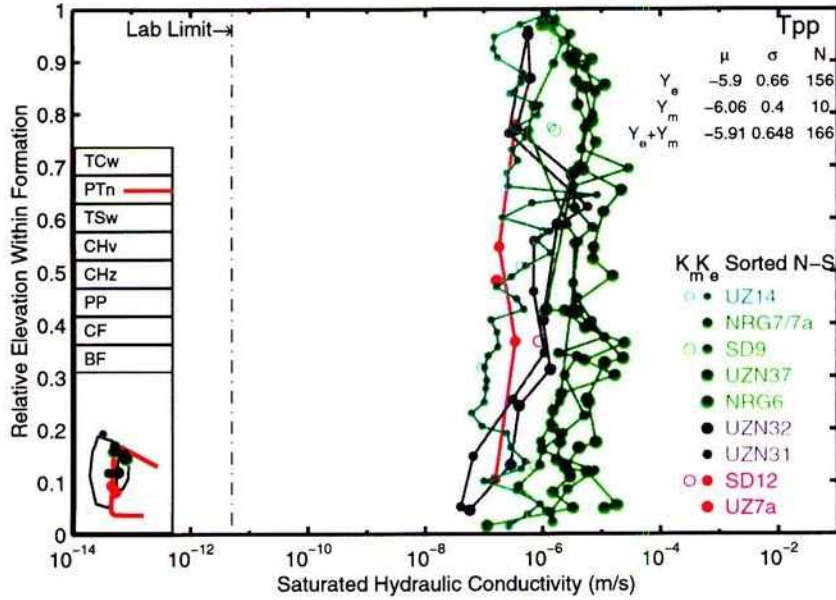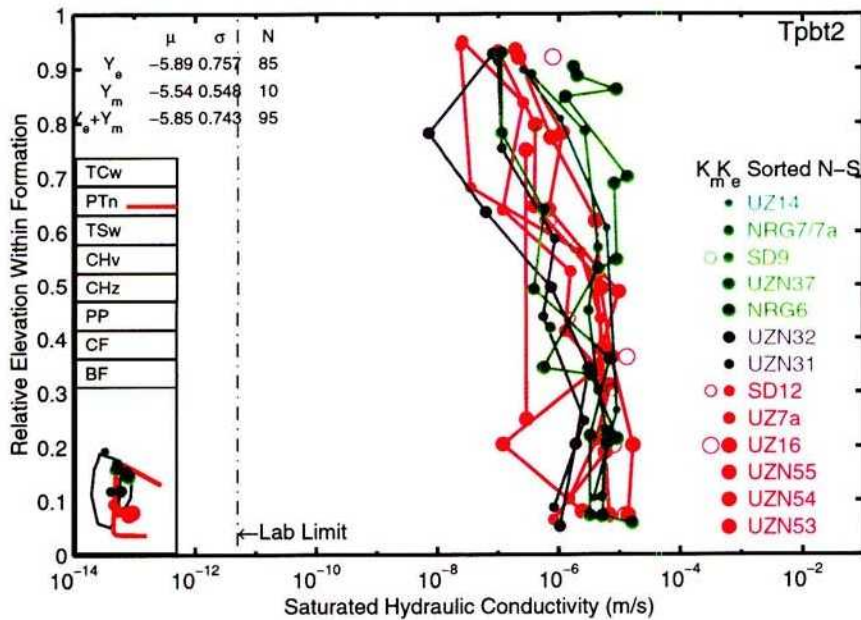
Figure 3-42: 9/17/97. All CNWRA-estimated and USGS-measured K_{sat} values in formation: (a) Tpp (**FormK_Tpp_c.eps**), and (b) Tpbt2 (**FormK_Tpbt2_c.eps**).
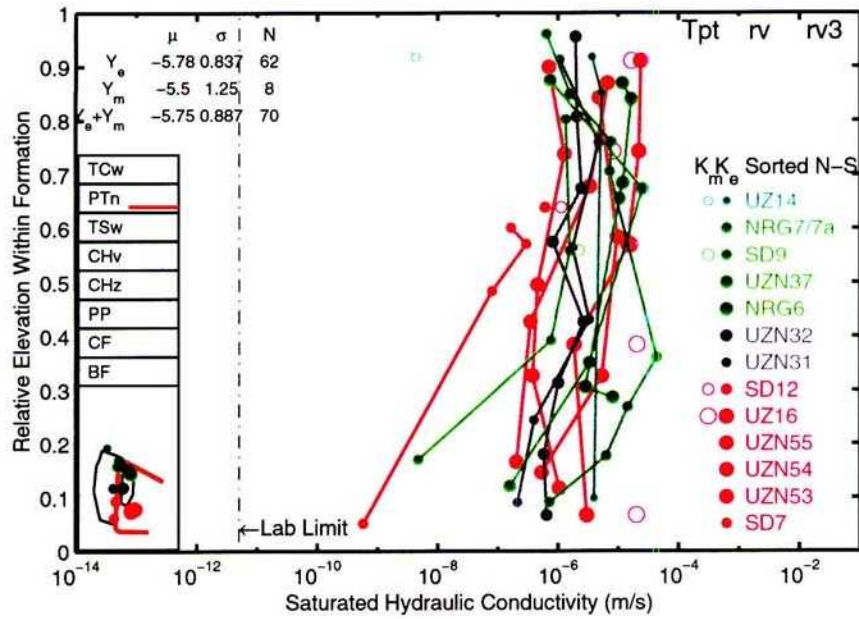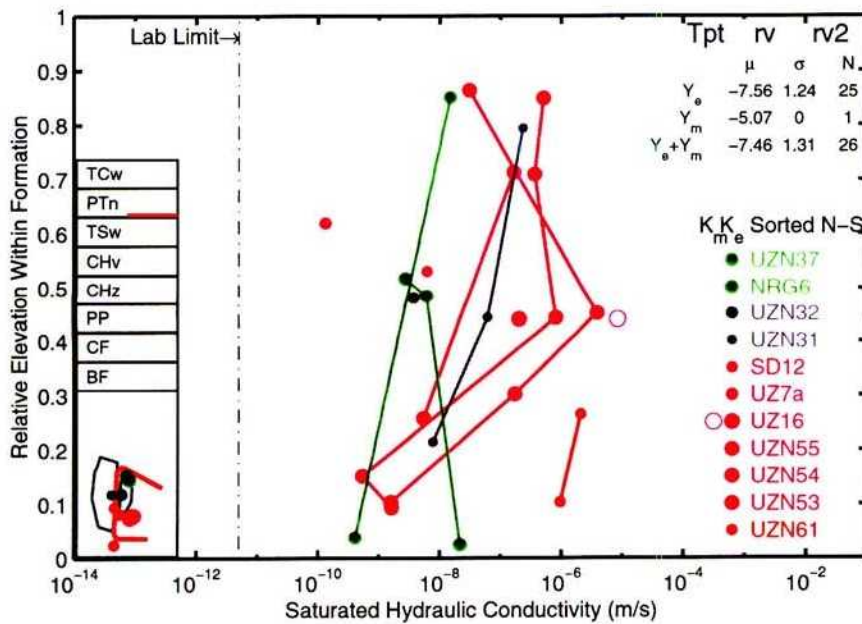
Figure 3-43: 9/17/97. All CNWRA-estimated and USGS-measured K_{sat} values in formation: (a) Tptrv3 (**FormK_Tptrv3_c.eps**), and (b) Tptrv2 (**FormK_Tptrv2_c.eps**).
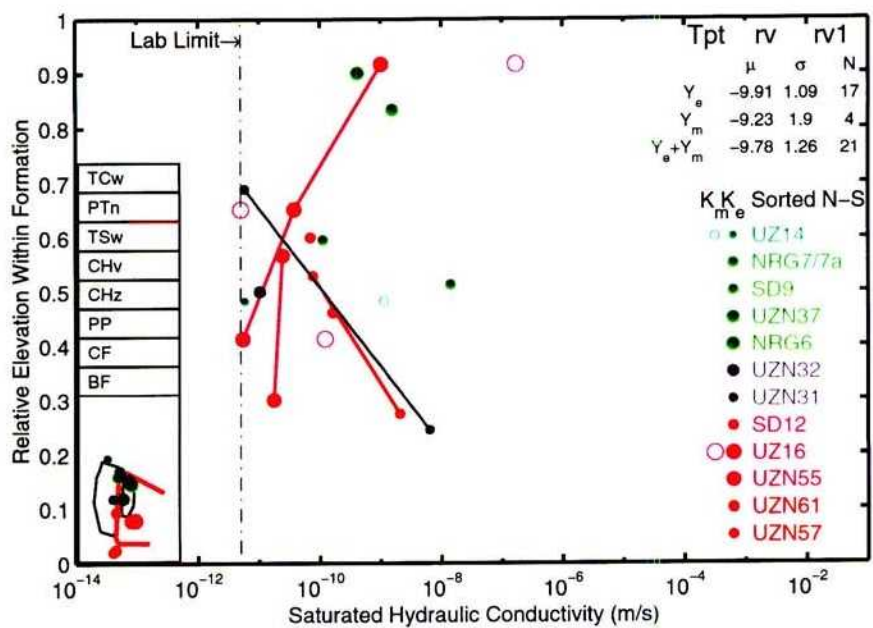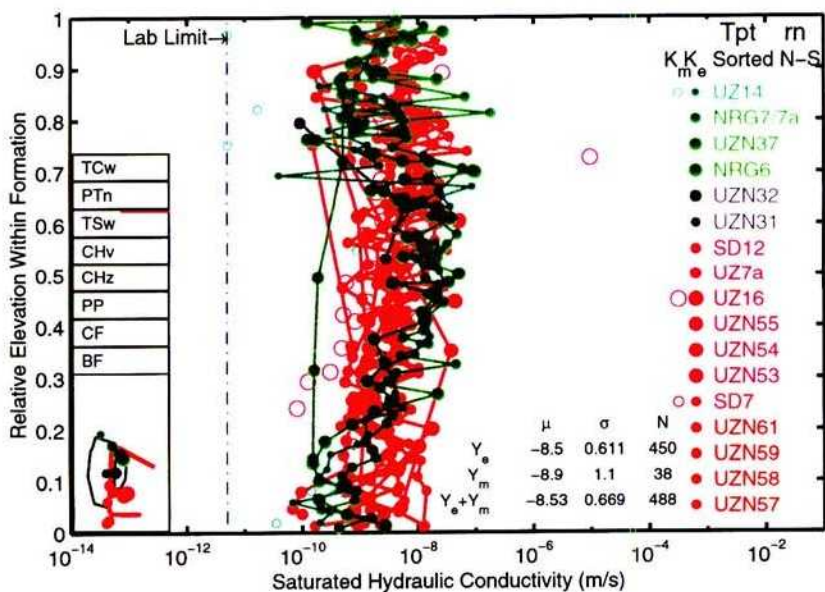
Figure 3-44: 9/17/97. All CNWRA-estimated and USGS-measured K_{sat} values in formation: (a) Tptrv1 (**FormK_Tptrv1_c.eps**), and (b) Tptrn (**FormK_Tptrn_c.eps**).
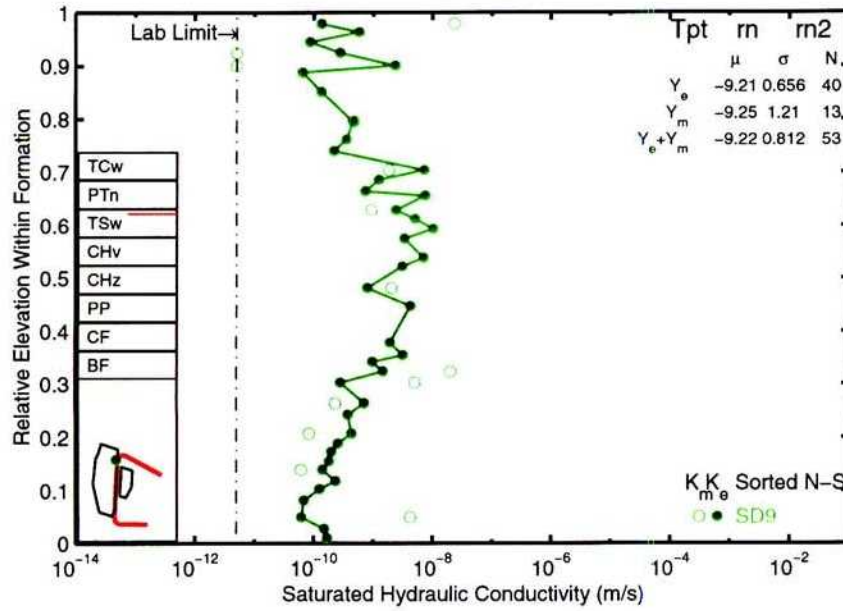
(a)
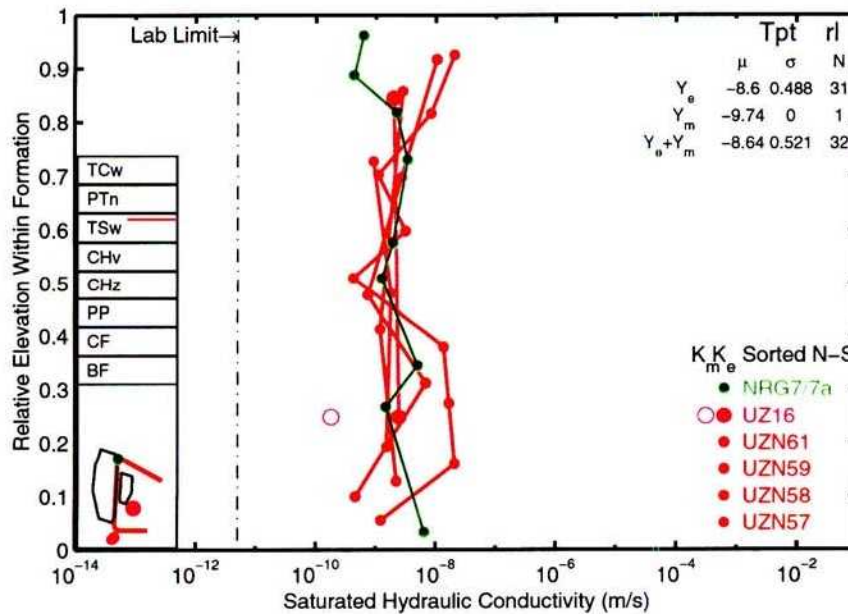
(b)

Figure 3-45: 9/17/97. All CNWRA-estimated and USGS-measured K_{sat} values in formation: (a) Tptrn2 (**FormK_Tptrn2_c.eps**), and (b) Tptrl (**FormK_Tptrl_c.eps**).
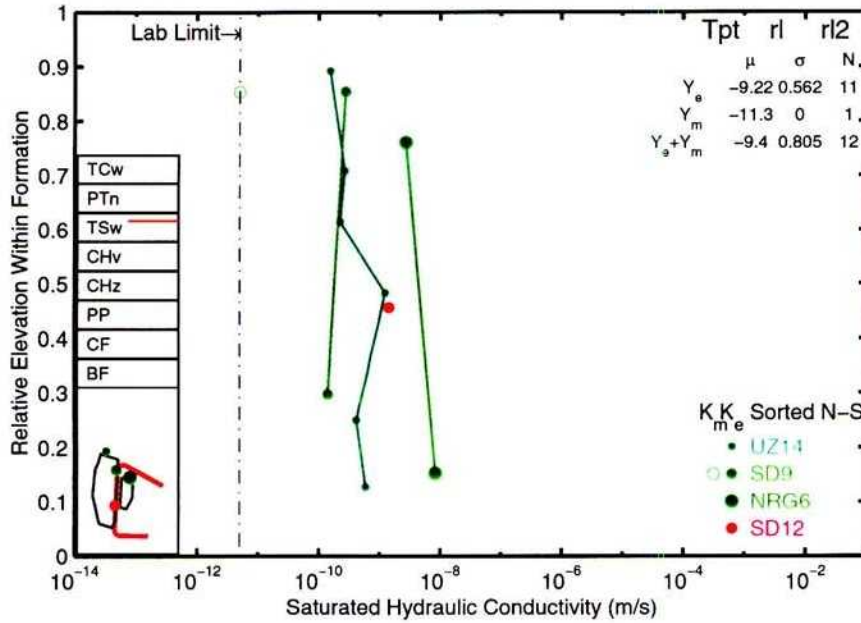
(a)
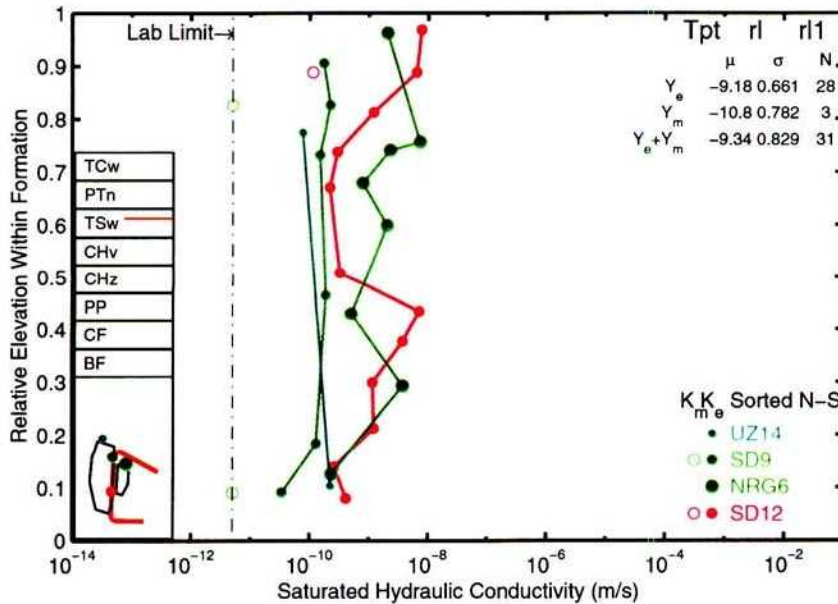
(b)

Figure 3-46: 9/17/97. All CNWRA-estimated and USGS-measured K_{sat} values in formation: (a) Tptrl2 (**FormK_Tptrl2_c.eps**), and (b) Tptrl1 (**FormK_Tptrl1_c.eps**).
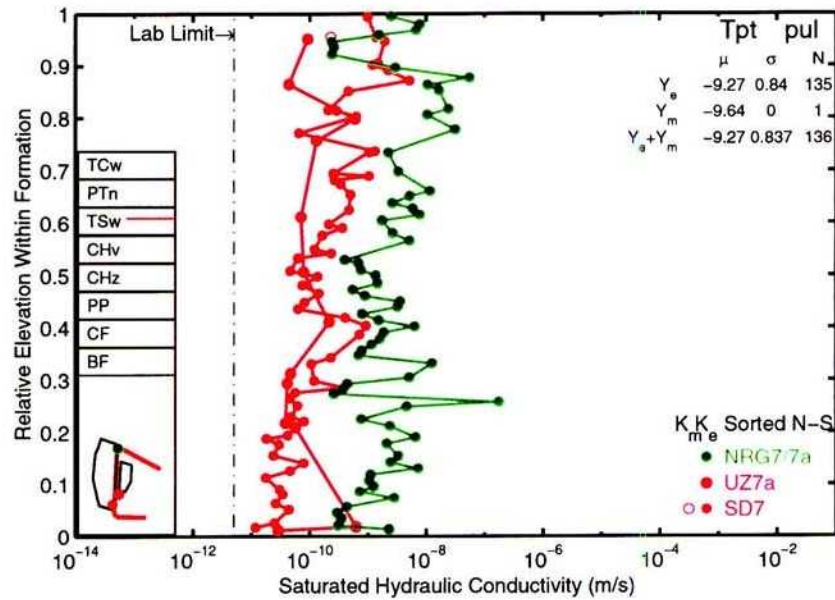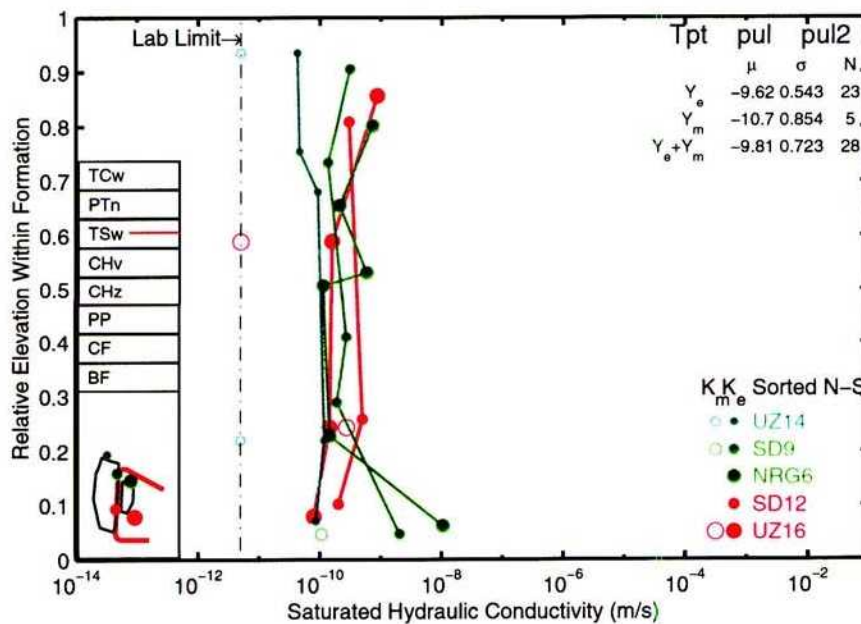
Figure 3-47: 9/17/97. All CNWRA-estimated and USGS-measured K_{sat} values in formation: (a) Tptpul (**FormK_Tptpul_c.eps**), and (b) Tptpul2 (**FormK_Tptpul2_c.eps**).
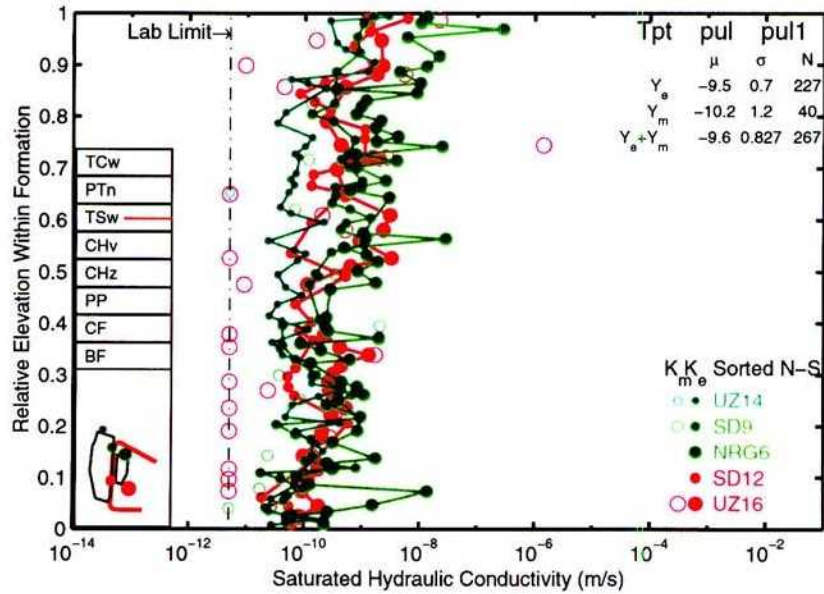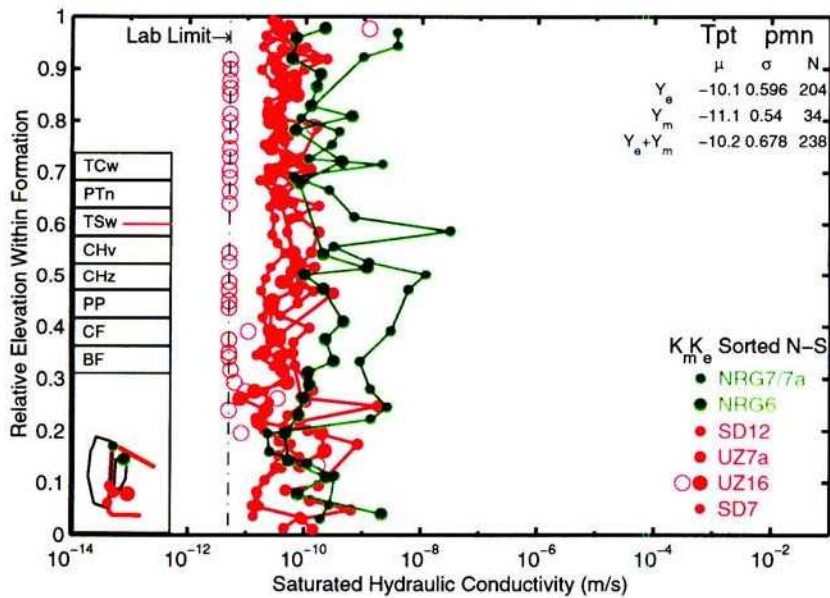
Figure 3-48: 9/17/97. All CNWRA-estimated and USGS-measured K_{sat} values in formation: (a) Tptpul1 (**FormK_Tptpul1_c.eps**), and (b) Tptpmn (**FormK_Tptpmn_c.eps**).
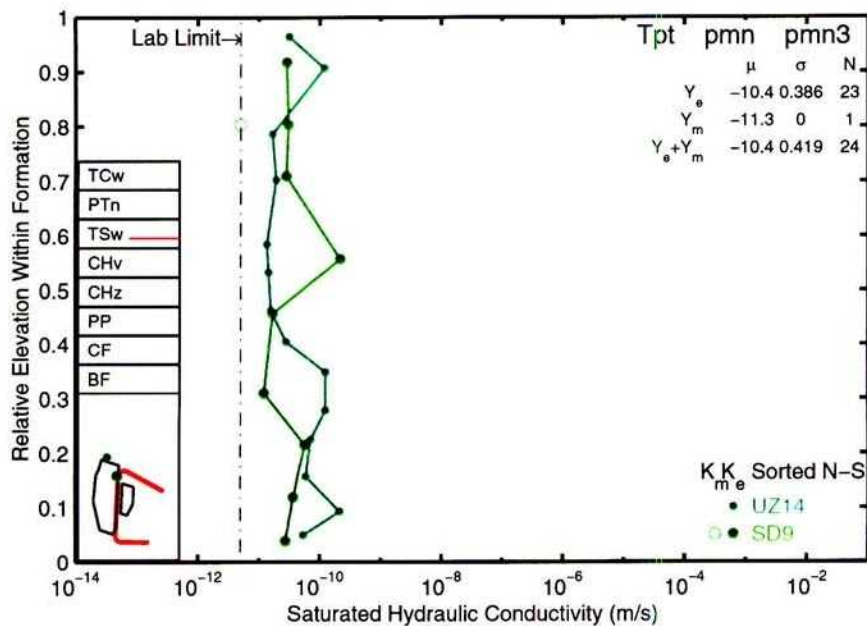
(a)
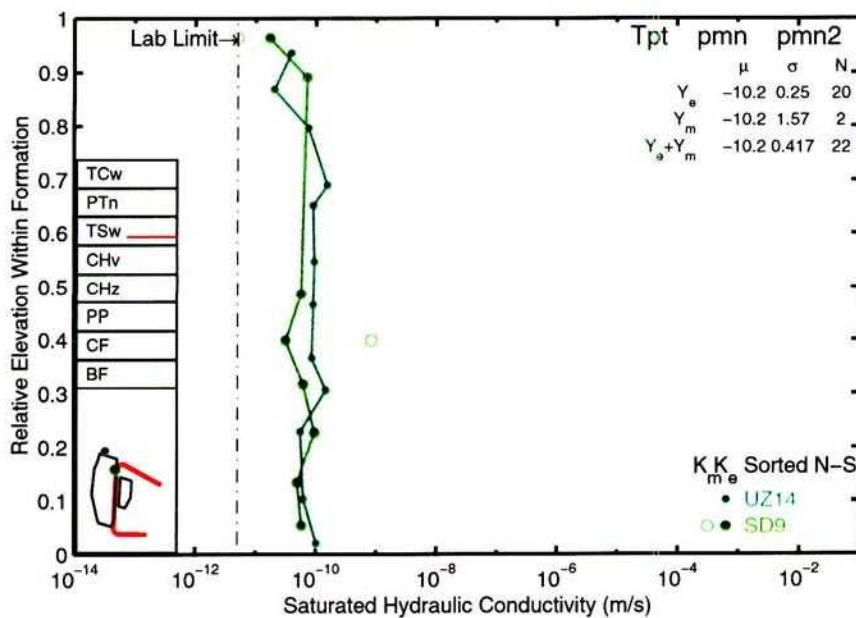
(b)

Figure 3-49: 9/17/97. All CNWRA-estimated and USGS-measured K_{sat} values in formation: (a) Tptpmn3 (**FormK_Tptpmn3_c.eps**), and (b) Tptpmn2 (**FormK_Tptpmn2_c.eps**).
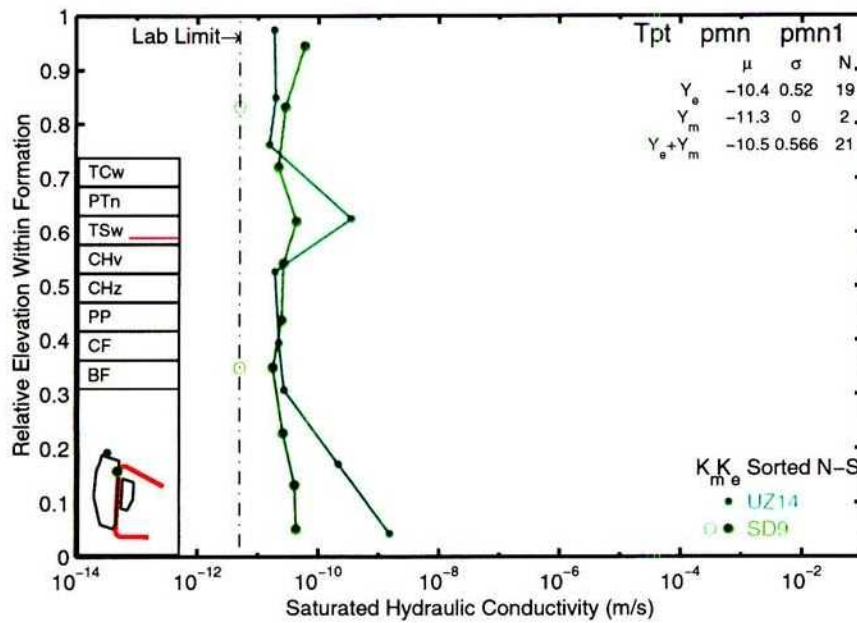
(a)
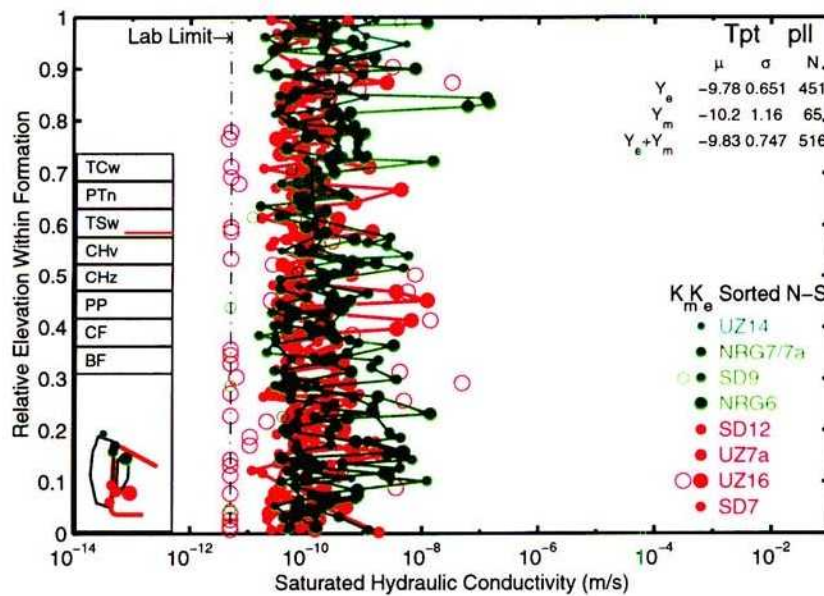
(b)

Figure 3-50: 9/17/97. All CNWRA-estimated and USGS-measured K_{sat} values in formation: (a) Tptpmn1 (**FormK_Tptpmn1_c.eps**), and (b) Tptpll (**FormK_Tptpll_c.eps**).
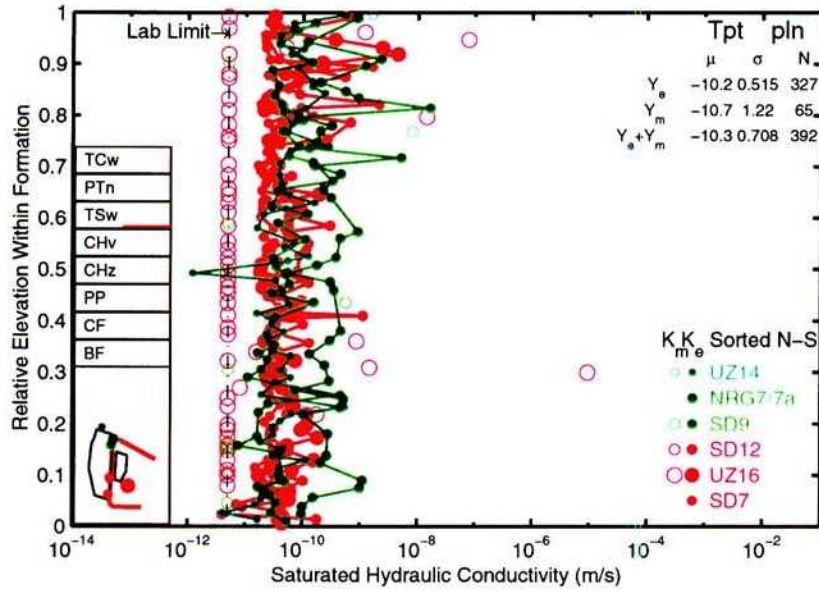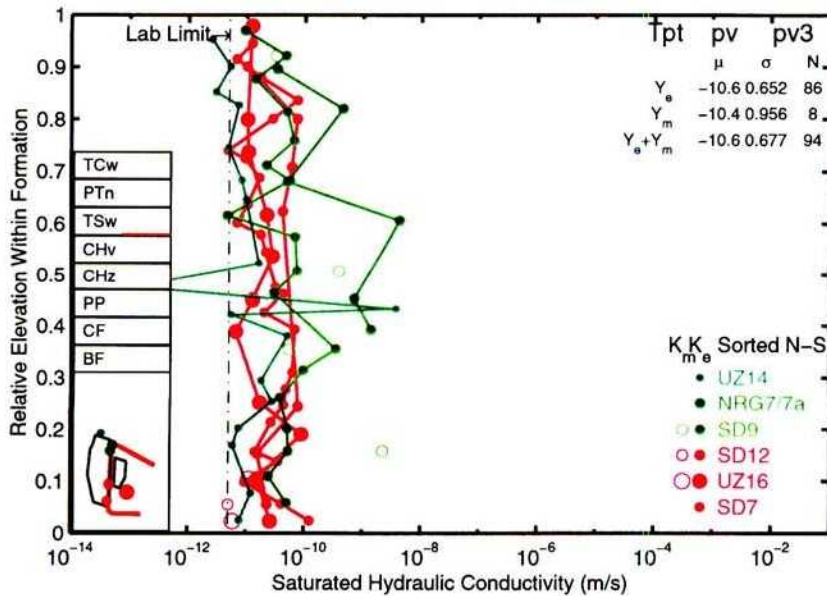
Figure 3-51: 9/17/97. All CNWRA-estimated and USGS-measured K_{sat} values in formation: (a) Tptpln (**FormK_Tptpln_c.eps**), and (b) Tptpv3 (**FormK_Tptpv3_c.eps**).
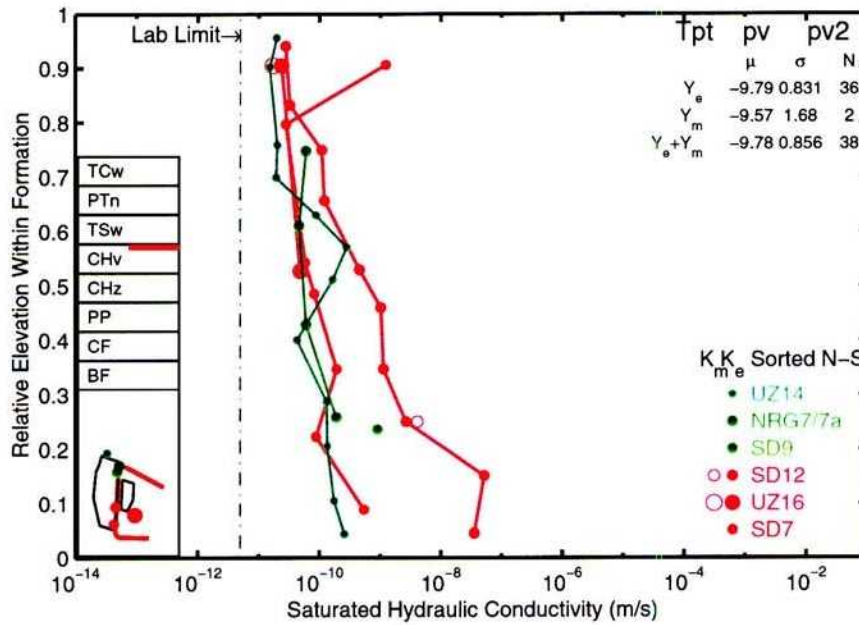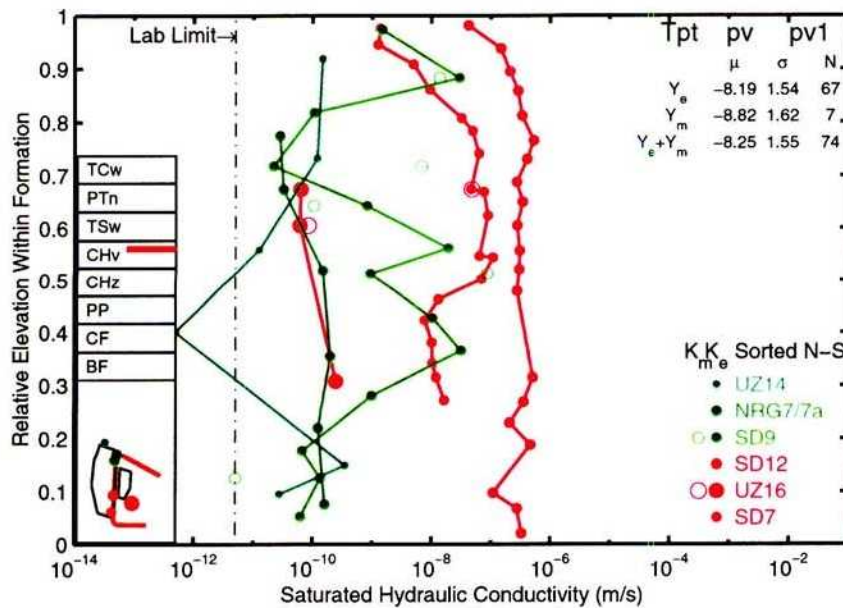
Figure 3-52: 9/17/97. All CNWRA-estimated and USGS-measured K_{sat} values in formation: (a) Tptpv2 (**FormK_Tptpv2_c.eps**), and (b) Tptpv1 (**FormK_Tptpv1_c.eps**).
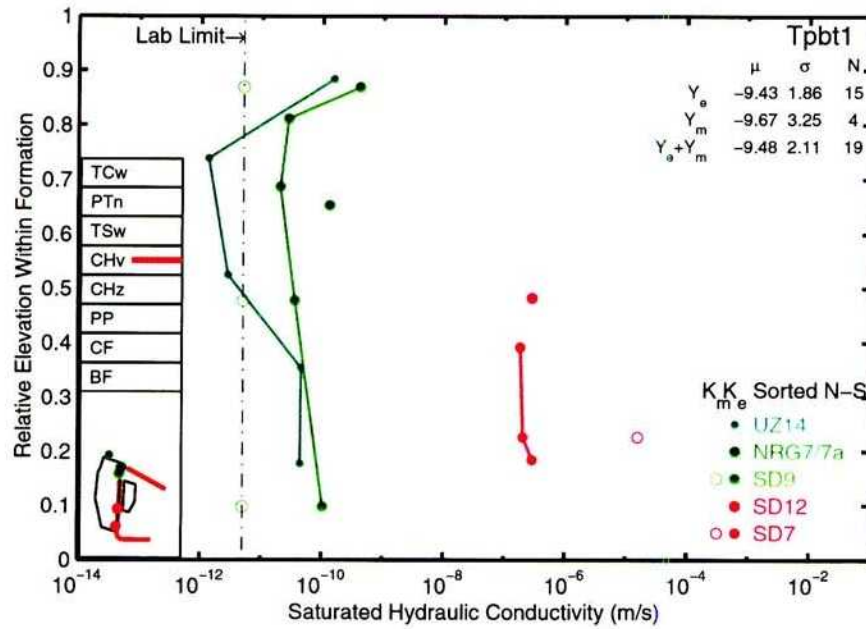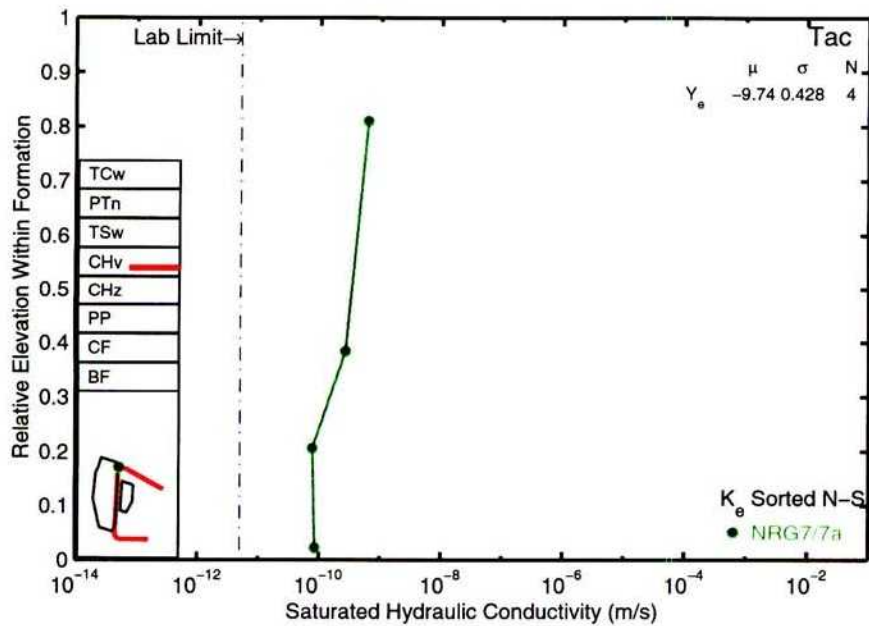
Figure 3-53: 9/17/97. All CNWRA-estimated and USGS-measured K_{sat} values in formation: (a) Tpbt1 (**FormK_Tpbt1_c.eps**), and (b) Tac (**FormK_Tac_c.eps**).
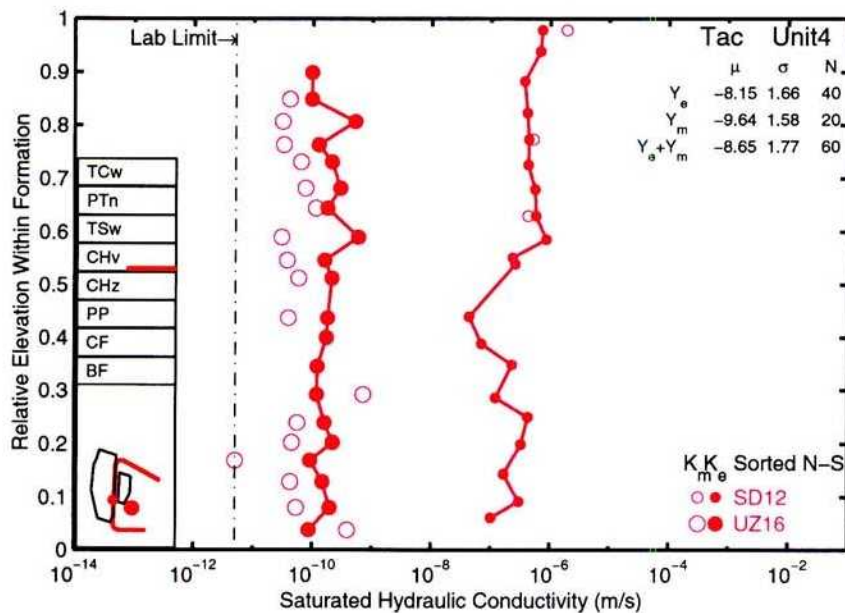
(a)
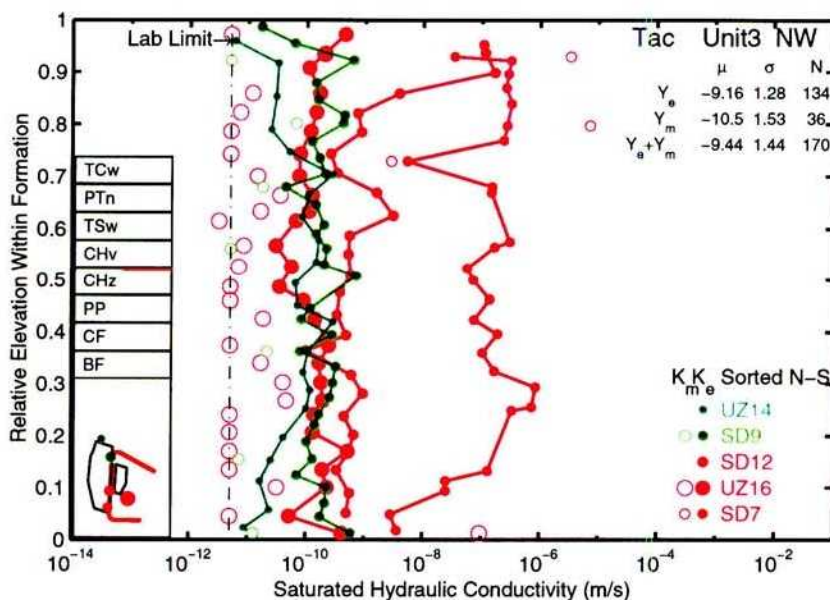
(b)

Figure 3-54: 9/17/97. All CNWRA-estimated and USGS-measured K_{sat} values in formation: (a) TacUnit4 (**FormK_TacUnit4_c.eps**), and (b) TacUnit3NW (**FormK_TacUnit3NW_c.eps**).
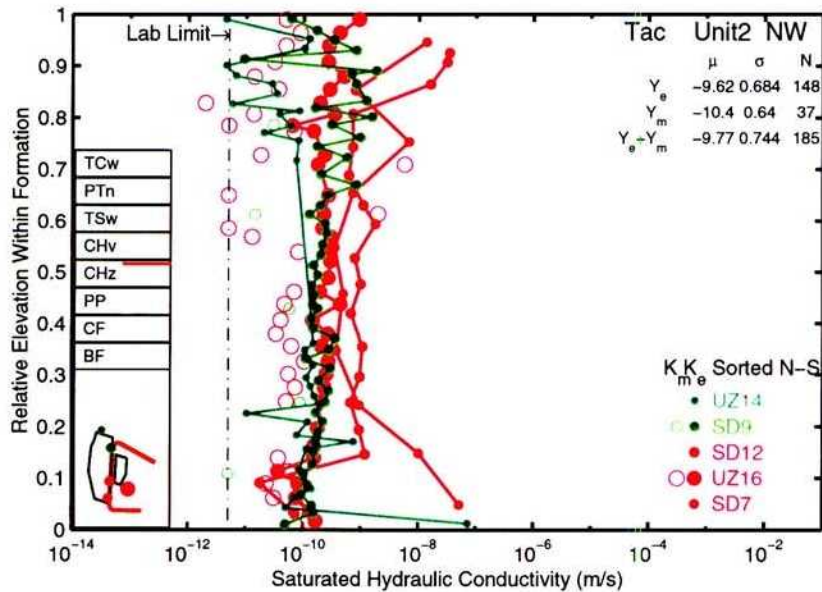
(a)
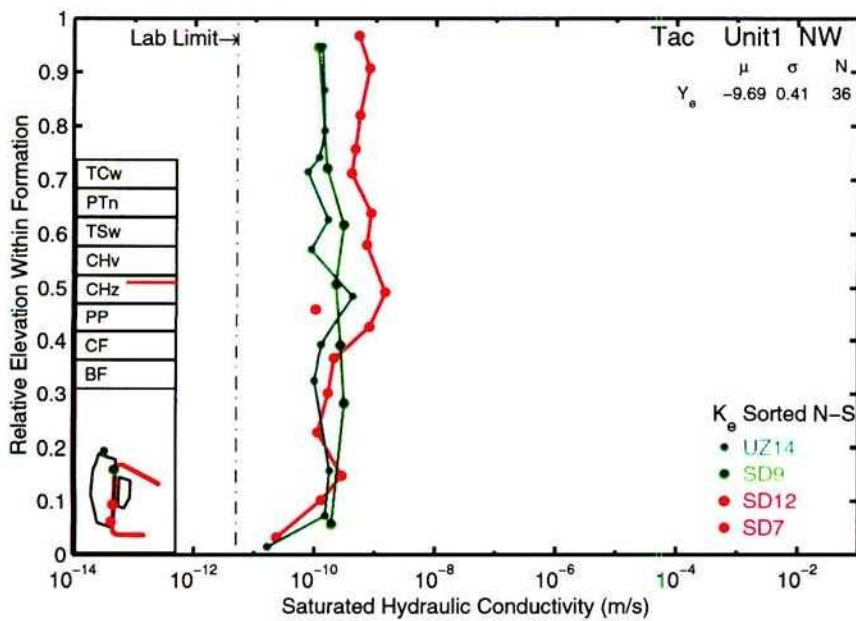
(b)

Figure 3-55: 9/17/97. All CNWRA-estimated and USGS-measured K_{sat} values in formation: (a) TacUnit2NW (**FormK_TacUnit2NW_c.eps**), and (b) TacUnit1NW (**FormK_TacUnit1NW-_c.eps**).
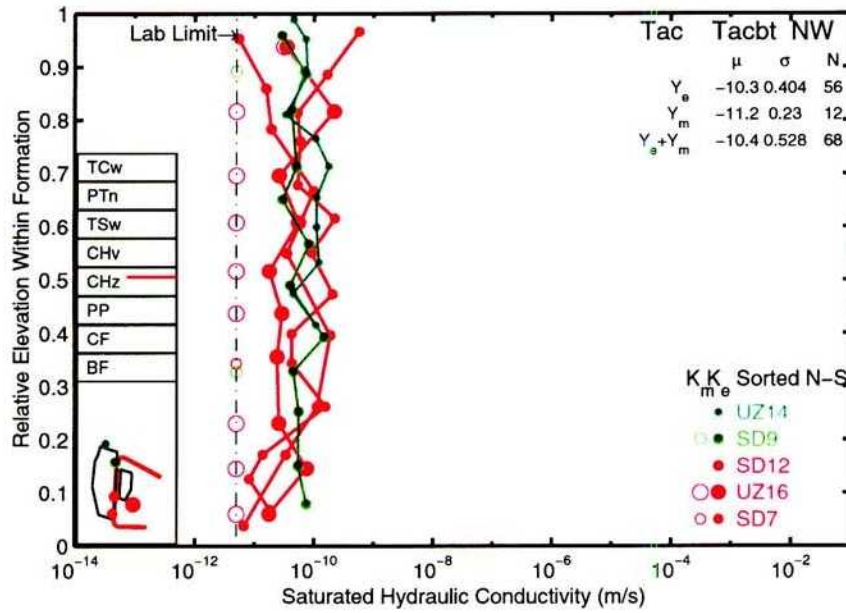
(a)
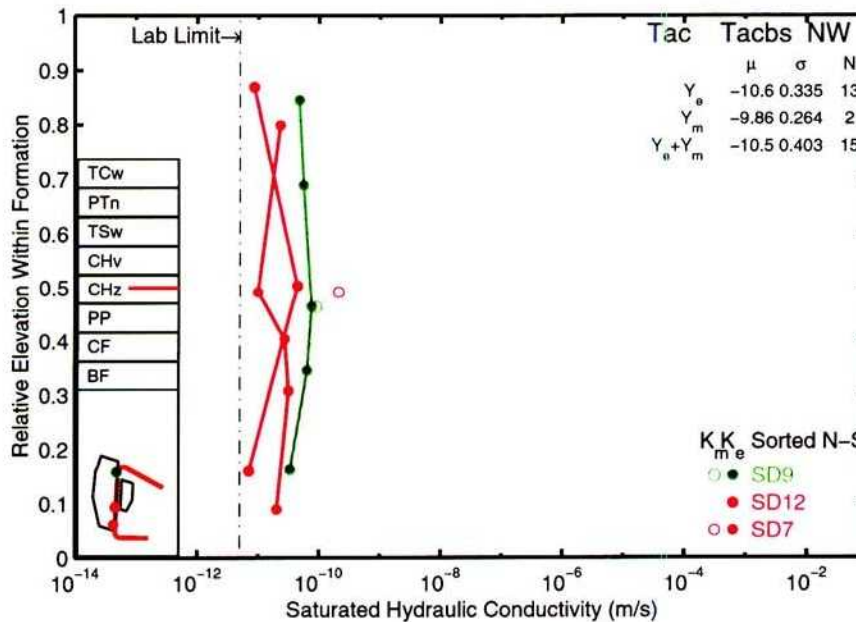
(b)

Figure 3-56: 9/17/97. All CNWRA-estimated and USGS-measured K_{sat} values in formation: (a) TacbtNW (**FormK_TacbtNW_c.eps**), and (b) TacbsNW (**FormK_TacbsNW_c.eps**).
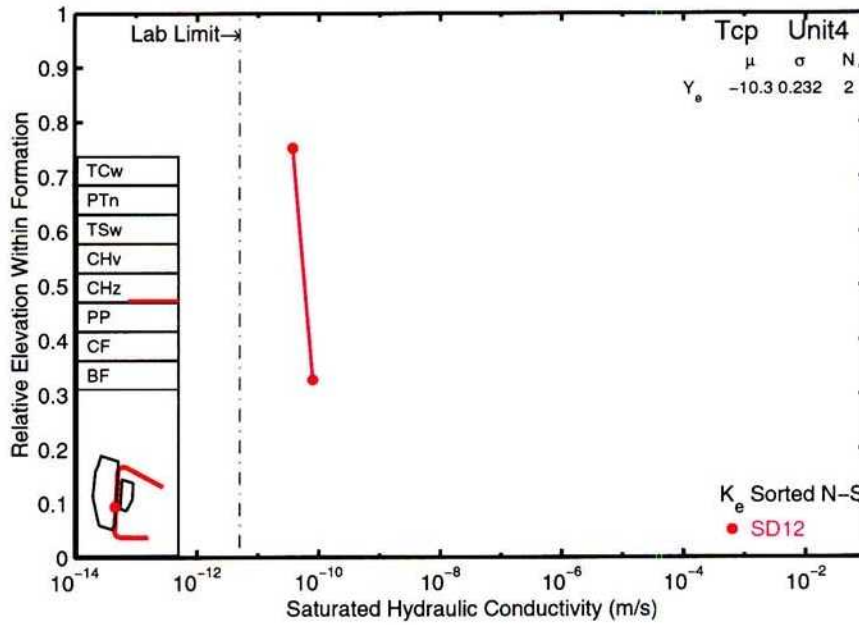
(a)
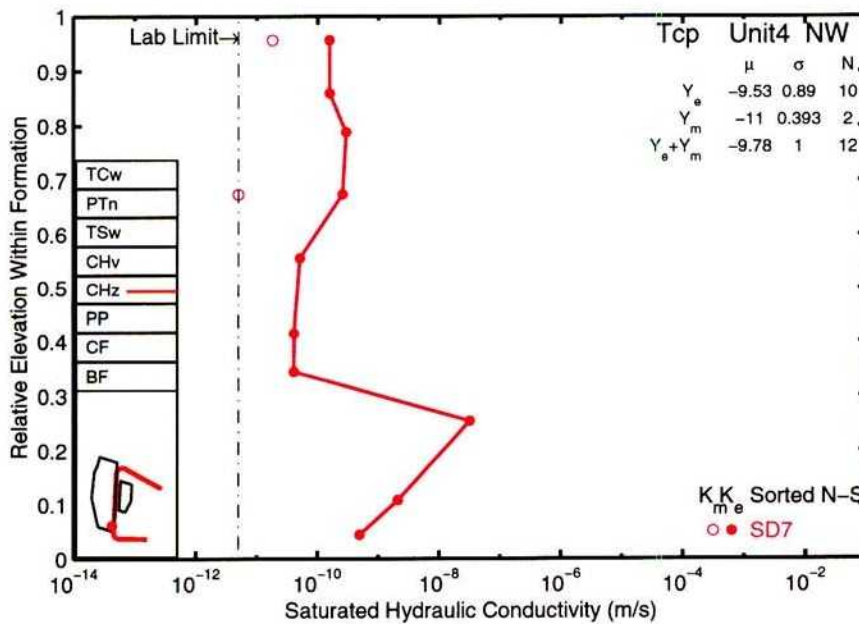
(b)

Figure 3-57: 9/17/97. All CNWRA-estimated and USGS-measured K_{sat} values in formation: (a) TcpUnit4 (**FormK_TcpUnit4_c.eps**), and (b) TcpUnit4NW (**FormK_TcpUnit4NW_c.eps**).
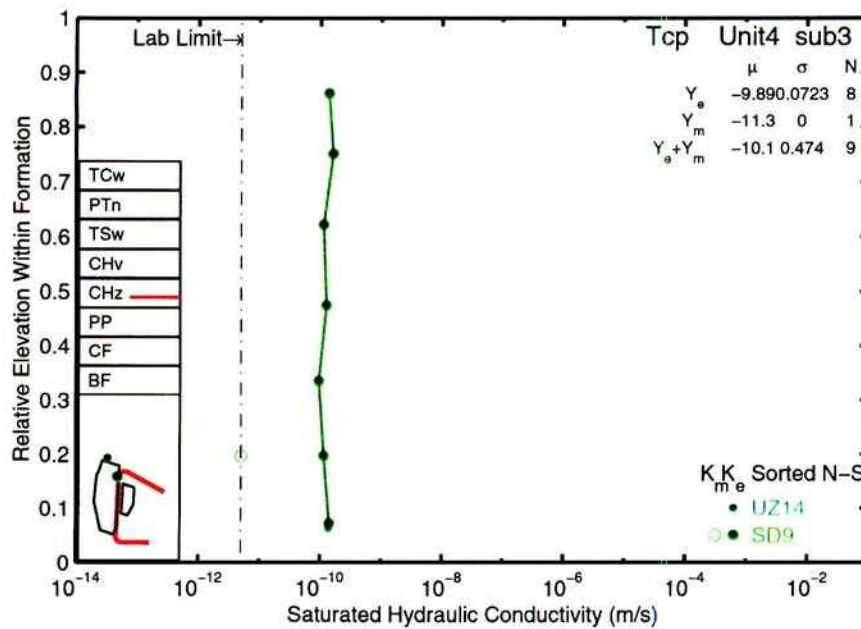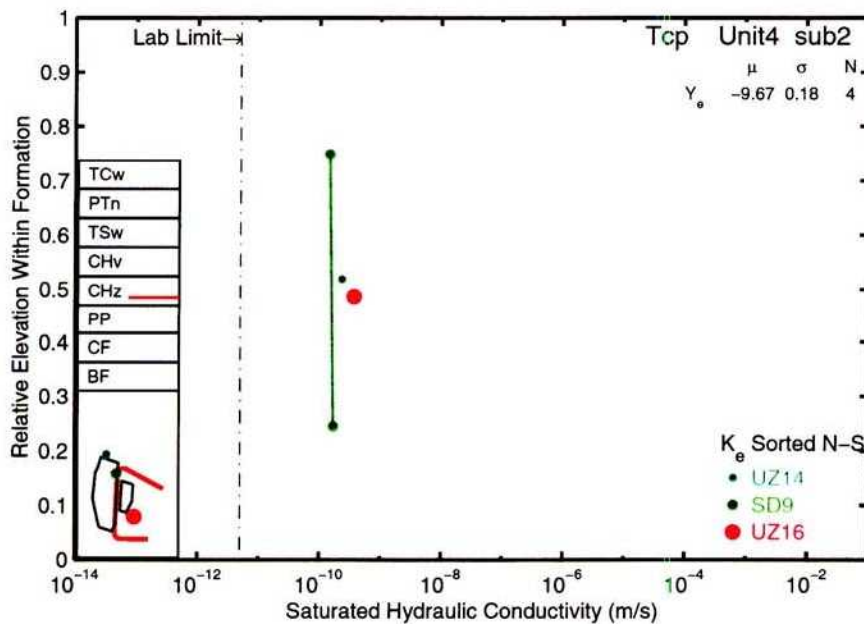
Figure 3-58: 9/17/97. All CNWRA-estimated and USGS-measured K_{sat} values in formation: (a) TcpUnit4sub3 (**FormK_TcpUnit4sub3_c.eps**), and (b) TcpUnit4sub2 (**FormK-_TcpUnit4sub2_c.eps**).
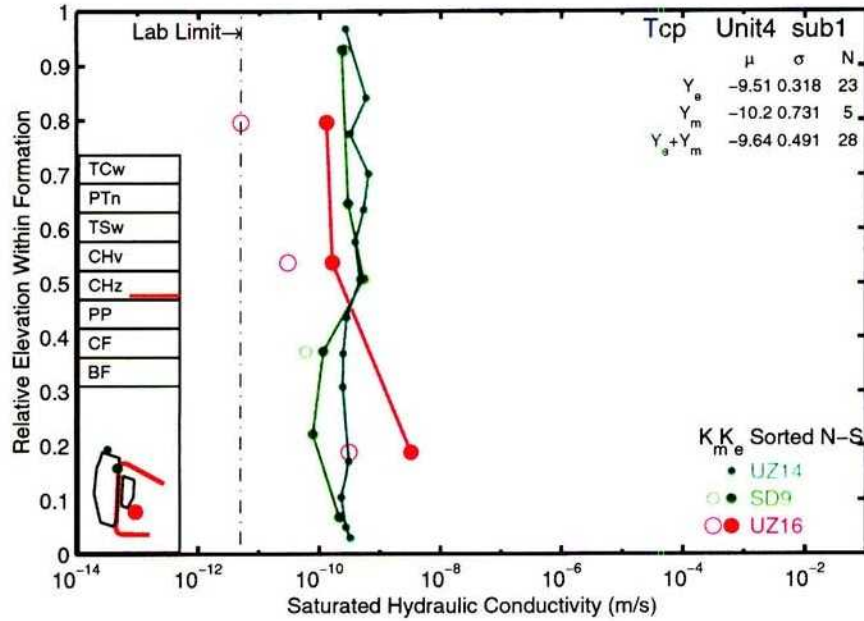
(a)
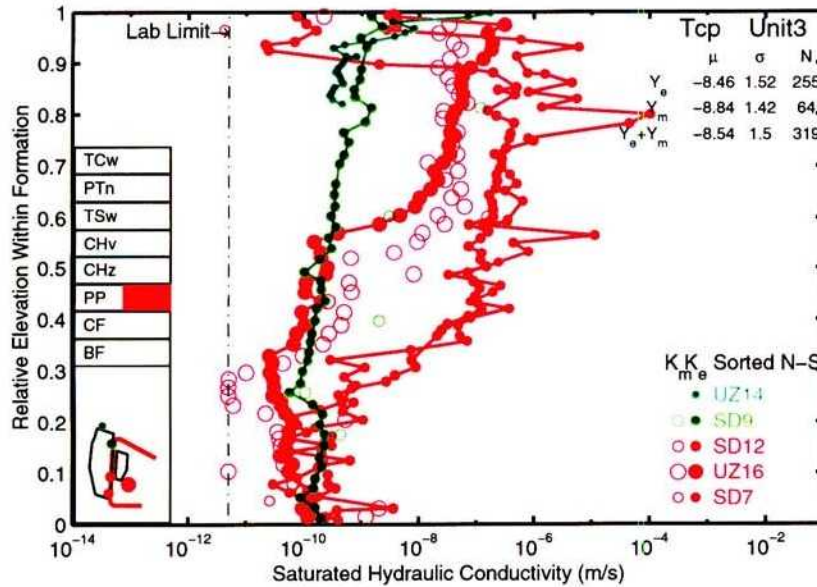
(b)

Figure 3-59: 9/17/97. All CNWRA-estimated and USGS-measured K_{sat} values in formation: (a) TcpUnit4sub1 (**FormK_TcpUnit4sub1_c.eps**), and (b) TcpUnit3 (**FormK_TcpUnit3_c.eps**).
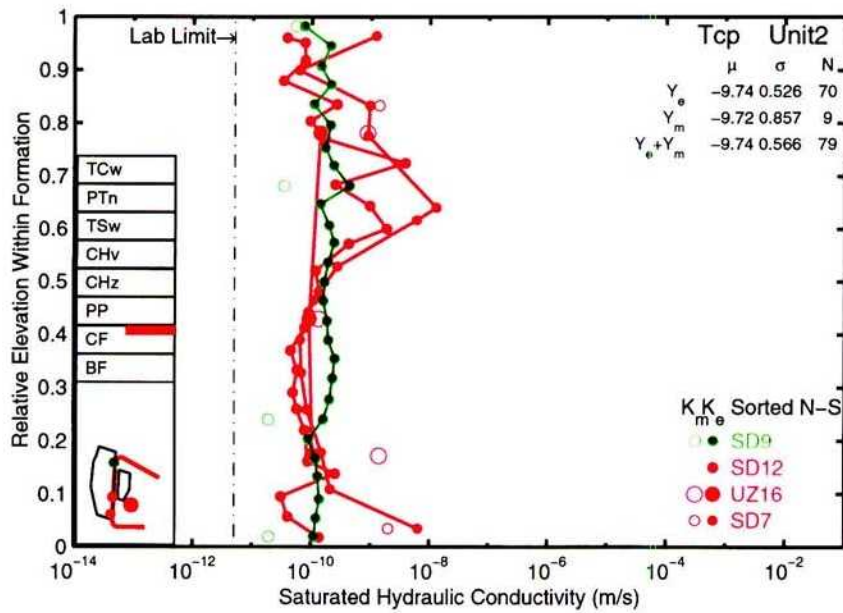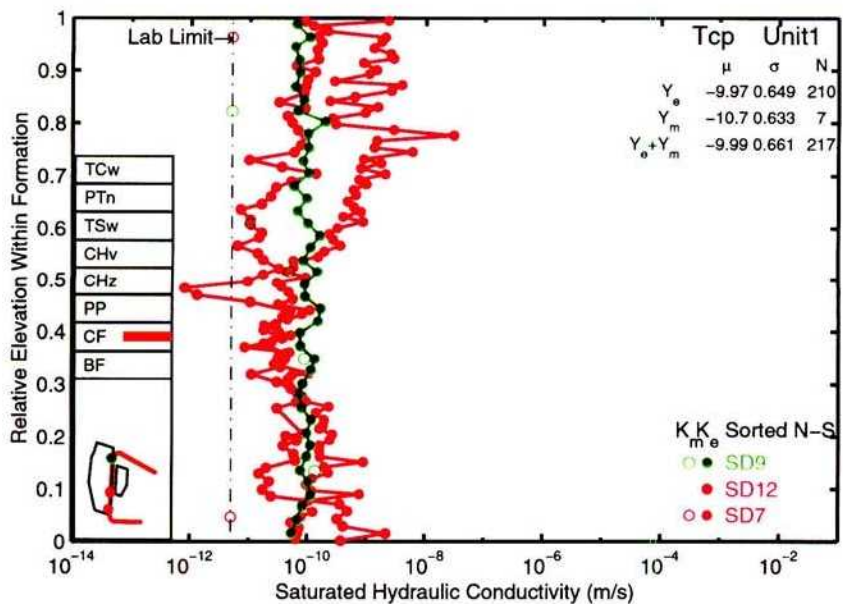
Figure 3-60: 9/17/97. All CNWRA-estimated and USGS-measured K_{sat} values in formation: (a) TcpUnit2 (**FormK_TcpUnit2_c.eps**), and (b) TcpUnit1 (**FormK_TcpUnit1_c.eps**).
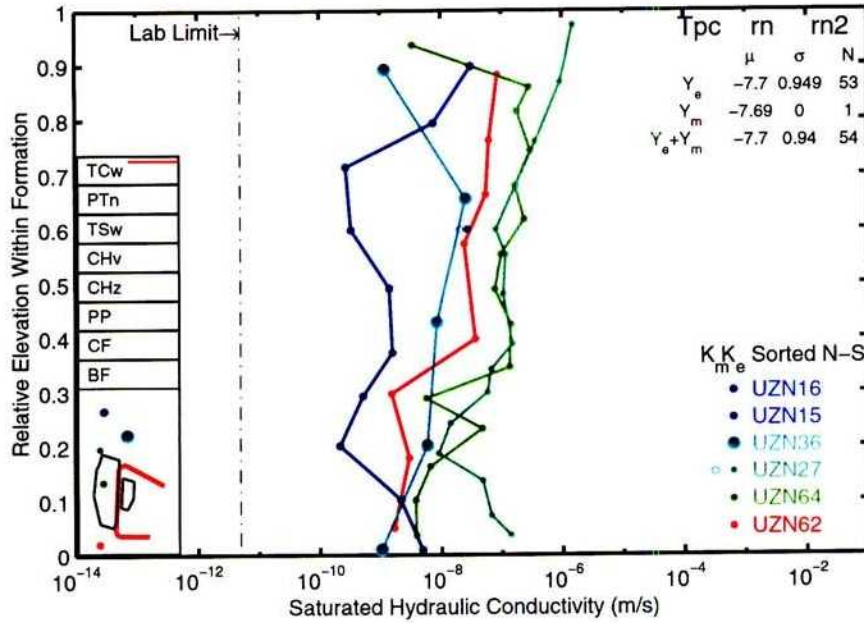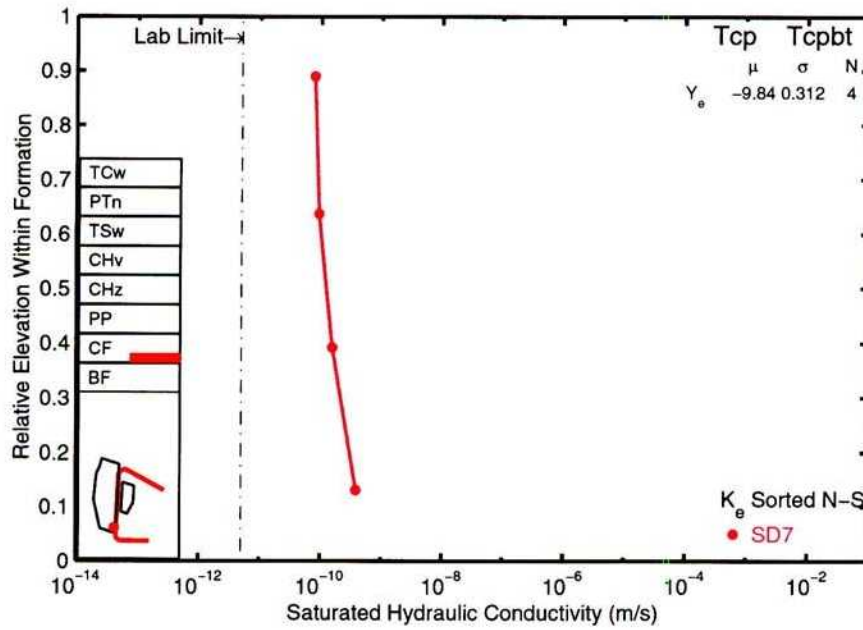
(a)
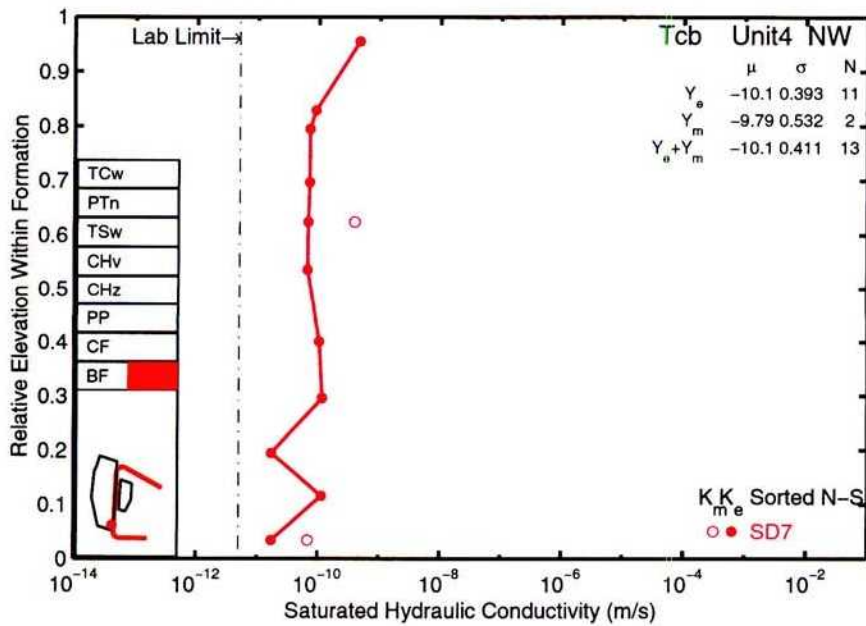
(b)

Figure 3-61: 9/17/97. All CNWRA-estimated and USGS-measured K_{sat} values in formation: (a) Tcpbt (**FormK_Tcpbt_c.eps**), and (b) TcbUnit4NW (**FormK_TcbUnit4NW_c.eps**).
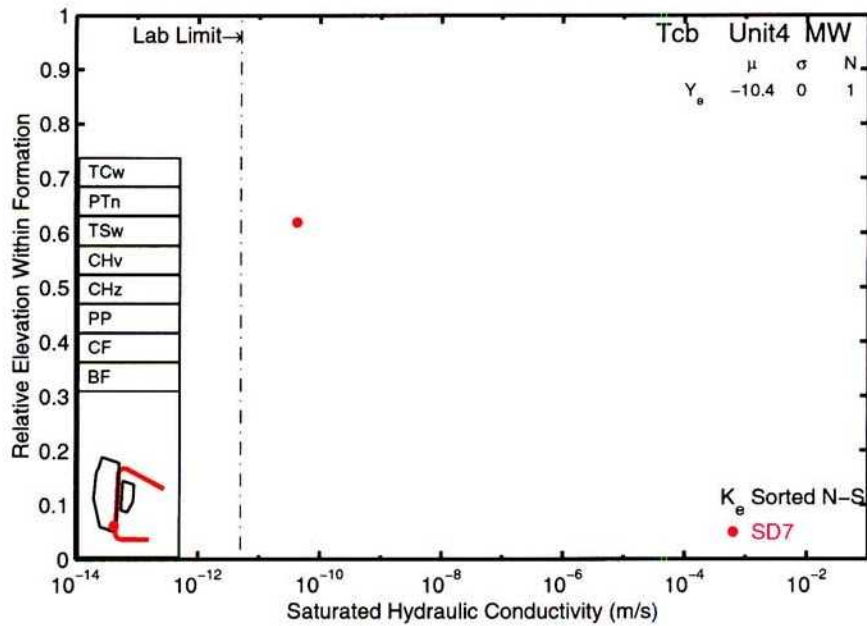
(a)
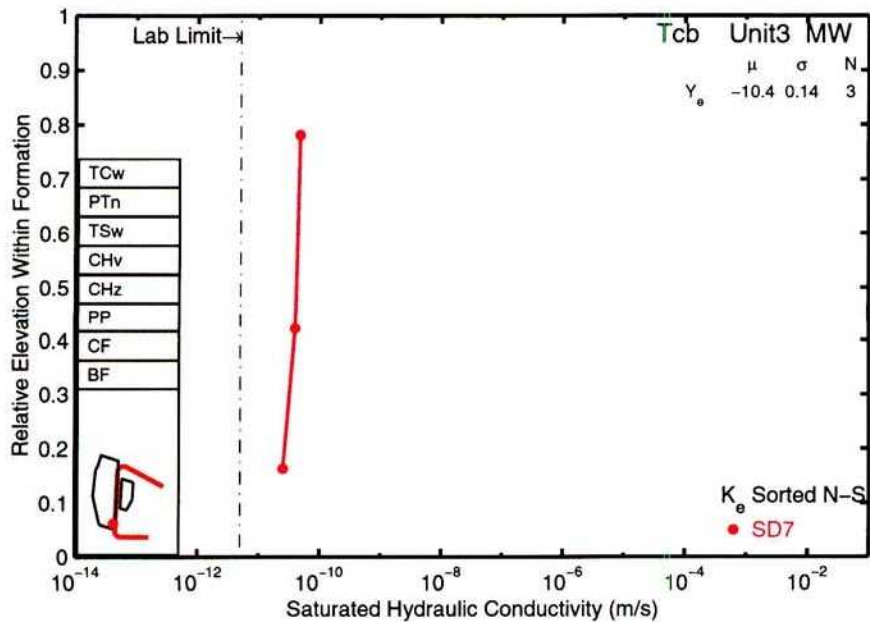
(b)

Figure 3-62: 9/17/97. All CNWRA-estimated and USGS-measured K_{sat} values in formation: (a) TcbUnit4MW (**FormK_TcbUnit4MW_c.eps**), and (b) TcbUnit3MW (**FormK-_TcbUnit3MW_c.eps**).
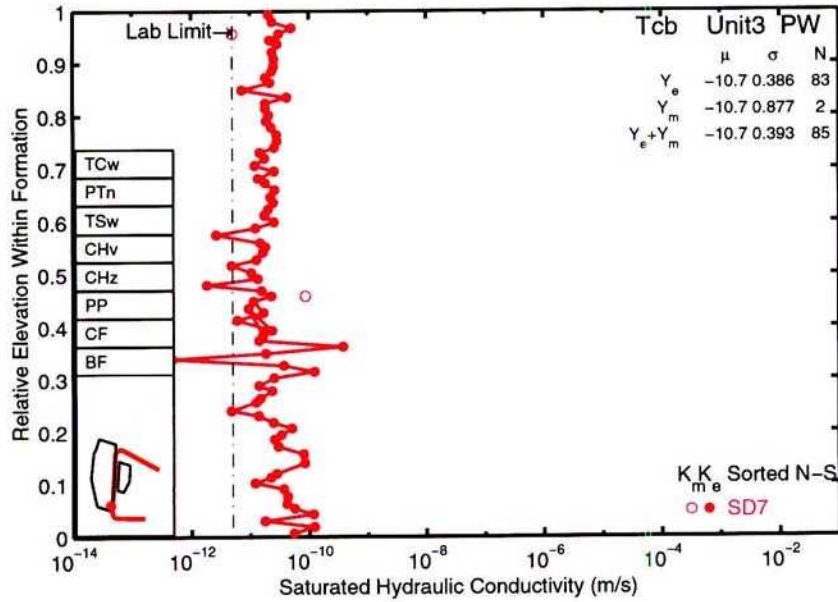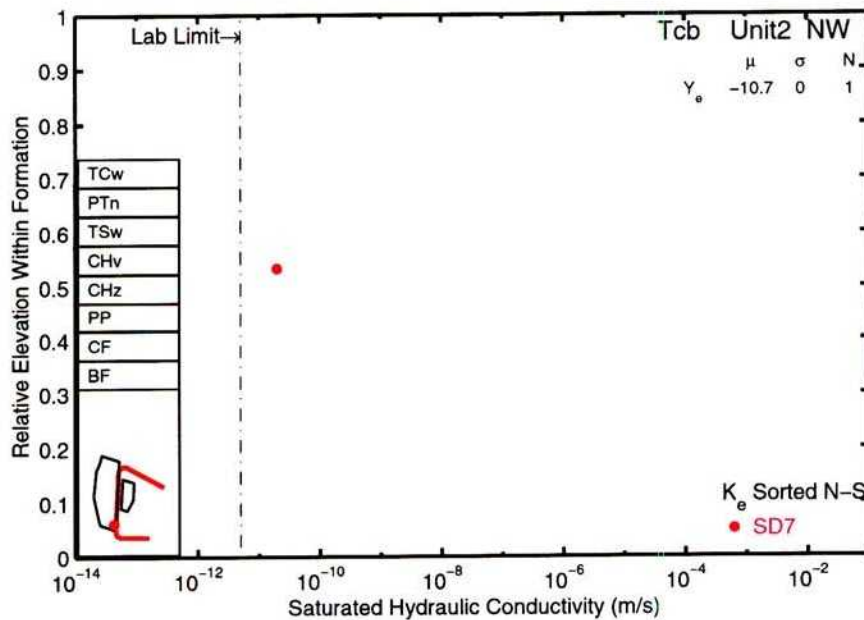
Figure 3-63: 9/17/97. All CNWRA-estimated and USGS-measured K_{sat} values in formation: (a) TcbUnit3PW (**FormK_TcbUnit3PW_c.eps**), and (b) TcbUnit2NW (**FormK_TcbUnit2NW-_c.eps**).
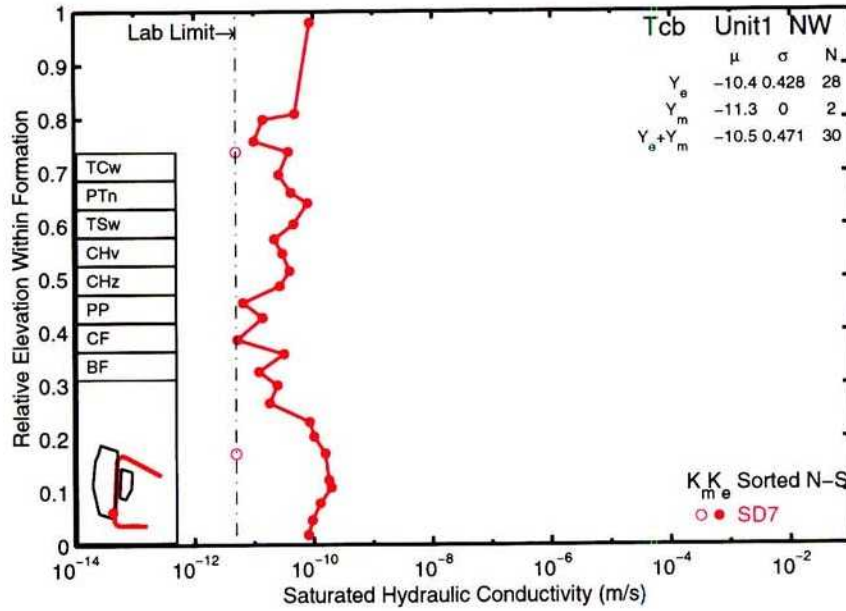
(a)
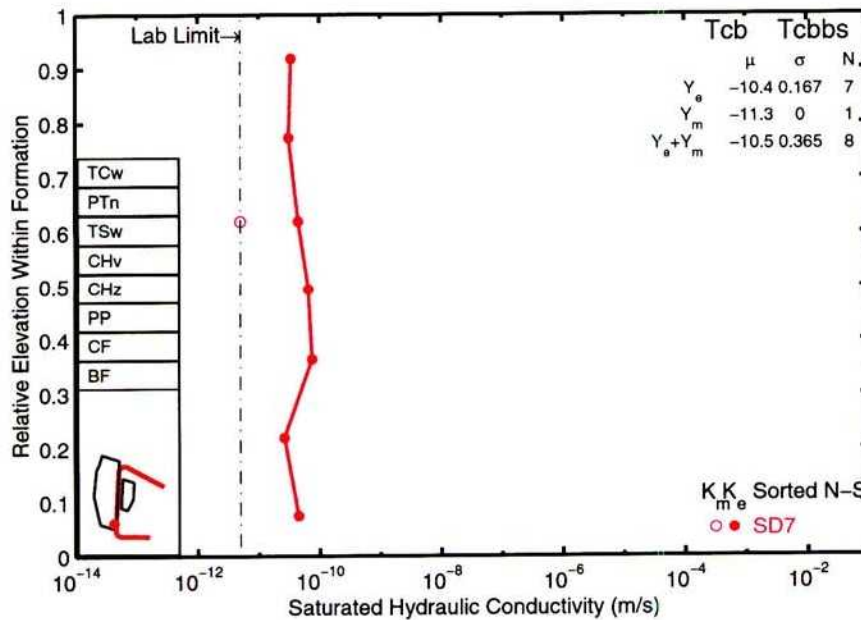
(b)

Figure 3-64: 9/17/97. All CNWRA-estimated and USGS-measured K_{sat} values in formation: (a) TcbUnit1NW (**FormK_TcbUnit1NW_c.eps**), and (b) Tcbbs (**FormK_Tcbbs_c.eps**).
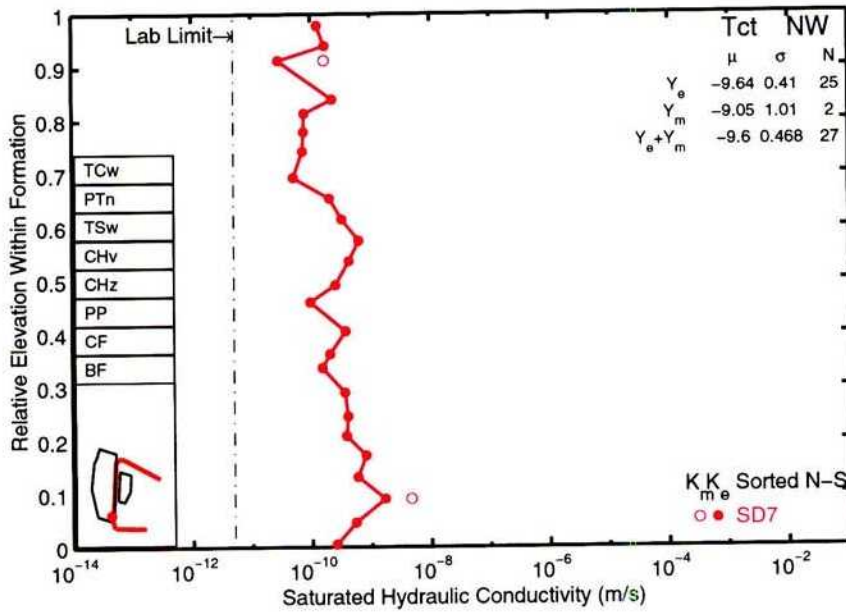
Figure 3-65: 9/17/97. All CNWRA-estimated and USGS-measured K_{sat} values in formation TctNW (**FormK_TctNW_c.eps**).

Table 3-1: Statistical description of $Y = \log_{10}[K_{sat}\ (m/s)]$ in TCw.

Formation			SAS Estimated			Measured			All		
Form	Zone1	Zone2	μ	σ	N	μ	σ	N	μ	σ	N
Tpc	rn	rn4	-9.497	0.769	19				-9.497	0.769	19
Tpc	rn	rn3	-7.541	0.566	62	-6.875	0	1	-7.53	0.568	63
Tpc	rn	rn2	-7.704	0.949	53	-7.693	0	1	-7.703	0.94	54
Tpc	rn	rn1	-8.064	1.31	17	-7.69	0	1	-8.043	1.27	18
Tpc	rl	rl2	-9.05	0.588	5				-9.05	0.588	5
Tpc	rl	rl1	-9.917	0.908	9				-9.917	0.908	9
Tpc	pul		-9.201	0.566	49	-8.985	1.53	2	-9.193	0.597	51
Tpc	pmn		-9.841	0.761	32				-9.841	0.761	32
Tpc	pll		-9.774	0.758	181	-11.14	0.48	14	-9.872	0.82	195
Tpc	pln	plnh	-10.15	0.662	169	-11.3	0	8	-10.2	0.69	177
Tpc	pln	plnc	-10.1	0.706	272	-10.99	0.523	17	-10.15	0.727	289
Tpc	pv	pv2	-9.93	0.994	54				-9.93	0.994	54

Table 3-2: Statistical description of $Y = \log_{10}[K_{sat} \ (m/s)]$ in PTn.

Formation			SAS Estimated			Measured			All		
Form	Zone1	Zone2	μ	σ	N	μ	σ	N	μ	σ	N
Tpc	pv	pv1	-7.851	1.43	76	-7.741	1.89	10	-7.839	1.48	86
Tpbt4			-6.947	1.41	20	-6.784	2.59	3	-6.925	1.53	23
Tpy			-7.97	1.36	85	-6.803	1.09	12	-7.826	1.38	97
Tpbt3			-6.99	0.804	55	-6.405	2	8	-6.915	1.03	63
Tpp			-5.903	0.66	156	-6.058	0.4	10	-5.913	0.648	166
Tpbt2			-5.885	0.757	85	-5.539	0.548	10	-5.849	0.743	95
Tpt	rv	rv3	-5.784	0.837	62	-5.503	1.25	8	-5.752	0.887	70
Tpt	rv	rv2	-7.556	1.24	25	-5.074	0	1	-7.46	1.31	26

Table 3-3: Statistical description of $Y = \log_{10}[K_{sat} \ (m/s)]$ in TSw.

Formation			SAS Estimated			Measured			All		
Form	Zone1	Zone2	μ	σ	N	μ	σ	N	μ	σ	N
Tpt	rv	rv1	-9.907	1.09	17	-9.233	1.9	4	-9.778	1.26	21
Tpt	rn		-8.5	0.611	450	-8.903	1.1	38	-8.532	0.669	488
Tpt	rn	rn2	-9.215	0.656	40	-9.255	1.21	13	-9.225	0.812	53
Tpt	rl		-8.603	0.488	31	-9.741	0	1	-8.639	0.521	32
Tpt	rl	rl2	-9.222	0.562	11	-11.3	0	1	-9.396	0.805	12
Tpt	rl	rl1	-9.178	0.661	28	-10.85	0.782	3	-9.339	0.829	31
Tpt	pul		-9.265	0.84	135	-9.638	0	1	-9.268	0.837	136
Tpt	pul	pul2	-9.617	0.543	23	-10.69	0.854	5	-9.808	0.723	28
Tpt	pul	pul1	-9.503	0.7	227	-10.17	1.2	40	-9.603	0.827	267
Tpt	pmn		-10.11	0.596	204	-11.07	0.54	34	-10.25	0.678	238
Tpt	pmn	pmn3	-10.41	0.386	23	-11.3	0	1	-10.44	0.419	24
Tpt	pmn	pmn2	-10.2	0.25	20	-10.19	1.57	2	-10.2	0.417	22
Tpt	pmn	pmn1	-10.38	0.52	19	-11.3	0	2	-10.47	0.566	21
Tpt	pll		-9.776	0.651	451	-10.21	1.16	65	-9.831	0.747	516
Tpt	pln		-10.22	0.515	327	-10.74	1.22	65	-10.31	0.708	392
Tpt	pv	pv3	-10.59	0.652	86	-10.43	0.956	8	-10.57	0.677	94

Table 3-4: Statistical description of $Y = \log_{10}[K_{sat} \ (m/s)]$ below TSw (CHnv, CHnz, PP, UCF, UBF).

Formation			SAS Estimated			Measured			All		
Form	Zone1	Zone2	μ	σ	N	μ	σ	N	μ	σ	N
Tpt	pv	pv2	-9.793	0.831	36	-9.574	1.68	2	-9.781	0.856	38
Tpt	pv	pv1	-8.193	1.54	67	-8.825	1.62	7	-8.253	1.55	74
Tpbt1			-9.426	1.86	15	-9.675	3.25	4	-9.479	2.11	19
Tac			-9.738	0.428	4				-9.738	0.428	4
Tac	Unit4		-8.153	1.66	40	-9.636	1.58	20	-8.648	1.77	60
Tac	Unit3	NW	-9.159	1.28	134	-10.47	1.53	36	-9.438	1.44	170
Tac	Unit2	NW	-9.615	0.684	148	-10.4	0.64	37	-9.772	0.744	185
Tac	Unit1	NW	-9.693	0.41	36				-9.693	0.41	36
Tac	Tacbt	NW	-10.27	0.404	56	-11.23	0.23	12	-10.44	0.528	68
Tac	Tacbs	NW	-10.56	0.335	13	-9.865	0.264	2	-10.47	0.403	15
Tcp	Unit4		-10.26	0.232	2				-10.26	0.232	2
Tcp	Unit4	NW	-9.528	0.89	10	-11.02	0.393	2	-9.777	1	12
Tcp	Unit4	sub3	-9.894	0.0723	8	-11.3	0	1	-10.05	0.474	9
Tcp	Unit4	sub2	-9.667	0.18	4				-9.667	0.18	4
Tcp	Unit4	sub1	-9.513	0.318	23	-10.23	0.731	5	-9.642	0.491	28
Tcp	Unit3		-8.465	1.52	255	-8.841	1.42	64	-8.54	1.5	319
Tcp	Unit2		-9.742	0.526	70	-9.723	0.857	9	-9.739	0.566	79
Tcp	Unit1		-9.965	0.649	210	-10.73	0.633	7	-9.99	0.661	217
Tcp	Tcpbt		-9.836	0.312	4				-9.836	0.312	4
Tcb	Unit4	NW	-10.13	0.393	11	-9.785	0.532	2	-10.08	0.411	13
Tcb	Unit4	MW	-10.38	0	1				-10.38	0	1
Tcb	Unit3	MW	-10.44	0.14	3				-10.44	0.14	3
Tcb	Unit3	PW	-10.68	0.386	83	-10.68	0.877	2	-10.68	0.393	85
Tcb	Unit2	NW	-10.7	0	1				-10.7	0	1
Tcb	Unit1	NW	-10.41	0.428	28	-11.3	0	2	-10.47	0.471	30
Tcb	Tcbbs		-10.37	0.167	7	-11.3	0	1	-10.48	0.365	8
Tct		NW	-9.641	0.41	25	-9.053	1.01	2	-9.598	0.468	27

Based on the set of figures, there appears to be little in the way of systematic spatial variability in the material properties, either vertically or horizontally. The systematic variability that is present is almost exclusively associated with the bedded units (e.g., PTn, CH). Examples of possible systematic spatial variability within a subzone include: (i) Tpy (north/south), (ii) Tpcpv1 (east/west), (iii) units transitional from nonzeolitic to zeolitic.

Bedded units also tend to have the largest unsystematic variability. This can be seen in the tables, in which most bedded units have standard deviations greater than 1 and most low-permeability units have standard deviations less than 1. Some of the lower variability in the low-permeability units is due to including those K_{sat} values at the laboratory limit for measured K_{sat} when calculating the statistical measures.

There is little point in breaking several of the zones into subzones, at least based on K_{sat}. Candidates for consolidation include:

- Tpcrn3 through Tpcrn1 (μ ranges from -7.53 through -8.04)

- Perhaps Tpcrl2 through Tpcpul (μ ranges from -9.05 through -9.92)

- Tpcmn through Tpcpv2 (μ ranges from -9.84 through -10.2)

- Tpp through Tptrv3 (μ ranges from -5.75 through -5.91)

- Tptrn through Tptrl1 (μ ranges from -8.53 through -9.40)

- Tptpul through Tptpull (μ ranges from -9.27 through -9.81)

- Tptpmn through Tptpv3 (μ ranges from -9.83 through -10.47)

- Tac Unit3 through Tac Unit1 (μ ranges from -9.44 through -9.77)

- Tacbt through Tacbs (μ ranges from -10.44 through -10.47)

- All Tcp Unit4 subzones (μ ranges from -9.64 through -10.26)

- Tcp Unit2 through Tcpbt (μ ranges from -9.74 through -9.99)

- All Tcb (μ ranges from -10.08 through -10.7)

9/23/97 Investigation of USGS retention properties. $\boxed{\text{SAS}}$

The USGS has only presented data for retention properties on core samples obtained from outcrops (Flint et al., 1996), to the best of my knowledge. As documented in the 1/22/97 entry, these data were entered electronically by A. Ramos from Appendix II in the report by Flint et al. (1996). I created two *Matlab* files, show_reten.m and ss_logpcap_eval.m, in *$HOME2/AmbientKTI/-3Ddata*, to investigate the retention properties.

The procedure Flint et al. (1996) followed was to use RETC for the data of each core sample individually, obtaining van Genuchten α and m, then regressing these into a global relationship. Thoughts on the Flint et al. (1996) procedure are discussed in the 9/21/96 entry, but in short my opinion is that it would be more fruitful to try to perform simultaneous regressions.

The idea behind today's investigation is to create a regression for all measured points simultaneously, using the intrinsic *Matlab* function fmins to minimize

$$u = \sum_{i=1}^{N} [\log_{10}(P_{mi}) - \log_{10}(P_{ei})]^2, \tag{3-16}$$

$$P_e = P_0(\theta^{-1/m} - 1)^{1-m}, \tag{3-17}$$

$$\log_{10}(P_{0i}) = a_0 + a_1 V_{1i} + a_2 V_{2i}, \tag{3-18}$$

$$m_i = b_0 + b_1 V_{3i} + b_2 V_{4i}. \tag{3-19}$$

where

$\quad u \quad$ is the objective function,

$\quad P_m \quad$ is measured capillary pressure,

$\quad P_e \quad$ is estimated capillary pressure,

$\quad m \quad$ is van Genuchten $m = 1 - 1/n$,

$\quad P_0 \quad$ is bubbling pressure (the reciprocal of van Genuchten α in the units used here),

$\quad V_{ji} \quad$ are the variables being regressed against, and

$\quad a_j, b_j \quad$ are the regression constants.

Flint et al. (1996) report pairs of volumetric water content (VWC) and capillary pressure (P_c) in their Appendix II. Data from two subsamples (TS47s, CH60s) were discarded, as properties (e.g., porosity) for the parent core samples were either not determined or were not reported in the electronic data set. Several VWC/P_c pairs had only one of the pair reported, or had a zero value for VWC; these pairs were also discarded.

The measured porosity of some core samples was not consistent with the VWC reported at

a P_c of 0.01 bar [note that Flint et al. (1996) assume full saturation at 0.01 bar]. Accordingly, for the purposes of regression, effective saturation was calculated by multiplying all VWC values for a sample by $0.999/VWC_0$, where VWC_0 is VWC at 0.01 bar; also, the porosity for each subsample was assumed to be VWC_0. Because of this inconsistency, the core-sample value for the difference between porosity at 65 and 105 °C was used as a candidate regression parameter, but not either porosity value individually.

All combinations of 1-parameter and 2-parameter fits for both P_0 and m were exhaustively checked for the best value of u. The 8 candidate regression variables, v, included VWC_0, bulk density at both 65 and 105 °C, particle density at both 65 and 105 °C, and change in porosity, bulk density, and particle density between 65 and 105 °C. The optimal fit provided by the best set and the worst set of parameters was not greatly different, differing by only about one-third, and all optimal fits were on the order of 10 (mean error for a measured/estimated P_0 pair is about one order of magnitude). The insensitivity to regression parameter is probably due to: (i) a high degree of correlation between the various parameters for each sample, and (ii) considerable noise in the data. A spot check for several combinations of parameters suggests that worse fits would be obtained for P_0 rather than $\log_{10}(P_0)$ and for $\log_{10}(m)$ rather than m.

9/24/97 Thoughts on assignment of layer properties.

The actual flow path of a water particle in a heterogeneous medium is likely to be quite tortuous. Under certain restrictive conditions, a heterogeneous porous medium can be replaced with an equivalent homogeneous porous medium. When saturated flow is 1D, and the flow is perpendicular to the heterogeneity (like a bundle of tubes), the flow is in parallel and the equivalent K_{sat} is the area-weighted arithmetic average of K_{sat} for the individual tubes. When saturated flow is 1D, and the flow is parallel to the heterogeneity (layers), the flow is in series and the equivalent K_{sat} is the length-weighted harmonic average of the individual tube K_{sat} s. If the heterogeneity relationship is more complicated, or the flow is not saturated, the picture muddies considerably and a unique K_{sat} cannot be determined in general.

When dealing with unsaturated media, the actual task is to determine equivalent values of K_{sat}, ε, α, m, and dispersivity so that a box containing the equivalent porous medium behaves like a box containing the heterogeneous medium, over the range of fluxes of interest. For YM, there is a tremendous upscaling that must be accomplished, from the core scale (5 cm on a side) to the formation scale (1 to 100 m thick by km^2).

A method that is useful for upscaling, and I believe is used in the petroleum industry, involves repeatedly averaging stochastically generated blocks of material, with each averaging occurring at a larger scale. At each scale, one creates the equivalent medium for 2, 4, or 8 blocks (depending on dimensionality). Averaging is typically performed for steady state conditions.

In the most rigorous approach, one would create a series of simulations with the original medium. For YM conditions, each simulation would presumably have 8 or more blocks, pressure conditions imposed at top and bottom, and no-flow conditions on the vertical sides (allowing lateral flow within the domain but not between averaging blocks). The equivalent properties would then be found by matching the flux and travel time results for each of the boundary conditions. It seems to me that the best that one could hope for would be to end up with pressure matches for the top and bottom of the formation and arbitrary variation in between.

It seems that one might do well trying to obtain an equivalent porous medium composed of several distinct media with different volumetric fractions; the distinct media might be preselected, with the job becoming obtaining the volumetric fractions. A first approach to picking media might be to: (i) determine the porosity distribution (for example) of a layer, (ii) pick out say 8 quantiles for porosity, and (iii) assign mean values for the other properties in each quantile.

In the case of YM, my feeling is that heterogeneity has much smaller correlation lengths in the vertical than in the horizontal, particularly for bedded tuffs. Welded tuffs should be almost isotropic at a small scale.

I think that an approach with merit would be to create many short columns, perhaps a correlation length in vertical dimension, pick a set of values of the medium properties for each end, and assume that the properties vary linearly/loglinearly between ends. The sets of properties should be appropriately correlated. The equivalent-medium properties can be obtained from building up a retention curve and a relative-permeability curve for the equivalent medium by averaging the contributions from each of the columns.

Actually, using the theory that lateral redistribution of pressure is efficient enough that pressure everywhere at the same relative height within a layer is approximately equal and gravity drainage is the primary condition of interest, a better approach would be to simply generate the arithmetic-mean response curves for each layer by imposing a gravity-drainage assumption for a series of capillary pressures and abstracting the mean responses. Arithmetic means should be taken of $k(P_c)$ and $\theta(P_c)$. It should be relatively efficient to calculate K_{sat}, α, and m for the effective medium using this approach.

9/29/97 More thoughts on assignment of layer properties.

A major component of generating layer properties by averaging core-sample properties is generating the set of random core-sample properties that are to be averaged. In order to generate properties, the statistical distribution of the properties must be known. However, these properties can only be estimated from the sampled values. According to Benjamin and Cornell (1970), in their section 4.1.2, the mean of a distribution estimated from samples is itself a random variable, normally distributed in the limit of many samples. Benjamin and Cornell (1970), in their section 4.3.2, further note that regression equations have uncertain coefficients as well.

The sample mean, $\bar{X}$, and sample variance, S^2, of n observations, X_i, from a random distibution are

$$\bar{X} = \frac{1}{n} \sum_{i=1}^{N} X_i, \tag{3-20}$$

$$S^2 = \frac{1}{n-1} \sum_{i=1}^{N} (X_i - \bar{X}). \tag{3-21}$$

The expected value and variance of $\bar{X}$ are

$$\mathrm{E}[\bar{X}] = m_X, \tag{3-22}$$

$$\mathrm{Var}[\bar{X}] = \frac{\sigma_X^2}{n}, \tag{3-23}$$

where m_X and σ_X are the true mean and standard deviation of the underlying physical process. Note that the variance of $\bar{X}$ would include correlation terms if the observations were not mutually independent. The expected value and variance of S^2 are

$$\mathrm{E}[S^2] = \sigma_X^2, \tag{3-24}$$

$$\mathrm{Var}[S^2] = \frac{2\sigma_X^4}{n-1}, \tag{3-25}$$

where it is assumed that X is normally distributed when deriving the expression for $\mathrm{Var}[S^2]$.

The regression equations have the form

$$y_j = a + \sum_{i=1}^{N} b_i x_{ij} + \epsilon_j, \tag{3-26}$$

where y_j is the jth observation of the predicted variable y, the x_{ij} values represent observations of N predictor variables, and ϵ_j represents a normally distributed zero-mean noise. To estimate the

a and b_i constants, one chooses $\hat{a}$ and $\hat{b}_i$ such that the sum of squares, or

$$\sum_{j=1}^{M} \left[y_j - \left(\hat{a} + \sum_{i=1}^{N} \hat{b}_i x_{ij} \right) \right]^2, \tag{3-27}$$

is minimized by taking the derivative with respect to the coefficients, yielding

$$\sum_{j=1}^{M} 2 \left[y_j - \left(\hat{a} + \sum_{i=1}^{N} \hat{b}_i x_{ij} \right) \right] (-1) = 0, \tag{3-28}$$

$$\sum_{j=1}^{M} 2 \left[y_j - \left(\hat{a} + \sum_{i=1}^{N} \hat{b}_i x_{ij} \right) \right] (-x_{kj}) = 0, \tag{3-29}$$

where $k = 1, 2, \ldots, N$. The equations reduce to

$$M \left(\bar{y} - \hat{a} - \sum_{i=1}^{N} \hat{b}_i \bar{x}_i \right) = 0, \tag{3-30}$$

$$\sum_{j=1}^{M} y_j x_{kj} - \hat{a} \bar{x}_k - \sum_{i=1}^{N} \hat{b}_i x_{ij} x_{kj} = 0, \tag{3-31}$$

$$\bar{y} = \frac{1}{n} \sum_{j=1}^{M} y_i, \tag{3-32}$$

$$\bar{x}_k = \frac{1}{n} \sum_{j=1}^{M} x_{kj}, \tag{3-33}$$

and finally to

$$\hat{a} = \bar{y} - \sum_{i=1}^{N} \hat{b}_i \bar{x}_i, \tag{3-34}$$

$$\sum_{j=1}^{M} y_j x_{kj} - M \hat{a} \bar{x}_k - \sum_{i=1}^{N} \hat{b}_i x_{ij} x_{kj} = 0, \tag{3-35}$$

$$\bar{y} = \frac{1}{M} \sum_{j=1}^{M} y_j, \tag{3-36}$$

$$\bar{x}_k = \frac{1}{M} \sum_{j=1}^{M} x_{kj}. \tag{3-37}$$

Benjamin and Cornell (1970) note that the obvious estimator for σ^2, the assumed-constant variance of Y given x, is the average of the squared residuals. This turns out to be

$$s^2 = \hat{\sigma}^2 = \frac{1}{M - N - 1} \sum_{j=1}^{M} \left[y_j - \left(\hat{a} + \sum_{i=1}^{N} \hat{b}_i x_{ij} \right) \right]^2. \tag{3-38}$$

Further, when the sample size is sufficiently large, $N = 1$, the values of y_i are uncorrelated, and the values of y_i have the same variance,

$$B = \sum_{j=1}^{M} c_j y_j, \tag{3-39}$$

$$c_j = \frac{x_j - \bar{x}}{\sum_{j=1}^{M}(x_j - \bar{x})^2}, \tag{3-40}$$

$$E[B] = E\left[\sum_{j=1}^{M} c_j y_j\right] = \sum_{j=1}^{M} c_j E[y_j] = a \sum_{j=1}^{M} c_j + b \sum_{j=1}^{M} c_j x_j = b, \tag{3-41}$$

$$\mathrm{Var}[B] = \mathrm{Var}\left[\sum_{j=1}^{M} c_j y_j\right] = \sum_{j=1}^{M} c_j^2 \mathrm{Var}[y_j] = \mathrm{Var}[y_j]\frac{\sum_{j=1}^{M} x_j^2 - M\bar{x}}{(\sum_{j=1}^{M} x_j^2 - M\bar{x})^2} = \frac{s^2}{M s_X^2}, \tag{3-42}$$

$$\mathrm{Var}[A] = \mathrm{Var}[\bar{y} - b\bar{x}] = \frac{\mathrm{Var}[y_j]}{M} + \bar{x}^2 \mathrm{Var}[B] = \frac{s^2}{M}\left(1 + \frac{\bar{x}^2}{s_X^2}\right). \tag{3-43}$$

Expanding upon the procedure outlined in section 4.3.2 by Benjamin and Cornell (1970), the corresponding estimators for two-variable regression equations are

$$B_1 = \frac{C_{10}C_{22} - C_{20}C_{12}}{C_{11}C_{22} - C_{12}C_{21}}, \tag{3-44}$$

$$B_2 = \frac{C_{20}C_{11} - C_{10}C_{21}}{C_{11}C_{22} - C_{12}C_{21}}, \tag{3-45}$$

$$C_{10} = \sum_{j=1}^{M}(x_{1j} - \bar{x}_1)y_j, \tag{3-46}$$

$$C_{20} = \sum_{j=1}^{M}(x_{2j} - \bar{x}_2)y_j, \tag{3-47}$$

$$C_{11} = \sum_{j=1}^{M}(x_{1j}^2 - \bar{x}_1^2) = M s_1^2, \tag{3-48}$$

$$C_{22} = \sum_{j=1}^{M}(x_{2j}^2 - \bar{x}_2^2) = M s_2^2, \tag{3-49}$$

$$C_{12} = C_{21} = \sum_{j=1}^{M}(x_{1j}x_{2j} - \bar{x}_1\bar{x}_2) = M s_{12} = M\rho s_1 s_2, \tag{3-50}$$

$$C_{11}C_{22} - C_{12}C_{21} = M^2 s_1^2 s_2^2 (1 - \rho^2), \tag{3-51}$$

where ρ is the correlation coefficient. The equations can be arranged to yield

$$B_1 = \sum_{j=1}^{M} \beta_{1j} y_j, \tag{3-52}$$

$$B_2 = \sum_{j=1}^{M} \beta_{2j} y_j, \tag{3-53}$$

$$\beta_{1j} = \frac{C_{22}(x_{1j} - \bar{x}_1) - C_{12}(x_{2j} - \bar{x}_2)}{M^2 s_1^2 s_2^2 (1 - \rho^2)}, \tag{3-54}$$

$$\beta_{2j} = \frac{C_{11}(x_{2j} - \bar{x}_2) - C_{21}(x_{1j} - \bar{x}_1)}{M^2 s_1^2 s_2^2 (1 - \rho^2)}. \tag{3-55}$$

Noting that

$$\sum_{j=1}^{M} \beta_{1j} = 0, \tag{3-56}$$

$$\sum_{j=1}^{M} \beta_{1j} x_{1j} = 1, \tag{3-57}$$

$$\sum_{j=1}^{M} \beta_{1j} x_{2j} = 0, \tag{3-58}$$

the corresponding variances are

$$\mathrm{Var}[B_1] = \mathrm{Var}[y_j] \sum_{j=1}^{M} \left(\frac{C_{22}(x_{1j} - \bar{x}_1) - C_{12}(x_{2j} - \bar{x}_2)}{C_{11}C_{22} - C_{12}C_{21}} \right)^2$$

$$= s^2 \frac{C_{22}}{C_{11}C_{22} - C_{12}C_{21}} = \frac{s^2}{M} \left[\frac{1}{s_1^2(1 - \rho^2)} \right], \tag{3-59}$$

$$\mathrm{Var}[B_2] = \mathrm{Var}[y_j] \sum_{j=1}^{M} \left(\frac{C_{11}(x_{2j} - \bar{x}_2) - C_{21}(x_{1j} - \bar{x}_1)}{C_{11}C_{22} - C_{12}C_{21}} \right)^2$$

$$= s^2 \frac{C_{11}}{C_{11}C_{22} - C_{12}C_{21}} = \frac{s^2}{M} \left[\frac{1}{s_2^2(1 - \rho^2)} \right], \tag{3-60}$$

$$\mathrm{Var}[A] = \mathrm{Var}[\bar{y} - b_1 \bar{x}_1 - b_2 \bar{x}_2] = \frac{\mathrm{Var}[y_j]}{M} + \bar{x}_1^2 \mathrm{Var}[B_1] + \bar{x}_2^2 \mathrm{Var}[B_2]$$

$$= \frac{s^2}{M} \left[1 + \frac{\bar{x}_1^2}{s_1^2(1 - \rho^2)} + \frac{\bar{x}_2^2}{s_2^2(1 - \rho^2)} \right]. \tag{3-61}$$

Note that when x_1 and x_2 are not correlated ($\rho = 0$), the expressions for the variances simplify.

These ideas can be generalized to be handled using matrix algebra, as listed by, for example, Lapin (1983). The set of observations,

$$\hat{y}_j = A + \sum_{i=1}^{N} B_i x_{ji} + \epsilon, \tag{3-62}$$

---

can be written in matrix form as

$$\mathbf{y} = \mathbf{Xb} + \epsilon, \tag{3-63}$$

where $\mathbf{y}$ is the column of observations, $\mathbf{X}$ is the matrix of individual-variable observations (each row is a data point and each column is a variable, with the first column all ones), $\mathbf{b}$ is the vector of unknown coefficients. Rewriting, the coefficients are found by solving

$$\mathbf{b} = (\mathbf{X}'\mathbf{X})^{-1}\mathbf{X}'\mathbf{y}. \tag{3-64}$$

The sum of squared residuals is

$$S_{Y \cdot 12\ldots}^2 = \frac{1}{M - N - 1}(\mathbf{y}'\mathbf{y} - \mathbf{b}'\mathbf{X}'\mathbf{y}), \tag{3-65}$$

and the sample variance-covariance pairs are provided by

$$S_{Y \cdot 12\ldots}^2 (\mathbf{X}'\mathbf{X})^{-1} = \frac{1}{M - N - 1}(\mathbf{y}'\mathbf{y} - \mathbf{b}'\mathbf{X}'\mathbf{y})(\mathbf{X}'\mathbf{X})^{-1}, \tag{3-66}$$

where the standard error for b_k is the square root of the kth diagonal element.

The above discussion relates to estimating K_{sat} in core samples using other measured properties (i.e., saturation, porosity). In previous entries, it was found that the best regression equation for predicting K_{sat} from measured properties is

$$\log_{10}(K_{sat}) = a + b_1\theta_{65} + b_2\varepsilon_{sample} + \epsilon. \tag{3-67}$$

The best-fit regression equations found before are:

$$\log_{10}(K_{sat}) = -10.1846 - 6.57021 \log 10(\theta_{65}), \tag{3-68}$$

$$= -7.62342 - 3.79487\theta_{65} + 6.30827\varepsilon_{sample}, \tag{3-69}$$

$$= -5.96958 - 11.3334\,VWC_{105} + 7.20616\varepsilon_{65} + 3.4806\log_{10}(\varepsilon_{sample}), \tag{3-70}$$

where a subscript of 65 denotes the measurement at 65 °C, a subscript of 105 denotes the measurement at 105 °C, a subscript of *sample* denotes the subsample measurement, θ is saturation, ε is porosity, and VWC is volumetric water content. For these equations, the sample coefficient of multiple determination, $R^2 = 1 - [\sum(Y - \hat{Y})]/[\sum(Y - \bar{Y})]$, total sum of squared error, S^2, and standard error of b_k (using Equation 3-66) are as shown in Table 3-5. The standard errors correspond to the coefficents listed as above. Notice that as the explained error increases, the uncertainty in the coefficients also increases.

There are uncertainties in the regression-equation coefficients as well as the underlying properties. In order to estimate layer-wide K_{sat} values given a statistical description of all relationships,

Table 3-5: Statistical properties of regression on K_{sat}.

Source	R^2	S^2	Standard Error in Equation Coefficient			
			a	b_1	b_2	b_3
USGS database	0.512	–	–	–	–	–
1-Parameter	0.574	1.25	6.20×10^{-3}	8.31×10^{-2}	–	–
2-Parameter	0.715	0.84	4.03×10^{-2}	3.90×10^{-2}	1.81×10^{-1}	–
3-Parameter	0.735	0.78	3.17×10^{-1}	3.06×10^{-1}	7.97×10^{-1}	2.19×10^{-1}

first the underlying populations of θ and ε must be generated using the statistical descriptions of the two variables. Since the two variables are correlated, an appropriate procedure is to first generate the distribution for one, using sample statistics, then generate the distribution for the other using conditional mean and variance (Benjamin and Cornell, 1970, section 3.6.3). Assuming mutual normality,

$$\mu_{Y|X} = \mu_Y + \rho \frac{\sigma_Y}{\sigma_X}(x - \mu_x), \qquad (3\text{-}71)$$

$$\sigma^2_{Y|X} = (1 - \rho^2)\sigma^2_Y. \qquad (3\text{-}72)$$

Once the underlying population samples are determined, these are plugged into the regression equation for $\log_{10}(K_{sat})$ and random noise (ϵ) applied based on the standard deviation about the regression plane. The integrated value for K_{sat} can then be determined from the population.

Since each of the coefficients in the equations are themselves uncertain, the coefficients must also be sampled. The resulting distribution of average K_{sat} more fully reflects the underlying uncertainties than a single averaged value using the mean coefficients determined from regression analysis.

A difficulty arises when considering retention properties. The USGS procedure, in which retention properties are determined for each core sample individually and the regression coefficients are then determined, lends itself to the same kind of analysis discussed above for K_{sat}, although the variability in the individual saturation measurements is muted. The procedure I followed (using all core samples simultaneously to determine retention parameters) does not lend itself to the determination of regression-parameter uncertainties, even though the overall fit to the data is at least as good as obtained with the USGS procedure.

10/2/97 Layer properties. $\boxed{\mathcal{SAS}}$

I created *Matlab* routine do_ksat_layerest.m to estimate K_{sat} for each layer. The idea is to generate many realizations of θ_{65} and ε_{sample}, use the regression equation for $\log_{10}(K_{sat})$ with ϵ added, and take the mean of the collection of realizations. I found that the underlying distributions for θ_{65} and ε_{sample} were sometimes quite skewed if they were near one end of their range (e.g., ε near 0 or θ near 1). The Type-I largest- and smallest-value distributions (Benjamin and Cornell, 1970, Section 3.3.3) conveniently describe shapes similar to the apparent skewed distributions. In cases where computed skew is less than half of the skew for the Type-I distribution, I assume that the distribution is normal; otherwise, the appropriate Type-I distribution is used.

There are difficulties in estimating bounded properties such as ε or θ using unbounded distributions. I made no attempt to resolve this problem, except for using the skewed distributions, primarily because some reported measured values fell outside the physically valid range and the regression is based on the full reported range of measured values. I do not believe that there should be a strong impact on estimated values for K_{sat}.

As it turns out, the linearity of the regression equation allows correlation between ε and θ to be ignored when calculating geometric mean. I verified this by comparing cases having normal distributions for both ε and θ. Identical geometric and means were obtained (to within the noise from 10^4 samples) considering correlation and neglecting correlation. However, correlation does appear to have an impact on arithmetic mean, as much as 2 orders of magnitude.

The comparison between data, USGS estimates, and my estimates are shown in Table 3-6. During repeated trials with the same number of realizations, the geometric mean of my estimated K_{sat} varies in the 3rd decimal place, while the arithmetic mean varies within a factor of about 1/3. In most cases, the geometric mean calculated using the many-realization approach was within a factor of 3 of the USGS estimate for the same layer. The USGS estimates are significantly different from my estimate (at least an order of magnitude) for 11 of the 30 layers; when there is a significant discrepancy my estimates usually honor the measured values somewhat better. Explanations for cases with estimates at least an order of magnitude difference include: (i) no measured K_{sat} values (CCR); (ii) measured K_{sat} is between the 2 estimates and K_{sat} subsamples are not representative (CW); (iii) measured K_{sat} values are between the 2 estimates (BT3, TR, TM1); and (iv) USGS estimates are significantly further from measured values (CMW, CNW, TC, PV3, PP3, BF3).

It is interesting to note that an arithmetic-mean layerwide K_{sat}, appropriate when gravity drainage is occurring and pressure is equalized horizontally within the layer, suggests that current

---

MAI estimates (<30 mm/yr or $<10^{-9}$ m/s) can be accommodated as deep percolation in the TSw without recourse to fracture flow. At and below the potential repository, only the TM1, BT, and BF3 units would perhaps require fracture flow to accommodate MAI rates.

10/7/97 Display of estimated fits. $\boxed{\mathcal{SAS}}$

The *Matlab* routine do_ksat_layerest.m used to estimate layer properties was augmented to plot the ε, θ, and K_{sat} values for the core samples and generated realizations. The figures are displayed on the following pages. There were 10^6 realizations used to generate mean values; only 1 in 20 realizations are plotted. In each figure, the mean (arithmetic for ε and θ, geometric for K_{sat}) of each sample set is denoted with a large circle and crosshair; the crosshair has the same color as the corresponding data source.

Table 3-6: Layerwise estimates of K_{sat} (m/s). 10^{-10} m/s is equal to 3.16 mm/yr.

Unit	Measured		USGS Estimate		SAS Estimate		
	Number Obs.	Geom. Mean	Number Obs.	Geom. Mean	Number Obs.	Geom. Mean	Arith. Mean
CCR	0	–	9	1.55×10^{-12}	10^5	1.05×10^{-10}	2.27×10^{-9}
CUC	3	3.81×10^{-8}	101	3.86×10^{-8}	10^5	3.01×10^{-8}	2.09×10^{-5}
CUL	1	1.25×10^{-8}	98	5.72×10^{-10}	10^5	1.25×10^{-9}	3.06×10^{-6}
CW	38	7.27×10^{-12}	599	3.77×10^{-12}	10^5	8.88×10^{-11}	6.43×10^{-9}
CMW	4	4.98×10^{-10}	90	8.84×10^{-12}	10^5	9.48×10^{-11}	6.30×10^{-9}
CNW	8	3.06×10^{-8}	101	2.55×10^{-7}	10^5	8.84×10^{-9}	9.52×10^{-6}
BT4	3	1.64×10^{-7}	32	6.77×10^{-7}	10^5	1.22×10^{-7}	5.85×10^{-5}
TPY	2	3.31×10^{-8}	43	1.68×10^{-8}	10^5	2.39×10^{-9}	5.18×10^{-7}
BT3	18	2.81×10^{-7}	85	7.85×10^{-7}	10^5	6.80×10^{-8}	2.75×10^{-6}
TPP	10	8.75×10^{-7}	156	3.65×10^{-6}	10^5	1.26×10^{-6}	2.58×10^{-5}
BT2	19	3.17×10^{-6}	170	1.86×10^{-6}	10^5	8.54×10^{-7}	3.45×10^{-5}
TC	10	8.82×10^{-11}	71	6.15×10^{-13}	10^5	5.42×10^{-10}	2.55×10^{-8}
TR	45	1.67×10^{-9}	438	3.98×10^{-10}	10^5	3.20×10^{-9}	6.85×10^{-8}
TUL	51	5.44×10^{-11}	455	2.26×10^{-10}	10^5	4.50×10^{-10}	1.36×10^{-7}
TMN	39	8.98×10^{-12}	266	1.50×10^{-11}	10^5	6.91×10^{-11}	2.74×10^{-9}
TLL	65	6.22×10^{-11}	451	7.20×10^{-11}	10^5	1.69×10^{-10}	8.71×10^{-9}
TM2	48	2.59×10^{-11}	225	1.79×10^{-11}	10^5	6.82×10^{-11}	1.68×10^{-9}
TM1	17	6.88×10^{-12}	102	4.85×10^{-12}	10^5	4.63×10^{-11}	5.59×10^{-10}
PV3	8	3.73×10^{-11}	86	1.53×10^{-13}	10^5	2.61×10^{-11}	1.09×10^{-8}
PV2	4	7.32×10^{-10}	39	7.39×10^{-11}	10^5	1.56×10^{-10}	5.76×10^{-8}
BT1	9	5.87×10^{-10}	79	2.60×10^{-9}	10^5	4.40×10^{-9}	2.55×10^{-5}
CHV	6	5.51×10^{-7}	69	2.13×10^{-7}	10^5	4.29×10^{-8}	1.68×10^{-6}
CHZ	87	2.88×10^{-11}	293	1.08×10^{-10}	10^5	1.79×10^{-10}	3.40×10^{-9}
BT	14	9.14×10^{-12}	69	1.40×10^{-11}	10^5	4.70×10^{-11}	4.58×10^{-10}
PP4	8	2.72×10^{-11}	47	9.61×10^{-11}	10^5	2.37×10^{-10}	3.88×10^{-9}
PP3	30	2.00×10^{-8}	166	2.93×10^{-10}	10^5	1.79×10^{-8}	1.51×10^{-5}
PP2	25	2.84×10^{-10}	140	5.60×10^{-11}	10^5	1.89×10^{-10}	2.44×10^{-9}
PP1	27	4.88×10^{-11}	245	3.15×10^{-11}	10^5	1.01×10^{-10}	4.36×10^{-9}
BF3	2	2.09×10^{-11}	86	2.10×10^{-12}	10^5	2.12×10^{-11}	1.93×10^{-10}
BF2	5	3.96×10^{-11}	65	5.03×10^{-11}	10^5	8.53×10^{-11}	1.29×10^{-9}

Figure 3-66: 10/7/97. **Disp_DBstat_CCR_c.eps**. Measured and generated formation values for (a) saturation and porosity, (b) saturation and estimated saturated hydraulic conductivity, and (c) porosity and estimated saturated hydraulic conductivity.
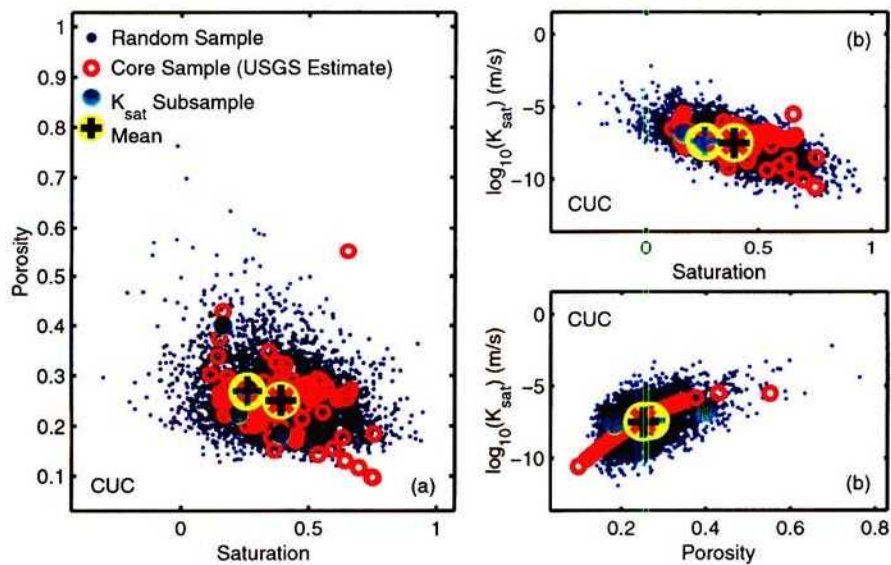
Figure 3-67: 10/7/97. **Disp_DBstat_CUC_c.eps**. Measured and generated formation values for (a) saturation and porosity, (b) saturation and estimated saturated hydraulic conductivity, and (c) porosity and estimated saturated hydraulic conductivity.
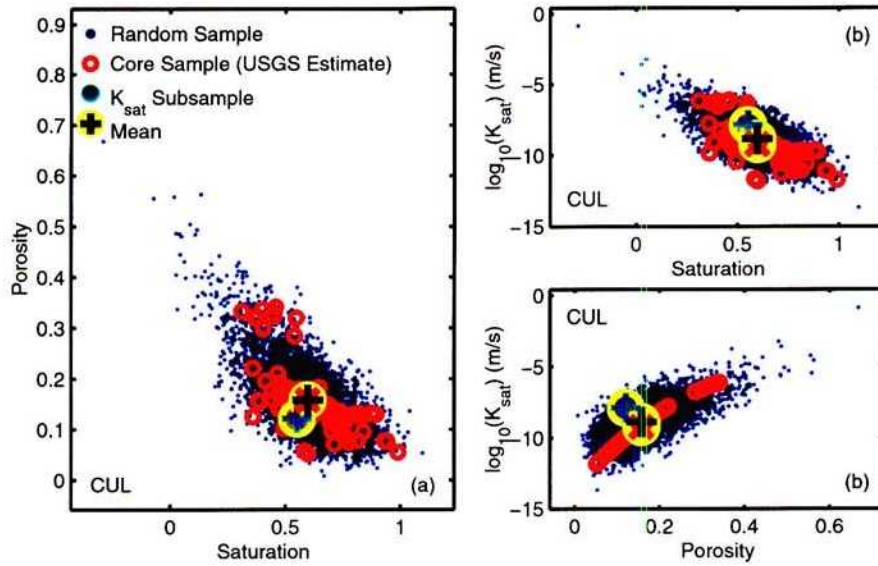
Figure 3-68: 10/7/97. **Disp_DBstat_CUL_c.eps**. Measured and generated formation values for (a) saturation and porosity, (b) saturation and estimated saturated hydraulic conductivity, and (c) porosity and estimated saturated hydraulic conductivity.
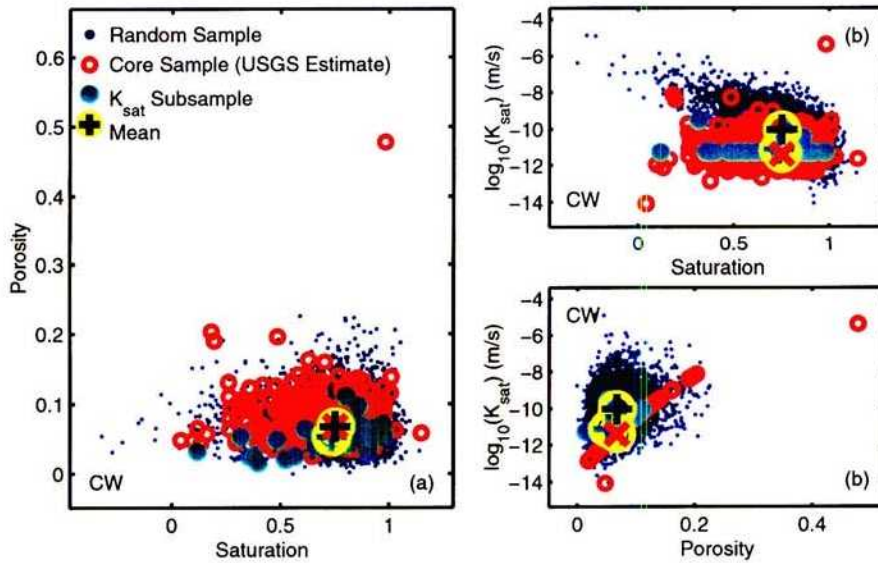
Figure 3-69: 10/7/97. **Disp_DBstat_CW_c.eps**. Measured and generated formation values for (a) saturation and porosity, (b) saturation and estimated saturated hydraulic conductivity, and (c) porosity and estimated saturated hydraulic conductivity.
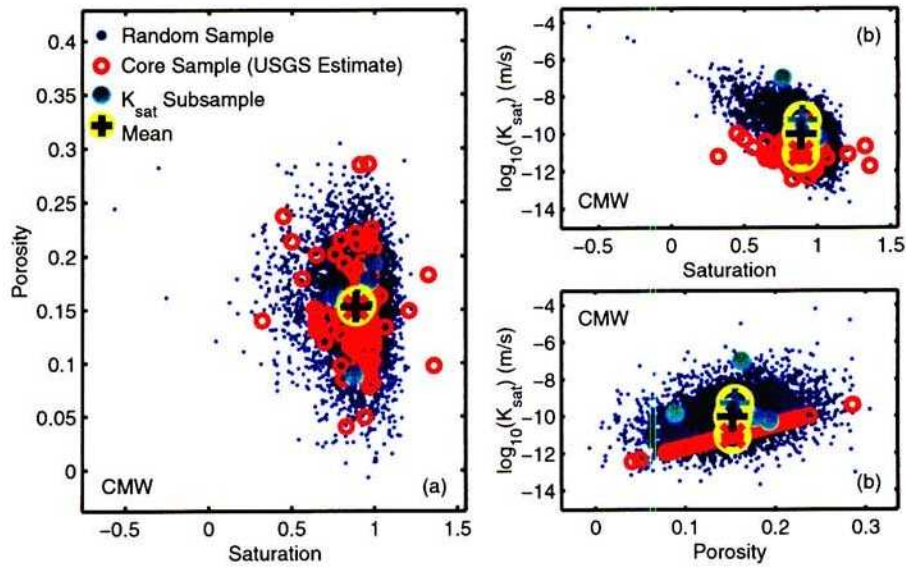
Figure 3-70: 10/7/97. **Disp_DBstat_CMW_c.eps**. Measured and generated formation values for (a) saturation and porosity, (b) saturation and estimated saturated hydraulic conductivity, and (c) porosity and estimated saturated hydraulic conductivity.
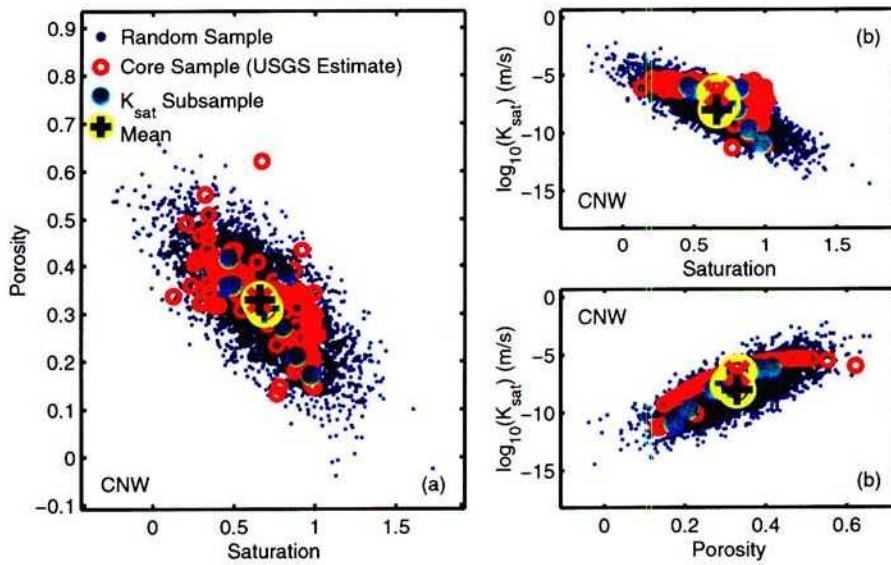
Figure 3-71: 10/7/97. **Disp_DBstat_CNW_c.eps**. Measured and generated formation values for (a) saturation and porosity, (b) saturation and estimated saturated hydraulic conductivity, and (c) porosity and estimated saturated hydraulic conductivity.
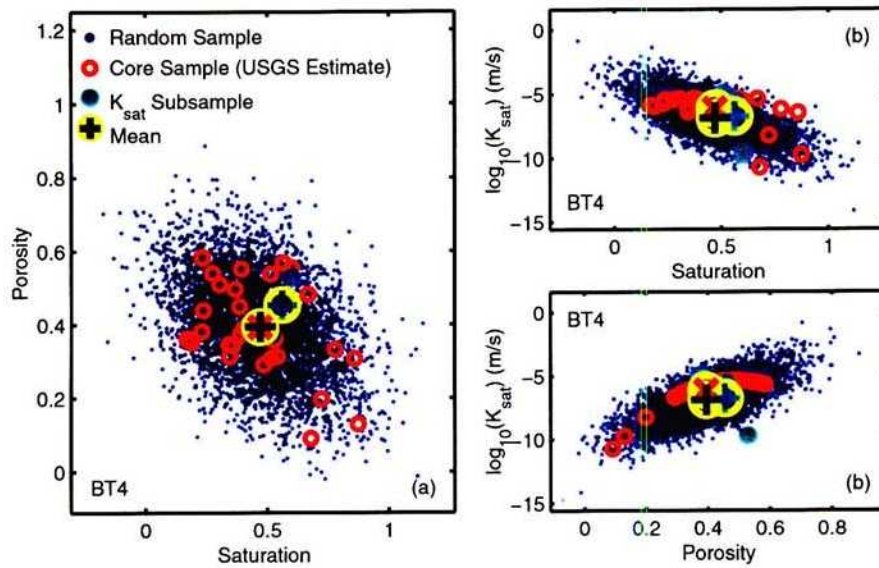
Figure 3-72: 10/7/97. **Disp_DBstat_BT4_c.eps**. Measured and generated formation values for (a) saturation and porosity, (b) saturation and estimated saturated hydraulic conductivity, and (c) porosity and estimated saturated hydraulic conductivity.
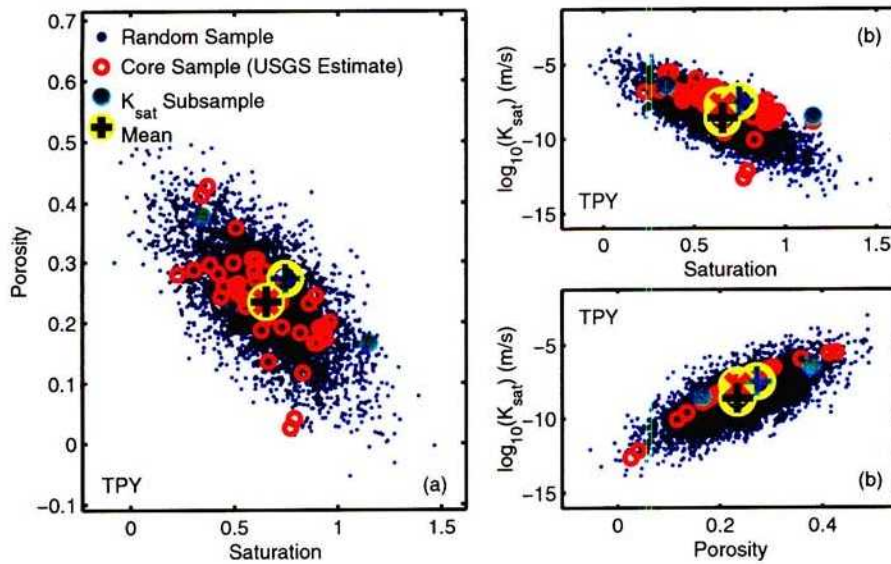
Figure 3-73: 10/7/97. **Disp_DBstat_TPY_c.eps**. Measured and generated formation values for (a) saturation and porosity, (b) saturation and estimated saturated hydraulic conductivity, and (c) porosity and estimated saturated hydraulic conductivity.
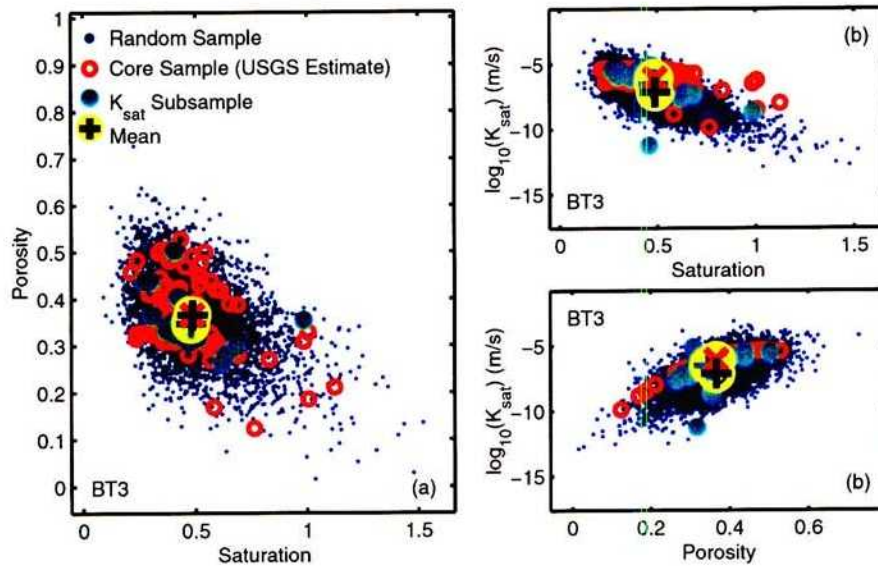
Figure 3-74: 10/7/97. **Disp_DBstat_BT3_c.eps**. Measured and generated formation values for (a) saturation and porosity, (b) saturation and estimated saturated hydraulic conductivity, and (c) porosity and estimated saturated hydraulic conductivity.
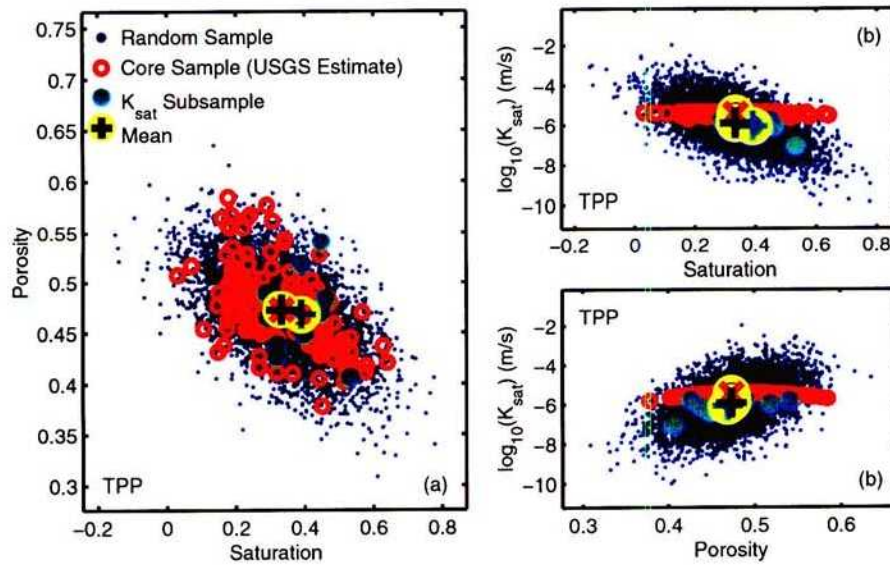
Figure 3-75: 10/7/97. **Disp_DBstat_TPP_c.eps**. Measured and generated formation values for (a) saturation and porosity, (b) saturation and estimated saturated hydraulic conductivity, and (c) porosity and estimated saturated hydraulic conductivity.
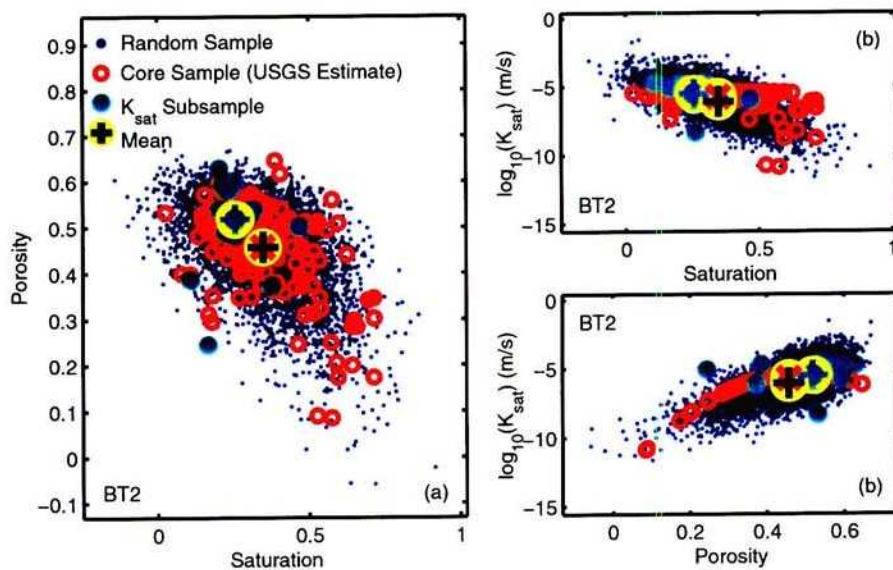
Figure 3-76: 10/7/97. **Disp_DBstat_BT2_c.eps**. Measured and generated formation values for (a) saturation and porosity, (b) saturation and estimated saturated hydraulic conductivity, and (c) porosity and estimated saturated hydraulic conductivity.
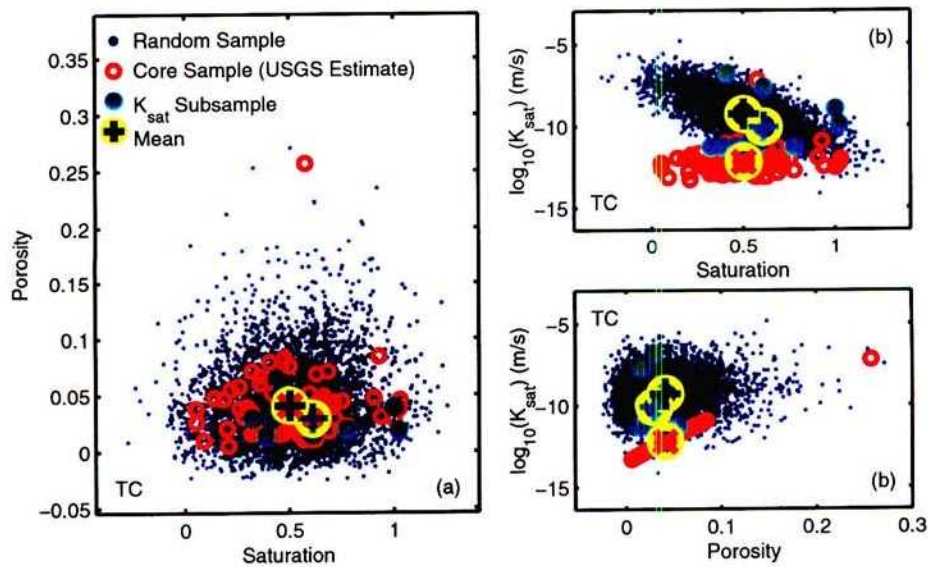
Figure 3-77: 10/7/97. **Disp_DBstat_TC_c.eps**. Measured and generated formation values for (a) saturation and porosity, (b) saturation and estimated saturated hydraulic conductivity, and (c) porosity and estimated saturated hydraulic conductivity.
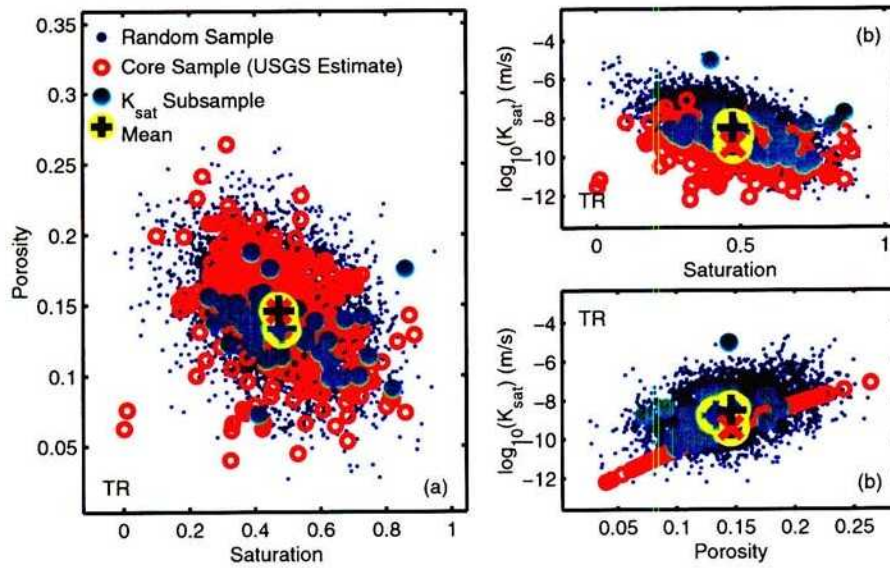
Figure 3-78: 10/7/97. **Disp_DBstat_TR_c.eps**. Measured and generated formation values for (a) saturation and porosity, (b) saturation and estimated saturated hydraulic conductivity, and (c) porosity and estimated saturated hydraulic conductivity.
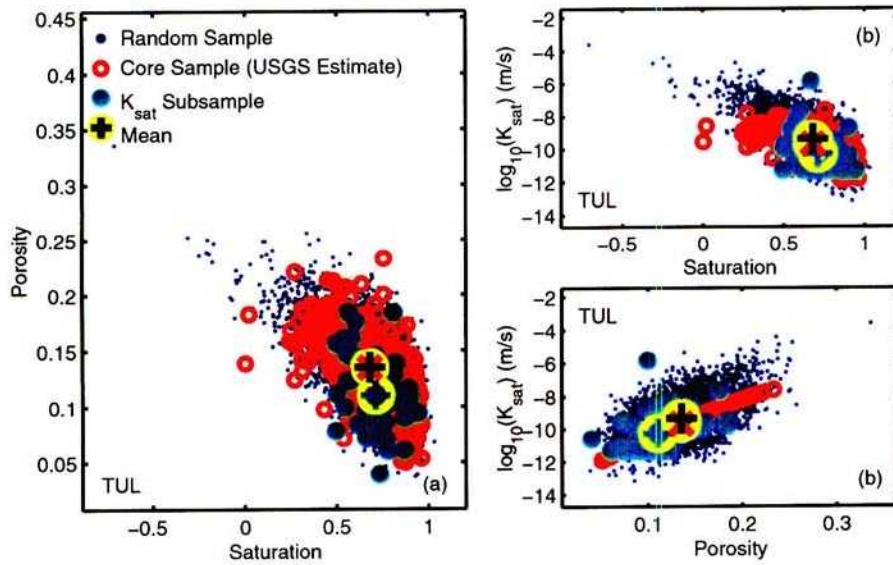
Figure 3-79: 10/7/97. **Disp_DBstat_TUL_c.eps**. Measured and generated formation values for (a) saturation and porosity, (b) saturation and estimated saturated hydraulic conductivity, and (c) porosity and estimated saturated hydraulic conductivity.
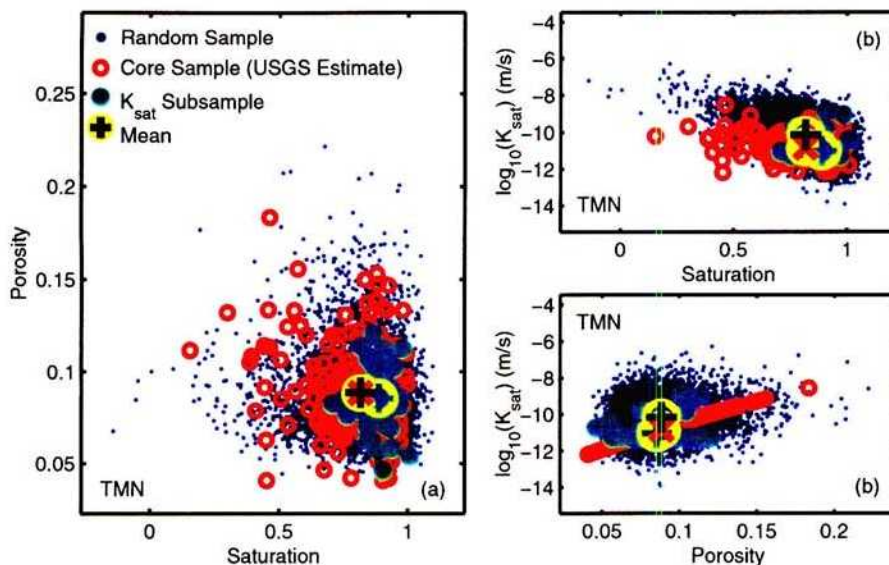
Figure 3-80: 10/7/97. **Disp_DBstat_TMN_c.eps**. Measured and generated formation values for (a) saturation and porosity, (b) saturation and estimated saturated hydraulic conductivity, and (c) porosity and estimated saturated hydraulic conductivity.
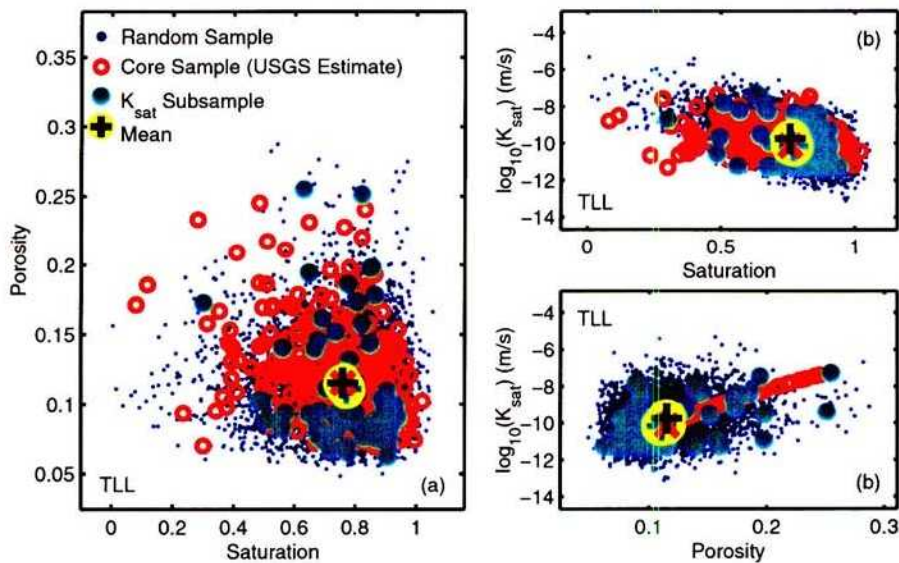
Figure 3-81: 10/7/97. **Disp_DBstat_TLL_c.eps**. Measured and generated formation values for (a) saturation and porosity, (b) saturation and estimated saturated hydraulic conductivity, and (c) porosity and estimated saturated hydraulic conductivity.
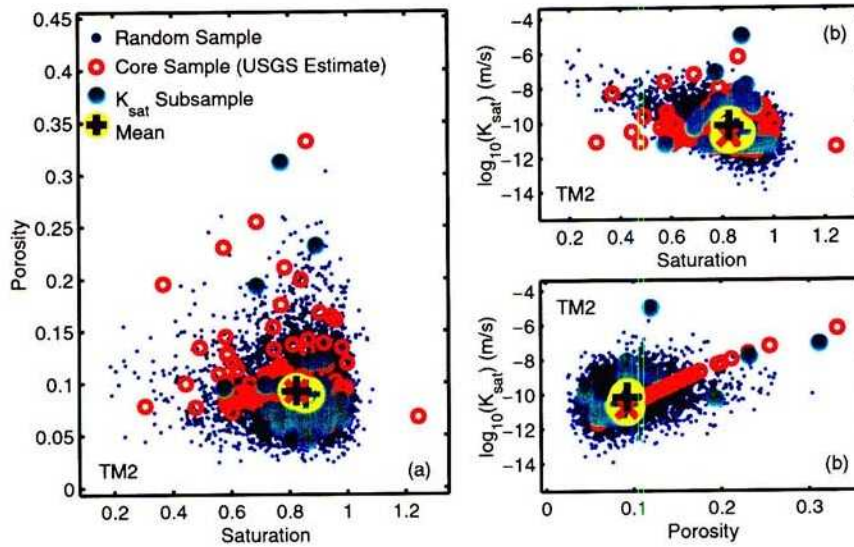
Figure 3-82: 10/7/97. **Disp_DBstat_TM2_c.eps**. Measured and generated formation values for (a) saturation and porosity, (b) saturation and estimated saturated hydraulic conductivity, and (c) porosity and estimated saturated hydraulic conductivity.
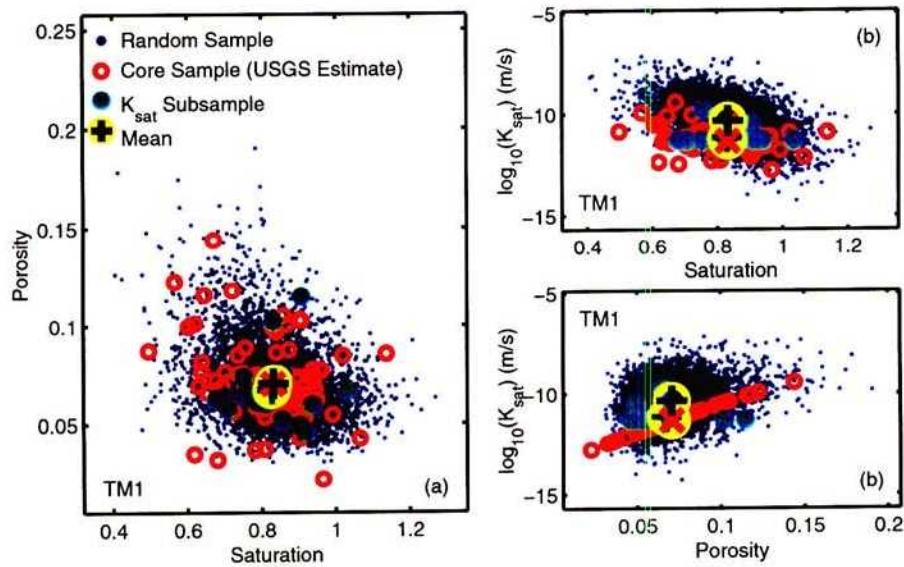
Figure 3-83: 10/7/97. **Disp_DBstat_TM1_c.eps**. Measured and generated formation values for (a) saturation and porosity, (b) saturation and estimated saturated hydraulic conductivity, and (c) porosity and estimated saturated hydraulic conductivity.
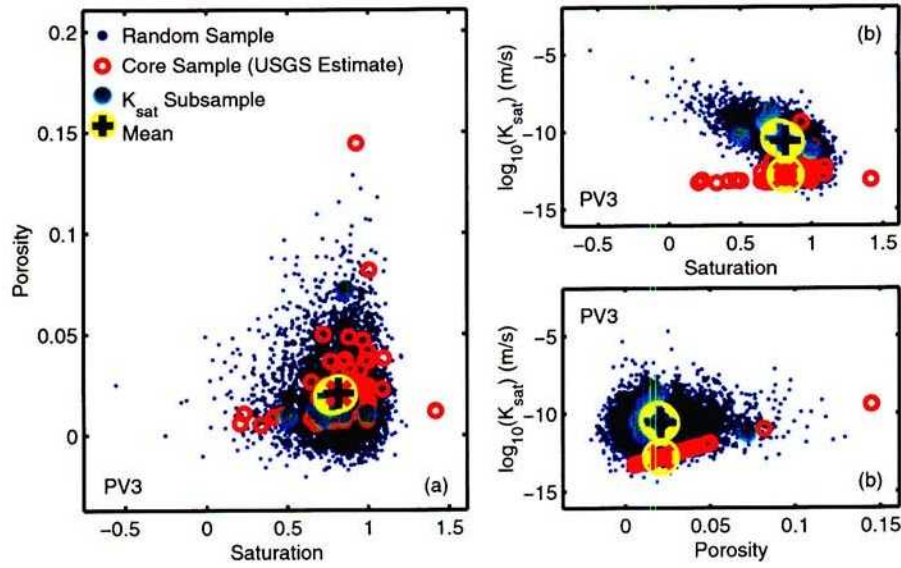
Figure 3-84: 10/7/97. **Disp_DBstat_PV3_c.eps**. Measured and generated formation values for (a) saturation and porosity, (b) saturation and estimated saturated hydraulic conductivity, and (c) porosity and estimated saturated hydraulic conductivity.
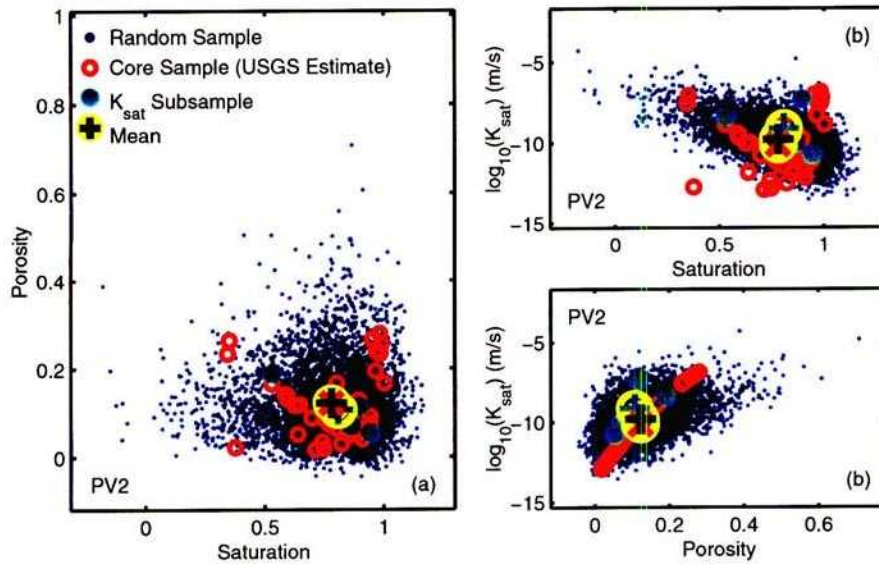
Figure 3-85: 10/7/97. **Disp_DBstat_PV2_c.eps**. Measured and generated formation values for (a) saturation and porosity, (b) saturation and estimated saturated hydraulic conductivity, and (c) porosity and estimated saturated hydraulic conductivity.
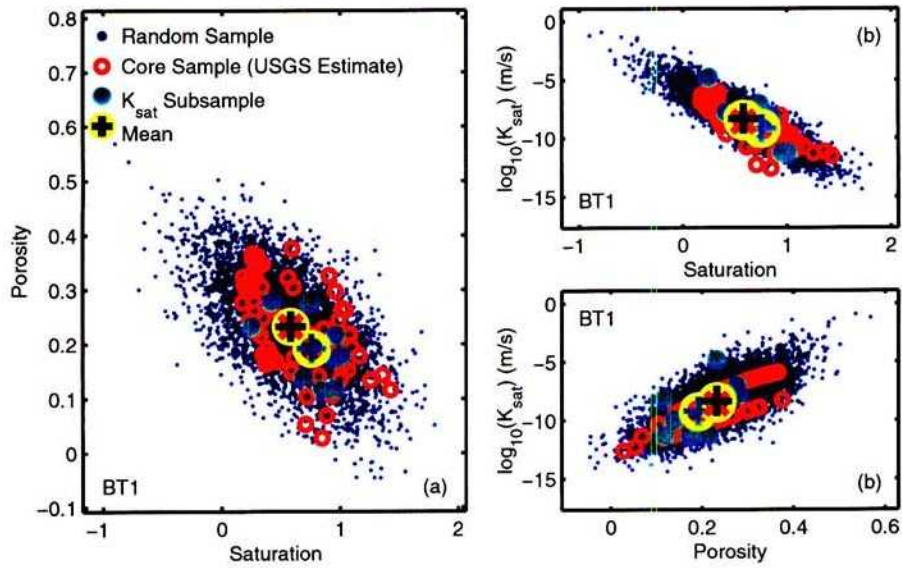
Figure 3-86: 10/7/97. **Disp_DBstat_BT1_c.eps**. Measured and generated formation values for (a) saturation and porosity, (b) saturation and estimated saturated hydraulic conductivity, and (c) porosity and estimated saturated hydraulic conductivity.
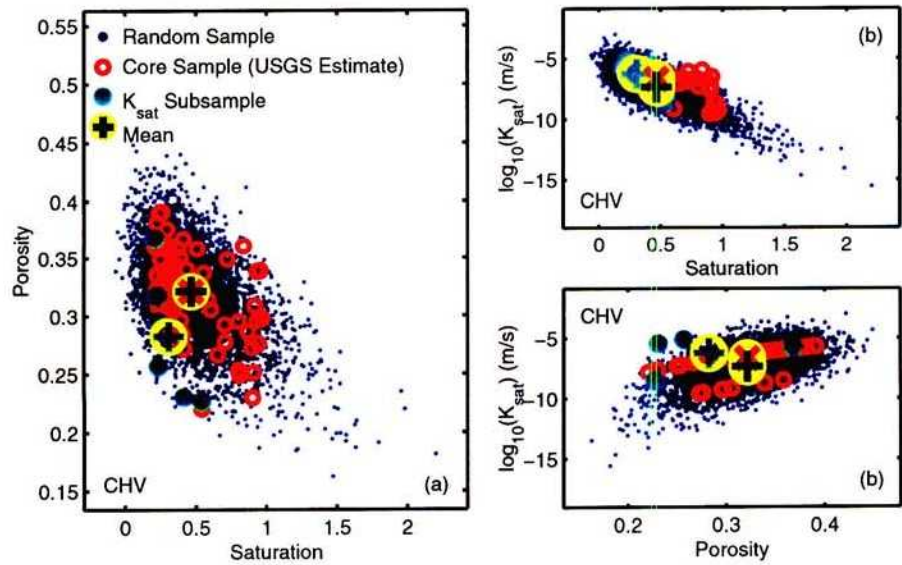
Figure 3-87: 10/7/97. **Disp_DBstat_CHV_c.eps**. Measured and generated formation values for (a) saturation and porosity, (b) saturation and estimated saturated hydraulic conductivity, and (c) porosity and estimated saturated hydraulic conductivity.
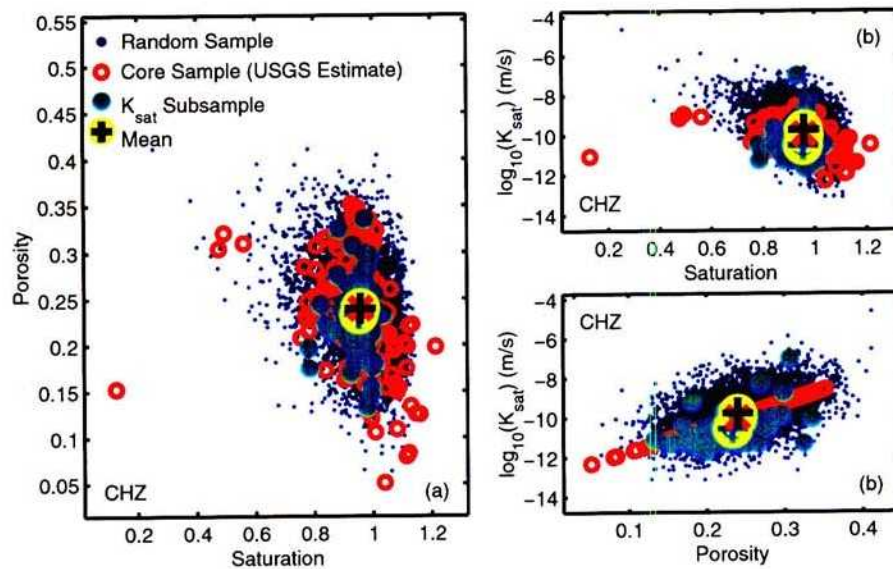
Figure 3-88: 10/7/97. **Disp_DBstat_CHZ_c.eps**. Measured and generated formation values for (a) saturation and porosity, (b) saturation and estimated saturated hydraulic conductivity, and (c) porosity and estimated saturated hydraulic conductivity.
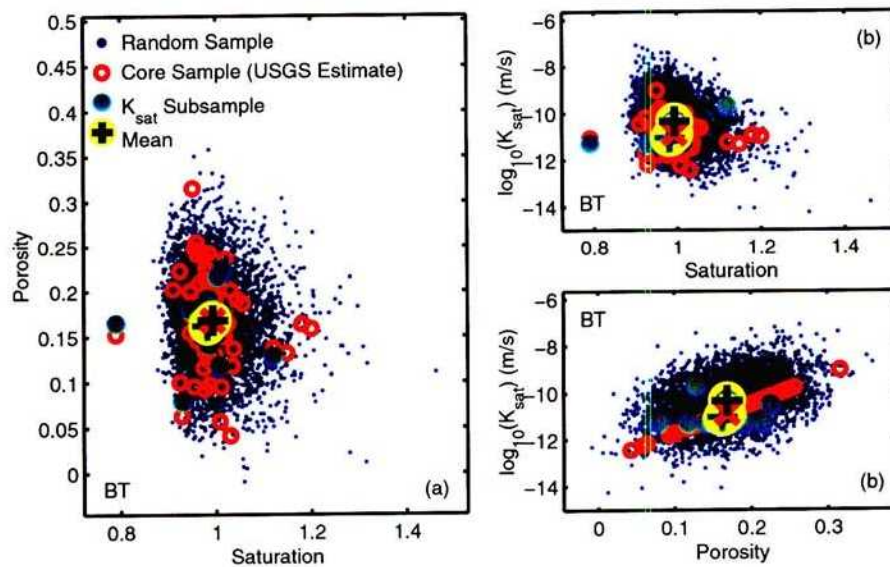
Figure 3-89: 10/7/97. **Disp_DBstat_BT_c.eps**. Measured and generated formation values for (a) saturation and porosity, (b) saturation and estimated saturated hydraulic conductivity, and (c) porosity and estimated saturated hydraulic conductivity.
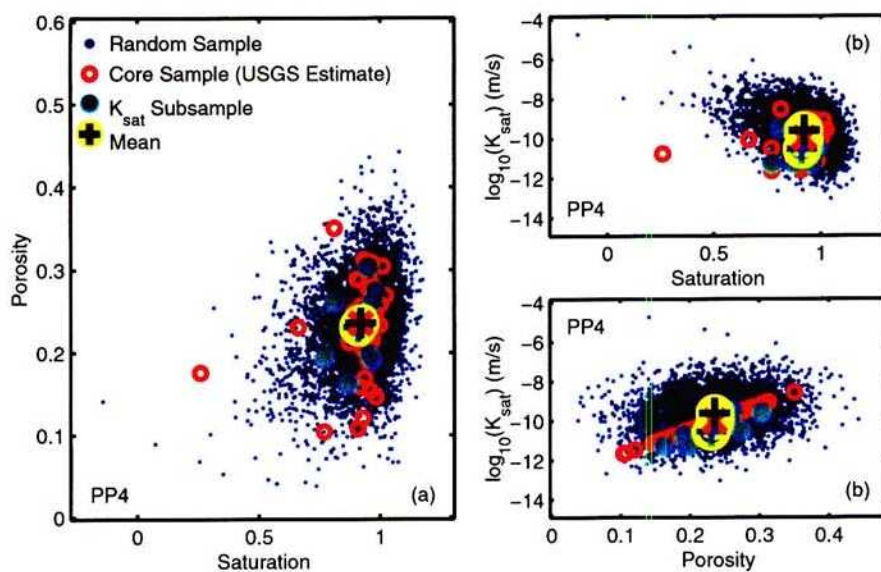
Figure 3-90: 10/7/97. **Disp_DBstat_PP4_c.eps**. Measured and generated formation values for (a) saturation and porosity, (b) saturation and estimated saturated hydraulic conductivity, and (c) porosity and estimated saturated hydraulic conductivity.
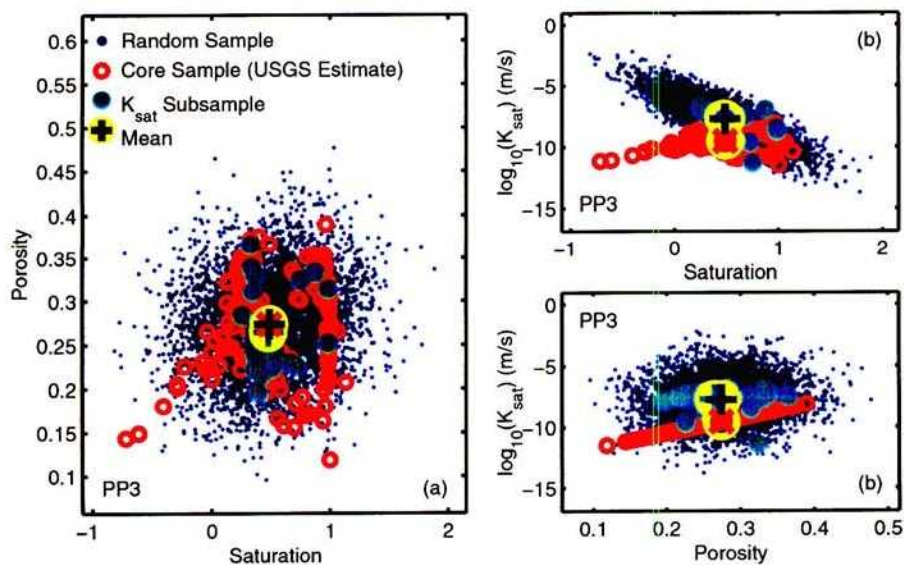
Figure 3-91: 10/7/97. **Disp_DBstat_PP3_c.eps**. Measured and generated formation values for (a) saturation and porosity, (b) saturation and estimated saturated hydraulic conductivity, and (c) porosity and estimated saturated hydraulic conductivity.
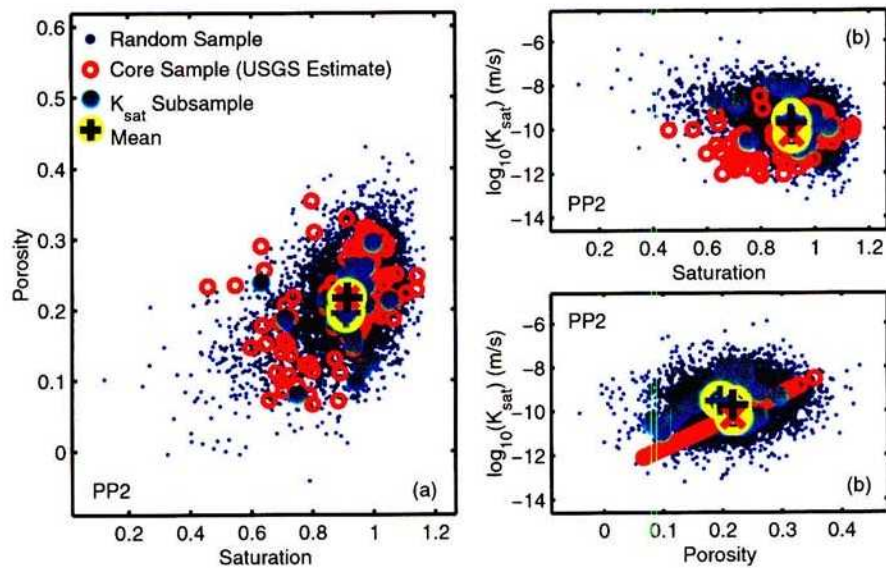
Figure 3-92: 10/7/97. **Disp_DBstat_PP2_c.eps**. Measured and generated formation values for (a) saturation and porosity, (b) saturation and estimated saturated hydraulic conductivity, and (c) porosity and estimated saturated hydraulic conductivity.
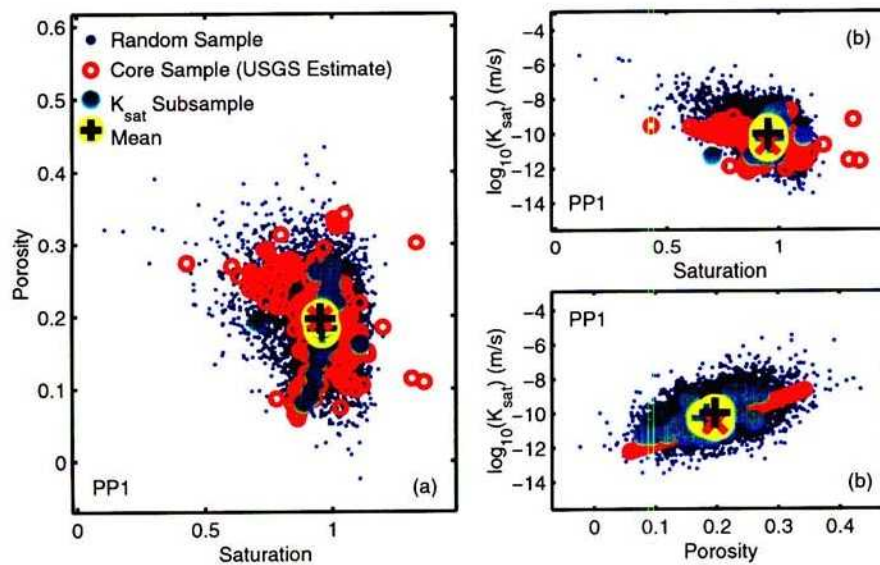
Figure 3-93: 10/7/97. **Disp_DBstat_PP1_c.eps**. Measured and generated formation values for (a) saturation and porosity, (b) saturation and estimated saturated hydraulic conductivity, and (c) porosity and estimated saturated hydraulic conductivity.
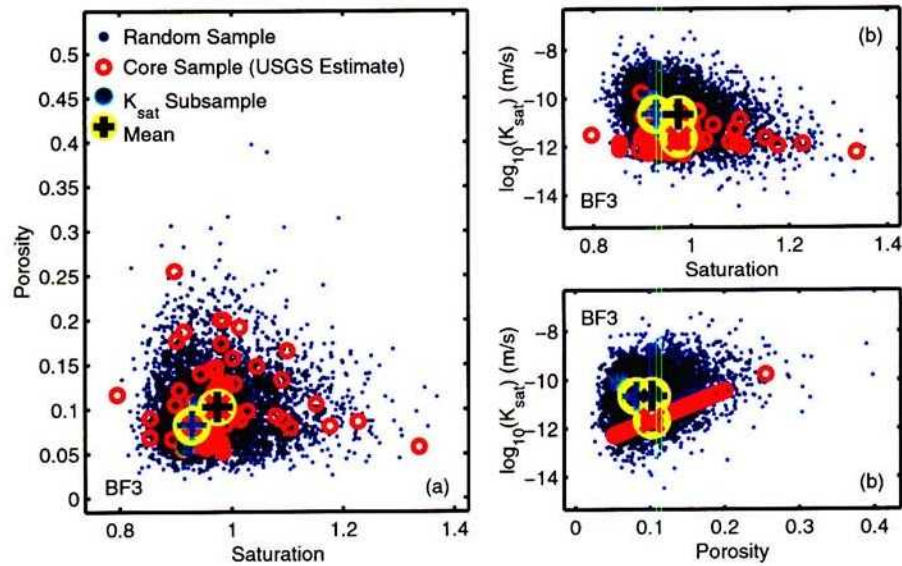
Figure 3-94: 10/7/97. **Disp_DBstat_BF3_c.eps**. Measured and generated formation values for (a) saturation and porosity, (b) saturation and estimated saturated hydraulic conductivity, and (c) porosity and estimated saturated hydraulic conductivity.
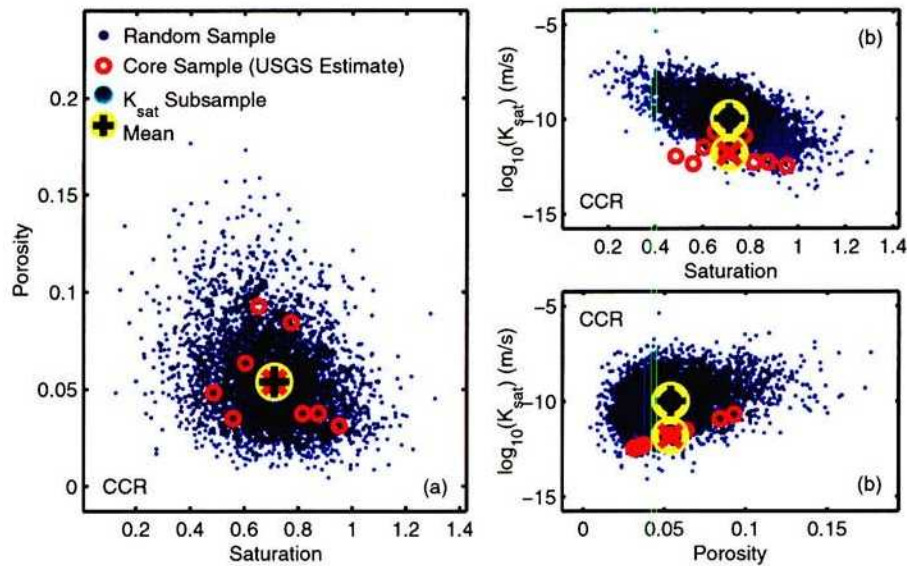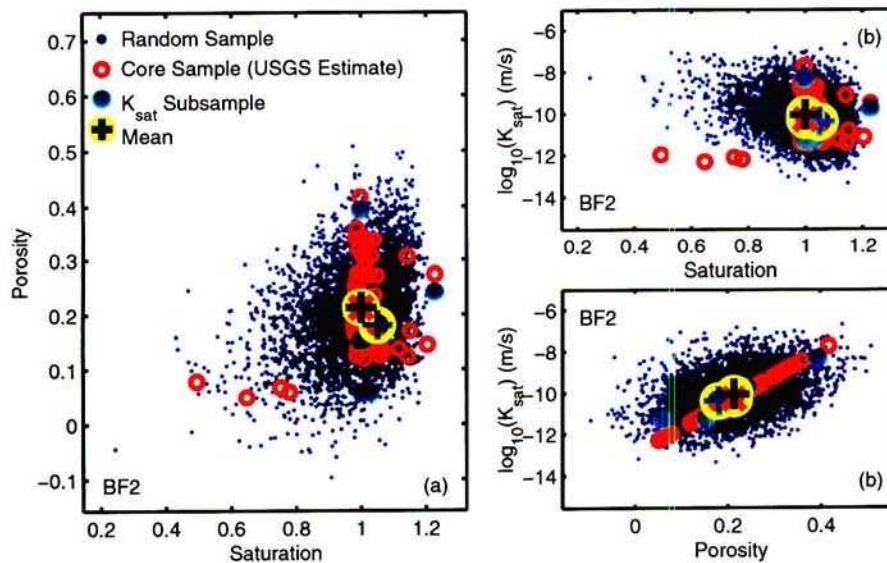

Figure 3-95: 10/7/97. **Disp_DBstat_BF2_c.eps**. Measured and generated formation values for (a) saturation and porosity, (b) saturation and estimated saturated hydraulic conductivity, and (c) porosity and estimated saturated hydraulic conductivity.

10/10/97 Further insights into statistics.

I obtained further insight into the inferences that can be derived from retention data while on a trip to San Antonio. Some of the comments that Robert Mason made last week and yesterday sank in, and reading chapters by Mason et al. (1989) also provided insight. The actual object of the retention measurements is to be able to provide the capillary pressure/moisture content relationship for all core samples, even though this will be done in numerical simulations.

The regression equation was originally written

$$u = \sum_{i=1}^{N} [\log_{10}(P_{mi}) - \log_{10}(P_{ei})]^2, \tag{3-73}$$

$$P_e = P_0(\theta^{-1/m} - 1)^{1-m}, \tag{3-74}$$

$$\log_{10}(P_{0i}) = a_0 + a_1 V_{1i} + a_2 V_{2i}, \tag{3-75}$$

$$m_i = b_0 + b_1 V_{3i} + b_2 V_{4i}. \tag{3-76}$$

where

u is the objective function,

P_m is measured capillary pressure,

P_e is estimated capillary pressure,

m is van Genuchten $m = 1 - 1/n$,

P_0 is bubbling pressure (the reciprocal of van Genuchten α in the units used here),

V_{ji} are the variables being regressed against, and

a_j, b_j are the regression constants.

In the original equation, it turns out that the components of $\log_{10}(P_{0i})$ are linearly incorporated, so that uncertainty in the a_i values would be directly estimated if the expression for m_i were also linearly incorporated. However, the nonlinear nature of the equation makes it difficult to directly estimate the uncertainty of the b_i coefficients.

In section 26.3 by Mason et al. (1989), the first difficulty is addressed by an approximation for the components of **X** in Equation 3-66 (repeated below)

$$S_{Y \cdot 12\ldots}^2 (\mathbf{X}'\mathbf{X})^{-1} = \frac{1}{M - N - 1}(\mathbf{y}'\mathbf{y} - \mathbf{b}'\mathbf{X}'\mathbf{y})(\mathbf{X}'\mathbf{X})^{-1}, \tag{3-77}$$

where the standard error for b_k is the square root of the kth diagonal element and the entries of **X** are the observed predictor variables X_{ij} in linear estimation. When the observations are explained by $f(X_{ij}, \beta_k)$, the approximation is to use $w_{ir} = \partial f(X_{ij}, \beta_k)/\partial \beta_r$ instead of X_{ij}.

The w_{ir} components are as follows:

$$\frac{\partial f(\theta, \beta_k)}{\partial \beta_r} = \frac{\partial \log_{10}(u)}{\partial \beta_r} = \frac{1}{\ln 10} \frac{1}{u} \frac{du}{dm} \frac{\partial m}{\partial \beta_k} \tag{3-78}$$

$$\frac{du}{dm} = \frac{d[(\theta^{-1/m} - 1)^{1-m}]}{dm} \tag{3-79}$$

$$\tag{3-80}$$

It would probably be easier to evaluate this function numerically than analytically.

As pointed out by R. Mason, a second difficulty arises from the considerable noise in the measurements, so that estimates of the uncertainties in van Genuchten coefficients may be strongly affected by measurement noise. In fact, the noise is probably more due to resolution problems. At high VWC, VWC is easy and P is difficult to measure (P is reported in quanta of 1.4 bar, with many repetitions of low values). At low VWC, VWC is difficult and P is easy to measure, (VWC is reported in quanta of 0.001, with many repetitions of low values). The issue of measurement error is dealt with in chapter 28.1 by Mason et al. (1989). Additional information must be included to handle measurement error, typically ρ (the correlation between predictor and response errors) and $\lambda = \sigma_v^2/\sigma_u^2$ (the ratio of measurement-error variances for response and predictor variables). The maximum-likelihood estimators for intercept and slope are

$$b_0 = \bar{y} - b_1 \bar{x}, \tag{3-81}$$

$$b_1 = s(\lambda, \theta) + [s(\lambda, \theta)^2 + t(\lambda, \theta)]^{1/2}, \tag{3-82}$$

$$s(\lambda, \theta) = \frac{s_{yy} - \lambda s_{xx}}{2(s_{xy} - \theta s_{xx})}, \tag{3-83}$$

$$t(\lambda, \theta) = \frac{\lambda s_{xy} - \theta s_{yy}}{s_{xy} - \theta s_{xx}}. \tag{3-84}$$

The original text does not raise t to a power; this should be checked. *Correction dated 5/3/00: I double-checked with R. Mason today and the form is correct as displayed.* $\boxed{\mathcal{SAS}}$

The structural-model approach for estimating uncertainty in the presence of measurement errors yields the following expressions:

$$\hat{\mu}_x = \bar{x}, \tag{3-85}$$

$$\hat{\sigma}_x^2 = s_{xx} - \hat{\sigma}_u^2, \tag{3-86}$$

$$\hat{\sigma}_v^2 = \lambda \hat{\sigma}_u^2, \tag{3-87}$$

$$\hat{\sigma}_u^2 = \frac{s_{yy} - 2b_1 s_{xy} + b_1^2 s_{xx}}{(b_1 - \theta)^2 + (\lambda - \theta^2)}. \tag{3-88}$$

Assuming that ρ is zero (measurement errors in x and y are uncorrelated), the equations reduce to:

$$s(\lambda, \theta) = \frac{s_{yy} - \lambda s_{xx}}{2 s_{xy}},$$

(3-89)

$$t(\lambda, \theta) = \lambda,$$

(3-90)

$$\hat{\sigma}_u^2 = \frac{s_{yy} - 2 b_1 s_{xy} + b_1^2 s_{xx}}{b_1^2 + \lambda}.$$

(3-91)

Although there is undoubtedly measurement error in the USGS data, quantifying the error is not straightforward and is primarily due to resolution rather than other factors. For the time being, it is probably not necessary to account for measurement error; this can be revisited at a later time if deemed appropriate.

10/12/97 Documentation of layer properties and retention estimation.   ☐

A first attempt to estimate layerwide-average K_{sat} is reported in Table 3-7. These values were calculated by a *Matlab* routine I created called do_ksat_layerdev.m. The routine used was copied to an archive file with the designation .archive101297. In the table, the mean and standard deviation of both geometric and arithmetic averages are calculated, incorporating uncertainties in both the regression coefficients and the descriptions of θ and ε. A total of 10^4 parameter realizations were used for each realization of the regression coefficients; 10^4 realizations of the regression coefficients were used as well.

In the plots displayed in the entry for 10/7/97, correlation was incorporated whenever one of the two variables appeared to be normally distributed but was not incorporated when both were deemed to be skewed. In the estimation of layer statistics, correlation was always considered by using a form of the skewed equations with the mean of the skewed distribution subtracted out. Realizations of the variable with the most skew are generated first, using the CDF as before, then realizations of the other variable. Realizations of the second variable are found using a mean and standard deviation calculated using the expressions for $\mu_{Y|X}$ and $\sigma_{Y|X}$ discussed in the entry for 9/29/97, and calculating the CDF for the second variable with $\sigma_{Y|X}$ and the original skew. This procedure is only different from before when both variables are skewed (e.g., welded units).

As discussed in the entry for 9/23/97, a complete set of regressions were performed for the available retention data. The best fits were obtained when P_0 was fit using VWC and a particle density (either at 65 or 105 °C, although the 105 °C fits were slightly better), with relatively little

Table 3-7: Estimates of mean and standard deviation for average K_{sat} (m/s) over a layer, reported as $\log_{10}(K_{sat})$. Both geometric and arithmetic means are reported. 10^4 replicates of 10^4 realizations were used.

Unit	Geometric Average		Arithmetic Average	
	$\hat{\mu}$	$\hat{\sigma}$	$\hat{\mu}$	$\hat{\sigma}$
TMN	-10.16	0.5332	-8.606	0.5823
TLL	-9.773	0.5779	-7.895	0.6724
TM2	-10.16	0.4844	-8.830	0.5032
TM1	-10.33	0.4282	-9.251	0.4302
PV3	-10.58	0.6842	-8.643	0.7880
PV2	-9.804	0.8403	-7.529	0.9314
BT1	-8.350	1.4034	-4.619	1.4593
CHV	-7.362	0.9665	-5.730	0.9685
CHZ	-9.744	0.4669	-8.449	0.4848
BT	-10.33	0.3830	-9.335	0.3852
PP4	-9.622	0.5635	-8.440	0.5702
PP3	-7.736	1.4243	-4.815	1.4526
PP2	-9.716	0.5971	-8.609	0.5981
PP1	-9.989	0.5459	-8.449	0.5885
BF3	-10.67	0.3766	-9.685	0.3792
BF2	-10.07	0.6496	-8.892	0.6529

impact from the m estimate. The best fits for m using two parameters were obtained when both particle and bulk densities were used. The worst fits were obtained when porosity information was neglected when estimating both P_0 or m.

When either P_0 or m was estimated using 1 parameter while the other was estimated using 2 parameters, the best fits were obtained with the 2-parameter model using VWC and particle density (again with the 105°C estimate for particle density slightly better than the 65°C estimate) with either bulk density or VWC. In both cases, if the parameter in the 1-parameter fit was restricted to be one of the parameters in the 2-parameter fit, the best estimate was obtained using VWC for the repeated parameter.

If no more than 2 parameters are to be measured for the combination of P_0 and m, again the best two are particle density and VWC. The best fit was obtained with VWC and particle

density at 105°C for P_0 and either of the two alone for m (VWC provides a slightly better fit). If only one parameter is to be used for both, ε is best, followed by bulk density (65°C is slightly better). The best combinations over all categories are shown in Table 3-8. The best combinations with restrictions on the number of parameters, as well as the worst fits, are shown in Table 3-9.

The generally poor showing for ε (as opposed to VWC) might be because a subsample of the original core was used for retention measurements while the subsample porosity is significantly variable at the sub-core scale.

Table 3-8: Best estimated fits to retention data using USGS outcrop data.

Fit Type	P_0		m		$SS^{1/2}$
	X_1	X_2	X_1	X_2	
Best Fit	ρ_p^{105}	VWC_0	ρ_b^{65}	ρ_p^{105}	8.84
	ρ_p^{105}	VWC_0	ρ_b^{105}	ρ_p^{105}	8.86
	ρ_p^{105}	VWC_0	ρ_b^{65}	ρ_p^{65}	8.86
	ρ_p^{105}	VWC_0	ρ_b^{65}	ρ_b^{105}	8.87
	ρ_p^{105}	VWC_0	ρ_b^{65}	$\Delta\rho_b$	8.87
	ρ_p^{105}	VWC_0	ρ_b^{65}	ρ_b^{105}	8.87
	ρ_p^{105}	VWC_0	ρ_b^{65}	$\Delta\varepsilon$	8.88
	ρ_p^{105}	VWC_0	ρ_b^{105}	$\Delta\varepsilon$	8.88
	ρ_p^{105}	VWC_0	$\Delta\rho_b$	VWC_0	8.89
	ρ_p^{105}	VWC_0	ρ_p^{65}	VWC_0	8.90
	ρ_p^{105}	VWC_0	$\Delta\varepsilon$	VWC_0	8.90
	ρ_p^{105}	VWC_0	ρ_b^{65}	VWC_0	8.91
	ρ_p^{105}	VWC_0	ρ_b^{65}	$-$	8.91
	ρ_p^{105}	VWC_0	ρ_b^{105}	$\Delta\rho_p$	8.92
	ρ_p^{105}	VWC_0	ρ_b^{105}	VWC_0	8.92
	ρ_p^{105}	VWC_0	ρ_b^{105}	$-$	8.92
	ρ_p^{105}	VWC_0	$\Delta\rho_p$	VWC_0	8.94
	ρ_p^{105}	VWC_0	VWC_0	$-$	8.94
	ρ_p^{65}	VWC_0	ρ_b^{65}	ρ_p^{105}	8.95
	ρ_p^{65}	VWC_0	ρ_b^{105}	VWC_0	8.95
	ρ_p^{65}	VWC_0	ρ_b^{105}	ρ_p^{105}	8.95
	ρ_p^{105}	VWC_0	$\Delta\rho_b$	$\Delta\rho_p$	8.97
	ρ_p^{105}	VWC_0	ρ_p^{65}	$\Delta\rho_b$	8.98
	ρ_p^{105}	VWC_0	ρ_p^{65}	$\Delta\varepsilon$	8.99
	ρ_p^{105}	VWC_0	$\Delta\rho_b$	$\Delta\varepsilon$	8.99

Table 3-9: Restricted fits to retention data using USGS outcrop data.

Fit Type	P_0		m		$SS^{1/2}$
	X_1	X_2	X_1	X_2	
$N(P_0) = 1$	VWC_0	–	ρ_p^{105}	VWC_0	9.28
	ρ_b^{65}	–	ρ_p^{105}	VWC_0	9.39
	ρ_b^{105}	–	ρ_p^{105}	VWC_0	9.40
	VWC_0	–	ρ_p^{65}	VWC_0	9.51
	ρ_b^{105}	–	ρ_p^{65}	VWC_0	9.61
$N(m) = 1$	ρ_p^{105}	VWC_0	ρ_b^{65}	–	8.91
	ρ_p^{105}	VWC_0	ρ_b^{105}	–	8.92
	ρ_p^{105}	VWC_0	VWC_0	–	8.94
	ρ_p^{105}	VWC_0	$\Delta\rho_b$	–	9.00
	ρ_p^{105}	VWC_0	$\Delta\varepsilon$	–	9.00
$N(P_0 + m) <= 3$	ρ_p^{105}	VWC_0	ρ_b^{65}	ρ_p^{105}	8.84
	ρ_p^{105}	VWC_0	ρ_b^{105}	ρ_p^{105}	8.86
	ρ_p^{105}	VWC_0	$\Delta\rho_b$	VWC_0	8.89
$N(P_0 + m) <= 2$	ρ_p^{105}	VWC_0	VWC_0	–	8.94
	ρ_p^{105}	VWC_0	ρ_p^{105}	–	9.00
	ρ_p^{65}	VWC_0	ρ_p^{65}	VWC_0	9.08
$N(P_0) = 1, N(m) = 1$	VWC_0	–	ρ_p^{105}	–	10.3
	VWC_0	–	ρ_p^{65}	–	10.4
	VWC_0	–	$\Delta\varepsilon$	–	10.7
	VWC_0	–	$\Delta\rho_b$	–	10.7
	VWC_0	–	$\Delta\rho_p$	–	10.7
$N(P_0 + m) = 1$	VWC_0	–	VWC_0	–	10.7
	ρ_b^{65}	–	ρ_b^{65}	–	11.3
	ρ_b^{105}	–	ρ_b^{105}	–	11.3
	$\Delta\rho_b$	–	$\Delta\rho_b$	–	12.3
Worst Fit	ρ_p^{105}	$\Delta\rho_b$	$\Delta\varepsilon$	$\Delta\rho_p$	12.5
	ρ_p^{65}	$\Delta\rho_b$	$\Delta\rho_b$	$\Delta\rho_p$	12.5
	ρ_p^{105}	–	ρ_p^{105}	–	12.5
	ρ_p^{65}	–	ρ_p^{105}	–	12.5
	ρ_p^{105}	$\Delta\rho_p$	ρ_p^{105}	$\Delta\rho_b$	12.5

10/13/97 Retention estimation.

The similarity between estimates of fit to the retention data can be explained by correlation between parameters. Correlation coefficients between VWC_0 and other parameters are as follows:

- $\rho_b^{65} = -0.915$,

- $\varepsilon^{65} = 0.883$,

- $\rho_p^{65} = -0.706$,

- $\rho_b^{105} = -0.917$,

- $\varepsilon^{105} = 0.904$,

- $\rho_p^{105} = -0.689$,

- $\Delta\rho_b = -0.462$,

- $\Delta\varepsilon = 0.551$, and

- $\Delta\rho_p = 0.522$.

One would expect that little additional explanatory power is achieved when a highly correlated parameter is added. The relative success of the cases with VWC and ρ_p^{105} for estimating P_0 may be due to the lack of correlation between the pair; note that the next best group of fits is provided by cases with the next worse correlation (i.e., VWC and ρ_p^{65}). It appears that the overall fit is best when VWC, ρ_b, and ρ_p are all used, while ρ_b and ρ_p are measured at different temperatures. On the other hand, the Δ parameters have relatively low correlation to VWC and little explanatory power. Apparently deviations in properties occurring due to drying have relatively little explanatory power.

The best overall fit only uses 3 measured variables (not 4); however, there is not a tremendous dropoff when only 2 variables are measured ($SS^{1/2}$ goes from 8.84 to 8.94). For simplicity of generating random realizations and due to the relatively good fit, the estimation of layerwise properties will use the best 2-variable model (5 coefficients):

$$P_0 = a_1 + b_{11} VWC_0 + b_{12}\rho_p^{105}, \tag{3-92}$$

$$m = a_2 + b_{21} VWC_0. \tag{3-93}$$

The best-fit coefficients for the 2-variable model are reported in Table 3-10. Following the procedure for estimating uncertainty in coefficients discussed in the 10/10/97 entry, the uncertainty for the best-fit coefficients are also reported in Table 3-10. For this set of coefficients, R^2 is 0.865.

Table 3-10: Statistical properties of regression on retention parameters.

Statistic	P_0 Coefficients			m Coefficients	
	a_1	b_{11} (VWC_0)	b_{12} (ρ_p^{105})	a_2	b_{21} (VWC_0)
$\hat{\mu}$	12.512	-4.51416	-3.80632	0.302373	0.115806
$\hat{\sigma}$	1.0494	0.41451	0.313008	0.0127992	0.0523755

One can estimate new coefficients using the $\partial f/\partial \beta$ matrix with the previous best-fit coefficients used to evaluate f. One would expect that there would be little difference in the two sets of coefficients. It is somewhat disconcerting that a different set of coefficients are in fact obtained. The estimated values for the P_0 coefficients are slightly different, but the estimated values for the m coefficients are quite different (roughly the same magnitude but with opposite sign). In particular, using the newly found coefficients to regress for m results in m values that are always negative! The $\hat{\sigma}$ values in Table 3-10 were evaluated with the new coefficients for self-consistency; values estimated using the old coefficients to multiply the matrix are roughly 4 times larger. Despite the obvious deviation from near-linearity implied by this finding, estimates for $\hat{\sigma}$ appear to be qualitatively reasonable and so will be used for further work.

In order to generate samples with more than 2 correlated parameters, the following form will be used:

$$\mathbf{u} = \mathbf{C}\epsilon, \tag{3-94}$$

where $\mathbf{u}$ is the vector of normalized variates [$u_i = (x_i - \mu)/\sigma$], $\mathbf{C}$ is the correlation matrix, and ϵ is normally distributed [$N(0,1)$] noise. This matrix form is the lag-0 simplification of a lag-0/lag-1 expression by Matalas (1967). The actual realization of x_i is directly calculated from u_i for normally distributed variables. For skewed variables, my idea is to use u_i to obtain the cumulative probability, $F(u_i)$, assuming that u_i is a normal variate, then get the value for u_i in the skewed distribution that has the same $F(u)$ using table lookup. A revised u_i can be obtained from table lookup on $F(u)$ for the skewed variable, and finally x_i is calculated from the revised u_i. The procedure may break down when the variables are greatly skewed.

I just noticed that Lapin (1983) discusses a method for estimating bounds on correlation coefficients using normally distributed Fisher's Z'. The formulas are

$$Z' = \frac{1}{2} \ln \left(\frac{1+r}{1-r} \right),$$ (3-95)

$$\mu_{Z'} = \frac{1}{2} \ln \left(\frac{1+\rho}{1-\rho} \right),$$ (3-96)

$$\sigma_{Z'} = \frac{1}{(n-3)^{1/2}},$$ (3-97)

where n is the number of samples and r is the estimated ρ. A realization for ρ is found by rearranging:

$$\rho_i = \frac{b_i - 1}{b_i + 1},$$ (3-98)

$$b_i = \exp[2(Z' + \sigma_{Z'} \epsilon_i)],$$ (3-99)

where ϵ_i denotes a sample from a $N(0,1)$ distribution. Each of the correlation coefficients within $\mathbf{C}$ can presumably be sampled independently using this procedure.

10/16/97 Retention-estimation progress.

A *Matlab* routine, do_laydev_all.m, was created in the *$HOME2/AmbientKTI/3Ddata* directory, to investigate the layer-average hydraulic properties for each microstratigraphic unit. The procedure was outlined before, and is summarized below.

- Estimate regression coefficients and their uncertainties for K_{sat} using est_ksat_params.m. The regressed fit is for θ^{65} and ε_{sample}.

- Estimate regression coefficients and their uncertainties for P_0 and m using est_reten_params.m The regressed fit for P_0 is for VWC_0 and ρ_p^{105}. The regressed fit for m is for VWC_0.

- Assume that the statistics for ε^{65} are equivalent to the statistics for ε_{sample}.

- Assume that the statistics for ε^{65} are equivalent to the statistics for VWC_0.

- Generate many realizations of the regression coefficients predicting $\log_{10}(K_{sat})$, $\log_{10}(P_0)$, and m. Use the same realizations for each layer so that layer combinations can be considered with comparable regressions.

- For each microstratigraphic layer of interest:

- Estimate mean, standard deviation, skew, and cross-correlations for θ^{65}, ε^{65}, and ρ_p^{105}.

- Estimate standard deviation of the mean, standard deviation, and cross-correlations.

- For each statistic realization in a layer:

  * Sample the mean, standard deviation, and cross-correlation for θ^{65}, ε^{65}, and ρ_p^{105}.

  * Generate many samples of the predictor properties.

  * Predict regressed variables from the samples. Noise is included for K_{sat} but not the retention properties (there is no direct way to calculate per-sample noise).

  * Calculate layer-wide, channel, and nonchannel hydraulic-property averages at various levels of capillary pressure.

  * Calculate hydraulic properties for the averages.

Using this procedure, some preliminary observations can be made. For the purposes of discussion, I will denote high-flux samples as channels and low-flux samples as barriers, although "barrier" would be more properly termed "noncontributor." I will denote cases with all samples included as "composite." To determine whether a sample is a channel or a barrier, the samples are first sorted by flux and the cumulative flux from lowest to highest is found. Barrier samples are those samples with cumulative flux less than a small fraction of the total flux (e.g., 0.01 of total flux), with the fraction of samples defined as a barrier denoted by f_b. Channel samples are the remaining samples, with the fraction of samples defined as a channel denoted by f_c. Aggregate parameters are defined as the parameters derived from performing a regression to fit the layer-mean properties [i.e., arithmetic mean of (i) all samples, (ii) channels, (iii) barriers].

- For any particular set of regression coefficients, the predicted variability of m is rather small within a formation, while the variability of K_{sat} and P_0 is quite significant.

- Welded units tend to have aggregate properties that are quite similar to the core sample properties, while nonwelded units tend to have aggregate properties that are somewhat different.

- f_c tends to decrease as conditions become drier.

- f_c tends to be larger for welded units.

- Under dry conditions, f_c can be miniscule for nonwelded units, implying that extreme channelling would occur.

- Both P_0 and m tend to be lower than composite in channels and higher than composite otherwise, while K_{sat} is opposite in behavior.

- Average velocity tends to be slower than that predicted using average channel flux, saturation, and porosity. In nonwelded tuffs, the discrepancy can be as much as 2 to 3 orders of magnitude; in welded tuffs, the discrepancy is generally well less than an order of magnitude. As fluxes increase, the discrepancy decreases.

- For nonwelded tuffs (based on several BT2 realizations)

    - Aggregate K_{sat} tends to be slightly larger than averaged K_{sat} (a factor of 2 or so) for all three categories.

    - Channel K_{sat} tends to be larger than composite K_{sat} by up to an order of magnitude.

    - Barrier K_{sat} tends to be more than an order of magnitude less than composite K_{sat}.

    - There is not much difference between averaged channel, barrier, and composite P_0 and m.

    - Both aggregate P_0 and aggregate m tend to decrease relative to the comparable averaged property. The decreases are more extreme when extracting P_0 and m from retention than from conductivity.

    - m tends to decrease by 15 to 35 percent using retention fits.

    - P_0 tends to decrease by 1 to 4 orders of magnitude using retention fits.

    - Fraction of samples corresponding to channels can be less than 0.01 and greater than 0.3.

- For nonwelded tuffs (based on several TMN realizations)

    - Aggregate K_{sat} tends to be slightly larger than averaged K_{sat} (a factor of 3 or so) for all three categories.

    - Channel K_{sat} tends to be larger than composite K_{sat}, by about an order of magnitude.

    - Barrier K_{sat} tends to be more than an order of magnitude less than composite K_{sat}.

    - There is negligible difference between averaged channel, barrier, and composite P_0 and m.

    - Both aggregate P_0 and aggregate m tend to decrease relative to the comparable averaged property. The decreases are more extreme when extracting P_0 and m from retention than from conductivity, but the changes are only by a few percent.

    - Fraction of samples corresponding to channels can be less than 0.1 and greater than 0.4.

10/20/97 Hydraulic-property preliminary results.

I set off a set of runs to get a feel for the behavior of the estimates. I tried to do a 12-hr simulation, which should have been possible with 150 realizations of regression coefficients, 6 microstratigraphic layers, and 10^4 realizations of hydraulic properties per realization of regression coefficients. Preliminary trials took 50 seconds for one set of hydraulic-property realizations. Surprisingly, the entire set took more than 2 days. I hope this is due to paging due to the size of memory used to save the results in one array.

Several observations can be made from the first set of results.

- There is very high correlation between layer-average properties (i.e., $\rho > 0.996$ for P_0, $\rho > 0.91$ for m) estimated using retention and conductivity values for units TMN, TLL, TM2, TM1, and PV3. In the less-welded PV2, $\rho = 0.96$ for P_0 and $\rho = 0.68$ for m.

- There is very low correlation between one layer-average property and any other ($\max[\text{abs}(\rho)] < 0.092$ for all layers other than PV2, and < 0.3 for PV2).

- There is high correlation (> 0.9) between layer-average K_{sat} and both channel and barrier K_{sat}; however, the means are different, with channel K_{sat} larger and barrier K_{sat} lower than layer-average.

- As channel flow becomes a smaller fraction of the total flow,

  - Both channel and barrier K_{sat} increase (but continue to bracket the mean); changes can be more than 2 orders of magnitude. Correlation with layerwide properties also decreases (as low as 0.7), more so for the barrier realizations.

  - P_0 is essentially unaffected.

  - Channel m tends to decrease with a concomitant decrease in correlation with layerwide properties. The deterioration in correlation is more marked with properties determined from conductivity; ρ ranges from 0.63 to 0.94. The change in mean is more marked with properties determined from retention; $\text{mean}(\Delta m)$ ranges from -0.011 to -0.068.

- The velocity discrepancy can only be estimated at low fluxes (e.g., 0.01 mm/yr), as fluxes greater than K_{sat} cannot be satisfied with matrix-only gravity drainage. It is disturbing that complex numbers pop up, as K_{sat} should generally be large enough to accommodate. The complex numbers arise when porosity is negative, a problem for layers with porosity less than 0.1. Based on cases that may include complex velocities, I find that:

– Even at 0.01 mm/yr, layers TM1, PV3, and PV2 have complex velocities in at least one realization; PV3 has more than half of the velocities complex.

– The correlation between velocity using averaged values and aggregate values is not particularly large at best, deteriorating as welding decreases.

10/21/97 More hydraulic-property preliminary results.

I fixed the problem with complex velocities in two steps. The first step was to provide an additional distribution option for generating raw-property samples. When every value of the generating population is positive, the skew is positive, and the skew of the base-10 logarithm is less than half that of the raw variables, the invoked distribution is lognormal rather than extreme-value. This step took care of most of the complex-variable problem; however, an occasional few velocities still were created with very small imaginary parts (apparently roundoff error, since the imaginary part is typically 10^{-16} times smaller than the real part). I simply took the real part of the velocities in such cases.

At the same time as fixing the complex-velocity problem, I changed the output so that only information for one layer at a time is in memory. This removed the problem with computational speed, suggesting that memory limitations were causing paging.

10/28/97 Hydraulic-property results.

The results from 500 realizations of material properties are shown in the following figures, all generated using files **show_several_laydev.m** and **show_laydev.m** in the *$HOME2/Ambient-KTI/3Ddata* directory. The generating files are archived with **archive102897** appended. In the following figures, subfigures a through f are entitled **LayMat_Ks_XXX_c.eps**, **LayMat_Corr_-XXX_c.eps**, **LayMat_Pr_XXX_c.eps**, **LayMat_Pk_XXX_c.eps**, **LayMat_Mr_XXX_c.eps**, and **LayMat_Mk_XXX_c.eps**, respectively, where **XXX** refers to the microstratigraphic layer.

The results are also displayed in Table 3-11 (K_{sat} results), Table 3-12 (van Genuchten α results), and Table 3-13 (van Genuchten n results). My calculations were performed using P_0 and m, then converted to the corresponding α and n to be consistent with USGS results.

Table 3-11: Estimates of microstratigraphic K_{sat}. Geometric means and standard deviations are of $\log_{10}(K_{sat})$ are shown.

| Unit | Core (USGS) | | Core (CNWRA) | | Geometric Mean of Equivalent Layer | | | | | | | |
| | | | | | Full | | $Q_{Bfrac} = 0.001$ | | $Q_{Bfrac} = 0.01$ | | $Q_{Bfrac} = 0.1$ | |
	μ	σ	μ	σ	μ	σ	μ	σ	μ	σ	μ	σ
TMN	1.50×10^{-11}	0.57	6.91×10^{-11}	0.56	3.59×10^{-9}	0.65	5.66×10^{-9}	0.71	1.20×10^{-8}	0.76	8.09×10^{-8}	0.81
TLL	7.20×10^{-11}	0.76	1.67×10^{-10}	0.65	2.39×10^{-8}	0.95	5.84×10^{-8}	1.2	1.92×10^{-7}	1.3	1.32×10^{-6}	1.2
TM2	1.79×10^{-11}	0.77	6.79×10^{-11}	0.53	3.51×10^{-9}	0.63	5.52×10^{-9}	0.69	1.18×10^{-8}	0.77	8.12×10^{-8}	0.85
TM1	4.85×10^{-12}	0.52	4.66×10^{-11}	0.46	6.39×10^{-10}	0.50	8.03×10^{-10}	0.49	1.21×10^{-9}	0.49	3.60×10^{-9}	0.50
PV3	1.53×10^{-13}	0.54	2.59×10^{-11}	0.65	2.64×10^{-8}	1.0	1.43×10^{-7}	1.4	6.74×10^{-7}	1.4	2.32×10^{-6}	1.1
PV2	7.39×10^{-11}	1.9	1.55×10^{-10}	0.80	6.78×10^{-8}	1.2	2.44×10^{-7}	1.4	8.97×10^{-7}	1.5	4.44×10^{-6}	1.3
BT1	2.60×10^{-9}	1.8	4.38×10^{-9}	1.7	4.53×10^{-4}	1.6	8.02×10^{-3}	1.7	2.71×10^{-2}	1.6	4.38×10^{-2}	1.6
CHV	2.13×10^{-7}	0.99	4.30×10^{-8}	1.1	3.34×10^{-6}	1.0	6.08×10^{-6}	1.0	1.09×10^{-5}	1.0	3.84×10^{-5}	1.0
CHZ	1.08×10^{-10}	0.61	1.79×10^{-10}	0.53	4.07×10^{-9}	0.58	5.56×10^{-9}	0.59	9.38×10^{-9}	0.62	3.68×10^{-8}	0.67
BT	1.40×10^{-11}	0.63	4.69×10^{-11}	0.41	4.88×10^{-10}	0.49	5.95×10^{-10}	0.49	8.67×10^{-10}	0.49	2.39×10^{-9}	0.49
PP4	9.61×10^{-11}	0.69	2.37×10^{-10}	0.50	3.75×10^{-9}	0.67	4.98×10^{-9}	0.74	7.95×10^{-9}	0.75	3.01×10^{-8}	0.77
PP3	2.93×10^{-10}	0.67	1.81×10^{-8}	1.4	1.82×10^{-5}	1.5	6.40×10^{-5}	1.5	1.89×10^{-4}	1.6	1.12×10^{-3}	1.5
PP2	5.60×10^{-11}	0.76	1.91×10^{-10}	0.46	2.61×10^{-9}	0.69	3.21×10^{-9}	0.69	4.82×10^{-9}	0.69	1.55×10^{-8}	0.72
PP1	3.15×10^{-11}	0.69	1.02×10^{-10}	0.62	4.86×10^{-9}	0.67	7.83×10^{-9}	0.71	1.65×10^{-8}	0.76	1.02×10^{-7}	0.82
BF3	2.10×10^{-12}	0.48	2.12×10^{-11}	0.38	2.58×10^{-10}	0.58	3.16×10^{-10}	0.60	4.64×10^{-10}	0.64	1.32×10^{-9}	0.71
BF2	5.03×10^{-11}	1.0	8.43×10^{-11}	0.55	1.49×10^{-9}	0.77	1.99×10^{-9}	0.78	3.25×10^{-9}	0.80	1.17×10^{-8}	0.86

Table 3-12: Estimates of microstratigraphic van Genuchten α (bar^{-1}). USGS estimate is from Table 8 by Flint (1996) and is probably arithmetic. CNWRA estimates are geometric, with $\log_{10}(\alpha)$ standard deviations shown.

Unit	Core (USGS)			Core (CNWRA)			$\psi - \theta$		$k - \theta$	
	N	μ	σ	N	μ	σ	μ	σ	μ	σ
TMN	3	0.064	0.013	266	0.170	0.168	0.184	1.571	0.183	1.577
TLL	3	0.273	0.105	451	0.279	0.156	0.416	1.588	0.245	1.578
TM2	1	0.047	0.005	225	0.238	0.174	0.290	1.570	0.219	1.579
TM1	1	0.022	0.002	102	0.169	0.164	0.154	1.566	0.164	1.579
PV3	3	0.010	0.003	86	0.022	0.119	0.010	1.512	0.024	1.545
PV2	1	1.255	0.652	39	0.046	0.329	0.013	1.556	0.064	1.553
BT1	2	9.800	8.695	79	0.061	0.445	0.091	1.516	0.092	1.572
CHV	2	9.800	8.695	69	0.068	0.537	0.054	1.523	0.159	1.607
CHZ	4	0.394	0.125	293	0.101	0.269	0.064	1.513	0.092	1.560
BT	1	0.015	0.001	69	0.145	0.366	0.072	1.579	0.214	1.659
PP4	1	0.010	0.001	47	0.180	0.317	0.037	1.558	0.195	1.584
PP3	3	1.817	0.599	166	1.443	0.310	0.841	1.623	1.392	1.633
PP2	3	0.072	0.012	140	0.437	0.293	0.271	1.610	0.398	1.623
PP1	2	0.179	0.060	245	0.139	0.413	0.151	1.577	0.274	1.649
BF3	1	0.036	0.010	86	0.316	0.249	0.265	1.612	0.442	1.653
BF2	1	0.012	0.001	65	0.151	0.442	0.099	1.590	0.207	1.611

Observations that were made in the 10/20/97 entry are well supported with the additional realizations. Note that correlation is generally very low between material properties, with very high correlation between P_0 estimated from retention data versus conductivity data and somewhat less high correlation between m obtained from the same pair of data sets.

In general, I expect that it may not be necessary to be sophisticated when using the retention properties estimated using the regression approach outlined herein. The variation in retention properties between channel and barrier is relatively small and no strong correlation appears to exist between material properties.

The results outlined here, although based on USGS-estimated core-sample properties, are strikingly different in several ways. The USGS-presented estimates of average core-sample properties (Flint, 1996) have considerably smaller variation in P_0 and considerably larger variation in m.

Table 3-13: Estimates of microstratigraphic van Genuchten n. USGS estimate is from Table 8 by Flint (1996).

Unit	Core (USGS)			Core (CNWRA)			$\psi - \theta$		$k - \theta$	
	N	μ	σ	N	μ	σ	μ	σ	μ	σ
TMN	3	1.470	0.076	266	1.455	0.005	1.437	0.030	1.438	0.028
TLL	3	1.294	0.051	451	1.461	0.008	1.449	0.035	1.448	0.030
TM2	1	1.713	0.078	225	1.456	0.008	1.438	0.030	1.445	0.029
TM1	1	2.141	0.267	102	1.450	0.005	1.427	0.030	1.442	0.028
PV3	3	1.592	0.127	86	1.438	0.004	1.424	0.039	1.428	0.033
PV2	1	1.310	0.075	39	1.463	0.020	1.401	0.060	1.421	0.035
BT1	2	1.294	0.072	79	1.491	0.021	1.460	0.065	1.433	0.038
CHV	2	1.294	0.072	69	1.514	0.010	1.391	0.052	1.416	0.037
CHZ	4	1.290	0.037	293	1.493	0.013	1.426	0.056	1.474	0.041
BT	1	1.909	0.111	69	1.475	0.013	1.453	0.039	1.418	0.035
PP4	1	3.035	0.404	47	1.492	0.014	1.410	0.047	1.454	0.039
PP3	3	1.455	0.071	166	1.502	0.014	1.437	0.048	1.475	0.043
PP2	3	1.603	0.081	140	1.487	0.015	1.445	0.038	1.468	0.040
PP1	2	1.454	0.078	245	1.482	0.014	1.402	0.037	1.403	0.035
BF3	1	1.680	0.202	86	1.458	0.010	1.417	0.032	1.413	0.032
BF2	1	2.477	0.275	65	1.486	0.021	1.361	0.041	1.427	0.038

The USGS estimates for the 15 layers I considered are based on a total of 31 samples.

My estimated range in layer-average P_0 is typically 8 to 10 orders of magnitude, with a standard deviation equivalent to more than an order of magnitude. My estimated geometric-mean van Genuchten α for each layer ranges from 0.0097 to 1.39 bar^{-1}, with a standard deviation for $\log_{10}(\alpha)$ of between 1.51 and 1.66, while the USGS core sample data has a range from 0.01 to 9.8 bar^{-1} in the same layers (apparently arithmetic mean, since there are no more than 4 samples for any layer).

On the other hand, my estimated range in m is quite small, with relatively little variation between layers. The estimated layer-average m ranges from 0.264 to 0.321, with standard deviation ranging from 0.0134 to 0.0341. Equivalently, layer-average n ranges from 1.36 to 1.46, with standard deviation ranging from 0.0279 to 0.652. For the same layers, the USGS mean values for n range from 1.29 to 3.035, with standard errors ranging from 0.037 to 0.404.
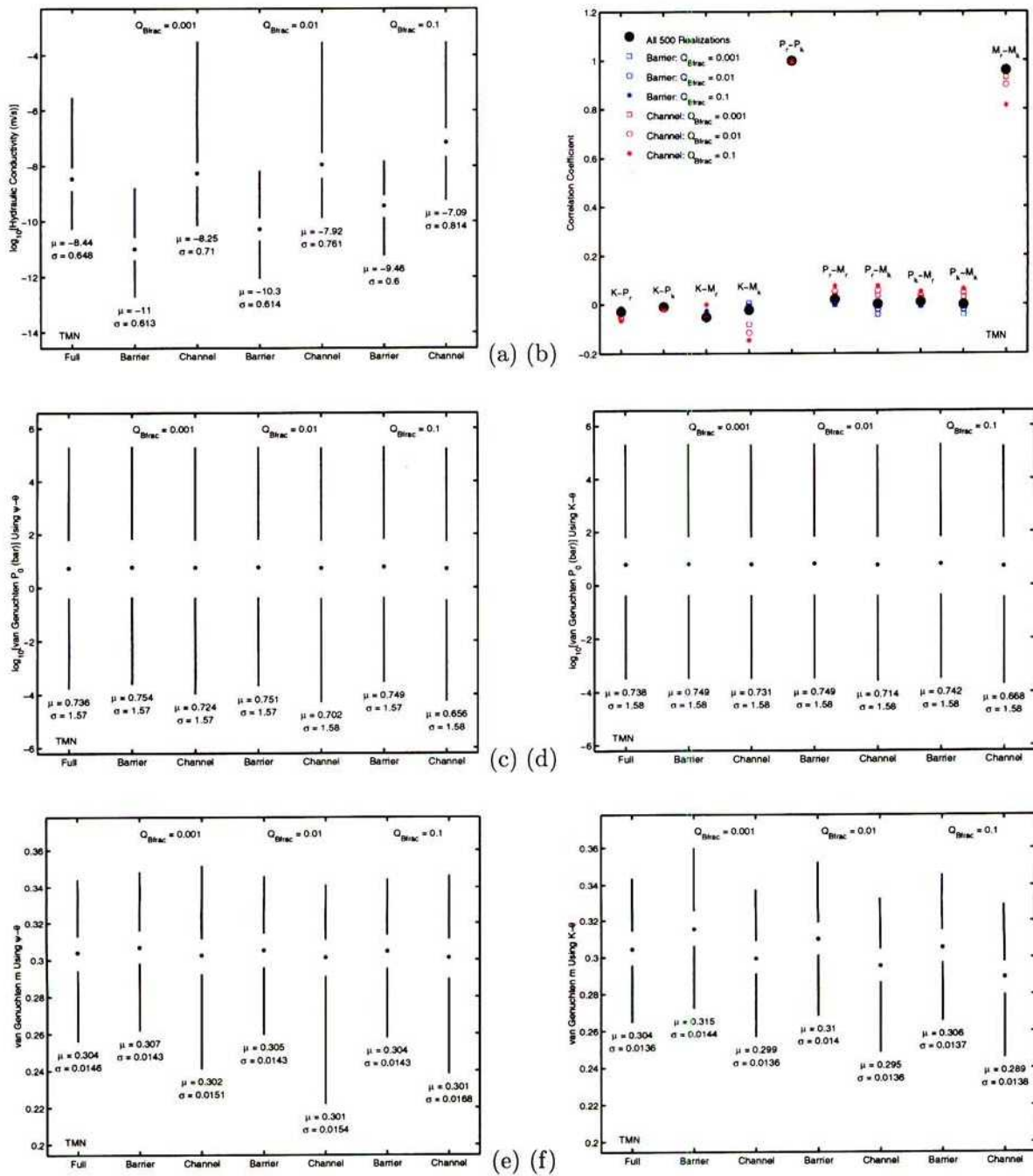
Figure 3-96: 10/28/97. Estimated properties for layer TMN. Correlation between material properties (b), and quartiles for: (a) equivalent K_{sat}, P_0 using retention and conductivity (c and d, respectively); and m using retention and conductivity (e and f, respectively).
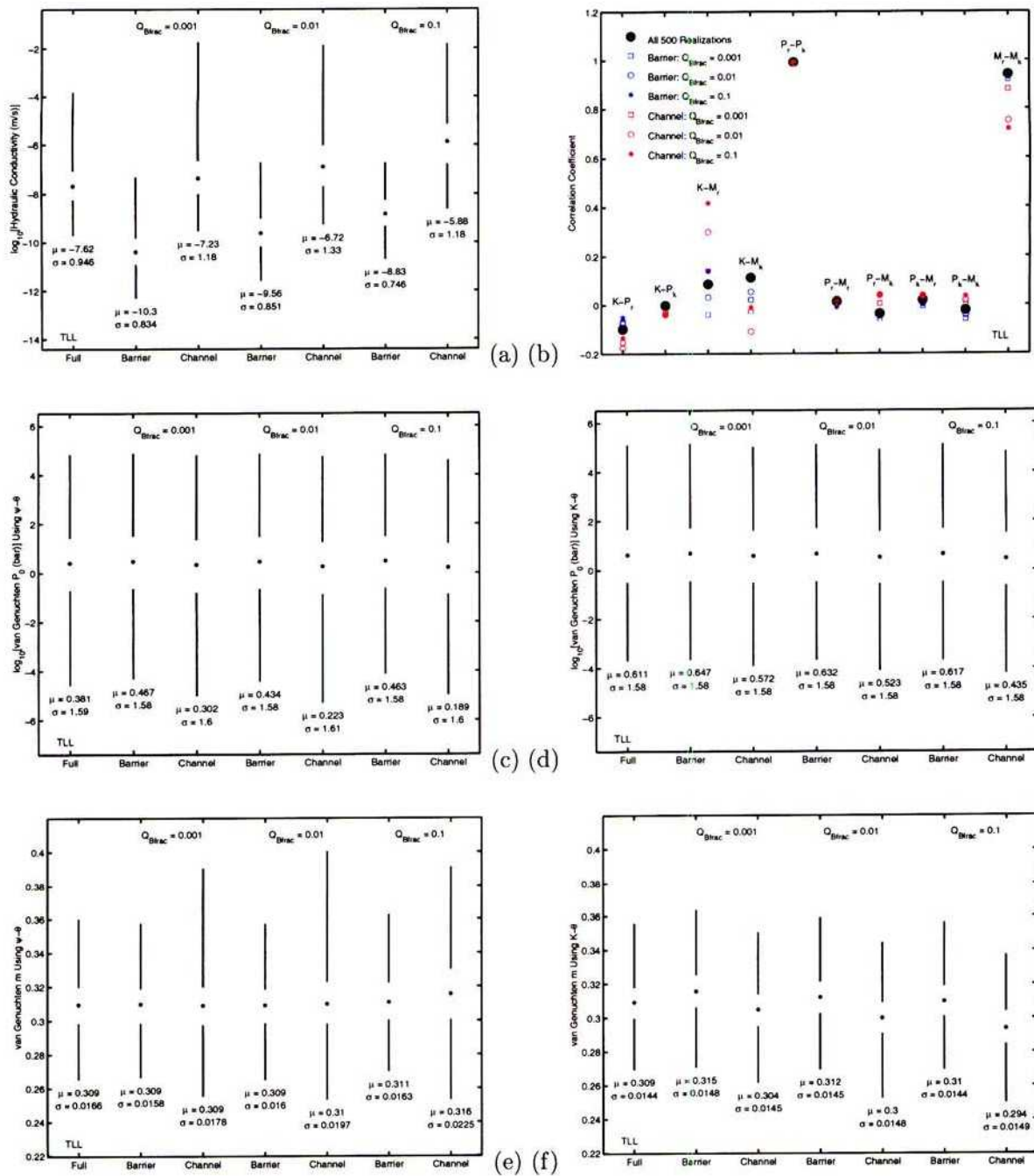
Figure 3-97: 10/28/97. Estimated properties for layer TLL. Correlation between material properties (b), and quartiles for: (a) equivalent K_{sat}, P_0 using retention and conductivity (c and d, respectively); and m using retention and conductivity (e and f, respectively).
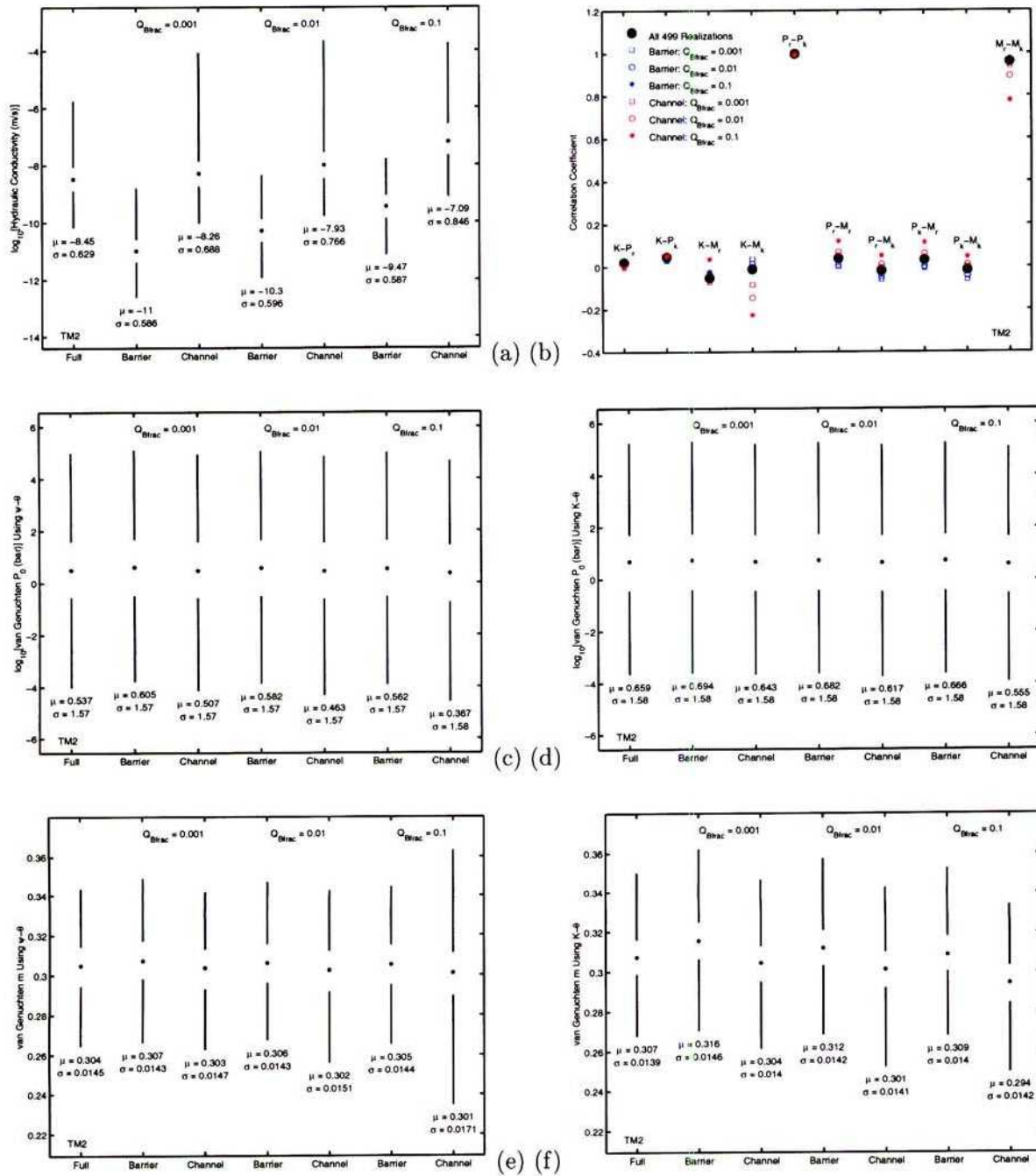
Figure 3-98: 10/28/97. Estimated properties for layer TM2. Correlation between material properties (b), and quartiles for: (a) equivalent K_{sat}, P_0 using retention and conductivity (c and d, respectively); and m using retention and conductivity (e and f, respectively).
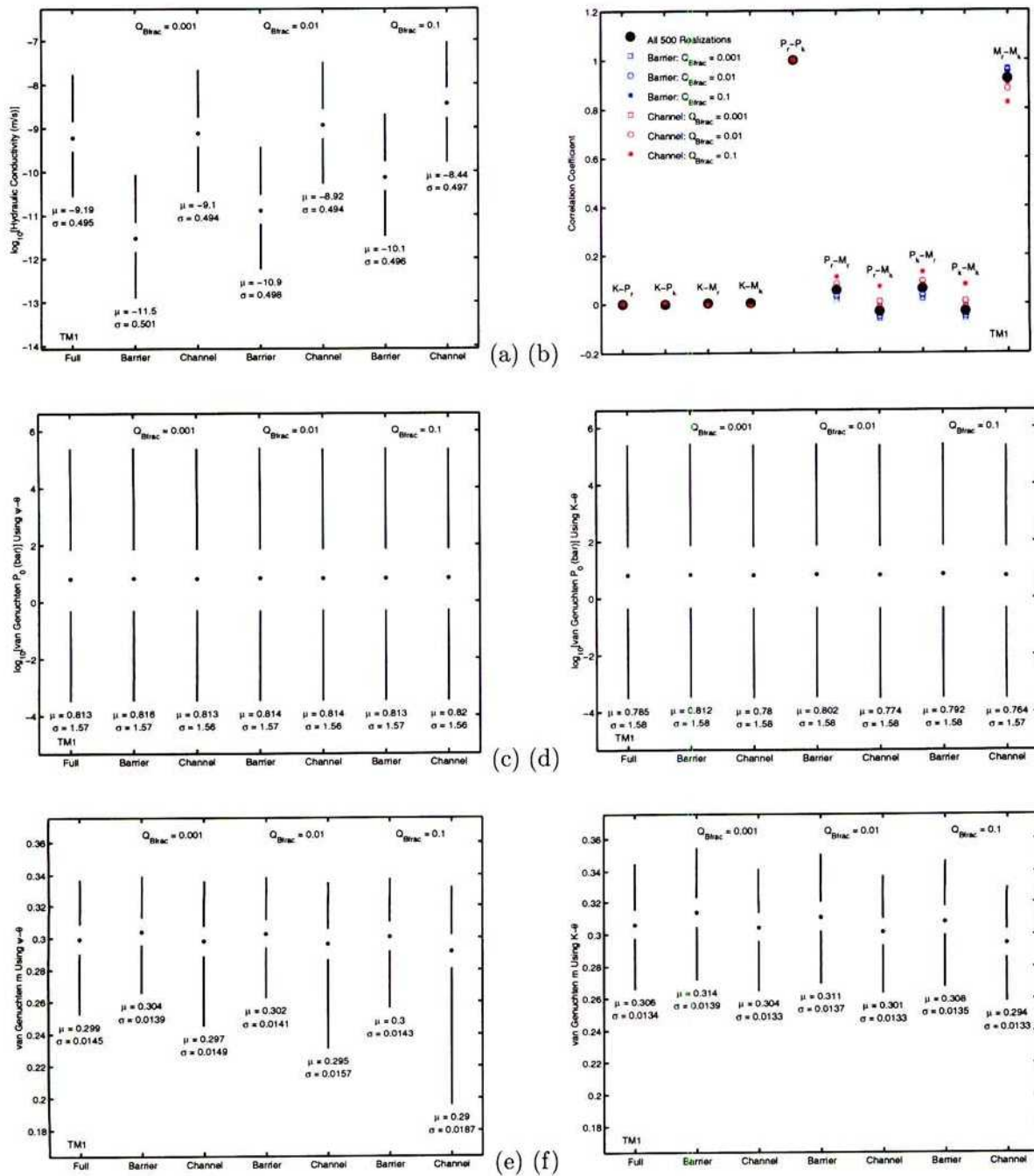
Figure 3-99: 10/28/97. Estimated properties for layer TM1. Correlation between material properties (b), and quartiles for: (a) equivalent K_{sat}, P_0 using retention and conductivity (c and d, respectively); and m using retention and conductivity (e and f, respectively).
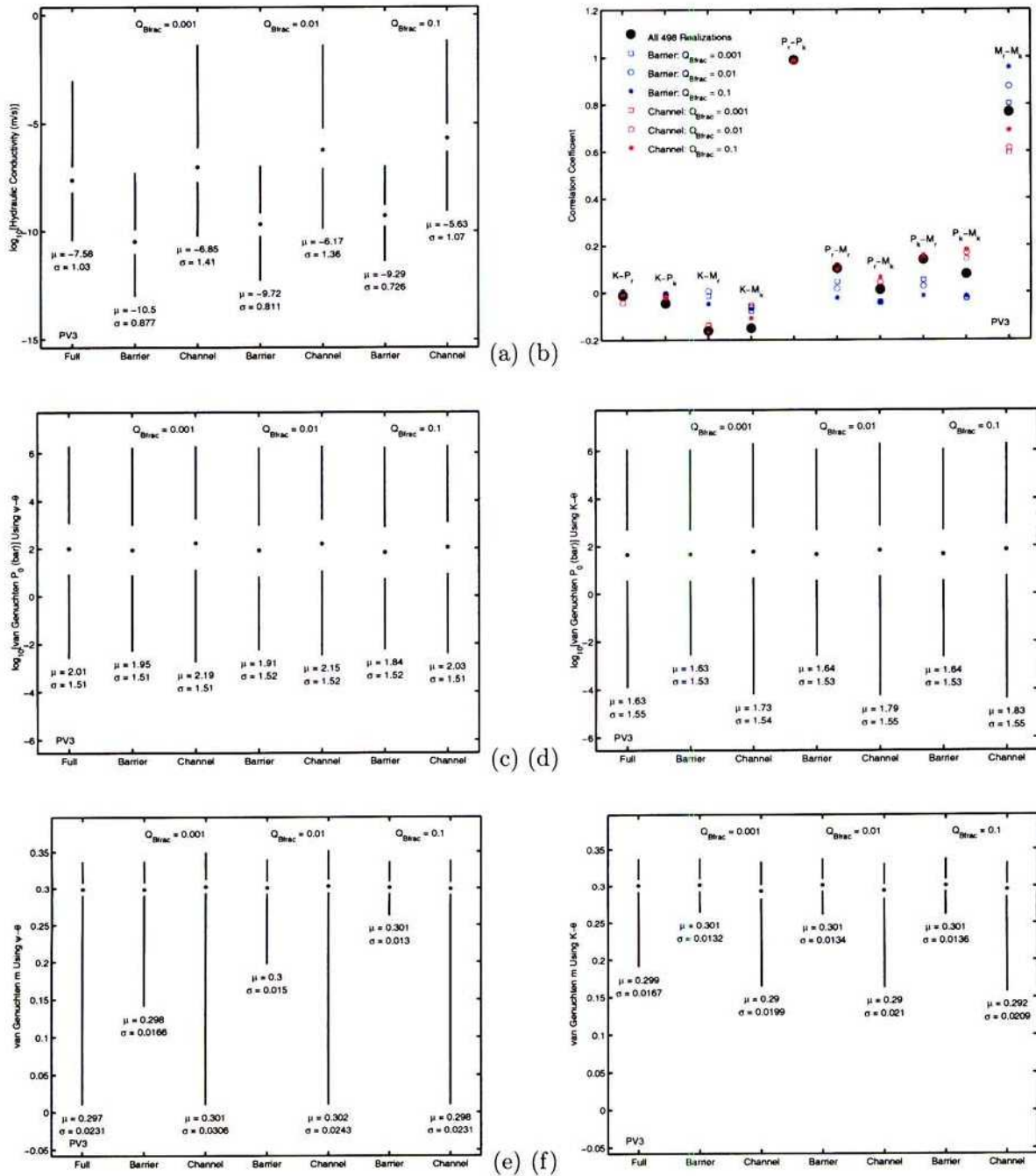
Figure 3-100: 10/28/97. Estimated properties for layer PV3. Correlation between material properties (b), and quartiles for: (a) equivalent K_{sat}, P_0 using retention and conductivity (c and d, respectively); and m using retention and conductivity (e and f, respectively).
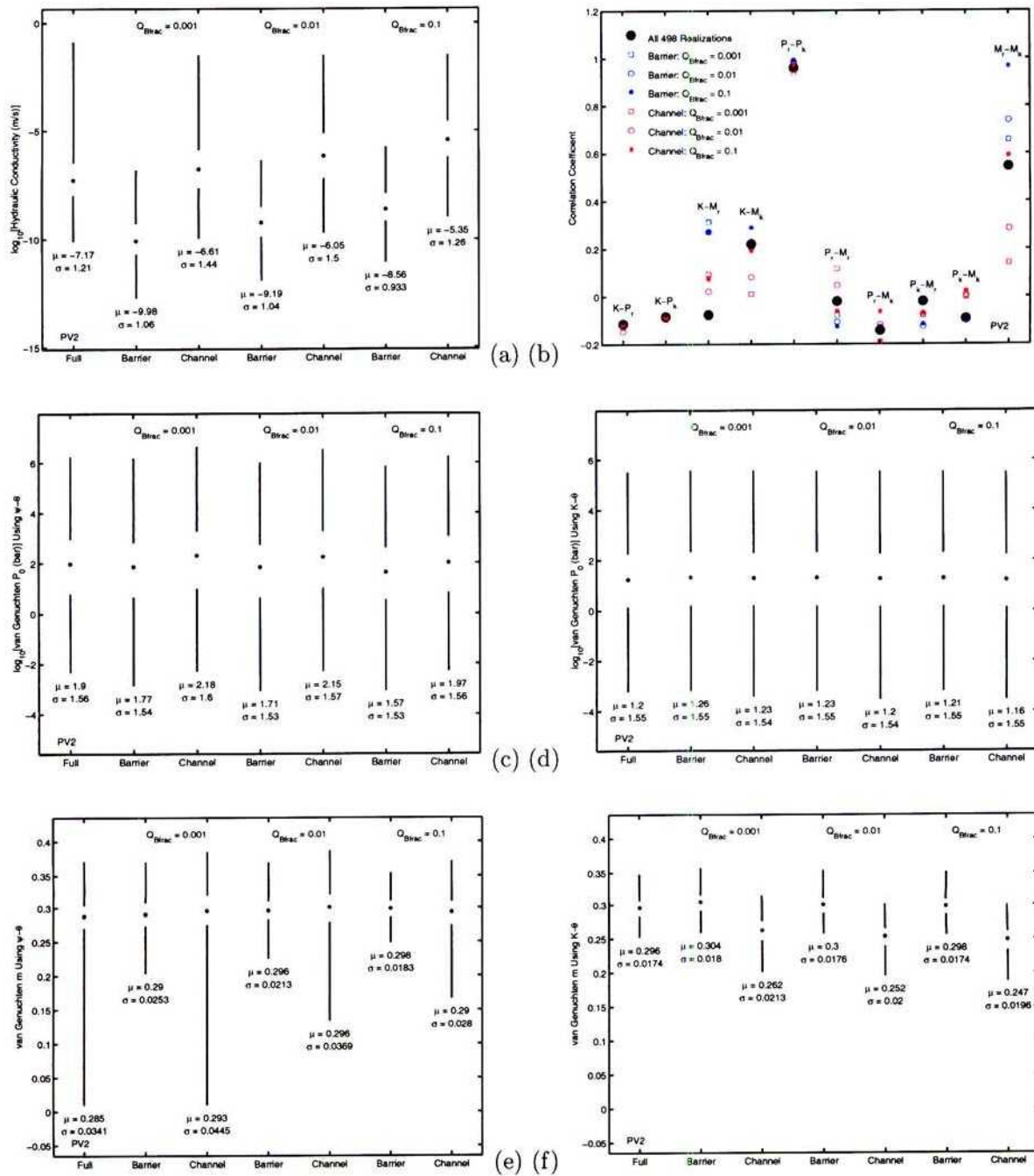
Figure 3-101: 10/28/97. Estimated properties for layer PV2. Correlation between material properties (b), and quartiles for: (a) equivalent K_{sat}, P_0 using retention and conductivity (c and d, respectively); and m using retention and conductivity (e and f, respectively).
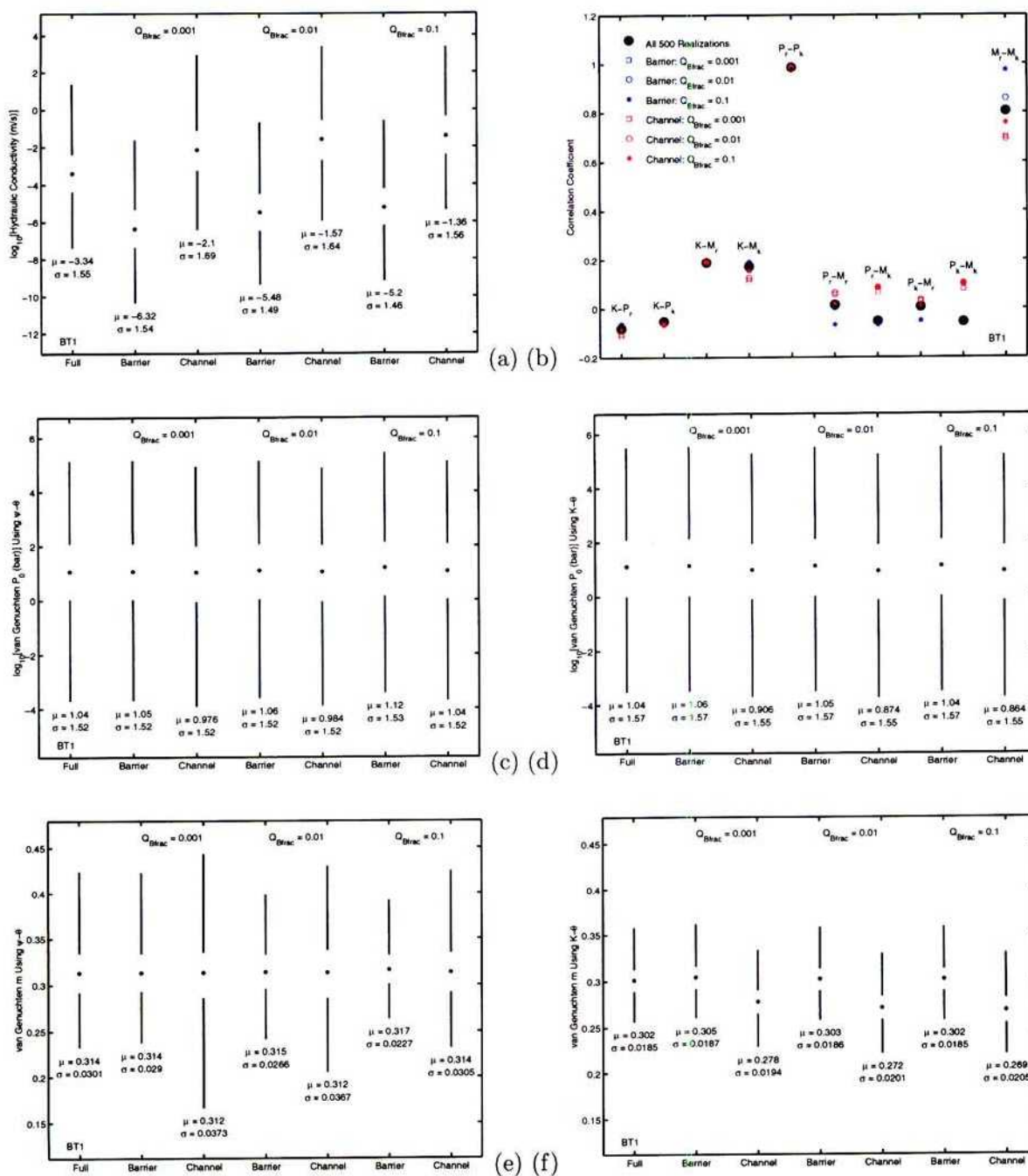
Figure 3-102: 10/28/97. Estimated properties for layer BT1. Correlation between material properties (b), and quartiles for: (a) equivalent K_{sat}, P_0 using retention and conductivity (c and d, respectively); and m using retention and conductivity (e and f, respectively).
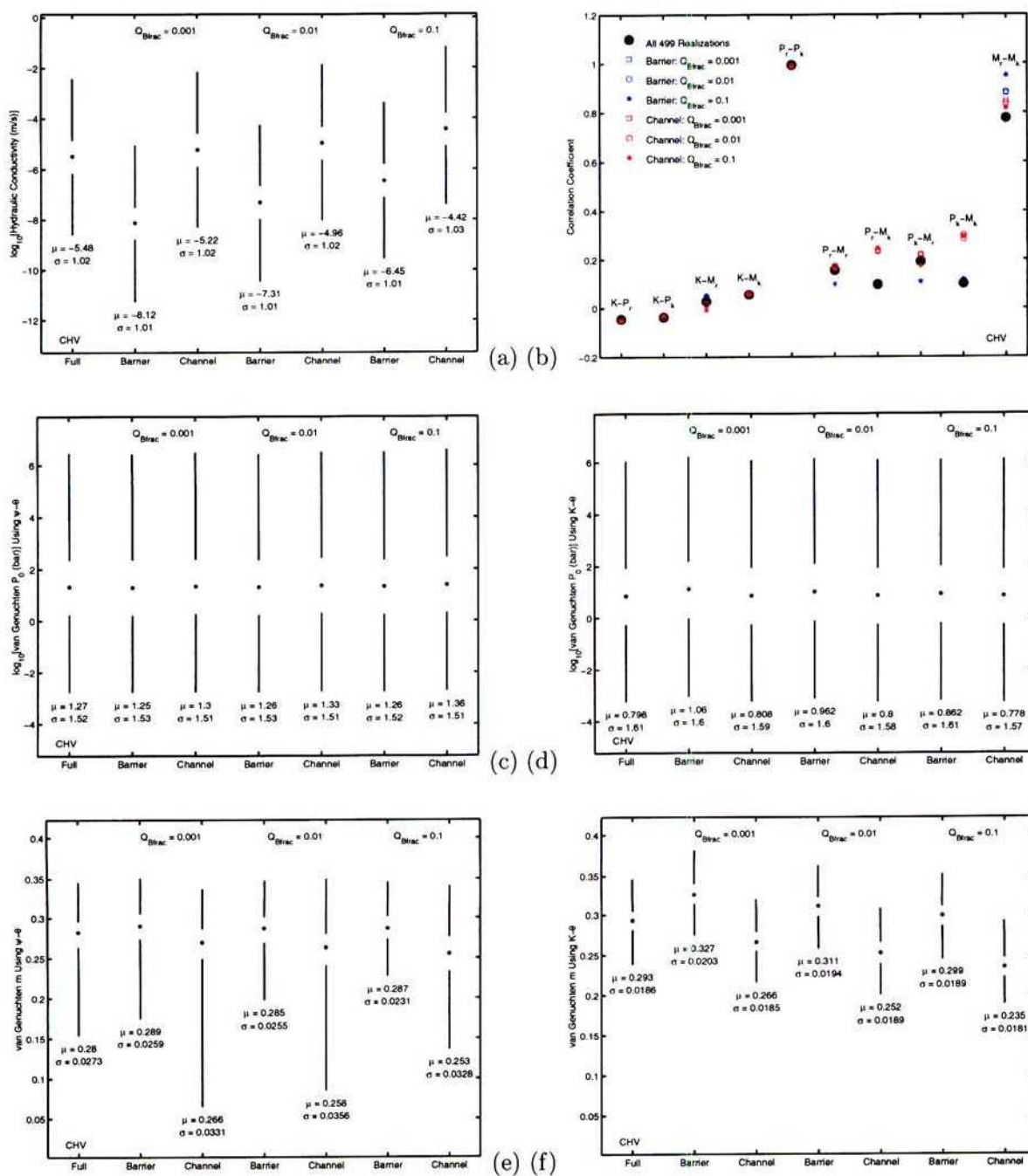
Figure 3-103: 10/28/97. Estimated properties for layer CHV. Correlation between material properties (b), and quartiles for: (a) equivalent K_{sat}, P_0 using retention and conductivity (c and d, respectively); and m using retention and conductivity (e and f, respectively).
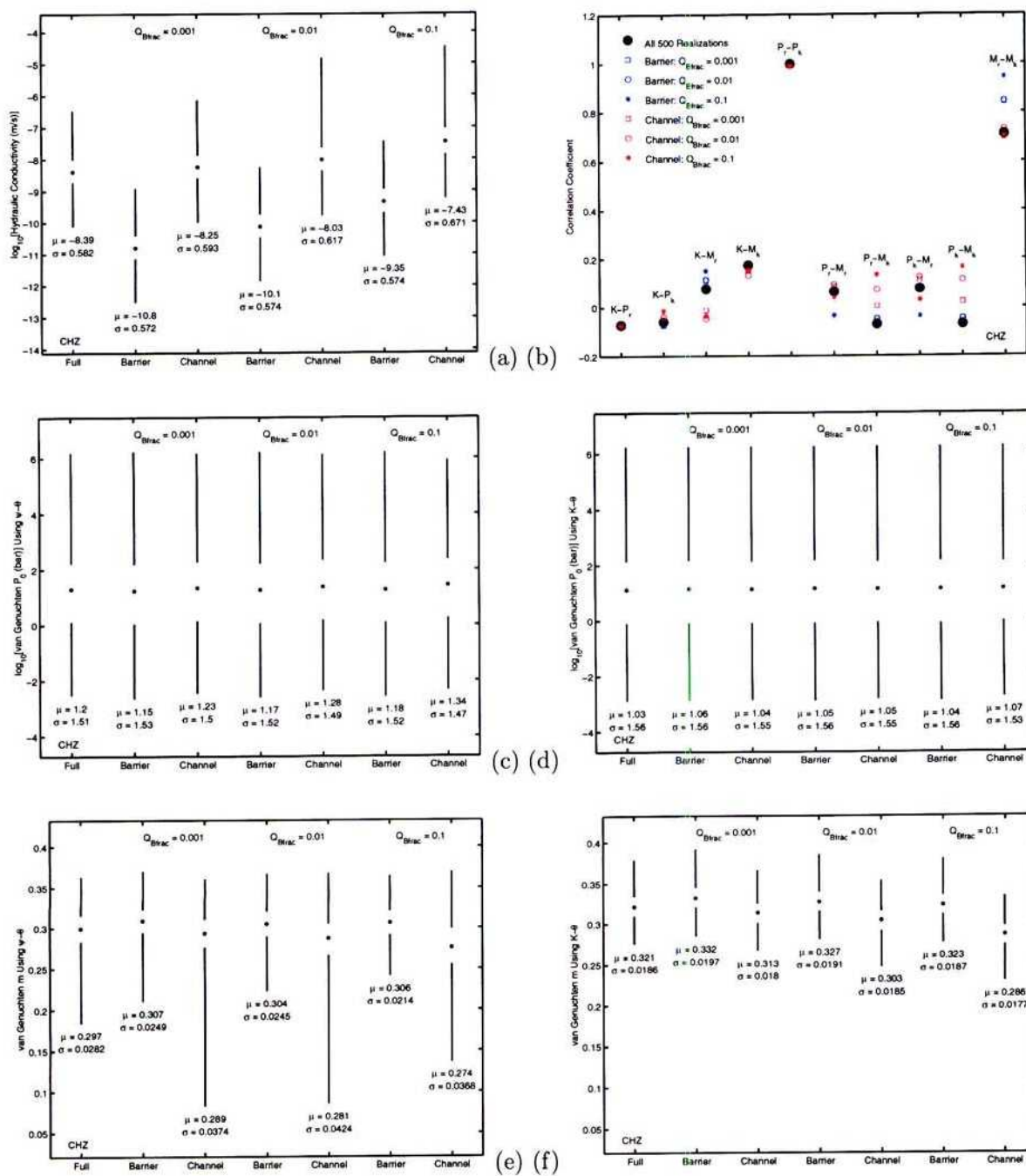
Figure 3-104: 10/28/97. Estimated properties for layer CHZ. Correlation between material properties (b), and quartiles for: (a) equivalent K_{sat}, P_0 using retention and conductivity (c and d, respectively); and m using retention and conductivity (e and f, respectively).
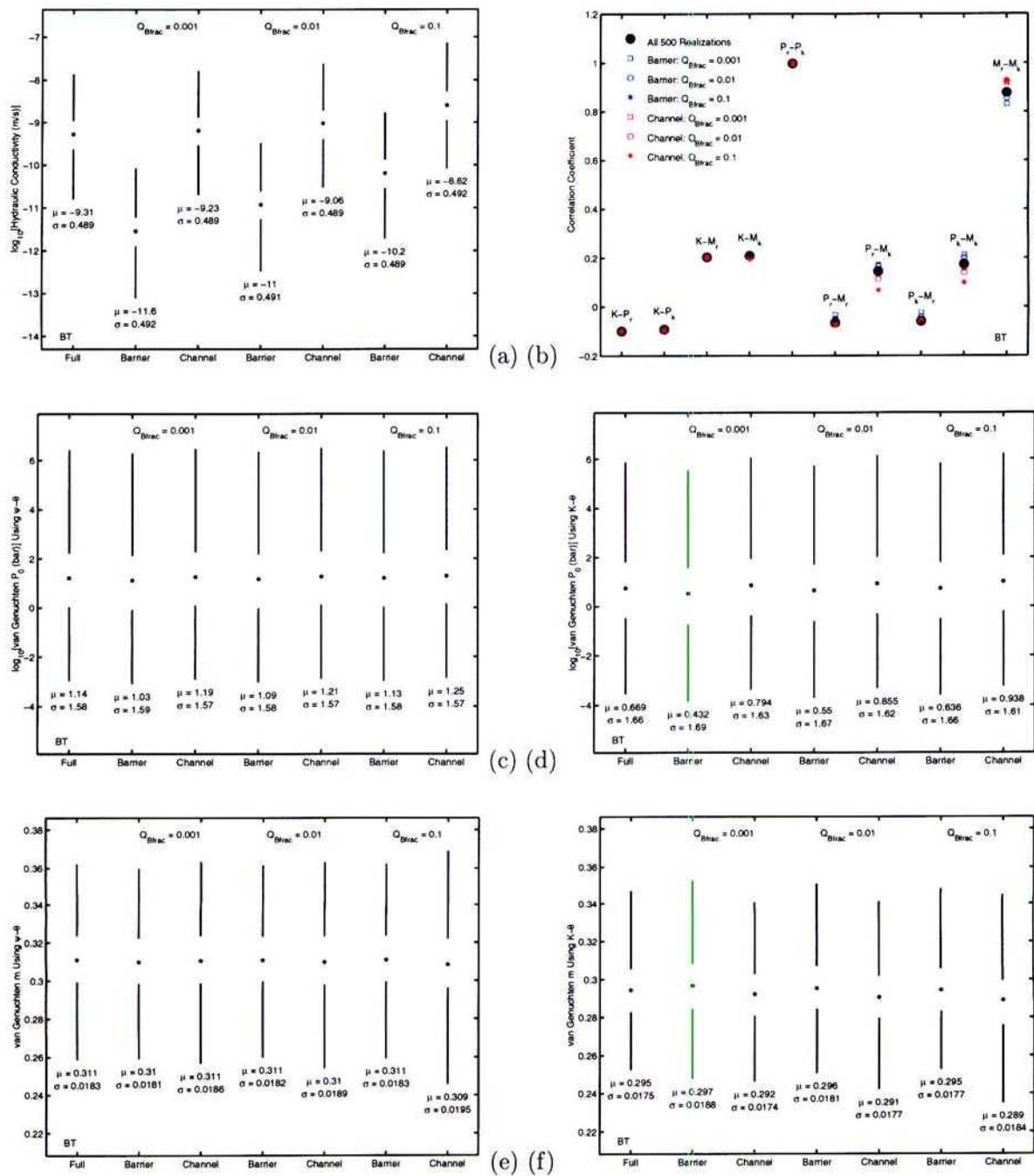
Figure 3-105: 10/28/97. Estimated properties for layer BT. Correlation between material properties (b), and quartiles for: (a) equivalent K_{sat}, P_0 using retention and conductivity (c and d, respectively); and m using retention and conductivity (e and f, respectively).
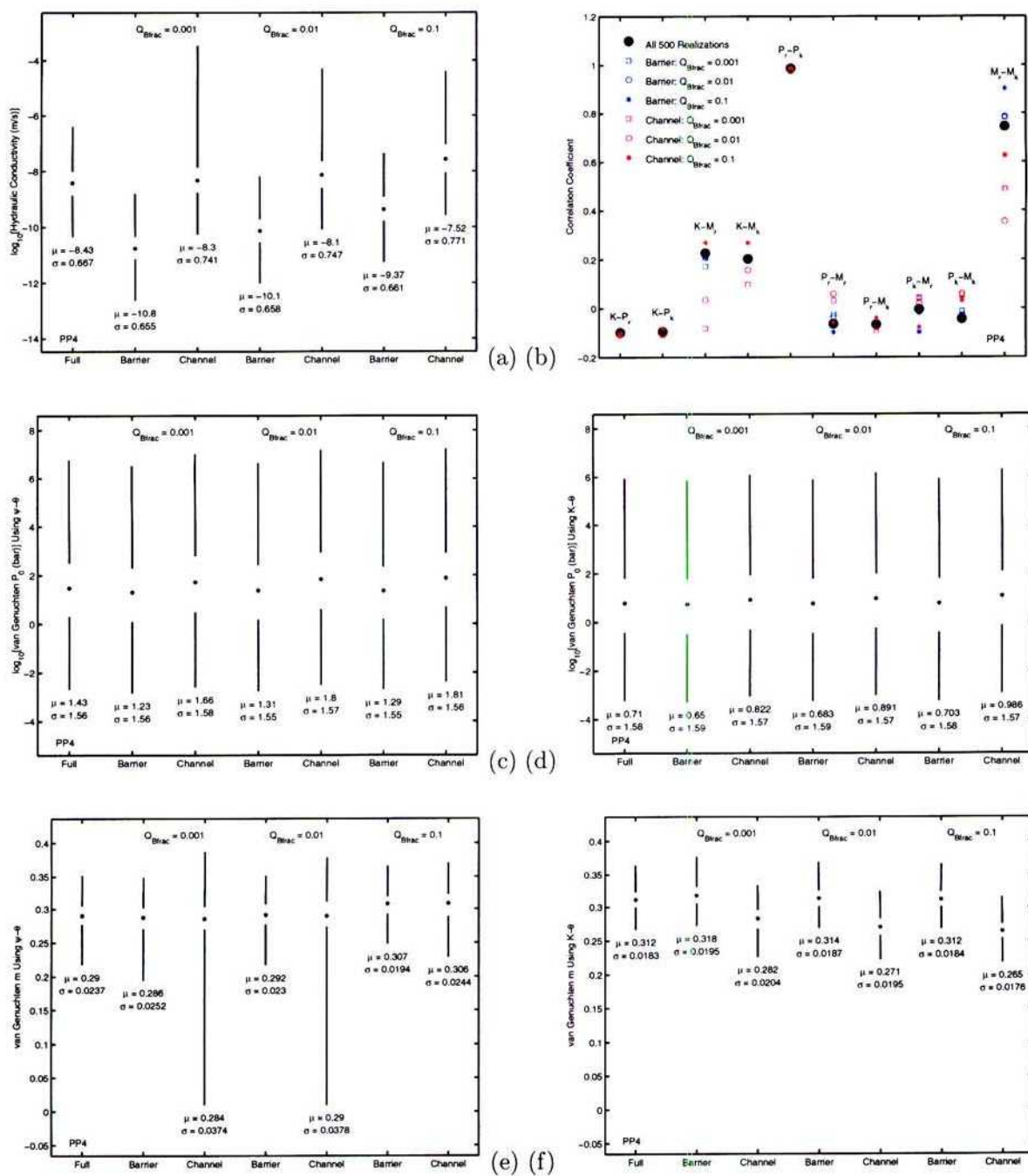
Figure 3-106: 10/28/97. Estimated properties for layer PP4. Correlation between material properties (b), and quartiles for: (a) equivalent K_{sat}, P_0 using retention and conductivity (c and d, respectively); and m using retention and conductivity (e and f, respectively).
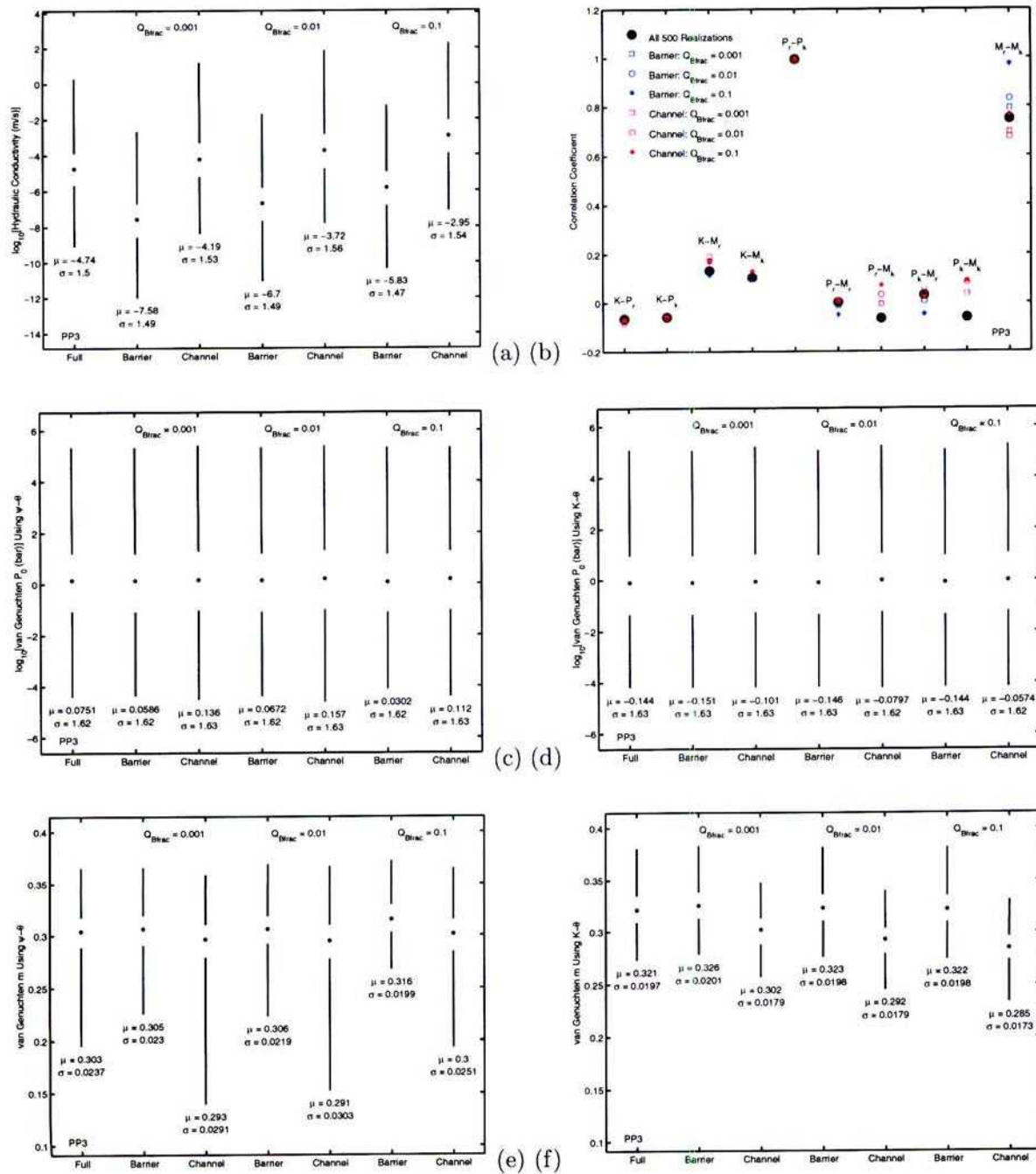
Figure 3-107: 10/28/97. Estimated properties for layer PP3. Correlation between material properties (b), and quartiles for: (a) equivalent K_{sat}, P_0 using retention and conductivity (c and d, respectively); and m using retention and conductivity (e and f, respectively).
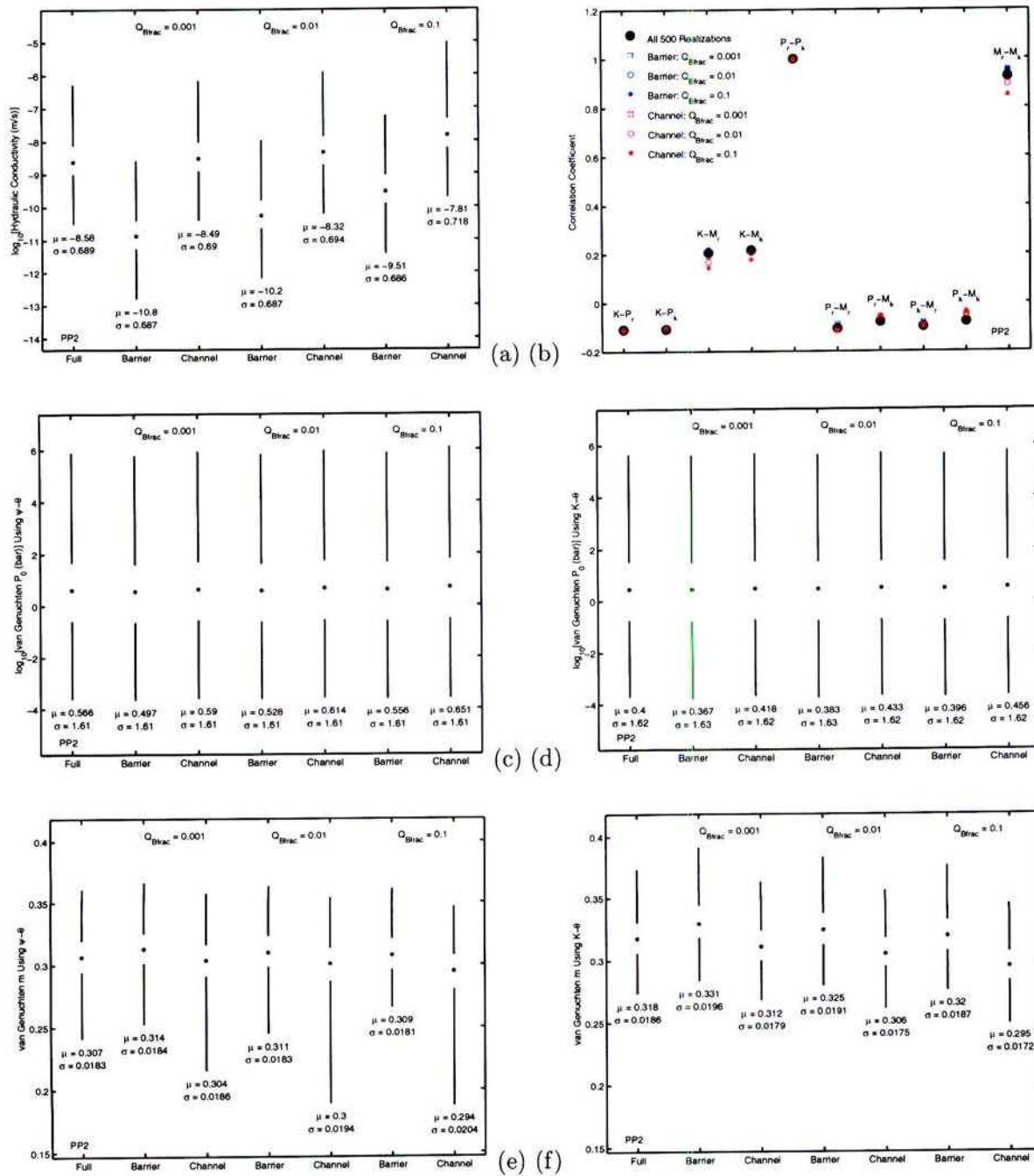
Figure 3-108: 10/28/97. Estimated properties for layer PP2. Correlation between material properties (b), and quartiles for: (a) equivalent K_{sat}, P_0 using retention and conductivity (c and d, respectively); and m using retention and conductivity (e and f, respectively).
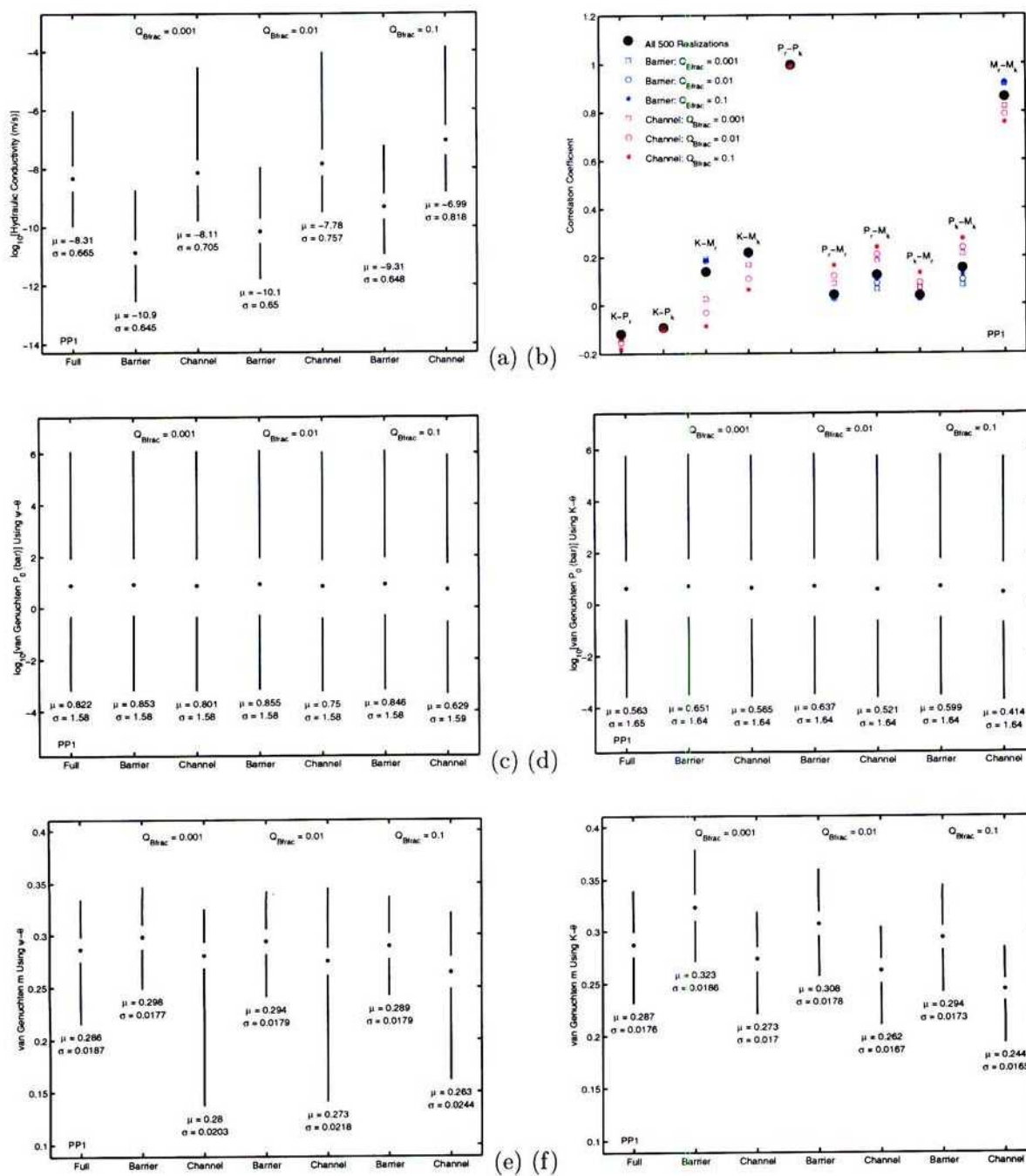
Figure 3-109: 10/28/97. Estimated properties for layer PP1. Correlation between material properties (b), and quartiles for: (a) equivalent K_{sat}, P_0 using retention and conductivity (c and d, respectively); and m using retention and conductivity (e and f, respectively).
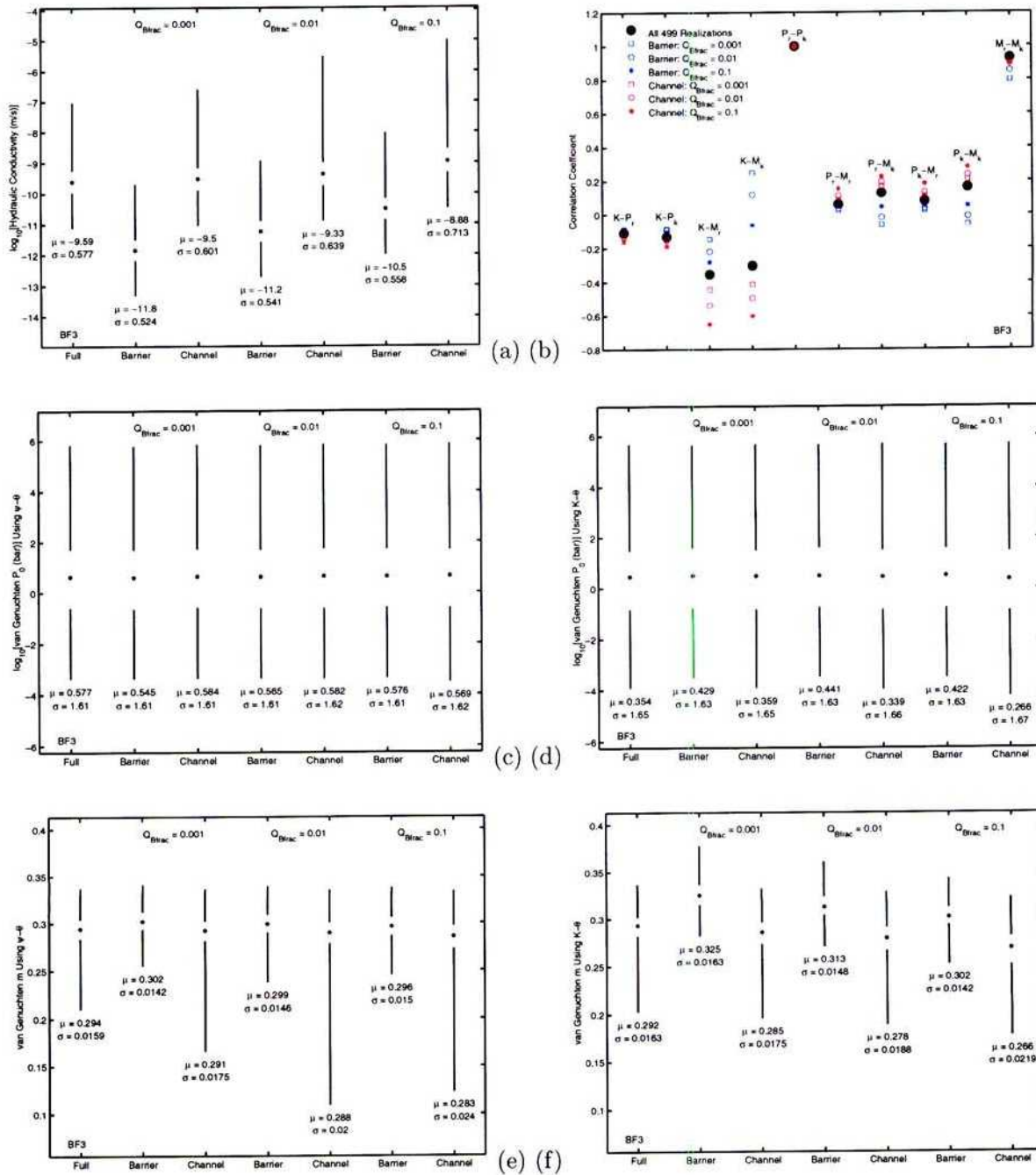
Figure 3-110: 10/28/97. Estimated properties for layer BF3. Correlation between material properties (b), and quartiles for: (a) equivalent K_{sat}, P_0 using retention and conductivity (c and d, respectively); and m using retention and conductivity (e and f, respectively).
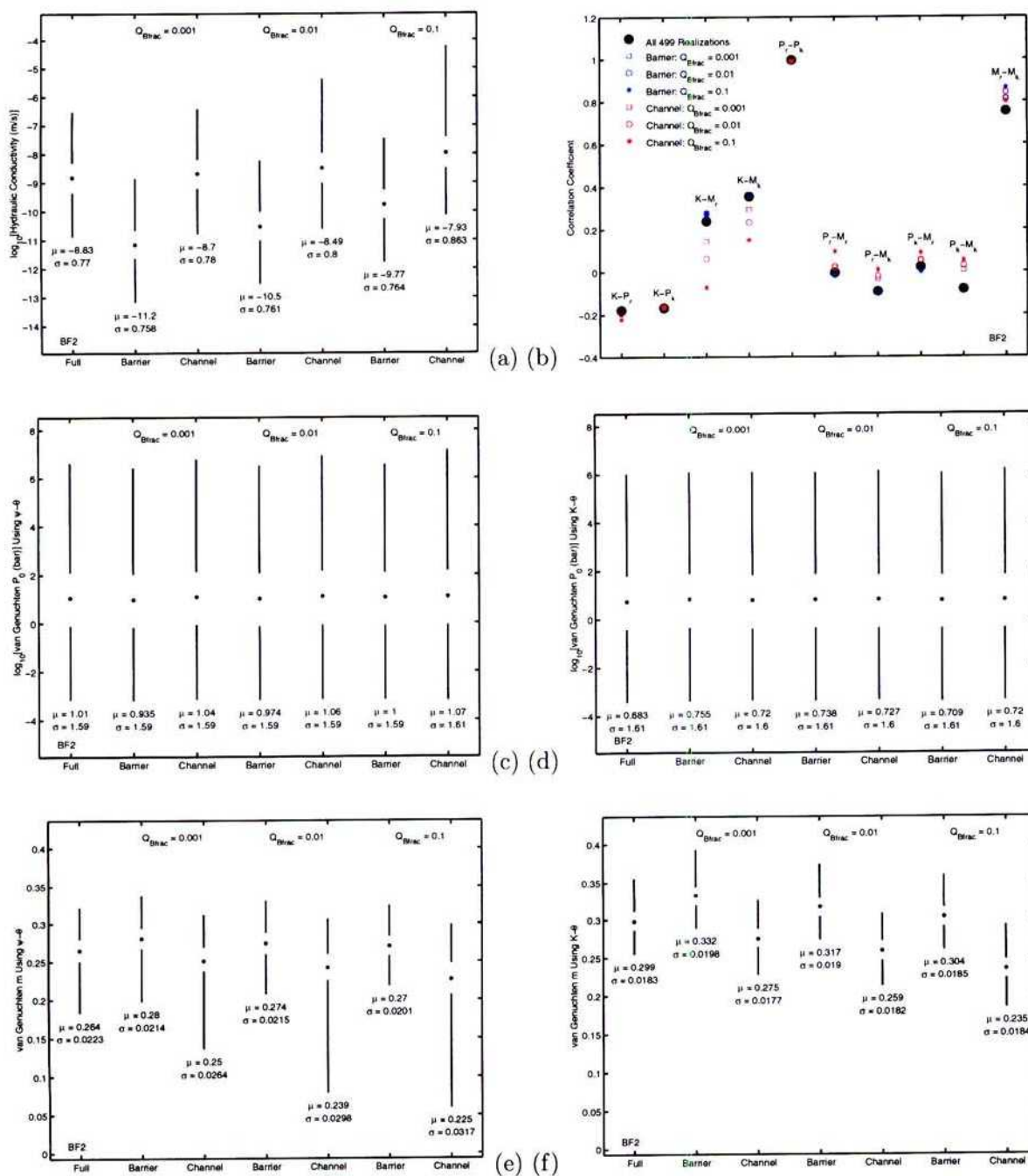
Figure 3-111: 10/28/97. Estimated properties for layer BF2. Correlation between material properties (b), and quartiles for: (a) equivalent K_{sat}, P_0 using retention and conductivity (c and d, respectively); and m using retention and conductivity (e and f, respectively).

11/8/97 Further hydraulic-property discussion. $\boxed{\mathscr{SAS}}$

After pondering the results shown in the previous entries, it occurred to me that the actual object of the exercise is to create properties that appropriately describe the bulk properties of each layer. The bulk properties of interest are the average flux and average velocity as a function of pressure. Actually, the bottom line result is a description of equivalent velocity as a function of percolation flux.

I realized that one way to achieve this goal is to use an optimization approach to simultaneously minimize deviations from both flux and velocity with the same set of equivalent properties. Equivalent hydraulic properties are imposed to describe hydraulic conductivity over a range of suctions. In the previous entry, only the flux was matched; the key idea is to also match velocity, by allowing four properties to be simultaneously determined. The four properties of interest are K_{sat}, P_0, van Genuchten m, and porosity.

In the implementation, I am able to use unconstrained minimization for these constrained parameters by transforming them for the optimization process. Both K_{sat} and P_0 are solved using their logarithm while both m and ε are required to lie within the $(0, 1)$ range using the transform

$$Y = \frac{1}{2} \log[X/(1 - X)], \tag{3-100}$$

where X represents the original parameter and Y is the transformed parameter.

My first attempt to match both average flux and average velocity simply matched the average velocity for the realizations with a percentage of the largest flux. In order to find average flux: (i) sort the realizations from smallest to largest flux; (ii) calculate cumulative flux; and (iii) calculate average velocity using the realizations, from largest to smallest flux, that contribute to the target percentage of total flux. For example, the largest-flux realizations contributing to 99.9 percent of the total flux might be used to calculate velocity. I tried 99.9, 99, and 90 percent of total flux at first go.

As it turned out, the flux-determining properties did not change significantly as the target changed. The porosity, however, changes dramatically.

One small detail of implementation: I weight the optimization realizations so that the region of fluxes centered on 50 mm/yr are weighted strongest, with the weighting decreasing exponentially as the fluxes are farther away from this value. The idea is to obtain the best match in the region

of the curves most likely to be used at YM. The weighting function is

$$w_i = \exp[-|\bar{y}_i - \log(50)|/4], \tag{3-101}$$

where $\bar{y}_i$ represents the logarithm of average flux for a layer (mm/yr) and w_i is the weight for that flux. The decay is relatively small.

The approach, as outlined, has an element of arbitrariness associated with it. How does one pick the percentage of total flux to use? It finally occurred to me to use a flux-weighted velocity,

$$\bar{V} = \frac{\sum qv}{\sum q}, \tag{3-102}$$

so that the largest flux realizations are weighted the most. A significant advantage of the approach is that no arbitrary tuning parameter is used.

After a few welded layers have been processed, it appears that the flux-weighted measure again does not change hydraulic properties significantly, except for the porosity. Generally, the flux-weighted measure provides a smaller porosity than that arising from using the realizations with 50 percent of the total flux. The flux-weighted porosity is typically 2 to 3 orders of magnitude less than the bulk porosity. The implication is that, if the water indeed moves in channels, it may move *within the matrix* on the order of 1 to 10 m/yr! And in very localized channels, which are difficult to find!

11/11/97 Results of velocity-weighted hydraulic properties.

The first 200 realizations for each of the 16 layers of interest (TMN through BF2) have been completed and are reported in Table 3-14. The results are extracted using calc_layerequiv.m. Each realization takes about 90 seconds on my Sparc 20. These results are in subdirectory *Realization6*. Three sets of properties are fairly similar to the corresponding properties reported in Table 3-11, Table 3-12, and Table 3-13 for the full layer averages. The saturated hydraulic conductivity is quite similar while the retention properties are less close; in particular, van Genuchten m and n tend to be smaller than the previous results, typical of materials with a mixture of pore sizes. Porosity (not previously reported) is far smaller than the bulk porosity for each layer, representing by far the biggest change in properties. Mean equivalent porosity ranges from 3.8×10^{-6} to 0.0035 for the different layers, and appears to be roughly lognormally distributed.

Table 3-14: Estimates of microstratigraphic hydraulic properties using flux-weighted velocity. The mean and standard deviation of the base-10 logarithm of all properties is reported except for van Genuchten n and m. Note that $\log_{10}(200) = 2.3$.

Unit	N	$\log_{10}(K_{sat})$ (mm/yr)			$\log_{10}(\alpha)$ (bar^{-1})		m		n		$\log_{10}(\epsilon)$	
		μ (m/s)	μ	σ	μ	σ	μ	σ	μ	σ	μ	σ
TMN	200	-8.39	2.11	0.69	0.2559	1.4745	0.287	0.034	1.406	0.062	-3.67	0.512
TLL	200	-7.16	3.34	0.99	0.9930	1.4997	0.295	0.031	1.420	0.060	-3.64	0.428
TM2	200	-8.28	2.22	0.74	0.6465	1.4935	0.275	0.033	1.381	0.060	-3.42	0.455
TM1	200	-9.12	1.38	0.50	0.2112	1.4778	0.267	0.028	1.367	0.050	-2.94	0.301
PV3	200	-7.59	2.91	1.10	0.0113	1.4350	0.298	0.015	1.424	0.030	-5.42	0.409
PV2	199	-7.30	3.20	1.28	0.0117	1.4967	0.280	0.044	1.394	0.081	-4.48	0.632
BT1	199	-3.32	7.17	1.71	0.1150	1.4643	0.296	0.054	1.429	0.106	-3.58	0.362
CHV	189	-5.13	5.37	0.95	0.0921	1.4224	0.144	0.058	1.173	0.080	-2.73	0.258
CHZ	199	-8.12	2.38	0.63	0.1115	1.4057	0.210	0.059	1.272	0.095	-2.85	0.343
BT	200	-9.29	1.21	0.49	0.0962	1.4558	0.292	0.031	1.416	0.060	-2.46	0.295
PP4	200	-8.56	1.94	0.66	0.0319	1.4567	0.286	0.039	1.405	0.074	-3.36	0.574
PP3	199	-4.80	5.70	1.50	1.2326	1.5022	0.284	0.045	1.401	0.080	-3.71	0.391
PP2	200	-8.48	2.02	0.73	0.4346	1.5210	0.276	0.031	1.383	0.058	-3.36	0.783
PP1	192	-7.97	2.53	0.80	0.2886	1.4701	0.171	0.057	1.212	0.083	-3.04	0.344
BF3	192	-9.50	1.00	0.66	0.3863	1.4655	0.242	0.064	1.328	0.101	-2.68	0.290
BF2	195	-8.51	1.99	0.96	0.1293	1.5411	0.165	0.070	1.207	0.103	-3.07	0.572

The curve-fitting algorithm had difficulty fitting hydraulic properties in some of the layers. When this occurs, K_{sat} is many orders of magnitude larger than it should be; otherwise, K_{sat} is within a factor of two or so for the various cases. Similarly, m can be extremely small, well less than 10^{-3}. The problem appears to be worst in CHV, PP1, BF3, and BF2, with particularly small values of equivalent m, although it may be that the unreasonably small m values aris from cases with misfit properties (very large K_{sat}, very small m). Usually the hydraulic properties are determined reasonably for nearly all of the flux-weightings even when one or two are off. I significantly cut down on occurrences of fitting error for the flux-weighted-velocity cases by using the final guess for the 50-percent flux case as the starting guess for the flux-weighted-velocity case. Apparently starting with porosity too large can bollux things. In Table 3-14, I eliminate all cases where flux-weighted K_{sat} is greater than six orders of magnitude greater than the minimum K_{sat} for the property set or m is less than 0.001.

When rerunning, I will start with the properties determined in the previous flux-weighting case for each subsequent flux-weighting case with the same collection of realizations, except that porosity will be multiplied by 0.1. Trial runs using this new strategy with CHZ appear to have much more self-consistent results.

I noticed that the standard deviation of $\log_{10}(K_{sat})$ appears to increase roughly linearly with the mean of $\log_{10}(K_{sat})$ for the different layers. The ratio of mean to standard deviation is generally within an order of magnitude across the different layers.

11/13/97 Notes.

Simulations with the revised approach have partially been redone for the layers with problems in the first set of flux-weighted velocities. The problems have not been eliminated, but have been greatly reduced. Only a maximum of 1 simulation per 200 has problems, rather than up to 9. I will try one more time by imposing a second try when the first has m below 0.001. These results are being put in subdirectory *Realization7*.

An idea occurred to me regarding a way to approach UZFT. The sensitivity studies have shown that having matrix flow will tend to have a noticeable impact on dose measures. It doesn't make a difference what order the layers are contacted when release rates to the water table is of primary interest. What might make more sense is to generate artificial layers with similar matrix properties. Equivalent properties can be determined so that the same travel time is provided as would result from all 16 microstratigraphic layers in succession.

A computational savings may be realized by noticing that UZFT really only requires that one leg be provided with the equivalent velocity and retardation characteristics. It is no problem to provide the equivalent velocity in 1D tubes, by dividing the travel time required to traverse intervening layers by the corresponding distance. The problem becomes identifying appropriate retardation characteristics. Intuitively one would expect that some sort of travel-time weighted retardation may be appropriate. Luckily retardation is linear.

References

Benjamin, J. R. and C. A. Cornell. 1970. *Probability, Statistics, and Decision for Civil Engineers.* New York, NY: McGraw-Hill.

Buesch, D. C., R. W. Spengler, T. C. Moyer, and J. K. Geslin. 1996. *Proposed Stratigraphic Nomenclature and Macroscopic Identification of Lithostratigraphic Units of the Paintbrush Group Exposed at Yucca Mountain, Nevada.* Open-File Report 94-469, United States Geological Survey, Denver, CO.

Flint, L. E. 1996. *Matrix Properties of Hydrogeologic Units at Yucca Mountain, Nevada.* Milestone 3GUP604M, Department of Energy, Las Vegas, NV.

Flint, L. E., A. L. Flint, C. A. Rautman, and J. D. Istok. 1996. *Physical and Hydrologic Properties of Rock Outcrop Samples at Yucca Mountain, Nevada.* Open-File Report 95-280, United States Geological Survey, Denver, CO.

Lapin, L. 1983. *Probability and Statistics for Modern Engineering.* Boston, MA: PWS Publishers.

Mason, R. L., R. F. Gunst, and J. L. Hess. 1989. *Statistical Design & Analysis of Experiments With Applications to Engineering and Science.* New York, NY: John Wiley & Sons.

Matalas, N. C. 1967. Mathematical Assessment of Synthetic Hydrology. *Water Resources Research 3*(4), 937–945.

Montazer, P. and W. E. Wilson. 1984. *Conceptual Hydrologic Model of Flow in the Unsaturated Zone, Yucca Mountain, Nevada.* Open-File Report 84-4345, United States Geological Survey, Lakewood, CO.

Rautman, C. A., L. E. Flint, A. L. Flint, and J. D. Istok. 1995. *Physical and Hydrologic Properties of Rock Outcrop Samples From a Nonwelded to Welded Tuff Transition, Yucca Mountain, Nevada.* Water-Resources Investigations Report 95-4061, United States Geological Survey, Denver, CO.

Scott, R. B. and J. Bonk. 1984. *Preliminary Geologic Map (1:12,000 scale) of Yucca Mountain, Nye County, Nevada, with Geologic Cross Sections.* Open-File Report 84-494, United States Geological Survey, Denver, CO.

4   Ambient Hydrology KTI – Model Development

Account Number: **20-1402-861**

Collaborators: **Randy Fedors, Gordon Wittmeyer, Jim Winterle**

Directories: **$HomeTwo/Numeric/Breath and as noted**

Objective: Perform documentation of conceptual model and code development for subsurface flow and transport, particularly regarding infiltration. Work documenting coding work and bug fixes is documented elsewhere in the Scientific Notebook. Conceptual model development may include: (i) enhanced one-dimensional (1D) simulation capability (*i.e.*, vegetation uptake, matrix-fracture interactions, true N-phase simulation, snow and ice, transport of tracers); (ii) two-dimensional (2D), 2.5D, or three-dimensional (3D) watershed-scale modelling; (iii) 2D, 2.5D, or 3D hillslope-scale modelling; (iv) diversion of infiltration due to the PTn layer; (v) discrete-fracture simulations.

2/9/98 Initial entry.

Work exploring results from infiltration studies performed under the Ambient Hydrology KTI is documented elsewhere in this Scientific Notebook. In order to improve the transparency of computational model development, conceptual-model development is documented in one or more separate chapters. This particular chapter documents the development of enhancements to the *breath* code. It may be that the resulting code is so significantly changed that a new name is required, although politically it would probably be better to call it *breath*. I have a fondness for calling a new code VaporWare (Vapor for short), and enhancements that result in at least 2D simulations may be renamed.

The overarching developmental philosophy for new code is to maintain extensibility from 1D through 3D applications. Accordingly, some of the TOUGH and MODFLOW ideas will be followed. In particular, strict segregation between physics and computation should be followed. Thus, modules for equations of state should not be dependent on the computational scheme or dimensionality.

As dimensionality is added it should be possible to use previously defined lower-dimensionality schemes as plug-ins. For example, a 2D model should be able to have locally 1D segments overlain using the same variables (*e.g.*, fractures within a matrix, overland flow). Similarly, a 3D model should be able to accommodate both 1D and 2D elements.

Ideally, the code should end up able to accommodate a wide variety of temperatures, ranging from below freezing to above boiling. It should also be possible to accommodate several simultaneous phases (air, water, oil) and several simultaneous components. Despite the generality in desirable physics, reduced complexity should also be accommodated with no lack of computational efficiency.

At its most complex, YM should only require the following elements: (i) 1D finite element, (ii) 1D finite volume, (iii) 2D triangle finite element, (iv) 2D quad finite element, (v) 2D finite volume, (vi) 3D prism (2.5D triangle) finite element, (vii) 3D brick finite element, and (viii) 3D finite volume. The difference between finite element and finite volume is in the definition of the unknown. In finite elements, the unknowns are located at the nodes (and edges, for mixed finite elements) and the elements are responsible for handling flow processes. In finite volumes, the unknowns are located at the center of the volume (and connections, for mixed finite volumes) and connections are responsible for handling flow processes. Finite volumes are simpler and arguably more accurate when they can be applied, but sharp discontinuities are difficult to accommodate. Finite elements are more complex to code and use, but can easily handle sharp discontinuities. The finite element approach allows adjacent elements, with different material properties, to share unknown values. The finite volume approach, on the other hand, must smear material properties over the distance between element centers.

The biggest mistake made during the coding of *breath* was made at the outset of the project. There was a choice between using C and Fortran. I selected Fortran for the possible benefits of sharing software and possible efficiencies if *breath* were to be used on supercomputers. So far, no sharing has occurred and workstations are approaching the capacity of supercomputers. There are several benefits of using C that have not been realized from this decision, including: (i) strong organizational capabilities (*e.g.*, structures, pointers to functions), (ii) portable error-catching capabilities, and (iii) strong development tools for program input (*e.g.*, flex, bison). Fortran-90 includes most C and C++ functionality, with far stronger array operations, but does not have the input-language tools.

Significant additional development should abandon the Fortran-77 language due to the above shortcomings. The fastest and most extensible procedure for development would be to base further code on *Matlab*, as there is a wealth of tools already developed and available as part of the *Matlab* package. *Matlab* is based on a very strong programming language, with many of the best features of both C and Fortran-90, was originally designed for numeric operations on arrays, and has a built-in Graphical User Interface (GUI) builder. The array-based nature of the *Matlab* language is easy to program in; code that is inefficient in the interpreted *Matlab* language can be replaced with compiled C code using a code translator supplied by *Matlab* or by independent programming.

Matlab is able to support standalone executable programs written in C or Fortran without requiring *Matlab* to be invoked, although I have not done so and do not know what would be required for porting applications. *Matlab* is used on numerous operating systems, so portability may not be a tremendous issue.

Coding in C/C++ overcomes questions about portability and is the second most favored approach. Using an environment called Jacquard, which I developed at UVM before joining the Center for Nuclear Waste Regulatory Analyses (CNWRA), much of the functionality of *Matlab* can be recovered and portability assured. At the time Jacquard was developed, there were several features that *Matlab* couldn't easily duplicate, but they are gradually being included in *Matlab*. The current version of Jacquard requires an SGI workstation for graphics, but is modular enough to adapt to OpenGL with minimal disruption.

2/10/98 Vegetation modelling. $\boxed{\text{SAS}}$

Model Rationale and Background

The intent of the plant uptake model is to plausibly take up water from the soil and from within fractures at YM under climatic conditions ranging from slightly drier than current to full glacial maximum. The model is intended to be an add-on to *breath*, and the implementation will be 1D to start. Ideally, a minimum of information should be required by the model, and that information should be readily estimated. It is not desirable that the characteristics of individual plants (*e.g.*, a sagebrush or a juniper) are specified in detail; rather, the simulation should reflect the aggregate behavior of several plants within a community (*i.e.*, the lateral extent captured by the 1D model should be on the order of a grid block within the Geographic Information System (GIS) model, or approximately 30 m x 30 m).

Typical models within the literature tend to provide a static distribution of root density or maximum root density with depth, and link uptake to the root density. The simplest approach is to proportionately take up water to satisfy transpiration requirements according to the maximum root density. A slightly more complex approach takes into account the relative soil moisture when apportioning uptake with depth. A final approach is to treat the plant as a continuum and take account of potential variation within the plant. The plant-continuum approach is easily extended into a dual-continuum formulation, representing the plant and the soil as two continua linked by leakage across the root hairs. A far more complex approach is to discretely model the individual

---

roots, requiring the use of a 3D simulator. My experience is that this approach is extremely slow, although this may be due in part to inefficient coding. Adaptive calculation of root-density distributions is not common, although the agricultural literature should account for changing uptake patterns during the growing season.

As the model increases in complexity, there are tradeoffs with both computational efficiency and data requirements. For example, the simplest model requires only the root density function and the transpiration rate, while as the model increases in complexity additional information such as soil-root uptake parameters and plant-transport parameters are required, and the calculations increase in complexity. On the other hand, as the models increase in complexity, the burden of appropriately apportioning rates of uptake with depth increasingly is shifted to the simulator, enabling increased plausibility. More is known or can be inferred about plant responses in general than uptake in the complex fractured-bedrock system at YM, so that there is real benefit in transferring as much burden as possible to the simulator within the bounds of feasible computational effort. For example, providing the root density function for soil overlying fractured bedrock is quite difficult to determine and would be required for each climatic scenario considered, while reasonable uptake and transport parameters are available in the literature or can be calculated. If the model adaptively calculates a root density function based on allowable growth rates and uptake information during the simulation, this function can not only be examined for plausibility (thereby providing ground-truth capability) but could provide basic information for the scientific community.

Two simple conceptual models for roots might be appropriate: (i) the vertical stem with horizontal roots branching at each node, and (ii) the cloud-o'-roots, with all roots branching from the main stem. Both models would split the plant into 3 conceptual regimes: (i) hair roots, where uptake from the soil takes place; (ii) transport system; and (iii) leaf system. The second model does not exclude the multiple root branching that plants exhibit: it does assume, in essence, that transport from hair to leaf occurs along independent channels within the same root. The first model would require that a separate set of plant potentials be simultaneously determined at each node point, resulting in a set of simultaneous equations to solve, while the second model can determine the nodal potentials without requiring a set of simultaneous equations to be solved. The computationally more complex first model would enable leakage of water from roots into dry soil. The second model may tend to overestimate the amount of biomass committed to roots by not accounting for the transmission efficiency gained by larger roots. Operationally, there may be little difference between the two models, as resistance losses in the transport system are typically small relative to losses across the root hairs and within the leaves, so that potentials within the transport system are relatively uniform. Uptake fluxes in both models would be controlled by resistance loss across the leaf area. Accordingly, the simpler model should be explored.

One area that requires a good deal of thought is the appropriate transpiration parameterization. This area is common to all of the models and will likely be difficult to resolve. Typically one parameterizes potential transpiration according to leaf area, and modifies this by the ability of the root system to deliver at the potential rate. Key information required for this approach is potential transpiration rate per leaf area, potential rates of change of leaf area with time, and modifications of the potential rates according to environmental conditions. Values of these parameters are likely species dependent, but it may be possible to regress some sort of relationship between climatic variables and plant uptake parameters if there is strong variability between species.

The potential rates are partly seasonal, but are also partly dependent upon plant-devised heuristic strategies. For example, shrubs may require adequate rainfall in the fall for growth in the spring (Beatley, 1974), otherwise remaining dormant. Different shrubs have a different tolerance for fall rainfall, so that there is a spectrum of responses to account for. Shrubs may emit a water-soluble growth-inhibiting compound that must be washed away before dormancy is averted. It should be simple to incorporate a module that simulates this behavior. A simple model would be

$$\frac{\partial c}{\partial t} = \alpha(c - c_{max}) - \beta q_{rain}, \tag{4-1}$$

where α and β represent seasonally dependent rate constants such that a good fall rain would remove any accumulated buildup and a poor fall rain would result in significant concentration, c, of the growth-inhibiting substance. Any potential rate, G, might then be dependent on the depletion in c, so that $G = G_{min} + G_{max}(1 - c/c_{max})$.

Adaptive modification of biomass distributions according to environmental conditions is another area that requires significant effort to resolve plausibly. Plants tend to allocate roots adaptively to maximize uptake of a growth-limiting resource (typically nitrogen, phosphorus, or water). The strategy is to grow and respond rapidly to environmental conditions at the end-member locations (hair roots, leaves) and grow slowly in major transport systems. Thus, there are numerous time scales to resolve: (i) minute-to-minute transpiration, (ii) growth and death of end members within days to weeks, and (iii) growth and death of transport systems within seasons or years. Simple parameterization will be key, but allocation of the resource within the plant should be taken into account in order to limit growth according to environmental constraints.

Model Overview

The following model provides a tight linkage between transpiration, temperature, soil moisture, and vegetation biomass, and should be able to resolve uptake at any time scale of interest. There are

relatively few parameters, and most of them can be estimated fairly easily. The model is formulated in terms of a single limiting nutrient, which could be either moisture or some chemical compound. Modelling the nutrient transport serves as a surrogate for detailed consideration of the details of transpiration, storage, and respiration. Transport of the chemical compound in the porous matrix must be modelled. If the limiting compound is not water, this will require an additional transport simulation, and sources must be considered. I would expect that the transport simulation might use a time-averaged flow field and a larger time step than the water simulation.

The model presupposes that vegetation will preferentially allocate growth to maximize uptake of the limiting nutrient, but not transpire more than required to satisfy respiration and possibly cooling requirements. Note that cooling requirements are not necessarily an issue for the sparse vegetation of desert shrubs as the leaves are well coupled with the atmosphere, according to David Groeneveld, but might be for the piñon-juniper association due to its denser vegetation. Vegetation is assumed to have built-in rate limits on the growth of the three modelled plant-system components (root hairs, transport, and leaves). Given ample supplies of the nutrient, any one of the three components may limit transpiration rates, although usually either transfer across the root hairs or stomatal resistance should be rate-limiting. While the nutrient is not available in sufficient quantities to support the biomass, vegetation biomass is trimmed at characteristic rates.

The interplay between growth, death, and uptake provides the adaptivity to environmental conditions that can capture vegetation adaptation to climatic change. The parameters are fairly general, but must be tuned to match observed conditions. Some of the parameters may depend on climate; for example, it may be that growth rates are slower under cooler conditions.

Nutrient allocation is assumed to follow a strict hierarchy. The demands of the current biomass are satisfied first. Any surplus nutrient goes into storage. If surplus nutrient exists once the storage is at capacity, growth occurs to maximize nutrient uptake. Nutrient-inspired transpiration is limited once maximal growth rates are achieved, so that there is no surplus nutrient uptake unless cooling is needed.

If there is a deficit in nutrient uptake, so that not even current biomass demands are satisfied, the nutrient is removed from storage to satisfy demands. If this is still not sufficient, biomass is trimmed until the available nutrient is sufficient for biomass demands. Note that storage should be large enough to supply biomass demands for one to several days. Also note that the growth and death rates should be much slower for the transport system than for either root hairs or leaves, as there is much greater capital expense involved in growing the transport system.

In actuality, both water and one or more nutrients may be limiting at any particular time.

The above conceptual model could be easily extended to account for multiple potentially limiting factors, by assuming that only one factor at a time is limiting. Such work is beyond the immediate scope of the analysis.

Soil System

The soil system is conceived of as being penetrated by roots spaced more-or-less uniformly. Within the soil, moisture flow is modelled as usual, except for the uptake term. Uptake from the soil is controlled by average distance from root to bulk soil center as

$$q_{uptake} = \frac{K(\theta)\Delta\phi}{\tau_{soil}\lambda_s/2}.$$ (4-2)

where $K(\theta)$ is the soil hydraulic conductivity, $\Delta\phi$ is the drop in potential from soil to root-hair wall, and $\tau\lambda_s/2$ represents an average length from soil to root hair including tortuosity effects (such as might occur with fractures). The λ_s parameter might be determined by

$$\lambda_s = A_{plant}/(\lambda_h + \lambda_t),$$ (4-3)

which shows that the distance travelled in the soil is inversely proportional to the length of the root system. The A_{plant} (area encountered by the plant) parameter is problematic, as it is an absolute area and the parameter of interest in the leaf system is leaf area per unit area. Perhaps A_{plant} can be parameterized in terms of a maximum Leaf area index (LAI) coefficient, maximum leaf area, and root/shoot ratio.

Root-Hair System

The root-hair system is extremely dynamic. Vegetation does not invest heavily in creating root hairs, so they tend to be quite opportunistic. Root hairs are only present where horizontal lateral roots exist. In the model, root hairs are parameterized by λ_h, the length of root hair per unit cross-sectional area, and θ_h, the ratio of λ_h to the maximum able to be accommodated by the transport system. The maximum that the transport system can accommodate is proportional to lateral transport-system length, λ_t, according to

$$\lambda_h = \kappa_{ht}\theta_h\lambda_t.$$ (4-4)

It is assumed that root-hair growth is affected by nutrient-uptake availability, transport-root capacity, and temperature. A format of such a root-growth model is

$$\frac{\partial \lambda_h}{\partial t} = \gamma_h(T, S_{soil})\kappa_{ht}(1 - \theta_h)\lambda_t U_{soil}. \tag{4-5}$$

Note that this model accounts for temperature effects, soil strength, transport-system support capacity, and nutrient-uptake availability. The temperature dependence should be such that no growth occurs above and below cutoff temperatures and maximal growth occurs in some optimal range. Soil strength reflects both soil moisture and soil resistance.

Uptake into the root-hair system is dependent on the soil conditions and the root-hair conditions. Uptake across the hair interface is proportional to the gradient from the soil to the hair,

$$q_{hair} = C(\theta_h)\Delta\phi, \tag{4-6}$$

where q_{hair} is flux into the hair, $C(\theta_h)$ is the conductance (conductivity divided by wall thickness) of the hair wall, and $\Delta\phi$ is the drop in potential from soil to hair interior. The conductance should drop to zero as θ_h approaches zero.

Transport System

The transport system is conceptually divided into a main vertical stem and a continuum of horizontal lateral roots. Each 1D element has a stem. Stems can be inactive (*i.e.*, below the rooting depth), but there are no gaps in the active stem system. Each stem element has the potential for horizontal lateral roots. The highest inactive stem element retains the potential for growing horizontal lateral roots, so that the rooting zone can extend downwards.

The vertical system is parameterized by A_{stem}, the area of the active stem. Growth of the vertical stem is dependent on time-averaged flux of water through the stem. As any chemical nutrient is very dilute and does not affect flow, the stem capacity is independent of any chemical nutrient. Fluxes within the stem are described by

$$q_{stem} = -\kappa_{stem}A_{stem}\nabla\phi, \tag{4-7}$$

where κ_{stem} is the conductivity per unit area. Note that flux is also linearly dependent on the stem area.

The lateral component of the transport system consists of nominally horizontal roots, parameterized by λ_t (length of lateral root per unit area) and A_{stem}. Fluxes within the lateral component

of the transport system are described by

$$q_{lat} = \frac{\kappa_{stem} A_{stem} \Delta\phi}{\tau\lambda_t/2}.$$ (4-8)

where κ_{stem} is the conductivity per unit area, $\Delta\phi$ is the drop in potential from hair to stem, and $\tau\lambda_t/2$ represents an average distance from hair to stem.

It is assumed that transport-root growth is affected by root-hair usage, soil strength, and temperature. A format of such a root-growth model is

$$\frac{\partial\lambda_t}{\partial t} = \gamma_t(T, S_{soil})\theta_h\lambda_t$$ (4-9)

Note that this model accounts for temperature effects, soil strength, transport-system support capacity, and nutrient-uptake availability. The temperature dependence should be such that no growth occurs above and below cutoff temperatures and maximal growth occurs in some optimal range. Soil strength reflects both soil moisture and soil resistance.

In both the vertical and lateral components of the transport system, flux is proportional to the active cross-sectional area. The evolution of the cross-sectional area might be described by

$$\frac{\partial A_{stem}}{\partial t} = \gamma_{stem}(T)(\nabla\phi - \nabla\phi_{opt}),$$ (4-10)

where it is assumed that there is some optimal gradient in potential and time-averaged potentials are used. The assumption is that active stem area handles average flows. It is not clear where the optimal gradient in potential will come from, perhaps by using estimates of typical active-stem area, time-averaged transpiration rate, and conductivity for some shrubs.

Leaf System

The leaf system controls the transpiration rate, manipulating the potential within the plant by changing the stomatal conductance. By adjusting stomatal conductance, transpiration rates are adjusted, the potential at the top of the stem is adjusted, and fluxes across the roots are adjusted.

Flux across the leaf/atmosphere boundary is controlled by

$$q_{leaf} = A_l C_{leaf}\Delta\phi,$$ (4-11)

where A_l represents the leaf area exposed to the atmosphere per unit area, C_{leaf} is the leaf/atmosphere interface conductance, and $\Delta\phi$ is the drop in potential from leaf to atmosphere. C_{leaf} is controlled by the stomates.

A_l is the product of plant cover and LAI, and is the parameter of interest when describing leaves.

Transpiration Observations

In this section, all observations (with corresponding citations) are collected by Kozlowski and Pallardy (1997).

Respiration has been found to be strongly dependent on temperature. Typically, respiration varies linearly with temperature below about 10 °C, exponentially with temperature between 10 and 25 °C, and may decrease above 35 °C. The rate of increase in the exponential range is characterized by the Q_{10} value (relative change in respiration for a 10 °C change in temperature), which ranges from 1.4 to 3.4 for cypress, 2 for scotch pine, and 2.9 for loblolly pine.

Respiration tends to be reduced by water stress but does not appear to be as strongly impacted as by temperature. Respiration demand is roughly halved at -48 bar for loblolly pine, but stress actually increases respiration to 150 percent at about -28 bar. Respiration decreases, increases, and decreases, as stress becomes successively more negative. Kozlowski and Pallardy (1997) state that respiration generally decreases somewhat with drying.

Respiration tends to be greater with young vegetation parts and parts with high proportions of living tissue (*e.g.*, leaves, root hairs). Leaves were found to account for 50 percent of transpiration in a 60-year-old beech forest, 60 percent in a tropical rain forest, and 32 percent in a young loblolly stand. Respiration from all branches has been found to be about half of the total autotrophic respiration in a loblolly pine plantation. Almost all of the root respiration is in the fine roots; more than 95 percent of root respiration for pine and birch stands is in the fine roots. Seasonal production of CO_2 in a loblolly pine plantation peaked at 0.05, 0.2, 1, and 14 gCO_2 m^{-2} hr^{-1} for roots, branches, stem, and foliage; the first three dropped to about 0.02 during winter while foliage bottomed out at about 3.

Moisture uptake is reduced as the soil temperature drops (although it is not clear what confounding processes take place). A number of pines exhibit roughly linear decreases in uptake as the soil drops from 25 °C to 0 °C, ranging from roughly 15 to 40 percent of the 25 °C uptake. The reduction was greatest with the temperate pines. The reduction is attributed to permeability decrease of roots and viscosity increase in water.

Permeability varies within parts of vegetation. In northern white cedar, leaf specific conductivity (LSC), which is defined as the rate of flow in a stem or branch caused by a unit of pressure potential gradient, is about 30 times greater in stems than small twigs. Conductivity of red pine roots was about 50 times greater than in the stem and increased away from the stem. Resistance to water flow in whole shoots of maples is estimated as 50 percent in leaves and petioles, 35 percent in branches, and 15 percent in the trunk.

3/4/98 Vegetation modelling continued.

Transport System

The λ_s parameter really represents a measure of space-fillingness. Perhaps a better parameterization would be something like

$$\lambda_s = \beta \left[\frac{(\rho_h + \rho_t)_0}{(\rho_h + \rho_t)} \right]^\alpha, \tag{4-12}$$

where β is a soil-dependent scaling constant [L], α is a plant-dependent fractal constant, and the root length densities [L/L^3] are normalized to a plant-dependent value. Root-length density is often used (Caldwell, 1994). Actually, probably only ρ_t need be considered, since hair roots are assumed not to venture far from the transport roots, leaving

$$\lambda_s = \beta \left(\rho_{to}/\rho_t \right)^\alpha. \tag{4-13}$$

The fractal constant captures the space-fillingness. A perfectly space-filling root system in 2D would have $\alpha = 1$, while a very poorly space-filling root system in 2D would have α close to 0. The point can be illustrated by considering a unit square with a root system represented by squares within the area. Each square has a root length of 4 times the side length. The boxes are placed so that the side length for each box is an integer multiple of the side length of the innermost box. In this case, the average distance from the furthest point in the soil from a box is approximately half the side length of the smallest box.

Consider the case where we halve the average soil/root distance each iteration. The inner-box side length has a sequence of (0.5, 0.25, 0.125, ...), or $1/2^n$. The corresponding soil-root distance has a sequence of $1/2^{n+1}$. The corresponding root length has a sequence of (2, 6, 14, 30, ...), or $2 \times (2^n - 1) \approx 2^{n+1}$. The sequence indicates that λ_s is proportional to the reciprocal of λ_t in this efficiently space-filling scheme, corresponding to $\alpha = 1$.

In a perfectly inefficient scheme, λ_s remains constant regardless of changes in λ_t. This situation corresponds to $\alpha = 0$.

The same ideas apply in 3D, except that a perfectly space-filling root system would have $\alpha = 2$ (i.e., $N - 1$, where N is the number of spatial dimensions). I would expect the root system to be fairly efficient in exploring the soil space, so values of α may be on the order of 1.3 to 1.5.

Fitter (1994) discusses architecture and biomass allocation of root systems. An interesting point is raised, that specific root length (length of root per unit mass) is a good correlate of root diameter, with finer roots having greater specific root length. This observation should be followed up; it may lead to a parametric relationship between ρ_t and A_{stem}.

3/27/98 Discrete-fracture ideas.

Most of the flow modeling at the drift scale has assumed that fracturing occurs as a continuum. As a rough approximation, I think that 5 fractures per grid block should be sufficient for this assumption. Mapped fracture densities are between 0.5 and 5 per meter in the Topopah Spring welded (TSw) unit (Sonnenthal et al., 1997), where mapping only accounts for fractures with traces of at least 1 m. Assuming that fracture densities are roughly 5 per meter, which should include some of the smaller, unmapped fractures, grid blocks need to be at least 1 m in dimension to make the continuum approximation valid. Incorporating discontinuities at this resolution may not be feasible in a continuum model, particularly if the details of the fractures are required. On the other hand, a flow-routing scheme similar to my geomorphic modeling work may enable extremely fine grids to be evaluated. I want to develop the ideas here for future reference.

The key idea that I used in the watershed modeling is that topography dominates flow routing. When this is true, it is possible to sort the grid blocks by elevation and calculate routings once and for all. When flows occur in films, in large apertures, this assumption is also valid. I expect that the assumption begins to break down once capillary forces are involved.

Several approaches might be tried. It may be possible to generate constitutive relationships for individual fractures. Very fine rough-aperture grids might be created, hooked together into a few intersections, and the characteristics of flow as features are modified might be examined. Perhaps the individual fractures could be upscaled into a continuum using a probability distribution to capture flow diversions. At some point it would be possible to incorporate matrix interaction using quasi-linear approaches and BEM methods, including the effects of fracture coatings on flow.

The first order of business is to identify the appropriate flow characteristics for an individual fracture. A fracture will generally have either a thin film of water covering both walls (perhaps only a few molecules thick) or will be filled with water. Note that relative humidities are likely to be almost 1, which will mediate the thickness of the film as well. Some fractures may have carbonate or opal fillings.

In the case of a fracture filled with carbonate or opal, flow occurs through vapor transport and Darcy's law. Resistance to flow is due to the permeability of the filling material and the thickness of the aperture (no turbulence). In the case of a water-filled fracture, the resistance is due to viscous effects and is proportional to the cube of the aperture (no turbulence). In the case of film flow, capillary effects are dominant for thin films and become less important as the film gets thicker.

Let me recap flow laws in terms of 2D fracture flow of an incompressible fluid with local coordinates ξ and η. Flux is generally of the form

$$\mathbf{q} = -bK(\theta)\nabla(P + \rho gz), \tag{4-14}$$

where b is the fracture aperture, $K(\theta)$ is different for the different flows, and the remaining symbols are the usual suspects. For porous media, classical retention relationships (*e.g.*, van Genuchten relationships) are appropriate. For laminar flow between two smooth plates,

$$\mathbf{q} = -\frac{b^3}{12\mu}\nabla(P + \rho gz), \tag{4-15}$$

where μ is viscosity and again b is the fracture aperture. For laminar film flow on a smooth plate,

$$\mathbf{q} = -\frac{b^3}{3\mu}\nabla(P + \rho gz), \tag{4-16}$$

where b is the film thickness. Note that a fracture can carry almost 4 times as much flow under gravity conditions if only one side of the fracture is wetted. For laminar flow in a capillary,

$$\mathbf{q} = -\frac{\pi r^4}{8\mu}\nabla(P + \rho gz), \tag{4-17}$$

where r is the capillary radius; average velocity is $\mathbf{q}/\pi r^2$. The laminar-flow expressions are presented in Chapter 2 of Bird et al. (1960).

Tetsu Tokunaga and Jiamin Wan presented studies of film flow on tuff surfaces to the UZFM Expert Elicitation panel on December 19, 1996, including an analysis of measured and theoretical velocities for film flow in partially filled capillary tubes (representing pores). It appears that pores of 5 μm and larger may contribute significant fluxes. A vertical capillary tube of radius r was

considered full when the water surface had a radius of $2r$, corresponding to a matric head (m) of $-\gamma/2\rho gr$ and an average velocity of $\rho gr^2/15\mu$. It seems that the average velocity should actually be smaller than $\rho gr^2/16\mu$ (half-full capillary flow).

It seems to me that I have seen a derivation someplace that builds up film flow using the bundle-of-capillary tubes idea, similar to the approach used by van Genuchten. Certainly it should be straightforward to relate the van Genuchten α and m values to pore-size distributions. The velocity distribution in a capillary half-tube should be dependent on head through the curvature of the meniscus, which implies that the flux of the pore set can be obtained through integration. The bigger question is what happens when the flow is wet enough to have capillarity acting on asperities larger than pores.

The computational approach for a discrete fracture should be based on a rectangular or triangular grid, with two unknowns per grid point: the head for each wall averaged over the film thickness. When the aperture is filled with water, the two unknowns are equal. If there is a fracture coating, perhaps an additional unknown is needed.

4/22/98 System of equations for vegetation model. $\boxed{\mathcal{SAS}}$

My current thinking on equations for the vegetation model is presented below. Much of the preliminary reasoning has been discussed before, so new ideas are the focus of the discussion. The equations have fairly well gelled, unless noted otherwise. Most of the basic ideas have been passed through Dani Or, with some discussion with David Groeneveld.

The vegetation model consists of four active types of variables. Three variables describe roots and are dispersed throughout the soil column, while one describes leaves (consisting of one layer). For current climatic conditions, the sparseness of the above-ground portion of the vegetation does not require much detail; however, the density of vegetation on higher-elevation sites suggests that it may be desirable to include multiple leaf layers to account for shading and cooling effects.

The four variables are all dimensionless, representing volume of biomass per unit volume $[L^3/L^3]$. Subscripts for variables are:

    l represents leaves
    v represents vertical roots
    t represents transverse roots
    h represents hair roots

The volume quantities for roots are straightforward to calculate. Each root has a length density (*e.g.*, ρ_v represents the length of vertical roots per unit volume [L/L^3]). Each also consists of a characteristic cross-sectional area for a root (*i.e.*, A_v is the vertical-root cross-sectional area [L^2]). These are multiplied together to create the dimensionless variable (*e.g.*, $\Theta_v = \rho_v A_v$). The unit volume is the 1D element thickness times the unit area.

The volume quantities for leaves are similarly straightforward to deal with. The typical quantity describing leaf density used by plant biologists is LAI, or the projected leaf surface area per unit ground surface area. To calculate Θ_l, LAI is multiplied by half of the typical leaf thickness (note each leaf has two sides). If the leaves are needles, LAI is multiplied by half of the typical radius to obtain Θ_l. The unit volume is a typical plant height times the unit area. If several leaf elements are used (when plant densities are greater), then the unit volume is the 1D leaf-element thickness times the unit area (similar to the root elements).

Length density and cross-sectional area should be related, with a greater length density also creating a greater cross-sectional area. I propose a relationship in the form

$$\left(\frac{\rho_i}{\rho_{io}} \right) = \chi \left(\frac{A_i}{A_{io}} \right)^{\beta}, \tag{4-18}$$

where χ and β are constants. The relationship between the two is not important for vertical roots, as only A_v has an impact on plant performance.

The contact between plant leaves and the atmosphere degrades as more leaves are present. For example, desert shrubs are well-connected to the atmosphere while the inner parts of piñon pines are not. Perhaps a similar relationship between LAI and leaf thickness will capture the less-efficient connection and increased cooling-transpiration demand as the leaf biomass increases.

The plant-dynamic scheme is broken into three broad components: (i) calculation of potential biomass growth and death rates, (ii) calculation of actual biomass growth and death rates, and (iii) calculation of plant-uptake rates (the quantity of interest). The scheme avoids complications of detailed consideration of photosynthesis, respiration, and plant growth. Instead, all interactions are translated into terms of one surrogate limiting nutrient, which might be water or might be a nutrient such as nitrogen or phosphorus. It would be possible to extend the approach to consider multiple limiting nutrients, but this will not be done in the near future.

A logical plant-growth time step is one day, thereby eliminating the considerations of detailed allocation under solar stress. Over the course of the day, the plant obtains a certain amount of the limiting nutrient through soil-moisture uptake. Conceptually, the nutrient is allocated between cell respiration, cell biomass, storage, wastage, and reproduction. Reproductive usage is implicitly

handled by an efficiency factor taxing uptake. The plant is assumed to allocate the remaining nutrient so as to maximize the expected plant-available nutrient at the end of the next time step.

In order to impose the scheme, it is necessary to quantify the options available to the plant for nutrient allocation and the costs associated with each option. The options available for each plant component are straightforward. The plant can allocate just enough nutrient to the plant component to satisfy expected respiration demands (*i.e.*, stand pat). The nutrient allocation can be increased beyond the stand-pat value, yielding plant growth proportional to the increased nutrient, up to the maximum-growth amount. Or the nutrient allocation can be decreased from the stand-pat value, down to no allocation, resulting in biomass death proportional to the shortfall in nutrient.

Net nutrient usage is the most important part of the cost structure. The direct cost of nutrient usage is straightforwardly calculated by taking into account how much nutrient is consumed by the biomass. Opportunity costs are also associated with nutrient allocation. In particular, transport roots are conduits for flow from the hair roots to the leaves. These roots are slow and expensive to grow. The roots reach a balance between uptake capacity during peak parts of the year (*i.e.*, spring) and respiration demand during the remainder of the year. If the plant did not account for the opportunity cost required to grow them, the roots would be quickly killed during the offseason and the plant would diminish from year to year. Accordingly, it makes sense to incorporate the same penalty to killing roots as it does to growing them.

The second type of opportunity cost results from the dependence of one plant component on densities of another plant component. For example, there is a limit to how many root hairs can be supported by the transport system. Accordingly, there may be advantage to growing additional transport roots in order to support higher densities of hair roots. This advantage must be accounted for in nutrient allocation.

Potential growth and death rates are also straightforward to calculate. Some death is assumed to unavoidably occur due to old age, regardless of nutrient allocation. Growth is assumed to occur proportionally to the allocation of nutrient above the respiratory requirement, up to a limiting rate. Death is assumed to occur proportionally to the allocation of nutrient below that necessary for respiration, again up to a limiting value (complete death depends on the time constant).

A typical root-growth rate is formulated as

$$\frac{\partial \Theta_i}{\partial t} = \gamma_i(T, S_{soil}) \left(1 - \frac{\rho_i}{\chi_{ij}\rho_j}\right) \left(\frac{\Xi - \Xi_r}{\Xi_r}\right) - \omega_{age}\Theta_i, \tag{4-19}$$

where

Θ_i is dimensionless mass of root component i

ρ_i is length density of root component i

ρ_j is length density of root component j

χ_{ij} is the maximum length of root component i per unit length of root component j

γ_i is the maximum growth rate of component i

T is temperature

S_{soil} is soil strength

Ξ is allocated nutrient mass ($\Xi_r \leq \Xi \leq \Xi_r + \Xi_g$)

Ξ_r is the nutrient mass required to meet all respiration needs

Ξ_g is the nutrient mass required to provide full growth

ω_{age} is the death rate due to old age

The root-growth formulation exhibits a one-way dependence, with hair roots dependent on transverse roots and transverse roots dependent on vertical roots. Vertical roots do not have this growth limitation.

A typical root-death rate is formulated as

$$\frac{\partial \Theta_i}{\partial t} = \left(\omega_i(T) \frac{\Xi - \Xi_r}{\Xi_r} - \omega_{age} \right) \Theta_i, \tag{4-20}$$

where

Θ_i is dimensionless mass of root component i

ρ_i is length density of root component i

ω_i is the maximum death rate of component i

T is temperature

Ξ is allocated nutrient mass ($0 \leq \Xi \leq \Xi_r$)

Ξ_r is the nutrient mass required to meet all respiration needs

ω_{age} is the death rate due to old age

The leaf growth formulation has the same general format for growth

$$\frac{\partial \Theta_l}{\partial t} = \gamma_l(T) \left(1 - \frac{\Theta_l}{\chi_{lv} \Theta_v} \right) \left(\frac{\Xi - \Xi_r}{\Xi_r} \right) - \omega_{age} \Theta_l, \tag{4-21}$$

and death

$$\frac{\partial \Theta_l}{\partial t} = \left(\omega_l(T) \frac{\Xi - \Xi_r}{\Xi_r} - \omega_{age} \right) \Theta_l. \tag{4-22}$$

4/23/98 Continuation of equations for vegetation model. $\boxed{\mathscr{SAS}}$

Each plant component is assumed able to store some amount of the limiting nutrient in easily plant-available form. It is assumed that each plant component has the same relative saturation of the limiting nutrient, and each component changes the relative saturation at the same rate. When a plant component dies, the easily available nutrient in the component returns to the plant. The total plant-available storage of the nutrient is characterized by

$$\Xi_s = \sum_{i=1}^{N} C_{si}\rho_{Bi}\Delta z_i \Theta_i \theta_\eta, \tag{4-23}$$

where

    Ξ_s is total mass of plant-available nutrient $[M/L^2]$

    C_s is maximum mass of plant-available nutrient per unit biomass $[M/M]$

    θ_η is the fraction of the available plant-available nutrient storage used up $[-]$

    ρ_{Bi} is biomass density of root component i $[M/L^3]$

    Δz_i is the thickness of element i

Each plant component is assumed to require some amount of the limiting nutrient in non-retrievable form in order to grow. It is assumed that each plant component uses up a certain mass of nutrient per unit biomass. The total non-retrievable storage of the nutrient is characterized by

$$\Xi_b = \sum_{i=1}^{N} C_{bi}\rho_{Bi}\Delta z_i \Theta_i, \tag{4-24}$$

where

    Ξ_b is total mass of nutrient irretrievably used in biomass $[M/L^2]$

    C_b is mass of irretrievable nutrient per unit biomass $[M/M]$

Each plant component is assumed to require some amount of the limiting nutrient for respiration each time step. The total respiration of the nutrient is characterized by

$$\Xi_r = \sum_{i=1}^{N} C_{ri}(T)\rho_{Bi}\Delta z_i \Delta t \Theta_i, \tag{4-25}$$

where

    Ξ_r is mass of nutrient expended in respiration per unit biomass $[M/L^2]$

    C_r is rate of nutrient mass expenditure in respiration per unit biomass $[M/M/t]$

The limiting nutrient is taken up by the plant during the course of a time step, with plant components that are based on the choices made in the previous time step. The uptake of soil water

is based on potential flow within the plant, similar to the potential flow in the soil. There are two continua modeled, the vertical plant continuum and the soil continuum. There is leakage from one continuum to the next.

The flux from a soil node to a vertical-plant node is proportional to the head gradient. There are three legs: (i) soil to hair, (ii) across the hair boundary to the transverse root, and (iii) through the transverse root. Flow through a leg is through horizontal porous-media flow:

$$q_i = -\frac{K_i(T)}{\rho g}\frac{\partial P}{\partial x} \tag{4-26}$$

or

$$q_i = -\frac{C_i(T)}{\rho g}\Delta P, \tag{4-27}$$

where

q is water flux [L/T]

K is conductivity [L/T]

C is conductance [1/T]

T is temperature [K]

ρ is water density [M/L^3]

g is acceleration due to gravity [L/T^2]

P is pressure [M/L T^2]

Within the soil, K is the soil conductivity, which is dependent on soil moisture and temperature. The characteristic length for the soil leg is hypothesized to be dependent on the length density of transverse roots, with the form

$$\lambda_s = \beta \left(\rho_{to}/\rho_t\right)^\alpha. \tag{4-28}$$

As with the following equations, a subscript with a o denotes a reference value.

Within the root hair, conductance is used rather than conductivity. The primary resistance to flow is assumed to be across the hair walls, so that resistance within the hair itself can be neglected. Resistance across the root hair is assumed to have a component that depends on soil moisture, and is proportional to surface area. The formulation for root-hair conductance is

$$C_h = C_{ho}\frac{\mu(T_o)}{\mu(T)}\left(\frac{A_t}{A_{to}}\right)^{1/2}\frac{\rho_h}{\rho_{ho}}f(\theta), \tag{4-29}$$

where

T is temperature [K]

μ is viscosity [M/L T]

A is characteristic cross-sectional root area [L^2]

$f(\theta)$ is a yet-undetermined function of soil moisture [–]

The reduction of the root-hair conductance as a function of soil moisture accounts for shrinkage of the root hair away from the soil, providing an air gap, when the soil is dry. The dependence on A_h and ρ_h is through the surface area available for uptake.

The most poorly defined conductivity/conductance is for the transverse roots. For the time being, a conductivity function,

$$K_t = \frac{k_t A_t}{\mu(T)} \tag{4-30}$$

and a characteristic length,

$$\lambda_t = \frac{\beta}{\tau} \left(\frac{\rho_t}{\rho_{to}} \right)^\alpha, \tag{4-31}$$

will be combined into a conductance,

$$C_t = \frac{K_t}{\lambda_t}, \tag{4-32}$$

where

k is a dimensionless coefficient [–]

τ is tortuosity [–]

β is a plant-dependent length factor [L]

α is a plant-dependent scaling factor [–]

The vertical roots use the same type of conductivity relationships as the transverse roots, except that the characteristic length is directly available from the numerical model, leading to the formulation

$$q_v = -\frac{k_v A_v}{\tau \mu} \frac{\partial}{\partial z}(P + \rho g z). \tag{4-33}$$

Leaves will be treated using a conductance, with the maximum conductance proportional to effective leaf surface area,

$$C_l = C_{lo} \frac{\mu(T_o)}{\mu(T)} \frac{\Theta_l}{\Theta_{lo}}. \tag{4-34}$$

The actual conductance can range from zero to this limit, based on projected nutrient uptake demand and the transpiration required to meet this goal. The conductance can increase arbitrarily as necessary to restrict transpiration, with no more transpiration occurring during a time step than is necessary to meet projected needs.

4/29/98 Continuation of equations for vegetation model.

I have just read several chapters summarizing root behavior (Waisel et al., 1996). There are several points that I take away from the discussions.

- Root hairs are not the only source of uptake, but they do enlarge the available surface area. Some plants do without.

- New roots are more effective at uptake than old roots, but the respiratory requirements are larger as well.

- Radial conductivity is roughly two orders of magnitude smaller than axial conductivity, expressed in per-unit-area terms.

- There may be a reduction in conductivity at high flux rates. This may be due to multiple flow pathways, one primarily responding to hydraulic gradients and the other primarily responding to osmotic gradients.

- Root growth may be limited by solute-concentration requirements rather than water availability.

- Plants may be healthier when they transpire at greater rates than is required for peak growth.

The dependence of roots on temperature has two components: (i) growth and (ii) death. It is generally agreed that growth occurs when temperatures are within an optimal range and dies off for warmer or cooler temperatures. Similarly, there is a band of temperature that roots can endure within, with hotter or cooler temperatures causing death. The temperature dependence should be in relative terms.

The data presented by McMichael and Burke (1996) suggests shapes of relative growth rates as a function of temperature looking like a (i) (skewed) normal or lognormal, (ii) bi-exponential, or (iii) triangular distribution. These three shapes should be provided when considering the relative growth rate, with parameters of optimal temperature and (i) standard deviation, (ii) cool and warm extinction coefficients, and (iii) minimum and maximum temperatures. Reported optimum temperatures ranged from 5 to 37 °C, with desert succulents having optima of about 30 °C. I would expect that the optimum temperature of the indigenous plants within a climatic regime is related to mean annual temperature (MAT), simply because the plants are selected to adjust to the climatic conditions.

Death rates are also affected by temperature. Nobel (1996) reports that *Agave deserti* and *Ferocactus acanthodes* have complete root death occurring at roughly 56 to 63 °C. If the root growth occurs under 15 °C warmer temperatures, the temperature tolerance is extended slightly (4 to 5 °C). *A. deserti* started exhibiting root death at about 20 °C lower than complete death, while *F. acanthodes* was completely stressed in only 8 or 9 °C. Both species have a sigmoidal dropoff, commensurate with a normal distribution for stress resistance. Similarly, sufficiently cool temperatures kill roots. A sigmoidal increase in death rate might be modelled as

$$\Lambda = 3\varsigma^2 - 2\varsigma^3, \tag{4-35}$$

$$\varsigma = \frac{T - T_i}{T_d - T_i}, \tag{4-36}$$

where Λ is the relative temperature-dependent death rate and ς is the fraction of the distance the temperature has reached between incipient stress (T_i) and completely stressed (T_d). It is theoretically tempting to use the CDF for a normal distribution, which can be approximated by a 6th-order polynomial with an error of less than 1.5×10^{-7} using equation 26.2.19 in Abramowitz and Stegun (1972). In the absence of further information, this function might be used for both hot and cool extremes.

A plant would presumably operate best at a particular temperature, with both decay of growth rates and rise of death rates symmetric about the optimal temperature. However, there are absolute temperature bounds on plant capabilities, represented by some subfreezing temperature and some near-boiling temperature. I would postulate that plants with an optimal temperature somewhere near 20 °C (for example) might actually have symmetric rates about the optimal, with a tolerance range of perhaps 25 to 40 °C on either side of the optimal. However, as plants become adapted to temperatures further from this symmetry value, the tolerance band becomes skewed. For example, MAT significantly above the symmetry range may skew the distribution about the adapted plant's optimum so that the lower tail is stretched while the upper tail is compressed. Conversely, MAT significantly below the symmetry range may skew the distribution so that the lower tail is compressed and the upper tail is stretched. For both of these cases, the overall bounds are likely to be narrower. The few data in McMichael and Burke (1996) generated this concept. Taking it one step further, I would suggest that the optimal temperature is likely to occur for temperatures in seasons with predictable moisture-uptake availability (*i.e.*, spring in warmer climates, summer in cooler climates).

The impact of mechanical impedance on root growth rates is discussed by Bennie (1996), in which it is proposed that relative root growth rate is exponentially dependent on mechanical

impedance, using the formula

$$\frac{R}{R_{max}} = e^{-0.6931 \frac{Q_p}{Q_{0.5}}}, \tag{4-37}$$

where R is the root elongation rate, R_{max} the maximum rate at very low impedance, Q_p is the penetrometer pressure [MPa], and $Q_{0.5}$ is the penetrometer pressure corresponding to $R/R_{max} = 0.5$. Bennie (1996) further suggest that the diameter of root laterals are proportional or nearly proportional to impedance.

Soil strength would appear to provide the linkage between root length density and root diameter. The average diameter is the quantity of interest. The average diameter is calculated using the balance equation,

$$(M_o - M_d + M_g)d_{ave}^{n+1} = (M_o - M_d)d_{ave}^n + M_g^n d_{grow}^n, \tag{4-38}$$

where M_o is mass of old roots, M_d is mass of dying roots, M_g is mass of new roots, d_{ave} is average diameter of the old roots, d_{grow} is average diameter of the new roots, and superscripts n and $n+1$ refer to the current and next time step. There is a need for soil-strength descriptions as a function of moisture content, however, for this to be useful.

Moreshet et al. (1996) summarize information on root permeability.

Nobel (1996) demonstrates that a cost-benefit analysis on root growth allocation, using carbon taken up through photosynthesis for costs and water transpiration as the benefit, predicts quite well the measured amounts of new and old roots for *A. deserti*. The new and old roots had identical relative distributions with depth. Note that *A. deserti* roots have low respiration costs, so that the ratio of water uptake costs to carbon costs are enhanced relative to other species. Although I had conceived of a soil nutrient as the limiting nutrient, carbon should also be a good way to approach the nutrient balance cost-benefit analysis.

4/30/98 Continuation of equations for vegetation model.

Allocation of nutrients is an optimization problem that the plant must solve each time step. Actual plants are genetically programmed to respond to external stimuli such as season, light levels, temperatures, and soil-moisture availability. In the vegetation model, these stimuli are accounted for through their impact on nutrient utilization.

The nutrient optimization problem is solved through a mass-balance approach with coeffi-

cients based on the marginal benefit of the allocation. The mass balance equation is stated

$$\alpha \left(\frac{d\Xi_s}{d\alpha} + \sum_{i=1}^{N} c_i \frac{d\Xi_i}{d\alpha} + W \right) = \Xi_u - \sum_{j=1}^{M} \alpha_i \frac{d\Xi_j}{d\alpha_j},$$
(4-39)

where

α is an adjustable weight $(0 \le \alpha \le 1)$,

c_i is the benefit/cost ratio (allocation weight),

$d\Xi_i/d\alpha$ is the rate of nutrient usage in plant element i per unit change in α,

W is net nutrient wastage,

Ξ_u is net nutrient uptake, and

Ξ_j is a constrained value (0 or 1) for α,

The algorithm proceeds as follows:

- Initialize by setting W to zero and consider all plant elements $(M = 0)$

- Calculate the chord-slope approximation to c_i based on the difference between maximum and zero nutrient allocation

- Repeat until done

  - Calculate α

  - Select the case where αc_i is furthest outside the valid range of 0 to 1

  - If there is no invalid case, done

  - Set c_i to the corresponding limit and move that variable to the summation on the right-hand side

- Calculate the transpiration limit for the next step based on the nutrient allocation

The benefit/cost coefficient represents the expected benefit of allocating a unit of nutrient to the plant element. A generic benefit, B, is used in the following; a good candidate for the benefit might be the expected plant-available nutrient storage. The benefit to cost for nutrient allocation to plant element i is

$$\frac{dB}{d\Xi_i} = \left(\frac{dB_r}{d\Xi_i} + \frac{dB_u}{d\Xi_i} \right),$$
(4-40)

where Ξ_i is the nutrient mass allocated to plant element i and subscripts r and u refer to changes to the benefit due to respiration and uptake, respectively. There is an additional term for overall plant storage.

The nutrient used for respiration is calculated using the optimal respiration rate per unit biomass. The benefits for uptake are evaluated for two nutrient allocations, $\Xi_i = 0$ and $\Xi_i = \Xi_r + \Xi_g$ (*i.e.*, maximal growth and maximal death of the biomass). Uptake benefits are generally due to changes in conductance.

5/1/98 Continuation of equations for vegetation model. $\boxed{\mathscr{SAS}}$

The components I've been referring to as root hairs really better describe "new" roots. The formulation might be changed to have "old" lateral roots, "new" lateral roots, and root hairs. Each type has characteristic properties, and both take up water. I would consider effective uptake surface area to be much smaller than actual surface area for the old roots, effective surface area to be somewhat less than actual surface area for new roots, and effective surface area to be about equal to actual surface area for root hairs. The conversion between new and old roots follows a mass balance approach, with the conversion rate dependent on average new-root age. Average new-root age is calculated using

$$(M_n - M_d - M_c + M_g)a_{ave}^{n+1} = (M_n - M_d - M_c)(a_{ave}^n + \Delta t), \tag{4-41}$$

where M_n is mass of new roots, M_d is mass of dying roots, M_c is mass of roots switching from new to old, M_g is mass of newly generated roots, a_{ave} is average age of the new roots, Δt is size of the time step, and superscripts n and $n + 1$ refer to the current and next time step. Note that newly generated roots have zero age.

Several other approaches might be used to handle conversions from new to old roots. A straightforward way to handle the problem would be to bin the ages. For example, if the time step was one day and roots switched from new to old after 60 dy, 10 6-dy bins might be constructed. Each time step, 1/6 of the contents of each bin might be passed to the next bin, with the contents of the last bin becoming old roots. Death is applied proportionately to each bin. Alternatively, the new root ages might be considered to have a normal distribution, with a mean and standard deviation. The mean and standard deviation could be used to calculate the conversion to old, updating both with the newly generated roots.

8/17/98 Equations for soil-genesis model. $\boxed{\mathscr{SAS}}$

The entry for 5/19/98 was moved to the chapter on geomorphology modeling for clarity and continuity. Continued work on the subject is in that chapter.

3/25/99 Plant activity considerations.

This entry is intended to clarify my thoughts on procedures for handling plant growth.

In an annual cycle for a perennial shrub, there are several phases:

- Early growth, in which most fine roots and leaves appear. Transport systems are under-utilized.

- Sustained growth, in which the entire plant grows more or less in equilibrium and allocates resources to reproduction. All systems are well utilized.

- Die-back, in which fine roots and leaves die but the transport system is maintained.

- Minimal maintenance, in which a bare minimum of transpiration occurs to satisfy the respiration needs of the transport system.

A common thread through the cycle is an emphasis on maintaining the resource-intensive transport infrastructure.

Plant growth/death can be handled as a constrained optimization problem, allocating nutrient uptake to respiration and growth processes. The constrained optimization problem results from the allocation of nutrients taken up during a day. The nutrients are allocated to respiration demands, growth, and reproduction. Transpiration can be adjusted by the plant to curtail uptake to the most that can be used by the plant, thus minimizing waste. Objectives addressed by the allocation process include:

- Maximizing overall long-term growth

- Maximizing reproduction

Note that reproduction generally requires replacement of existing biomass subsequent to death.

One way to treat the optimization is to maximize nutrient uptake through a global assessment. Each time step, the sensitivity of nutrient uptake to change in plant properties is calculated, where a plant property is any vegetation density component in a computational segment. If there are 20 segments, each with 4 vegetation densities, a first-order sensitivity calculation is calculated by perturbing each of the eighty components and assessing changes in uptake. If the sensitivity

calculation is cheap, this approach is fine, but may be unattractive if the sensitivity calculation requires the solution of a matrix equation.

An alternate way to get at the same thing is by doing a local optimization using local characteristics. A good criterion for allocation is the efficiency of transport through the component. If the component is oversized, it should be cut back; if the component is undersized, it should grow. The criterion might be the deviation of chemical-potential gradient from a nominal gradient, or equivalently a flux per unit area; if the gradient or flux is smaller than nominal, it is too efficient and needs pruning.

As the plant system is hierarchical, subcomponents should exert pressure on a component if they are close to capacity, since capacity is achieved in favorable environments. In order to achieve this goal, the nominal gradient should correspond to the subcomponents at something less than full capacity; subcomponents at greater than this nominal value will supply more flux than the nominal and put pressure on the component to expand. A target value might be something like 80 percent of capacity, to enable growth. The local strategy results in a simple sensitivity test for growth and death. Note that the environment provides forcings for the finest roots and leaves, with wet conditions providing a strong impetus for growth.

Respiration demand is another factor that needs to be accounted for. There should be incentive for allocating nutrient to respiration demand. The incentive should be much stronger than incentives for growth and death, and the relative weight should be proportional to the cost of replacement (higher-order components have stronger priority than lower-order components like fine roots and leaves). In other words, not satisfying respiration demands is painful, and high-order components feel relatively greater pain.

The optimization problem can be formulated as

$$\max \sum_i W_r C_n (R_i - R_{io}) + W_g C_n (G_i - G_{io}), \tag{4-42}$$

where W_r is the weight assigned to respiration, C_n is the nutrient cost per unit biomass, R_i is nutrient allocation to satisfy respiration demand, R_{io} is respiration demand for nutrients, W_g is the weight assigned to growth/death, G_i is nutrient allocation to growth, and G_{io} is maximum growth demand for nutrients. The optimization problem is subject to the constraints

$$0 \le R_i \le R_{io} \tag{4-43}$$

$$0 \le G_i \le G_{io} \tag{4-44}$$

$$G_i = 0 \qquad \text{when } R_i < R_{io} \tag{4-45}$$

3/26/99 More plant activity considerations.

Another approach replaces optimization with a set of partial differential equations that change mass/root-length density according to local fluxes. The idea is to change the allocated mass according to the ratio between actual flux and nominal capacity. The partial differential equation for density change based solely on flux (no other limiting factors) is simply

$$\frac{\partial \rho}{\partial t} = \alpha \frac{q - q_o}{q_o} \rho \tag{4-46}$$

where ρ is the current density, α is a time constant related to cost of growth, q is the actual time-averaged flux over the time period, and q_o is the nominal time-averaged flux corresponding to ρ. Note that the multiplier of ρ should be greater than -1 (for plants, this condition is almost certainly reached for daily time steps, as either the time constant is larger than a day (for transport) or the q ratio doesn't drop to 0 instantaneously).

Growth can be constrained by capacity limits as well. Incorporating capacity constraints yields

$$\frac{\partial \rho}{\partial t} = \alpha \left(\frac{q - q_o}{q_o} \right) \left(\frac{\rho_o - \rho}{\rho_o} \right) \rho \tag{4-47}$$

where ρ_o represents the density at capacity.

The q_o values can be estimated from dividing typical flux values by typical active cross-sectional areas, leaf areas, or root-uptake surface areas, respectively. For example, if a shrub transpires an average of 1 mm/d under nominal conditions, dividing the respective areas by this rate gives nominal flux values per unit area. Hopefully ballpark estimates are sufficient for these parameters.

The time constants arise from considerations of response times under optimal conditions. For example, the time constant for main shrub roots might be on the order of a year, while the time constant for fine roots might be on the order of days. The time constant for leaves is probably on the order of weeks.

It is not clear whether the time constant should be different for death and growth. It can be argued that leaves and fine roots die quicker than they grow, while main transport systems may be reversed. The time constant may change according to environmental stress, with faster death rates and slower growth rates for a wet year after two dry years than for the same wet year after a wet year.

3/27/99 More plant activity considerations.

$\boxed{\mathcal{SAS}}$

I coded up a test case for multiple vegetation types simultaneously extracting water from a stagnant column to examine the partial-differential-equation approach and associated constants. The test was of a 50-cm column of soil with no evaporation or bedrock fluxes, and the vegetation was assumed to achieve a vapor density of 2×10^{-5} gm/cm^3 (with atmospheric vapor density of 2×10^{-6} gm/cm^3 and reasonable turbulence). It quickly became apparent that I had to reduce the plant conductivity by the fraction of the total area occupied by plant stems. The actual conductance of stem roots should be like a sand, which has the range of roughly 10^{-9} cm^2 to 10^{-5} cm^2. The higher end may be too conductive, while a value in the midrange seems to give somewhat plausible results.

The conductance of the fine roots is questionable: a fairly small value seems to be necessary.

Allowing the plants to adjust root density according to the nominal-flux criterion for the test problem results in a pressure profile in the soil and plant continua that is almost identical even when the plants initially have sufficiently low densities that the plant pressures are much lower than the soil pressures while supplying vapor flux at the maximum rate. At early times, the plants proliferate exponentially at all depths. As the top dries out, plants that start loosing water adjust the fine-root biomass density down to cut transfer losses.

The permeability of the plant transport strongly affects the dryout profile. For permeabilities comparable to relatively fine sands, a sharp drying front develops. For relatively coarse sands, the front is much more diffuse. For low-permeability transport systems, the transport density tends to drop off more rapidly with depth.

I realized that the change in density term should read

$$\frac{\partial \rho}{\partial t} = \left(\frac{q - q_o}{q_o} \right) \left(\frac{\rho_o - \rho}{\rho_o} \right) \rho \qquad (4\text{-}48)$$

with the terms in front of ρ on the right-hand side limited to $\pm \alpha$. There is still some question in my mind as to how constraints from nutrients can be accommodated.

7/19/99 Generic equations.

$\boxed{\mathcal{SAS}}$

It is useful to have a capability for solving generic 1D equations and systems of equations in which the actual equations and coefficients are defined through easily modified scripts and the work of

equation assembly, equation solution, and state variable manipulations are handled with generic solvers. If done properly, coding up a different equation should be very fast.

There are several types of 1D equations that should be accommodated. These include a diffusion equation, a transport equation, and a phase balance equation. The form of a diffusion equation is

$$\frac{\partial u}{\partial t} - \nabla \cdot (K \nabla u) = Src;$$ (4-49)

a transport equation is

$$\frac{\partial u}{\partial t} + \nabla(vu) - \nabla \cdot (K \nabla u) = Src;$$ (4-50)

and a phase balance equation is

$$\frac{\partial M}{\partial t} - \nabla \cdot [K(\nabla u + G \nabla z)] = Src.$$ (4-51)

In the above, u, M, and z represent state variables; K, v, and G represent parameters; and Src represents source terms.

The generic form of all of these equations is

$$\frac{\partial M}{\partial t} + \nabla \cdot q = Src.$$ (4-52)

The system form of the generic equations is

$$\sum_j \left[\alpha_{ij} \frac{\partial M_{ij}}{\partial t} + \nabla \cdot \beta_{ij} \mathbf{q}_{ij} = Src_{ij} \right],$$ (4-53)

where an i subscript represents the primary state variable, a j subscript represents secondary state variables, $\mathbf{q}$ is flux, and the α and β variables are flags for inclusion of terms in the equation. Fully implicitly discretizing this system using a finite volume approach in 1D,

$$\sum_j \left\{ \alpha_{ij} \left[\frac{M_{ij}}{\Delta t} \right]_n^{n+1} + \beta_{ij} \left. \frac{\Delta \mathbf{q}_{ij}}{\Delta x} \right|^{n+1} = Src_{ij}|^{n+1} \right\};$$ (4-54)

rearranging yields

$$\sum_j \left\{ \alpha_{ij} [M_{ij}]_n^{n+1} V + \beta_{ij} \Delta t \, \Delta \mathbf{q}_{ij}|^{n+1} = V \Delta t \, Src_{ij}|^{n+1} \right\},$$ (4-55)

where Δ denotes a difference operator (Δt is the time step and other quantities are the difference between one side of the volume and the other) and V is the volume of the element ($V = \Delta x$).

When the system includes nonlinearities, a first-order increment is added to the equation set

$$\sum_j \left\{ \alpha_{ij} \left[M_{ij} \right]_n^m V + \beta_{ij} \Delta t \, \Delta \mathbf{q}_{ij} |^m - V \Delta t \, Src_{ij} |^m \right\}$$

$$+ \sum_k \sum_j \left\{ \alpha_{ij} V \, M_{ij} |_m^{m+1} + \beta_{ij} \Delta t \Delta \left(\mathbf{q}_{ij} |_m^{m+1} \right) - V \Delta t \, Src_{ij} |_m^{m+1} \right\} = 0, \qquad (4\text{-}56)$$

where u is an unknown, n is the time step level, and m is the iteration level (implicitly at the $n+1$ time step). This form also works for linear equations, as the incremental part of the time derivative is the only active part and the remainder of the terms cancel except for the incremental part.

The generic solver needs to handle the following fluxes, (i) $\mathbf{q} = -K \nabla u$ (diffusion), and (ii) $\mathbf{q} = \mathbf{v} u$ (advection). When u represents elevation, gravity-dependent flux is accommodated, which implies a loose definition of state variable. It would be useful to enable specification of K for adjacent finite volumes and have the generic solver provide the appropriate interface value (*e.g.*, harmonic mean, geometric mean, upstream value, flux-limited value). The solver also needs to handle the following zeroth- and first-order sources (i) $Src_{ij} = f_{ij}$ (specified source), (ii) $Src_{ij} = \lambda_{ij} u_j$ (decay), and (iii) $Src_{ij} = \Lambda_{ij}(u_j - u_i)$ (transfer).

The various increment terms are approximated by the generic expansions for variable c (taking advantage of the chain rule)

$$c|_m^{m+1} = \left(\frac{\partial c}{\partial \chi} \right)^m \delta \qquad (4\text{-}57)$$

$$(c \nabla u_j)|_m^{m+1} = c^m \left(\frac{\partial u_j}{\partial \chi} \right)^m \nabla \delta + \left(\frac{\partial u_j}{\partial \chi} \right)^m \delta \nabla \chi^m, \qquad (4\text{-}58)$$

$$(c u_j)|_m^{m+1} = \left[c^m \left(\frac{\partial u_j}{\partial \chi} \right)^m + \left(\frac{\partial c}{\partial \chi} \right)^m u_j^m \right] \delta, \qquad (4\text{-}59)$$

$$\delta = \chi|_m^{m+1}. \qquad (4\text{-}60)$$

Typically δ is solved for rather than u.

The individual applications should provide α_{ij}, β_{ij}, K_{ij}, $\mathbf{v}_j$, λ_{ij}, Λ_{ij}, and f_{ij}. For each of these values, the corresponding array of sensitivity coefficients should also be provided. In *Matlab*, storage could be sparse for each of these arrays if significant numbers of coefficients are zero. Of course, storage is not a constraint in 1D.

In multiphase flow and transport, constraints on volume fractions and mass fractions are applied. Constraints on mass fractions are applied for each phase by adding together all species mass-balance equations for the phase, replacing one mass fraction with a weighted sum of the

others, and neglecting the corresponding species balance equation in favor of the summed equation. Constraints on volume fractions are applied by summing together the equations for all phases, replacing one volume fraction with a weighted sum of the others, and neglecting the corresponding phase equation in favor of the summed equation. Mechanisms should be provided to do this, with automatic switching to constrain the largest volume fraction and largest mass fraction in each phase (avoiding roundoff error).

A second type of facility may be nice. It is possible to strictly enforce nonnegativity or boundedness through transforms. A log transform enforces nonnegativity at the cost of disallowing zero values (useful for concentration), while a tanh transform enforces boundedness between -1 and 1 at the cost of disallowing the limiting values (useful for saturation or mass fraction after adaptation). Both of these transforms can be applied after the coefficient array is assembled by multiplying columns in the coefficient array corresponding to the transformed variable. These transforms are

$$\frac{\partial()}{\partial \ln \chi} = \frac{1}{\chi}\frac{\partial()}{\partial \chi} \tag{4-61}$$

$$\frac{\partial()}{\partial \tanh \chi} = \text{sech}^2(\chi)\frac{\partial()}{\partial \chi} \tag{4-62}$$

The reverse transform is easily obtained after solution.

9/3/99 Uptake/dispersal relationships.

A transfer function for uptake was developed for a 1D system last April. In actuality, uptake should be developed in a radial system. Dispersal from the leaf surfaces to the far field can also be treated in a radial system or in a cascade of radial systems (leaf to canopy, canopy to far field). The leaf to far field system is simpler, but doesn't account for clumping; perhaps in a highly diffusive system clumping doesn't matter.

As shown by Bear (1979), steady diffusive flux between two concentric cylinders (*e.g.*, far field and well) is

$$Q = Aq_r = 2\pi r B K \partial\phi/\partial r = \text{constant} \tag{4-63}$$

where Q is radial flux, A is area, q_r is specific radial discharge, B is cylinder length, K is conductivity, ϕ is potential, and r is radius. This can be rearranged and integrated to yield

$$\frac{Q}{2\pi B}\ln\left(\frac{R}{r_w}\right) = \int_{\phi_w}^{\phi} K\,d\phi. \tag{4-64}$$

When K is a constant, flux into the well is defined as

$$Q = 2\pi B K \ln\left(\frac{r_w}{R}\right)(\phi - \phi_w).$$
(4-65)

Correction dated 11/15/01: Equation 4-65 is written incorrectly and the results are applied through today. The correct expression is

$$Q = \frac{2\pi B K}{\ln(R/r_w)}(\phi - \phi_w).$$
(4-66)

Note that when R is slightly larger than r_w (say $R = R_w + \Delta$), $\ln(R/r_w) \approx \Delta/r_w$ and flux into the well is defined as

$$Q = \frac{2\pi B r_w K}{\Delta}(\phi - \phi_w) = AC(\phi - \phi_w).$$
(4-67)

where conductance $C = K/\Delta$.

All of the following equations until today's date will remain uncorrected, with the assumption that $K \ln(r/R)$ should be replaced with $K/\ln(R/r)$. $\boxed{\text{SAS}}$

When K is assumed exponential [the Gardner approximation: $K = K_o \exp(\alpha\phi)$ for negative ϕ], flux into the well is defined as

$$Q = 2\pi B \ln\left(\frac{r_w}{R}\right)\left[\frac{K(\phi) - K(\phi_w)}{\alpha}\right].$$
(4-68)

When there are two concentric cylinders, each with a constant K (say K_s for soil and K_p for plant wall), flux continuity requires that

$$2\pi B K_s \ln\left(\frac{r_w}{R}\right)(\phi_s - \phi_w) = 2\pi B K_p \ln\left(\frac{r_p}{r_w}\right)(\phi_w - \phi_p).$$
(4-69)

In the case

$$Q = ac(h - h_1) = bc(h_1 - h_2),$$
(4-70)

simplification and rearrangement yields

$$Q = \frac{abc}{a + b}(h - h_2).$$
(4-71)

Defining $Y_s = K_s \ln(r_w/R)$ and $Y_p = K_p \ln(r_p/r_w)$,

$$\phi_w = \frac{Y_s \phi_s + Y_p \phi_p}{Y_s + Y_p},$$
(4-72)

and rearranging yields

$$Q = 2\pi B \left(\frac{Y_s Y_p}{Y_s + Y_p}\right)(\phi_s - \phi_p) = 2\pi B Y_e(\phi_s - \phi_p).$$
(4-73)

This relationship can be used directly for the uptake function. A particularly straightforward conceptual model for uptake within a 1D slice has N vertical cylinders uniformly distributed in the horizontal plane (note that gravity is not important at the scales being considered). With the assumption that the transport roots have little resistance compared to the soil/plant-wall system, the plant pressure can be assumed spatially uniform within the volume. Uptake length root density can be defined as

$$\rho_{ru} = \frac{NB}{AB},$$

(4-74)

where ρ_{ru} is uptake root length density [L/L^3], B is the slice thickness [L], and A is the area of the slice [L^2]. The radius from root to far field is calculated by assigning equal area to each root, yielding

$$\pi R^2 = A/N = \frac{1}{\rho_{ru}}$$

(4-75)

$$R = \left(\frac{1}{\pi \rho_{ru}}\right)^{1/2}$$

(4-76)

Thus, the exchange radius is simply related to the uptake biomass.

Total transfer flux within the slice is

$$Q_{tot} = 2\pi N B Y_e(\phi_s - \phi_p),$$

(4-77)

and specific transfer flux is

$$q = \frac{Q_{tot}}{AB} = \frac{2\pi N B Y_e}{AB}(\phi_s - \phi_p)$$
$$= 2\pi \rho_{ru} Y_e(\phi_s - \phi_p).$$

(4-78)

This relationship should work for generic volumes (not just slices in a 1D model). Typically a model would specify the uptake-root radii and plant-wall conductivity, adjusting Y_e and ρ_{ru} according to changes in soil conductivity and biomass.

The simple model for dispersal is similar to the model for uptake, except that the exchange surfaces are assumed to be spheres uniformly distributed throughout a volume V. Each sphere represents 2 stomates. By analogy to the uptake reasoning, steady diffusive flux between two concentric spheres (*e.g.*, far field and stomate) is

$$Q = A q_r = 4\pi r^2 K \partial \phi / \partial r = \text{constant}.$$

(4-79)

This can be rearranged and integrated to yield (assuming K constant)

$$\frac{Q}{4\pi K}\left(\frac{1}{r_w} - \frac{1}{R}\right) = \phi - \phi_w,$$

(4-80)

so flux into the stomate is

$$Q = 4\pi \left(\frac{R r_w}{R - r_w} \right) K(\phi - \phi_w)$$

$$\approx 4\pi r_w K(\phi - \phi_w) \tag{4-81}$$

where the simplification occurs if $r_w \ll R$.

The value for R can be estimated by equating the volume of a sphere with radius R to the total volume divided by the number of stomate pairs, or

$$\frac{4\pi R^3}{3} = \frac{V}{N_s}, \tag{4-82}$$

where N_s is the total number of stomates in the volume V. Each plant has a characteristic number of stomates per leaf area, λ_s. When the leaf biomass is characterized by a leaf area density, ρ_l,

$$N_s = \lambda_s \rho_l V, \tag{4-83}$$

yielding an estimate for R of

$$R = \left(\frac{3}{4\pi \lambda_s \rho_l} \right)^{1/3} \tag{4-84}$$

A stomate is actually a 2D cavity, not a sphere. Assuming that a stomate pair is equivalent to one sphere (one stomate on each side of the leaf), equality of areas yields

$$A = 2(\pi r_s^2) = 4\pi r_w^2 \tag{4-85}$$

$$r_w = r_s / \sqrt{2} \tag{4-86}$$

Typical values from Kozlowski and Pallardy (1997) are $r_s = 3 \times 10^{-6}$ m, $\lambda_s = 3 \times 10^8$ m^{-2}, and $LAI = 2$ (where LAI represents the value for the canopy). Assuming a slab thickness of 0.1 m, $\rho_l = LAI/0.1 \approx 20$ m^{-1}. Let r_c is the radius of a disk containing the canopy (assume 0.5 m) and R_f is the far field for the disk (assume 2 m). Plugging in, $r_w \approx 2 \times 10^{-6}$ m, while $R \approx [3/(4\pi)(3 \times 10^8)(20)]^{1/3} \approx 3 \times 10^{-4}$ m. Clearly $r_w \ll R$ for the example, and flux from the stomate to the far field in the canopy must be dominated by the resistance at the stomate itself.

Specific transfer flux (flux per volume) is represented by

$$q = \frac{(N_s/2)4\pi r_w K}{V}(\phi - \phi_w) \tag{4-87}$$

yielding a specific transfer flux in the form

$$q = \frac{\lambda_s \rho_l V 2\pi r_w K}{V}(\phi - \phi_w)$$

$$= 2\pi r_w \lambda_s \rho_l K(\phi - \phi_w). \tag{4-88}$$

Interestingly, the specific transfer flux is independent of the distance to the far field.

If the transfer is assumed to occur only within the plant canopy, which is represented by a disk, equating the cylinder formula to the flux produced in the disk yields

$$Q = 2\pi BK \ln \left(\frac{r_c}{R}\right) (\phi - \phi_c) = (2\pi r_c^2 B) 2\pi r_w \lambda_s \rho_l K (\phi_c - \phi_w). \qquad (4\text{-}89)$$

Using the relationships

$$a = \ln \left(\frac{r_c}{R}\right)$$

$$b = 2\pi r_c^2 r_w \lambda_s \rho_l$$

$$c = 2\pi BK \qquad (4\text{-}90)$$

yields

$$Q = 2\pi BK \frac{ab}{a+b}(\phi - \phi_w). \qquad (4\text{-}91)$$

Using the same typical values for estimates, $b = 2\pi(0.5)^2(2\times 10^{-6})(3\times 10^8)(20) \approx 2\times 10^4$. Obviously $a \ll b$, so the transfer from the canopy to the far field is the rate-limiting step instead of transfer from stomates to the canopy. However, application requires a relationship between biomass and the ratio between canopy radius and far-field radius.

9/5/99 More dispersal relationships.

$\boxed{S\!\!AS}$

One conclusion from the prior analysis is that transfer rates may be greatly overpredicted if stomates are considered uniformly distributed throughout an atmospheric slice near the ground surface, rather than localized within a canopy, since transfer rates from individual stomates were found to be independent of far-field distance. An unsettling implication of the disk analysis is that transfer is not affected by the number of stomates, which should be flat wrong. However, diffusion rates within the canopy would have to be orders of magnitude smaller within the canopy than within the inter-canopy areas to make the two resistances comparable. Presumably boundary-layer effects would provide reduction in diffusion rates just at the leaf surface, especially since the length scale for diffusion from stomate to canopy is about 1 mm, where the boundary layer is presumably strongest. Note that for 300 stomates/mm^2, there are many stomates within the effective radius for each stomate and the point estimate is misleading. Instead, we can return to the leaf scale to perform the analysis.

There are two types of leaves to consider, needles (*e.g.*, pine, ephedra) and plates (most other species). The needle case will be handled using cylinders, similarly to the uptake root analysis. The plate case will be handled using spheres, similarly to the stomate analysis.

Cylinder

Assume that each leaf is represented by a vertical cylinder extending from the top to the bottom of the individual slices, just like the uptake root analysis. A cylinder has a characteristic inner and outer radius, r_p and r_w, characterizing an outer wall punctured by stomates. Each needle has a characteristic length, b, so each cylinder consists of $n_n = B/b$ needles stacked atop each other, where B is the thickness of the canopy layer under consideration. Treating the leaf as a two-layer system within the canopy (leaf wall and far field), specific flux within a volume within the canopy is represented by

$$q = 2\pi \rho_{cd} Y_e (\phi_a - \phi_p) \tag{4-92}$$

$$Y_e = Y_a Y_p / (Y_a + Y_p)$$

$$Y_a = K_a \ln(r_w/R_c)$$

$$Y_p = K_p \ln(r_p/r_w) \tag{4-93}$$

where ρ_{cd} represents an equivalent dispersal length density within the canopy, R_c is the far field radius within the canopy, K_a is the conductivity of the far field, and K_p is the conductivity of the plant wall. The ρ_{cd} parameter is related to the more commonly measured parameters LAI (leaf area per unit ground surface area) and r_c through surface area equality within a slice,

$$(2\pi r_w) N_c B = LAIA(A_c B)/V_c \tag{4-94}$$

$$\rho_{cd} = \frac{N_c B}{A_c B}, \tag{4-95}$$

where A_c is the area of the canopy, V_c is the volume of the canopy, and N_c is the number of cylinders in the canopy slice. Substitution yields

$$2\pi r_w \rho_{cd} = LAI(A/V_c) \tag{4-96}$$

$$\rho_{cd} = \frac{LAIA}{2\pi r_w V_c} \tag{4-97}$$

By assigning equal plan-view area to each leaf cylinder,

$$R_c = \left(\frac{1}{\pi \rho_{cd}}\right)^{1/2}. \tag{4-98}$$

For the purposes of estimation, assume $r_w = 1$ mm, $LAI = 0.1$ (averaged over plant support area), $H_c = 1$ m, $b = 1$ cm, $B = 10$ cm, $r_c = 0.5$ m, and $A = 10$ m². With these approximations, $\rho_{cd} \approx 200$ m/m³ and $R_c \approx 0.04$ m. Using a typical air conductivity of $K = 1.5$ cm/s and typical stomatal conductivities of 0.15 and 1.5 cm/s (based on Table 12.1 by Kozlowski and Pallardy

(1997)), $0.1K < Y_p < K$ and $Y_a \approx 2K$, or $0.1K < Y_e < (2/3)K$. Presumably desert vegetation would have conductivies in the lower part of the conductivity range.

The horizontal canopy to far field flux continuity requires

$$Q = 2\pi B K \ln\left(\frac{r_c}{R}\right)(\phi - \phi_c) = (A_c B)2\pi\rho_{cd}Y_e(\phi_c - \phi_w). \tag{4-99}$$

Using the relationships

$$a = \ln\left(\frac{r_c}{R}\right)$$
$$b = A_c\rho_{cd}Y_e/K$$
$$c = 2\pi B K \tag{4-100}$$

yields

$$Q = 2\pi B K \frac{ab}{a+b}(\phi - \phi_w). \tag{4-101}$$

Using the same typical values for estimates, $a \approx -2$ and $b = 0.735(200)(0.1 \text{to} 0.7)$ (implying $16 < b < 110$). Again $a \ll b$, so the transfer from the canopy to the far field is the rate-limiting step instead of transfer from needles to the canopy. Note that if the diffusion within the canopy accounted for boundary layer effects, K within the canopy would be significantly smaller than K outside the canopy. If this effect were 1 to 2 orders of magnitude, both intercanopy and intracanopy diffusion would be of the same order of magnitude. Also note that the value of LAI represents a well-watered condition. When $Y_p = 0.1K$, a drop of one order of magnitude in LAI makes the leaf and far field resistances of the same order of magnitude, while a drop of two orders of magnitude makes the local resistance dominant. An extra order of magnitude drop is required for the other extreme.

If eddy diffusion is invoked, K is linearly proportional to wind velocity, which in turn logarithmically varies with distance from a surface. At the surface, molecular diffusion is the only active mechanism for transporting vapor ($0.25 \text{ cm}^2/\text{s}$); eddy diffusion tens of meters from the surface may be orders of magnitude larger.

Sphere

Assume that each leaf is represented by a sphere with radius r_w. A characteristic sphere radius is found by equating surface areas,

$$\frac{4\pi r_w^2}{3} = 2A_l \tag{4-102}$$

$$r_w = \left(\frac{3A_l}{2\pi}\right)^{1/2} \tag{4-103}$$

where A_l is the area of one side of the leaf. From the stomate analysis, flux for one leaf is

$$Q = 4\pi \left(\frac{R_d r_w}{R_d - r_w}\right) K(\phi - \phi_w). \tag{4-104}$$

The value for R_d can be estimated by equating the volume of a sphere with radius R_d to the total volume divided by the number of leaves,

$$\frac{4\pi R_d^3}{3} = \frac{V}{N_l}, \tag{4-105}$$

where V is the volume of the canopy slice $(A_c B)$ and N_l is the total number of leaves in the volume V. It is convenient to define a leaf area density within the canopy as total leaf area divided by canopy volume, or

$$\rho_{ac} = \frac{LAI A}{V_c}, \tag{4-106}$$

where V_c is the canopy volume. Using this density, N_l can be estimated by

$$N_l = \rho_{ac} \frac{B A_c}{2A_l}. \tag{4-107}$$

Substituting,

$$\frac{4\pi R_d^3}{3} = \frac{V}{\rho_{ac} V/(2A_l)} = \frac{2A_l}{\rho_{ac}} \tag{4-108}$$

$$R_d = \left(\frac{3A_l}{2\pi \rho_{ac}}\right)^{1/3} \tag{4-109}$$

For the purposes of estimation, assume $A_l = 1$ cm^2, $LAI = 0.1$ (support areal average), $V_c = 0.3$ m^3, $B = 0.1$ m, $r_c = 0.5$ m, and $A = 10$ m^2. With these approximations, $r_w \approx 0.7$ cm, $\rho_{ac} \approx 1.3$ m^2/m^3, $N_l \approx 500$, $V \approx 0.08$ m^3, and $R_d \approx 3.3$ cm. Neither R_d nor r_w can be neglected in determining flux in this case.

The canopy to far field flux continuity requires

$$Q = 2\pi BK \ln\left(\frac{r_c}{R}\right)(\phi - \phi_c) = 4\pi\left(\frac{R_d r_w}{R_d - r_w}\right) K N_l(\phi_c - \phi_w). \tag{4-110}$$

Using the relationships

$$a = \ln\left(\frac{r_c}{R}\right)$$

$$b = 2\left(\frac{R_d r_w}{R_d - r_w}\right)\left(\frac{\rho_{ac} A_c}{2 A_l}\right)$$

$$c = 2\pi BK \tag{4-111}$$

yields

$$Q = 2\pi BK \frac{ab}{a+b}(\phi - \phi_w). \tag{4-112}$$

Using the same typical values for estimates, $a \approx -2$ and $b \approx 70$. Again, $a \ll b$, so the transfer from the canopy to the far field is the rate-limiting step instead of transfer from leaves to the canopy. With one to two orders of magnitude drop in LAI, the two components are of comparable magnitude; with three orders of magnitude drop, plant resistance is dominant.

One more approach might be examined, extending the concepts used here. The approach uses a cascade of leaf to branch cylinder, branch cylinder to canopy, and canopy to far field. This begins to get complex and the payback may be limited.

9/6/99 More dispersal relationships.

Generic relationship

When conductivity is constant within the canopy and far field, both the cylinder and the sphere relationships boil down to the form

$$Q = 2\pi BK_a \frac{ab}{a+b}(\phi - \phi_w), \tag{4-113}$$

where

$$a = \ln\left(\frac{r_c}{R}\right)$$

$$b_c = 2\pi r_c^2 \rho_{cd} Y_e / K_a$$

$$Y_e = Y_a Y_p / (Y_a + Y_p)$$

$$Y_a = K_a \ln(r_w / R_c)$$

$$Y_p = K_p \ln(r_p / r_w)$$

$$b_s = 2\left(\frac{R_d r_w}{R_d - r_w}\right)\left(\frac{\rho_{ac} A_c}{2A_l}\right) \tag{4-114}$$

where b_c is b for the cylinder case and b_s is b for the sphere case. Conductivity in these cases represents a vapor eddy diffusion coefficient (although some checking needs to be done to get the right units).

Boundary layer theory suggests that the mean velocity field increases away from a fixed surface. The increase can be described as a power law (Brutsaert, 1982),

$$\bar{u} = C_p u_*(z/z_0)^m \tag{4-115}$$

$$u_* = (\tau_0/\rho)^{1/2} \tag{4-116}$$

where u_* is the friction velocity. For neutral conditions $C_p \approx 5.5$ to 6.0 and $m = 1/7$. The parameter z_0 can be as small as 0.001 cm for mud flats and ice; presumably individual leaves are similarly smooth.

As discussed earlier, steady diffusive flux between two concentric cylinders (e.g., far field and well) is

$$Q = Aq_r = 2\pi r B K \partial\phi/\partial r = \text{constant}, \tag{4-117}$$

which can be rearranged to provide

$$\frac{Q}{2\pi B}\int_{r_w}^{R}\frac{1}{rK}\,dr = \phi - \phi_w. \tag{4-118}$$

Diffusivity is often considered proportional to mean velocity, or $D = \alpha\bar{u}$. When $K = \beta(r - r_w)^m$ (blithely using the 1D expression in radial coordinates),

$$\frac{Q}{2\pi B}\int_{r_w}^{R}\frac{1}{\beta r(r - r_w)^m}\,dr = \phi - \phi_w. \tag{4-119}$$

Approximating the r term in the integral as the mean of the limits yields

$$\frac{Q}{2\pi B} \int_{r_w}^{R} \frac{1}{\beta r (r - r_w)^m} \, dr \approx \frac{Q}{\pi B \beta (1 - m)(r_w + R)}(R - r_w)^{1-m} = \phi - \phi_w. \tag{4-120}$$

9/8/99 More dispersal relationships. $\boxed{SAS}$

The relationships developed to date have made me uneasy because of the insensitivity of resistance to leaf area. I expect that a shrub would only put out enough leaves to start reaching the point of no return, not slam past the point by orders of magnitude. Why would a shrub put out so many leaves that there is no marginal benefit in adding an additional leaf? I discussed this issue with Dani Or and he brought up the point that my integrations thus far neglected consideration of the path from the far field of individual leaves to the canopy perimeter. In effect, I placed all leaves at the perimeter, although the volume relations are not right for this case.

Let's look at the effect of uniformly spreading leaves throughout the volume without regard to canopy. This assumption was looked at with the stomates to some extent. The assumption is that the layer is well mixed, so the analysis does not depend on the details of the canopy distribution. Using the stomate analysis, we find

$$Q_l = 4\pi \left(\frac{R r_w}{R - r_w} \right) K(\phi - \phi_w) \tag{4-121}$$

$$\frac{4\pi}{3} R^3 = \frac{V}{N_l} = \frac{V}{V \rho_l / A_l} = \frac{A_l}{\rho_l} \tag{4-122}$$

$$R = \left(\frac{3 A_l}{4 \pi \rho_l} \right)^{1/3} \tag{4-123}$$

$$r_w = \left(\frac{A_l}{4\pi} \right)^{1/2} \tag{4-124}$$

$$q = \left(\frac{N_l}{V} \right) Q_l = \frac{4\pi \rho_l}{A_l} \left(\frac{R r_w}{R - r_w} \right) K(\phi - \phi_w)$$

$$\approx \frac{\rho_l K}{r_w}(\phi - \phi_w) = \rho_l K \left(\frac{4\pi}{A_l} \right)^{1/2}(\phi - \phi_w) \tag{4-125}$$

where A_l is now total surface area for a typical leaf, ρ_l is the leaf area per unit volume on an areal basis, and a subscript w represents the leaf surface. Generally $r_w \ll R$, as with the stomate analysis, leading to the last approximation. The last form is satisfyingly simple and linearly dependent on leaf area density; the fuller form is not quite linearly dependent on leaf area density. An offline example suggests that the fuller form is appropriate once LAI (defined for the canopy) starts getting

larger than 1; however, the approximate form is only 12 percent too small for $LAI = 10$ in the example.

9/13/99 More dispersal relationships.

The previous analysis can be adapted for the case where just the canopy is concerned. In this case,

$$q = \frac{4\pi\rho_{lc}}{A_l}\left(\frac{Rr_w}{R - r_w}\right)K(\phi - \phi_w) = \lambda K(\phi - \phi_w) \tag{4-126}$$

$$R = \left(\frac{3A_l}{4\pi\rho_{lc}}\right)^{1/3} \tag{4-127}$$

$$r_w = \left(\frac{A_l}{2\pi}\right)^{1/2} \tag{4-128}$$

where A_l is total surface area for a typical leaf, ρ_{lc} is the leaf area per unit volume within the canopy, λ is a transfer coefficient, and a subscript w represents the leaf surface.

Let's return to the idea of overall transfer from plant to far field. The dispersal relationship above is only step one. Step two is dispersal from within canopy to the canopy edge, and step three is dispersal from the canopy edge to far field (analyzed before).

The step two analysis has a difficulty, in that strictly speaking dispersal depends on the local value of ϕ, which varies throughout the canopy. Assuming dispersal takes place uniformly through-out the canopy ($q = $ constant), however, integration is straightforward assuming a cylindrical slice with thickness B within the canopy

$$\frac{1}{r}\frac{d}{dr}\left(r\frac{d\phi}{dr}\right) + \frac{q}{K} = 0, \tag{4-129}$$

where K is the conductivity in the canopy. This can be integrated to yield

$$\frac{d\phi}{dr} + \frac{qr}{2K} = 0 \tag{4-130}$$

$$\phi - \phi_0 + \frac{qr^2}{4K} = 0 \tag{4-131}$$

Evaluating at the canopy edge,

$$\phi_0 = \phi_c + \frac{qr_c^2}{4K} \tag{4-132}$$

$$\phi_c - \phi + \frac{q}{4K}(r_c^2 - r^2) = 0 \tag{4-133}$$

where r_c is the radius of the canopy. Further assuming that an effective canopy ϕ can be used to provide an equivalent q, define ϕ_m as ϕ at the radius enclosing half of the canopy area, or $r_m^2 = r_c^2/2$. Plugging in results in the relationships

$$\phi_c - \phi_m + \frac{\lambda K}{4K}(\phi_w - \phi_m)(r_c^2 - r_m^2) = 0$$

$$\phi_m\left(1 + \frac{\lambda r_c^2}{8}\right) = \phi_c + \phi_w\frac{\lambda r_c^2}{8}$$

$$\phi_m = \alpha\phi_c + (1-\alpha)\phi_w$$

$$\alpha = \frac{1}{1 + (\lambda r_c^2/8)}$$

$$q = \lambda K[\phi_w - \alpha\phi_c - (1-\alpha)\phi_w] = \frac{\lambda K}{1 + (\lambda r_c^2/8)}(\phi_w - \phi_c) \qquad (4\text{-}134)$$

$$\phi_c - \phi + \frac{2\lambda}{8 + \lambda r_c^2}(\phi_w - \phi_c)(r_c^2 - r^2) = 0 \qquad (4\text{-}135)$$

$$\phi_0 = \phi_c + \frac{2\lambda r_c^2}{8 + \lambda r_c^2}(\phi_w - \phi_c) \qquad (4\text{-}136)$$

The total flux at a particular radius r is

$$Q = -2\pi K B\frac{\partial\phi}{\partial r} = \frac{2\pi r Bq}{2} = \frac{8\pi r B\lambda K}{8 + \lambda r_c^2}(\phi_w - \phi_c). \qquad (4\text{-}137)$$

Flux continuity at the canopy fringe for the canopy relationship and for a cylinder between the canopy and far field requires (flux defined as positive from leaf to far field)

$$Q = 2\pi BK\ln\left(\frac{R_f}{r_c}\right)(\phi_c - \phi) = \frac{8\pi r_c B\lambda K}{8 + \lambda r_c^2}(\phi_w - \phi_c). \qquad (4\text{-}138)$$

Using the relationships

$$a = \ln\left(\frac{R_f}{r_c}\right)$$

$$b = \frac{4\lambda r_c}{8 + \lambda r_c^2}$$

$$c = 2\pi BK \qquad (4\text{-}139)$$

yields

$$Q = 2\pi BK\frac{ab}{a+b}(\phi - \phi_w). \qquad (4\text{-}140)$$

Using typical values for estimates ($r_c = 0.5$ m, $R_f = 2$ m, $A_l = 1$ cm^2, $\rho_{lc} = 3$ m^2/m^3), calculated values are $r_w = 2.8\times 10^{-3}$ m, $R_w = 2.\times 10^{-2}$ m (leaf far field radius), $\lambda = 1.2\times 10^3$ m^{-2}, $a = 1.4$, and $b = 7.8$. These values provide a restriction factor $ab/(a+b)$ that is fairly insensitive to

leaf area density. For sensitivity to leaf area, b should be significantly smaller than a; b is linearly dependent on ρ_{lc}. If the ratio of canopy radius to far field radius increases, sensitivity to leaf area increases.

9/14/99 Other dispersal issues.

Transpiration is dependent on the difference between vapor density at the leaf and far field vapor density. It is typically assumed that the vapor density at the leaf surface is the saturated vapor density at the leaf temperature. In the sparse canopies of most desert shrubs, air and leaf temperature should be fairly close. Using the air temperature for leaf transpiration should provide a reasonable estimate of leaf vapor density.

9/17/99 Eddy diffusivity.

The formulation provided thus far uses the terminology of conductivity [L/T] and potential [L] to give a volume flux. Mass transfer is better stated in terms of vapor density.

Bare-soil evaporation in *breath* has used the idea of a logarithmic velocity profile to provide a quasi-steady two-point conductance (soil and far atmosphere, such as 2 m elevation). Conductance is iteratively determined based on wind speed and atmospheric stability. If transpiration is included at discrete elevations, the profile must include elevation-dependent velocity and thus elevation-dependent conductivity. This becomes more problematic as vegetation is included, as vegetation not only modifies the velocity profile through roughness but provides a source of vapor and energy. It may be desirable to discretize the profile in some way, which would require local values of conductivity.

Brutsaert (1982) discusses various approaches to characterizing transport of momentum, heat, and vapor in the lower atmosphere, and some of the explanation here is lifted from his text.

The lower atmosphere is broken into several layers. In the immediate vicinity of the surface, turbulence is affected by the roughness elements and may be damped by viscous effects. Brutsaert (1982) terms the lower layer the *interfacial (transfer) sublayer*. In smooth flow (*e.g.*, over ice or mud) it is called the *viscous sublayer*, with thickness on the order of $30\nu/u_*$, where ν is the kinematic viscosity and u_* is the friction velocity ($u_* = \sqrt{\tau/\rho}$), τ is momentum flux (stress), and ρ is density. Over a rough surface, the interfacial sublayer is called the *roughness sublayer*, with thickness on the order of the mean height of the roughness obstacles. If the rough surface is porous or permeable to

the air stream, the interfacial sublayer can be called the *canopy sublayer*. Molecular diffusivities for vapor and heat are of the same order as kinematic viscosity, so in the interfacial sublayer scaling lengths for vapor, sensible heat, and momentum are very similar.

The next layer up is the *surface sublayer*, with the lowermost portion termed the *dynamic sublayer*. The dynamic sublayer extends to roughly 1 to 10 m above the surface, depending on atmospheric stability; the entire surface sublayer extends to about 10 m above the surface. In the dynamic sublayer, density stratification is negligible so that stability is not a concern and profiles are logarithmic.

Above the surface sublayer, the *defect sublayer* extends to an elevation of about 100 to 1000 above the surface, and the free atmosphere lies above. None of the vapor density measurements available for simulation are within the defect sublayer; most are at 2 m above the surface, at the top edge border of the dynamic sublayer. Accordingly, the defect layer and the free atmosphere will not be considered further.

The dynamic sublayer is the most tractable analytically. From dimensional analysis,

$$\frac{u_*}{z(d\bar{u}/dz)} = \kappa \tag{4-141}$$

where $\bar{u}$ is mean horizontal wind speed and κ is von Kármán's constant (roughly 0.4). Direct integration yields

$$\bar{u}_2 - \bar{u}_1 = \frac{u_*}{\kappa} \ln\left(\frac{z_2}{z_1}\right). \tag{4-142}$$

The zero-velocity intercept is called z_{0m}, the momentum roughness parameter. If the surface is rough, an offset distance d is used in the similarity formulation, yielding

$$\bar{u}_2 - \bar{u}_1 = \frac{u_*}{\kappa} \ln\left(\frac{z_2 - d}{z_1}\right). \tag{4-143}$$

Note that this relationship breaks down when $z \leq d$, and is not correct when z is slightly larger than d. The relationship for $\bar{u}$ when $z - d \gg z_{0m}$ is

$$\bar{u} = \frac{u_*}{\kappa} \ln\left(\frac{z - d}{z_{0m}}\right). \tag{4-144}$$

Other analyses replace $(z - d)$ with $(z - d + z_{0m})$.

A similar analysis for vapor flux (surface to air), E, yields

$$E = -\frac{a_v \kappa u_*}{\ln\left[(z_2 - d)/(z_1 - d)\right]}(\rho_{v2} - \rho_{v1}) \tag{4-145}$$

---

where ρ_v is the (mean) vapor density and a_v is the ratio of water and momentum von Kármán constants ($a_v \approx 1$ is thought reasonable for practical purposes). The vapor roughness length, z_{0v}, is defined as the zero intercept of $(\rho_{vs} - \rho_v)$ data plotted against $\ln(z - d)$, where ρ_{vs} is the surface value of ρ_v. The relationship for ρ_v when $z - d \gg z_{0v}$ is

$$E = -\frac{a_v \kappa u_*}{\ln\left[(z - d)/z_{0v}\right]}(\rho_v - \rho_{vs}) \tag{4-146}$$

A similar analysis for sensible heat flux (surface to air), H, yields

$$H = -\frac{a_h \kappa u_* \rho c_p}{\ln\left[(z_2 - d)/(z_1 - d)\right]}(\theta_2 - \theta_1) \tag{4-147}$$

where θ is the (mean) potential temperature, a_h is the ratio of heat and momentum von Kármán constants ($a_h \approx 1$ is thought reasonable for practical purposes), and c_p is the specific heat for constant pressure. The heat roughness length, z_{0h}, is defined as the zero intercept of $(\theta_s - \theta)$ data plotted against $\ln(z - d)$, where θ_s is the surface value of θ. For most practical purposes, θ can be replaced by $\bar{T}$ or T for short. The relationship for T when $z - d \gg z_{0h}$ is

$$H = -\frac{a_h \kappa u_* \rho c_p}{\ln\left[(z_2 - d)/(z_1 - d)\right]}(T - T_s) \tag{4-148}$$

When considering effects in the canopy sublayer, it is convenient to use the vertical continuity relationship for momentum,

$$-\frac{d\tau}{dz} + D_f = 0, \tag{4-149}$$

where τ is the horizontal shear stress and D_f is the momentum sink term (drag experienced by the foliage per unit volume of air. It is generally assumed that shear stress is proportional to velocity gradient through

$$\tau = \rho K_m \frac{d\bar{u}}{dz}, \tag{4-150}$$

where K_m is the eddy viscosity [L^2/T].

In the dynamic sublayer, $D_f = 0$, implying τ is a constant, denoted by τ_0. Eliminating $d\bar{u}/dz$ from Equation 4-141 and Equation 4-150 yields the relationship

$$K_m = \frac{\kappa \tau_0}{\rho u_*}(z - d) = \frac{\kappa^2 \bar{u}_2}{\ln[(z_2 - d)/z_{0m}]}(z - d) \tag{4-151}$$

for K_m within the dynamic sublayer. Eddy diffusivities for vapor and sensible heat may be slightly larger than for momentum, but for practical purposes the differences may be neglected.

In a canopy, D_f is assumed proportional to $\bar{u}^2$ through

$$D_f = \frac{A_f C_d \rho}{2}\bar{u}^2 \tag{4-152}$$

where A_f is the surface area (both sides) of leaves per unit volume of air and C_d is a drag coefficient. A_f is related to leaf area index (one-sided area of leaves per unit ground surface area) through

$$2LAI = \int_0^{h_0} A_f \, dz. \tag{4-153}$$

Depending on the assumptions for K_m and $A_f C_d$, one gets different profiles for velocity. The exponential profile for $\bar{u}$ is obtained by assuming $K_m \propto |d\bar{u}/dz|$ and $A_f C_d$ is constant (essentially a uniform canopy): *Correction dated 04/30/02: Actually $K_m \propto |d\bar{u}/dz|^{-1}$, but the remainder is correct* $\boxed{\mathcal{SAS}}$

$$\bar{u} = \bar{u}(h_0) \exp(-a_w \xi), \tag{4-154}$$

where a_w is an extinction coefficient and $\xi = (h_0 - z)/h_0$. The eddy viscosity relationship for this case is expressed as

$$K_m = K_m(h_0) \exp(-a_m \xi), \tag{4-155}$$

where $K_m(h_0)$ is the value of K_m at h_0 and $a_m = (2a_d - a_w)$ is an extinction coefficient that probably is close to a_d and a_w. Measurements suggest that a_w increases with both canopy density and canopy flexibility. Reported values for a_w are between 0.4 and 0.8 for sparse rigid elements (citrus orchard, wooden pegs, bushel baskets); between 1 and 2 for moderately dense semirigid elements (corn, rice, larch, christmas trees, sunflower, and plastic strips); and between 2 and 4 for dense flexible elements (wheat, oats, immature maize). A series of measurements for maize during a growing season suggest that $a_w \propto h_0^m$, where h_0 is in cm, m is in the range of approximately $1/3$ to $1/2$, and the proportionality constant is roughly 5 to 6 for $m = 1/2$ and 2.3 for $m = 1/3$. Another analysis suggests that

$$a_w = \frac{A_k h_0}{h_0 - d}, \tag{4-156}$$

where A_k is slightly smaller than or equal to 1. For a dense canopy, $d \approx 2h_0/3$, suggesting $a_w \approx 3$.

Brutsaert (1982) suggests that a workable approximation is to join the canopy sublayer with the dynamic sublayer at h_0, yielding

$$K_m(h_0) = \kappa u_* (h_0 - d + z_{0m})$$
$$= \frac{\kappa^2 \bar{u}_2}{\ln[(z_2 - d + z_{0m})/z_{0m}]} (h_0 - d + z_{0m}) \tag{4-157}$$

$$\bar{u}(h_0) = \frac{u_*}{\kappa} \ln\left(\frac{h_0 - d}{z_0 m}\right) \tag{4-158}$$

Turbulent transfer of a scalar inert mixture is governed by

$$-\frac{dF}{dz} + S_f = 0, \tag{4-159}$$

---

where F is the vertical specific flux of the mixture and S_f is the source term from the foliage. With the assumption that the profile for a scalar is roughly similar to that of momentum, the eddy diffusivity profile for a uniform canopy is expressed as

$$K_c = K_c(h_0)\exp(-a_s\xi),\qquad(4\text{-}160)$$

where $K_c(h_0)$ is the value of K_c at h_0 and a_s is an extinction coefficient that is of the same order of magnitude as a_m and a_w. Various values for a_s are reported ranging from 2.2 through 4.25, all for dense canopies. The lowest value is the lowest end of a range for wheat; the highest is for a pine forest. Presumably a_s would be smaller for sparse desert vegetation.

Most of the available information on vegetation is for dense canopies. Claassen and Riggs (1993) examined the roughness length and displacement height for Sonoran desert vegetation, dominated by creosote bush. For these vegetation, they found that $z_{0m} \approx 0.145h_0$, in agreement with Brutsaert (1982) observations, but $d \approx 0$, suggesting that the roughness elements are sparsely spaced. Further, the roughness elements in the Sonoran desert vegetation were found to be approximately uniformly distributed through the canopy. These results are likely to be fairly typical of vegetation scenarios through those associations likely to be present at YM that are now at lower elevations than piñon-juniper, and perhaps even for piñon-juniper.

Based on the above information, it may be sufficient to simply use a formulation for evapotranspiration that includes only the canopy and dynamic sublayers. This is always adequate when the measurement point is at 1 m elevation above the surface and is adequate under neutral conditions when the measurement point is even as high as 50 to 100 m elevation. There should be relatively little error for a measurement point of 2 m elevation (typical of YM observations) even when the atmosphere is very unstably stratified, although Brutsaert (1982) notes that under stable conditions the logarithmic profile is not representative. The advantage of neglecting stability considerations is that no iteration is necessary to calculate eddy diffusivities.

10/9/99 Summary of updake/dispersal relations. $\boxed{\text{SAS}}$

Musings about uptake and dispersal, and equation developments, are dispersed through too many pages and are pretty diffuse. The relationships are developed in a more compact and unified form here.

Analysis of steady-state series obeying

$$Q = c_1(v_0 - v_1) = c_2(v_1 - v_2) = c_i(v_{i-1} - v_i),\qquad(4\text{-}161)$$

where c is conductance and v is the corresponding potential, yields a useful relationship between the various potentials in the form

$$Q = c_e(v_0 - v_n), \tag{4-162}$$

$$c_e = \frac{\prod_i c_i}{\sum_i \left(\prod_{j \neq i} c_j\right)}. \tag{4-163}$$

The most important cases are 2 layers $[c_{e2} = c_1 c_2 / (c_1 + c_2)]$ and 3 layers $[c_{e3} = c_1 c_2 c_3 / (c_1 c_2 + c_1 c_3 + c_2 c_3)]$. With these relationships in hand, it is possible to mix and match solutions for specific types of layers to develop multilayer equations.

Three-layer cases will be considered here (two for roots). In all cases, there is a transfer resistance across the plant root or leaf wall. There is a resistance from the plant surface to the far field: in the case of leaves, this resistance can be broken into two parts, leaf to canopy and canopy to far field. Wall resistance will be considered 1D. Resistance to the far field will be considered in cylindrical coordinates, while resistance within a plant canopy will be considered in spherical coordinates.

One-dimensional mass fluxes across the plant wall per unit area are described by

$$q_m = C(\phi_w - \phi_p), \tag{4-164}$$

where q_m is the local mass flux per unit area $[\text{M/T L}^2]$, C is wall conductance, ϕ_w is potential at the outside of the wall, and ϕ_p is potential at the inside of the wall. Total mass flux across all plant walls is described by

$$Q_m = A_w q_m = A_w C(\phi_w - \phi_p), \tag{4-165}$$

where A_w is the total wall area over which flux occurs.

Three types of potential are of interest: (i) head [L], (ii) pressure $[\text{M/L T}^2]$, and (iii) density $[\text{M/L}^3]$. The first two forms are used for uptake, the third for dispersal into the atmosphere. In all cases, C times ϕ must end up with units of M/TL^2, so that the appropriate conductance units for the three cases are:

$$C_h = \frac{\rho K}{\Delta} \qquad [\text{M/T L}^3] \tag{4-166}$$

$$C_p = \frac{K}{g\Delta} \qquad [\text{T/L}] \tag{4-167}$$

$$C_d = \frac{D_a}{\Delta} \qquad [\text{L/T}] \tag{4-168}$$

where K is soil conductivity [L/T], Δ is the length that diffusion occurs across [L], and D_a is atmospheric dispersivity $[\text{L}^2/\text{T}]$.

Mass fluxes from an outer to an inner surface in a spherical system are described by

$$Q_m = 4\pi r_i r_o C(\phi_o - \phi_i), \tag{4-169}$$

where r represents a radius [L]; C is again a conductance; and the i and o subscripts represent the inner and outer surfaces, respectively. This case represents leaves dispersing to a far field. Total mass flux within a volume is the mass flux for one sphere times the number of spheres.

Mass fluxes from an outer to an inner surface in a cylindrical system are described by

$$Q_m = 2\pi B C \Delta \ln\left(\frac{r_i}{r_o}\right)(\phi_o - \phi_i), \tag{4-170}$$

where B is the thickness of the system. This case represents a canopy dispersing to a far field or a set of vertical uptake roots in a horizontal slice. Total mass flux within a volume is the mass flux for one cylinder times the number of cylinders.

Using the analysis for a local spherical system, assuming that there are numerous local systems uniformly distributed within a cylindrical system, and that the outer potential for each system is adequately described by the potential at the radius enclosing half of the cylinder's area, mass fluxes from one of a number of local spherical sources to the outer surface of the cylindrical system are described by

$$Q_m = \frac{8\lambda C}{8 + \lambda r_o^2}(\phi_o - \phi_i) \tag{4-171}$$

$$\lambda = \frac{4\pi N_w r_o r_i}{V} \tag{4-172}$$

where N_w is the number of local sources and V is the volume of the cylindrical system. This case represents leaves in a canopy dispersing to the edge of the canopy.

3/2/00 Methodology for eddy diffusivity.

Discussion of eddy diffusivity was brought out in the entry for 9/17/99. A finite-volume formulation for vertical continuity of flux is being implemented in *breath*.

The vertical continuity of momentum flux is

$$-\frac{d\tau}{dz} + D_f = 0, \tag{4-173}$$

where τ is the horizontal shear stress and D_f is the momentum sink term (drag experienced by the foliage per unit volume of air). It is generally assumed that shear stress is proportional to velocity

gradient through

$$\tau = \rho K_m \frac{d\bar{u}}{dz},\tag{4-174}$$

where K_m is the eddy viscosity $[L^2/T]$ and $\bar{u}$ is mean horizontal wind speed. Similarly, vapor mass flux and sensible heat flux are

$$E = \alpha_v K_m \frac{d\bar{\rho}_v}{dz}\tag{4-175}$$

$$H = \rho c_p \alpha_h K_m \frac{d\bar{T}}{dz}\tag{4-176}$$

where α_v and α_h are K_v/K_m and K_h/K_m, respectively. Continuity equations are yielded in the form

$$\frac{dE}{dz} + S_v = 0\tag{4-177}$$

$$\frac{dH}{dz} + S_e = 0\tag{4-178}$$

where S_v and S_e are sources of vapor and heat, respectively.

Assuming that the canopy has uniform roughness elements and the eddy diffusivity is joined at h_0,

$$K_m = \bar{u}_2 K_o \exp(-a_m \xi)\tag{4-179}$$

$$K_o = \frac{\kappa^2 (h_0 - d + z_{0m})}{\ln[(z_2 - d + z_{0m})/z_{0m}]}\tag{4-180}$$

$$\xi = \begin{cases} (h_0 - z)/h_0 & \text{for } z \le h_0 \\ 0 & \text{for } z \ge h_0 \end{cases}\tag{4-181}$$

where z_2 is the measurement height, h_0 is the height of the canopy, d is the displacement height, z_{0m} is the momentum roughness parameter, and a_m is an extinction coefficient dependent on vegetation density.

As a consequence of neglecting consideration of stability, it is straightforward to derive the profile of K_m. In fact, all but the windspeed component can be supplied at long intervals (*e.g.*, weekly) and scaled by windspeed.

3/9/00 Methodology for vegetation.

The previous discussion of dispersal of vapor from leaves has neglected one salient feature: the vegetation adaptively adjusts the leaf resistance to achieve target conditions within the plant. Thus, a relatively simple formulation for dispersal can be achieved.

The simple formulation for dispersal is a two-step process: (i) transfer across the leaf boundary, and (ii) transfer to the bulk atmosphere. It is convenient to characterize leaves as spheres uniformly embedded in a continuum, without considering the details of cover distribution. It is assumed that the atmosphere is a well-mixed continuum. For this case, total flux from inner to outer surface of one sphere is

$$Q_m = 4\pi r_i r_o D_a (\rho_i - \rho_o)/(r_o - r_i),$$
(4-182)

where Q_m is the mass flux of vapor, r_i is the equivalent radius of the leaf, r_o is the equivalent radius of the volume enclosing each leaf, ρ_o is the far-field vapor density, ρ_i is the leaf-surface vapor density, and D_a is the vapor diffusivity (vapor diffusion plus eddy diffusivity). Assuming that $r_o \gg r_i$ and accounting for all leaves simultaneously yields

$$q_m = \rho_l (D_a/r_i)(\rho_i - \rho_o) = \rho_l C_a (\rho_i - \rho_o)$$
(4-183)

where ρ_l is leaf area per unit volume, A_l is surface area for a typical leaf, $C_a = D_a/r_i$ is bulk conductance, and q_m is mass flux per unit volume.

The flux across the leaf surface is

$$Q_m = A_w D_v (\rho_p - \rho_i)/(r_i - r_p),$$
(4-184)

where A_w is the total wall (stomate) area over which flux occurs, D_v is the vapor diffusion coefficient, ρ_p is the plant vapor density, and $r_i - r_p$ is the thickness of the leaf for diffusion. Accounting for all leaves simultaneously yields

$$q_m = (\rho_l A_w D_v/A_l)(\rho_p - \rho_i)/(r_i - r_p)$$
(4-185)

Letting $F_s = A_w/A_l$ and $C_v = D_v/(r_i - r_p)$,

$$q_m = \rho_l F_s C_v (\rho_p - \rho_i)$$
(4-186)

Combined flux from inner leaf to far field is

$$Q_m = C(\rho_p - \rho_o)$$
(4-187)

$$C = \rho_l \frac{C_a C_v F_s}{C_a + F_s C_v}$$
(4-188)

As developed previously, the equivalent radius of a leaf is

$$r_i = \left(\frac{3A_l}{2\pi}\right)^{1/2}$$
(4-189)

where A_l is the area of one side of the leaf. Note that A_l is much larger than A_w, since stomates only cover a fraction of the leaf surface.

The far-field radius can be estimated from the leaf-area density within a horizontal slice,

$$r_o = \left(\frac{3A_l}{2\pi\rho_l}\right)^{1/3} \tag{4-190}$$

where ρ_l is the leaf area density within the horizontal slice (which includes canopy and intercanopy in the estimate). Leaf area density can be estimated from LAI, the canopy height, and some estimate of how LAI is distributed vertically within the canopy. Note that canopy height is also required for the eddy diffusivity.

A key feature of this formulation is the strong dependence of transpiration flux on both ρ_l and F_s, which are under direct control of the plant. Given a set of leaves already in place, plants can rapidly adjust stomate apertures to limit fluxes. Over longer periods, plants can add or subtract leaves.

F_s can be defined as

$$F_s = F_{smax}\epsilon_T\epsilon_P \tag{4-191}$$

where F_{smax} is maximum fraction of the leaf area devoted to stomates, $0 \leq \epsilon_T \leq 1$ is a reduction factor due to temperature, and $0 \leq \epsilon_P \leq 1$ is a reduction factor to maintain pressure constraints within the plant. Typically ϵ_T is parabolic with air temperature.

The computational approach to maintaining plant pressure conditions requires an iterative approach to estimating ϵ_P. This is done by matching the flux to the shoots with the dispersion from the leaves to the atmosphere. The plant requires that the pressure in the leaves is above some threshold (e.g., 15 bar). As a first guess, the procedure sets $\epsilon_P = 1$. If the plant pressure is less than the threshold, ϵ_P is reduced until flux continuity is satisfied with leaf pressure at the lower threshold. Flux within the plant can be estimated with the threshold pressure as a boundary condition. Since ρ_p is known for the threshold pressure, the ϵ_P can be determined to match the atmospheric conditions.

Vegetation adjusts LAI, cover, and root densities over time according to environmental influences. A straightforward way to account for this adjustment is through the differential equation,

$$\frac{\partial\xi}{\partial t} = (\alpha_d + \omega\alpha_g)(\bar{q} - q_{targ}) \tag{4-192}$$

where ξ is some plant density, α_d is the death rate ($\bar{q} < q_{targ}$), α_g is the growth rate ($\bar{q} > q_{targ}$), and $\bar{q}$ is a time-averaged flux (length of averaging depends on the component; leaves and fine roots use

shorter periods), q_{targ} is a target time-averaged flux, and $0 \leq \omega \leq 1$ is an adjustment to account for environmental and phenological constraints.

The ω adjustment factor may consist of several components. Seasonal growth is included as a 0 or 1 multiplier. Limits due to available capacity are also included. For example, the limits of LAI or leaf area density on cover density might be expressed as

$$\omega_c = 1 - \xi/\xi_{max} \tag{4-193}$$

where ξ might represent LAI or leaf area density and ξ_{max} is the absolute maximum allowed by the available cover. Thus, growth rates go to zero as capacity is reached and only by adding additional cover can additional LAI be achieved.

The same type of relationship is used for cover and root length density. The ξ_{max} limit on cover is based on the total root length (root length density integrated over the soil column). Note that ξ_{max} is larger than would be predicted by the equilibrium root/shoot ratio. I would estimate ξ_{max} as the absolute maximum cover capacity per total root length.

Uptake is parameterized using a relationship between fine roots and soil conductance in cylindrical coordinates. Like dispersal from leaves, both the soil conductivity and a conductance across the root surface determine overall conductance from soil to plant. Overall conductance is a function of fine-root length density and the capability of the fine roots to transfer water. It is assumed that the conductance of the fine roots goes to zero if the soil would extract moisture from the plant. Although in actuality there is a network of larger roots spreading from the trunk of the shrub, with very dynamic water and fine roots, the characterization simplifies this into a network of long-lived fine roots that open and close based on moisture conditions. Opening and closing reflect the rate that the finest roots grow and die. Only information on fine-root densities for wet conditions and response times for wetting and drying pulses are important. Note that the fine-root densities are primarily important for estimating the soil response.

The ω adjustment factor for fine roots also includes a depth factor limit, expressed as

$$\omega_c = 1 - d/d_{max} \tag{4-194}$$

where d is the depth below ground surface. Thus, growth rates go to zero as a species-dependent depth is reached. This limiting factor should produce an exponential profile over several growth/decay cycles.

3/11/00 Continued methodology for vegetation. $\boxed{\mathscr{SAS}}$

Summarizing the various components of the vegetation to be modeled:

- Transpiration. Transpiration is a function of leaf area density under atmosphere-limiting conditions. Transpiration is a function of a minimum plant potential under soil-limiting conditions.

- Uptake. Uptake conductance is a function of fine-root-length density under moist conditions (soil pressure is greater than plant pressure). Uptake conductance goes to zero under dry conditions (soil pressure is less than plant pressure). Fine-root conductance responds at the time scales of fine roots, but the length density responds at the time scales of large roots.

- Changes in leaf area density. Required information includes earliest and latest growth date, maximum LAI for a given cover, temperature preference for growth, growth rate (*e.g.*, time to doubling) under optimal conditions, death rate (*e.g.*, time to halving) under dry conditions, target flux rate, and averaging period for fluxes.

- Changes in cover. Required information is growth and death rate, seasonal growth on-off flag, temperature dependence for growth, maximum cover per total root length, target flux rate, and averaging period for fluxes.

- Changes in root-length density. Required information is growth and death rate, seasonal growth on-off flag, temperature dependence for growth, target flux rate, and averaging period for fluxes.

- Changes in fine-root-length density. Required information is growth and death rate, seasonal growth on-off flag, temperature dependence for growth, maximum fine-root-length density per root-length density, target flux rate, and averaging period for fluxes.

- Reference values. These include typical area of a leaf, typical leaf vapor diffusion length, and typical fine-root diameter.

The dynamic vegetation variables tracked in the computational model are:

- Canopy height.

- Root depth.

- Leaf area density in each element above ground surface. As a first cut, assume that leaf area density is uniform from top of the canopy to the ground.

- Cover fraction. As a first cut, assume that vegetation forms cylinders to translate between leaf area density, LAI, cover, and shoot length density.

- Root length density. This is the transport root density.

- Fine-root length density in each element below ground surface. This is the uptake root density.

For growth relationships, it is necessary to have some way of relating the root length densities to cover á la a root/shoot ratio. There should be some relation between cover and canopy height as well.

4/28/02 Return to methodology for vegetation.

A simple model approach is being implemented in *breath* to handle vegetation as a first cut. The approach basically assumes that all parts of the plant are directly connected to the trunk at the ground surface, with a single variable of plant pressure at the ground surface. This is simpler than assuming that vegetation is a continuously connected continuum, which would require a plant pressure at each node.

The previous version of the atmospheric condition is expanded to discretize the atmospheric boundary layer column. Discretization allows vapor released by transpiration to reduce evaporation by increasing atmospheric vapor density above the ground, thereby reducing gradients at the ground surface. The atmospheric velocity profile within the vegetation will be reduced to account for drag, also increasing resistance to evaporation.

Flux continuity is imposed on the plant continuum. Total flux from the soil to the plant trunk is

$$q_p = \sum_{i=1}^{N} C_{spi}[(P_i - P_G) + \rho g(z_i - z_G)]$$

(4-195)

where q_p is total upward flux at the plant trunk and C_{spi} is total soil-plant conductance for pressure from subsurface node i. This can be rewritten as

$$P_G = \frac{\sum_{i=1}^{N} C_{spi}[P_i + \rho g(z_i - z_G)] - q_p}{\sum_{i=1}^{N} C_{spi}}$$

(4-196)

Flux from leaf surfaces to the atmosphere is written

$$q_{LA} = C_{LA}(\rho_L - \rho_A) \tag{4-197}$$

where C_{LA} is total leaf-atmosphere conductance for vapor density. Conductance is controlled by both atmospheric conditions and the plant's ability to close stomates, so that $0 \le C_{LA} \le C_{max}$. Vapor density at the leaf is always essentially saturated, since capillary effects on reducing vapor density are not strong under normal plant conditions. Note to check: certain xeric plants may have plant water that is treated to have lower vapor pressure (*e.g.*, salt covering leaves).

There is a leg of the journey in the shoots between the ground surface and the leaves. Flux continuity requires that

$$q_{LA} = C_p[P_G - P_L + \rho g(z_G - z_L)] \tag{4-198}$$

where C_p is pressure conductance in the shoots and $q_p = \sum_i q_{LAi}$. Rewriting,

$$P_L = [C_{LA}(\rho_L - \rho_A)/C_p] + P_G + \rho g(z_G - z_L) \tag{4-199}$$

Assuming that the plant will close stomates if leaf pressure drops below a target leaf pressure of P_{targ}, the reduced conductance that maintains flux continuity is

$$C_{LAred} = \frac{C_p[P_G - P_{targ} + \rho g(z_G - z_L)]}{\rho_L - \rho_A} \tag{4-200}$$

At night and whenever the atmosphere is more saturated than the leaf (essentially never in the desert), leaf conductance is zero.

As a simplification, neglecting transport losses in the shoots sets the target pressure at the ground surface. Assuming M levels of leaf discharge to the atmosphere,

$$q_p = \sum_{j=1}^{M} C_{LAj}(\rho_L - \rho_{Aj})$$
$$= \sum_{i=1}^{N} C_{spi}[(P_i - P_{targ}) + \rho g(z_i - z_G)] \tag{4-201}$$

The target leaf flux is achieved by setting

$$C_{LAj} = \frac{q_p}{\sum_{j=1}^{M} C_{LAmaxj}(\rho_L - \rho_{Aj})} C_{LAmaxj} \tag{4-202}$$

so that conductances for the plant at all elevations are reduced by the same percentage.

5/01/02 Prototype results.

I coded a prototype in *Matlab* to investigate the expected behavior of the vegetation models before actually adding them to *breath*. Actually, two prototypes were coded, one for the soil (water uptake) and one for the atmosphere (vapor dispersal). The idea of creating prototypes in *Matlab* is to ensure that all models are self-consistent and to provide guidance on parameter values.

At this time the soil prototype considers two uptake options:

- Uptake based on a single control pressure (my simple scheme)

- Uptake using the UNSAT-H scheme (Fayer, 2000)

The prototype considers two atmospheric-demand options:

- Specified PT demand (generally "unlimited")

- UNSAT-H PT demand based on the 1st formula (equation 4.48 by Fayer (2000))

I also put in growth algorithms for uptake and transport roots similar to the algorithms documented previously. These algorithms were modified to use normalized terms, but the idea is the same.

The prototype does not consider evaporation or soil-moisture redistribution, since I'm just looking at the uptake algorithms.

I've been testing the various options while narrowing in on parameters. It's taken some time to make sure that all the relationships and parameters have consistent units, but now there is an example problem that seems to be fairly self-consistent and similar to the cheatgrass example in the UNSAT-H code.

The example problem is a soil column 150 cm deep. Roots are allowed to penetrate to the bottom while root-length density (RLD) exponentially decreases from the top. I've made estimates of RLD based on the biomass distribution and assumed root diameter and root mass density.

The initial conditions are essentially saturated; partway through I rewet the column to the initial condition. With growth, the simulation starts with very low RLD values; without growth, the values are roughly calibrated.
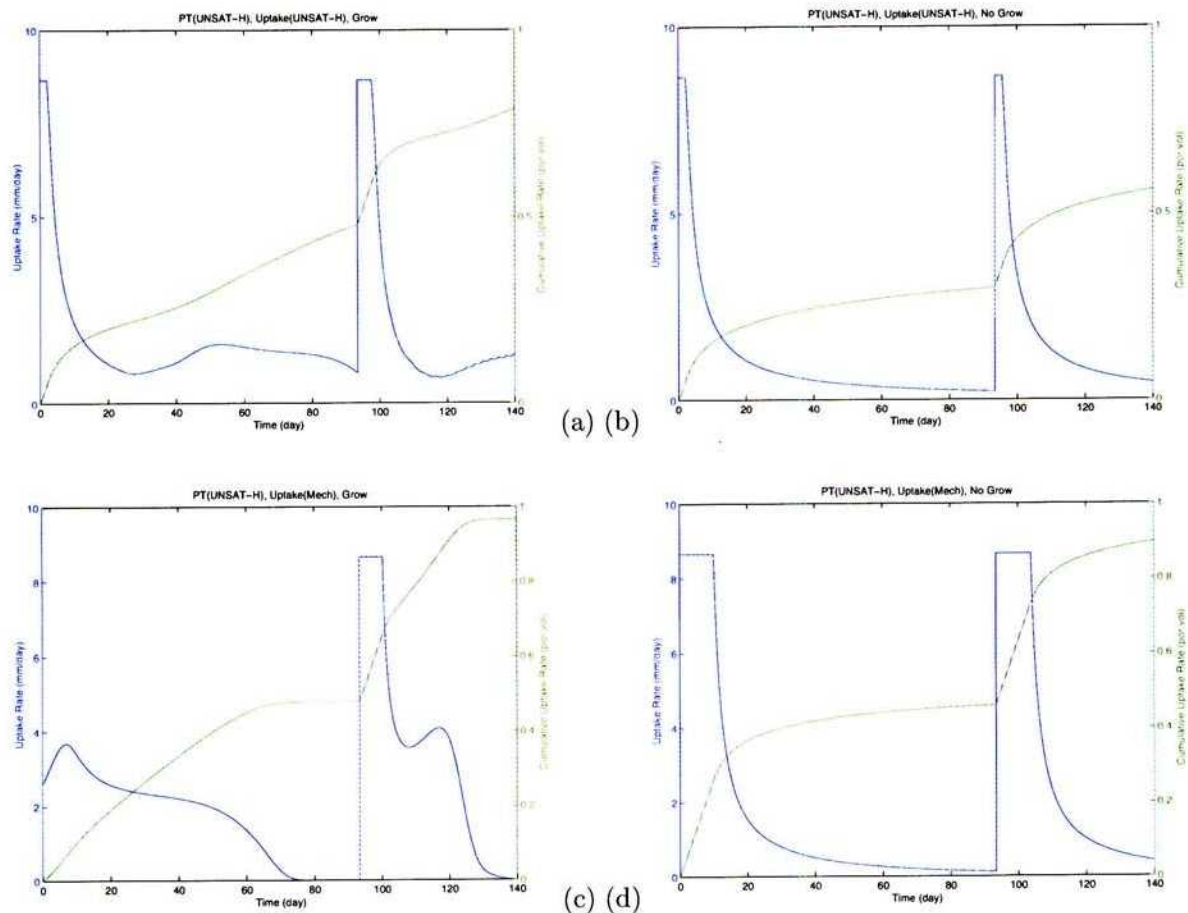
Figure 4-1: 5/01/02. Time history of predicted total uptake for 150-cm deep example problem with UNSAT-H limits to transpiration based on LAI. Root growth is allowed in (a) and (c), but not in (b) and (d). The UNSAT-H uptake model is used in (a) and (b); the mechanistic model is used in (c) and (d).

Figure 4-1 illustrates the behavior of the different model combinations for the example problem. Both the UNSAT-H and mechanistic uptake models are used with grow and no-grow options.

I've tried mixing and matching the different options to see what they predict. Several results become apparent.

- It is not appropriate to use the UNSAT-H uptake model with infinite atmospheric demand,

since it will completely dry in the first step

- It is more difficult to use the mechanistic uptake model with infinite atmospheric demand if growth is not allowed, since calibration is then required

- Without growth and with the UNSAT-H atmospheric demand, the two uptake models are qualitatively similar in total uptake but the mechanistic model predicts more uptake (about 50 percent more in the example), since uptake at depth can compensate for loss of moisture at the top in the mechanistic model

- With growth, a secondary bulge of uptake can occur after the main peak occurs, since roots are gradually adjusting themselves to the appropriate configuration

- With growth, the two events have different root configurations and thus behave differently. For this example, uptake progresses from top to bottom in the first event and from bottom to top in the second (since RLD is higher at the bottom after the dryout period). The result is that uptake peaks much quicker in the second event. However, if the roots started out with a high density, they may quickly dry the soil and die, leaving the second event to have a slower response than the first.

5/02/02 More prototype results.

The second prototype is to provide a mechanistic model for limits on transpiration based on above-ground dispersal. The prototype calculates the windspeed profile while accounting for momentum uptake by vegetation. Windspeed is in turn used to estimate both bulk vapor dispersivity and the boundary-layer vapor conductance, which are combined to provide an overall vapor conductance from leaves to the atmosphere. The soil is allowed to have a specified vapor density (*e.g.*, saturated) or be a no-flow boundary (typical if it has dried out and vegetation is transpiring).

It turns out that the leaf boundary layer resistance can be far larger than the bulk atmospheric resistance. In all of my formulations to date, I had ignored this component. Within the boundary layer, vapor diffusion occurs with the rate determined by molecular diffusion across the boundary layer. Nobel (1991) presents relationships for boundary-layer thickness including

$$\delta^{bl} = \begin{cases} c_{bl}(d/v)^{1/2} & \text{flat leaf or cylinder} \\ c_{bl}(d/v)^{1/2} + c_2/v & \text{sphere} \end{cases} \tag{4-203}$$

where

δ^{bl} boundary-layer thickness [L]

d representative length [L]

v wind speed [L/T]

c_{bl} coefficient [L/T$^{1/2}$]

c_2 coefficient [L^2/T]

In the following, it is assumed that v has units of L/s and d has consistent length unit. For a flat leaf with d representing leaf length in downwind direction, $c_{bl} = 4$ mm/s$^{1/2}$ is approximately correct. For a cylinder with d representing diameter, $c_{bl} = 5.8$ mm/s$^{1/2}$ is appropriate. For a sphere with v in m/s, $c_{bl} = 2.8$ mm/s$^{1/2}$ and $c_2 = 0.25$ mm·m/s.

Another resistance that Nobel (1991) discusses is the resistance across the stomatal depth. He notes that the actual stomatal depth must be augmented by the effective stomatal radius to capture the dispersal of vapor from the small area of the stomate over the entire leaf area. The vapor conductance is written

$$C_{st} = \frac{D_v}{\delta^{st} + r^{st}} \tag{4-204}$$

where

δ^{st} stomate depth [L]

r^{st} representative length [L]

v wind speed [L/T]

c_{bl} coefficient [L/T$^{1/2}$]

c_2 coefficient [L^2/T]

When I included the resistance based on a flat leaf or cylinder, transpiration dropped to a fraction of the original for shrubs.

As a plausibility check, Groeneveld and Warren (1992) present some measurements of evapotranspiration (ET) in Owens Valley for relatively well-watered shrubs. As an example, total transpiration over a day is roughly 1.5 mm for an areal-average LAI of about 0.47, with a water table depth of about 3 m.

Assuming that the stomate properties are at the extreme xeric edge of the typical range ($\delta_{st} + r^{st} = 60$ μm and leaf-area fraction for stomates is 0.002), LAI is 0.45, temperature is 38 °C, and relative humidity is 0.15 (atmospheric values are midday values), the model estimates a rate of 1.2 mm/day. Assuming that this rate applies for the 14 daylight hours yields about 0.7 mm/day. Shortly after sunrise, relative humidity is about 0.4 and temperature is about 26 °C, which yields a rate of about 0.44 mm/day (or 0.26 mm/day if applied over 14 of the 24 hours). These values are

lower than but comparable to the values presented by Groeneveld and Warren (1992). Transpiration rate doubles if area fraction doubles or if stomate depth halves, both of which are still on the xeric end of their ranges. A four-fold increase in transpiration is larger than observed by Groeneveld and Warren (1992).

The stomate properties can be expressed as an effective diffusion distance using the formula

$$\delta^*_{st} = \frac{\delta_{st} + r^{st}}{A_{st}/A_l} \tag{4-205}$$

where A_{st} is total stomate area (number of stomates times stomate area) and A_l is total leaf area. The range for δ^*_{st} using the values from Nobel (1991) is roughly 0.125 to 3 cm. The leaf boundary layer thickness is roughly in the range of 0.01 to 0.04 cm for shrubs in windy areas, and the leaf boundary layer can be neglected except under very still conditions. However, plants at the leaky end are affected by the boundary layer and it should not be neglected for these plants.

For the same set of Owens Valley sites, Groeneveld (1989) examines root density issues. Maximum measured root densities (comparable to the uptake roots) reach 78 cm/cm^3 at a grassy site but only 9.3 cm/cm^3 at a site without grasses. These values are thought to include dead roots as well as living roots, thus are probably upper-bound values. Roughly translating to YM, one would expect root densities to be lower based on much lower LAI and shorter growing season. A simple scaling based on both LAI and growing season brings the equivalent rooting density for the grass-free site to about 0.8 cm/cm^3.

In the rooting example, achieving soil-limited uptake rates of a few mm/day with rooting densities of about 1 cm/cm^3 appears to require that root conductance is reduced by several orders of magnitude from the typical values (1 to 5×10^{-7} m/s/MPa) cited by Nobel (1994). Reducing RLD by a comparable magnitude while keeping root conductance fixed also works. There is a discrepancy that may be partly due to overcounting roots (dead roots may stay around for a very long time), and partly due to soil limitations not playing a role until soil is quite dry.

In the growth model, achieving a target RLD is done by adjusting the flux trigger for growth and death. Increasing the growth trigger flux shuts off growth earlier, thus reducing RLD.

5/04/02 More results. $\boxed{SAS}$

The issue of distributing LAI over the year takes a twist with the Owens Valley phreatophytes. Groeneveld and Warren (1992) estimates LAI for shrubs using the relationship

$$LAI = a\exp[-c(J - b)^2] \tag{4-206}$$
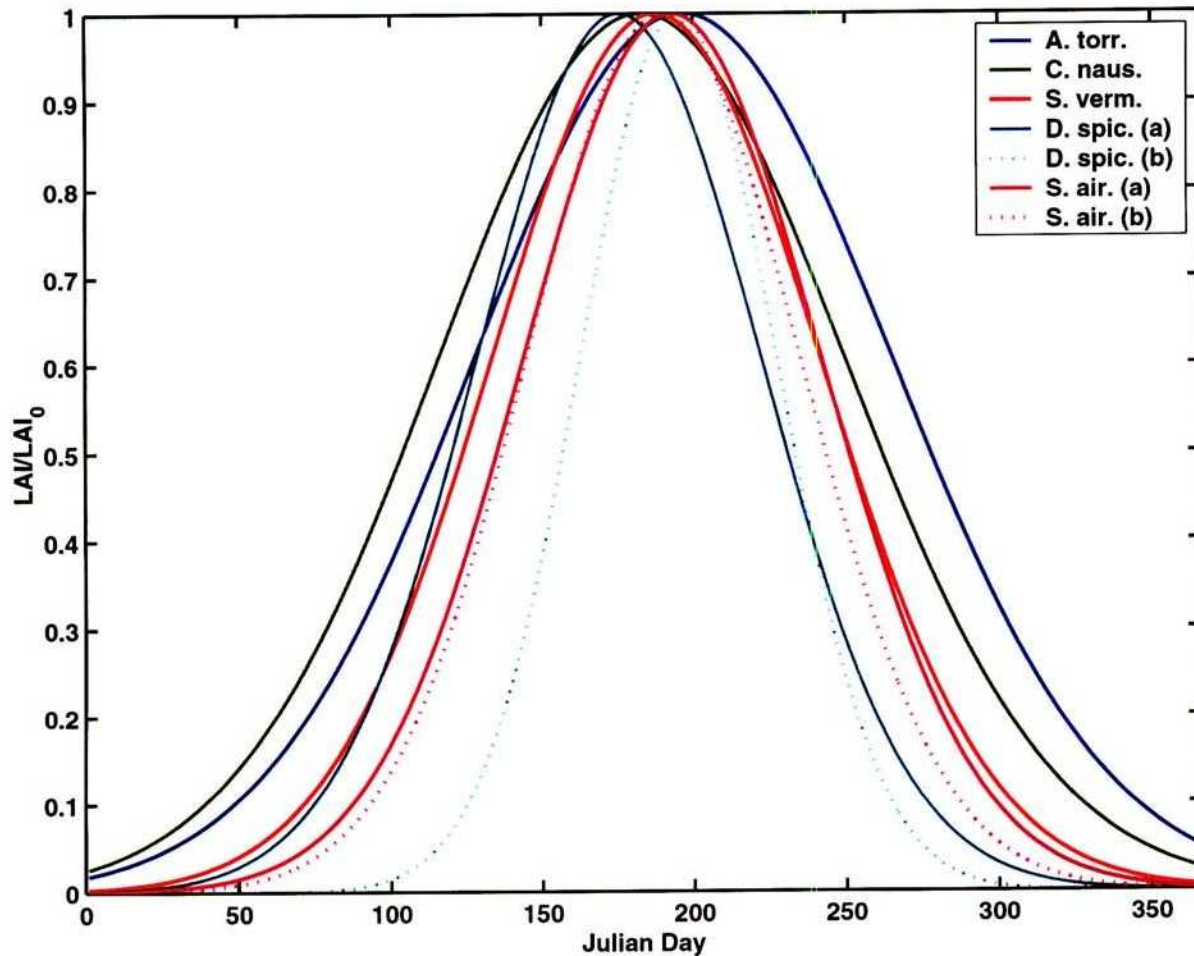
Figure 4-2: 5/04/02. Normalized annual LAI curves for well-watered shrubs at Bishop, CA.

where J is Julian day. The normalized curves are shown in Figure 4-2.

Ranges of 49 to 98 day are obtained for $c^{-1/2}$, with the larger value having appreciable LAI during winter and the smaller having a gap of perhaps 100 day (about the period of night-time freezing). Interestingly, the driving vapor density gradient for transpiration has a fairly similar shape, albeit muted; a workable approximation for well-watered target LAI might be

$$LAI = LAI_0 \left(\frac{\rho_{vs} - \rho_a}{\rho_0} \right)^p \tag{4-207}$$

where

LAI_0 reference LAI

ρ_{vs} saturated vapor density

ρ_a atmospheric vapor density

ρ_0 reference vapor density

p exponent

The p exponent might be near 1 for the cases with appreciable winter LAI and larger for no winter LAI. I don't have a basis for picking the exponent. However, it does appear from the Owens Valley observations that leaf growth (at least in warm months) can return to the curve quickly after a drop off.

Part of the effect is also due to available photosynthetic photon flux density (PPFD), since daily total shortwave radiation is about 3 times greater in the summer than in the winter.

As a thought, curves for projected leaf area reported by Groeneveld and Warren (1992) have a mismatch at day 1 and day 365 unless the offset is at 183 days. A better interpolator uses a power of a sine wave

$$s(J, b) = \frac{\sin[(2\pi/366)(J - b + 90)] + 1}{2} \tag{4-208}$$

$$f(J) = v_{min}(1 - s^p) + v_{max}s^p \tag{4-209}$$

As p goes to ∞, the distribution becomes peakier.

The curves for projected leaf area have b ranging from day 175 to day 196. The mean minimum, average, and maximum daily temperature for the 48-yr length of record, and shortwave radiation outside the atmosphere at Bishop's latitude, are plotted in Figure 4-3. As it turns out, PPFD peaks about day 172 while temperature peaks about day 205, which suggests that the leafing strategies are partly determined by temperature (or vapor density gradient) and partly by PPFD.

A convenient way to handle multiple influences is to use a weighted average

$$s_*(J) = \frac{\sum_i w_i s(J, b_i)^{p_i}}{\max[\sum_i w_i s(J, b_i)^{p_i}]} \qquad 0 \le w_i \le 1 \tag{4-210}$$

$$b_* = \sum_i w_i b_i \tag{4-211}$$

$$1 = \sum_i w_i \tag{4-212}$$

$$f_*(J) = v_{min}(1 - s_*^p) + v_{max}s_*^p \tag{4-213}$$

If there are two influences and $p_1 = p_2$, the w_i values are uniquely determined. If $p_1 > p_2$, the $f_*(J)$ curve peak skews towards b_1.
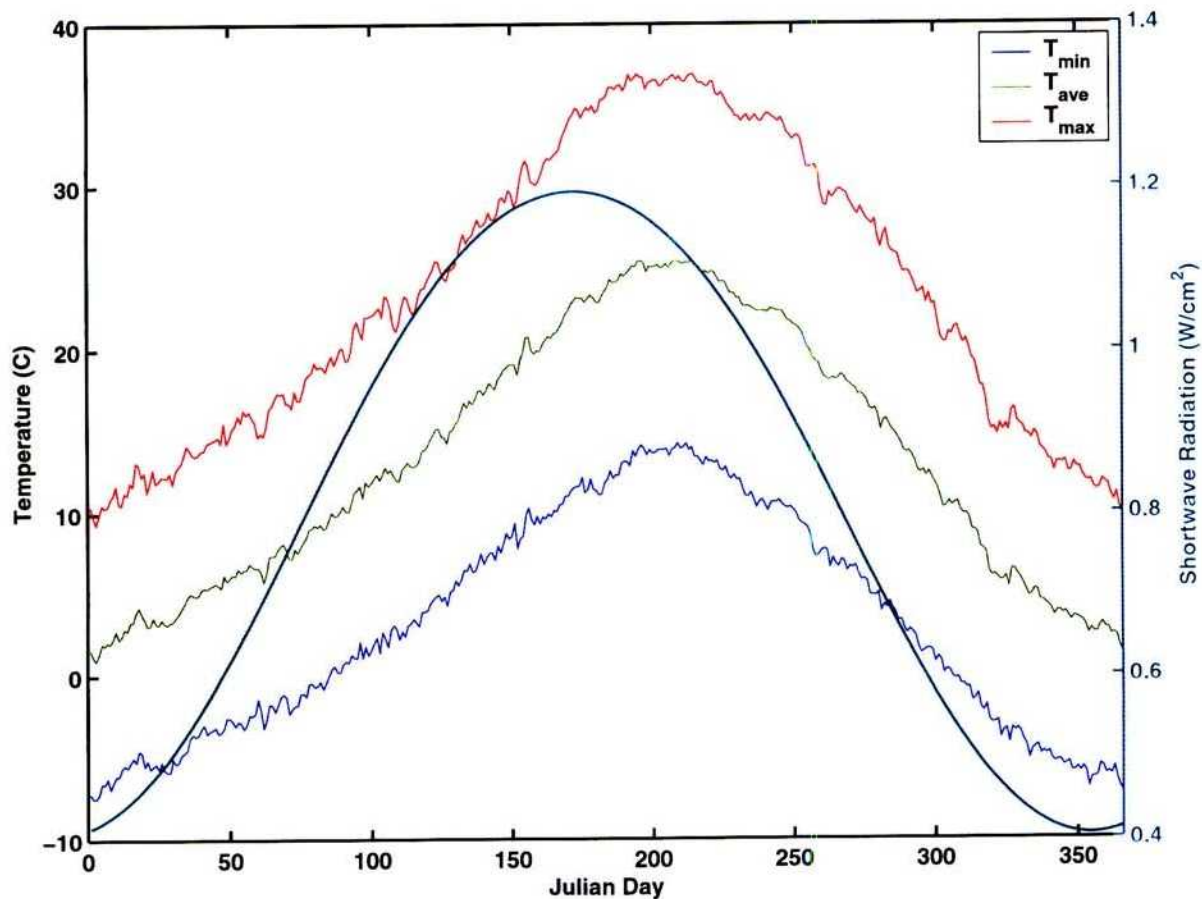
Figure 4-3: 5/04/02. Minimum, average, and maximum average daily temperature; and average daily shortwave radiation outside the atmosphere; all at Bishop, CA.

Rather than using sines, one could also use other functions based directly on meteorological parameters such as temperature and shortwave radiation. I propose combining a parabolic function for temperature (parameters are T_{mid} and T_{off}) and linear function of shortwave radiation in the form

$$f = \left[\frac{f_t f_r}{w_r f_t + (1 - w_r) f_r} \right]^p \tag{4-214}$$

where $0 \le w_r \le 1$ is the relative importance of radiation. Several examples of the different combinations of weighting-function parameters are shown in Figure 4-4, showing the effect of different temperature and radiation utilization strategies. The intent is to match preferences for individual species and use site conditions to determine the location on the curve. This approach will automatically adjust maximum LAI based on site conditions, a great benefit when doing sensitivity

analyses such as dropping temperature a fixed amount.

Dated erratum list.

$\boxed{\text{SAS}}$

A current list of errata, copied or expanded from the in-text notation.

Correction dated 11/15/01: In entry dated 9/3/99, Equation 4-65 is written incorrectly and the results are applied through today. The correct expression is

$$Q = \frac{2\pi BK}{\ln(R/r_w)}(\phi - \phi_w).$$ (4-215)

Note that when R is slightly larger than r_w (say $R = R_w + \Delta$), $\ln(R/r_w) \approx \Delta/r_w$ and flux into the well is defined as

$$Q = \frac{2\pi B r_w K}{\Delta}(\phi - \phi_w) = AC(\phi - \phi_w).$$ (4-216)

where conductance $C = K/\Delta$.

All of the following equations until today's date will remain uncorrected, with the assumption that $K\ln(r/R)$ should be replaced with $K/\ln(R/r)$.

Correction dated 04/30/02: In entry dated 9/17/99, actual assumption of relationship between K_m and $\bar{u}$ is that τ is essentially conserved, thus $K_m \propto |d\bar{u}/dz|^{-1}$. The expressions are otherwise correct.
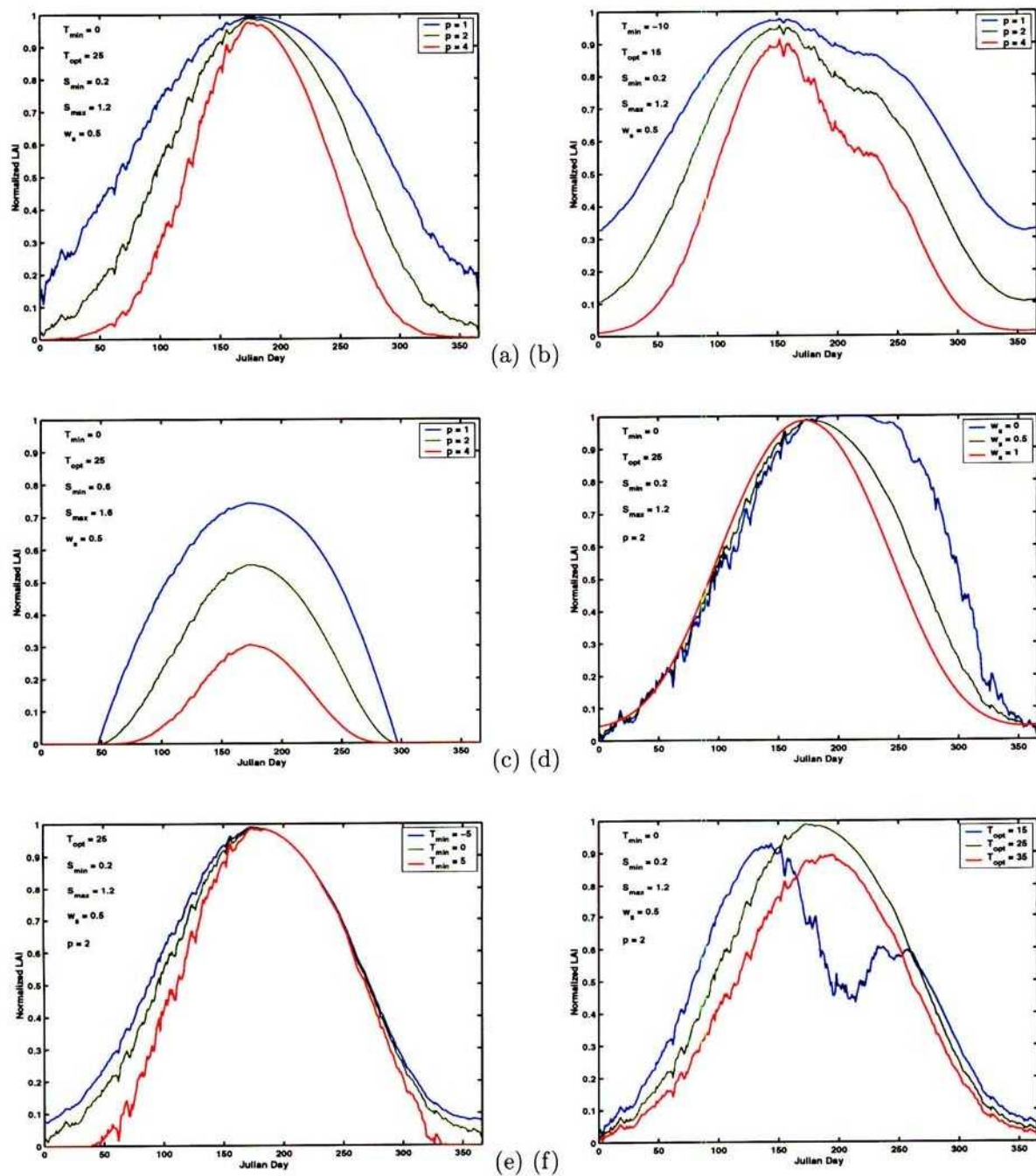
Figure 4-4: 5/04/02. Composite LAI-allocation weighting functions for temperature and shortwave radiation, (a) warm-weather species, (b) cold-weather species, (c) high-radiation species, (d) varying allocation weight, (e) varying minimum temperature, and (f) varying maximum temperature.

References

Abramowitz, M. and I. A. Stegun. 1972. *Handbook of Mathematical Functions.* New York, NY: Dover Publications, Inc.

Bear, J. 1979. *Hydraulics of Groundwater.* New York, NY: McGraw-Hill.

Beatley, J. C. 1974. Phenological Events and Their Environmental Triggers in Mojave Desert Ecosystems. *Ecology 55,* 856–863.

Bennie, A. T. P. 1996. Growth and Mechanical Impedance. In Y. Waisel, A. Eshel, and U. Kafkafi (Eds.), *Plant Roots: The Hidden Half,* pp. 453–470. New York, NY: Marcel Dekker, Inc.

Bird, R. B., W. E. Stewart, and E. N. Lightfoot. 1960. *Transport Phenomena.* New York, NY: John Wiley & Sons.

Brutsaert, W. 1982. *Evaporation into the Atmosphere: Theory, History, and Applications.* Dordrecht, The Netherlands: Kluwer Academic Publishers.

Caldwell, M. M. 1994. Exploiting Nutrients in Fertile Soil Microsites. In M. M. Caldwell and R. W. Pearcy (Eds.), *Exploitation of Environmental Heterogeneity by Plants,* Chapter 12, pp. 325–347. San Diego, CA: Academic Press.

Claassen, H. C. and A. C. Riggs. 1993. *An Estimate of the Roughness Length and Displacement Height of Sonoran Desert Vegetation, South-Central Arizona.* Water-Resources Investigation Report 92-4065, United States Geological Survey, Denver, CO.

Fayer, M. J. 2000. *UNSAT-H Version 3.0: Unsaturated Soil Water and Heat Flow Manual.* PNNL-13249, Pacific Northwest Laboratory, Richland, WA.

Fitter, A. H. 1994. Architecture and Biomass Allocation of Root Systems. In M. M. Caldwell and R. W. Pearcy (Eds.), *Exploitation of Environmental Heterogeneity by Plants,* Chapter 11, pp. 305–323. San Diego, CA: Academic Press.

Groeneveld, D. P. 1989. Shrub rooting and water acquisition on threatened shallow groundwater habitats in the Owens Valley, California. In *Symposium on Cheatgrass Invasion, Shrub Dieoff, and other Aspects of Shrub Biology and Management,* Las Vegas, NV, pp. 221–237.

Groeneveld, D. P. and D. C. Warren. 1992. Chapter E. Total transpiration from land areas estimated from hand-held porometer measurements. In D. H. Wilson, R. J. Reginato, and K. J. Hollett (Eds.), *Evapotranspiration Measurements of Native Vegetation, Owens Valley, California, June 1986,* Water-Resources Investigations Report 91-4159, Sacramento, CA, pp. 49–59. United States Geological Survey.

Kozlowski, T. T. and S. G. Pallardy. 1997. *Physiology of Woody Plants* (Second ed.). New York, NY: Academic Press.

McMichael, B. L. and J. J. Burke. 1996. Temperature Effects on Root Growth. In Y. Waisel, A. Eshel, and U. Kafkafi (Eds.), *Plant Roots: The Hidden Half*, pp. 383–396. New York, NY: Marcel Dekker, Inc.

Moreshet, S., B. Huang, and M. G. Huck. 1996. Water Permeability of Roots. In Y. Waisel, A. Eshel, and U. Kafkafi (Eds.), *Plant Roots: The Hidden Half*, pp. 659–678. New York, NY: Marcel Dekker, Inc.

Nobel, P. S. 1991. *Physicochemical and Environmental Plant Physiology*. San Diego, CA: Academic Press.

Nobel, P. S. 1994. Root-Soil Responses to Water Pulses in Dry Environments. In M. M. Caldwell and R. W. Pearcy (Eds.), *Exploitation of Environmental Heterogeneity by Plants*, pp. 285–304. San Diego, CA: Academic Press.

Nobel, P. S. 1996. Ecophysiology of Roots of Desert Plants, with Special Emphasis on Agaves and Cacti. In Y. Waisel, A. Eshel, and U. Kafkafi (Eds.), *Plant Roots: The Hidden Half*, pp. 823–844. New York, NY: Marcel Dekker, Inc.

Sonnenthal, E. L., C. F. Ahlers, and G. Bodvarsson. 1997. Fracture and Fault Properties for the UZ Site-Scale Flow Model. In G. S. Bodvarsson, T. M. Bandurraga, and Y. S. Wu (Eds.), *The Site-Scale Unsaturated Zone Model of Yucca Mountain, Nevada, for the Viability Assessment*, LBNL-40376, Berkeley, CA, pp. 7-1–7-33. Lawrence Berkeley Laboratory.

Waisel, Y., A. Eshel, and U. Kafkafi (Eds.). 1996. *Plant Roots: The Hidden Half* (Second ed.). New York, NY: Marcel Dekker, Inc.

8 Thermal Hydrology KTI

Account Number: **20-5708-663**
Collaborators: **Ronald T. Green**
Directories: **As noted**

Objective: The overall objective of the thermal hydrology KTI is to assess the impacts of possible thermal loading due to the proposed Yucca Mountain (YM) repository on the subsurface hydrology. The near-field KTI also is investigating potential effects of the thermal loading, but with perhaps more of an emphasis on the impact on geochemistry and hence hydrology. Out of the entire hydrology-thermal-mechanical-chemical (HTMC) group, the thermal hydrology KTI is essentially HT while the near-field KTI is more HTC.

2/1/96 Initial entry.

The reorganization of the CNWRA into KTI units occurred less than two weeks ago. At this point, organizational issues have been resolved. Detailed task descriptions have not been promulgated as of yet. This initial entry is a brain-storming task to put together ideas for future work within the task, which should also mesh with work to be performed under the near-field task and the ambient-hydrology KTI.

After discussion with Ron, it is clear that there are two areas that I can contribute: boundary conditions (i.e., infiltration, temperature) and matrix-fracture flow investigations.

In the realm of boundary conditions, a relatively quick investigation might be undertaken that examines the impact of the repository on surface processes. Two questions arise immediately: (i) is the ground surface well-represented by a specified-temperature condition, or should there be some interaction with the atmosphere á la *breath*; and (ii) is there an effect on infiltration rates due to the thermal load imposed by the repository?

A simple sensitivity test can be made using *breath*. Assuming that thermal equilibrium occurs rapidly relative to the change in energy release, and that half of the energy moves upwards, a quasi-steady-state energy flux can be calculated which combines the geothermal flux and the repository loading. The energy flux can be applied at the bottom of the column, thereby allowing the column temperatures to equilibrate. Presumably this is a no-nevermind issue, but the analysis should take little effort and any unforeseen impacts should be obvious. Also, the robustness of the

surface temperature condition can be quickly examined; extending the analysis to seasonal-average and annual-average conditions for temperature would be straightforward.

Matrix-fracture interaction analysis options are less well defined. Ideas have arisen: (i) Sitakanta would like to do a laboratory analysis with a fractured thin slab, in which it appears that the best information would be a videotape of the wetting front; (ii) Ron Green has resurrected the idea of an infiltration test at the Peña Blanca site, where an adit lies about 8 m below a cleared surface and a reasonably large fracture can be traced to the surface; and (iii) I have thought about extending *breath* to quasi-2D or 3D to investigate matrix-fracture interaction with discrete fractures, which could possibly be extended to handle large thermal effects á la TOUGH and possibly even geochemistry for near-field analyses. The experimental work needs to be properly linked with YM and appropriate numerical experiments need to be designed to justify the code development.

4/19/96 Boundary condition evaluations.

In line with the initial entry, a series of surface condition evaluations will be performed. The idea is to look at the sensitivity of both infiltration and temperature to the upward thermal fluxes due to the repository. A series of several upward fluxes will be examined, with a maximum that is the maximum flux the repository can generate. Since the 2-cm cases are the fastest to run, I'll use the standard 2-cm case I have used for shallow infiltration simulations under the ambient hydrology KTI. In every case, fifty or one hundred years of annual-average conditions will be used to set up the thermal profile. With the thermal conditions set, additional 20-yr runs with standard hourly conditions will be used to check the impact on infiltration. A subsidiary step will be to check that the thermal regime under different climatic regimes is the same for different depths of alluvium, despite different infiltration rates.

The quoted thermal loads in TSPA-95 (TRW, 1995) range from 20 MTU/acre through 100 MTU/acre, where the conversion factor is about 1 kW/MTU. Other work quoted in TSPA-95 used 28, 57, and 114 kW/acre for the loading. Using the conversion factor of 1 acre = 4.047×10^3 m^2, corresponding power densities are approximately:

20 kW/acre 5 W/m^2.

28 kW/acre 7 W/m^2.

40 kW/acre 10 W/m^2.

80 kW/acre 20 W/m^2.

100 kW/acre 25 W/m^2.

120 kW/acre 30 W/m^2.

As a comparison, the annual average incident shortwave radiation is 250 W/m^{2}and annual average longwave radiation of 320 W/m^2. With albedo of slightly greater than 0.25 for shortwave radiation, this yields roughly 400 W/m^{2}net incoming radiation. Assuming an average emissivity times Stefan-Boltzmann constant on the order of 5.2×10^{-8} W/m^{2}K^4, radiating 400 W/m^{2}would require an annual average temperature of 296.15 K. Radiating 415 W/m^{2}requires an annual average temperature of 298.89 K for the same emissivity. One would expect that the top boundary temperature should vary by less than 2.5 °C, thus a constant-temperature top boundary condition is really not bad at all for deep simulations.

On the other hand, one might expect that the lower boundary condition temperature might be more strongly impacted by the repository, both due to smaller ambient thermal fluxes and due to the relatively closer distance between the repository and the common bottom condition at the water table. As Gordon is currently constructing a regional-scale transport model, it makes sense to piggy-back a thermal examination onto the model. The issue may have been addressed in the past...

References

TRW. 1995. *Total System Performance Assessment–1995: An Evaluation of the Potential Yucca Mountain Repository.* B00000000-01717-2200-00136, TRW Environmental Safety Systems Inc., Las Vegas, NV.

9 Thermal Hydrology KTI

Account Number: **20-1402-661**
Collaborators: **Goodluck Ofoegbu, Ronald T. Green**
Directories: **As noted**

Objective: The overall objective of the thermal hydrology KTI is to assess the impacts of possible thermal loading due to the proposed YM repository on the subsurface hydrology. The near-field KTI also is investigating potential effects of the thermal loading, but with perhaps more of an emphasis on the impact on geochemistry and hence hydrology. Out of the entire hydrology-thermal-mechanical-chemical (HTMC) group, the thermal hydrology KTI is essentially HT while the near-field KTI is more HTC.

7/5/98 Initial entry.

Background

Last week Goodluck contacted me regarding a modeling task with a milestone date at the end of August. The task evaluates two-phase flow within a fracture under thermal loads from the repository. The approach he has used thus far is to have detailed modeling in a fairly restricted area (roughly 20 m laterally by roughly 50 m vertically). Apparently the approach is extremely computationally demanding, due to the small elements (hence small time steps) required to accurately handle the fracture.

The idea that Goodluck had was to handle the rock matrix with a simplified approach, using a Boundary Integral Equation Method (BIEM) approach. A BIEM approach is most effective when the domain is not discretized, rather placing any mesh along discontinuities (boundaries are special cases of discontinuities). Elimination of domain discretization is accomplished by use of a Green's function specific to the equation. Such a Green's function is available for only a few (linear or quasi-linear) equations. The steady-state potential equation is particularly useful, as the Green's function is easy to use in one-dimensional (1D), two-dimensional (2D), and three-dimensional (3D). There are two approaches for time-dependent potential problems with fixed boundaries: (i) use a time-dependent Green's function (I recall from about ten years ago that this approach is fairly inaccurate and clumsy); or (ii) take the Laplace transform of the problem, solve in Laplace space with the appropriate Green's function, and (numerically) invert.

The steady-state potential equation is often used for thermal conduction or isothermal saturated flow. It should also be appropriate for isothermal vapor diffusion. At YM, unsaturated conditions exist. When the unsaturated conductivity is described by an exponentially decaying function of potential, the problem is quasilinear and can be handled using a special Green's function, at the cost of iteration when the boundaries are not completely first-type boundaries. If the range in potential within the domain is sufficiently small, any conductivity can be approximated using the exponential function. In the TSw, the matrix is essentially saturated but the fractures are quite unsaturated, so that one could either approximate the conductivity from the equivalent-continuum assumption or use K_{sat} in the matrix and provide discrete fractures to handle flows in excess of matrix K_{sat}.

The potential equation is most straightforward to use when all coefficients within the domain are constants (i.e., conductivities are spatially invariant) and all nonlinearities are confined to the discontinuity mesh. Piecewise-constant coefficients are straightforwardly handled by discretizing the boundaries between the discontinuities. Arbitrarily varying coefficients require domain discretization, negating much of the BIEM advantage, although some fairly restrictive conductivity distributions can be handled without domain integration.

For immiscible free-surface problems where the solution within the domain is rapid relative to the movement of the boundary (i.e., a quasi-steady state exists), the time-varying solution can be obtained by determining the velocity of the free surface at any instant and updating the position of the free surface. Classic examples of this approach are the phreatic-surface problem and the moving sharp-interface problem. The approach requires that two compatibility equations are available relating potential and the gradient of potential normal to the interface (e.g., $\phi_1 = \phi_2$, $q_1 = q_2$).

Definition of Problem

The particular problem that Goodluck is considering is a single vertical fracture within a porous matrix. At the top of the fracture, a liquid flux is applied. A drift with heat source is located at the bottom of the fracture, raising some portion of the domain to above boiling. It is desired to quantify the liquid flux into the drift as a function of time; if no liquid reaches the drift, the distance that the liquid penetrates in the fracture is desired as a function of time.

As noted above, the solution procedure using MULTIFLO is too computationally demanding for significant analysis. The original idea put forth by Goodluck is to approximate energy transport

in the matrix as occurring solely through conduction. Liquid (film flow) and vapor are considered in the fracture, but no mass is allowed to cross the matrix-fracture interface. A solution procedure was developed by Frank Dodge for liquid, vapor, and energy fluxes within the fracture given the thermal state of the matrix at the fracture boundary.

In addition to the numerical difficulties exhibited by MULTIFLO, Goodluck expressed dissatisfaction with some of the properties of the solver for the fracture system. Several actual or potential weaknesses with the approach are apparent after cursory examination (noting that it is quite possible I may have missed some point of the development). The method assumes that the fluid mixture in the fracture has a different temperature than the rock matrix, and the mixture has uniform temperature throughout the fracture. It appears that continuity of total water flux is not assured (i.e, liquid poured in the top of the fracture may not escape through the bottom of the fracture in the form of vapor). The proposed neglect of mass exchange across the matrix-fracture interface may seriously misrepresent vapor fluxes. No mention was made of the dependence of thermal conductivity on moisture content.

Goodluck expressed a desire to examine approaches that might be extended past the current problem. In addition, I have long wanted to develop a technique that could be used to examine discrete-fracture flows under ambient flow conditions, with particular interest in fracture-drift interactions. I believe that the BIEM can be developed into a powerful approach to handle both situations. The following approach can be used for both 2D and 3D simulations (although the equations will be specialized for 2D until further interest is expressed). The numerical approach can be applied to the thermal problem, the ambient problem, and discrete-fracture problems in the saturated zone (in order of increasing simplicity). The approach is developed for the 2D thermal problem, as the other physical scenarios represent simplifications of the overall method and the 3D scenarios are identical in general approach, simply swapping out the Green's functions for the 3D equivalent and using triangles instead of linear elements.

General Boiling-Isotherm Solution Approach

The philosophy of the BIEM approach developed here is to simplify the physics while hopefully not mutilating them.

Once boiling temperatures are widely reached there are three zones (upper nonboiling, middle boiling, and lower nonboiling) separated by two boiling isotherms. The top boundary condition for the upper nonboiling zone is specified flux and temperature, while the bottom boundary condi-

tion for the lower nonboiling zone is specified pressure and perhaps temperature. In all zones, the non-vapor component of the gas phase is assumed to be hydrostatically distributed (no bulk movement). It is assumed that the boiling isotherm represents a sharp transition between a dessicated zone with vapor movement but no liquid movement, and a nearly saturated zone with liquid movement but no vapor movement. Within discrete fractures, this restriction is lifted but the fracture only can exchange mass with the matrix based on the phase in the matrix (i.e., in the boiling zone only vapor can exchange while in nonboiling zones only liquid can exchange).

It is assumed that both temperature and fluids redistribute quickly relative to the movement of the isotherm, so that a quasi-steady state exists for all components. Drifts are modeled as point energy sources.

When discontinuities separate the region into bounded parcels, it can be advantageous to artificially separate the parcels at the penalty of doubling the unknowns along the discontinuity. If the Green's function is different in each region, then the separation must take place (e.g., if the discontinuity separates a saturated zone from an unsaturated zone). The resulting matrix equation is larger than before but no longer full. In this case, the BIEM for a given potential field requires that four variables are defined at a discontinuity: the potential on each side of the discontinuity and the gradient on each side of the discontinuity. Additional equations are included to the system to ensure compatibility of potential and flux. Typical compatibility equations ensure that potential is continuous and flux is continuous, although one can simulate impermeable or semipermeable features, highly permeable features, sources/sinks, and specified potentials.

It is also possible to treat the discontinuities as interior to the domain, but only the jump in potential and the jump in gradient remain as unknowns (one supplemental compatibility equation is required). The method results in a fully populated matrix.

One mass balance compatibility equation at the isotherm links liquid pressure to vapor pressure using the vapor-pressure reduction for unsaturated porous media. The other relates the velocity of the isotherm to the mass flux rates and mass transfer rate across the isotherm, which are in turn related to energy transfer across the isotherm. The primary unknowns are pressure and pressure gradient for a phase.

The temperature at the isotherm is specified on both sides of the isotherm to be the boiling temperature, so that the primary unknowns are the temperature gradients on either side of the isotherm or source strength along the line feature.

General Fracture Solution Approach

Fractures represent potential fast pathways for fluxes as well as discontinuities. It is assumed that pressure and temperature are continuous between the fracture and the matrix. The fracture is discretized into line segments (2D) or triangles (3D), with potential linearly varying between nodes, normal derivative of potential constant over an element, and source/sink terms constant over the portions of the element associated with a node (e.g., half the element for lines and one-third of the element for source/sink terms). If an unknown potential or source/sink term is required, a contour integral is performed with the base point at the node. If an unknown normal derivative is required, a contour integral is performed with the base point at the element centroid.

Within the fracture, standard equations for fluid and energy flow are used. It is assumed that liquid and vapor pressures are in equilibrium, both within the fracture and between fracture and matrix, and the equilibrium is a function of temperature. If necessary, it is possible to consider the effect of a skin between fracture and matrix limiting the mass exchange. It is further assumed that relative permeability and saturation within the fracture is a function of pressure and temperature.

Compatibility at the Boiling Isotherm

At the isotherm, pressure in the vapor is determined by saturated vapor pressure at the boiling temperature times the relative humidity (considered solely as a function of the liquid pressure). The compatibility of pressures at the boiling isotherm is nonlinear. A reasonable approach for this nonlinearity is to assume an initial liquid pressure distribution along the isotherm and solve for the increment in pressure. The procedure uses the linearization

$$P_v^{m+1} \approx P_v^m + \frac{dP_v}{dP_l}\Delta P_l, \tag{9-1}$$

where liquid and vapor are denoted by l and v, P is pressure, m represents the iteration level, and the unknown being determined is ΔP_l.

The temperature at the isotherm is specified as the boiling temperature. The boiling temperature might be considered a function of pressure, represented by the sum of air pressure and vapor pressure. Note that air pressure is assumed hydrostatic (a small correction).

The compatibility equations for mass and energy fluxes are coupled through the velocity of

the isotherm. The velocity, V, of a discontinuity (shock) in a phase is

$$V = \frac{q_2 - q_1}{\varepsilon(\theta_2 - \theta_1)},$$ (9-2)

where q is flux, ε is porosity, θ is saturation (or mass fraction times saturation, for vapor), and the subscript represents the side of the discontinuity. Note that as the flux equilibrates, the velocity of the discontinuity goes to zero. Similarly, the velocity of an energy discontinuity between liquid and vapor is

$$V = \frac{E_{UZ} - E_{TZ} - h_{fg}q_c}{C_{UZ} - C_{TZ}},$$ (9-3)

$$E = c_l q_l + c_v q_v - K\frac{\partial T}{\partial n},$$ (9-4)

where E represents total energy flux; UZ and TZ denote the unsaturated zone (liquid) and thermal zone (vapor), respectively; q_c is the mass flux across the interface (positive for condensation of vapor at the interface); c_l and c_v represent enthalpy per unit mass of liquid and vapor; K is the bulk thermal conductivity; h_{fg} is the enthalpy associated with phase change; and C represents total energy capacitance.

Assuming liquid is on side 2 and vapor on side 1, the velocity of the discontinuity can be represented as

$$V_l = R_l(q_l - q_c),$$ (9-5)

$$V_v = R_v(q_c - q_v),$$ (9-6)

$$V_e = C_l q_l - C_v q_v - C_c q_c + \epsilon,$$ (9-7)

$$R_l = 1/\varepsilon(\theta_{l2} - \theta_{l1}),$$ (9-8)

$$R_v = 1/\varepsilon(\theta_{v2} - \theta_{v1}),$$ (9-9)

$$C_l = c_l/(C_{UZ} - C_{TZ}),$$ (9-10)

$$C_v = c_v/(C_{UZ} - C_{TZ}),$$ (9-11)

$$C_c = h_{fg}/(C_{UZ} - C_{TZ}),$$ (9-12)

$$\epsilon = \left(K_{UZ}\frac{\partial T_{UZ}}{\partial n} - K_{TZ}\frac{\partial T_{TZ}}{\partial n}\right)/(C_{UZ} - C_{TZ}).$$ (9-13)

For compatibility, $V_l = V_v = V_e$.

Equating the velocities from liquid and vapor,

$$q_c = \frac{R_l q_l + R_v q_v}{R_l + R_v}.$$ (9-14)

Equating the velocities from liquid and energy, and substituting for q_c,

$$q_l[R_l(R_v - C_l + C_c)] = -q_v[C_v(R_l + R_v) + R_v(C_c - R_l)] + \epsilon(R_l + R_v). \tag{9-15}$$

The relationship between liquid flux in the nonboiling zone and vapor flux in the boiling zone depends on the temperature gradients on both sides of the isotherm as well as the storage capacities for mass and energy.

The energy-flux balance compatibility condition is not explicitly specified. The specified-temperature condition along the isotherm is equivalent to an energy source/sink along the isotherm, with the magnitude of the source determined in the solution process. The magnitude of the source is implicitly compatible with the mass fluxes through the velocity constraints.

Once the solution has been determined, the isotherm is updated using any of the expressions for velocity:

$$\mathbf{x}^{n+1} = \mathbf{x}^n + \mathbf{V}\Delta t. \tag{9-16}$$

Note that the velocity solved for is actually the velocity magnitude in the direction normal to the isotherm.

Matrix Governing Equations

The quasisteady governing equation for vapor flow in the boiling zone is

$$\nabla \cdot [\rho_v k\lambda(\nabla P + \rho g\nabla z)] + \nabla \cdot D\nabla\rho_v = 0, \tag{9-17}$$
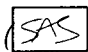
where P is gas pressure, k is intrinsic permeability, λ is mobility (relative permeability divided by viscosity), g is acceleration due to gravity, z is elevation, D is the diffusion constant, and ρ_v is vapor density.

Assuming the ideal gas law is valid,

$$P = \rho RT, \tag{9-18}$$

and the air component is pneumostatic $(\nabla P_a + \rho_a g\nabla z = 0)$,

$$\rho_v\nabla P = \frac{R}{2}\nabla T\rho_v^2 = \frac{R}{2}(T\nabla\rho_v^2 + \rho_v^2\nabla T). \tag{9-19}$$

The correct equation is ($\boxed{SAS}$, dated 9/5/98):

$$\rho_v\nabla P = R\rho_v\nabla T\rho_v = \frac{R}{2}T\nabla\rho_v^2 + R\rho_v^2\nabla T. \tag{9-20}$$

Leaping to a gross approximation for the equation coefficients, by assuming that it is acceptable to use a representative mean value for T, k, λ, ρ, and D, the governing equation can be written

$$A_1 \nabla^2 \rho_v^2 + A_2 \nabla^2 T + A_3 \nabla^2 z + A_4 \nabla^2 \rho_v = 0, \tag{9-21}$$

$$A_1 = \left\langle \frac{RTk\lambda}{2} \right\rangle, \tag{9-22}$$

$$A_2 = \left\langle \frac{R\rho_v^2 k\lambda}{2} \right\rangle, \tag{9-23}$$

$$A_3 = \left\langle \rho_v^2 k\lambda \right\rangle, \tag{9-24}$$

$$A_4 = \left\langle D \right\rangle. \tag{9-25}$$

The braces denote the representative value. The representative values might be obtained by averaging several point values strategically located within the domain after each nonlinearity iteration. The new governing equation is a sum of Laplacians, each of which can be written as a boundary integral.

The correct expression for A_2 is $A_2 = < R\rho_v^2 k\lambda >$ (𝒮𝒜𝒮 , *dated 9/5/98).*

The governing equation for energy in the boiling zone can be written

$$\nabla \cdot (C\mathbf{q}) - \nabla \cdot (K_e \nabla T) = 0, \tag{9-26}$$

$$\mathbf{q} = -A_1 \nabla \rho_v^2 - A_2 \nabla T - A_3 \nabla z, \tag{9-27}$$

where C is specific enthalpy for the air mixture, $\mathbf{q}$ is flux of the air mixture, and K_e is thermal conductivity. Assuming all coefficients are spatially invariant allows the energy equation to be calculated as a sum of Laplacians that can be solved using boundary integrals. Presumably the gradients of the variables are relatively small in the problem of interest so that the use of a representative value is not so bad.

Note that the Green's function for a Laplacian is (Liggett and Liu, 1983)

$$G = \ln r \qquad \text{in 2D}, \tag{9-28}$$

$$G = 1/r \qquad \text{in 3D}. \tag{9-29}$$

The mass and energy equations represent a coupled system of two equations with (essentially) two unknowns (ρ_v and T).

In the nonboiling zone, the mass balance equation is stated

$$\nabla \cdot K(\nabla P + \rho g \nabla z) = 0. \tag{9-30}$$

If $K = K_{sat}\exp(\alpha P)$, the governing equation can be converted to

$$\nabla^2\phi = s^2\phi, \tag{9-31}$$

which is quasilinear, with the following substitutions

$$\phi = \exp(-sz)\int_{-\infty}^{P} K\,\mathrm{d}P = \frac{K_{sat}}{\alpha}\exp(\alpha P - sz), \tag{9-32}$$

$$s = \frac{\rho g \alpha}{2}. \tag{9-33}$$

The correspondence between fluxes is

$$\frac{\partial q}{\partial n} = K(P)\frac{\partial P}{\partial n} = \exp(sz)\left[\frac{\partial\phi}{\partial n} + s\phi\frac{\partial z}{\partial n}\right]. \tag{9-34}$$

The Green's function for the quasilinear case is (Pullan and Collins, 1987)

$$G = K_0(sr) \qquad \text{in 2D}, \tag{9-35}$$

$$G = \exp(-sr)/r \qquad \text{in 3D}, \tag{9-36}$$

where K_0 is the modified Bessel function of the second kind of order 0. Any effects of temperature on K and ρ are neglected.

The energy balance equation in the nonboiling zone is

$$\nabla \cdot (K_e \nabla T) = 0. \tag{9-37}$$

In the nonboiling zone, mass and energy fluxes are assumed independent. The restriction of independence is a consequence of the quasilinear approximation for unsaturated flow.

Fracture Governing Equations

The same governing equations apply in the fractures as in the matrix, except that mass fluxes are two-phase rather than one-phase. The approximations of constant coefficients need only be applied within each element. The fracture equations should be quite standard. However, it is desirable to have pressure and temperature continuity from fracture to matrix. If these are not continuous (a fracture coating, for example), the resistance of the layer must be characterized. If the connection is totally shut off, then the matrix and fracture must have twice as many unknown values.

Interchange with the matrix is handled through distributed sources/sinks centered on fracture nodes. These sources and sinks enter into the compatibility equations for the matrix and are directly applied in the fracture equations.

General BIEM Approach

The following section is modified from Stothoff (1991).

The Green's function, or direct boundary element, approach is followed herein, due to the generality of the approach and the ease of incorporating extensions to the basic formulation. An excellent derivation of the approach is presented by Liggett and Liu (1983), along with associated computer code.

The Green's function approach takes advantage of Green's theorem. The first form of Green's theorem states that, for a function V satisfying the divergence theorem

$$\int_\Omega \nabla \cdot V \, d\Omega = \int_\sigma \mathbf{n} \cdot V \, d\sigma, \tag{9-38}$$

where V is represented by $V = \phi_1 \nabla \phi_2$, and both ϕ_1 and ϕ_2 are scalar functions of space,

$$\int_\Omega \nabla \cdot \phi_1 \nabla \phi_2 \, d\Omega = \int_\sigma \mathbf{n} \cdot \phi_1 \nabla \phi_2 \, d\sigma. \tag{9-39}$$

A symmetric form of this is derived by applying the first form of the Green's theorem to the second part of the left hand side, reversing the role of ϕ_1 and ϕ_2, resulting in the second form of the Green's theorem

$$\int_\Omega (\phi_1 \nabla^2 \phi_2 - \phi_2 \nabla^2 \phi_1) \, d\Omega = \int_\sigma \mathbf{n} \cdot (\phi_1 \nabla \phi_2 - \phi_2 \nabla \phi_1) \, d\sigma. \tag{9-40}$$

If an appropriate function G is found which satisfies the relationship

$$\nabla^2(G) = \delta(\mathbf{p} - \mathbf{d}), \tag{9-41}$$

where $\mathbf{p}$ represents a base point and $\mathbf{d}$ represents a field point, it is called the Green's function for the problem, and Equation 9-40 may be written in the form

$$\int_\Omega (\phi \nabla^2 G - G \nabla^2 \phi) \, d\Omega = \int_\sigma \mathbf{n} \cdot (\phi \nabla G - G \nabla \phi) \, d\sigma. \tag{9-42}$$

The second part of the volume integral is identically zero, and the Laplacian in the first part of the volume integral may be replaced by the Dirac delta function, resulting in

$$\alpha \phi(\mathbf{p}) = \int_\sigma \left(\phi(\mathbf{d}) \frac{\partial G}{\partial n}(\mathbf{p}, \mathbf{d}) - G(\mathbf{p}, \mathbf{d}) \frac{\partial \phi}{\partial n}(\mathbf{d}) \right) d\sigma, \tag{9-43}$$

where the notation $\partial\phi/\partial n$ is shorthand for the expression $\mathbf{n} \cdot \nabla\phi$. This is the basic representation for the direct boundary integral method used herein. With this representation, ϕ may be found at any base point $\mathbf{p}$ by setting the field point $\mathbf{d}$ to the locus of points defining the surface. For the free space Laplace equation in two dimensions,

$$G = \frac{\ln(r)}{2\pi};$$ (9-44)

and for the free space Laplace equation in three dimensions,

$$G = \frac{1}{4\pi r},$$ (9-45)

where $r = |\mathbf{p} - \mathbf{d}|$. The coefficient α depends on the location of the point $\mathbf{p}$ relative to the jump in potential along σ, as it arises from the exclusion of the singular point $\mathbf{p} = \mathbf{d}$ from Ω; α is 0 if $\mathbf{p}$ is outside Ω, 1 if $\mathbf{p}$ is wholly within Ω, and $\frac{1}{2}$ if on a smooth portion of the boundary.

If $\mathbf{p}$ lies at a non-smooth portion of the boundary, α corresponds to the interior angle the boundary makes at the point. Note that $\partial\phi/\partial n$ does not have a unique value at points where the boundary is not smooth, as there is no well-defined normal direction! This difficulty is handled by defining $\partial\phi/\partial n$ by pieces, with discontinuities occurring at angle points.

Equation 9-43 expresses the value of potential at a point as a sum of a weighted integral of the potential around σ and a weighted integral of the normal derivative of the potential around σ. If both of these values are known, in theory the potential may be found at any internal or boundary point. Liggett and Liu (1983) report that solutions tend to deteriorate near σ, due to what is termed the "boundary layer" effect. This arises due to the sharp change in α at σ, and care must be taken to minimize this numerical artifact.

In a well-posed problem, either ϕ or $\partial\phi/\partial n$ is defined around σ. For boundary integral methods to work, the missing boundary values must be available; in order to generate the missing set of boundary values, a number of strategies are commonly used. In the most common approach, both ϕ and $\partial\phi/\partial n$ are discretized into point values and interpolating functions between the point values, with a resultant set of N unknown values. Equation 9-43 is applied directly at the N locations where an unknown value is desired, resulting in a complete set of N equations in N unknowns. This is denoted by the matrix equation

$$\mathbf{H}\phi = \mathbf{G}\frac{\partial\phi}{\partial n},$$ (9-46)

where $\mathbf{H}$ comprises the integrals, dependent on the geometry of the problem, which multiply the discretized point values of ϕ, and $\mathbf{G}$ comprises the corresponding integrals for the point values of $\partial\phi/\partial n$. In practice, this equation is rearranged so that known values are multiplied through and

placed on the right hand side, and unknown values are moved to the left hand side, resulting in the familiar system of equations

$$\mathbf{Au} = \mathbf{b}, \tag{9-47}$$

where $\mathbf{A}$ is a square matrix, $\mathbf{u}$ is the vector of unknowns, and $\mathbf{b}$ is a vector of known information.

If the Green's function is satisfied identically along a portion of σ, the corresponding portion of σ need not be discretized; for example, a Green's function can be constructed which explicitly takes into account no-flow conditions on a boundary, using the method of images. The free space Green's function accommodates infinite boundaries, and only *finite* boundaries need be discretized. This property is in stark contrast to domain method requirements.

Another approach uses the derivative of Equation 9-43 to evaluate the normal derivative at the boundary directly. The derivative of ϕ in an arbitrary direction $\mathbf{n_p}$ may be written in the form

$$\alpha \frac{\partial \phi}{\partial n_{\mathbf{p}}}(\mathbf{p}) = \frac{\partial}{\partial n_{\mathbf{p}}} \left[\int_{\sigma} \left(\phi(\mathbf{d}) \frac{\partial G}{\partial n}(\mathbf{p}, \mathbf{d}) - G(\mathbf{p}, \mathbf{d}) \frac{\partial \phi}{\partial n}(\mathbf{d}) \right) \, d\sigma \right]. \tag{9-48}$$

Equation 9-48 may be evaluated at any point for which equation Equation 9-43 is valid, with a caveat for a base point $\mathbf{p}$ on σ. When the base point is not on the boundary, the derivative of the integrals may be taken inside the integral, resulting in

$$\alpha \frac{\partial \phi}{\partial n_{\mathbf{p}}}(\mathbf{p}) = \int_{\sigma} \left(\phi(\mathbf{d}) \frac{\partial^2 G}{\partial n_{\mathbf{p}} \, \partial n}(\mathbf{p}, \mathbf{d}) - \frac{\partial G}{\partial n_{\mathbf{p}}}(\mathbf{p}, \mathbf{d}) \frac{\partial \phi}{\partial n}(\mathbf{d}) \right) \, d\sigma. \tag{9-49}$$

On the other hand, when the base point is on σ, the singularities resulting from coincidence of the base point $\mathbf{p}$ and the field point $\mathbf{d}$ in Equation 9-49 are too strongly singular to be integrated directly. As is shown by Ingber and Mitra (1989), the resulting integral may be evaluated in the finite-part sense, or Equation 9-48 may be evaluated by taking the derivative *after* performing the integration. In either case, both the boundary and the normal gradient must be smoothly varying at the point of evaluation in order to perform the requisite operations. This precludes the use of Equation 9-48 at either angle points or jumps in normal gradient values. The more straightforward approach for evaluating Equation 9-48 is to take the derivative of the integral, rather than trying to evaluate the integral in the finite-part sense.

I have played with some of the approaches in the past. My experience suggests that the standard approach is simplest and produces quite acceptable results. Many of the difficulties faced by other practitioners are due to using higher-order interpolation along the boundary. The piecewise linear ϕ and piecewise constant $\partial \phi / \partial n$, together with adequate numbers of elements, is quite sufficient to avoid most difficulties.

7/16/98 Summary of matrix/fracture equations.   ⟨SAS⟩

Generic Matrix/Fracture Interaction Equations

The generic equations for a fracture interacting with a matrix include resistance across the fracture to matrix flow (e.g., through fracture coatings or air space), lateral flow in the fracture, and sources in the fracture. The fracture equations are formulated in 2D using the concept of integrated finite volumes. A simple but general formulation for balance within each fracture volume, incorporating diffusive flux within the fracture, sources in the fracture, and exchange with the matrix, is

$$Q_{si} = \sum_j \lambda_e (\phi_j - \phi_i) + Q_{ci}, \tag{9-50}$$

where Q_{si} represents exchange between matrix and fracture at node i, $\lambda_e = b_e K_e / L_e$ is the elemental conductance between nodes i and j, b_e is fracture thickness, K_e is fracture conductivity, L_e is fracture length, ϕ is potential (e.g., temperature), and Q_{ci} is the source arising within the control volume. The formulation is linear unless λ or Q_{ci} are nonlinear. The generality of the formulation is extended when the divergence of net advective flux within the fracture control volume is included into Q_{ci}.

The exchange between matrix and fracture is assumed to occur uniformly along the fracture walls, with the source apportioned so as to create the same gradient in matrix potential along the fracture wall. The fraction of total flux from the source at node i allocated to element e (attached to node i) is

$$F_{ei} = \frac{(K_1 + K_2)_e L_e}{\sum_m (K_1 + K_2)_m L_m}, \tag{9-51}$$

where the summation is over the number of elements connected to node i and subscripts 1 and 2 represent sides of the fracture. Assuming that the flux is uniformly distributed along the element, the rate supplied to the fracture walls is

$$q_{se} = \frac{\sum_j F_{ej} Q_{sj}}{L_e \sum_j}, \tag{9-52}$$

where the summation is over the number of nodes attached to the element (2 in 2D). Expanding,

$$q_{se} = \sum_i [\sum_j C_{eik}(\phi_j - \phi_i) + M_{ei} Q_{ci}], \tag{9-53}$$

$$C_{eik} = \lambda_k M_{ei}, \tag{9-54}$$

$$M_{ei} = \frac{F_{ei}}{L_e \sum_i}, \tag{9-55}$$

where the summation in i is over the number of nodes attached to element e, the summation in j is over the number of nodes with connections to node i, and k represents the element between nodes i and j. Note that the form of the equation is also appropriate in 3D (2D fractures) if L_e represents the area of the element when calculating q_{se} and if the width of the connection is included in λ_e.

It is important to note that the value of ϕ in the flux equations represents an average value within the fracture that may differ from the matrix if there is resistance to transfer between the fracture and matrix.

The general boundary integral formulation for flow in the matrix provides values for u or $\partial u/\partial n$ at particular points on the boundary or within the domain of interest. The formulation is quite simple:

$$\sum_i \alpha_i u_i = \int_\sigma \left(G \frac{\partial u}{\partial n} - u \frac{\partial G}{\partial n} \right) \, \mathrm{d}\sigma + \int_{\sigma_M} \left(G \Delta \frac{\partial u}{\partial n} - \Delta u \frac{\partial G}{\partial n} \right) \, \mathrm{d}\sigma_M, \tag{9-56}$$

$$= \int_\sigma \left(G \frac{\partial u}{\partial n} - u \frac{\partial G}{\partial n} \right) \, \mathrm{d}\sigma + \int_{\sigma_M} \left(-G q_s - \Delta u \frac{\partial G}{\partial n} \right) \, \mathrm{d}\sigma_M, \tag{9-57}$$

where G is the Green's function, q_s is the flux entering the fracture, σ represents the domain boundary, σ_M represents discontinuities within the domain, and α_i is the fraction of the point in region i (the point may be partially within several domains). If the point is completely within the domain, $\alpha = 1$. On a smooth boundary, $\alpha = 1/2$.

The BIEM requires that all terms within the integrals are known before ϕ can be explicitly evaluated at any point. A well-specified problem does not provide all terms. In order to define the missing terms, a set of linear equations is formed by writing one equation for each unknown. Choosing the representation of piecewise-linear u and piecewise-constant $\partial u/\partial n$, equations along the boundary are written at nodes wherever there is an unspecified value of u and are written at element centroids wherever there is an unspecified value of $\partial u/\partial n$.

In the case where the fracture ϕ is dominated by matrix interaction (e.g., when ϕ is temperature), the fracture value for ϕ is the numerical average of the matrix ϕ surrounding the point. In this case, u might represent $K\phi$, where K represents conductivity (piecewise constant by region). Flux is represented by $q = -K\nabla\phi = -\nabla u$. Through-flux from matrix to matrix across the fracture may be limited by increased resistance within the fracture, and the matrix blocks may have different conductivities.

In this situation, the general form of the equation written at the discontinuity nodes in the

middle of the fracture (not at a fracture intersection) is

$$\alpha_1 u_1 + \alpha_2 u_2 = \int_\sigma \left(G\frac{\partial u}{\partial n} - u\frac{\partial G}{\partial n} \right) \, d\sigma + \int_{\sigma_M} \left(-Gq_s - \Delta u\frac{\partial G}{\partial n} \right) \, d\sigma_M, \qquad (9\text{-}58)$$

where the subscripts 1 and 2 represent matrix sides 1 and 2 of the fracture and q_s is defined by fracture mass balance considerations. The unspecified values of q_s require ϕ within the fracture, while Δu is also unspecified. Choosing ϕ within the fracture (piecewise linear between nodes) and Δu (piecewise constant for elements) as variables to be determined, the left-hand-side can be rewritten

$$\alpha_1 u_1 + \alpha_2 u_2 = (\alpha_1 + \alpha_2) \left(\frac{2K_1 K_2}{K_1 + K_2} \right) \phi + \left[(\alpha_1 + \alpha_2) \left(\frac{K_2 - K_1}{K_1 + K_2} \right) + (\alpha_2 - \alpha_1) \right] \frac{\Delta u}{2}. \qquad (9\text{-}59)$$

As Δu is only piecewise constant, the arithmetic average of the values attached to the node is used. Note that the following relationships are used:

$$u = K\phi \qquad (9\text{-}60)$$

$$u_1 = \bar{u} - \Delta u/2 \qquad (9\text{-}61)$$

$$u_2 = \bar{u} + \Delta u/2 \qquad (9\text{-}62)$$

$$\bar{\phi} = \frac{1}{2}(\phi_1 + \phi_2) \qquad (9\text{-}63)$$

$$\bar{\phi} = \frac{1}{2K_1 K_2} [(K_1 + K_2)\bar{u} + (K_1 - K_2)\Delta u/2] \qquad (9\text{-}64)$$

$$\Delta\phi = 2\left(\frac{K_1 - K_2}{K_1 + K_2} \right) \bar{\phi} + \frac{2}{K_1 + K_2}\Delta u \qquad (9\text{-}65)$$

In this general case, both ϕ and Δu must be determined, but insufficient equations are generated if only nodes are used. An additional set of equations is derived by taking the derivative with respect to the normal direction of the discontinuity, yielding

$$\frac{\partial}{\partial n}(\alpha_1 u_1 + \alpha_2 u_2) = \frac{\partial}{\partial n}\left[\int_\sigma \left(G\frac{\partial u}{\partial n} - u\frac{\partial G}{\partial n} \right) \, d\sigma + \int_{\sigma_M} \left(-Gq_s - \Delta u\frac{\partial G}{\partial n} \right) \, d\sigma_M, \right]. \qquad (9\text{-}66)$$

This derivative equation can only be used where the discontinuity is smooth, due to integration difficulties for the high-order singularities arising when the integration passes through the base point. Because of this limitation, Δu is defined as piecewise constant so that enough equations can be generated to determine the unknown values.

The derivative equation is used to impose the restriction on flux normal to the fracture.

The left-hand-side is rearranged in terms of ϕ and Δu to yield

$$\frac{\partial}{\partial n}(\alpha_1 u_1 + \alpha_2 u_2) = (\alpha_1 + \alpha_2)\frac{K_r}{b}\Delta\phi - \left(\frac{\alpha_1 K_1 + \alpha_2 K_2}{K_1 + K_2}\right)q_s \tag{9-67}$$

$$= \frac{1}{K_1 + K_2}\left[2(\alpha_1 + \alpha_2)\frac{K_r}{b}((K_1 - K_2)\phi + \Delta u) - (\alpha_1 K_1 + \alpha_2 K_2)q_s\right] \tag{9-68}$$

$$= \frac{1}{K_1 + K_2}\left[2\frac{K_r}{b}((K_1 - K_2)\phi + \Delta u) - \frac{1}{2}(K_1 + K_2)q_s\right], \tag{9-69}$$

where $\alpha_1 = \alpha_2 = \frac{1}{2}$ by virtue of the smoothness of the boundary.

Several simplifications may occur. When $K_r = 0$, the matrix is forced to interact completely with the fracture (no flow bypasses the fracture). When the matrix has the same $K = K_m$ on each side of the fracture, the left-hand-side terms become

$$\alpha_1 u_1 + \alpha_2 u_2 = (\alpha_1 + \alpha_2)K_m\phi + (\alpha_2 - \alpha_1)\frac{\Delta u}{2}, \tag{9-70}$$

$$\frac{\partial}{\partial n}(\alpha_1 u_1 + \alpha_2 u_2) = \frac{K_r}{bK_m}\Delta u - \frac{1}{2}q_s. \tag{9-71}$$

If, instead, the drop in ϕ across the fracture is negligible, then the derivative equation is not needed and $\alpha_1 u_1 + \alpha_2 u_2 = (\alpha_1 K_1 + \alpha_2 K_2)\phi$. If the matrix conductivity is also identical on either side of the fracture, the left-hand-side term further simplifies to $\alpha_1 u_1 + \alpha_2 u_2 = (\alpha_1 + \alpha_2)K_m\phi$.

Complications can occur in the left-hand-side of the nodal equation at junctions between fracture sets or at the end of the fracture, due to ambiguities in specifying Δu at the node. If the fracture ends in a uniform matrix $(K_1 = K_2 = K_m)$, then $\alpha_1 = \alpha_2 = 1/4$ and the Δu portion of the term is zero. If the fracture lies along a material discontinuity, discretization continues along the discontinuity with no ambiguity. If the fracture node represents a junction between fracture sets, the left-hand-side term becomes

$$\sum_i \alpha_i u_i = \sum_i \alpha_i K_i[\bar{\phi} + \frac{\sum_k(\phi_i - \phi_k)}{\sum_k}] \tag{9-72}$$

$$\phi_i - \phi_k = 2\left(\frac{K_k - K_i}{K_i + K_k}\right)\bar{\phi} + \frac{2}{K_i + K_k}(u_i - u_k) \tag{9-73}$$

where the summation over i represents the number of matrix blocks contacting node i and the summation over k represents the number of fracture elements contacting matrix block i. The junction equation is valid in both 2D and 3D, and reduces to the simpler formulation. Note that the junction equation is valid for any case where material discontinuities meet, as long as $\bar{\phi}$ is the value that is solved for at the junction.

7/17/98 Simpler formulation of matrix/fracture equations. $\boxed{\text{S\hspace{-1pt}S}}$

Localized Matrix/Fracture Interaction Equations

A slightly different generic case arises if there is local resistance to transferral from the fracture to the matrix (e.g., fluid flow in the fracture resists transferral due to a fracture coating). The local-resistance case is more straightforward to code than the generic case considered previously, due to the more straightforward representation for fracture mass balance.

The nodal balance equation is the fracture mass balance. For fracture node i,

$$\sum_j \lambda_{ij}(\phi_j - \phi_i) + \sum_k L_k[C_{k1}(\phi_k - \phi_{k1}) + C_{k2}(\phi_k - \phi_{k2})] + Q_{ci} = 0, \qquad (9\text{-}74)$$

where the summation over j represents the number of nodal connections exchanging with node i and the summation over k represents the number of elements attached to node i. The potential in the fracture is denoted by ϕ, while the potential in the matrix is denoted by ϕ_1 and ϕ_2 (for sides 1 and 2 of the fracture, respectively).

For element centroids in this case, assume

$$q_{se} = C_{e1}(\phi_e - \phi_{e1}) + C_{e2}(\phi_e - \phi_{e2}). \qquad (9\text{-}75)$$

The left-hand-side of the derivative equation is

$$\alpha\frac{\partial}{\partial n}(u_1 + u_2) = 2\alpha\left(\frac{K_f}{b}(\phi_2 - \phi_1) - q_s\right) = \frac{K_f}{b}(\phi_2 - \phi_1) - q_s \qquad (9\text{-}76)$$

where

$$q_s = 2\bar{C}\phi_e - (2\bar{C}\bar{\phi} + \frac{\Delta C \Delta \phi}{2}), \qquad (9\text{-}77)$$

$$\bar{\phi} = \frac{1}{2K_1K_2}\left[(K_1 + K_2)\bar{u} + (K_1 - K_2)\frac{\Delta u}{2}\right], \qquad (9\text{-}78)$$

$$\Delta\phi = \frac{1}{K_1K_2}\left[(K_1 - K_2)\bar{u} + (K_1 + K_2)\frac{\Delta u}{2}\right], \qquad (9\text{-}79)$$

$$\bar{C} = \frac{1}{2}(C_1 + C_2), \qquad (9\text{-}80)$$

$$\Delta C = C_2 - C_1. \qquad (9\text{-}81)$$

There are two equations with two unknowns (Δu and q_s), where the second equation is a mass-balance statment for q_s. Note that $\bar{u}$ is directly obtained from an evaluation of the normal-equation

integral and ϕ_e is the average of the surrounding nodal values for fracture potential. As C_1 and C_2 become large, potentials become nearly identical across the fracture. One can consider an arbitrarily thin layer of the matrix to be the resistant layer if no fracture coating exists.

Assigning conductances (conductivity divided by thickness) is consistently performed by considering the case where three distinct (and isotropic) layers form the fracture. In sequence, the layers might represent a fracture coating (1), fluid (2), and another fracture coating (3). The total conductance for flow normal to the fracture is then

$$C_{norm} = \frac{\theta}{\sum_i^3 b_i/K_i} + \frac{(1-\theta)K_{bypass}}{\sum_i^3 b_i}, \tag{9-82}$$

while the total conductance for flow along the fracture is

$$C_{tang} = \frac{\sum_i^3 b_i K_i}{L \sum_i^3 b_i}. \tag{9-83}$$

The fraction of the surface area of the fracture contributing to fracture/matrix exchange is denoted by θ; the remainder is assumed to contribute to fracture-bypass fluxes (e.g., through matrix-to-matrix contact along asperities) with conductivity K_{bypass}. The consistent representation for conductances becomes

$$C_{e1} = \frac{\theta}{b_1/K_1 + b_2/(2K_2)}, \tag{9-84}$$

$$C_{e2} = \frac{\theta}{b_3/K_3 + b_2/(2K_2)}, \tag{9-85}$$

$$\bar{C} = \frac{1}{2}(C_{e1} + C_{e2}), \tag{9-86}$$

$$\Delta C = C_{e2} - C_{e1}, \tag{9-87}$$

$$\frac{K_f}{b} = C_{norm}, \tag{9-88}$$

$$\lambda_e = C_{tang}. \tag{9-89}$$

These representations are consistent even if the fracture coatings do not exist ($b_1 = 0$ and/or $b_3 = 0$).

Rearranging the derivative-equation left-hand-side for an element centroid,

$$\alpha\frac{\partial}{\partial n}(u_1 + u_2) = C_{norm}\left(\frac{K_1 - K_2}{K_1 K_2}\right)\bar{u} + C_{norm}\left(\frac{K_1 + K_2}{K_1 K_2}\right)\frac{\Delta u}{2} - q_s, \tag{9-90}$$

while the statement for q_s (also at the centroid) is

$$q_s = 2\bar{C}\phi_e - \left[\bar{C}\left(\frac{K_1 + K_2}{K_1 K_2}\right) + \frac{\Delta C}{2}\left(\frac{K_1 - K_2}{K_1 K_2}\right)\right]\bar{u}$$

$$- \left[\frac{\bar{C}}{2}\left(\frac{K_1 - K_2}{K_1 K_2}\right) + \frac{\Delta C}{4}\left(\frac{K_1 + K_2}{K_1 K_2}\right)\right]\Delta u. \tag{9-91}$$

In these expressions, $\bar{u}$ is determined by an integral, Δu is the unknown to be determined at the centroid, and ϕ_e is the average of the fracture potentials for the nodes determining the element. The C values should be derived from the K and b values as noted above.

7/20/98 Matrix formulation of matrix/fracture equations.

Simplifications occur when the fracture does not interact with the matrix or lateral flow in the fracture can be neglected, so that $q_s = 0$ and only one equation need be solved at the centroid:

$$\alpha \frac{\partial}{\partial n}(u_1 + u_2) = C_{norm}\left(\frac{K_1 - K_2}{K_1 K_2}\right)\bar{u} + C_{norm}\left(\frac{K_1 + K_2}{K_1 K_2}\right)\frac{\Delta u}{2}. \tag{9-92}$$

If the matrix also has the same conductivity on each side of the fracture, the left-hand-side reduces to

$$\alpha \frac{\partial}{\partial n}(u_1 + u_2) = \left(\frac{C_{norm}}{K_m}\right)\Delta u. \tag{9-93}$$

If the matrix and fracture interact but the matrix has the same conductivity on each side of the fracture, the two equations are

$$\alpha \frac{\partial}{\partial n}(u_1 + u_2) = \left(\frac{C_{norm}}{K_m}\right)\Delta u - q_s, \tag{9-94}$$

$$q_s = 2\bar{C}\phi_e - \frac{2\bar{C}}{K_m}\bar{u} - \frac{\Delta C}{2K_m}\Delta u. \tag{9-95}$$

If the fracture has no particular resistance to flow normal to the fracture (e.g., it is simply a material discontinuity), the formulation does not require the use of the derivative equation, but can use the standard equation with a left-hand-side in the form:

$$\alpha\left(\frac{K_1 + K_2}{K_2 - K_1}\right)\Delta u \tag{9-96}$$

(note that the continuity of potential requires that $\bar{u} = (K_1 + K_2)\phi$ and $\Delta\phi = (K_2 - K_1)\phi$).

Combining all of these cases into a generic format, a BIEM equation for any material-derived discontinuity can be written at the element centroids in terms of (i) values for ϕ at the surrounding nodes, (ii) jumps in u at the centroid, (iii) integrals of the normal equation, and (iv) integrals of the derivative equation. In the most complex cases, both Equation 9-97 and Equation 9-98 are

required; otherwise only one is. The full equations are

$$a_{11}q_s + a_{12}\Delta u = b_{11}\left[\int_\sigma \left(G\frac{\partial u}{\partial n} - u\frac{\partial G}{\partial n}\right)\mathrm{d}\sigma + \int_{\sigma_M}\left(-Gq_s - \Delta u\frac{\partial G}{\partial n}\right)\mathrm{d}\sigma_M\right]$$

$$+b_{12}\frac{\partial}{\partial n}\left[\int_\sigma \left(G\frac{\partial u}{\partial n} - u\frac{\partial G}{\partial n}\right)\mathrm{d}\sigma + \int_{\sigma_M}\left(-Gq_s - \Delta u\frac{\partial G}{\partial n}\right)\mathrm{d}\sigma_M\right], \qquad (9\text{-}97)$$

$$a_{21}q_s + a_{22}\Delta u + a_{23}\phi_e = b_{21}\left[\int_\sigma \left(G\frac{\partial u}{\partial n} - u\frac{\partial G}{\partial n}\right)\mathrm{d}\sigma + \int_{\sigma_M}\left(-Gq_s - \Delta u\frac{\partial G}{\partial n}\right)\mathrm{d}\sigma_M\right], \qquad (9\text{-}98)$$

where

$$a_{11} = -1 \qquad (9\text{-}99)$$

$$a_{12} = \frac{C_{norm}}{2}\left(\frac{K_1 + K_2}{K_1 K_2}\right) \qquad (9\text{-}100)$$

$$b_{11} = -C_{norm}\left(\frac{K_1 - K_2}{K_1 K_2}\right) \qquad (9\text{-}101)$$

$$b_{12} = 1 \qquad (9\text{-}102)$$

$$a_{21} = -1 \qquad (9\text{-}103)$$

$$a_{22} = -\frac{\bar{C}}{2}\left(\frac{K_1 - K_2}{K_1 K_2}\right) - \frac{\Delta C}{4}\left(\frac{K_1 + K_2}{K_1 K_2}\right) \qquad (9\text{-}104)$$

$$a_{23} = 2\bar{C} \qquad (9\text{-}105)$$

$$b_{21} = \bar{C}\left(\frac{K_1 + K_2}{K_1 K_2}\right) + \frac{\Delta C}{2}\left(\frac{K_1 - K_2}{K_1 K_2}\right). \qquad (9\text{-}106)$$

Equation 9-97 can be referred to as the Δh equation while Equation 9-98 can be referred to as the Δg equation.

The fracture mass balance equation for fracture node i is

$$\sum_j C_{tangij}(\phi_j - \phi_i) + \sum_k A_{nfk}q_{sk} + Q_{ci} = 0, \qquad (9\text{-}107)$$

where A_{nfk} is the area of the fracture exchanging with the matrix that is associated with the node ($A_{nfk} = L_k/2$ in 2D), the summation over j represents the number of nodal connections exchanging with node i and the summation over k represents the number of elements attached to node i.

7/27/98 Partial results of testing.

I used the Jacquard program, which I had developed while at the University of Vermont, to incorporate the ideas on boundary element simulation of fracture/matrix interaction. The Jacquard program incorporates a BIEM module based on the code I developed in my dissertation work. The module intent was to enable interpolation based on the Laplace equation. I had worked out approaches for some of the possible discontinuity formulations at that time, and included them in the code to help document my thinking, but only tested the coding for normal-equation boundaries and line-potential discontinuities. Resistance and material-change discontinuities were incorporated but not verified.

The fracture formulations developed above can be simplified to represent other discontinuities, thereby allowing components of the fracture formulation to be tested independently. As of today, the Jacquard module includes the following discontinuities:

- Specified-head boundaries

  - Normal-equation for unknown $\partial\phi/\partial n$
  - Derivative-equation for unknown $\partial\phi/\partial n$

- Specified-gradient boundaries

- Line discontinuities

  - Change in matrix properties
  - Specified-potential
  - Specified-source
  - Specified-flux
  - Specified-potential-jump
  - Thin inclusion (no lateral flow in inclusion) with or without change in matrix properties
  - Thin inclusion (lateral flow in inclusion) with or without change in matrix properties

I have tested almost all of these cases, checking for plausibility but without verifying numerical accuracy in most cases. The only case not checked at least summarily is the inclusion with lateral flow and a change in matrix properties.

The test cases are loosely based on the YM repository. The ultimate problem of interest is a vertical fracture with liquid and vapor flux, with the fracture penetrating a drift. The test domain extends roughly 1000 m horizontally both sides of the drift, and roughly 100 m vertically both sides of the drift. Testing of a particular discontinuity may use either horizontal or vertical discontinuity orientations. In general, potentials are specified at the top and bottom of the domain, with the sides open (semi-infinite). Near the drift, these side boundary conditions have little effect.

The plausibility tests were valuable in identifying several minor coding problems, both in the original code and in the additions. The formulations appear to work fairly well at worse and very well at best.

A particularly weak formulation is for a thin inclusion without lateral flow when the conductance of the inclusion is small. This case is like a low-conductivity lens. Apparently the matrix becomes poorly conditioned when the conductivity drops below a few orders of magnitude less than the matrix. The singularity term, which goes on the diagonal, is proportional to the conductance. As the singularity term goes to zero, conditioning becomes very poor. Physically the problem appears when the conductance is small enough to significantly reduce flow. The difficulty is more apparent when potential is not centered on zero (i.e., extra digits required to represent the potential reduce the number of significant digits used in computations). I don't consider the thin-barrier formulation particularly reliable.

Two comparisons were made for direct confirmation of results. An analytic solution is available when the problem is 1D. I tested the boundary contours for a box, no-flow on two opposing sides and specified-potential on the other two sides. This test identified a problem with the derivative-equation integrations (required for the fracture formulation). The problem was remedied, and analytic solutions were obtained both for the normal-equation approach and the derivative-equation approach, even when the grid was rotated ninety degrees.

The second comparison used the PDE tools supplied with *Matlab* to check the solution for a box with a fracture. The box is 20 m horizontally and 100 m vertically, with a fracture on one vertical side. The fracture was assigned the same material property as the matrix. A uniform sink was applied within the fracture, comparable to the energy removed by latent heat for flows representative of YM. The solutions from *Matlab* and the BIEM approach are identical at the boundaries, to the resolution visible from contour plots. This problem will be revisited with Goodluck for more stringent testing.

Before testing with *Matlab*, I modified the fracture formulation to have fracture potentials supplied at the element centroids rather than the nodes. The solutions generated with the unknown

potentials at nodes suffered from numerical instability, with alternate potentials above and below the "true" solution. Instability become noticable for sources orders of magnitude smaller than would be expected for YM problems. The reformulation completely eliminated the instability.

I used the *Matlab* PDE tools to play with the effect of conductivity in the fracture. When the fracture conductivity is comparable to the matrix conductivity, the solution appears to be prone to the same type of instability that was observed in the BIEM approach. When the fracture conductivity is large or small enough, the solution behaves well. One would expect that other codes would have similar difficulties.

7/30/98 Updated Observations. $\boxed{\mathcal{SAS}}$

Goodluck and I tested the BEM code against Abaqus yesterday. Essentially the same problem was used as when I tested the code against *Matlab*, with a slightly different thermal conductivity and a larger extraction rate. We compared vertical transects along the fracture, the far boundary, and the middle of the domain. We also compared horizontal transects at -25, 0, and 25 m (the quarter- and midpoints). These comparisons are plotted in Goodluck's notebook. The results are about as good as was achieved in the comparison against *Matlab*.

The Abaqus fracture was applied as a simple extraction flux along the portion of the boundary corresponding to the fracture. This procedure reduces or eliminates the problems associated with extreme differences in discretization and material properties. After the successful testing, Goodluck and I devised a simple procedure for estimating the penetration zone using this observation of numerical simplicity. If we assume that the total energy extracted from the rock due to boiling is known for a given liquid flux (i.e., latent heat), and we further assume that the energy is extracted in a range of temperatures above and below the boiling point (e.g., ± 5 °C), the problem reduces to predicting the location of the top and bottom of the sink zone. The location of the sink zone should be found fairly straightforwardly through iteration.

The simplified procedure misses three aspects of the problem, however. The implicit assumption is that all liquid flux is converted to vapor flux continuing down the fracture so that there is no recirculation above the boiling zone. The latent heat released upon condensation, thereby warming the condensation zone, is not accounted for. Also, the water entering the system must be warmed from the original temperature to the boiling temperature (above the top boiling zone) and must be cooled to the bottom temperature (below the bottom boiling zone), providing additional energy sinks. One would expect that these effects would be important in different domains. In particular,

the release of heat from condensation would be most important near the boiling zone, while the heating/cooling of water would act all the way along the fracture outside the condensation zone.

In order to form a heat pipe, there must be excess capacity for moisture movement beyond that required to transfer the incoming water to the bottom of the domain. It should be possible to estimate the excess capacity, which in turn provides an estimate for the maximum magnitude of recirculation and the maximum amount of energy bound up in the recirculation cycle. The excess capacity is overestimated by the difference between the maximum gravity flux and the actual flux in the fracture (vapor flux needs some capacity unless it occurs in the matrix).

It is reasonable to assume that the excess flux will not always be mobilized. Rather, the excess flux will not exceed that which creates a monotonic temperature distribution.

A slight modification to the problem may serve to capture the full behavior a bit better. The boiling/condensation behavior is more like a source dipole than a sink, with unbalanced components (some of the latent heat is removed through downward vapor flux, which balances the flux entering the top of the fracture). Perhaps the source and the sink can each be modeled as triangularly distributed over a certain temperature range, where the ranges overlap. An additional source/sink term can be applied uniformly along the fracture from the boundary to the boiling temperature, with a total strength that required to raise the liquid from the initial temperature to boiling. The net source/sink term at any particular location is simply the sum of the three. Note that when the fracture extends above and below the drift, the latent heat lost from above the drift is deposited below the drift, and heat is lost from the liquid as it cools to the bottom boundary temperature. Both of these effects would tend to bring the top reflux zone closer to the drift than the bottom zone would be.

As a practical matter, I would expect that the boiling pattern might drop off rapidly below boiling and not so rapidly above boiling, peaking slightly above boiling. Similarly, I would expect that the condensation pattern would drop off rapidly above boiling and not so rapidly below boiling, peaking slightly below boiling.

A heat-pipe effect would develop from these assumptions. It has to be seen whether the heat pipe bears any resemblance to the heat pipe that develops when fluid motion is explicitly considered. The approach implicitly assumes that the fluid moves readily relative to the flux of energy in the rock. In addition, the approach implicitly assumes that the flux in the fracture is essentially at the carrying capacity for the fracture (so that no excess recirculation can take place).

1/13/99 Fracture junctions.

I am returning to the process of developing a BEM code sufficient for a poster next month. My existing code is adequate for a relatively few matrix blocks, if some additional coding is performed to handle intersecting fractures. The procedure generates a large square full matrix, however, restricting the applicability due to computational effort (both in solving the matrix equations and due to the global support for each unknown).

An attractive alternative approach may be to develop the BEM code as a type of finite element code, which would produce a matrix structured similar to a finite element code, with reduced support for each node. I anticipate that such a code would be dramatically faster. The development process may be just a little too long for the poster time frame, but the possibility for speedup is tempting nevertheless. Definitely a production code should use the finite element ideas.

In pondering the physics of fracture flow in unsaturated systems, I realized that there are some fundamental differences between saturated and unsaturated systems. In saturated systems, capillarity is not an issue and flow is driven by head differences and conductivity can be treated as a bulk property. In unsaturated systems, capillarity may have a strong influence on flow, with flow directions that would be possible in saturated systems barred due to capillary effects. A good demonstration was presented by Nicholl and Glass (1995) with a field experiment at YM that showed an infiltration pulse at the large-block experimental site bypassing some fractures by simply stopping at the junction. The key factor that has been neglected is the physics at fracture intersections.

There are basically two situations: a filled fracture meeting the junction and a partially empty fracture meeting the junction. The partially empty fracture is dominated by film flow and capillarity is not important. The filled fracture, however, may or may not allow flow into the junction depending on conditions at the junction. In effect, there is a highly nonlinear conductance just at the exit of the fracture; at low flows and at high flows, the conductance is one, while when the fracture is just saturated with minimal overpressure, flows may be zero due capillarity. The translation of these physical considerations has not been made to numerical simulators, as far as I am aware.

A numerical approach to account for these effects is somewhat complicated. The standard equation under steady-state saturated conditions is a mass balance for junction N,

$$\sum_j C_j(\phi_j - \phi_N) = 0, \qquad (9\text{-}108)$$

where C is a conductance and ϕ is a potential. Solving for ϕ_N and rearranging, flux from the junction into volume i is

$$q_{Ni} = \frac{\sum_j C_i C_j (\phi_j - \phi_i)}{\sum_j C_j}. \tag{9-109}$$

This relationship assumes that no losses occur and there is a single potential at the junction. This relationship works for vapor flux and conduction.

If film flow is occurring in all incoming junctions, the situation may be the same or may be different. For example, consider a near-vertical joint and a slanted intersecting joint, both with entering film flow. In a saturated system, flow would likely join and move into all down-sloping fractures. In the unsaturated system, however, flows from the slanted fracture would tend to be completely diverted into the near-vertical fracture unless the near-vertical fracture became saturated. Similarly, flow in the near-vertical fracture will tend to be diverted into the slanted fracture due to surface tension pulling water around the corner. Note that, if the slanted fracture is capable of carrying the flow, only a small diversion would have the effect of completely cutting off vertical flow. Thus, the local structure at the fracture openings may play a rather important role in flow processes.

At a fully saturated 2D pipette network, the connections should default to the Equation 9-109 formula. A simplified approach may be effective for an unsaturated intersection. Assuming that the fractures are straight and the intersection has an offset, two incoming and two outgoing fractures can be defined.

The incoming fractures could be both unsaturated, both saturated, or one of each. If exactly one fracture is saturated and the hydrostatic pressure is not enough to overcome capillarity, the junction conductance for that fracture is 0; otherwise, the conductance is 1.

All flux is assumed to divert into the outgoing fracture on the down side of the offset joint, unless the fracture must be saturated to carry the flux; in this case, the excess spills into the other fracture.

The pressure in the primary outgoing fracture controls outgoing fluxes. The pressure at the incoming junction can be calculated from this (or be assumed the same), which in turn controls incoming fluxes.

The bottom line expression for unsaturated conditions can be formulated as

$$\sum_j C_j(\phi_j, \phi_N)(\phi_j - \phi_N + \Delta\phi_{jN}) = 0, \tag{9-110}$$

where $\Delta\phi_{jN}$ accounts for capillary effects and C_j is upstream weighted. The flux from volume i across the junction into volume j is

$$q_{ij} = \frac{C_i C_j C_{ij}(\phi_i - \phi_j)}{(C_i C_j + C_i C_{ij} + C_j C_{ij})}, \tag{9-111}$$

where C_{ij} is the conductance linking i and j in the junction. Note that $0 \leq C_{ij} < \infty$, with no flow when $C_{ij} = 0$ and the harmonic average between C_i and C_j recovered as C_{ij} becomes very large.

One approach for determining the unsaturated conductances under conditions of complete film flow is semi-explicit, so that it may have problems with stability. Given the potentials at the surrounding volumes, a local mass balance can be explicitly constructed. Assuming fully upstream weighted fluxes and slanted fractures, incoming film fluxes can be calculated. The outgoing fluxes are allocated preferentially according to offset geometry, so that the conductances can be explicitly calculated. Note that there are 9 possible offset configurations, which reduce to 4 basic configurations that need be considered: (i) 2 entering funneling to a split (4 of 9 cases); (ii) 2 reflections, with the chance of overflow (3 of 9); (iii) a zig zag with dual inputs (1 of 9); and (iv) horizontal or near-horizontal fractures (1 of 9). A case with no offsets reduces to the reflections or horizontal split.

1/14/99 More fracture junctions.

The problem of fracture intersections under unsaturated conditions can be simplified tremendously with the simple shift of considering each intersection as an internal boundary condition. In this case, the details of flow inside the intersection need not be considered and the only condition is an appropriate mass balance at the intersection. It turns out that only three types of mass balance equations suffice for all combinations of offset and fracture orientation. Ultimately, there should be a transition to handle fully saturated fractures, which may be due to using a marker potential at the outlet(s) to the junction.

Note that under saturated conditions, the flux into any one fracture volume is a function of the surrounding potentials (see Equation 9-109). For fully upstream-weighted film flow, the corresponding flux is a function of the upstream potential only and the fracture slope. Actually, film flux is dependent on the energy slope, which should only play a role in the transition between film and saturated flow.

The mass balance equation set for the funnel case is

$$q_3 = -\lambda(q_1 + q_2) \tag{9-112}$$

$$q_4 = -(1 - \lambda)(q_1 + q_2), \tag{9-113}$$

where q_1 and q_2 are incoming fluxes, q_3 and q_4 are outgoing fluxes, and λ is a weighting factor.

Typically, λ is set knowing the last value of the incoming fluxes, letting one fracture receive all flux up to its capacity and the other receive any overflow. If both are filled to capacity, λ smoothly transitions from the threshold value for both having incipient filling to the corresponding saturated-flow parallel conductance weighting (is this the same value?).

The set for the reflection and zigzag cases is

$$q_3 = -(1 - \lambda_1)q_1 - \lambda_2 q_2 \tag{9-114}$$

$$q_4 = -\lambda_1 q_1 - (1 - \lambda_2)q_2, \tag{9-115}$$

where the λ values are weighting factors set using the same considerations as in the funnel cases. In this case, however, it may be useful to maintain a potential inside the outgoing fractures to determine the direction of crossover flow.

In all of the above cases, film flow is assumed to occur with incoming fluxes, so that the incoming directions are determined from the slope of the fractures. Because film-flow flux is written as a function of potential, the outgoing fluxes are functions of the incoming potentials.

The case of capillary exclusion can be incorporated as well, with the idea of an internal boundary condition working here too.

When flow reduces to the case of a single outlet or a single inlet, the set of balance relationships is, for completeness,

$$q_2 = -\lambda_1 q_1 \tag{9-116}$$

$$q_3 = -\lambda_2 q_1 \tag{9-117}$$

$$q_4 = -(1 - \lambda_1 - \lambda_2)q_1, \tag{9-118}$$

where q_1 represents flux at either the single inlet or the single outlet.

The case with horizontal fractures is indeterminant, since the horizontal flow direction is not necessarily known *a priori*. For early simulator experiments, it would be best to not confuse the issue with horizontal fractures.

1/15/99 More fracture junctions.

The issue of transition between saturated and film-flow systems must be addressed for the fracture approach.

In saturated systems, it is straightforward to include an extra equation to solve for the pressure at the junction. Flux interchanging between junction and fracture i is written by

$$q_i = C_i(\phi_i - \phi_N) = C_i(P_i - P_N + \rho g(z_i - z_N), \tag{9-119}$$

where $C_i = b^3/12\mu$ from parallel-plate theory.

The same equation applies for film-flow systems, except that $C_i = b^3/3\mu$. There is a significant loss of efficiency due to the resistance of a second wall; a smooth transition in coefficients will be necessary for mixed saturated/film flow if the film thicknesses are asymmetric (perhaps due to large apertures). If the fracture is narrow enough to have numerous contacts, potentials are likely to be the same on either face and the flows would be symmetric or nearly symmetric on both faces, so that the transition is automatically smooth.

Generally $C_i = C_i(P)$, which can be written in the form $PC_i'(P)$ for inclusion in the matrix equations. Unless the junction is saturated, $P_i = P_N$ and upstream weighting can be used. Near the transition between unsaturated and saturated systems, there may be some effect from P_N even under unsaturated conditions.

In funnel and zigzag configurations, a single value for P_N is sufficient to determine outflow for both outlets. In reflection configurations, probably a single value would be adequate, but some care in switching would be necessary since the outlets are independent at low flows and linked at higher flows. The best option would be to use the potential for the outlet that is closest to its capacity during an iteration.

1/18/99 More fracture junctions.

Dani and I discussed the ideas of flow routing through fracture junctions today. One point that Dani made was that there may be film flow on both sides of a fracture, particularly at low flux rates. Without this consideration, I had identified a total of 45 possible configurations for 2 fractures with block movement along either fracture (rather than the 9 identified a few entries ago). There are 3 configurations for the subhorizontal fractures (slope less than, equal to, and greater than horizontal, respectively); 3 configurations for the subvertical fractures (slope less than, equal to, and greater

than vertical, respectively); and 5 configurations accounting for offsets [right-lateral or left-lateral along either fracture (4 possibilities), or no offset].

As discussion proceeded, it became clear that the routing of film fluxes through a junction is a bit more complex than just the consideration of geometry and fracture capacities. The additional component accounts for the diversion length of fluid before it forms a drop. The diversion length increases as the entry-fracture slope steepens and flux decreases. The effect of the diversion is to preferentially change the geometric offset based on film fluxes and fracture slope.

1/19/99 More fracture junctions.

Following up on the idea of symmetric/asymmetric flows, it occurred to me that it is likely that the top and bottom of narrow fractures are at the same chemical potential, due to the numerous asperities. The difference in elevation is perhaps insignificant. However, gravity may tend to pull water particles away from the hanging wall and pull water particles towards the footwall. In turn, absorbance forces may be reduced in the hanging wall and increased in the footwall. Presumably gravity would be more important as the film becomes thicker and absorption forces affect a smaller fraction of the film.

The problem of routing can also be looked at as a matter of tracking fluxes on individual faces or matrix blocks. For all configurations (except perfectly vertical/horizontal) there is one upper block that drips from the corner and one that tends to divert laterally. Once dripping occurs, it may encounter any of the footwall fracture faces for each of the four fracture segments, depending on offset geometry.

When the incoming subhorizontal fracture film intersects the footwall of the subvertical fracture, diversion always occurs into the subvertical fracture. If the hanging wall is intersected, diversion always occurs; however, if there is offset on the subvertical fault, dripping may occur onto the upper-block footwall and the possibility of diversion exists.

1/22/99 Fracture-junction routing algorithm.

There are two criteria for determining whether a junction is completely saturated: (i) all surrounding nodes are saturated, or (ii) film-flow inputs are greater than output capacity. When the junction is saturated, the solution process is linear and straightforward, geometry doesn't determine flow directions, and both upstream and downstream potentials determine flow. There can be between

one and three entries and exits.

When the junction is completely dominated by film flow, routing is dominated by face geometries, film-flow capacity, and the distance drops move laterally on hanging faces before dripping occurs, and only the upstream potential determines fluxes. Unless there are horizontal fractures, there are two entries and two exits.

When the junction has a mixture of film and saturated flows, it is necessary to consider capillarity to determine if a saturated fracture is an entry, exit, or neutral fracture. It is probably reasonable to assume that both corners touching a saturated fracture have the same potential. Note that the conditions for flux are a combination of the film and saturated conditions.

An algorithm for calculating film-flow routing (with no fracture saturated) is as follows:

- Calculate the flux capacity for each face

- Find incoming faces and estimate the incoming fluxes

- Sort block corners by elevation

- From highest corner to lowest, route incoming-face fluxes to a downstream face

    - Fixed drip (2 incoming faces): drip on underlying footwall (steeper footwall face wins in a tie)

    - No drip (2 outgoing footwall faces): do nothing

    - Lateral diversion (1 incoming and 1 outgoing footwall face): route from incoming to outgoing

    - Hanging-wall diversion (outgoing face is hanging wall): route along outgoing face to capacity, calculate lateral diversion for the remaining fluxes, and route the remaining at that point

- Accumulate the upstream flux for each face and the fraction of the upstream-face fluxes that make it to the downstream face

- Calculate the weights for outgoing fractures using the face information

The algorithm depends on the previous iteration to provide incoming fluxes; however, for low flux rates the weights will generally be independent. The only exception is if lateral diversion occurs before dripping, and if the diversion may cause dripping to reach different faces with different fluxes.

Mass balance is implicit with the completely film-flow formulation. Mass balance can be implicit with the completely saturated formulation.

1/25/99 Algorithm with some saturated fractures. $\boxed{S\!A\!S}$

There are several cases where a mixture of saturated and unsaturated fractures is relatively straight-forward. When there are three saturated fractures, the formulation is essentially that of the fully saturated case, with one unknown potential at the junction. When two opposed fractures are saturated, unless dripping occurs the formulation is essentially two independent fully saturated problems. The flux on a face attached to the saturated fracture is given by Equation 9-109.

2/16/99 Observations after the Witherspoon symposium. $\boxed{S\!A\!S}$

Paul Witherspoon made an observation regarding how difficult the YM problem is, due to the coupled HTMC processes in fractures during the thermal pulse. It occurred to me that the boundary integral approaches that I have been investigating are ideal for elastic deformation (or so I have repeatedly read). It should be relatively straightforward to implement a classic elastic solid deformation model, with the resulting impacts on fracture apertures and permeability due to normal and shear strains.

After pondering some more, it occurred to me that perhaps the chemistry effects could also be incorporated. The restrictions are similar to the restrictions placed on moisture redistribution, although perhaps somewhat more stringent.

The boundary integral approach is most easily applied for several conditions: (i) steady state, (ii) quasi-steady matrix, or (iii) completely disconnected matrix. The steady state condition is the easiest, as only boundary integrals and discontinuity values are required. The quasi-steady matrix is also fairly straightforward, with the matrix essentially acting as a special finite-volume element. A completely disconnected matrix is also straightforward, as only fracture equations need be considered.

When the matrix participates to an intermediate extent, the unmodified boundary integral approach fails due to the deviation from required assumptions. Typical failures are due to transience at an intermediate time scale. When the matrix behavior exhibits transience on time scales comparable to the problem time scales, standard domain discretization methods are required. However, when some matrix interaction is limited to a skin about the fracture and the remainder is

either quasi-steady or disconnected, the finite volumes representing fractures can be replaced with a finite-volume mesh extending perpendicular to the fracture. Either a 1D extension or a full grid can be used, depending on the problem.

The skin approach is probably appropriate for YM chemistry near the drifts during the thermal pulse, where the skins represent thin precipitation/dissolution fronts. Note that the assumption of quasi-steady THM components with transient C components may be appropriate for YM. The description of the TH fractures would have layered permeability as described previously, while it may be possible to neglect the layering for the M components. It may be that only the C components require a finite-volume mesh.

Another thought occurred to me recently: a multiple-continuum system can be conceived of as a type of layered aquifer/aquitard system. There is a Green's function developed for the latter case (Cheng and Morohunfola, 1993a; Cheng and Morohunfola, 1993b) that may be specialized for multiple overlapping continua. The presented solutions are for cases where the responses of the aquitards are significant, using Laplace transforms. However, the development should be able to be simplified to neglect the aquitard transience. The ideas may be of some use in considering saturated problems.

References

Cheng, A. H.-D. and O. K. Morohunfola. 1993a. Multilayered Leaky Aquifer Systems 1. Pumping Well Solutions. *Water Resources Research 29*(8), 2787–2800.

Cheng, A. H.-D. and O. K. Morohunfola. 1993b. Multilayered Leaky Aquifer Systems 2. Boundary Element Solutions. *Water Resources Research 29*(8), 2787–2800.

Ingber, M. S. and A. K. Mitra. 1989. The evaluation of the normal derivative along the boundary in the direct boundary element method. *Applied Mathematical Modelling 13*, 32–40.

Liggett, J. A. and P. L.-F. Liu. 1983. *The Boundary Integral Equation Method for Porous Media Flow*. London, England: George Allen & Unwin.

Nicholl, M. J. and R. J. Glass. 1995. A Field Experiment Exploring Fracture Network Geometry, Connectivity, and Unsaturated Flow Processes. *Supplement to Eos, Transactions 76*(46), F196.

Pullan, A. J. and I. F. Collins. 1987. Two- and Three-Dimensional Steady Quasi-Linear Infiltration From Buried and Surface Cavities Using Boundary Element Techniques. *Water Resources Research 23*(8), 1633–1644.

Stothoff, S. A. 1991. *A Boundary Integral Technique for Modelling Two-Phase Flow in Porous Media*. Ph. D. thesis, Princeton University, Princeton, NJ.

10   Iterative Performance KTI

Account Number: **20-5708-761**
Collaborators: **Robert Baca, Gordon Wittmeyer**
Directories: **As noted**

Objective: Perform analysis of the spatial and temporal distribution of moisture fluxes at YM. The emphasis under this project is on abstracting detailed process-level simulations into forms that are more amenable to performance assessment needs (e.g., probability distributions). In addition, periodic review of DOE work may be performed.

3/25/96 Audit review of TSPA-95.

Over the last few days I have been reviewing the approaches taken to estimate percolation fluxes impacting waste-package corrosion, and matrix and fracture velocities used to calculate transport of radionuclides, in the TSPA-95 document by TRW (1995). There are a number of internal inconsistencies and what appears to be just plain errors, particularly in the calculation of transport velocities. The major errors appear to be in the mountain-scale (transport) calculations, where parameter uncertainty is not passed through to velocity calculations in a self-consistent manner. In addition, the treatment of the ECM is not conventional, insofar as it is assumed that fractures are either completely saturated or completely empty depending on matrix saturation, which may drastically underpredict fracture velocities. In the drift-scale analysis, the variation in percolation flux is unsubstantiated and the information gathered on the fraction of packages being dripped on as a function of infiltration is ignored under climatic variation.

As I understand it, the primary thrust in the audit review is to perform some relatively straightforward calculations to check on the TRW results. I plan to perform a calculation of the probability distribution for quantities needed in the transport simulations such as matrix and fracture velocities and fluxes, as well as the partition of infiltration flux between matrix and fractures. My suspicion is that I will get a somewhat wider distribution for matrix velocity, perhaps log-normal rather than log-uniform, and a distribution for fracture velocities which yield much faster velocities in general. In addition, by running many more realizations than the 120 performed by TRW, I expect to expand the limits of their velocity ranges as well.

3/26/96 TSPA-95 comparison.

The work in the audit review is located in *$HOME2/Matlab/TSPA95Cols*. In order to set up a comparison, the same raw information used for the TSPA-95 report is used, which is derived from Schenker et al. (1995). The Schenker et al. (1995) report appears to have been excerpted for the TSPA-93 report (Sandia National Laboratories, 1994), as much of the information is identical. The Schenker et al. (1995) report describes the probabilistic behavior of each parameter using a beta function. Over the range $[a, b]$, the beta function produces a probability density function (PDF), $p(x)$, given by

$$p(x) = C(x - a)^{\alpha}(b - x)^{\beta}, \tag{10-1}$$

where C is a normalizing constant and α and β are used to define the shape of the function. By requiring that the integral of the PDF over the range is 1, one finds that

$$C = \frac{1}{\int_a^b (x - a)^{\alpha}(b - x)^{\beta}\, dx} = (b - a)^{-(1 + \beta + \alpha)}\frac{\Gamma(2 + \alpha + \beta)}{\Gamma(1 + \alpha)\Gamma(1 + \beta)}, \tag{10-2}$$

where

$$\Gamma(x) = \int_0^{\infty} t^{(x-1)} \exp(-t)\, dt. \tag{10-3}$$

All TSPA-95 hydraulic variables are described using a beta distribution or a constant value.

The best way to get randomly sampled values for a generic x is to push a uniformly sampled random variable through the cumulative probability distribution, retrieving the x value that has a cumulative probability less than the input random variable. For the beta distribution, the cumulative probability distribution is not convenient to manipulate directly, as the integral is not nice. A way around this is to construct a table of probabilities and find the cumulative normalized sum. A new *Matlab* function entitled **beta_dist.m** retrieves the values for a single set of beta-distributed probabilities, and **beta_dist_set.m** retrieves a set for all layers.

The **beta_dist.m** routine works by evaluating the unnormalized probability at 1001 evenly-spaced x locations. For cases with negative α or β, the beta function predicts infinite probability at the endpoint; I got around this by enforcing zero probability at any endpoint corresponding to a negative power. The cumulative sum is calculated and the resultant values are normalized. I plotted up each of the probability functions and compared them to the plots in the back of the Schenker et al. (1995) report. Schenker et al. (1995) provide a probability distribution for the data samples and for some of the layers also provide scaled probability distributions that are

supposed to represent the effective properties for the layer. I entered the scaled values for layers 1 through 7 (Tiva Canyon welded through Calico Hills/Prow Pass zeolitic nonwelded), and the plots in the back of the report are for the data only, but these should be relatively close. It appears that there are a few obvious errors. In particular, the residual saturations can be as high as 1, with no enforcement of the requirement that residual is less than porosity, and the layer 3C scaled parameters are completely outrageous. I can see why residual saturation was treated as a layer constant in the TSPA-95 work and I shall do the same for this task.

Correlations between parameters are not mentioned in the TSPA-95 document and only touched on by Schenker et al. (1995) on one page. Apparently the data is too sparse to do any comparisons other than for porosity and permeability. Several of the layers show significant correlation between porosity and permeability (a correlation coefficient between 0.467 and 0.929), but more than half show a negative or small correlation. According to the Leverett (1941) theory, scaling can be performed by the so-called J function,

$$J(S) = \frac{P_c}{\gamma\sqrt{k/\varepsilon}}, \tag{10-4}$$

where P_c is capillary pressure, γ is surface tension, k is intrinsic permeability, and ε is porosity. The J function is a dimensionless function of saturation (S). I expect that using such a scaling law would affect predicted velocities quite significantly.

3/28/96 TSPA-95 velocity comparison.   ⟦𝒮𝒜𝒮⟧

After setting up the beta distribution function, 10^4 realizations of independently sampled matrix properties were created for each of the layers denoted in the Schenker et al. (1995) report as

1 Tiva Canyon welded (TCw);

2 Paintbrush nonwelded (both modes 1 and 2 output) (PTn);

3C Topopah Spring welded–composite (TSw);

3R Topopah Spring welded–repository (TSw);

4 Topopah Spring vitrophyre (TSv);

5 Calico Hills/Prow Pass nonwelded–vitric (CHnv);

6 Calico Hills/Prow Pass nonwelded–zeolitic (CHnz);

7 Prow Pass welded (PPw).

Parameters were calculated using **make_param.m** and placed in a *Matlab* binary file, **param_uc_10000.mat**.

The method-of-lines (MOL) work discussed in the ODE-solver task is directly applicable for the comparison of steady-state velocities used in transport simulations. Accordingly, pertinent *Matlab* MOL routines were brought into *$HOME2/Matlab/TSPA95Cols* and stripped down to the simplest possible 1D matrix-fracture forward solver routines. The overall run routine is **run_forward_set.m**, which calls other routines as needed. The material-property routines are **calc_vg_wtcond.m**, for the true equivalent-continuum model (ECM) of matrix-fracture flow, as presented by Klavetter and Peters (1986), and **calc_vg_t2cond.m**, which represents my conceptualization of the TOUGH2 implementation described in the TSPA-95 report (TRW, 1995). Using the TSPA-95 stratigraphy, the four layers encountered in the integration from the water table to the repository are, in order, (i) CHnz (121.2 m), (ii) CHnv (80.7 m), (iii) TSv (8.4 m), and (iv) TSw (111.2 m).

As a first test, the forward solution for the true ECM model was run over the elevation range that appeared to be used in the TSPA-95 report. Solutions depended on hydraulic properties, of course, but averaged less than half a minute for the low-flow case (0.05 mm/yr), and less than two minutes for the high-flow case (2 mm/yr). The high-flow case kicked in some fracture flow, which slows the solver down considerably. The runs were performed from the water table to the repository, essentially assuming gravity drainage always occurs at the repository level.

The TOUGH2 implementation, as I understand it, uses the matrix properties to calculate a matrix conductivity. In addition, if the matrix saturation is above some criterion, the fractures are assumed saturated and the fracture conductivity is set to the saturated value, which is added to the matrix conductivity to get a total conductivity. If the matrix saturation is below the criterion, fractures are treated as not present. Fracture pressure is never calculated. I presume that matrix and fracture conductivities are weighted according to the liquid volume fraction in each, as is usual with the equivalent continuum approach.

When I ran the low-infiltration case, there was no particular difficulty, as the fractures were not active. However, the high-infiltration case did not provide a solution. Upon further investigation, it turns out that for a wide range of fluxes, it is mathematically impossible to get a steady state solution with the step-conductivity approach; I only presume that either numerical error must allow a solution somehow or I misunderstand the approach.

As an example, consider the integration up from a water table with a flux greater than the matrix saturated conductivity but less than the combined conductivity. Neglecting the fractures, pressure increases upwards in order to force water downwards at the appropriate rate. With the fractures, pressure decreases upwards since gravity is more than sufficient to push water downwards. If the switching criterion is at saturation, for example, any infinitesmal upwards spatial increment must have a lower pressure than the water table but requires that the next infinitesmal increment must have a greater pressure again, since the fractures have switched off. In a finite-volume code, pressure can oscillate above and below the criterion value node by node. For the MOL approach, there is no fixed node spacing so there is no admissible solution above the roundoff spacing length scale.

Implementing a delta range for the step to take place over, allowing a unique conductivity for every pressure, turns out to work but the integration process seems to be extraordinarily slow for reasonably small deltas (e.g., one percent of the matrix saturation range).

It occurs to me that for the purposes of the audit, only a high and a low flux need be considered, which should ease computational burden.

4/4/96 TSPA-95 audit closeout. $\boxed{\text{SAS}}$

The procedure for calculating the TSPA-95 conductivity is explained by Xiang et al. (1995) in another TRW report, and it turns out that the procedure is not as bad as I thought. The pressure in the matrix and fracture continua are separate, but defined, and the fractures are not forced to be either fully on or fully off. Instead, it is assumed that the capillary pressure/saturation relationship is linear above the threshold saturation for both the matrix and the fractures. The lower capillary pressure is well-defined for the matrix, but undefined for the fractures. The TRW procedure for defining the lower fracture capillary pressure is not presented; I presume some cutoff saturation stands in for zero (e.g., 10^{-8}) and the corresponding capillary pressure is used.

I implemented my understanding of the TRW ECM in an updated version of **calc_vg_t2cond.m**. Using the first 50 hydraulic-property realizations in **param_uc_10000.mat**, I ran a total of 9 sets of 50 simulations, representing 3 flux rates (2, 0.1, and 0.01 mm/yr) and 3 ECM models (single-pressure, or classical; $\sigma = 1$; and $\sigma = 0.95$). The σ-based ECM is the TRW ECM, where σ is the threshold matrix saturation above which fracture flow kicks in. For each simulation, 69 summary statistics were obtained for each layer, including number of ODE points in the layer. For each of 17 physical quantities, (i) the maximum observed, (ii) the minimum observed, (iii) the integral-

average value, and (iv) the integral-average deviation were calculated using **calc_run_summary.m** and stored in summary output files with names such as **ECM1-50_Q0.01_s-1.mat**. The digits following the "ECM" represent the hydraulic-property realization in **param_uc_10000.mat** (here realizations 1 through 50). The number after the "Q" represents infiltration flux in mm/yr. The number after the "s" represents the ECM model σ (-1 denotes the single-pressure ECM). The summarized physical quantities include matrix, fracture, and bulk velocities, saturations, moisture contents, etc. The quantities are labeled where defined in **calc_run_summary.m**.

For a parameter (V, for example), the integral-average ($\bar{V}$) and integral-average deviation (V') are defined by

$$\bar{V} = \frac{\int_{Z_a}^{Z_b} V \, dZ}{\int_{Z_a}^{Z_b} dZ}, \tag{10-5}$$

$$V' = \left(\frac{\int_{Z_a}^{Z_b} (\bar{V} - V)^2 \, dZ}{\int_{Z_a}^{Z_b} dZ} \right)^{1/2}. \tag{10-6}$$

The integrals are performed over the range of ODE points that are within a particular layer.

In the work for the TSPA-95 audit, only the integral-average quantities are examined in detail. The other information is stored for future examination.

As a measure of the impact of the assumptions embedded in the TSPA-95 ECM models, a travel-time measure is defined for the 4-layer system:

$$T = \sum_{i=1}^{4} \frac{L_i}{\bar{V}_{mi} F_{mi} + \bar{V}_{fi} F_{fi}}, \tag{10-7}$$

where L_i is the thickness of layer i, F_m and F_f are the fraction of flux in matrix and fractures, and $\bar{V}_m$ and $\bar{V}_f$ are the integral-average velocities in matrix and fractures.

In order to examine the statistical distribution of the travel times, a *Matlab* routine was created, **calc_5pt_stats.m**, which calculates the quartiles for a vector. Using the created *Matlab* routine **show_5pt_plots.m**, the distribution for T is displayed in Figure 10-1 for the 3 models, the two bounding fluxes, and two conceptualizations of V_f. The TSPA-95 definition of V_f is incorrect, dividing fracture flux by porosity rather than moisture content; the two V_f conceptualization are the correct and incorrect V_f definitions.
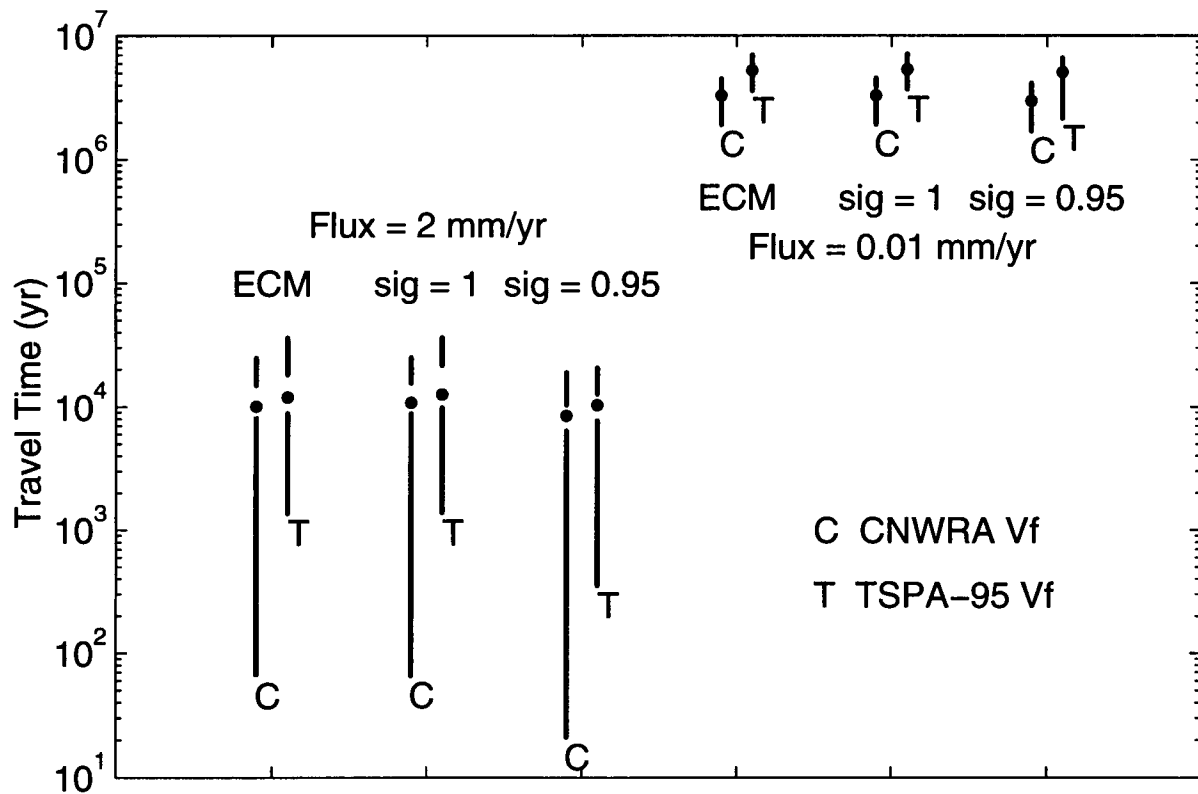
Figure 10-1: 4/4/96. Travel-time statistics for 50-realization simulations using different fluxes, ECM conceptualizations, and fracture-velocity conceptualizations.

Several general observations can be made based on Figure 10-1.

- The single-pressure ECM (denoted ECM in Figure 10-1) yields almost identical results as the σ-based ECM with $\sigma = 1$ (denoted sig = 1).

- The σ-based ECM with $\sigma = 0.95$ (denoted sig = 0.95) yields slightly faster travel times than the other models, consistent with claims in the TSPA-95 report. The major impact on travel time is found when fracture flow dominates (i.e., high infiltration rates, all layers exhibiting fracture flow).

- Misrepresenting the fracture velocity yields consistently slower travel times, by a factor of two to three, in the low-infiltration case.

- Misrepresenting the fracture velocity has less effect in the high-infiltration case, except that

the fastest travel-time outliers are more than an order of magnitude faster for the CNWRA measure.

The last two observations are somewhat surprising *a priori*, insofar as the low-infiltration cases have very little fracture flow to impact travel times and most high-infiltration cases, which have much higher fracture-flow contributions, are insensitive to errors in calculating fracture velocities. It can be seen that even a small amount of fracture flow in a low-infiltration case has noticable impact on overall travel time. In high-infiltration cases, however, the TSw, TSv, and CHnz layers all exhibit significant fracture flow and only the nonwelded CHnv layer is dominated by matrix flow. Accordingly, the bulk of the travel time is spent traversing the CHnv layer; only those few cases with significant fracture fluxes in the CHnv layer demonstrate the effects of incorrect fracture velocity calculations in the high-infiltration scenario.

A further examination of the abstraction process was undertaken using 320 hydraulic-property realizations and the classical ECM (including the 50 realizations summarized in Figure 10-1). In Figure 10-2, created by **$HOME2/Matlab/TSPA95Cols/calc_trav_stat.m**, the success of the abstraction process is summarized. Curve A represents the summary statistics for the 320 realizations. Curves B and C use the TSPA-95 procedure to abstract PDFs for the velocities and flux distributions, with 320 randomly sampled realizations for each layer. Curve B uses the TSPA-95 fracture velocity definition, while curve C defines the velocity fracture using the average moisture content for all cases with velocities greater than 10^{-13} m/s. Curve D presents the summary of 320 realizations using the TSPA-95 PDFs exactly.

Several observations can be drawn from Figure 10-2.

- In matrix-dominated flow ($q_{inf} = 0.01$ mm/yr), the TSPA-95 abstraction process with a modified V_f appears to capture the travel time statistics reasonably well, and the incorrect V_f yields consistently slow travel times.

- With significant fracture flow, the TSPA-95 abstraction process yields mean travel times 3 to 5 times faster than the mean travel times of the generating simulations.

- The travel times for the generating simulations are strongly clustered about the mean travel time, while the TSPA-95 abstraction travel times tend to be more spread out.
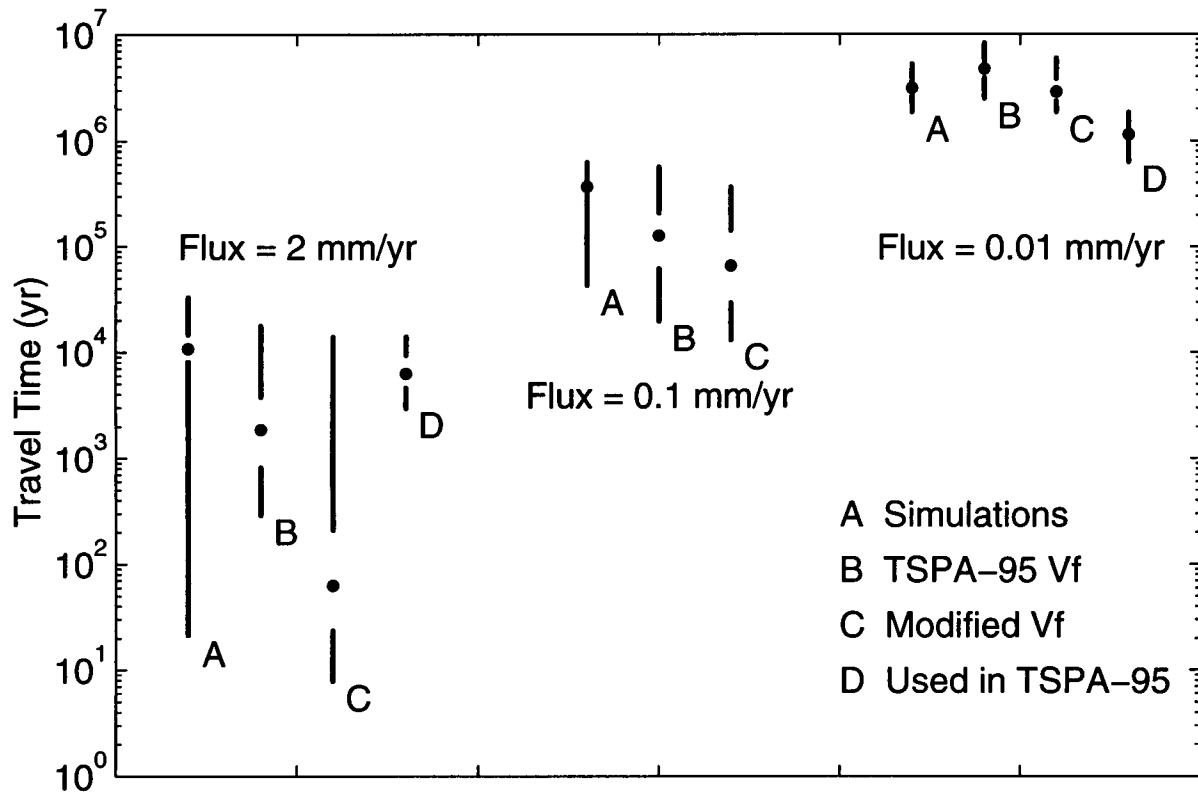
Figure 10-2: 4/4/96. Travel-time statistics for 320-realization simulations using classical ECM conceptualization, as well as abstracted PDFs using TSPA-95 approaches.

4/5/96 More TSPA-95 audit closeout.

As part of the audit review, I generated sets of scatterplots and histograms comparing various assertions of the TSPA-95 approach. These were not used in the write-up of the audit. For completeness, I am presenting them here.

The first set of scatterplots, shown in Figure 10-3, is based on the 50 hydraulic-property realizations used for all three ECM approaches. The four subplots represent each of the four layers, and were created using *Matlab* routine **show_plots.m**. The size of the symbol represents infiltration flux, with larger symbols denoting larger fluxes. Generally the ECM models only diverge significantly with higher fluxes.

The second set of scatterplots, shown in Figure 10-4, follows the same approach as Figure 10-
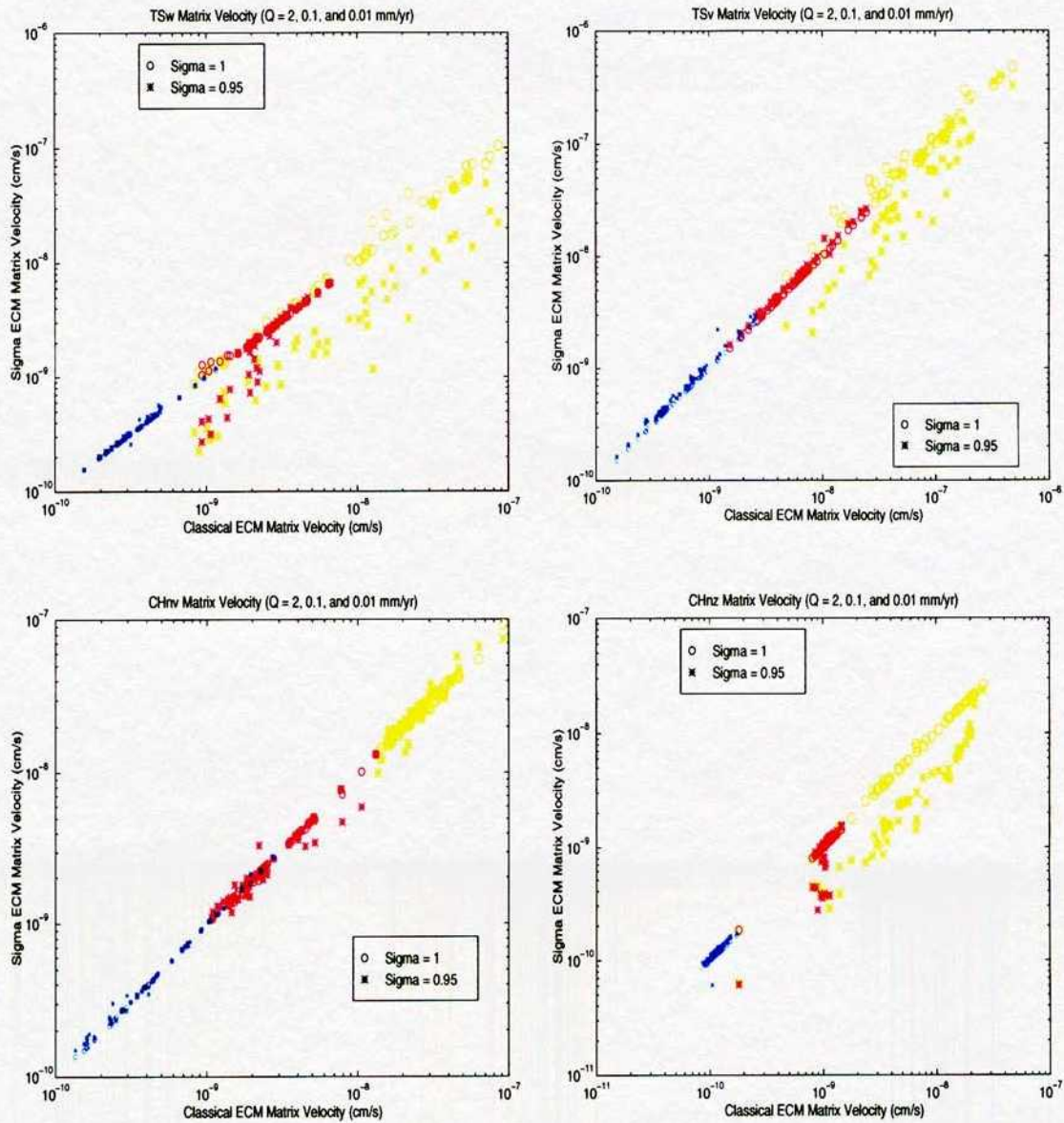
Figure 10-3: 4/5/96. Comparison of TSPA-95 matrix velocities predicted by the ECM models in the (a) TSw, (b) TSv, (c) CHnv, and (d) CHnz layers.

3, except that the fracture velocities are shown instead. The plots were created using *Matlab* routine **show_plots.m**. Not shown are the points with essentially zero fracture velocities, although there are significant numbers of cases with one model predicting high velocity while another predicts essentially zero. Note that low and medium infiltration rates often do not yield significant fracture flow and these cases are not shown.

The third set of scatterplots, shown in Figure 10-5, shows the fraction of flow in the fractures versus fracture velocities for each of the infiltration rates and layers. The plots were created using *Matlab* routine **show_plots.m**. Again, cases without significant fracture flow or fracture velocity are not shown. A very strong linear relationship occurs for the omitted points.

The fourth set of scatterplots, shown in Figure 10-6, shows the significant fracture velocities versus the matrix velocities for each of the infiltration rates and layers. The plots were created using *Matlab* routine **show_plots.m**. By dividing both velocities by infiltration flux, the respective sets of curves align much better. High matrix velocities yield low fracture velocities; above a threshold range, fracture velocities are essentially zero. The fracture-velocity dropoff behavior at high matrix velocities in the CHnz layer is followed in an exaggerated way for the other layers.

The first set of histograms, shown in Figure 10-7, shows the frequency of occurrence for matrix velocities. The plots were created using *Matlab* routine **scat_plot_stats.m**. Only the classical ECM model was used, but 320 hydraulic-property realizations are used. The base-10 log of the resultant velocities was binned into 10 evenly spaced bins from the minimum to the maximum velocity for each infiltration rate and layer. A strong tendency towards a bell-shaped log distribution is apparent.

The second set of histograms, shown in Figure 10-8, shows the frequency of occurrence for fracture velocities. The plots were created using *Matlab* routine **scat_plot_stats.m**. Only the classical ECM model was used, but 320 hydraulic-property realizations are used. The base-10 log of the resultant velocities was binned into 10 evenly spaced bins from 10^{-9} cm/s to the maximum velocity for each infiltration rate and layer. Any fracture velocities below 10^{-9} cm/s were put into the lowest bin.

9/3/96 Thoughts on TSPA-95 detailed audit.

Some of the results discussed above were presented at a Technical Exchange with the DOE in Denver. I presented a comparison of the DOE approach with the two different ECMs with the DOE abstraction and the NRC abstraction, plotting the sets of simulations discussed before in
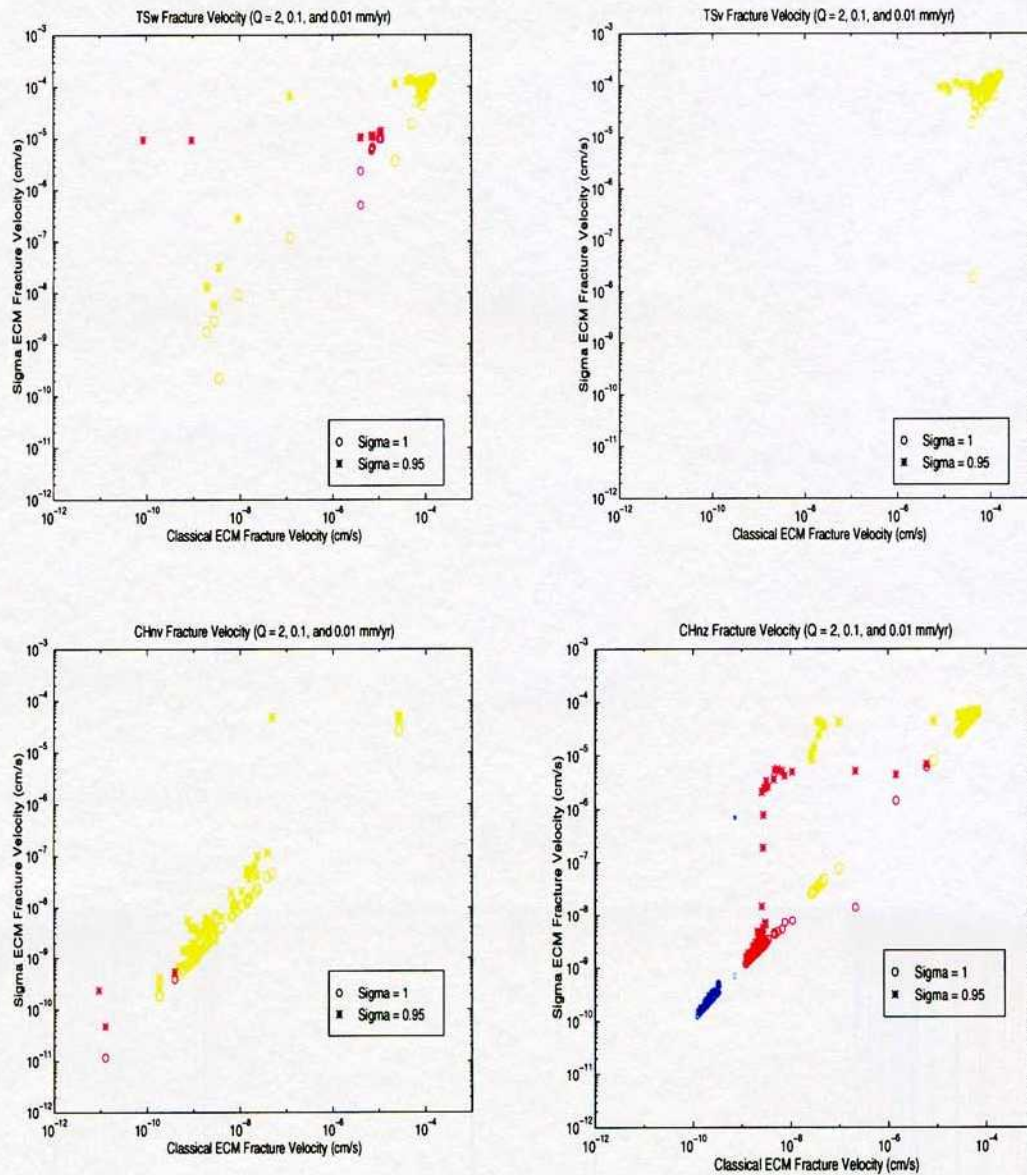
Figure 10-4: 4/5/96. Comparison of TSPA-95 fracture velocities predicted by the ECM models in the (a) TSw, (b) TSv, (c) CHnv, and (d) CHnz layers.
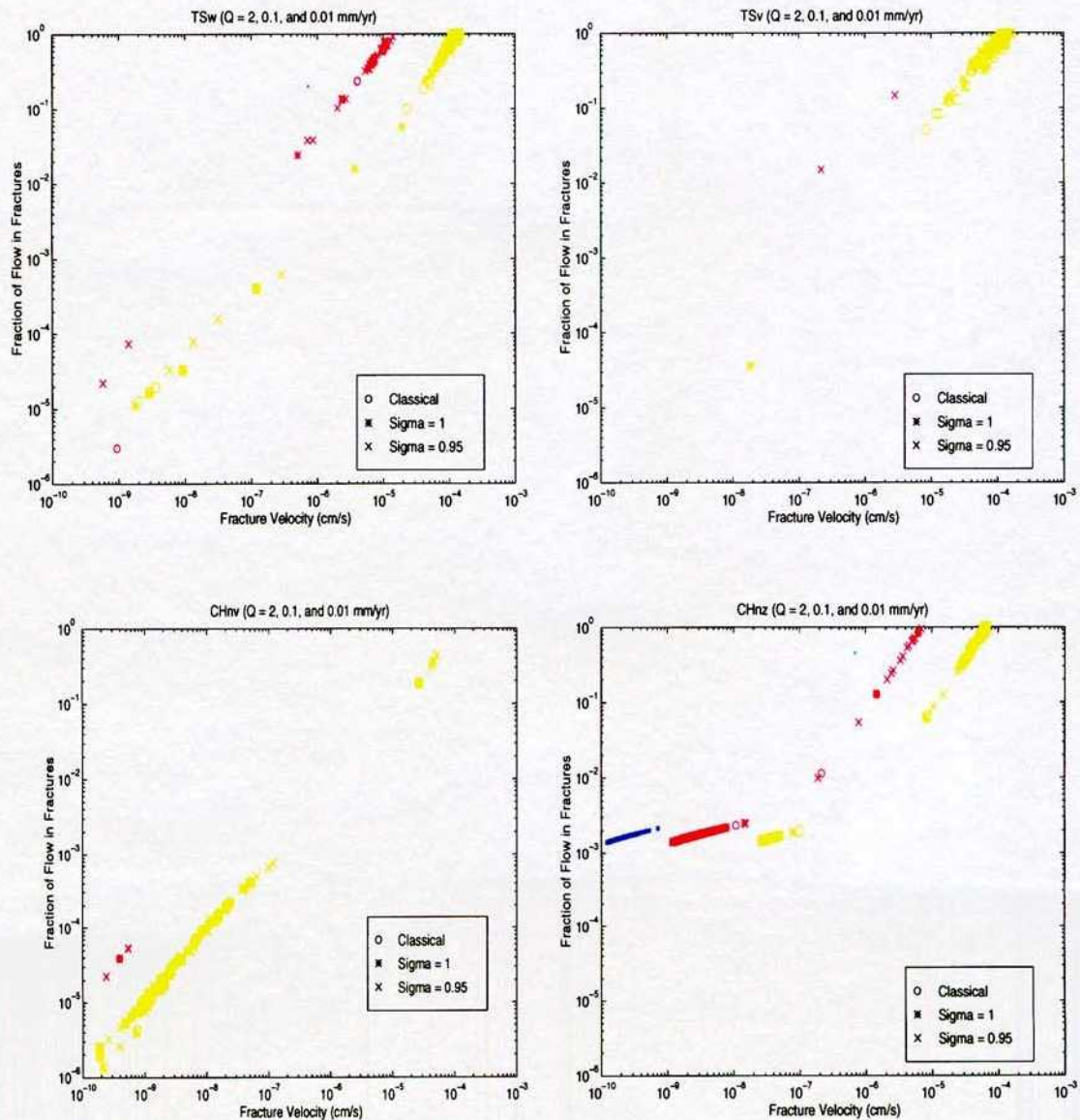
Figure 10-5: 4/5/96. Comparison of TSPA-95 fracture velocities to fraction of flow in fractures as predicted by the ECM models in the (a) TSw, (b) TSv, (c) CHnv, and (d) CHnz layers.
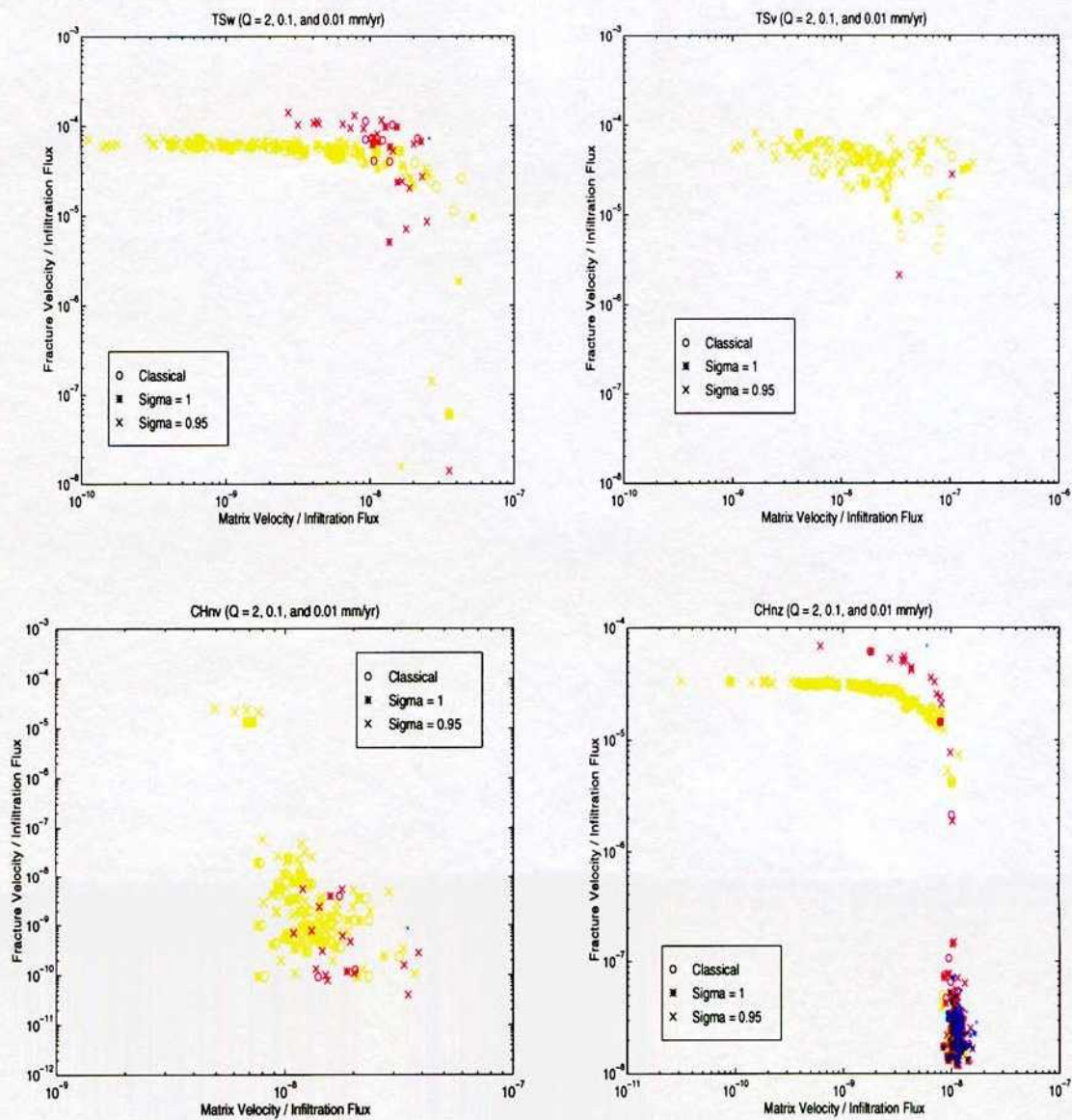
Figure 10-6: 4/5/96. Comparison of TSPA-95 scaled matrix velocities to scaled fracture velocities as predicted by the ECM models in the (a) TSw, (b) TSv, (c) CHnv, and (d) CHnz layers.
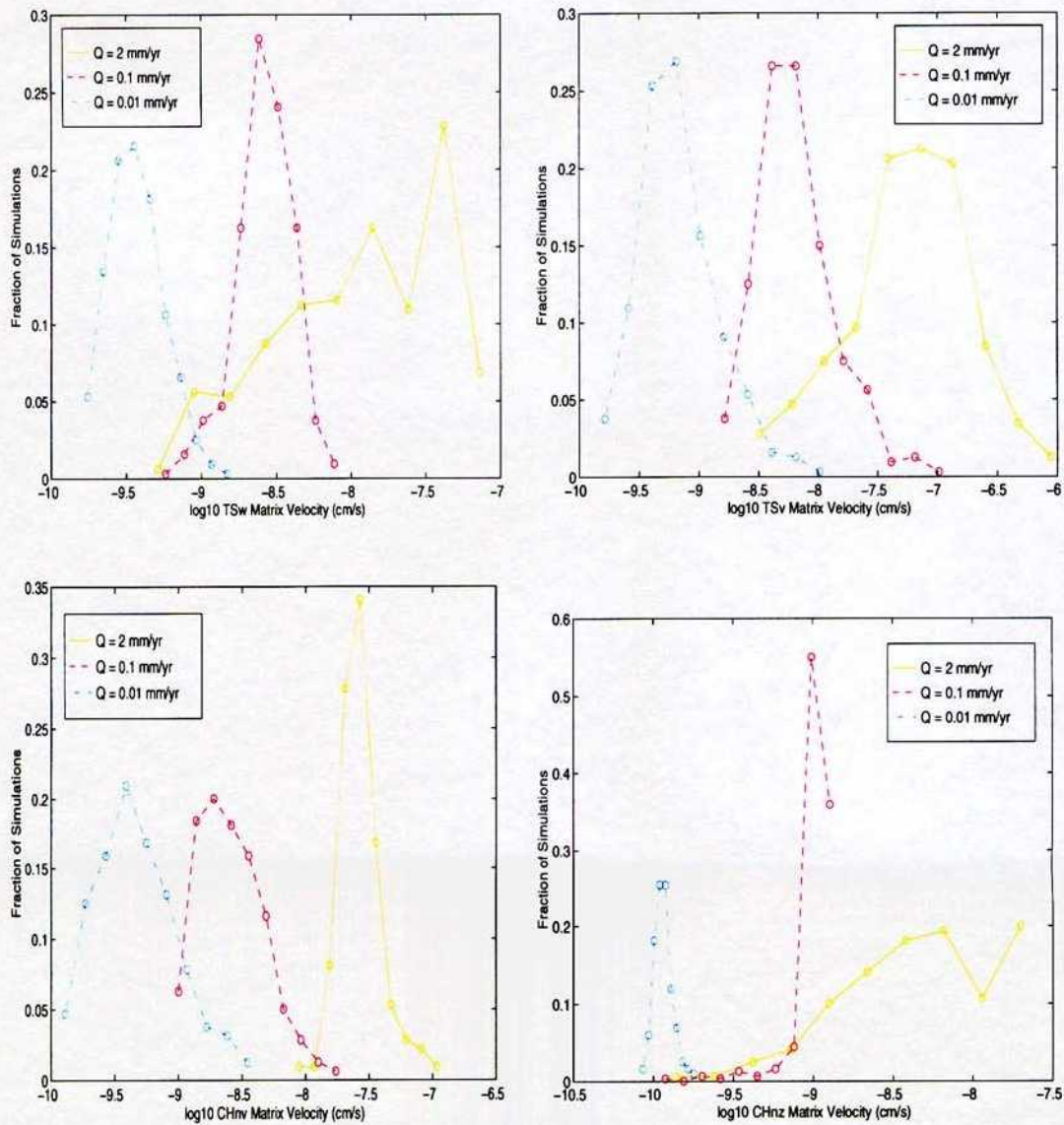
Figure 10-7: 4/5/96. Histogram of TSPA-95 matrix velocities for the classical ECM model in the (a) TSw, (b) TSv, (c) CHnv, and (d) CHnz layers.
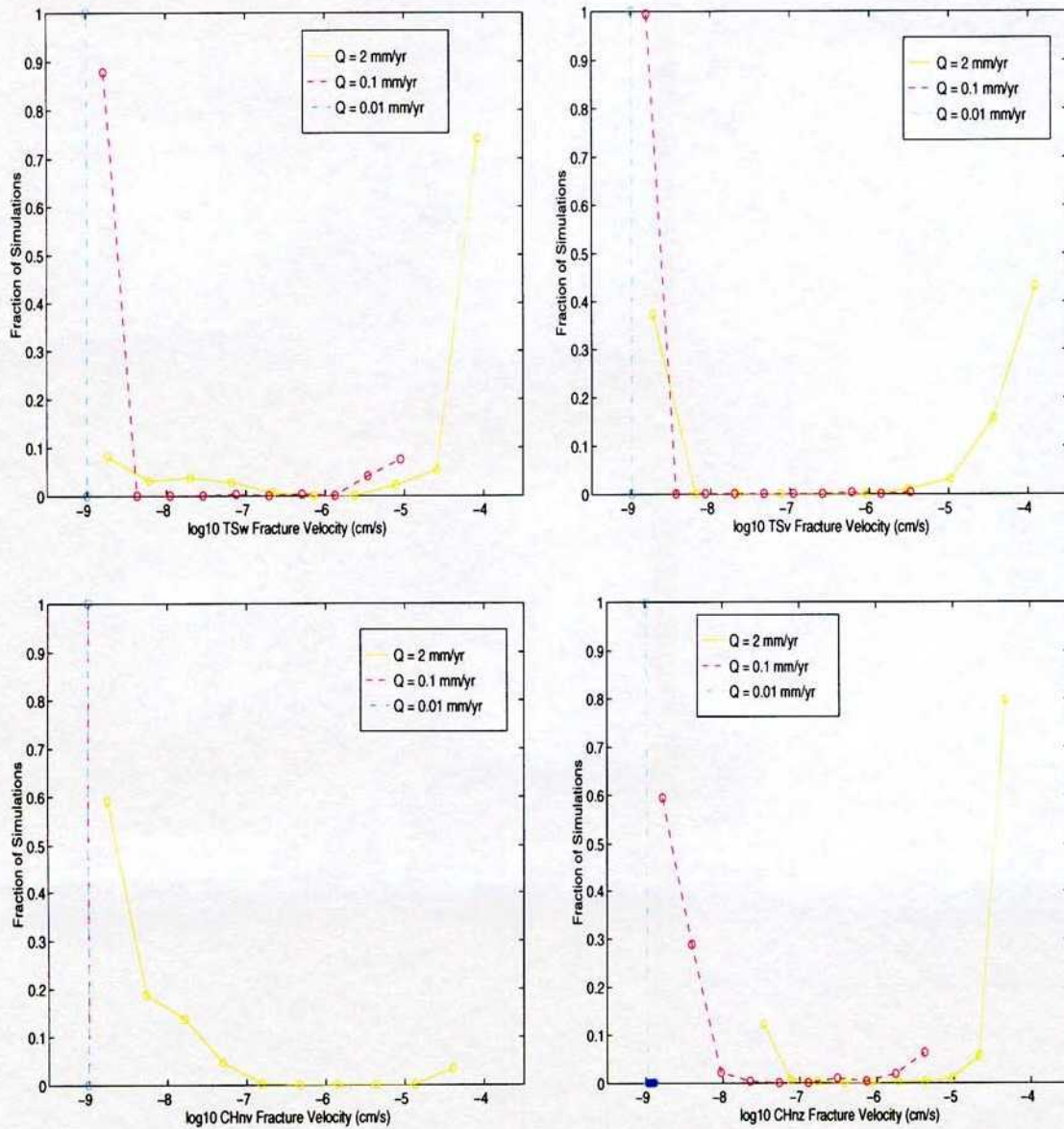
Figure 10-8: 4/5/96. Histogram of TSPA-95 fracture velocities for the classical ECM model in the (a) TSw, (b) TSv, (c) CHnv, and (d) CHnz layers.

terms of cumulative density functions (CDFs) for conservative-particle travel times. These plots confirm the conclusions I discussed in previous entries. The plots are generated using **tech_plots.m**, which further uses **calc_gwtt_stat.m** to plot curves from the simulations.

In general, the comparisons between the DOE and NRC approaches were well received by the DOE and gave the DOE staff some insight into the methods. The DOE staff did express surprise that the drift-scale approximations did not receive similar attention, however, as they believe that the drift-scale approximations are crucial to the predictions that the TSPA-code makes. In summary, the drift-scale analysis assumes that:

- The infiltration flux can be represented as a percolation flux that is lognormally distributed over the area of the column with a mean equal to a specified value and a standard deviation arbitrarily equal to 0.5,

- The matrix properties at the drift scale are also lognormally distributed based on Schenker et al. (1995) properties,

- The random percolation fluxes and matrix properties are independent,

- The matrix has fluxes up to the saturated conductivity,

- Any flux in the matrix diverts around the drift,

- Drip rates are equal to the flux in the fracture assuming that the flux in the fracture only occurs if the matrix does not have capacity for the flux,

- An arbitrary catchment area of four times the waste package is present, and

- Using the expected flux rate for every package results in approximately the same release rates that would occur from using the actual flux rate for each package.

Possible weak points in the discussion are:

- There is no justification for the standard deviation used in the percolation flux distribution,

- There is no consideration of correlation between matrix properties and local percolation flux,

- There is no consideration of lateral flow effects (all matrix flux must somehow cram around the drift),

- There is no consideration of dual permeability effects (local strengthening or weakening of the fracture flow),

- There is no explicit consideration of drip effects on package failure time, and

- There is no consideration of reduction in effective matrix flux area due to rewetting times for the matrix (after the cool-down period, presumably the matrix takes considerable time to re-wet, during which the interior of the matrix block is essentially unsaturated).

In addition, there is no consideration of the spatial distribution of the infiltration fluxes (each column has any spatial information completely washed out).

9/4/96 More thoughts on TSPA-95 detailed audit. $\boxed{\mathcal{SAS}}$

I discussed the impact of drips on package failure time with Sridhar today. The current thinking is that waste-package failure is due to a water film on the package, which can either occur due to drips or relative humidity. The TSPA-95 approach is to lump all of this behavior into a relative humidity term, with corrosion only starting when temperature drops below 100 °C and relative humidity is above a threshold (75 to 85 percent). The current EBSPAC approach is moving towards calculating chemistry at the drift wall based on the ECM model in Multiflo, and assuming that each drift has drips, so that drips may contact the package earlier than the 100 °C cutoff. Drip formation is not well established in this approach. ECM simulations performed by Peter Lichtner suggest that up to 100 ka are required to rewet the repository. Some sort of linkage between ECM and drip would be desirable according to Sridhar.

Based on the thoughts to date, we have promised to Rex Wescott that we would assess assumptions in TSPA-95 regarding:

- Independence of flux and permeability. The assessment of uncorrelated flux and permeability distributions will examine the impact of correlation in the calculations simply by repeating the analysis with correlated parameters.

- Variability of flux and permeability. The assessment will repeat the analysis with a range of standard deviations.

- Spatial dependency of infiltration flux. The assessment will repeat the analysis with the infiltration distribution explicitly carried through the analysis.

In addition, I would like to examine several related issues, but to be prudent these will not be promised.

- Impact of rewetting time on dripping fluxes. The idea is to examine how long it will take after the thermal pulse for the matrix to reach pre-pulse conditions. I suspect that fracture flow will dominate for at least tens of thousands of years.

- Impact of discrete-fracture flow on drips. With discrete fractures, it may be that matrix properties are relatively unimportant indicators of drip distributions.

The additional issues would require additional code development.

9/7/96 Drift-scale analysis.

One approach for a first cut at the drift-scale analysis include the following tasks:

- Get the TSPA-95 column outlines and the IPA-2 column outlines into UTM coordinates and assign DEM pixels to each column.

- Assemble software to create a PDF for q_{drip} given a PDF for K_{sat} and a value of q_{infil}.

- Create a table of q_{drip} PDFs as a function of average infiltration:

  - Scale a "standard" infiltration distribution to provide a desired average infiltration over YM at the repository level.
  - Adjust the distribution to accommodate intermediate processes (smoothing and/or focussing).
  - Assemble a PDF describing q_{drip} by examining the column pixel by pixel.
  - Repeat for remaining infiltration rates.

- Localize dripping fluxes to discrete locations relative to drifts.

- Calculate release rates for each of the models.

Several what-if scenarios can be examined relatively quickly using this basic format:

- Perfectly vertical fluxes.

- Lateral diffusion of vertical fluxes (i.e., Laplace smoothing).

- Localization of vertical fluxes (i.e., faulting/perching).

- Localization and subsequent lateral diffusion of vertical fluxes (i.e., faulting/perching then Laplace smoothing).

Very relevant extended analysis includes examining the effects of:

- Long-range impacts on fracture fluxes (i.e., fracture flow initiated above the drift level even though the drift level is highly permeable such as can happen in dual-permeability models).

- Time-dependent matrix saturation (i.e., cool-down rewetting fluxes).

My hunch is that fracture flow is strongly initiated but weakly dissipated. If so, the presence of a low-permeability TSw microstratum will initiate fracture flow that continues for extended distances downwards despite a more-permeable matrix. If so, q_{drip} at the repository will be less sensitive to K_{sat} at the repository than the TSPA-95 approach and instead will be an integral measure of the vertical distribution of the matrix properties. The point may have considerable impact on the analysis approach.

I also suspect that fracture flow will be much more prevalent during the cool-down period as the matrix slowly rewets. Although the thermal pulse may indeed strongly redistribute water in the matrix due to vapor transport during heating, I don't think this will be so active during cooling. If the matrix is relatively dry, then it cannot conduct water and any flux must be in the fractures. However, fracture flux must also be diverted to refill the matrix, so presumably there will be less overall flux at the repository.

9/8/96 Drift-scale analysis.

Assuming that the matrix hydraulic conductivity can be described using a lognormal PDF, as the TSPA-95 analysis does (Section 7.3 of TRW, 1995), an equivalent assumption is that $Y = \ln(K_{sat})$ is described by a normal distribution. The normal probability density function is described by

$$f_X(x) = \frac{1}{\sigma\sqrt{2\pi}} \exp\left[-\frac{1}{2}\left(\frac{x-\mu}{\sigma}\right)^2\right], \tag{10-8}$$

where x is the random variable, μ is the mean value of x, and σ is the standard deviation of x Benjamin and Cornell (1970). The standardized normal distribution is described by

$$f_U(u) = \frac{1}{\sqrt{2\pi}} \exp(-u^2/2), \tag{10-9}$$

$$u = \frac{x-\mu}{\sigma}, \tag{10-10}$$

so that

$$f_X(x) = \frac{1}{\sigma} f_U\left(\frac{x-\mu}{\sigma}\right).$$
(10-11)

The corresponding cumulative density function (CDF) is described by

$$\begin{aligned}
F_X(x) = P[X \le x] &= P\left[U \le \frac{x-\mu}{\sigma}\right] \\
&= F_U\left(\frac{x-\mu}{\sigma}\right) \\
&= \frac{1}{\sqrt{2\pi}} \int\limits_{-\infty}^{u} \exp(-u^2/2)\,\mathrm{d}u.
\end{aligned}$$
(10-12)

A related integral, the error function, is defined (Section 7.1.1 of Abramowitz and Stegun, 1972)

$$\mathrm{erf}(t) = \frac{2}{\sqrt{\pi}} \int\limits_{0}^{t} \exp(-t^2)\,\mathrm{d}t;$$
(10-13)

thus, for $u \ge 0$, Abramowitz and Stegun (1972) (Section 26.2.29) show

$$\mathrm{erf}(u) = 2F_U(u\sqrt{2}) - 1, \qquad \text{or equivalently}$$
(10-14)

$$F_U(u) = [\mathrm{erf}(u/\sqrt{2}) + 1]/2.$$
(10-15)

Note that $F_U(-u) = 1 - F_U(u)$ for a normal distribution, so that the limitations of having $u \ge 0$ for the error function can be overcome.

Equation 10-15 can be used to develop a *Matlab* function that provides a CDF for $q_{perc} - K_{sat}$ given a value for q_{drip}, since *Matlab* provides a function for the error function but not for the normal-distribution CDF. The idea is to discretize the range $0 \le q_{drip} \le \max(q_{perc})$ with a long vector (e.g., 1000 entries) for q_{drip}. For each pixel in the column, the values of K_{sat} that correspond to the q_{drip} vector entries can be determined and the CDF evaluated for those particular values. The CDF value corresponding to $q_{drip} = 0$ should be evaluated with $K_{sat} = q_{perc}$. The calculated CDF for each pixel should be normalized by the number of pixels that will be accumulated.

The outlined procedure can be used to develop a CDF equivalent to the TSPA-95 approach as well. Instead of providing an infiltration distribution equivalent to the distribution estimated from surface considerations, a distribution can be provided that is simply random noise about a mean value.

A difficulty comes when one assumes that insofar as there is observed spatial correlation in matrix properties, thus there may be some correlation between q_{perc} and K_{sat}. For example, lateral redistribution may result in higher q_{perc} in areas with high K_{sat} and lower q_{perc} in areas with low K_{sat}. If x and y are jointly normal distributions, then (Benjamin and Cornell, 1970)

$$\mu_{Y|X} = E[Y|X = x] = \mu_Y + \rho \frac{\sigma_Y}{\sigma_X}(x - \mu_X), \tag{10-16}$$

$$\sigma_{Y|X} = (1 - \rho^2)^{1/2}\sigma_Y, \tag{10-17}$$

where ρ is the correlation coefficient. For the case of jointly normal distributions, an estimate for the CDF can therefore be built up in a similar way as outlined previously, except that the q_{perc}s input as a set of pixel values adjust the mean and standard deviation of $\ln(K_{sat}$ for each pixel individually according to the value of ρ. Presumably correlation between K_{sat} and q_{perc} should be handled using the corresponding logarithms.

9/9/96 First drift-scale results.

I created several *Matlab* files in */home2/sierra/stothoff/Matlab/TSPA95Drift* to investigate the behavior of TSPA-95 assumptions on dripping fluxes. Two questions are easily investigated using the TSPA-95 or related approaches assuming that infiltration fluxes are randomly distributed: (i) what is the impact of correlation between q_{perc} and K_{sat}, and (ii) what is the impact of the standard deviation of q_{perc} and K_{sat}.

Two calculational approaches were investigated. The first approach directly calculates the CDF for $q_{perc} - K_{sat}$ for each entry of an input vector of q_{perc}, directly using the CDF for K_{sat} to calculate the CDF for specific values of q_{drip}. The direct approach results in apparently rather good estimates for the low range of q_{drip}, but is a little noisy at the upper end if there are not a lot of q_{prec} values in the vector. The second approach extends the TSPA-95 approach, estimating a CDF from long input vectors of random q_{perc} and K_{sat}. For the same computational effort, longer vectors can be used for the indirect approach, so the indirect approach results in nice upper tails but is questionable for small values of q_{drip}. The two methods appear to yield quite comparable results with reasonably long input vectors and correlations that aren't too big. There is significant disagreement between the $\rho = 1$ cases.

The few cases that I have run while experimenting with vector sizes and code testing are beginning to show some trends. The most consistent trend is the increasing probability of not exceeding fluxes that are larger than the mean q_{perc} as the correlation increases (i.e., large q_{drip}

is less likely as ρ increases). However, this does not mean that $E[q_{drip}|q_{perc} > K_{sat}]$ necessarily decreases.

Another trend that is worth examining is the probability of $q_{drip} > 0$ (i.e., the number of waste packages being dripped upon). Preliminary results indicate that for cases with the mean q_{perc} less than the mean K_{sat}, increasing ρ decreases the probability of $q_{drip} > 0$, while for the mean q_{perc} greater than the mean K_{sat}, increasing ρ increases the probability that $q_{drip} > 0$.

Finally, as the standard deviation of q_{perc} increases, there is a trend towards broader q_{drip}, and larger expected values of q_{drip}.

In the process of examining the data used for the TSPA-95 analyses, I cannot find direct links between Schenker et al. (1995) data and the TSPA-95 data. It appears that some uncited reanalysis of the data occurred, so that the mean values for TSw are 2.37×10^{-10} m/s for Schenker et al. (1995) and 2.0×10^{-11} m/s for TSPA-95. The Schenker et al. (1995) results do not have a standard deviation, but report a coefficient of variation; assuming that $CV = \sigma/|E[\log_{10}(K_{sat})]|$ yields the σ for TSw reported in TSPA-95.

9/10/96 Investigation of coding and sensitivity.

In order to test the software that will be used to estimate fluxes based on a surface distribution of annual-average infiltration, I continued comparing the two approaches for calculating the CDF for q_{drip}. I found some bugs in the *Matlab* code for the $\rho = 1$ case; now the two approaches match quite well for all values of ρ.

A representative set of parameters were decided on to examine the behavior of the assumptions carefully. It was assumed that μ_q/μ_k, σ_q/σ_k, and ρ were important determinants of behavior classes, so several sets of cases were run systematically varying these parameters. The preliminary observations were investigated more completely with the more-robust software.

Several points were verified.

- For all cases, the fraction of the area seeing $q_{drip} > 0$ increases with increasing ρ when $\mu_q > \mu_k$ and decreases with increasing ρ when $\mu_q > \mu_k$. In other words, as ρ increases, the area fraction moves further from 0.5.

- When $\mu_q = \mu_k$, the fraction of the area seeing $q_{drip} > 0$ is 0.5; this fraction increases as q_{perc} increases.

- When $\sigma_q \ll \sigma_k$, $E[q_{drip}]$ decreases with increasing ρ, regardless of the magnitude of q_{perc}, while when $\sigma_q \gg \sigma_k$, $E[q_{drip}]$ increases with increasing ρ if $\mu_q < \mu_k$ and decreases otherwise.

- As $|\mu_q - \mu_k| \to 0$, the impact of ρ becomes large, particularly as ρ approaches 1 or $|E[Q] - E[K]|$ becomes large.

- As σ_q/σ_k increases,

    - the fraction of the area seeing $q_{drip} > 0$ moves towards 0.5,

    - a broader range of $q_{drip} > 0$ occurs, and

    - $E[q_{drip}]$ increases.

An argument for correlation between K_{sat} and q_{perc} might be that the spatial structure for K_{sat} has high correlation lengths, so that lateral redistribution may take place. When $K_m \gg q_{perc}$, there would be positive correlation between K_m and q_{perc}. When $K_m \ll q_{perc}$, there may be negative correlation between K_m and q_{perc}, as there could be increased density of fracturing as welding increases concommitant with decreased matrix permeability. Behavior where K_m and q_{perc} are roughly the same order of magnitude is not apparent (no correlation?).

9/12/96 Further investigation of sensitivity.   ⟦𝒮𝒜𝒮⟧

I created two plots yesterday that showed the impact of ρ and σ_q/σ_k, respectively, on the dripping-flux CDF for ratios of $10^{E[\log_{10}(q_{perc})] - E[\log_{10}(K_m)]}$ ranging from 0.01 to 100. Gordon noticed that the expected values of q_{drip} seemed rather large compared to the expected values of q_{perc} that I was discussing. After some digging, I realized this was due to confusing the mean of the logs with the log of the mean.

The Schenker et al. (1995) data as used in TSPA-95 is provided in terms of base-10 logarithms. In order to convert from base-10 to natural logarithms, Section 4.1.22 in Abramowitz and Stegun (1972) states

$$\log_{10} z = \ln z / \ln 10 = \log_{10} e \ln z. \tag{10-18}$$

Also, on page 267 of Benjamin and Cornell (1970), the relationship between the log of the mean and the mean of the log is provided,

$$m_{\ln Y} = \ln m_Y - \frac{1}{2}\sigma_{\ln Y}^2. \tag{10-19}$$

Table 10-1: Behavior of dripping-flux CDF using the Schenker et al. (1995) TSw description and the base-case infiltration distribution estimate. $E[K] = 5.27$ mm/yr *[Note 10/28/96: $10^{E[Y]} = 0.62$ mm/yr, where $Y = \log_{10}(K)$, but $E[K] = 5.27$ mm/yr]* and $\sigma_{\log_{10} K} = 0.9$.

$E[q_{perc}]$ (mm/yr)	Laplace Passes	$\sigma_{\log q}/\sigma_{\log K}$	$E[q_{drip}]$ (mm/yr)	$E[f_{drip}]$
15.1	0	2.08	16.7	0.79
15.1	1	0.71	14.9	0.87
5.26	0	2.08	5.8	0.69
5.26	1	0.71	5.1	0.76
1.83	0	2.08	2.00	0.55
1.83	1	0.71	1.75	0.61

Based on 10-18 and the computational verification that $\mu[\ln(10^X)] = \ln(10)\mu(X)$ and $\sigma[\ln(10^X)] = \ln(10)\sigma(X)$, where X is a base-10 lognormal distributed random variable, we see that

$$\ln m_Y = \ln(10)\log(m_Y) = m_{\ln Y} + \frac{1}{2}\sigma_{\ln Y}^2$$

$$= \ln(10)m_{\log Y} + \frac{1}{2}(\ln(10)\sigma_{\log Y})^2; \tag{10-20}$$

$$\log m_Y = m_{\log Y} + \frac{1}{2}\ln(10)\sigma_{\log Y}^2. \tag{10-21}$$

These relationships allowed me to relabel the plots and send them off to Rex Wescott. The plots were generated using **show_CDF_set.m**.

As a followup, I created a base-case *AAI* distribution using the functions defined in my second paper on infiltration. Using this distribution, I created a CDF in just the same way as before. I also scaled this distribution by $(5.27/15.1)$ and $(5.27/15.1)^2$, to bracket the $E[K]$. The CDF for each flux case was created using the *AAI* distribution directly and a four-way Laplace-smoothed distribution. The statistics on these cases are shown in Table 10-1. The smoothing step crudely allows lateral redistribution, and lowers the standard deviation of q_{perc} by a factor of 2.7. Based on the previous results, lowering σ_q would be expected to greatly lower $E[q_{drip}]$ and decrease f_{drip} a fair amount. However, with the input *AAI* distribution, an extremely interesting behavior is observed, with $E[q_{drip}]$ decreasing only slightly and $E[f_{drip}]$ actually increasing significantly.

9/13/96 Thoughts on creating an IPA drip model. $\boxed{\mathcal{SAS}}$

The work over the last week has assumed that the statistics generated from a set of core samples could indeed be applied to describe processes that are appropriate for a continuum scale much

larger than the core samples. Calculating a dripping flux by subtracting K_m from q_{perc} is only reasonable on a scale where there are many fractures within an REV, and is essentially dependent on assuming that the ECM approach is valid. At the scale of the continuum, however, much of the variability in the matrix properties is lost due to averaging. Thus, one would presume that $\sigma_{\log_{10} K}$ should be significantly lower than the value previously used, 0.9. It should be straightforward to calculate $\sigma_{\log_{10} K}$ simply by creating random fields on a fine grid, using the statistical properties presented by Sandia and USGS workers, then averaging over appropriate volumes. In fact, there is probably a sill associated with the data; the sill value may be adequate for the purposes of using a more-representative value for $\sigma_{\log_{10} K}$. Istok et al. (1994) find that the variogram of both porosity and $\log(K_{sat})$ for the shardy base of the PTn can be modelled as a pure sill, at least for horizontal separation distances greater than 25 or 50 m. The vertical variogram was also fit with a pure-sill model; minimum separation distance is 0.02 of undefined units that I suppose are relative stratigraphic elevation (running 0 to roughly 30 m), suggesting 60 cm is minimum separation elevation.

The second difficulty with the approach is the assumption that the spatial distribution of q_{drip} is patchy, but still a continuum with a calculable saturation level. In fact, I would suspect that fractures flow either locally saturated or locally dry, with only a few fractures actually saturated. If this bimodal distribution is correct, flowing water only exists in a miniscule fraction of the area where $f_{drip} > 0$, although the flux is locally quite large. In turn, many waste packages that are nominally in the zone with $f_{drip} > 0$ will not be dripped upon at all if the localization is strong; the remaining would have fluxes much larger than $E[q_{drip}]$.

10/1/96 PDFs for matrix and fracture properties. $\boxed{\mathcal{SAS}}$

Yesterday I was tasked by Randy Manteufel and Bob Baca to provide PDFs for matrix and fracture permeabilities, porosities, and van Genuchten βs in layers involving UZ and SZ radionuclide transport for an IPA simulation to be run starting tomorrow. I have been gathering information on properties informally for the past few months, under the Ambient KTI, but have not looked at the lower layers in any detail.

A set of borehole samples, including locations, are available from the data set Gerry Stirewalt had George Rice assemble last year, totalling 582 saturated conductivity samples (14 boreholes) and 509 porosity samples (13 boreholes). The boreholes are identified in the data file but the data source attributions must come from George. The Schenker et al. (1995) data set used in TSPA-93 has information on all of the desired parameters, but it appears that: (i) the overlap between

any pair of data set sources is imperfect, (ii) the labeling between the Rice data set and IPA2 is not consistent, and (iii) the TSPA-93 and IPA2 stratigraphies do not perfectly correspond. The TSPA-93 stratigraphy includes a Topopah Spring vitrophyre layer and a Tram welded unit both missing in IPA2, while I assume that the Upper Crater Flat nonwelded unit in IPA2 is missing from TSPA-93 and the Middle Crater Flat nonwelded unit in IPA2 corresponds to the Bullfrog nonwelded unit.

A set of outcrop-sample information (Flint et al., 1996) postdating the previous analyses augments the data available. The samples provide a detailed picture of microlayering through the Topopah Springs unit, several samples of the Calico Hills zeolitized unit, two samples of the Prow Pass unit, and no samples from deeper units. The 10 Flint et al. (1996) Calico Hills zeolitized samples have a mean of 7.9×10^{-11} m/s as opposed to the mean of 1.93×10^{-10} m/s for the 51 samples presented by Schenker et al. (1995); the means are essentially identical. The 18 Flint et al. (1996) Topopah Springs samples have a mean of 1.2×10^{-10} m/s as opposed to the mean of 2.37×10^{-10} m/s for the 66 samples presented by Schenker et al. (1995); again the means are essentially identical. However, the outcrop information suggests that there may be stratigraphic variation, with two orders of magnitude change across microlayers, that is not accommodated in the lumped sampling.

Both TSPA-93 and IPA2 recognize that there are scale effects involved in going from core samples to field samples, which will tend to reduce the overall variance. The IPA2 approach to accommodating the scale effects appears to take 100 realizations of a 1D column with point locations spread 10 m apart (to represent uncorrelated values) and use a harmonic mean for each set of K_{sat} values. The TSPA-93 approach creates a scaled coefficient of variation based on the unit thickness and correlation length.

It appears to me that scaling parameters independently is dangerous, since in fact the parameters are correlated. Instead, a more satisfying approach would be to generate a set of 3D random fields of parameters and numerically perform flow simulations to build up the response from which the parameters can be estimated. The steady-state ODE approach Gordon and I have been investigating may be applicable here. However, this approach would take several weeks to get working. An intermediate approach would be to do this in 1D, which would be considerably faster to generate. The quick-and-dirty scheme is to reprise the IPA2 approach or TSPA-93 approach.

10/3/96 Estimated PDFs for matrix and fracture properties.   ⌐SAS⌐

Several tasks were undergone to estimate PDFs for material properties (i.e., matrix and fracture permeability, porosity, and van Genuchten β.

- The set of data sources were reviewed. TSPA-93 and Schenker et al. (1995) sources and tables are identical aside from a corrected bulk density table in Schenker et al. (1995). The IPA2, TSPA-93, and CNWRA Earthvision data sources are partly disjunct, with none of the 3 data sets being a subset of any other. The TSPA-93 data set is significantly larger than the others; the Earthvision data only consist of matrix K_{sat} and porosity.

- Problems are noticable with the lower matrix data, particularly the Bullfrog unit. The unit is purportedly welded, and the TSPA-93 set has plausible properties while the IPA2 set appears to have nonwelded and welded units flipped. However, the original data source (used by both TSPA-93 and IPA2) is consistent with IPA2 usage. Note that the Upper and Middle Crater Flat units are not found in TSPA-93, although the IPA2 Middle Crater Flat may correspond to the TSPA-93 Bullfrog nonwelded. I assume that the TSPA-93 data is more representative and that the two Crater Flat properties are the same. Further, I use the IPA2 thicknesses for the Prow Pass, Upper and Middle Crater Flat, and Bullfrog units.

- Fracture properties are of course problematic. I don't believe that fracture properties strongly affect flow in the UZ but may in the SZ. The IPA2 properties are as good as any, since the TSPA-93 properties are calculated not measured. It might be worthwhile to examine the data that the TSPA-93 analysis was based on, since only one borehole is the same and different methods were used to derive distributions. If the intent of the PA runs is to identify key parameters, then the TSPA-93 distributions may be better than the IPA2 distributions, since the IPA2 distributions have lots of constant values.

- I decided that using the TSPA-93 data set with the IPA2 scaling approach was adequate for providing averaged UZ matrix estimates. The IPA2 approach is equivalent to creating many columns, getting the average for the column, and subsequently averaging the column averages. For permeability, the columns used harmonic means (series solution) with arithmetic averaging of the column means (parallel solution). For porosity, arithmetic and arithmetic means were used directly for matrix and on the logs for fracture. For van Genuchten β, arithmetic and arithmetic means were used on the log of β. I used 10^4 columns to accumulate statistics.

- In the averaging, a vertical correlation length is required. Rautman and Flint (1992) address

Table 10-2: Estimated matrix K_{sat} values (m^2).

Layer	Thick	CV(log)	Low	Mean	High
TSw	min	0.0685	2.62e-20	3.66e-18	5.11e-16
TSw	mean	0.0527	2.69e-20	1.40e-18	7.29e-17
TSw	max	0.0454	2.89e-20	9.25e-19	2.96e-17
CHn	min	0.095	8.30e-19	2.39e-16	6.89e-14
CHn	mean	0.0807	7.20e-19	1.08e-16	1.61e-14
CHn	max	0.0803	7.44e-19	1.08e-16	1.58e-14
CHz	min	0.0591	1.27e-20	1.12e-18	9.83e-17
CHz	mean	0.0549	1.32e-20	8.76e-19	5.82e-17
CHz	max	0.0482	1.48e-20	6.20e-19	2.59e-17
PPw	IPA2	0.0825	1.00e-18	1.52e-16	2.30e-14
UCF	IPA2	0.0467	1.75e-17	2.77e-16	4.37e-15
BFw	IPA2	0.0356	1.75e-18	1.92e-17	2.11e-16
MCF	IPA2	0.0469	1.73e-17	2.77e-16	4.43e-15

this for the TCw, PTn, and TSw units. For all three units considered simultaneously, a correlation length of 30 m was found appropriate; considering the layers independently yielded a scatter of correlation lengths. I used 30 m; IPA2 used 10 m. The larger correlation yields more uncertainty (a wider range of values). For the Prow Pass unit, the correlation length is greater than the thickness so the sample statistics were used. I used the thicknesses considered in IPA2 for units lower than CHnz unit. The TSPA-93 approach did not scale the fracture properties, implying that the properties were considered formational properties, so that scaling was not performed here either.

All calculations were done with *Matlab*, in *$HOME2/IPA/TSPA95/Data*. Matrix calculations were done using **do_layer_sets.m**, which calls **codell_ave.m**. Fracture calculations were done using **do_frac_sets.m**. The calculated matrix and fracture properties are shown in Tables 10-2 through 10-7. K_{sat} is in m/s; porosity and van Genuchten β are dimensionless. The plus and minus 3 standard deviation values are given for the minimum, mean, and maximum layer thicknesses. Probably the mean thickness should be used (note that van Genuchten β must be greater than 1). Where other information is unavailable on layer thicknesses, the IPA2 thicknesses are used. K_{sat} and β should be lognormal, porosity normal or lognormal.

Table 10-3: Estimated matrix porosity values.

Layer	Thick	CV	Low	Mean	High
TSw	min	0.291	0.0175	0.139	0.261
TSw	mean	0.206	0.053	0.139	0.225
TSw	max	0.169	0.0688	0.139	0.21
CHn	min	0.19	0.142	0.33	0.517
CHn	mean	0.158	0.175	0.331	0.488
CHn	max	0.155	0.177	0.331	0.485
CHz	min	0.104	0.21	0.306	0.402
CHz	mean	0.0946	0.219	0.305	0.392
CHz	max	0.0795	0.233	0.306	0.379
PPw	IPA2	0.168	0.145	0.292	0.439
UCF	IPA2	0.137	0.153	0.261	0.368
BFw	IPA2	0.179	0.0763	0.165	0.254
MCF	IPA2	0.136	0.154	0.261	0.367

Table 10-4: Estimated matrix van Genuchten β values.

Layer	Thick	CV(log)	Low	Mean	High
TSw	min	0.346	0.979	1.78	3.23
TSw	mean	0.245	1.16	1.78	2.71
TSw	max	0.202	1.25	1.78	2.52
CHn	min	0.386	0.855	2.70	8.54
CHn	mean	0.317	1.05	2.72	7.05
CHn	max	0.316	1.05	2.72	7.01
CHz	min	0.255	1.14	1.74	2.65
CHz	mean	0.227	1.19	1.74	2.53
CHz	max	0.191	1.27	1.74	2.39
PPw	IPA2	0.223	1.92	7.12	26.5
UCF	IPA2	0.346	0.979	1.78	3.25
BFw	IPA2	0.155	1.87	3.21	5.53
MCF	IPA2	0.346	0.978	1.78	3.23

Table 10-5: Estimated fracture K_{sat} values (m^2) translated from TSPA-93.

Layer	CV(log)	Low	Mean	High
TSw	0.369	1.26e-10	1.62e-09	2.07e-08
CHn	0.398	7.67e-11	1.20e-09	1.87e-08
CHz	0.31	6.01e-11	5.11e-10	4.35e-09
PPw	0.438	5.43e-11	1.12e-09	2.30e-08
UCF	0.219	3.40e-11	1.54e-10	7.01e-10
BFw	0.331	4.42e-11	4.35e-10	4.28e-09
MCF	0.219	3.40e-11	1.54e-10	7.01e-10

Table 10-6: Estimated fracture porosity values translated from TSPA-93.

Layer	CV(log)	Low	Mean	High
TSw	0.19	0.000270	0.001000	0.00372
CHn	0.169	0.000114	0.000365	0.00117
CHz	0.151	6.64e-05	0.000188	0.000535
PPw	0.136	4.95e-05	0.000127	0.000324
UCF	0.105	2.30e-05	4.75e-05	9.82e-05
BFw	0.183	0.000147	0.000520	0.00184
MCF	0.105	2.30e-05	4.75e-05	9.82e-05

Table 10-7: Estimated fracture van Genuchten β values.

Layer	CV(log)	Low	Mean	High
TSw	0.155	1.45	4.23	12.3
CHn	0.155	1.45	4.23	12.3
CHz	0.155	1.45	4.23	12.3
PPw	0.155	1.46	4.25	12.4
UCF	0.155	1.46	4.25	12.4
BFw	0.155	1.46	4.25	12.4
MCF	0.155	1.46	4.25	12.4

Table 10-8: Estimated areal-average infiltration values.

Region	Number	Raw Pixels			Smoothed Pixels		
		q_{infil} (mm/yr)	$\log_{10}(q_{infil})$ (mm/yr)	$\sigma_{\log_{10}}(q_{infil})$ (mm/yr)	q_{infil} (mm/yr)	$\log_{10}(q_{infil})$ (mm/yr)	$\sigma_{\log_{10}}(q_{infil})$ (mm/yr)
1	488	20.22	1.047	0.968	20.37	1.280	0.175
2	452	18.91	1.064	0.897	18.91	1.249	0.173
3	795	21.58	0.851	1.494	21.57	1.231	0.528
4	729	18.09	1.040	0.906	18.03	1.223	0.190
5	888	20.76	0.790	1.467	20.77	1.181	0.581
6	745	19.56	1.038	0.962	19.53	1.262	0.178
All	4097	19.96	0.952	1.194	19.96	1.232	0.384

10/9/96 Estimated PDFs for infiltration. $\boxed{\textit{SAS}}$

Infiltration estimates are used in the TPA code to drive releases from the waste packages. New sets of IPA simulations are being generated to provide best-estimate CDFs with as much new information incorporated as possible. I was tasked by R. Manteufel to provide a PDF for infiltration as well as the material properties generated previously.

Yesterday I digitized the outline of 6 columns approximately equivalent to the 83 MTU/acre (high heat load) repository presented in TSPA-95, in order to estimate the infiltration over each column. The column numbering is based on Figure 3.8-3 in TSPA-95, starting in the north and numbering faster from west to east. Somewhat surprisingly, the 6 columns had quite similar estimates for spatially averaged q_{infil}, as shown in Table 10-8, which is derived from the base-case AAI map. I expect that other maps would have similar variability patterns, although the mean may shift around somewhat. The three easterly blocks (2, 4, 6) have roughly 90 percent as much infiltration as do the three westerly blocks (1, 3, 5). One pass of data smoothing, in which the value of each cell is replaced by the average of the four neighboring east, west, north, and south cells, significantly smooths the variability in the $\log_{10}$ parameters, thereby shifting the mean of the $\log_{10}$ values, but does not significantly change the arithmetic mean values. Data smoothing crudely represents redistribution underground.

The variability patterns for q_{infil} are probably not unreasonable. However, the absolute magnitude of areal-average q_{infil} is not yet pinned down. At the ACNW meeting on September 26 and 27, 1996, G. Bodvarsson went through the data sources and numbers that the DOE is

using, with the lowest numbers coming from saturation and moisture data in boreholes (slightly under 1 mm/yr). Other information includes fracture coatings and perched water data (perhaps 2 mm/yr), environmental isotopes (1 to more than 10 mm/yr), temperature data (5 to 10 mm/yr), and infiltration estimates (not defined well, but suggested to be 5 or 7 mm/yr). None of the estimates was well defined. My infiltration estimates are somewhat higher, as shown in Table 10-8. The more direct estimates tend to yield higher estimates than the indirect estimates.

Using 7 numbers as a basis for estimation (1, 2, 2, 4.5, 6, 7.5, and 20 mm/yr for boreholes, fracture coatings, perched water, isotopes, Flint infiltration estimates, temperature estimates, and Stothoff infiltration estimates, respectively), the mean and standard deviation are 6.1 and 6.5 mm/yr, respectively. The mean and standard deviation of the $\log_{10}$ values are 0.60 and 0.44, respectively (yielding the power of the mean being 4 mm/yr). Based on this set of information, my feeling is that an expected q_{infil} might be lognormally distributed. Simply using the mean and standard deviation of the logs yields the 1- and 3-standard-deviation ranges of 1.45 to 11 and 0.19 to 84 mm/yr, respectively. Similarly, using just the DOE numbers yields 3.05 mm/yr and 0.34 for median and standard deviation of the logs, with 1- and 3-standard-deviation ranges of 1.39 to 6.67 and 0.29 to 31.9 mm/yr, respectively.

10/21/96 Return to drift-scale audit review. $\boxed{\mathcal{SAS}}$

I have been doing some more thinking about the detailed audit review of the drift-scale modeling, in conjunction with Rex and Bob Baca. The current plan is to feed various waste-package flux distributions into either SOTEC or EBSPAC to get out the full distribution of the radionuclide mass outside the waste package as a function of time. SOTEC is the source module for IPA2, and according to Sitakanta would require some modification to get it to work for my purposes. EBSPAC is to be the source module for IPA3, is much more suitable for my purposes, but Sitakanta wants to continue testing the code before it is used. One or the other code will be available to me starting Friday, depending on the status of the EBSPAC testing.

Preliminary results from two EBSPAC simulations were given to me by Sitakanta. The two cases correspond to 0.03 and 30 mm/yr fluxes onto the WP area. Some of the radionuclides (^{129}I, ^{99}Tc, ^{14}C, and ^{94}Nb) are almost completely released with 0.03 mm/yr WP fluxes. The remaining radionuclides appear to be solubility limited, and when fluxes go up 3 orders of magnitude either are almost completely released or increase releases by about 3 orders of magnitude, whichever is smaller. The radionuclides with significantly less release than inventory at the higher flux rate include ^{79}Se, ^{230}Th, ^{234}U, ^{236}U, ^{238}U, ^{239}Pu, ^{240}Pu, ^{242}Pu, and ^{243}Am. The remaining 12 radionuclides have

at least 90 percent released for the higher flux rate. Thus, there should be three categories of release: (i) insensitive to dripping flux due to complete release (4 nuclides), (ii) variably sensitive to dripping flux (8 nuclides), and (iii) linearly sensitive to dripping flux (9 nuclides). Some of the variably sensitive radionuclides are apparently daughter products.

The previous work I did for the review concentrated on the issue of the appropriateness of the drift-scale flux approximations. As discussed in September entries, the ECM model was used by DOE to partition flux between matrix and fractures, with the matrix required to saturate before any fracture flow occurs. I looked at the assumptions for matrix and q_{perc} distributions used by DOE, and used my *AAI* distributions for another q_{perc} distribution. Since then, two more items occur to me to examine: (i) the satiation parameter used in the TSPA-95 column model, and (ii) the use of dual-permeability (DK) models for percolation. The satiation parameter is only a slight modification to the ECM model, so it is easy to incorporate in the analysis. The use of DK models starts to address the relative weighting between fracture and matrix flow.

The use of a DK model should have several characteristics:

- A tight coupling between matrix and fracture in the PTn,

- Various matrix-fracture interaction strengths in welded units,

- Variable depths of repository below PTn, and

- Reasonable correlation lengths for matrix properties.

I expect that the correlation structure of the PTn could provide a strong impact on matrix/fracture fluxes at the top of the TSw unit. When the TSw linkage is weak, the PTn influence will propagate far into the TSw due to the high vertical correlation for matrix properties (Rautman and Flint (1992) suggest that a variogram for the TSw porosity has $\gamma = 5 + 20$Sph(61), with lengths in meters). For comparison, the horizontal variogram for porosity is on the order of 100 to 200 m for most units, with the zeolitic tuffs of the Calico Hills unit on the order of 900 m (Rautman and Flint, 1992).

My (unverified) instinct is that DK models should never have more matrix flow than ECM models, thus should have at least as much fracture flow. The DK model could then be used to predict the satiation parameter in the ECM model at the drift level. PTn properties will partly determine the pressure at the PTn/TSw interface, which will in turn partly determine the partitioning between matrix and fracture at the top of the TSw. The TSw properties at the interface

and repository should be essentially independent when the repository is more than 60 m below the interface. Assuming that the PTn and the TSw properties are independent, which I believe is a quite reasonable assumption, the partitioning between matrix and fracture at the top of the TSw is only partly correlated to the TSw properties at the interface and are not correlated to TSw properties at the repository.

Thought experiments on the impact of using DK models to determine the satiation parameter:

- With weak coupling between matrix and fracture in the TSw, the satiation parameter is a function of the PTn properties, the matrix/fracture interaction in the TSw, and the TSw properties through the column.

- As the matrix/fracture coupling increases, the PTn influence decreases and the TSw influence increases. In the limit, the ECM is recovered (satiation approaches 1).

- As the matrix/fracture coupling decreases, the PTn influence increases and the TSw influence decreases. In the limit, the fracture flow is completely determined at the interface, although the partitioning depends on the entire column. Satiation is almost independent of TSw properties at the repository.

10/28/96 Documenting detailed review.

I had observed on 9/9/96 that there appeared to be a discrepancy or reanalysis of the TSw matrix saturated conductivity between Schenker et al. (1995) (i.e., Table 3-9a) and TSPA-95 (i.e., Table 2.4-3). Upon re-examination, the value of $E[K_{sat}]$ reported in Table 2.4-3 of TSPA-95 is the geometric mean rather than the arithmetic mean, and with this understanding the two documents are consistent.

10/30/96 Documenting detailed review.

Two efforts are proceeding simultaneously for my analysis of drift-scale flow and release: (i) the interaction between matrix and fracture as it impacts the drift scale, and (ii) the release of radionuclides as a function of dripping flux. The writeup for both analyses will be included as one entry.

Analysis for the first effort is reaching completion. I found that when changing the standard deviation for q_{perc}, it makes a large difference whether comparison of the PDF for q_{perc} and matrix permeability is performed with the same expected value or the same expected value for the log. In the first (more logical) case, I get very similar behavior for the TSPA-95 approach and parameters as I do for the same approach while using my moving-averaged AAI map for q_{perc}. Increasing the standard deviation lowers the mean of the log distribution so that f_{drip} decreases drastically. In the second case, the big shift is in expected dripping flux.

One final assumption that I should examine is that the drift forms a barrier to flow when the matrix is saturated. The capillary barrier should only form when the matrix is unsaturated.

10/30/96 Documenting detailed review.

I coded up a quick-look check of various conceptual models, including the seeps-when-saturated version of TSPA-95 and a very simple attempt to get a handle on the impact of DK models. The seeps-when-saturated version of TSPA-95 does not change f_{drip} in the slightest, but does slightly increase $E[q_{drip}]$. When $E[K_m]$ is two orders of magnitude greater than $E[q_{perc}]$, the increase in $E[q_{drip}]$ is less than a factor of two and is negligible when $E[q_{perc}]$ is two orders of magnitude greater than $E[K_m]$.

The simple DK approach hypothesizes two independent regions with identical matrix-property distributions. The dripping flux is a weighted sum of the fracture fluxes; the model might also take into account seepage. The primary impact of the model is to increase f_{drip} significantly but decrease $E[q_{drip}]$ slightly (no more than a factor of 2). It is easy to incorporate more than two regions, which would presumably move things in the consistent direction but have less of an overall impact.

1/3/97 Documenting detailed review.

This entry serves as partial documentation for the activities performed to date for the detailed review of TSPA-95 drift-scale assumptions. EPSPAC simulations were conducted using EBSPAC Release 1.0β, with the executable code stored in *$HOME2/IPA/EPBSPAC/Release1.0beta*. EBSPAC simulations took place in *$HOME2/IPA/EPBSPAC/TSPA95Drift*. Input files are exactly the same as the example input files in the EBSPAC Release 1.0β documentation (Mohanty et al., 1996), except that the input flux is varied. EBSPAC simulations were run from a *Matlab*

driver called **runRRset.m**, which created output files for a set of 21 flow rates from 10^{-3} to 10^3 mm/yr averaged over the area of a WP (10.25 m^2). The output file names have the flow rate, in mm/yr, appended as an identifier (e.g., **summary.out.1e-03** represents the summary file for the 10^{-3} mm/yr simulation).

The reference problem is identical to that documented in Chapter 5 of the EBSPAC technical description (Mohanty et al., 1996), except it is assumed that failure occurs immediately upon emplacement and various fluxes are considered to obtain radionuclide releases as a function of q_{drip}. The example represents an interior WP undergoing a thermal loading of 80 MTU/acre. For the purposes of the example, it is assumed that q_{drip} enters through a breach in the failed waste package, pools inside, and exits through a lower breach. The waste is assumed to slowly break apart, with the pieces falling into the pooled water and dissolving. It is assumed that no percolation fluxes occur until the drift-wall temperature drops below 100 °C, at which time q_{perc} is immediately re-established at the WP and the interior of the WP begins to be filled. For the example problem, the temperature drops below 100 °C at approximately 3180 yr. Accordingly, although immediate WP failure is specified, the example problem is valid for all WPs failing before 3180 yr after emplacement.

Post-processing on the set of EBSPAC simulations was performed using **make_ebsnef_mat.m** and **make_treleasel_mat.m** as driver routines. Each post-processing routine formatted a set of output files into one *Matlab* binary file, **ebsnef_out.mat** and **treleasel_out.mat**, respectively, which represent release rates and cumulative release. These binary files are used in all calculations translating fluxes into cumulative radionuclide release.

In **ebsnef_out.mat**, radionuclide release rates are stored for each 21 radionuclides, for each of 21 dripping fluxes, at each 100-yr time instant for 10 ky.

In **treleasel_out.mat**, cumulative radionuclide releases are stored for each 21 radionuclides, for each of 21 values of q_{drip}, at 195 time instants over 10 ky.

A series of plots were generated to examine the release rates, both as a function of time and as a function of q_{drip}. Creation of the plots was driven using **show_ebspac_result.m**. Release rates as a function of dripping flux, at 4, 6, 8, and 10 ky, for all 21 radionuclides, are shown in Figure 10-9. In Figure 10-10, radionuclide release rates as a function of time are shown for various values of q_{drip}.

There is no release from the WP if q_{drip} is 1 mm/yr. For some of the radionuclides, release rates drop sharply at 7 ky. The waste completes breakup at 7 ky, at which time all of the waste
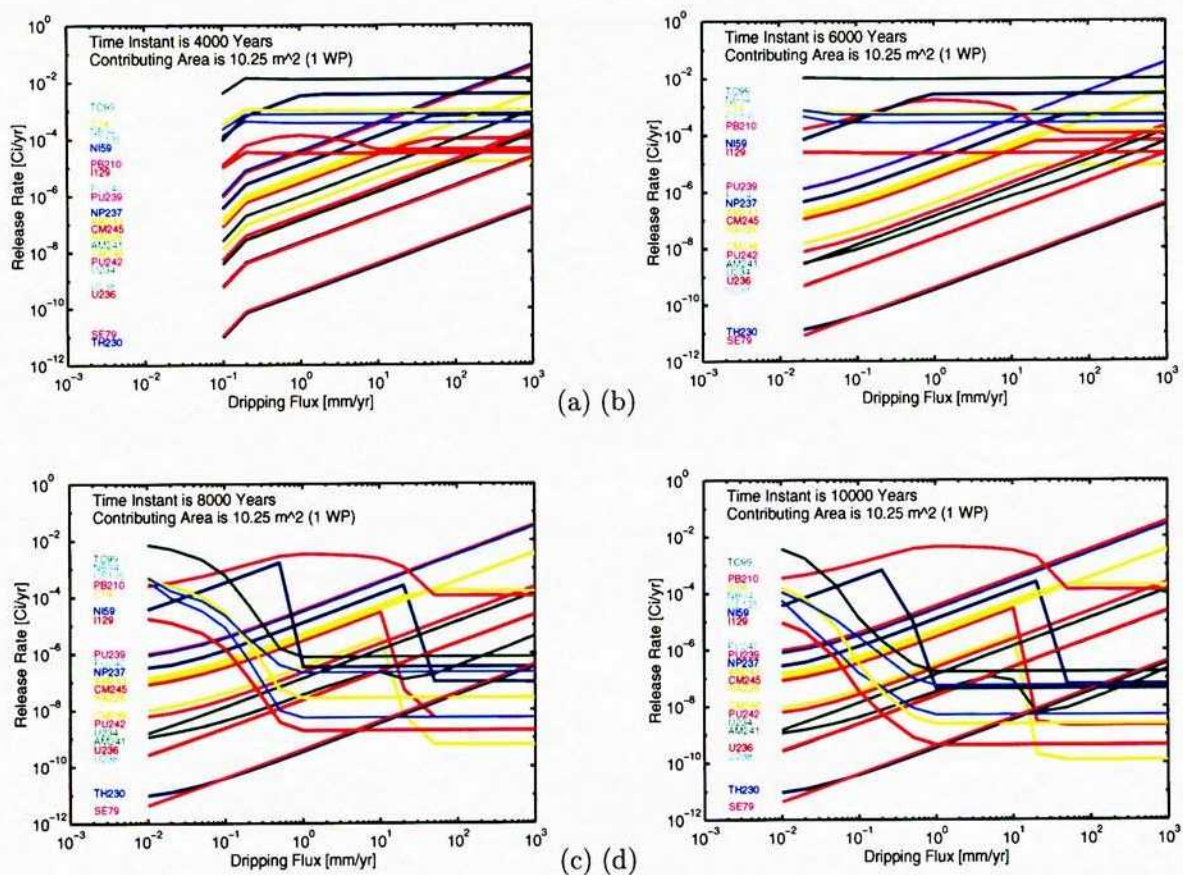
Figure 10-9: 1/3/97. Release rates for 21 radionuclides for EBSPAC nominal base case, as a function of dripping flux, at (a) 4 ky, (b) 6 ky, (c) 8 ky, and (d) 10 ky.

has fallen into the pool of water at the bottom of the WP. Until this time, there is a continuous source of fresh waste.

Two of the 21 radionuclides, ^{237}Np and ^{99}Tc, were selected as being representative of the release behavior of relatively long-lived radionuclides, having solubilities of 2.4×10^{-4} and 1, respectively. The expected release of the two radionuclides are presented in Figure 10-11 as a function of time for various values of $E[q_{drip}]$. The TSPA-95 calculational procedure was followed to generate the 133,000 realizations for K_m and q_{perc} used to construct Figure 10-11, using the same statistical values for K_m and q_{perc}, and using the same funnel factor of 4. However, cumulative radionuclide release was directly calculated for each realization, rather than calculating release using $E[q_{perc}]$.
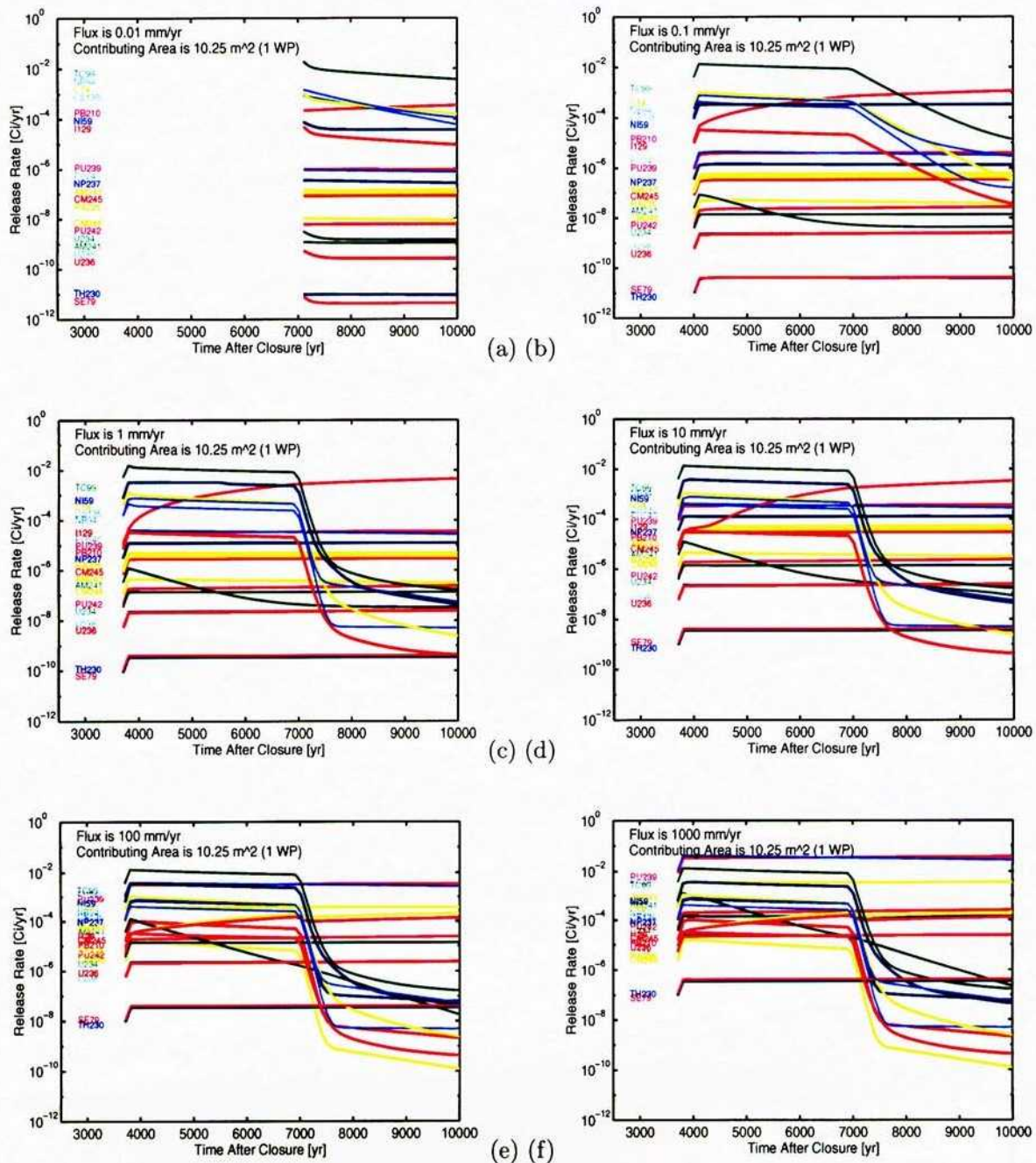
Figure 10-10: 1/3/97. Release rates for 21 radionuclides for EBSPAC nominal base case, as a function of time, for average dripping flux of (a) 10^{-2} mm/yr, (b) 10^{-1} mm/yr, (c) 10^0 mm/yr, (d) 10^1 mm/yr, (e) 10^2 mm/yr, and (f) 10^3 mm/yr.
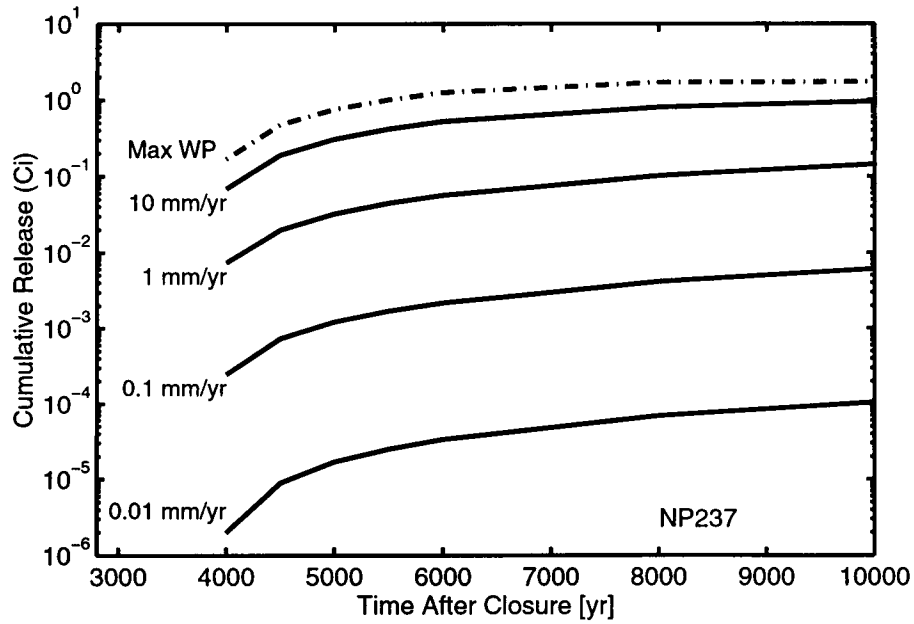
(a)
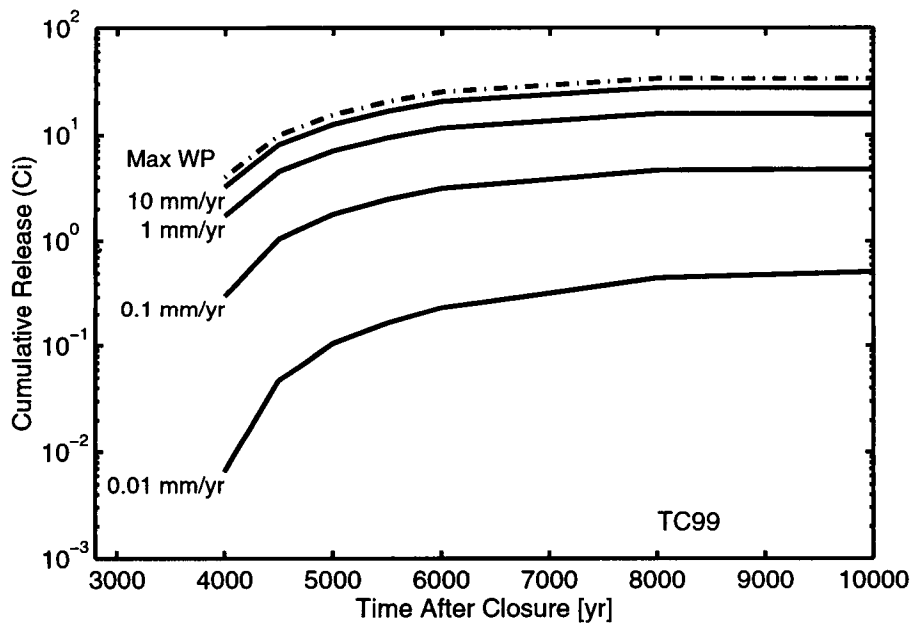
(b)

Figure 10-11: 1/3/97. Ratio of expected radionuclide release using the TSPA-95 procedure to the expected radionuclide release using direct calculation for (a) ^{237}Np and (b) ^{99}Tc.

Radionuclide release is proportional to $C_s q_{drip}$, where C_s is the solubility of the radionuclide, until the radionuclide is completely released from the WP. Based on Figure 10-11, [237]Np has a small enough value of C_s that expected radionuclide release is proportional to $C_s E[q_{perc}]$, at least for the lower part of the range of $E[q_{perc}]$, while ^{99}Tc has a large enough value of C_s that expected radionuclide release is relatively insensitive to $E[q_{perc}]$, especially for the higher part of the $E[q_{perc}]$ range. In both cases, releases are delayed for the lowest fluxes. As $E[q_{perc}]$ increases, more WPs are contacted by a sufficiently large q_{drip} that all of the radionuclide is released. Interestingly, using $E[q_{perc}]$ to calculate releases of [237]Np results in an overprediction of release for high $E[q_{perc}]$, as the significant fraction of WPs releasing all of the radionuclide is not accounted for; this overprediction also depends on the inventory of the radionuclide relative to the radionuclide solubility.

The TSPA-95 calculation of releases from the WP uses the expected value of q_{drip} for all WPs, $E[q_{drip}]$, to calculate an expected per-WP release. The expected per-WP release is then multiplied by the fraction of WPs that are contacted by drips. The TSPA-95 calculation should instead use the expected value of q_{drip} given that $q_{drip} > 0$, $E[q_{drip}|q_{drip} > 0]$, as WPs do not experience dripping when $q_{drip} = 0$. As $E[q_{drip}] < E[q_{drip}|q_{drip} > 0]$ whenever $f_{drip} < 1$, smaller releases will be predicted.

Two measures of computational accuracy are defined,

$$Y_1 = \log_{10} \{Q_r(E[q_{perc}])/E[Q_r]\} \tag{10-22}$$

$$Y_2 = \log_{10} \{Q_r(E[q_{drip}|q_{drip} > 0])/E[Q_r]\} \tag{10-23}$$

where Q_r is the cumulative release of the radionuclide. The impact of the two approaches to calculating releases is shown in Figure 10-12a and b, which show contour plots of Y_1 and Y_2, respectively, as a function of the ratio of $E[q_{perc}]$ to $E[K_m]$ and of time. The same simulations used in Figure 10-11 are used in Figure 10-12. The relatively low-solubility radionuclide, [237]Np, is shown in Figure 10-12. The relatively high-solubility radionuclide, ^{99}Tc, is not shown as releases are relatively less sensitive to the calculational approach.

As can be seen from Figure 10-12a, when $E[q_{drip}]$ is less than $E[K_m]$ release rates are underpredicted. For comparison, the lowest and highest values of $E[q_{perc}]$ considered in TSPA-95 are 0.01 and 2 mm/yr, respectively; these values correspond to a range of $E[q_{perc}]/E[K_m]$ of 0.002 to 0.4, respectively. For low fluxes and early times, releases can be underpredicted by an order of magnitude or greater. On the other hand, Figure 10-12b suggests that the correct formulation will slightly overpredict releases, and comparing the figures suggests that the two approaches yield equivalent releases for higher fluxes. Similar comparisons, not shown here, suggest that the calculational approach used in TSPA-95 decreases in conservativeness as the funnel factor
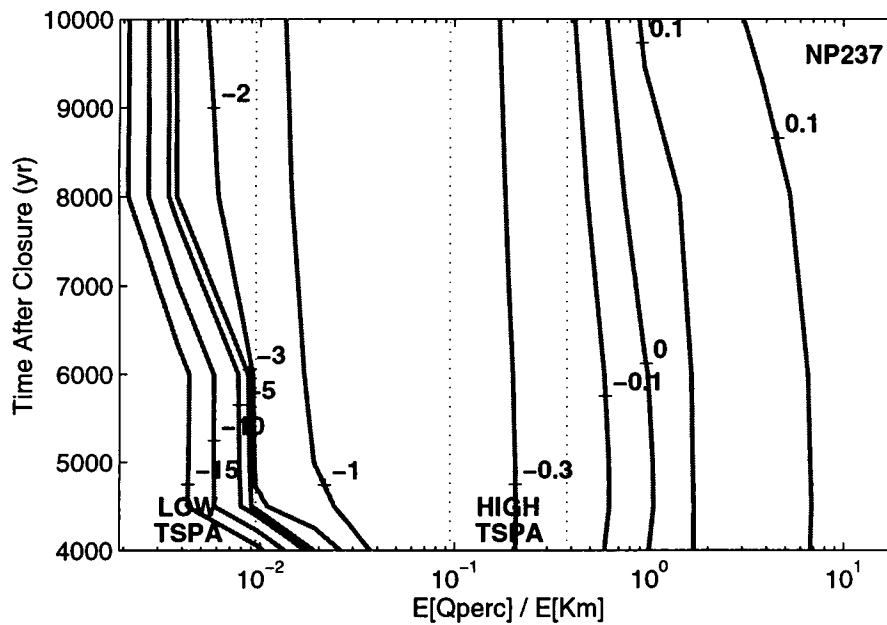
(a)
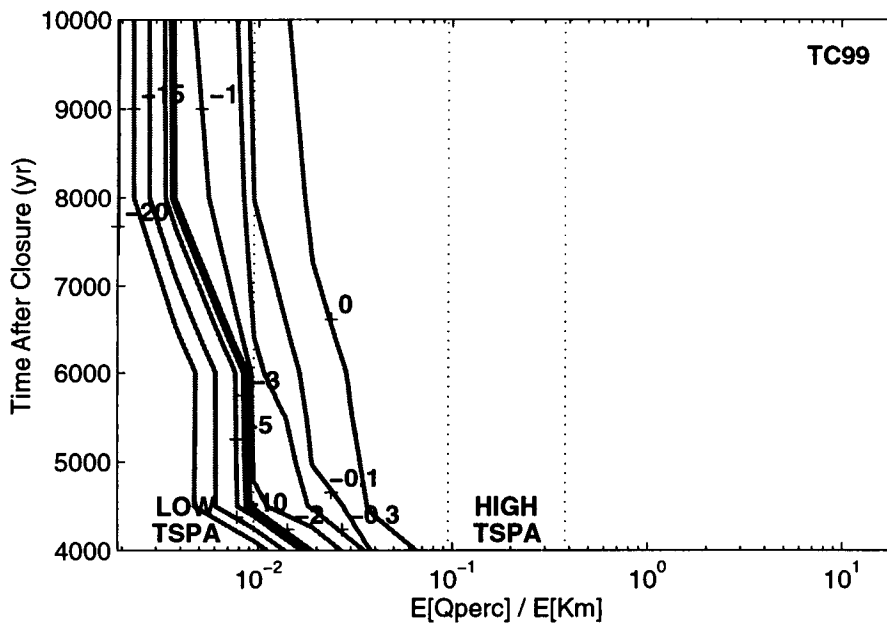
(b)

Figure 10-12: 1/3/97. Contour plot of ^{237}Np cumulative-release error, as a function of relative percolation flux and time since closure, for (a) the TSPA-95 approach (Y_1), and (b) the corrected approach (Y_2). *Correction dated 1/23/97: Part (b) is actually the Y_1 measure for ^{99}Tc. See entry dated 1/23/97 for referenced plot.* [signature]

decreases and as the standard deviation of q_{perc} increases.

For the simulations presented in TSPA-95, releases of all but the most soluble radionuclides are underpredicted by roughly a factor of two in the high-flux range and are underpredicted by roughly an order of magnitude in the low-flux range. Releases of the most soluble radionuclides are underpredicted by roughly and order of magnitude in the low-flux range but are slightly overpredicted in the high-flux range.

The dripping-flux model presented in TSPA-95 oversimplifies the behavior of moisture movement at the drift scale, with several features that are unsupported, questionable, or clearly nonconservative. For example, there is no justification presented in TSPA-95 for either the probability distribution for q_{perc} or the value picked for the standard deviation of flux. Presumably it can be argued that q_{perc} is somewhat controlled by K_m, through lateral redistribution, and therefore should have a similar probability distribution; however, the q_{perc} distribution might instead be dominated by the spatial distribution of infiltration if there is little lateral redistribution. As another example, the nonconservative assumption that there is no seepage into the drift from a saturated matrix is contradicted by evidence of low-temperature calcite and opal deposits inside lithophysae cavities. Nevertheless, the basic approach delineated in TSPA-95 provides a good framework to examine assumptions regarding drift-scale behavior.

A number of conceptual models based on the TSPA-95 model were constructed:

- The SDEV model varies one parameter in the TSPA-95 model, the standard deviation of q_{perc}, varying the parameter up and down by a factor of 2 from the TSPA-95 value while holding $E[q_{perc}]$ constant [2 abstractions].

- The CORR model is the same as the TSPA-95 model, but allowing K_m to be correlated to q_{perc}. As higher q_{perc} would presumably be associated with higher K_m for matrix-dominated cases and higher K_{bulk} for fracture-dominated situations, and assuming K_{bulk} is negatively correlated with K_m (higher fracture density in more densely-welded units), it is plausible to assume that q_{perc} is positively correlated to K_m when $q_{perc} < K_m$ and negatively correlated when $q_{perc} > K_m$.

- The AAI model replaces the distribution for q_{perc} with estimates for surface annual-average infiltration on 30 m x 30 m pixels, both with the raw estimate and a smoothed version qualitatively accounting for some degree of lateral redistribution from high flux to low flux [2 abstractions].

- The SITE model crudely accounts for fracture flow initiated above the repository, using the

TSPA-95 approach for 2 or 3 sites. For each realization, if $q_{perc} \geq K_m$ at the repository (1 site), the TSPA-95 approach is used. If $q_{perc} < K_m$, half of the fracture flux calculated for the site above the drift (site 2) is passed on as fracture flux to the drift and becomes q_{drip}. The same process is followed if there is a third site. Thus, there are multiple chances to initiate fracture flow in the SITE model [2 abstractions].

- The SEEP model is identical to the TSPA-95 model except that it is assumed that when the matrix is saturated, all matrix water enters the drift ($q_{drip} = q_{perc}$ when $q_{perc} > K_m$) [3 abstractions].

- The WEEP model represents an attempt to account for scale effects in fracture flow, and is somewhat similar to the weeps model used in TSPA-93 (Sandia National Laboratories, 1994). In the WEEP model, all q_{drip} for each set of 10, 100, or 1330 realizations is summed and assigned to one realization of each set, with the remaining realizations assigned zero fracture flow [3 abstractions].

- The SWEEP model is a combination of the SEEP and WEEP models, so that the matrix flow is assumed to seep into the drift for each realization that has $q_{perc} > K_m$, but the fracture flow is treated as with the WEEP model [3 abstractions].

In order to examine the impacts of the assumptions regarding q_{perc} on the predicted q_{drip} distributions, given the TSPA-95 probability density function for K_m, dimensionless curves are presented in Figure 10-13 to examine the probability of not exceeding particular values of q_{drip}. Each data point for a curve compares the corresponding value for q_{perc} against the cumulative probability that K_m is less than that value. Each q_{drip} curve is normalized by $E[K_{satiate}]$, where $K_{satiate}$ represents the satiated hydraulic conductivity as discussed in Section 7.2 of TSPA-95. Normalizing the curves allows one to examine the impact of a different mean $K_{satiate}$, assuming that the standard deviation of $\log_{10}(K_{satiate})$, or σ_Y [where $Y = \log_{10}(K_{satiate})$], does not change. Note that $Q = \log_{10}(q_{perc})$ in the figure. The figures were created by **show_CDF_set.m** in *$HOME2/Matlab/TSPA95Drift*.

Two pieces of information are extracted in the TSPA-95 report: (i) the fraction of packages with dripping (f_{drip}), and (ii) the expected value of dripping flux ($E[q_{drip}]$). In Figure 10-13, the intersection of a curve with the left axis is the probability that a package is dry; subtracting this value from 1 yields f_{drip}. The symbol on each curve denotes $E[q_{drip}]$.

The set of curves labelled *Delta* = 0 in Figure 10-13 represent the case where $E[K_{satiate}] = E[q_{perc}]$. If $E[K_{satiate}] = E[K_m] = 5$ mm/yr, the middle set of 3 curves represents $E[q_{perc}] = 5$
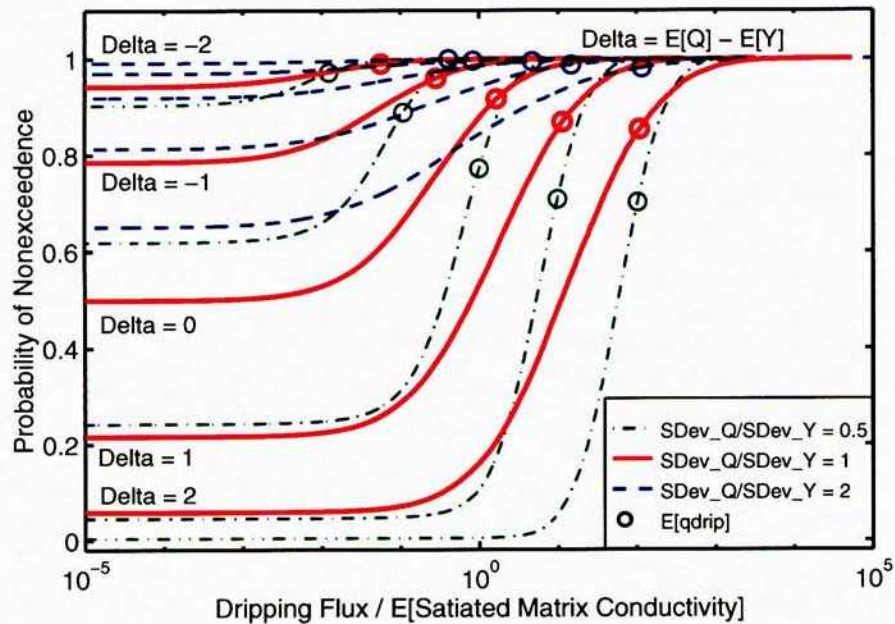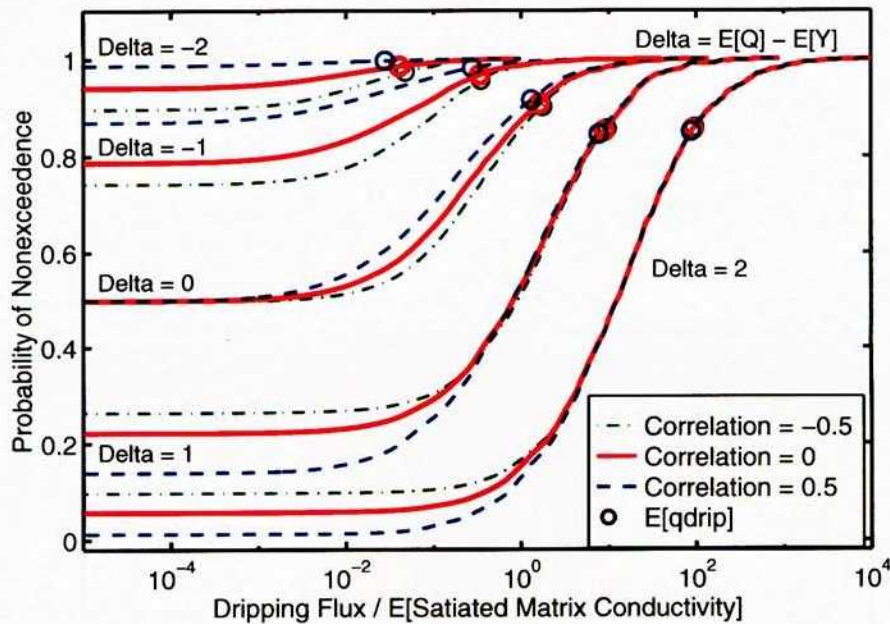
Figure 10-13: 1/3/97. Cumulative probability of not exceeding q_{drip} for various ratios of $E[q_{perc}]$ to $E[K_{satiate}]$ (Delta is the base-10 logarithm of the ratio), while varying (a) the standard deviation of $\log_{10}(q_{perc})$, and (b) the correlation between $\log_{10}(q_{perc})$ and $\log_{10}(K_{satiate})$.

mm/yr. The $Delta = 1$ set of curves might represent $E[K_{satiate}] = E[K_m] = 5$ mm/yr and $E[q_{perc}] = 50$ mm/yr, or it might represent $E[K_{satiate}] = 0.5$ mm/yr (i.e., the matrix saturation is low enough that relative permeability is 0.1) with $E[q_{perc}] = 5$ mm/yr. Changing from the $Delta = 0$ set to the $Delta = 1$ set increases the $E[q_{perc}]$ to $E[K_{satiate}]$ ratio by about an order of magnitude. Therefore, changing $E[q_{perc}]$ while holding $E[K_{satiate}]$ constant yields almost a one-to-one change in $E[q_{drip}]$; however, changing $E[K_{satiate}]$ while holding $E[q_{perc}]$ constant has minimal impact on $E[q_{drip}]$. The impact on f_{drip} is the same whether changing $E[q_{perc}]$ or $E[K_{satiate}]$ changes which curve set is considered.

Five sets of three curves are plotted in Figure 10-13a. Each of the five sets represents different ratios for $E[q_{perc}]$ to $E[K_{satiate}]$, ranging from $E[q_{perc}]/E[K_{satiate}] = 0.01$ to $E[q_{perc}]/E[K_{satiate}] = 100$ (i.e., $E[q_{perc}] = 0.05$ to 500 mm/yr when $E[K_{satiate}] = 5$ mm/yr or $E[q_{perc}] = 0.005$ to 50 mm/yr when $E[K_{satiate}] = 0.5$ mm/yr). Each of the three curves in a set represents different assumptions for the ratio of σ_Q to σ_Y, where σ_Q is the standard deviation of $\log_{10}(q_{perc})$ and σ_Y is the standard deviation of $\log_{10}(K_{satiate})$, and it is assumed that q_{perc} and $K_{satiate}$ are independent. The same five sets of curves are shown in Figure 10-13b, except that q_{perc} and $K_{satiate}$ are assumed to have a joint lognormal distribution; the correlation between q_{perc} and $K_{satiate}$ is varied and it is assumed that $\sigma_Q = \sigma_Y$.

Based on Figure 10-13a, both $E[q_{drip}]$ and f_{drip} can be significantly impacted by the assumptions for σ_Q. Increasing σ_Q tends to widen the probability distribution for q_{perc} and doubling σ_Q can increase $E[q_{drip}]$ by more than an order of magnitude. When $E[q_{perc}] < E[K_{satiate}]$, increasing σ_Q increases f_{drip}, more significantly for smaller values of $E[q_{perc}]$. On the other hand, when $E[q_{perc}] > E[K_{satiate}]$, increasing σ_Q decreases f_{drip}.

The assumptions for correlation between q_{perc} and $K_{satiate}$ have a minimal impact on $E[q_{drip}]$, as can be seen in Figure 10-13b. Correlation does have an impact on f_{drip}, however. When $E[q_{perc}]$ is less than $E[K_{satiate}]$, positive correlation decreases f_{drip}, and when $E[q_{perc}]$ is greater than $E[K_{satiate}]$, negative correlation decreases f_{drip}. Insofar as intuition suggests that there is likely to be positive correlation when $E[q_{perc}] < E[K_{satiate}]$ and negative correlation when $E[q_{perc}] > E[K_{satiate}]$, the assumption of independent distributions for q_{drip} and $K_{satiate}$ yields larger f_{drip} and is thus conservative.

The basis for the assumption that q_{perc} is lognormally distributed is not discussed in TSPA-95. One might point to a presumed impact of $K_{satiate}$ on redistribution of q_{perc}, and the observed lognormality of $K_{satiate}$, for this assumption. An approach for estimating q_{perc} variability that has not been explored propagates plausible patterns of q_{infil} to the repository level, with perhaps some

modification to account for local redistribution, to provide an estimate of the q_{perc} distribution. Estimated q_{infil} distributions have been developed by the NRC, based on mapped surface-property distributions (e.g., soil cover, slope, solar aspect) and shallow-infiltration simulations, to estimate q_{infil} independently for each 30 m by 30 m pixel of a digital elevation model (e.g., Stothoff and Bagtzoglou, 1996; Bagtzoglou et al., 1997). When flow is predominantly vertical, it is reasonable to assume that the spatial distribution of q_{infil} propagates down to the repository level with the spatial pattern essentially unchanged, perhaps with some redistribution from areas of high q_{infil} to areas of low q_{infil}.

Selecting a plausible q_{infil} distribution, which is generally typified by highest infiltration where soil cover is least, a 3 km EW by 4 km NS block centered on the repository was used to provide estimated q_{infil} for 13300 pixels. The estimated q_{infil} distribution was used directly for one estimate of the q_{perc} distribution. In order to estimate the impacts of subsurface redistribution from high-flux areas to low-flux areas, additional q_{perc} distributions were created by smoothing the q_{infil} distribution for each pixel by using the average of the 9 pixels centered on the pixel. Two distributions were created, by performing the smoothing once and twice, respectively. Finally, assuming that the q_{infil} magnitudes are questionable but that relative magnitudes may be better determined, the estimated q_{perc} values were normalized by multiples of $E[K_{satiate}]$, providing analogs for the sets of curves in Figure 10-13. The plot and associated calculations are driven from **show_YMaai_CDF.m** in *$HOME2/Matlab/TSPA95Drift*.

The cases presented in Figure 10-14 are quite comparable to those in Figure 10-13b, as the ratio of σ_Q to σ_Y is 1.9 for the unsmoothed case and 0.34 for the doubly smoothed case. As with the TSPA-95 distribution for q_{perc}, $E[q_{drip}]$ decreases as $E[q_{perc}]$ decreases for the q_{infil} distribution for q_{perc}. Smoothing does not have a large impact on $E[q_{drip}]$ and only a relatively small impact on f_{drip}. However, $E[q_{perc}]$ is one to two orders of magnitude greater than the TSPA-95 predictions for all values of q_{infil} considered, and f_{drip} is also significantly greater except for the highest values of q_{infil}.

Using **test_drip_model.m** in *$HOME2/Matlab/TSPA95Drift*, the SITE and SEEP cases are shown in Figure 10-15. For each curve, 10^4 realizations are employed, and a range of q_{perc} standard deviations are examined. For a given $E[q_{perc}]$, as σ_Q increases the median value of q_{perc} decreases; therefore, as σ_Q increases, only the high tail of the q_{perc} distribution results in a realization having positive q_{drip}. Essentially no realizations yield positive q_{drip} with σ_Q only a few times larger than σ_Y.

Sixteen abstractions of dripping-flux generation were created from the six conceptual models

Figure 10-14: 1/3/97. Cumulative probability of not exceeding q_{drip} for various ratios of $E[q_{perc}]$ to $E[K_{satiate}]$, scaling a surface-based AAI map to provide a q_{perc} distribution, while varying the nine-way smoothing of q_{perc}.

and the TSPA-95 model by varying parameters within the conceptual model. The impact of various q_{drip} model assumptions are examined by generating 13,300 realizations for K_m, q_{perc}, and any other quantities required for an abstraction. For each realization, q_{drip} is calculated using each abstraction model; f_{drip} and $E[q_{perc}]$ are directly calculated from the set of realizations using the TSPA-95 process. The abstractions were each subjected to a range of $E[q_{perc}]$ and funnel factor to examine the sensitivity to these parameters. A funnel factor larger than 1 corresponds to a focusing of flow towards the drift, while a funnel factor less than 1 corresponds to a diversion of flow away from the drift.
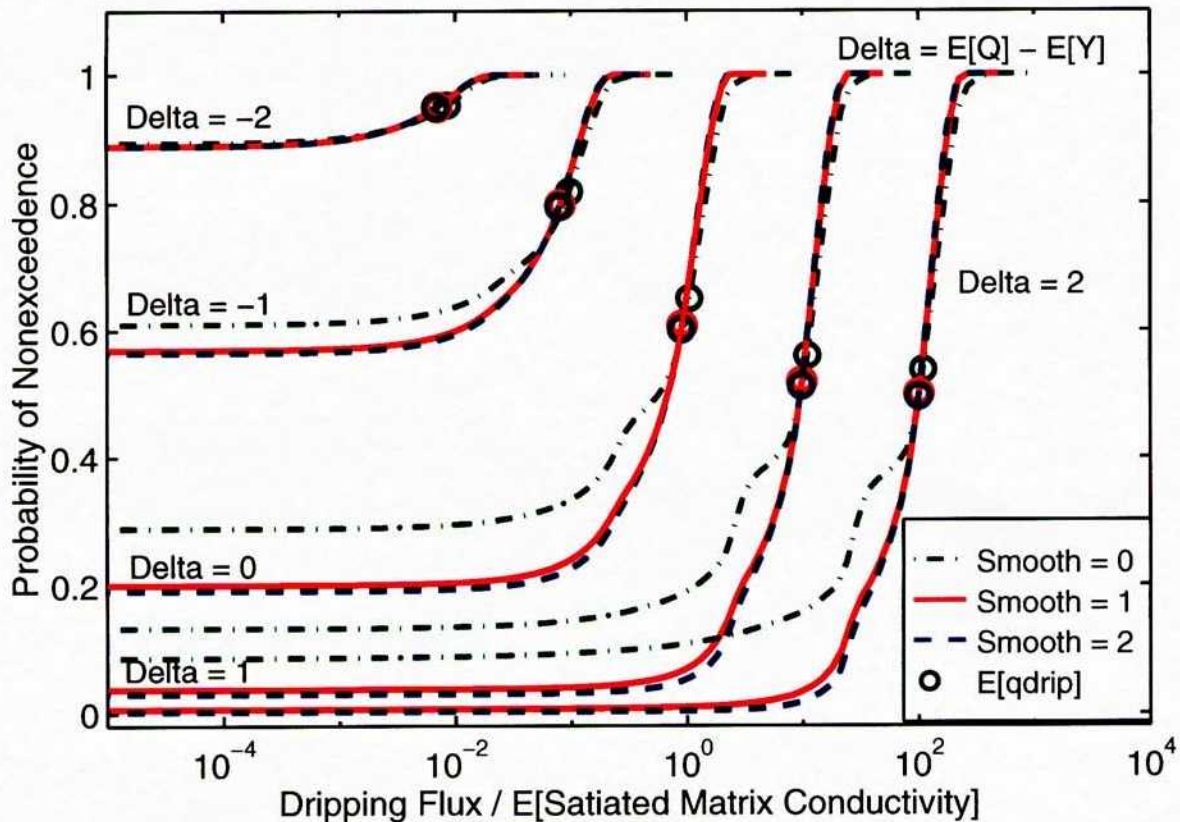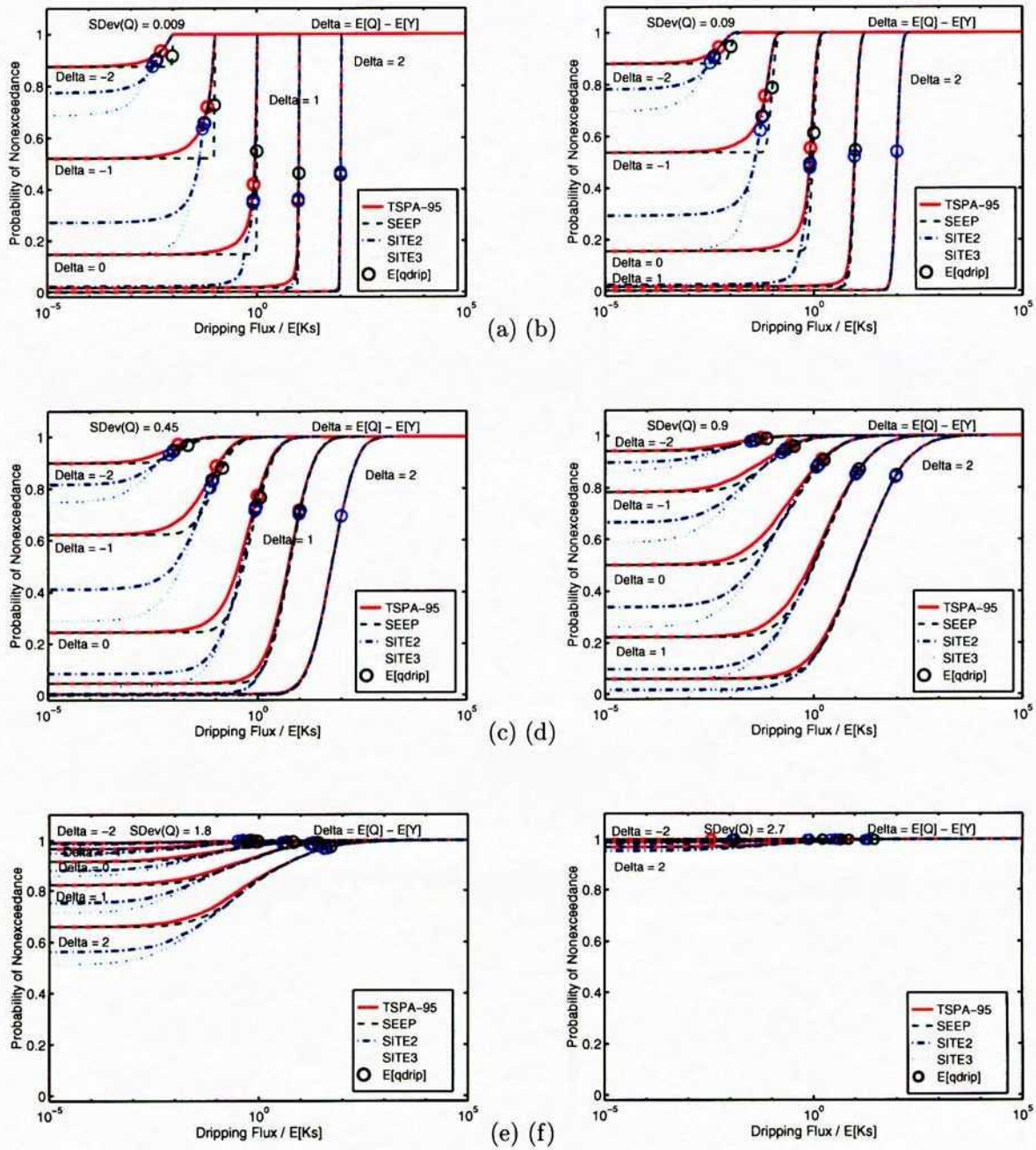
Figure 10-15: 1/3/97. Cumulative probability of not exceeding q_{drip} for various ratios of $E[q_{perc}]$ to $E[K_{satiate}]$, using the SEEP and SITE models, for a ratio of the standard deviation of $\log_{10}(q_{perc})$ to the standard deviation of $\log_{10}(K_{satiate})$ of (a) 0.01, (b) 0.1, (c) 0.5, (d) 1, (e) 2, and (f) 3.

The base-10 logarithm of the expected cumulative release of ^{99}Tc and ^{237}Np after 10 ky is contoured in Figure 10-16a and b, respectively, for all abstractions except for the WEEP and SWEEP models. In Figure 10-16c and d, corresponding WEEP and SWEEP model predictions are contoured, where cases with 10, 100, and 1330 realizations summed into one fracture flow realization in a WEEP or SWEEP set are denoted using dashed, dash-dot, and dotted lines, respectively, and the WEEP predictions are shown in gray. As a reference in each plot, the model predictions obtained using TSPA-95 assumptions are shown as a heavy line. For any particular contour level, abstractions resulting in contours to the left of the TSPA-95 model are more conservative. In general, the SITE and SEEP models are slightly more conservative than the TSPA-95 model. At low values of $E[q_{perc}]$, the AAI model is also more conservative than the TSPA-95 model, as is the SDEV model as the q_{perc} standard deviation decreases. However, the predictions of the various abstractions in Figure 10-16a and b are qualitatively quite similar. All plots were created using **show_detail_tspa.m** in *$HOME2/Matlab/TSPA95Drift* as a driver. *Matlab* files called by **show_detail_tspa.m** include **show_DScontours.m** and **do_Drip_contour.m**.

Very different predictions are obtained using the WEEP model, where each order of magnitude increase in the number of drifts required to contact one dripping fracture results in an order of magnitude decrease in the maximum cumulative radionuclide release, despite the same value of $E[q_{drip}]$. Each WP contacted by a fracture releases essentially all of the radionuclide in the WP, so that reducing the number of WPs that are contacted reduces the releases proportionately. The SWEEP model is more conservative than the TSPA-95 model at low $E[q_{perc}]$ but the localized fracture drips yield less-conservative predictions for high $E[q_{perc}]$. There is little or no difference between SWEEP model predictions for cases that have fracture flow for 100 or 1330 realizations summed into one realization, suggesting that seepage in cases with a saturated matrix could strongly impact release rates even with highly localized fracture flows.

The impact of the funnel factor can easily be assessed from Figure 10-16. The funnel factor has a strong impact on releases of low-solubility radionuclides and high-solubility radionuclides at low flows. On the other hand, releases are quite insensitive to the funnel factor for flow rates that are large enough to create rate-limited releases (i.e., high-solubility radionuclides at high $E[q_{perc}]$).

1/23/97 Updated documentation of detailed review. $\boxed{\mathcal{SAS}}$

Figure 10-12(b) had the incorrect plot to go with the caption for the 1/3/97 entry. The correct plot for Figure 10-12(b) is shown as Figure 10-17(a), generated using **show_DSrelcont('BASE', 'NP237', [], 1, 1)**. Figure 10-17(b) shows the error measures Y_1 and Y_2 for both ^{237}Np and
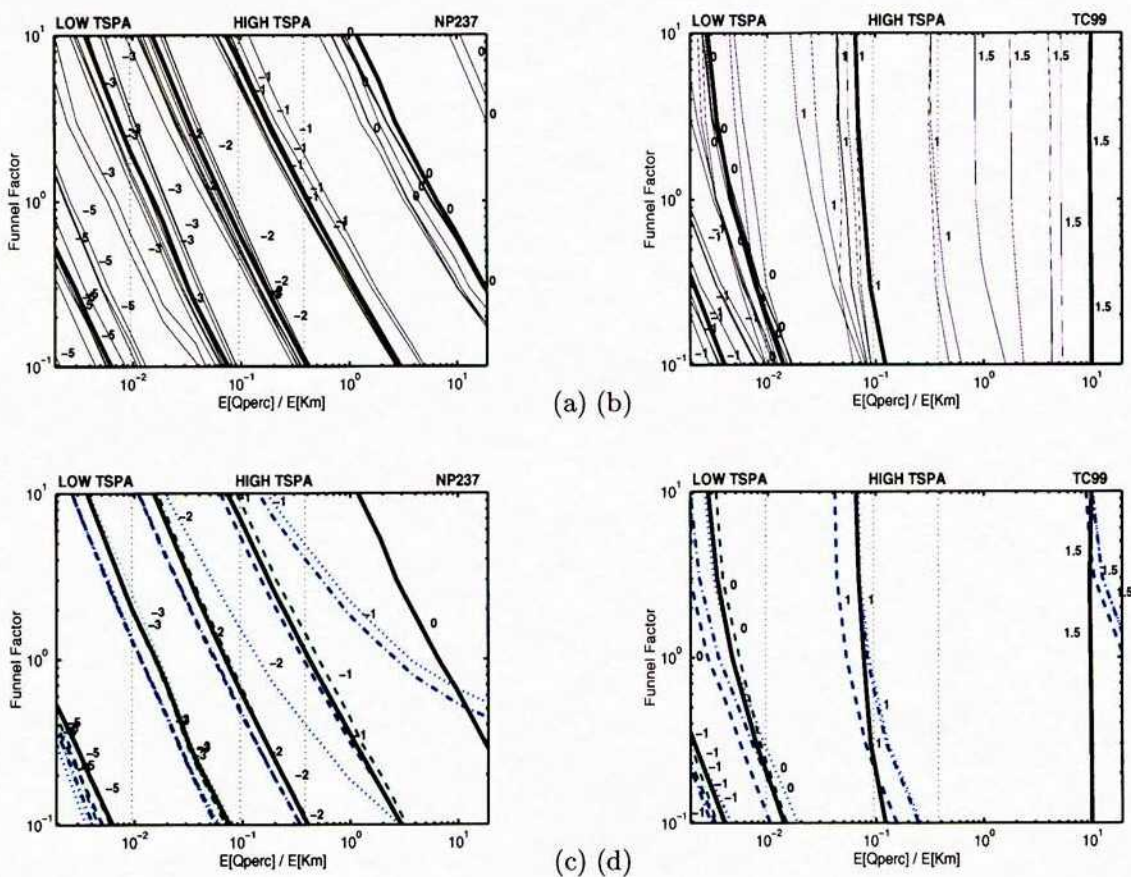
Figure 10-16: 1/3/97. Contours of the base-10 logarithm of expected cumulative release after 10 ky, as a function of relative percolation flux and funnel factor, for (a) ^{237}Np using the SDEV, AAI, SITE, and SEEP models, (b) ^{99}Tc using the SDEV, AAI, SITE, and SEEP models, (c) ^{237}Np using the WEEP and SWEEP models, and (d) ^{99}Tc using the WEEP and SWEEP models.

^{99}Tc at 10 ky; these are contoured as a function of time in Figure 10-12 and Figure 10-17(a). Figure 10-17(b) was generated using **show_DSrelcurve('Detail', [], 10000, 1)**.

1/27/97 WEEP and SWEEP CDF figures.

Using **show_CDF_snweeps.m** in **$HOME2/Matlab/TSPA95Drift**, cumulative density functions of dripping flux for the WEEP and SWEEP cases are shown in Figure 10-18. For each curve, 10^4 realizations are employed, and a range of $E[q_{perc}]$ values are examined. The standard deviation
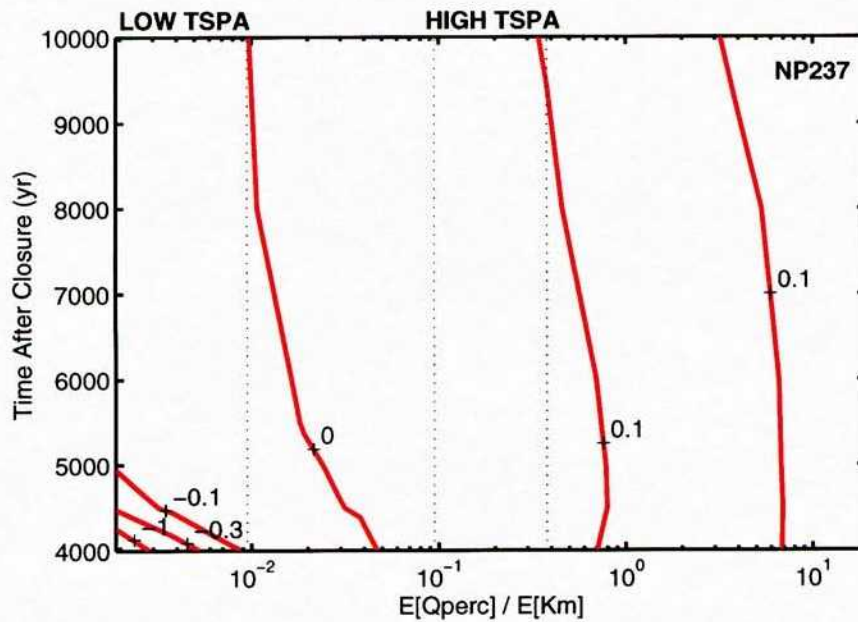
(a)
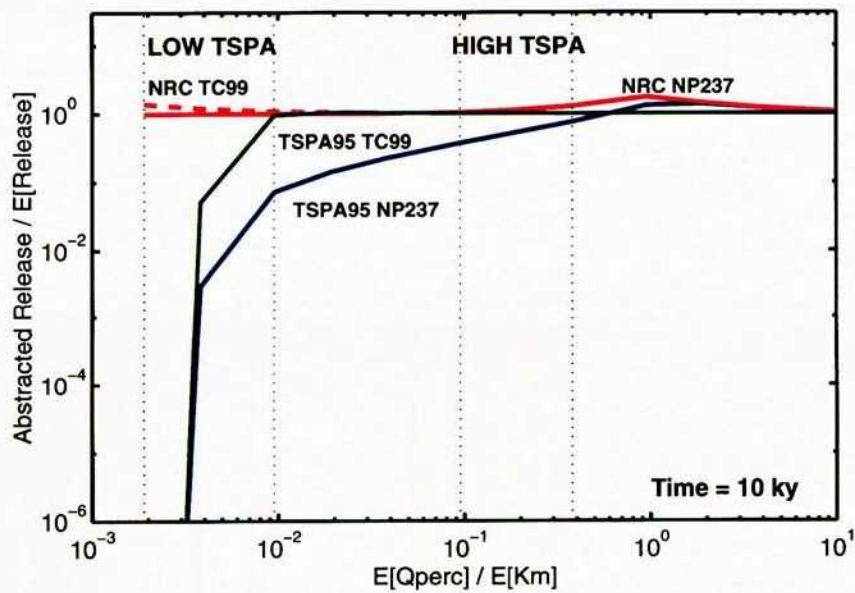
(b)

Figure 10-17: 1/23/97. (a) Contour plot of ^{237}Np cumulative-release error (Y_2), as a function of relative percolation flux and time since closure, and (b) Y_1 and Y_2 for both ^{237}Np and ^{99}Tc at 10 ky.

for q_{perc} is equal to σ_Y in all cases. The localization parameter is 10, 100, and 1000 for both the WEEP and SWEEP cases.
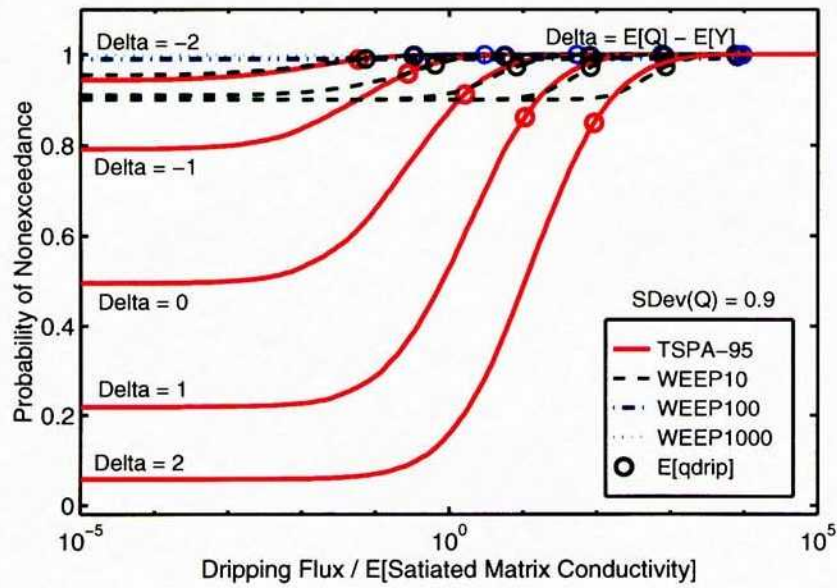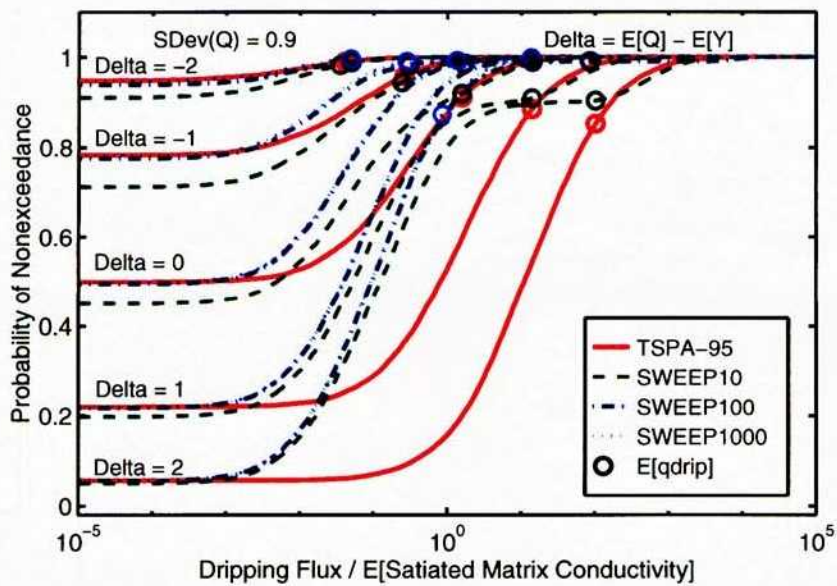
Figure 10-18: 1/27/97. Cumulative probability of not exceeding q_{drip} for various ratios of $E[q_{perc}]$ to $E[K_{satiate}]$, with a ratio of the standard deviation of $\log_{10}(q_{perc})$ to the standard deviation of $\log_{10}(K_{satiate})$ of 1, using (a) the WEEP and (b) the SWEEP model.

References

Abramowitz, M. and I. A. Stegun. 1972. *Handbook of Mathematical Functions*. New York, NY: Dover Publications, Inc.

Bagtzoglou, A. C., N. M. Coleman, E. C. Pearcy, S. A. Stothoff, and G. W. Wittmeyer. 1997. Unsaturated and Saturated Flow Under Isothermal Conditions. In B. Sagar (Ed.), *NRC High-Level Radioactive Waste Program FY96 Annual Progress Report*, Volume NUREG/CR-6513, No. 1, Washington, DC, pp. 10–1–10–28. Nuclear Regulatory Commission.

Benjamin, J. R. and C. A. Cornell. 1970. *Probability, Statistics, and Decision for Civil Engineers*. New York, NY: McGraw-Hill.

Flint, L. E., A. L. Flint, C. A. Rautman, and J. D. Istok. 1996. *Physical and Hydrologic Properties of Rock Outcrop Samples at Yucca Mountain, Nevada*. Open-File Report 95-280, United States Geological Survey, Denver, CO.

Istok, J. D., C. A. Rautman, L. E. Flint, and A. L. Flint. 1994. Spatial Variability in Hydrologic Properties of a Volcanic Tuff. *Ground Water 32*(5), 751–760.

Klavetter, E. A. and R. R. Peters. 1986. *Estimation of Hydrologic Properties of An Unsaturated, Fractured Rock Mass*. SAND84-2642, Sandia National Laboratories, Albuquerque, NM.

Leverett, M. C. 1941. Capillary Behavior in Porous Solids. *Transactions of the AIME 142*, 152–169.

Mohanty, S., G. A. Cragnolino, T. Ahn, D. S. Dunn, P. C. Lichtner, R. D. Manteufel, and N. Sridhar. 1996. *Engineered Barrier System Performance Assessment Code: EBSPAC Version 1.0 β, Technical Description and User's Manual*. CNWRA 96-011, Center for Nuclear Waste Regulatory Analyses, San Antonio, TX.

Rautman, C. A. and A. L. Flint. 1992. *Deterministic Geologic Processes and Stochastic Modeling*. SAND91-1925C, Sandia National Laboratories, Albuquerque, NM.

Sandia National Laboratories. 1994. *Total-System Performance Assessment for Yucca Mountain—SNL Second Iteration (TSPA-1993)*. SAND93-2675, Sandia National Laboratories, Albuquerque, NM.

Schenker, A. R., D. C. Guerin, T. H. Robey, C. A. Rautman, and R. W. Barnard. 1995. *Stochastic Hydrogeologic Units and Hydrogeologic Properties Development for Total-System Performance Assessments*. SAND94-0244, Sandia National Laboratories, Albuquerque, NM.

Stothoff, S. A. and A. C. Bagtzoglou. 1996. Subregional Hydrogeologic Flow and Transport Processes. In B. Sagar (Ed.), *NRC High-Level Radioactive Waste Research at CNWRA, July–*

December 1995, Volume CNWRA 95-02S, San Antonio, TX, pp. 9–1–9–20. Center for Nuclear Waste Regulatory Analyses.

TRW. 1995. *Total System Performance Assessment–1995: An Evaluation of the Potential Yucca Mountain Repository.* B00000000-01717-2200-00136, TRW Environmental Safety Systems Inc., Las Vegas, NV.

Xiang, Y., S. Mishra, and B. Dunlap. 1995. *Hydrologic Sensitivity Analysis for the Unsaturated Zone at Yucca Mountain, Nevada.* BAAAF00000-01717-0200-00008, Rev. 00, TRW Environmental Safety Systems Inc., Las Vegas, NV.

11   Iterative Performance KTI - Total Performance Assessment Phase 3

Account Number: **20-5708-761**
Collaborators: **Robert Baca**
Directories: **$HOME2/Matlab/TPA3, $HOME2/IPA/Phase3, as noted**

Objective: Providing input and analyses for Total Performance Assessment (TPA) Phase 3 exercises. The emphasis under this project is on abstracting detailed process-level simulations into forms that are more amenable to performance assessment needs (e.g., probability distributions).

1/10/97 Software requirements for UZFLOW. $\boxed{S\!A\!S}$

In *$HOME2/IPA/Phase3*, I developed a first-cut description of proposed software requirements for the UZFLOW module and supplied it to R. Manteufel. The description is included below in italics.

UZFLOW Module Technical Description

Introduction

The UZFLOW module is to provide time-dependent percolation-flux boundary conditions for the NFENV module, based on climatic change. As the module considers climatic change, it could easily be modified to provide other climate-dependent values such as water table elevations and irrigation rates.

Two modes should exist for the UZFLOW module, in which mean annual infiltration (mean annual infiltration (MAI)) is (i) directly specified as a randomly sampled variable, and (ii) mechanistically varied according to current interpretations of the linkage between climate and infiltration.

The first UZFLOW mode reproduces the IPA2 procedure, taking advantage of the generality of random-parameter sampling strategies that can be employed in the IPA3 code.

The second UZFLOW mode consists of (i) a climate simulator and (ii) a shallow-infiltration

simulator. The climate simulator generates a series of mean-annual precipitation and temperature values at discrete intervals, based on expert elicitation within 10 ky and Milankovich cycles for longer intervals. The shallow-infiltration simulator uses these mean-annual values to predict mean-annual infiltration in a highly abstracted manner, using a DEM containing elevation, soil depth, and bedrock characteristics in conjunction with abstracted transfer functions.

The shallow-infiltration simulator should be considered as representative of the spatial distribution of the MAI signal; however, the results should be normalized to a user-specified value to reflect calibration from other lines of evidence.

Climate Simulation

A standard auto-regressive time-series generation process will be used to generate a climatic record. At particular time instants, mean, standard deviation, and correlation matrix for mean annual precipitation (mean annual precipitation (MAP)) and mean annual temperature (mean annual temperature (MAT)) will be provided, either as a data file or as block data. The time instants will be sufficient to define climatic variation. Linear interpolation of the statistical parameters will be used to define the parameters at intermediate times.

A time series for MAP and MAT will be generated using the equation (Matalas, 1967)

$$\chi_k = A\chi_{k-1} + B\epsilon_i, \tag{11-1}$$

$$A = M_1 M_0^{-1}, \tag{11-2}$$

$$B = M_0 - M_1 M_0^{-1} M_1^T, \tag{11-3}$$

where the superscripts -1 and T denote the inverse and transpose of the matrix and ϵ is a random signal drawn from a normal distribution with zero mean and unit standard deviation. The matrices are defined as

$$M_0 = [\rho_0(i,j)], \tag{11-4}$$

$$M_1 = [\rho_1(i,j)], \tag{11-5}$$

where $\rho_0(i,j)$ is the correlation coefficient between variables i and j at the same time and $\rho_1(i,j)$ is the lag-1 correlation between variables i and j. Note that $\rho_0(i,i) = 1$, M_0 is symmetric, and M_1 is not necessarily symmetric. Variables MAP and MAT will be recovered from the deviation variable χ by taking into account the time-varying mean and standard deviation,

$$v_k = \chi_k s_k + m_k, \tag{11-6}$$

where

v_k *is the value of MAP or MAT at time k*

s_k *is the standard deviation of MAP or MAT at time k*

m_k *is the mean of MAP or MAT at time k*

A total of 9 parameters are provided as a function of time: m, s, and $\rho_1(i,i)$ for both MAP and MAT (6 parameters); $\rho_0(1,2)$; and both $\rho_1(1,2)$ and $\rho_1(2,1)$. The ρ parameters can probably be time-independent. The m and s parameters will be derived from the expert elicitation (DeWispelare et al., 1993) for the first 10 ky. Beyond 10 ky, both m and s will be functions of orbital mechanics (i.e., the Milankovich cycle):

$$m = \alpha(t)m_{current} + (1 - \alpha(t))m_{pluvial} \tag{11-7}$$

$$s = \alpha(t)s_{current} + (1 - \alpha(t))s_{pluvial} \tag{11-8}$$

where $\alpha(t)$ is a time-varying signal based on solar loading, further based on orbital mechanics. Parameters $m_{current}$, $m_{pluvial}$, $s_{current}$, and $s_{pluvial}$ for both MAP and MAT will come from interpretations of Devils Hole data and other sources.

Time steps will be on the order of decades to hundreds of years. Correlation between time steps may be zero at sufficiently long time intervals, in which case the values for ρ_1 are all 0 and the model simplifies considerably to

$$v_k = B\epsilon_k s_k + m_k. \tag{11-9}$$

Shallow Infiltration Transfer Functions

Transfer relationships have been developed for predicting MAI as a function of soil properties, soil depth, and meteorologic parameters such as MAP and MAT (Stothoff et al., 1996). Each of the soil properties is unknown; MAP and MAT are also unknown but will be provided from the climate simulator.

The hydraulic-property transfer relationships for deep soil is

$$\log_{10}\left(\frac{MAI}{MAP}k^{1/2}\right) = \alpha_0 + \alpha_1\left[\left(\frac{m}{m_0}\right)^2 - 1\right] + \alpha_2\left[\left(\frac{P_0}{P}\right)^{1/2} - 1\right] + \alpha_3\left[\left(\frac{\varepsilon}{\varepsilon_0}\right) - 1\right], \tag{11-10}$$

where k is intrinsic permeability, m is van Genuchten $m = 1 - 1/n$, P is bubbling pressure (the reciprocal of van Genuchten α in the units used here), ε is porosity, a subscript 0 represents a reference value for the parameter ($m_0 = 0.2$, $P_0 = 2000$ Pa, and $\varepsilon_0 = 0.3$), and the α values are hydraulic-parameter sensitivity constants. If k is less than 10^{-8} cm^2, MAI is zero.

The meteorologic-property transfer function for deep soil, neglecting longwave and shortwave radiation and windspeed, is

$$\log_{10}\left(\frac{MAI}{MAP}k^{1/2}\right) = J_{fit} \tag{11-11}$$

$$J_{fit} = \beta_0 + \beta_1\left[\left(\frac{MAV}{MAV_0}\right)^2 - 1\right]$$

$$+ j_1 M + j_2 T + j_3 M^2 + j_4 MT$$

$$+ j_5 T^2 + j_6 M^3 + j_7 M^2 T + j_8 MT^2 + j_9 T^3, \tag{11-12}$$

$$T = (MAT - MAT_0)/MAT_0, \tag{11-13}$$

$$M = \log_{10}(MAP/MAP_0), \tag{11-14}$$

where the β_i and j_i values are fitting coefficients, T is the relative change in MAT and M is the change in the base-10 log of the MAP multiplier. Base-case mean-annual values are used for normalizing: (i) $MAP_0 = 163$ mm/yr, (ii) $MAT_0 = 290$ K, and (iii) $MAV_0 = 4.5 \times 10^{-6}$ gm/cm³.

The transfer function for shallow soil over fractured welded bedrock, neglecting longwave and shortwave radiation and windspeed, is

$$\log_{10}\left[\frac{(MAI/MAP)}{I_{D0}}\right] = B^{\sqrt{1/2}}(J_{fit} - C_I) \tag{11-15}$$

$$B = \varepsilon\frac{b}{b_r} \tag{11-16}$$

where C_I, I_{D0}, and b_r values are all fitting coefficients. The β_i values and the j_i values are different in Equation 11-11 and Equation 11-15.

In addition, the transfer functions have corrections to account for solar aspect. Modification of the base-case MAI by solar radiation is estimated by calculating the north-south and east-west rotations of the ground surface, and interpolating within a table obtained from simulations using solar loads appropriate to surface rotations 30 degrees to the east, west, north, and south. The impact should be considered part of J_{fit}, so the sensitivity increases with depth.

A blending of the deep and shallow equations are required. I use the shallow equation for depths less than 5 m, the deep equation for depths greater than 10 m, and interpolate between the two for intermediate depths.

Formulae for predicting base meteorologic-property distributions under current climate are

$$MAP = \exp(4.26 + 0.000646Z) \tag{11-17}$$

$$MAT = 25.83 - 0.00840Z \tag{11-18}$$

$$MAV = \exp(-11.96 - 0.000341Z) \tag{11-19}$$

where Z is ground-surface elevation in meters, MAP is in mm/yr, MAT is in $^\circ C$, and mean annual vapor density (MAV) is in gm/cm^3. It should be adequate to ignore temporal variation in MAV and solar aspect.

Soil Depth

Three equilibrium balance equations are solved to calculate the equilibrium depth of alluvium over the YM region; (i) an overall alluvium mass balance, (ii) a sediment mass balance, and (iii) a hydraulic mass balance or stream-flow model. The overall mass balance for alluvium, the first equation, is

$$\nabla \cdot \mathbf{q}_{alluv} + Q_{wea} + \overline{Q_{str}} = 0, \tag{11-20}$$

where $\mathbf{q}_{alluv}$ is the flux of alluvium, Q_{wea} is the source of alluvium due to weathering, and $\overline{Q_{str}}$ is the time-averaged flux due to stream action. The erosion-balance model assumes that all processes are at equilibrium. Thus, the stream-flow model assumes that a representative spatially uniform rainfall rate is applied over the entire mountain, and the resulting equilibrium hydraulic flux distribution is used to calculate equilibrium sediment transport. As streamflow is actually highly episodic at YM, the equilibrium sediment-transport velocities and erosion/deposition rates must be adjusted to account for the time with no streamflow. Time averaged stream-action flux is approximated here by

$$\overline{Q_{str}} \approx F_{str}Q_{str}, \tag{11-21}$$

where F_{str} is the fraction of time stream flow occurs. The procedure is likely to under-represent the time average in headwater and overland-flow areas, and over-represent the time average in deep washes and downstream areas.

Flux of alluvium, other than through sediment transport, is assumed to occur through creep and is gravity-driven,

$$\mathbf{q}_{alluv} = -Kb\nabla Z, \tag{11-22}$$

where b is the depth of alluvium, Z is the ground surface elevation, and K is a creep conductance (assumed spatially constant here). The alluvium-flux term is similar to the short-range transport model used by Beaumont et al. (1992), except that here b varies with time and Z is constant, while

in the Beaumont et al. (1992) application, b is assumed constant and Z is allowed to vary over time.

A simple source term representing weathering is used here. It is assumed that alluvium protects the bedrock from weathering, so that weathering decreases exponentially with alluvial depth:

$$Q_{wea} = Q_0 \exp(-b/b_0) \tag{11-23}$$

where Q_0 is the source strength, and b_0 represents a weathering-protection alluvium depth. The weathering model has two fitting parameters, Q_0 and b_0, which can be used to match observed alluvium depths.

Erosion and deposition through stream action is calculated using the second equilibrium balance equation, a sediment-balance equation,

$$\nabla \cdot c_s \mathbf{q}_w - Q_{str} = 0, \tag{11-24}$$

where c_s is the concentration of the sediment in water and $\mathbf{q}_w$ is the flux of water. Following standard practices in the literature (e.g., Woolhiser et al. (1990)), a simple kinetic rate law is used to characterize erosion and deposition,

$$Q_{str} = C_g(c_s - c_{eq}), \tag{11-25}$$

where c_{eq} is the equilibrium sediment concentration for a reach along a stream bed and C_g is an equilibrium constant.

Numerous equilibrium sediment concentration capacity relationships exist in the literature (e.g., Yang (1973), Kilinc and Richardson (1973), Ackers and White (1973), Yalin (1963)). A particularly simple relationship is used herein (Meyer and Wischmeier, 1969), based on tractive force:

$$c_{eq} = C_s \frac{v^4}{h}, \tag{11-26}$$

where C_s is a constant, v is water velocity, and h is hydraulic depth.

For erosion, C_g is a constant describing the erodibility of the alluvium or bedrock. For deposition ($c_s > c_{eq}$), C_g assumes that particles have fall velocities and drag characteristics similar

to spheres (Fair and Geyer, 1954), and a coupled set of equations are used to calculate C_g:

$$v_s^2 = \frac{4}{3} \frac{g(S_s - 1)d}{C_D}, \tag{11-27}$$

$$C_D = \frac{24}{R} + \frac{3}{\sqrt{R}} + 0.34, \tag{11-28}$$

$$R = v_s d / \nu, \tag{11-29}$$

$$C_g = \frac{v_s}{h}\left(1 - \frac{c_{eq}}{c_s}\right), \tag{11-30}$$

where v_s is the particle settling velocity, g is the acceleration due to gravity, S_s is the particle specific gravity, d is the particle diameter, C_D is the drag coefficient, R is the Reynold's number, and ν is the kinematic viscosity.

The final equilibrium balance equation required to complete the alluvium-balance system is the water-balance equation,

$$\nabla \cdot \mathbf{q}_w + Q_{rain} = 0, \tag{11-31}$$

where Q_{rain} is the net rainfall. A standard practice in the literature is to use a kinematic-wave approximation for hydraulic flux in conjunction with the Manning hydraulic resistance law, so that (in metric units)

$$\mathbf{q}_w = \frac{S^{1/2} h^{5/3}}{n}, \tag{11-32}$$

where S is the slope and n is Manning's roughness coefficient.

Each of the three balance equations is solved using the same general finite-volume flow-routing approach. The DEM grid is discretized into square boxes, or nodes, with 1D connections to the nearest eight nodes. Taking advantage of the hyperbolic nature of the equations by assuming that upstream variables uniquely determine fluxes to downstream nodes, the nodes in the grid can be processed in order from highest to lowest elevation in one pass.

The water-balance equation is solved independently of the sediment- and alluvium-balance equations. In the water-balance equation, each node is processed using the algebraic equation,

$$A_i q_{rain} + \sum_{j=up} \frac{w_{ij} h_j^{5/3}}{n}\left(\frac{Z_j - Z_i}{\Delta_{ij}}\right)^{1/2} - \sum_{j=down} \frac{w_{ij} h_i^{5/3}}{n}\left(\frac{Z_i - Z_j}{\Delta_{ij}}\right)^{1/2} = 0, \tag{11-33}$$

where node i is the node being processed, node j is a neighboring node, A_i is the area associated with node i, q_{rain} is the rainfall rate minus infiltration, w_{ij} is the width of the 1D connection between nodes i and j, and Δ_{ij} is the distance between nodes i and j. Summing over upstream nodes is denoted by $j = up$, and summing over downstream nodes is denoted by $j = down$. On a square grid

with constant node spacing Δ, w_{ij} is $\Delta/2$ for nearest-neighbor connections and $\sqrt{2}\Delta/3$ for diagonal connections.

The sediment- and alluvium-balance equations are solved simultaneously, by requiring that each nodal alluvium depth and sediment concentration is compatible with outflow from the node. The algebraic balance equations are:

$$\sum_{j=up} c_{sj}Q_{wij} - \sum_{j=down} c_{si}Q_{wij} + \frac{A_i}{8}\sum_{j=down} \overline{C_{gij}(c_{eqij} - c_{si})} = 0, \tag{11-34}$$

$$\sum_{j=1}^{8} w_{ij}K_{ij}b_{up}\left(\frac{Z_j - Z_i}{\Delta_{ij}}\right) + A_iQ_0\exp(-b_i/b_0) - \frac{A_i}{8}\sum_{j=down} \overline{C_{gij}(c_{eqij} - c_{si})} = 0, \tag{11-35}$$

where b_{up} is the upstream alluvium depth. Alluvium depths are solved by bisection between a minimum depth of 0 m and a maximum depth (arbitrarily assumed to be 20 m here). The equilibrium sediment concentration is found during each bisection step.

The flow-routing approach works well when there are no local minima in the domain, so that there is a route from every node to the boundary. A physical local minimum cannot exist at equilibrium unless there is a physical mechanism for removing alluvium (e.g., wind transport). Typically, however, local minima are artifacts of the DEM resolution, as elevations are only reported to the nearest meter. Also, narrow features such as upstream wash channels, which are on the order of a meter wide, cannot be resolved with the 30-m DEM grid. About 0.5 percent of the nodes in the DEM are local minima, almost all occurring in wash bottoms but a few occurring along ridgetops. For these minimum nodes, a preprocessing step is performed to eliminate artificial local minima, by artificially raising minima nodes at least 10 cm above the lowest of the surrounding nodes. A number of passes are required to eliminate multinode basins.

There are a total of 11 adjustable parameters in the set of coupled balance equations, The 11 parameters, and values found to result in reasonable predictions of colluvium depths, are shown in Table 16-1. As F_{str}, K, and Q_0 control the relative importance of stream processes, colluvial diffusion, and weathering. These three parameters are not completely independent, so scaling the three parameters by the same constant does not modify the predicted colluvium distribution.

Within the mapped alluvium outline, a post-processing step is performed to provide more realistic alluvium depths. An exponential relationship of alluvial depth to surface slope was determined by regression,

$$b = 47\exp(-0.32s) \tag{11-36}$$

where s is the slope, in degrees, of the ground surface at the nearest grid point in the DEM. The coefficient of determination is 0.61 for the relationship, using information from 56 of the boreholes

Table 11-1: Adjustable parameters for creating colluvium distributions.

Name	Symbol	Base Value
Net rainfall rate	q_{rain}	5 cm/hr
Manning's roughness coefficient	n	0.1
Kinetic coefficient for alluvium scour	C_g	$0.1~\text{s}^{-1}$
Kinetic coefficient for bedrock scour	C_g	$0.002~\text{s}^{-1}$
Traction coefficient for sediment equilibrium	C_s	10^{-3}
Particle diameter	d	1 mm
Particle specific gravity	S_s	2.5
Alluvium creep conductance	K	10^{-12} m/s
Alluvium weathering rate	Q_0	$10^{-9}~\text{m}^3/\text{m}^2\text{s}$
Alluvium weathering depth	b_0	1 cm
Fraction of time in streamflow	F_{str}	30 min/100 yr

discussed by Fernandez et al. (1994). Wherever the slope is less than 10 degrees within the Scott and Bonk (1984) alluvium outline, the alluvium depths are calculated using Equation 11-36; otherwise, the colluvium-routing model predictions are used. Note that in the near future Equation 11-36 will be replaced with a slightly better relationship of the form

$$b = as^{-c}, \tag{11-37}$$

where a and c are constants.

Application of the Transfer-Function Model

The transfer-function model has the general flow of

- *Map pixels to subareas, either one pixel per subarea or all pixels per subarea, depending on the analyst.*

- *Create a base map for soil depth, either once or for each realization, depending on the analyst.*

- *Step through the sequence of meteorology time steps, saving MAP and MAT at each output step.*

- *Run the transfer functions for the mapped pixels corresponding to the subareas for each output step.*

- *Normalize the transfer functions by the user-defined value.*

Data Needs

Two DEM input files must be provided, one for elevation control and one for pixel classification (i.e., mapped alluvium, welded, nonwelded). For each classification, appropriate parameters need to be provided for the hydraulic and erosional relationships.

Sensitivity analyses will probably center on

- *Mean and standard deviation of climatic parameters,*

- *Soil depth, and*

- *Soil hydraulic properties.*

Accordingly, these variables should be able to be tweaked. Ideally, each variable should be able to be tweaked. I suggest that an auxillary file be read in with parameter tweaks, in the form

```
parname1: value1 # comment
parname2: value2 # comment
/ # End of Input Signal
```

The parameters should have a default value. If the tweak file does not exist, the defaults should be used.

2/17/97 Software description for UZFLOW.   ⌐SAS⌐

In *$HOME2/Matlab/TPA3*, I prototyped a version of the UZFLOW module in *Matlab* to test out functionality and ideas. The prototype is driven from **uzflow_test.m** and calls several additional routines.

Based on this mockup, I redefined the software description for UZFLOW, which is copied below in italics.

UZFLOW Module Technical Description

Introduction

The UZFLOW module provides time-dependent percolation fluxes at and below the repository level, based on climatic change. Primary clients for this information are the NFENV and UZFT modules. As UZFLOW considers climatic change, it might easily be modified to provide other climate-dependent values such as water table elevations and irrigation rates.

UZFLOW consists of (i) a climate simulator and (ii) a shallow-infiltration simulator. The climate simulator generates a series of mean-annual precipitation (mean annual precipitation (MAP)) and mean-annual temperature (mean annual temperature (MAT)) values at uniform time intervals. The shallow-infiltration simulator uses these mean-annual values to predict mean-annual infiltration (mean annual infiltration (MAI)) in a highly abstracted manner, using abstracted transfer functions on each pixel of a digital elevation model (DEM) containing elevation, soil depth, and bedrock characteristics. The pixels within each subarea (SA) are averaged to provide one MAI value for the SA. The SA values are then averaged in time to supply MAI at the output times requested by the user.

The mean values of MAP and MAT over the period of simulation are supplied from an input data file. It is suggested that these values are based on expert elicitation within 10 ky and Milankovich cycles or Devils Hole data for longer intervals.

The user specifies 7 parameters that are provided by the LHS sampler: (i) and (ii) change in the mean of MAP and MAT, respectively, at full glacial maximum; (iii) and (iv) standard deviation of MAP and MAT, respectively, about the mean over each sample period; (v) correlation between MAP and MAT perturbations about the mean; (vi) areally averaged MAI for the initial climate; and (vii) an index into a file containing normally distributed perturbations. IPA Phase 2 behavior is obtained by specifying that parameters (i) through (iv) are constant and zero.

Climate Simulation

A time-series generation process is used to generate a climatic record. An input file specifying mean values of MAP and MAT at particular points in the future is supplied, with enough points to define climatic variation. Linear interpolation of the statistical parameters is used to define the parameters at intermediate times. The values in the time history are normalized to LHS-sampled values for full-glacial conditions.

It is assumed that there is no correlation between perturbations in successive time periods. For a time period k, perturbations are generated using

$$\chi_{kj} = [\rho_{ij}]\epsilon_i \qquad (11\text{-}38)$$

where

j represents *MAP* or *MAT*

χ_{kj} is a vector of correlated perturbations

ϵ_i is a vector of independent normally distributed perturbations

ρ_{ij} is a correlation matrix

Variables *MAP* and *MAT* are calculated from χ by taking into account the time-varying mean and standard deviation,

$$v_{kj} = \chi_{kj}s_j + m_{kj}, \qquad (11\text{-}39)$$

where

j represents *MAP* or *MAT*

v_{kj} is the value of variable j at time k

s_j is the standard deviation of variable j *(constant in time)*

m_{kj} is the mean of variable j at time k

Shallow Infiltration Transfer Functions

Transfer relationships have been developed for predicting *MAI* as a function of soil properties, soil depth, and meteorologic parameters such as *MAP* and *MAT* (Stothoff et al., 1996). Each of the soil properties is unknown; *MAP* and *MAT* are also unknown but will be provided from the climate simulator.

Transfer relationships are in the form of perturbations about a mean value for *MAI*, in the form

$$\log_{10}\left(\frac{MAI}{MAP}\right) = \alpha_0 + \sum_{i=1}^{N} \alpha_i N(u_i) + \sum_{j=1}^{M} \beta_j N(v_j)\left[1 + \gamma \log_{10}\left(\frac{MAI}{MAP}\right)\right] \qquad (11\text{-}40)$$

where

N is a normalizing function appropriate for each variable

u_i, v_j represent hydraulic and meteorologic variables

$\alpha_i, \beta_j, \gamma$ are fitting constants

Soil properties and soil depths must be supplied for each pixel of the DEM. This information is uncertain. More than one realization for the properties could be provided by the user and LHS-sampled, as might be done for sensitivity analyses, but the typical user would probably not gain a great deal of benefit by having more than one realization for soil properties.

Formulae for predicting base meteorologic-property distributions under current climate are

$$MAP = \exp(4.26 + 0.000646Z) \tag{11-41}$$

$$MAT = 25.83 - 0.00840Z \tag{11-42}$$

$$MAV = \exp(-11.96 - 0.000341Z) \tag{11-43}$$

where Z is ground-surface elevation in feet, MAP is in mm/yr, MAT is in $^\circ C$, and mean annual vapor density (MAV) is in gm/cm^3. Solar aspect is calculated from the surface slope.

Application of the Transfer-Function Model

The transfer-function model has the general flow of

- *Map DEM pixels to subareas.*

- *Sample one or more base maps for soil depth and soil properties.*

- *Step through the sequence of uniform time steps, saving MAP and MAT at each step.*

- *Normalize MAP and MAT using the sampled full-glacial value.*

- *Run the transfer functions for the mapped pixels in the SAs.*

- *Average the pixel values within each SA.*

- *Normalize MAI by the user-defined initial value.*

- *Output average MAI over each output time step.*

3/1/97 UZFLOW module.

The UZFLOW module was converted from a *Matlab* prototype into FORTRAN, by S. Stothoff, over the period from 2/22/97 through 2/23/97. Debugging and testing began 2/24/97, immediately

linking to the TPA modules (i.e., there is no test driver routine). S. Stothoff verified that inputs were received from the sampler and data files as expected, and reasonable outputs were generated. Each function and subroutine was exercised, using the default tpa.inp data file provided for testing, except for the subroutine qclimate (23 lines of FORTRAN code plus comments). Total lines of code with comments are 1371, comprising the main UZFLOW module, uzflow.f, and a file included into each subroutine, uzflow.i. There are 572 total lines of code, not including comments, for the two files, so that approximately 58 percent of the two files represent comments or white space.

The UZFLOW departs from the Software Requirement Description (SRD) in a few ways. The most significant change is introduced by modifying the future history of climate specified from the input file **climate.inp** to refer to the fraction of full glacial for AAP and AAT, rather than absolute values of AAP and AAT. Also, an additional parameter is required for sampling, 'TimeStepForClimate[yr]'. In addition, a query routine, qclimate, was provided to enable other modules to get AAP, AAT, and fraction of full glacial at specified time instants.

A. Armstrong went through the code line by line on 2/27/97, checking that the code met specifications. An incorrect conversion factor for feet to meters was identified and corrected. Also, a number of FORTRAN-usage questions were raised and explained, regarding the use of double-precision constants, indexing into character strings, and undefined parameters. These questions were explained satisfactorily. Several usages that are extensions to standard FORTRAN-77 were also identified (e.g., do-enddo loops, do-while loops, character*(*) dimension statements). Each usage was justified as being consistent with standards set in previously coded modules.

3/14/97 NFENV and UZFLOW modules.   [SAS]

During the past week I developed and modified several subroutines involved with the NFENV module, and tested both the NFENV and UZFLOW modules.

The NFENV module work was associated with adding reflux capabilities, encapsulated in the nfhydro subroutine in the **nfenv.f** file, and calculating dripping flux onto WPs, encapsulated in the nfdrip subroutine in the **nfenv.f** file.

The reflux module uses the following parameters in the **tpa.inp** file:

- ThermalConductivityofYMRock[W/(m-K)]

- BoilingPointofWater[C]

- AreaMassLoading[MTU/acre]

- LengthOfRefluxZone[m]

- MaximumFluxInRefluxZone[m/s]

- ReleaseFractionForPerchedBucket

- PerchedBucketVolumePerSAarea[m3/m2]

Each parameter (except for the boiling point of water and areal mass loading) are sampled.

The logic for handling the reflux zone is based on using a bucket that continually fills through deep percolation and partially empties whenever it fills. The bucket also continually drains while the reflux zone is intersecting the drift horizon. The balance equation for the bucket is

$$\frac{\partial V}{\partial t} = q_{perc} - q_{reflux}(z_{repos}),$$

(11-44)

where

V is the volume of the bucket per unit area [L^3/L^2]

q_{perc} is the percolation flux [L^3/TL^2]

$q_{reflux}(z_{repos})$ is the liquid reflux at the repository horizon [L^3/TL^2]

It is assumed that if while the reflux zone intersects the repository, the liquid flux at the repository continues past the repository. Liquid reflux, q_{reflux}, is assumed to be linearly varying from a maximum value at the boiling isotherm to zero at a specified distance below the isotherm. If the isotherm is farther above the repository horizon than the thickness of the reflux zone, $q_{reflux}(z_{repos})$ is assumed to be zero.

While the repository is below boiling, the bucket drains with a flux equal to q_{perc}. In addition, half of the existing water stored in the bucket is assumed to drain at each time step. When the repository is above boiling, the bucket fills at the rate of $q_{perc} - q_{reflux}(z_{repos})$ until it exceeds capacity within a time step. A loop releases a user-specified fraction of the bucket volume until the stored volume is than a full bucket.

A reasonable size of the bucket might be the difference between saturated moisture content and ambient moisture content, multiplied by 10 to 100 m. For TSw, this criterion corresponds to a range of roughly 0.1 to 1 m^3/m^2.

The dripping module simply calculates the volumetric flux across the cross-sectional area of a waste package given the volumetric flux across the repository. Additional calculations for

localization and diversion is handled in the EBSPAC modules; for clarity, this should be moved to NFENV in the next iteration.

I tested the NFENV module by using inputs that generate constant q_{perc} over the length of the simulation and verifying that the magnitude of fluxes output from the module were consistent. I then used standard climatic inputs and again verified that the resulting flux magnitudes were consistent and reasonable compared to the constant-q_{perc} case.

I also tested the UZFLOW module, to a greater extent than previously, verifying that the IPA2 approach could be reproduced. Several bugs were found in subroutine get_climean, which reads in the mean values for the climate from the disk. These were fixed. I identified one additional bug tonight in subroutine get_climean that will need to be rectified in the next version – it is assumed that the start of the climatic history (i.e., current conditions) must have a fraction of full glacial maximum equal to zero. In actuality it might be different from zero, so that the weighting schemes should take this into account.

3/15/97 Thoughts on NFHYDRO module.

There are a couple of weaknesses in the NFHYDRO portion of the NFENV module that should be rectified for the next version of the TPA code.

It is assumed that the bucket drains half of its volume per time step once the temperature drops below boiling at the repository; this procedure should be replaced with a decay constant

$$\frac{\partial V}{\partial t} = \lambda V + q_{perc} \tag{11-45}$$

where λ is a decay constant.

It is assumed that the bucket flushes a multiple of a fixed volume if it overflows. It may be more realistic to simply pass the excess on directly (steady-state assumption), particularly for typical time steps.

Some accounting for the moisture in the dry-out zone needs to be done. A more realistic model provides three saturation levels, θ_{amb}, θ_{buck}, and θ_{dry}, corresponding to ambient, bucket, and dryout-zone saturations. Presumably $\theta_{buck} > \theta_{amb} > \theta_{dry}$. As the boiling isotherm moves up, the moisture in the new part of the dryout zone should be put into the bucket. The governing mass balance equation is

$$\varepsilon \left[\theta_{dry} \frac{\partial L_{dry}}{\partial t} + \theta_{buck} \frac{\partial L_{buck}}{\partial t} + \theta_{amb} \frac{\partial L_{amb}}{\partial t} \right] = q_{perc} - q_{reflux}(z_{repos}) - q_{flush}, \tag{11-46}$$

11-16

where L represents the height of a bucket, q_{flush} is the overflow flushed from a full bucket, and subscripts dry, $buck$, and amb represent the dryout-zone, perched-zone, and ambient-zone buckets, respectively. Note that $L_{amb} + L_{buck} + L_{dry} = L_{tot}$ is a constant, where L_{tot} is the maximum thickness for the calculation (perhaps TSw layer thickness) and L_{dry} is the height of the boiling isotherm above the repository level. Accordingly,

$$L_{amb} = L_{tot} - L_{dry} - L_{buck} \tag{11-47}$$

and

$$\varepsilon \left[\theta_{dry}\frac{\partial L_{dry}}{\partial t} + \theta_{buck}\frac{\partial L_{buck}}{\partial t} - \theta_{amb}\frac{\partial (L_{dry} + L_{buck})}{\partial t} \right] = q_{perc} - q_{reflux}(z_{repos}) - q_{flush}, \tag{11-48}$$

(noting that $\partial L_{tot}/\partial t = 0$), yielding

$$\varepsilon \left[(\theta_{dry} - \theta_{amb})\frac{\partial L_{dry}}{\partial t} + (\theta_{buck} - \theta_{amb})\frac{\partial L_{buck}}{\partial t} \right] = q_{perc} - q_{reflux}(z_{repos}) - q_{flush}. \tag{11-49}$$

With the adjusted mass balance equation, the height of the perched-zone bucket is tracked. As the repository heats up, L_{buck} remains zero until $q_{reflux}(z_{repos}) < q_{perc}$. A period of time exists, while $L_{buck} + L_{dry} < L_{tot}$, where $q_{reflux}(z_{repos}) + q_{flush} = 0$. While $L_{buck} + L_{dry} = L_{tot}$,

$$q_{flush} = q_{perc} - \varepsilon(\theta_{dry} - \theta_{buck})\frac{\partial L_{dry}}{\partial t}. \tag{11-50}$$

As the temperature drops, there may be another period of zero flux. Finally, as the boiling isotherm returns to the repository level, reflux kicks in to drain the perched-zone bucket.

A potential pitfall arises if the perched-zone bucket tries to generate negative thickness. Two obvious approaches can handle this situation: (i) collapse the perched-zone bucket and track the ambient-dry interface explicitly, or (ii) add a separate fracture-rewetting front accounting for sorption into the matrix. The first approach would tend to delay the arrival of rewetting at the repository, while the second approach promotes arrival of rewetting.

7/15/97 Documenting changes to UZFLOW module.

Over the course of testing, it became apparent that the regression formula for mean annual infiltration (MAI) used in the UZFLOW module was seriously in error beyond the range of values used for the regression. As documented in the 7/11/97 entry of the Ambient Hydrology KTI, a modified regression equation was proposed that extrapolates reasonably to the wet and cool extremes demanded by the TPA code.

As per a telecon with Tim McCartin, Dick Codell, and Neil Coleman, I have changed one constant in the regression equation to represent a fudge factor for all the unsampled parameters. The original practice was to calculate MAI under current conditions, using my formula, and scale the calculated MAI including climate change by the factor required to match the user-specified MAI under current conditions. The problem is that the regressed relationships are not linear, so that under climatic extremes excessive MAI may result. By adjusting the regression equation so that initial conditions are exactly matched, conditions under climatic extremes are also matched.

In order to match the condition, MAI is tabulated for various values of the fudge factor. Given the initial MAI to match, the matching fudge factor is found through interpolation within the table.

I implemented the equation in the last version of the UZFLOW module that I had been working on. A practice has been implemented in the interim with the rationale of eliminating warning and error messages, so as not to upset NRC, but is instead a poor coding practice that fosters modification errors. The one included file that I had created, with all parameter statements, dimensioning information, and common blocks, has been replaced with 6 included files (one for each common block) and all other information has been copied into each subroutine that it is used in. The module is about 1/3 larger, is unwieldy to read, and subject to modification errors due to the redundant statements. **I strongly deprecate this practice as cutting off one's nose to spite one's face**.

3/26/02 Documenting changes to UZFLOW module.

In January and February, 2000, I modified the UZFLOW module to read in a digital elevation model (DEM) table with expected MAI calculated at each pixel for various combinations of mean annual precipitation (MAP) and mean annual temperature (MAT). A preprocessor called ITYM is used to calculate expected MAI, accounting for uncertainties in hydraulic properties such as soil thickness, bedrock fractures, hydraulic conductivity, etc. Expected MAI is output from ITYM on a regular DEM grid; within UZFLOW, DEM pixels within each subarea are used to calculate average MAI for the subarea. With this strategy, UZFLOW is streamlined and uncertainty in the hydraulic properties can be accounted for.

Climatic variability is accounted for in UZFLOW, using a file with normally distributed random variables to perturb MAP and MAT on a series of uniform time steps. These values are averaged to the time steps used by the TPA code. Required parameters include standard deviations

of MAP and MAT, correlation between the two, time step size, and climate noise set (subset of the random-variable file).

Today I modified the ITYM/UZFLOW modules to be able to investigate the effect of hydraulic-property uncertainty within the TPA code. Two DEM tables replace the DEM table of MAI previously output from ITYM. The new tables are $\log_{10}(MAI)$ and the standard deviation of $\log_{10}(MAI)$. Within UZFLOW, MAI is calculated using

$$I = 10^{(Y+SN)} \tag{11-51}$$

where I is MAI, Y is $E[\log_{10}(MAI)]$, S is standard deviation of $\log_{10}(MAI)$, and N is a zero-mean, unit-variance sampled parameter. Both Y and S are interpolated using $\log_{10}(MAP$ and MAT, while N is a new sampled parameter called "UZFLOWShallowHydraulicPropertyDeviation".

Accounting for climatic variability increases MAI, since rare wet years account for a disproportionate amount of infiltration. However, abruptly varying water fluxes through the repository greatly slow transport calculations in the Total-System Performance Assessment (TPA) code. The current tables conceptually provide MAI as a function of a known MAP and MAT averaged over roughly a decade. The variability in these averaged climatic properties from one decade to the next is explicitly accounted for in UZFLOW as described above.

A further modification to the approach is possible to account for climatic variability at time scales longer than a decade by extending the current table in additional dimensions. In this approach, the effect of climatic variability can be shifted to the preprocessor at the cost of longer preprocessor runs and much larger files transferred from ITYM to UZFLOW. The UZFLOW module is simplified and as only the expected value of MAI is considered, the time history of MAI provided to the TPA code is smooth. The net effect is to increase MAI but eliminate any large pulses that might flush contaminants through the system.

The simplest approach is to only consider the expected response of MAI to climate after accounting for hydraulic-parameter variability and uncertainty. The idea is to first create the same internal table for MAI as a function of decadal-average MAP and MAT that is already generated. This first table represents the case with all variance equal to zero for longer-than-decadal periods. A large number of decadal perturbations to MAP and MAT are independently generated for each set of variability-describing parameters (*e.g.*, standard deviations of MAP and MAT), which represent a large number of realizations of the decadal variability. Table lookup can be used with the zero-variance table to get expected decadal MAI for each climate realization. The new values should be larger than the zero-variance case. Only the expected value of MAI as a function of mean MAP and MAT is passed from ITYM to UZFLOW.

In the simplest approach, variability due to mutual variation of hydraulic properties and climate is not considered. A more computationally intensive second approach would proceed similarly to the simple case for the zero-variance case, but would use the full suite of climate realizations for each hydraulic-property realization. In this case, a second table can be passed for the variance in expected MAI, which accounts for the uncertainty in hydraulic properties.

In both new approaches, the UZFLOW module would no longer need to sample a parameter for time step or correlation between MAP and MAT.

References

Ackers, P. and W. R. White. 1973. Sediment Transport: New Approach and Analysis. *Journal of the Hydraulics Division, American Society of Civil Engineers 99*(HY11), 2041–2060.

Beaumont, C., P. Fullsack, and J. Hamilton. 1992. Erosional control of active compressional orogens. In K. R. McClay (Ed.), *Thrust Tectonics*, London, pp. 1–18. Chapman & Hall.

DeWispelare, A. R., L. T. Herren, M. P. Miklas, and R. T. Clemen. 1993. *Expert Elicitation of Future Climate in the Yucca Mountain Vicinity*. CNWRA 93-016, Center for Nuclear Waste Regulatory Analyses, San Antonio, TX.

Fair, G. M. and J. C. Geyer. 1954. *Water Supply and Wastewater Disposal*. New York, NY: John Wiley & Sons.

Fernandez, J. A., J. B. Case, C. A. Givens, and B. C. Carney. 1994. *A Strategy to Seal Exploratory Boreholes in Unsaturated Tuff*. SAND93-1184, Sandia National Laboratories, Albuquerque, NM.

Kilinc, M. and E. V. Richardson. 1973. *Mechanics of Soil Erosion From Overland Flow Generated by Simulated Rainfall*. Hydrology Paper 63, Colorado State University, Fort Collins, CO.

Matalas, N. C. 1967. Mathematical Assessment of Synthetic Hydrology. *Water Resources Research 3*(4), 937–945.

Meyer, L. D. and W. H. Wischmeier. 1969. Mathematical Simulation of the Process of Soil Erosion by Water. *Transactions of the American Society of Agricultural Engineers 12*(6), 754–762.

Scott, R. B. and J. Bonk. 1984. *Preliminary Geologic Map (1:12,000 scale) of Yucca Mountain, Nye County, Nevada, with Geologic Cross Sections*. Open-File Report 84-494, United States Geological Survey, Denver, CO.

Stothoff, S. A., H. M. Castellaw, and A. C. Bagtzoglou. 1996. *Simulating the Spatial Distribution of Infiltration at Yucca Mountain, Nevada.* , Center for Nuclear Waste Regulatory Analyses, San Antonio, TX.

Woolhiser, D. A., R. E. Smith, and D. C. Goodrich. 1990. *KINEROS, A Kinematic Runoff and Erosion Model: Documentation and User Manual*. ARS-77, United States Department of Agriculture, Agricultural Research Service.

Yalin, Y. S. 1963. An Expression for Bed-Load Transportation. *Journal of the Hydraulics Division, American Society of Civil Engineers 89*(HY3), 221–250.

Yang, C. T. 1973. Incipient Motion and Sediment Transport. *Journal of the Hydraulics Division, American Society of Civil Engineers 99*(HY10), 1679–1704.

12 Breath code development

Account Number: **20-1402-863**

Collaborators: **As noted**

Directories: **Subdirectories of $HOME2/Numeric/Breath as noted**

Objective: Perform modifications to the *breath* code as required for infiltration analyses. Each version of the code is in a subdirectory labelled *V1.1*, *V1.2*, etc., located off of the main *breath* directory, *$HOME2/Numeric/Breath*.

2/17/96 Initial entry.

A bug was found in the calculation of temperature-dependent water viscosity. The fviscw2 routine calculated viscosity in centipoise, rather than poise, which is then converted to user units. Version 1.1, and beta versions of 1.2 and 1.3, had the correction made.

8/24/96 Planning for additional enhancements to *breath*.

breath has been used essentially without modification for numerous production runs over the last year, primarily investigating shallow infiltration processes with one or two layers. Although *breath* has performed reasonably well for these purposes, there are several significant areas that require enhancement for future planned studies at YM, including

- snow and snowmelt dynamics (important for future-climate studies),

- vegetation dynamics,

- atmospheric-pressure dynamics,

- discrete-fracture interactions,

- weather simulation,

- weather averaging,

- tracer pulses, and

- overland- and lateral-flow dynamics.

Most of these studies could be performed by enhancing the current 1D *breath* simulator; others require extending the 1D formulation to 2D and 3D.

During the production runs, some dissatisfaction with performance cropped up due to extremely long simulation times (i.e., several weeks to complete a 20-yr simulation). It became painfully clear that a restart capability was highly desirable, due to the inability to maintain computers up and running for such extended periods. In addition, speed of calculation continues to be an issue. It has been determined that roughly half of the computational effort is involved with function evaluations. For such long simulations, which may involve 10 to 100 million function evaluations, tabulated functions may drastically cut the function evaluation effort.

In the simulations, mass balance is also a critical issue, which has required that extremely refined grids be employed, both near the ground surface and at material interfaces. Two possible changes have been identified that may allow considerably coarser meshes to be used, at least for some time intervals: (i) using a finite-element approach at material interfaces, and (ii) using adaptive gridding. The change from a finite-volume approach, in which material interfaces are between nodes, to a true finite-element approach, in which material interfaces are between elements, will presumably cut the refinement requirements at the interfaces since a very small element at the interface has been used to minimize the impacts of improperly approximating fluxes across the interface. Using adaptive gridding is perhaps more problematical, since mass balance issues will be involved in regridding, and will be more useful in 1D than 2D or 3D. Also, adaptive gridding requires that material properties be specified by zone, as opposed to the current practice of specifying properties individually by element.

Based on the set of enhancements and extensions that have been identified, it appears that a generic multiphase, multicomponent, multicontinuum mass and energy transport simulator might be appropriate, developed in such a way that adding and subtracting simulation modules is extremely straightforward. The generic mass-component balance equation includes a storage term, an advective-transport term, a diffusive-transport term, and terms accounting for (i) decay, (ii) transfer across phase boundaries, (iii) transfer due to phase change, (iv) reaction with other components, and (v) external sources/sinks. In addition to such terms, the energy balance equation may consider radiation.

In general, a generic code consists of modules responsible for

- data input,

- mesh description and maintenance,

- discretization operations,

- functional relationships,

- state maintenance,

- balance-equation description,

- balance-equation assembly,

- matrix solvers,

- result analysis,

- output routines, and

- restart/debug routines.

It is highly desirable that these modules be as logically independent as possible, so that code maintenance can be localized. Although *breath* was originally coded in Fortran, modularity would be considerably enhanced using C or C++, as would maintenance of data structure and sophistication of input/output. As the computational portion of the code is typically on the order of 10 percent of total coding, and for many computer systems the computational speed of the two languages is comparable, recoding *breath* in C or C++ would be appropriate, particularly since much of this work can be done using a Fortran-to-C converter.

The organization of a generic code depends on the use to which the code will be put. At one extreme, a code may be used for extremely straightforward problems, with homogeneous properties and simple geometries. At the other extreme, extremely complex situations may also be encountered, with layering, embedded discontinuities, and random properties. In the first case, it is desirable to have strong data generation capabilities with minimalist input and global storage structure. In the second case, powerful input is required and each node/element may need individual data storage. These situations are further complicated by the possibility of different parameterization needs for different parts of the domain (e.g., a snow layer has different requirements than a Brooks-Corey medium or a dual-continuum medium).

The internal data structure must be suited both to sophisticated input facilities and to computational efficiency in matrix assembly. Three types of computer architecture are available, each with particular strengths and weaknesses: (i) serial machines (e.g., PCs, workstations), (ii) vector machines (e.g., Crays), and (iii) data-parallel machines (e.g., Connection machines). Appropriate assembly algorithms are considerably different for the three architectures. In general, though,

element-by-element or node-by-node assembly is most appropriate, since information regarding element discretization can be rather voluminous to store in RAM for 2D and 3D. From the standpoint of data input, however, it would be most efficient to assemble by using a process-level assembly process, thereby allowing several data storage schemes to be accommodated simultaneously.

8/25/96 Further planning.

An attractive approach to reconciling efficiency requirements is to maintain data by separate computational zones. With adaptive gridding in 1D, such a zone might be an individual layer. Transition nodes cause a problem – they might be stored independently or might be duplicated as necessary. In higher dimensions, a zone might consist of all triangles, or all dual-permeability elements. Adaptive and non-adaptive zones should be stored separately.

For peak performance in matrix assembly, all potentially state-dependent coefficients should be calculated and separated out to convenient storage before element-discretization operations are performed. Typically, such coefficients are more interesting to look at than element-discretization variables and storage should be smaller as well. Coefficients include capacitance terms, phase mobilities, diffusion coefficients, and derived state variables (e.g., density, viscosity, saturation, enthalpy).

8/26/96 Function handling ideas.

Each of the different types of coefficients discussed yesterday are typically calculated with functions. Ideally, three types of functions should be available: (i) internal hard-coded functions, (ii) tabular functions, and (iii) external user-defined functions. To minimize overhead of identifying pointers, variable names, etc., each function should perform processing in a vector manner (e.g., all nodes can be processed with one call to the function). The strategy has the drawback of requiring additional memory for temporary storage and perhaps some temporary pointer lists as well. The strategy is not suited to Fortran-77 (Fortran-90 may be better), but can be straight-forwardly implemented in C or C++.

Internal hard-coded functions may typically have several arguments, and the arguments may arbitrarily be vectors or constants depending on the user. This multiplicity of options can be handled by restricting internal functions to the straight-forward protocol outlined below. For simplicity of handling facilities, three variables should be passed into each function, (i) an array

handling the list of arguments, (ii) the number of arguments passed in (length of the array), and (iii) the number of vector entries to process. The argument-handling array is actually an array of structures, with each structure containing variables

- pointing to the data vector structure,

- pointing to the index vector structure, and

- maintaining pointers into the index vector.

Since these structures are cumbersome to address, predefined functions should be provided for common manipulations (i.e., pointer initialization, pointer increment, vector addressing). In addition, each function might define shorthand names for the variables, so that the function could end up looking like a normal scalar function with somewhat different interface and an internal loop.

Tabular functions should behave like internal hard-coded functions, with function parameters replaced by the table itself. In addition, a setup routine may be needed to define the table. A somewhat novel idea may be useful for highly heterogeneous systems for some functions, where the expense of function evaluations can be amortized in a partial table with perhaps 4 entries per node. Only when the nodal value goes out of bounds is it necessary to recalculate table entries, and it is expected that most nodes would need to recalculate entries only infrequently.

User-defined functions should assume that vector protocols are in use. The function has the number of arguments and their names predefined, as for the other types of functions, but this time a pair of variables are passed for each argument; (i) the vector/scalar of interest, and (ii) an index vector/scalar. The user-defined functions could utilize the Jacquard vector-C software that I developed at Vermont. Converting these routines to the new use should be straightforward. Alternatively, *Matlab* might be used instead.

9/4/96 Discretization handling ideas. $\boxed{\text{SAS}}$

There are many different physical systems that may be considered. There are also numerous philosophies for discretizing the physical systems, ranging from several flavors of finite element methods, finite difference methods, finite volume methods, and boundary integral methods. Various numerical methods are more appropriate depending on whether the underlying PDE is elliptic, parabolic, or hyperbolic in character. In addition, one can use static grids or adaptive grids. For

1D problems, quite sophisticated adaptive gridding can be performed; as the dimensionality of the problem increases, adaptive gridding becomes increasingly difficult.

Ideally, one would like the structure of the program to allow for generic discretization schemes, so that a scheme can be selected based on the special characteristics of the problem at hand. In order to do this, each general scheme should be modularized with an identical interface structure. Module categories include:

- mesh maintenance (adaptive gridding),

- mesh description (connectivity lists),

- mesh-independent parameters,

- mesh-dependent parameters and state variables,

- discretization description:

    - capacitance term,

    - flux terms,

    - source term,

    - cross-source term, and

    - boundary condition terms,

- matrix assembly, and

- matrix solution.

I envision the mesh-related module categories as separate categories, while the description modules are linked according to the discretization scheme. The various schemes require different levels of information–for example, finite volume schemes consist of 1D pipes and require no spatial information other than distances, while finite element schemes need information on the connections for each element, finite difference schemes implicitly handle the connection information and boundary element schemes also need information on the interfaces between regions. The matrix assembly modules should provide a uniform interface for each of the matrix solution schemes that might be available.

9/17/96 Documentation of version 1.2 for TOP-018. $\boxed{\mathcal{SAS}}$

A file called **Changes** in the subdirectory *V1.2/Src* of the main *breath* directory has been maintained since June, 1995. The file is quoted below (in slightly prettier format) for completeness of documentation, in order to comply with the requirements of TOP-018 for version 1.2.

5/12/96 Fixed bug in boundary condition for specified energy flux. Variable bcenet had incorrect reference for second boundary in thrm1bc.

2/17/96 Fixed bug in the calculation of temperature-dependent water viscosity. The fviscw2 routine calculated viscosity in centipoise, rather than poise, which is then converted to user units. Version 1.1, and beta versions of 1.2 and 1.3, had the correction made.

8/10/95 Fixed bug in evaporation calculations. Added time-averaging of pressure, pressure perturbations, and vapor density perturbations.

8/6/95 Fixed bug in routine calculating d(mobility)/d(mc), which divides by zero when saturated. Added evaporation calculations within domain.

8/5/95 Implemented signal catch routines in C to gracefully shut down when floating point error or interrupt signal thrown.

8/4/95 Fixed bug in time-averaging of perturbations of moisture content times gradient in temperature perturbation.

8/3/95 Added upstream weighting of conductivities to tracking routine for first-type flow boundary conditions. Added capability for tracking partial of vapor density wrt pressure and temperature, perturbations of moisture content times gradient in temperature perturbation.

7/28/95 Fixed error in upstream mobility coding and added option for upstream weighting of conductivities.

7/27/95 Fixed index problem for range output in real restart. Included upstream weighting of mobilities as an option a la TOUGH. Also included dptmax and dtemax checks, which are maximum changes for pressure and temperature in an iteration. Defaults are 100 and 2. An abort occurs as soon as a node hits one of these barriers.

7/25/95 Made floating-point constants and character variables tracked by name array in restart and set/echo calls.

7/23/95 Cleaned up boundary conditions for flux in flow equation. Now the elemental mobility is used, rather than the interface mobility between the two elements nearest the boundary.

7/16/95 Added grid peclet and grid courant calculations. All floating point variables are now tracked by name, just like arrays.

7/15/95 Reorganized common blocks further for binary output. Began work on summary output for time-averaging variables.

7/8/95 Added a few variables tracking averaged quantities.

7/4/95 All real variables dimensioned with mnnd/mnel/mnbc tracked in an equivalenced array, so that trace/snap/restart/set/echo all automatically get each variable.

6/27/95 Added capability for arithmetic/geometric/harmonic means for hydraulic conductivity and for vapor dispersion coefficient.

6/15/95 Added iovar variable and input command to specify the output file for restart variable dumps.

6/14/95 Added a const and a linear option to met command to define whether met variables are piecewise linear or piecewise constant.

6/13/95 Added a scale and a shift option to met command to change met variables from file values at runtime.

6/9/95 Added restart capabilities (actually just echo all variables in a format that *breath* can read). Dump to unit 6.

9/24/96 Bug fix in met command.

I tracked down several bugs in handling the maximum-time-step input from the met command. There was no problem when the boundary conditions were for side 0, as I usually assume, but the time step information was lost when boundary conditions were for side 1. The problem was that the t0bc and t1bc arrays had the time information put in the same array slot as the boundary conditions on reads, while otherwise it was assumed that timmax was in the array slot for side 0. This was fixed by generalizing the code to use the proper slot.

5/23/97 Check using fstudy and corrective actions.

$\boxed{SAS}$

Version 1.2 of *breath* was checked using a FORTRAN static analyzer code, for_study (called fstudy on bashful), provided by Cobalt Blue. SPARC version 2.0.1 was used for the test. A total of 3 syntax errors, 15 semantic errors, and 1181 warnings were reported by fstudy.

The vast majority of the warnings (700) were due to including file brecom.h, which contains specifications for all common blocks, into routines that did not use all common blocks. These warnings should be disregarded.

A total of 340 warnings dealt with subroutine initname, with 141 due to passing an array rather than the anticipated scalar, and an additional 199 due to mixing strings and arithmetic objects. Although it is generally deprecated, this behavior was specifically required during coding, and each of these warnings can be disregarded. One additional warning was due to not explicitly converting character to double precision. Although it is generally deprecated, this behavior was specifically required during coding, and the warning can be disregarded. This set of warnings are all generated by the scheme for providing a pointer and a name for all arrays, which is not handled gracefully in FORTRAN.

A total of 67 warnings dealt with passing the address of functions to subroutines, which apparently confuses fstudy. An additional 22 warnings dealt with passing a constant into a subroutine rather than a variable. These warnings can be disregarded.

A total of 28 warnings dealt with loss of precision (double precision to integer). In each case, the loss of precision was anticipated during coding, so each of these warnings can be disregarded.

A total of 12 warnings dealt with passing a scalar instead of an array. In each case, the dimension of the array passed to the subroutine is 1, so each of these warnings can be disregarded.

A total of 10 warnings dealt with including brecom.h into routines where it is not used. The included file defines implicit variable-name types, as well as providing common blocks; fstudy does not account for this. These do not have any impact on performance, so each of these warnings can be disregarded. In cases there were no repercussions, the statement was removed.

One warning is due to a missing function, initsig, which is a C routine for catching system signals. This warning can be disregarded.

A total of 8 reported syntax errors were generated by passing a DO-loop index into a sub-

routine, which potentially could change the value of the index. These messages can be disregarded, as in each case the subroutine treats the value as a flag and does not change its value.

The 3 reported syntax errors were due to extra commas in write statements in brvresty and brvrestz. These commas were removed.

A total of 7 reported syntax errors were due to variables being referenced before being set. These errors were each remedied. In rich1bc, variables a2, c1, and c2 were defined; the error was not encountered during simulations to date. In richbal, the test "kmobder .eq. 0" was replaced by already-defined logical variable ymbder; the error affects output of the Peclet number and was not encountered during simulations to date. In tmstep, variable conve0 was replaced by the correct variable (econv0); the error may modify time step sizes. In brvsnap, the section of code referring to variables kset and ksqe was obsolete and therefore was commented out; the error is harmless.

5/31/97 Implementation of unique header. $\boxed{S\!A\!S}$

One of the TOP-018 requirements is that output files are uniquely identified by run. The requirement is typically fulfilled by putting a time stamp in a header line. This requirement had not been implemented in *breath*, except that there is a capability to echo character strings that are defined in the input file. Part of my reluctance to implement headers was due to the non-portability of FORTRAN calls to get the current time, and part was due to the use of *Matlab* routines that scan the output for further processing and that are more conveniently implemented without a header line.

In order to complete an acceptable version of the code, I added two character-string variables (ztime and zversion) that hold the time at the start of the simulation and a version identifier, respectively. The time is obtained using a small routine in C that is coded within the brcatch.c module. By default, the headers are not output; variables are defined for each output stream that enable output. The changes were documented in the version 1.2 user's guide.

A fully compliant release was placed on a diskette and will become part of the QA documentation.

2/16/98 Revision of name initialization.

A known weakness with subroutine initname was fixed while porting *breath* to a Microsoft NT PC using Microsoft Fortran. Microsoft Fortran treats numeric and character data completely differently, so that it is not possible to use the same memory space for both. Most compilers warn, but do not fail, if overloading of memory space occurs.

It is possible to access a vector as either a column in an array or as a vector, if the array and vector are appropriately equivalenced. In *breath*, all vectors with equal lengths are equivalenced into columns of one array, so that IO routines deal with the array and numeric routines deal with a named vector. In order to determine the array column corresponding to a vector for IO, while enabling the addition of new columns without regard to the order of variables in the common block, initname puts a character string with the vector name into the first entry of the double-precision vector. The name is then retrieved and stored in a character name array that is ordered by array column.

The original formulation used a call to initname to access the first entry of a double-precision vector as a character*8 variable. The revised formulation accesses the first entry of a double-precision vector as an integer vector with length 2. The equivalent integer values for the first four characters are loaded into the first entry of the integer vector and the second four are loaded into the second entry. The new subroutine extrname extracts the character string from the encoded entries. There is now no overloading of character and numeric data types, although integer and floating-point data types are overloaded (so that compilers warn but should not fail). Note that the revised procedure would work with integer or single-precision variables if they were vectors of length at least 2.

4/19/02 New development work.

We've finally decided to go ahead and actually implement vegetation in *breath*. Several options are to be allowed, all in the quest for relatively simple models that capture the physics adequately. This entry summarizes the actual mathematical models that will be incorporated.

An extensive series of thoughts are included in the chapter entitled "Ambient Hydrology KTI – Model Development", in which the models that I developed are arrived at. I developed an approach for estimating transpiration based on plant geometry (*e.g.*, rootlets, leaves). This model is described immediately below, reproducing suggestions made to Randy. The vegetation dynamics

component may not be implemented immediately within *breath*, although something like it would probably be used to generate the input for *breath* if it is not implemented.

Randy also requested that I put in a model based on the approach used in UNSAT-H. This model is not used with heat transfer in UNSAT-H, although there is no particular reason that heat transfer cannot be solved as well.

Stothoff model summary

ABSTRACT

A simple vegetation-modeling approach is proposed, suitable for 1D, 2D, and 3D domains. Vegetation uptake is distributed throughout the soil matrix and instantaneously adjusts to atmospheric and soil conditions. Vegetation is assumed to transpire during daylight hours, with atmosphere control whenever pressure at a control point is above wilting and plant control otherwise. A vegetation continuum consists of uptake roots, a transport system, and leaves, and these simplified physiological components determine potential transpiration fluxes that are available for the plant. Evolution of the leaf component occurs according to simplified ordinary differential equations, with growth mediated by temperature and available moisture and death mediated by available moisture and component age. Other components are assumed either static or instantaneously adjusted. Relatively little plant-specific information is required for the model, but the approach is adaptable for both long-lived plant species (*e.g.*, shrubs) and short-lived species that may undergo a life cycle during the simulation.

Background

In project discussions, the most weight has been given to the calculation of evapotranspiration (ET) given a vegetation state, with several approaches considered. One approach is to calculate potential evapotranspiration (PET) based on environmental conditions, and distribute through the soil column as much of PET as the soil will provide based on some specified plant-root distribution (*e.g.*, an envelope exponentially decaying with depth). A second approach is to treat the vegetation continuum as a separate continuum, with pressure defined throughout. A third approach, adopted here, simplifies the second approach by only considering vegetation pressure at one control point.

All three approaches should provide similar answers given similar root distributions, since ET is usually plant controlled; the third option is simplest to implement in the existing code.

Less attention has been given to changing vegetation states over time, which is fairly well characterized for crops and poorly so for range vegetation. Project discussions have touched on how to change leaf area index (LAI) over time for shrubs, based on season or degree-days, but the exact mathematical relationships have not been agreed upon. The approach proposed here is relatively straightforward to implement and is relatively easy to calibrate to the available data.

Instantaneous ET fluxes

Current approach in *breath*

The immediate objective is to provide a simple model for vegetation uptake compatible with existing *breath* methodology, which only considers evaporation. The existing unvegetated model exchanges vapor with the atmosphere with

$$E = C_{sa}(\rho_{vs} - \rho_{va}) \tag{12-1}$$

where

$\quad E \quad$ soil-atmosphere evaporative moisture flux

$\quad C_{sa} \quad$ soil-atmosphere conductance

$\quad \rho_{vs} \quad$ vapor density in surface soil

$\quad \rho_{va} \quad$ vapor density in far-field atmosphere

The conductance is based on boundary-layer theory, and accounts for such factors as wind speed, surface roughness, and atmospheric stability. After a rainfall event, E is large and almost constant as the soil is able to supply atmospheric demand. As the soil dries, the soil is unable to supply water at the atmospheric demand and E drops as a function of $t^{1/2}$.

Proposed approach

Several assumptions are made regarding vegetative transpiration in the proposed approach.

- Pressure losses are negligible within the plant transport system

- Uptake roots respond instantaneously relative to moisture dynamics

- Transport roots respond slowly relative to moisture dynamics

- Leaf stomates respond instantaneously to atmospheric conditions

- Leaf stomates open as much as possible to achieve positive transpiration and internal pressure above wilting

- Uptake roots are characterized as an array of cylinders

- Leaves are characterized as an array of spheres

Proposed uptake model

The uptake model accounts for soil properties, root length density, and plant pressure status. The neglect of pressure losses within the plant system implies that pressure within the plant is essentially hydrostatic, so uptake is

$$q_u = C_u(P_s + \rho g z_s - P_v - \rho g z_v) = C_u(P_s^* - P_v) \tag{12-2}$$

$$Q_u = \int\limits_{-\infty}^{z_g} q_u \, dx \tag{12-3}$$

where

q_u local uptake flux per unit volume

Q_u total uptake flux per unit area

C_u soil-plant uptake conductance

P_s soil pressure

P_v vegetation pressure at a control point

z_s soil elevation

z_v control-point elevation

z_g ground-surface elevation

Uptake conductance is calculated assuming that roots are uniformly distributed cylinders

$$C_u = 2\pi \rho_{ru} H \left[\frac{K_s}{\ln(R/r_w)}, \frac{K_w}{\ln(r_w/r_p)} \right] \tag{12-4}$$

$$R = \left(\frac{1}{\pi \rho_{ru}} \right)^{1/2} \tag{12-5}$$

$$H(x,y) = \frac{2xy}{x+y} \tag{12-6}$$

where

ρ_{ru} uptake-root length density

K_s soil conductivity

K_w plant-wall conductivity

r_w outer radius of uptake root

r_p inner radius of uptake root

$H(x, y)$ harmonic-mean operator

Note that typically plant-wall conductance C_w is measured, where

$$C_w = \frac{K_w}{\ln(r_w/r_p)} \approx \frac{K_w}{r_w - r_p} \tag{12-7}$$

The requirement that $\rho_{ru} = 0$ if $P_v > P_s^*$ (the instantaneous response assumption) completes the model.

The uptake model requires only P_v, z_v, ρ_{ru}, C_w, and r_w in addition to quantities already calculated by *breath*. P_v is calculated as part of the flux-continuity component of the model, while the remainder are model inputs.

Uptake roots are not uniform throughout the column. Length density typically decays exponentially from the top. The initial distribution of ρ_{ru} in each grid cell will be provided as input. In transient-ρ_{ru} cases, rules for modifying ρ_{ru} over time can be specified.

Common agronomy approaches specify q_u in the general form

$$q_u = F_u q_0 \exp[-a(z - z_g)] \tag{12-8}$$

where F_u is a reduction factor based on soil moisture. The proposed model also reduces uptake as soil pressure drops, reaching zero before the control point reaches wilting. Reduction comes from both reduced pressure gradients and reduced soil conductivity. When ρ_{ru} is exponentially distributed, the uptake model has the same general behavior as common agronomy approaches.

Proposed dispersal model

The dispersal model accounts for leaf area density, atmospheric demand, and plant status.

$$q_d = F C_d [\rho_{vs}(T_l) - \rho_{va}] \tag{12-9}$$

$$Q_u = \int\limits_{z_g}^{\infty} q_d \, dx \tag{12-10}$$

where

F plant stomate control factor $0 \leq F \leq 1$

q_d local dispersal flux per unit volume

Q_d total dispersal flux (transpiration) per unit area

C_d plant-atmosphere dispersal conductance

ρ_{vs} saturated vapor density at leaf temperature

ρ_{va} atmospheric vapor density

T_l leaf temperature

Dispersal conductance is calculated assuming that leaves are uniformly distributed spheres within a layer

$$C_d = \frac{4\pi \rho_{ld}}{A_l} \left(\frac{Rr_w}{R - r_w} \right) D \approx \rho_{ld} D \left(\frac{4\pi}{A_l} \right)^{1/2} \tag{12-11}$$

$$R = \left(\frac{3A_l}{4\pi \rho_{ld}} \right)^{1/3} \tag{12-12}$$

$$r_w = \left(\frac{A_l}{4\pi} \right)^{1/2} \tag{12-13}$$

where

ρ_{ld} leaf area density

D atmospheric dispersivity

A_l area of one leaf

The simplification in C_d comes when $R \gg r_w$, which is usually the case for shrubs. Neglecting R is probably justified for all YM vegetation even under glacial conditions. At low transpiration rates, q_d is then linearly dependent on ρ_{ld} (hence LAI) and atmospheric dispersivity. At higher transpiration rates, ρ_{va} responds to the flux, increasing and reducing the gradient driving both evaporation and transpiration, so the linearity is lost.

The dispersal model requires F, $\rho_{vs}(T_l)$, ρ_{ld}, D, and A_l in addition to quantities already calculated by *breath*. F is calculated as part of the flux-continuity component of the model; A_l is model input; ρ_{vs} is calculated using air temperature (part of the boundary conditions), and D arises from the same boundary-layer theory as *breath* already uses.

As with ρ_{ru}, ρ_{ld} is distributed vertically. Typically only the vertically integrated value is known (*i.e.*, LAI). If the leaves are concentrated into one elevation (the "big leaf" approach), $\rho_{ru} = LAI/b$ where b is grid-block thickness. An easy assumption is that ρ_{ru} is uniformly distributed over a characteristic plant height that depends on climate.

The ρ_{ld} distribution is calculated in the form

$$\rho_{ld}(z) = LAI P_{ld}(z) \tag{12-14}$$

where

$$\int\limits_{z_g}^{\infty} P_{ld}\,\mathrm{d}z = 1 \tag{12-15}$$

Variation of $\rho_{ld}(z)$ over time reduces to specifying LAI over time, which is discussed below.

Proposed flux-continuity model

The approach requires that compatibility is maintained between uptake flux, dispersal flux, and plant physiology. Flux compatibility is stated by

$$F_d \sum_i q_{di} = F_u \sum_j q_{uj} \tag{12-16}$$

$$q_{di} = C_{di}(\rho_{vsi} - \rho_{vai}) \tag{12-17}$$

$$q_{uj} = C_{uj}(P_{sj}^* - P_v) \tag{12-18}$$

where F_d and F_u are fractions of the maximum possible dispersal and uptake fluxes, respectively ($0 \le F_d \le 1$ and $0 \le F_u \le 1$). These parameters are assumed to hold across all vegetation classes simultaneously.

The compatibility equation can be written in the form of

$$F_d q_{dm} = F_u q_{um} \tag{12-19}$$

where q_{dm} is the maximum possible dispersal flux over all vegetation classes (taking into account whether the plant type would actually be transpiring), and q_{um} is the maximum possible uptake flux over all vegetation classes (the plant is at its wilting pressure), The values for F_u and F_d are set by

$$F_u = \begin{cases} q_{dm}/q_{um} & \text{if } q_{dm} < q_{um} \\ 1 & \text{otherwise} \end{cases} \tag{12-20}$$

$$F_d = \begin{cases} q_{um}/q_{dm} & \text{if } q_{um} < q_{dm} \\ 1 & \text{otherwise} \end{cases} \tag{12-21}$$

All of the local values of q_{di} and q_{ui} for all vegetation classes are multiplied by the same factor.

In the simple case of one release point for vegetation above the ground (an assumption in the "big leaf" approach) in 1D, the atmosphere system must satisfy

$$q_3 = q_1 + q_2 = E + T \tag{12-22}$$

$$q_1 = C_1(\rho_s - \rho_m) \tag{12-23}$$

$$q_2 = F_d C_2(\rho_l - \rho_m) \tag{12-24}$$

$$q_3 = C_3(\rho_m - \rho_a) \tag{12-25}$$

where subscripts s, l, m, and a represent locations at the soil, leaf, mid-boundary-layer, and far-field atmosphere. This results in the solution for ρ_m as

$$\rho_m = \frac{C_1\rho_s + F_d C_2\rho_l + C_3\rho_a}{C_1 + F_d C_2 + C_3} \tag{12-26}$$

The corresponding actual transpiration flux is

$$
\begin{aligned}
Q_d &= F_d C_2(\rho_l - \rho_m) \\
&= F_d C_2\left[\rho_l - \left(\frac{C_1\rho_s + F_d C_2\rho_l + C_3\rho_a}{C_1 + F_d C_2 + C_3}\right)\right] \\
&= F_d C_2\left[\frac{C_1(\rho_l - \rho_s) + C_3(\rho_l - \rho_a)}{C_1 + F_d C_2 + C_3}\right]
\end{aligned} \tag{12-27}
$$

It is simple to solve a system of linear equations to get the intermediate densities and fluxes.

The F_d and F_u may vary across a time step, since ρ_m depends on F. The simplest way to handle this nonlinearity is to use the value at the start of the step. In essence, the plant makes a decision at the start of the step and holds it for the entire step.

The parameters that need specifying for the model include P_{vmin} and the transpiration-enable method. A simple transpiration-enable method would be to allow transpiration only if shortwave radiation is greater than zero (*i.e.*, daylight) or equal to zero (*i.e.*, nighttime, for CAM plants). Since shortwave radiation is provided as a boundary condition, no additional information is required.

Vegetation dynamics

Over a simulation that extends through a growing season, the vegetation must change state (*e.g.*, add/drop leaves). The three major components of the vegetation system are leaves, transport roots, and uptake roots.

The immediate goal for adding to *breath* is to keep the dynamics as simple as possible at first. As a first cut, the root system will not evolve over time. Uptake roots were assumed to instantaneously respond to changes in moisture in the previous section, in essence either completely dead or missing, or present at a capacity level. Evolution would occur if the capacity level changed over time. However, leaves are quite dynamic at the time scales of interest, so a dynamic-leaf-density model is presented below.

Leaf dynamics

We have agreed that leaves respond to season, and a common approach for agronomists is to use the concept of degree-days to describe the growing season. Degree days measure the accumulated time above freezing, weighted by the warmth when above freezing. Presumably one characterizes LAI or some equivalent as a function of degree-days during the growing season. Although data on rangeland species is lacking, in principle this is relatively straightforward to approximate.

A weakness of the degree-day approach in our case is that moisture is also required for growth, and (correct me if I'm wrong) this is not considered.

A way to get at the same thing as the degree-day approach with perhaps less effort, while incorporating moisture stress, is to formally integrate temperature-dependent growth relationships. A general expression for total leaf area density is written

$$\frac{\partial \rho_l}{\partial t} = \alpha_g(\rho_{og} - \rho_l)\left(\frac{\bar{F}}{F_{og}} - 1\right) - \alpha_d(\rho_l - \rho_{od})\left(1 - \frac{\bar{F}}{F_{od}}\right) - \alpha_a\rho_l\left(\frac{A}{A_{oa}} - 1\right) \tag{12-28}$$

where

ρ_l LAI
α rate constant [1/T]
A average leaf age
$\bar{x}$ moving time average of x

The three terms on the right-hand-side represent growth, death due to moisture stress, and death due to old age. The first term only operates when $\rho_l < \rho_{og}$ and $\bar{F} > F_{og}$ (*i.e.*, density less than maximum capacity and average respiration is more than a target threshold). The second term only operates when $\rho_l > \rho_{od}$ and $\bar{F} < F_{od}$ (*i.e.*, density greater than minimum capacity and average respiration is less than a target threshold). The last term only operates when $A > Aoa$ (*i.e.*, mean age is greater than some threshold age).

The α_g coefficient represents growth under optimal conditions. This is known to be temperature dependent, with a parabolic form. The form to include in the code is

$$f = |(T - T_{mid})/(T_{end} - T_{mid})| \tag{12-29}$$

$$\alpha_g = \alpha_{opt}(1 - f^2) \tag{12-30}$$

where $0 \leq f \leq 1$. Maximum growth occurs at an optimal temperature and there is a threshold cold temperature value where growth ceases. Note that Bromus has a lower cold temperature value than shrubs.

There should be a seasonal component as well, which might be handled as an on/off switch for growth.

For simplicity, I propose a similar but inverted relationship for α_d and α_a, with a cutoff maximum rate.

$$f = |(T - T_{mid})/(T_{end} - T_{mid})| \tag{12-31}$$

$$\alpha_d = \alpha_{mid} + f^2(\alpha_{end} - \alpha_{mid}) \tag{12-32}$$

where $0 \leq f \leq 1$. This describes a parabola.

The mean leaf age in days accumulated over a time step is calculated by

$$A = \frac{\Delta t \rho_g + (A + \Delta t)(\rho_l - \rho_d - \rho_a)}{\rho_g + \rho_l - \rho_d - \rho_a} \tag{12-33}$$

which adds new leaves at age Δt and removes leaves at the mean age. The densities represent accumulated changes over the day.

Time averaging of some variable x is performed using

$$\bar{x} \leftarrow \frac{\Delta t(x - \bar{x}) + T_{ave}\bar{x}}{T} \tag{12-34}$$

where T_{ave} is the averaging period.

The required information for the growth term includes growth start/stop period, optimal temperature, minimum growth temperature, maximal growth rate, threshold fraction of transpiration, maximum leaf area density, and transpiration averaging period.

The required information for the moisture-deficit death term includes minimum temperature, temperature at maximum death rate, minimum and maximum death rate, threshold fraction of transpiration, minimum leaf area density, and transpiration averaging period.

The required information for the old-age death term includes death rate and age trigger.

Note that due to the nonlinear temperature dependence of α_g and α_d, it is best to perform a moving average of these coefficients over a period of at least a day.

Summary of vegetation parameters

Parameter	Description
$\rho_{ru}(z)$	Root-length density distribution [L/L^3]
C_w	Conductance across uptake-root walls [1/T]
r_w	Outer diameter of uptake roots [L]
$P_{ld}(z)$	Relative leaf-area-density distribution [1/L]
A_l	Area of one leaf [L^2]
P_{vmin}	Minimum plant pressure at control point
z_v	Elevation of plant-pressure control point [L]
F_{enable}	Transpiration enable code (day/night/both)
α_{opt}	Unrestricted leaf growth rate at optimal temperature [1/T]
T_{opt}	Optimal temperature for leaf growth [K]
T_{min}	Minimum temperature for leaf growth [K]
α_{mid}	Minimum leaf death rate [1/T]
α_{end}	Maximum leaf death rate [1/T]
T_{mid}	Temperature for minimum leaf death rate [1/T]
T_{end}	Temperature for maximum leaf death rate [1/T]
ρ_{og}	Maximum distributed (not canopy) LAI [L^2/L^2]
ρ_{od}	Minimum distributed LAI for moisture-stress death [L^2/L^2]
F_{og}	Fractional transpiration rate required for growth
F_{od}	Minimum fractional transpiration rate before death starts
A_{oa}	Mean age at which leaves start dying [T]
T_{ave}	Averaging period for $\bar{F}$ and A [T]

UNSAT-H model summary

Driving force

UNSAT-H model

UNSAT-H bases transpiration on the use of PET and does not solve for heat transport at the same time. In all cases considered,

$$PET = T_p + E_p \qquad (12\text{-}35)$$

where PET is potential evapotranspiration, T_p is potential transpiration, and E_p is potential evaporation.

UNSAT-H allows PET to be either directly provided as a boundary condition, or calculated using the formula

$$PET = \frac{1}{s+\gamma}\left[sR_{ni} + \gamma 0.27(1 + U/100)(e_a - e_d)\right] \qquad (12\text{-}36)$$

where s is slope of the saturation-vapor-pressure/temperature curve [mb/K], R_{ni} is isothermal net radiation [mm/d], γ is psychropmetric constant [mb/K], U is 24-hr wind run [km/d], e_a is saturation vapor pressure at mean air temperature [mb], and e_d is actual vapor pressure [mb].

Two methods are provided in UNSAT-H to partition PET, both based on the ratio of T_p to net radiation, R_n. One relationship is in the form

$$\frac{T_p}{R_n} = a + bLAI^c \qquad \text{for } d \leq LAI \leq e \qquad (12\text{-}37)$$

where suggested values for cotton and grain sorghum are $a = d = 0$, $b = 0.52$, $c = 0.5$, and $e = 3.7$.

The second relationship simply apportions T_p/R_n over the growing season. The suggested relationship for cheatgrass is trapezoidal, with a peak growing season hard-coded from day 90 to day 150, and linear changes from germination to day 90 and from day 150 to senescence.

An adjustment factor is provided to scale T_p/R_n by biomass. The original measurements were based on 220 gm/m^2; thus, to double the T_p/R_n ratio, one provides UNSAT-H with a biomass of 440 gm/m^2(with the caveat that $0 \leq T_p/R_n \leq 1$).

Once E_p is determined, it is used as a flux boundary condition when the suction head is less than the air-dry value; otherwise, the top boundary condition is that the suction head value is

specified to be the air-dry value. The air-dry value is either user-specified or calculated based on atmospheric conditions and soil properties.

Implementation in *breath*

The evaporation boundary condition for *breath* is based on transport across a boundary layer. This eliminates the need for a boundary condition switching between vapor flux and specified pressure, and there is no reason to calculate an air-dry pressure. In the spirit of partitioning PET, the flux boundary condition due to evaporation will be the minimum of the boundary-layer flux and $PET - T$, where T is the total uptake flux.

Uptake distribution

UNSAT-H first distributes T_p through the soil depth based on root length density, ρ_r, converted into a root density function, RDF, that is the root length within each layer normalized by the total root length,

$$RDF = \frac{\int\limits_{z_0}^{z_1} \rho_r \, \mathrm{d}z}{\int\limits_{-\infty}^{\infty} \rho_r \, \mathrm{d}z} \tag{12-38}$$

The distributed uptake value for a layer is then multiplied by a factor, α_f, based on soil water content. As implemented, α_f is trapezoidal; $\alpha_f = 1$ for $\theta_d \leq \theta \leq \theta_n$, $\alpha_f = 0$ for $\theta \leq \theta_w$ or $\theta \geq \theta_n$, and α_f linearly varies between θ_w and θ_d.

There are several features of the implementation worth noting.

- The implementation abruptly cuts off at a threshold value at the wet end due to anaerobic conditions. This is objectionable numerically, since this is where the solution is already very twitchy even without the shock of a threshold. Further, it is rare that the soil is almost saturated so that neglecting the refinement is not likely to have a great impact.

- The use of water content is objectionable when the soil is heterogeneous, since a different set of parameters should be provided for each soil type

- The distribution formulation tends to underpredict uptake, since there is no provision for extra water to be taken from layers that have water when other layers are dry

For all these reasons, the distribution function described in the UNSAT-H documentation will not be implemented. Instead, the uptake model I developed will be used.

4/20/02 Status of revision. $\boxed{\text{SAS}}$

Over the last few weeks, I revised the input/output structure again. Revision was needed in order to add multiple vegetation types and discretize the atmospheric boundary layer.

The existing I/O structure basically had several types of variables, depending on whether they were defined as scalar values, by node, or by element, and what type of variable. Each type of variable is stored in a single large array that is equivalenced to a list of variables in a single common block. Thus, each variable can be accessed by name (good for computations) and by address within a large array (good for I/O).

Under the existing I/O structure, it is straightforward to add new variables if the variables have the same dimensions as an existing variable (changing a few spots in the include file and an initialization statement) but it would be significantly more tedious otherwise, since additional conditional loops would need to be added in several locations. It turns out that adding multiple vegetation types makes it desirable to allow variables to be referenced with dimensions in the input data set (*e.g.*, vlai(1), vlai(2), etc.). Since several new dimension sets were needed, I revised the I/O structure to make it easy to add whole new types of variables including ones with subscripts.

It turns out that somewhere in excess of 600 user-accessible variables are needed with vegetation included, with the exact number depending on the number of vegetation types. In addition, more than 25 different combinations of type and dimension are needed. With this large number of variables, it is really necessary to impose a strategy that can easily add and subtract variables while ensuring that transparent updating occurs wherever the I/O structure references the variable.

The strategy is to use *Matlab* to generate fortran modules. In the *Matlab* generating scheme, each variable only requires a one-line description in a table, including name, description, and initial value. A different table is used for each set of variables with a unique type and dimensions, and yet another table is used for parameters. A master table describes the characteristics of the variables in the other tables. This information, together with a list of synonyms for backward compatibility, is sufficient to generate the include file and a fortran module handling all initialization and I/O details that depend on the actual storage locations for the variables. The combined modules are over 2000 lines of code (including comments).

The run-time strategy for handling variables is based on a set of tables paralleling the *Matlab* tables. One set of tables describes the unique components of each variable, while another set describes the unique components of each group of variables. A large fraction of the generated code is a block-data module that initializes these tables.

Each I/O routine that accesses the variables by name calls a driver routine that locates the name and pointers to the location in memory. The I/O routine also passes the address of 4 functions, one for integer, real, logical, and character variables. The driver routine ultimately executes the appropriate function for the variable and passes the storage location to that function. Typical functions are for input, echoing, printing, and restarting.

As the input structure is quite significantly altered from before, there is always the possibility of bugs. I tested the revised code using the example files for version 1.2, which were specifically developed to test a wide variety of I/O options as well as physical scenarios. Some variables have different names, although synonyms are defined for most of the new names for backward compatibility, so the old input files all had to be modified to some extent. Each example pointed out one or more bugs, but ultimately all ran All but one of the examples provided exactly the same results as before (evidenced by a `diff` command on the output files), while the last example only differed in the 4th or 5th decimal place.

I expect that there may be a few more things to shake down, but I conclude that the new I/O structure is working pretty well. From this point on, it will be trivially easy to add new variables to *breath*, at least as far as I/O is concerned; before, revising I/O made adding new capabilities a daunting prospect.

4/24/02 Revised equations.

I've been testing a prototype in *Matlab*, which suggests revisions to the equations for dynamics. A revised form is discussed here.

Vegetation dynamics

Over a simulation that extends through a growing season, the vegetation must change state (*e.g.*, add/drop leaves). The three major components of the vegetation system are leaves, transport roots, and uptake roots. Leaves were discussed before. I am using a simple prototype to investigate the

effect of different strategies for allocating uptake (*e.g.*, hydrostatic, dual-continuum, and UNSAT-H). In the process, I am testing the importance of root evolution as well.

Root dynamics

Following the approach developed for leaves, uptake roots are assumed to change according to the relationship

$$\frac{\partial \rho_u}{\partial t} = \alpha_g \rho_u \left(\frac{\rho_{uog}}{\rho_u} - 1 \right) \left(\frac{\bar{F}}{F_{uog}} - 1 \right) - \alpha_d \rho_u \left(1 - \frac{\rho_{uod}}{\rho_u} \right) \left(1 - \frac{\bar{F}}{F_{uod}} \right) - \alpha_a \rho_u \left(\frac{A}{A_{uoa}} - 1 \right) \quad (12\text{-}39)$$

where

ρ_u root-length density for uptake roots

α rate constant [1/T]

A average age

The three terms on the right-hand-side represent growth, death due to moisture stress, and death due to old age. Each term only operates when the individual components are all positive, and the adjustment factors after the $\alpha \rho_u$ components for a term are assumed to be jointly in the range 0 to 1. The α coefficients are all assumed to be of the same form as the corresponding leaf coefficients.

The ρ_{uo} terms are tied to the local transport-root vertical-area density by assuming that an ever-increasing fraction of the transport area can be devoted to local uptake, using the form

$$\rho_{uo} = \beta_{tuo} \rho_t \left(\frac{z_g - z}{L_{tmax}} \right) \quad (12\text{-}40)$$

where

ρ_t vertical transport-root area density [L^2/L^2]

β_{tuo} maximum uptake-root length per unit ρ_l

z_g ground-surface elevation [L]

z local elevation [L]

L_{tmax} maximum transport-root depth [L]

The F_{uo} terms are tied to ρ_u using

$$F_{uo} = \beta_{quo} \rho_u \quad (12\text{-}41)$$

where

12-26

β_{quo} target uptake flux per unit ρ_u

Transport roots are assumed to change according to the relationship

$$\frac{\partial \rho_t}{\partial t} = \alpha_g \rho_t \left(\frac{\bar{F}}{F_{tog}} - 1 \right) - \alpha_d \rho_t \left(1 - \frac{\bar{F}}{F_{tod}} \right) - \alpha_a \rho_t \left(\frac{A}{A_{toa}} - 1 \right) \tag{12-42}$$

where terms are analogous to the uptake-root relationship. The α coefficients are all assumed to be of the same form as the corresponding uptake and leaf coefficients. Note that unlike the leaf and uptake relationships, no *a priori* upper or lower limits are imposed for transport roots.

The set of relationships drives root distributions towards a characteristic depth and density profile. Descriptions of the plant including maximum rooting depth and maximum uptake-root length per unit stem area tend to drive the allocation patterns towards ever-decreasing transport and maximum-uptake capacities with depth, although actual uptake capacity adjusts according to moisture.

4/26/02 Revised equations.

$\boxed{\mathcal{SAS}}$

I found that updating ρ from $d\rho/dt = \pm \alpha \rho$ using

$$\rho \leftarrow (1 + \alpha_d \Delta t)\rho \tag{12-43}$$

$$\rho \leftarrow (1 - \alpha_h \Delta t)\rho \tag{12-44}$$

where α_d is 1/time-to-doubling and α_h is 1/time-to-halving, did not work correctly unless $\alpha_d \Delta t = 1$ and $\alpha_h \Delta t = 1/2$. The error is because of compounding over many time steps. For example, in the limit of many tiny time steps the final ρ ends up a factor of e too large for doubling. The adjusted forms are

$$\alpha_d^* \Delta t = 1 + 2^{\alpha_d \Delta t} \tag{12-45}$$

$$\alpha_h^* \Delta t = 1 - (1/2)^{\alpha_h \Delta t} \tag{12-46}$$

for doubling and halving, respectively. In all of the growth equations discussed here, $\alpha \Delta t < 1$ and the adjustment is tacitly assumed.

5/06/02 Vegetation implementation.

$\boxed{\mathcal{SAS}}$

Based on the similarity between uptake patterns for the UNSAT-H and hydrostatic-mechanistic algorithms, even when adaptive root-length distributions are allowed, I am not going to look at

dual-continuum uptake patterns in the prototype at this time. Both algorithms tested suggest that shrub uptake is only limiting when plant (and soil) pressures are about at the wilting pressure for typical root-length densities. However, I will implement both uptake strategies, and an adaptive growth algorithm for roots.

The prototype investigations suggest that shrub transpiration is rate-limited by stomatal diffusion of water vapor, although for grasses and for shrubs under very still conditions there may be influence from the leaf boundary layer as well. Under most environmental conditions the necessary information for shrubs is stomate area density and dimensions. This is most easily handled by specifying these quantities on a per-leaf-area basis, and working with the more readily available LAI.

The leaf dynamics model discussed in the 4/19/02 entry depends on a target LAI for both growth and death. In the investigation of phreatophytic-shrub behavior in Owens Valley, CA, reported in the entry dated 5/2/02 in the chapter devoted to model development for the ambient hydrology KTI, LAI peaks somewhere between the peak day for shortwave radiation and the peak day for temperature, about a month later. This occurs for shrubs that are not moisture-limited, and LAI is measured as a function of Julian day. However, it is undesirable to use LAI described by day, since the function is site specific.

The implementation for LAI will be in terms of LAI per unit stem area. The following options will be provided

- Specified LAI/stem area

  - Time-varying input

  - Constant

- Specified target LAI for growth and death

  - Time-varying input

  - Constant

  - Functional form based on temperature and/or net radiation

The preferred functional form for target LAI (both growth and death) is in the form

$$LAI_{log} = LAI_{og} f(T, S_w)$$ (12-47)

$$f = \left[\frac{f_t f_r}{w_r f_t + (1 - w_r) f_r} \right]^p$$ (12-48)

$$f_t = P(T, T_{end}, T_{mid}, f_{tmin}, f_{tmax})^{p_t}$$ (12-49)

$$f_r = L(S_w, S_{lo}, S_{hi}, f_{rmin}, f_{rmax})^{p_r}$$ (12-50)

$$P(x, x_{end}, x_{mid}, v_{end}, v_{mid}) = v_{end} f_p + v_{mid}(1 - f_p)$$ (12-51)

$$f_p(x, x_{end}, x_{mid}) = \max(-1, \min[1, (x - x_{end})/(x_{mid} - x_{end})])^2$$ (12-52)

$$L(x, x_{lo}, x_{hi}, v_{lo}, v_{hi}) = (1 - v_{lo}) f_l + v_{hi} f_l$$ (12-53)

$$f_l(x, x_{lo}, x_{hi}) = \max(0, \min[1, (x - x_{lo})/(x_{hi} - x_{lo})])$$ (12-54)

which represents a parabolic dependence on temperature and a linear dependence on net radiation. Both models will be available for both parameters, and either can be neglected. Remember, the functional form represents the results of a long optimization search by the species and does not necessarily mean that transpiration constraints are at play.

The functional form is more flexible than is probably justified by the available data. I suggest setting $p_t = p_r = 1$ as a default.

The leaf-dynamic model needs to be modified based on the form of the LAI distribution over the year for the Owens Valley phreatophytes. The form is symmetric about the peak, which implies that shrubs voluntarily reduce LAI even without an apparent stress. Also, the prototype suggests that shrub transpiration is essentially unaffected by the windspeed profile. The implication is that individual shrubs primarily grow higher for reproductive success (perhaps for better radiation access, too) and that transpiration is not really responsive to the distribution of leaf-area density. Accordingly, the leaf-dynamics model is modified to the form

$$\begin{aligned}
\frac{\partial L}{\partial t} = {}& \alpha_{lg} L \left(\frac{L_{max}}{L} - 1 \right) \left(\frac{\bar{F}}{F_g} - 1 \right) \\
& - \alpha_{ld} L \left(1 - \frac{L_{max}}{L} \right) \\
& - \alpha_{ld} L \left(1 - \frac{L_{min}}{L} \right) \left(1 - \frac{\bar{F}}{F_d} \right) \\
& - \alpha_{la} \alpha_{ld} L \left(\frac{A}{A_d} - 1 \right)
\end{aligned}$$ (12-55)

where L is LAI and the F parameters represent fraction of stomates open. All terms in parentheses are dimensionless and clamped to the range of 0 to 1. In this form, LAI_{max} and LAI_{min} are the

target LAI values described just above. For completeness, the same model will be made available for F_g, F_d, and A_d although the simplest model would typically be used due to lack of information. Also, note that the age-death term may be most appropriate for annuals.

For additional flexibility, a saturation model based on the sigmoid function will be included as well to augment the linear ramp. A sigmoid function based on $\tanh(x)$ is

$$ f = \left(1 + \exp\left[\frac{x(L_1 - L_0) - (L_1 x_0 - L_0 x_1)}{x_1 - x_0} \right] \right)^{-1} \tag{12-56}$$

$$ L_0 = \ln\left(\frac{1}{\delta} - 1 \right) \tag{12-57}$$

$$ L_1 = \ln\left(\frac{1}{1 - \delta} - 1 \right) \tag{12-58}$$

where $0 \le \delta \le 1$ is a small offset, and x_0 and x_1 are the values of x where $f = \delta$ and $f = 1 - \delta$, respectively. The sigmoid is linear near its midpoint.

For consistency, the corresponding root parameters will have the same model dependencies available. Although no shortwave radiation hits roots, the plant can signal roots based on radiation. Also note that there is some basis for uptake roots having seasonal targets as well, since respiration is temperature-dependent.

5/20/02 Vegetation input.

Adding vegetation requires that new control variables be implemented. These are listed here for planning purposes. Each vegetation type has its own set of control variables. Control variables and options for vegetative fluxes are listed in Table 12-1. Control variables and options for vegetative growth are listed in Table 12-2.

The vegetation module should be considered an essentially standalone package from the standpoint of the main code. With this in mind, the vegetation module only needs to provide the main code with values for total vegetative uptake flux and the derivatives with respect to the state variables (pressure or vapor density, and temperature).

Table 12-1: Control variables and options for vegetative fluxes.

Variable	Option	Description
zvmodep		Vegetation pressure mode
	inactive	Vegetation not required
	none	Pressure not required
	hydrostatic	Hydrostatic pressure in vegetation -1 (stem) pressure solved for
	statevar	Pressure in vegetation solved for as a separate continuum (not implemented immediately)
zvuptake		Model for distributed uptake (limit is imposed by potential transpiration)
	none	No uptake required
	dtrancyl	Diffusive transfer with cylinder model
	limitvwc	Transpiration-determined uptake limited by volumetric-water-content function (UNSAT-H)
	limitp	Transpiration-determined uptake limited by pressure function (like UNSAT-H but with pressure function instead of water content)
zvpottran		Model for potential transpiration rate
	none	None required
	dtransph	Diffusive transfer with spherical model
	dtrancyl	Diffusive transfer with cylinder model
	netrad1	Rate determined by function of net radiation (UNSAT-H model)

Table 12-2: Control variables and options for vegetative growth.

Variable	Option	Description
zvglai		Vegetation LAI growth mode
	static	Determined from user input
	sine	Determined with sinusoidal function
	trap	Determined with trapezoidal function
	dynamic	Determined through dynamic growth model (not implemented immediately)
zvgleaf		Vegetation distributed-leaf growth mode
	static	Determined from user input
	dynamic	Determined through dynamic growth model (not implemented immediately)
zvgtrad		Vegetation transport-area-density growth mode
	static	Determined from user input
	dynamic	Determined through dynamic growth model (not implemented immediately)
zvgurld		Vegetation uptake length density growth mode
	static	Determined from user input
	equilib	Equilibrium mode
	dynamic	Determined through dynamic growth model (not implemented immediately)

References

13   Performance Assessment Research, Task 3 – Vertical ODE Solver

Account Number: **20-5704-193**

Collaborators: **Sitakanta Mohanty, Gordon Wittmeyer**

Directories: **$HOME2/Matlab/ODE → $ODE**

Objective: The first proposed objective put forth by Sitakanta on November 16, in a meeting with Gordon and myself, is to examine vertical fluxes of both liquid and vapor at YM under the influence of the geothermal gradient. Gordon used an ODE solver previously to handle liquid fluxes only. Immediately after the meeting, Bill Murphy mentioned to me that he had previously examined ^{14}C fluxes and concluded that diffusion is the dominant mechanism. Quickly checking this statement with a simple analytic solution for a homogeneous column, liquid flux may be supported up to 10 mm/yr.

Based on the meeting and on the ^{14}C results, the objective is two-fold: (i) create numerical tools to integrate the steady-state flow and transport equations, using an ODE solver where applicable; and (ii) use the tools to estimate what fluxes might be admissible with all sources of information. As *Matlab* has ODE solvers built in, the tools will be developed in *Matlab*.

12/23/95 Governing Equations.

$\boxed{\mathcal{SAS}}$

The basic nonisothermal multiphase, multicomponent flow and transport equations are the starting point for the development. The development is presented in Stothoff (1995).

Summary of governing equations

Mass balance

$$\frac{\partial}{\partial t}(\epsilon_\alpha \rho_\alpha \chi_\alpha^i) + \nabla \cdot (\epsilon_\alpha \rho_\alpha \chi_\alpha^i \mathbf{v}_\alpha) + \nabla \cdot \mathbf{j}_\alpha^i - S_\alpha^i - \epsilon_\alpha \rho_\alpha \chi_\alpha^i R_{m\alpha}^{\ i} = 0, \tag{13-1}$$

$$\mathbf{j}_\alpha^i = \epsilon_\alpha \rho_\alpha \chi_\alpha^i (\mathbf{v}_\alpha^i - \mathbf{v}_\alpha), \tag{13-2}$$

where

ϵ_α is the volume fraction for phase α,

ρ_α is the density of phase α,

χ_α^i is the mass fraction of species i in phase α,

$\mathbf{v}_\alpha$ is the mass-average velocity of phase α,

$\mathbf{j}_\alpha^i$ is the non-advective flux of phase α,

R_α^i is the external supply of species i in phase α, and

S_α^i is the exchange of mass with other phases of species i in phase α.

The following additional constraints must also be obeyed:

$$1 = \sum_{\alpha=1}^{N_{\text{phase}}} \epsilon_\alpha, \tag{13-3}$$

$$1 = \sum_{i=1}^{N_{\text{spec}}} \chi_\alpha^i, \tag{13-4}$$

$$1 = \sum_{\alpha=1}^{N_{\text{phase}}} \sum_{i=1}^{N_{\text{spec}}} S_\alpha^i. \tag{13-5}$$

The following definition is used throughout to average from a species-defined variable, B_α^i, to a phase-average quantity, B_α, (unless otherwise specified):

$$B_\alpha = \sum_{i=1}^{N_{\text{spec}}} \chi_\alpha^i B_\alpha^i \tag{13-6}$$

leading to the mass-averaged phase velocity,

$$\mathbf{v}_\alpha = \sum_{i=1}^{N_{\text{spec}}} \chi_\alpha^i \mathbf{v}_\alpha^i. \tag{13-7}$$

Note that there are other, comparable, averaging definitions, such as molar-averaging or volume-averaging (Bird et al., 1960).

The mass-averaged phase velocity for a fluid phase in a porous medium is assumed to be described using Darcy's law, so that

$$\mathbf{q}_\alpha = \epsilon_\alpha(\mathbf{v}_\alpha - \mathbf{v}_s) = -k\lambda_\alpha \cdot (\nabla P_\alpha + \rho_\alpha g \nabla z), \tag{13-8}$$

where

$\mathbf{q}_\alpha$ is the volumetric flux of phase α per unit area [L T^{-1}],

$\mathbf{v}_s$ is the velocity of the solid phase [L T^{-1}],

k is the intrinsic permeability [L^2],

λ_α is the mobility of phase α, or $k_{r\alpha}/\mu_\alpha$,

$k_{r\alpha}$ is the relative permeability of phase α, where $k_{r\alpha} = k_{r\alpha}(P_\alpha)$ [-],

μ_α is the dynamic viscosity of phase α [ML^{-1}T^{-1}],

P_α is the pressure of phase α [ML^{-1}T^{-2}],

g is the acceleration due to gravity [L T^{-2}], and

z is the elevation [L].

ODE form for equations

The equations that will be considered for the ODE solver consist of mass balance for the water species, mass balance for the liquid phase, mass balance for the total fluid mass, mass balance for the ^{14}C species, and global energy balance. The equations will all be steady state.

Mass balance equations for species

For mass balance of the water species in the aqueous phase, assume that dissolved species cause negligible diffusive flux of the water species ($\mathbf{j}_l^w = 0$), the mass fraction of the water species in the liquid water is approximately 1 ($\chi_l^w = 1$), and there is no external source of water. Subscript l refers to the liquid (water) phase, superscript w refers to the water species.

$$\nabla \cdot (\epsilon_l \rho_l \mathbf{v}_l) - S_l^w = 0. \tag{13-9}$$

For mass balance of the water species in the gas phase, assume there is no external source of vapor, but there may be gas-phase advection as well as diffusion within the gas phase. Subscript g refers to the gas phase, superscript w refers to the water species (vapor).

$$\nabla \cdot (\epsilon_g \rho_g \chi_g^w \mathbf{v}_g) + \nabla \cdot [\epsilon_g \rho_g \chi_g^w (\mathbf{v}_g^w - \mathbf{v}_g)] - S_g^w = 0. \tag{13-10}$$

For mass balance of the air species in the gas phase, assume there is no external source of air. Subscript g refers to the gas phase, superscript a refers to the air species (a mixture of everything but water vapor and ^{14}C.

$$\nabla \cdot (\epsilon_g \rho_g \chi_g^a \mathbf{v}_g) + \nabla \cdot [\epsilon_g \rho_g \chi_g^a (\mathbf{v}_g^a - \mathbf{v}_g)] - S_g^w = 0. \tag{13-11}$$

For mass balance of the ^{14}C species in the liquid phase, assume there is no external source of ^{14}C. Subscript l refers to the liquid phase, superscript c refers to the ^{14}C species.

$$\nabla \cdot (\epsilon_l \rho_l \chi_l^c \mathbf{v}_l) + \nabla \cdot [\epsilon_l \rho_l \chi_l^c (\mathbf{v}_l^c - \mathbf{v}_l)] - S_l^w = 0. \tag{13-12}$$

For mass balance of the ^{14}C species in the solid phase, assume there is no external source of ^{14}C, there is no movement of the solid phase, and there is no diffusion. Subscript s refers to the solid phase, superscript c refers to the ^{14}C species.

$$S_s^c = 0. \tag{13-13}$$

Exchange of mass between phases

Exchange of the water species with the solid phase is assumed zero ($S_s^w = 0$), as is exchange of the air species with the solid phase ($S_s^a = 0$).

The water species is assumed to partition between liquid and gas phases using an equilibrium relationship,

$$\rho_g^w = \rho_{vs} \exp\left(\frac{P_l M_w}{\rho_l^w RT}\right) \qquad \text{for } P_w < 0, \tag{13-14}$$

$$\rho_{vs} = a_1 \exp[a_2 - (a_3/T) - a_4 \ln(T)] \tag{13-15}$$

where

ρ_{vs} is saturated vapor density [M L^{-3}],

ρ_l^w is liquid water density [M L^{-3}],

P_l is the pressure of the liquid phase (water) [M L^{-1}T^{-2}],

T is temperature [K],

R is the ideal gas coefficient [8.3143 J mole^{-1}],

M_w is the molecular weight of water [18 gm mole^{-1}].

In the cgs system, $a_1 = 1$, $a_2 = 46.440973$, $a_3 = 6790.4985$, $a_4 = 6.02808$, T is in degrees Kelvin, and ρ_{vs} is in units of gm cm^{-3}.

In addition, ^{14}C is assumed to partition between liquid and gas phases using an equilibrium relationship,

$$\rho_l^c = (K_d)^c \rho_g^c, \tag{13-16}$$

where $(K_d)^c$ is a distribution coefficient (a typical value for YM is 40, according to Murphy (1995)).

12/30/95 First Results.

The first sets of simulations were run over the past few days. The simulations considered liquid and vapor fluxes for the UZ16 data set presented in (Baca et al., 1994, pp. 7-19–7-25). Two thermal cases were considered, isothermal and linear temperature variation as a surrogate for the geothermal gradient. For each thermal case, 6 moisture flux cases were considered, with input moisture fluxes changing from 10^{-3} to 100 mm/yr by an order of magnitude at a time. A number of input and coding errors were detected, but finally these were shaken out and the resulting simulations were found to be comparable to the simulations in Baca et al. (1994). The previous simulations considered net downward fluxes of 0.0086 mm/yr and 0.0135 mm/yr, but did not consider fracture flow. In the current work, a reference fractured continuum was assumed to exist in each unit having low permeability ($k < 10^{-8}$ cm^2).

As might be suspected, vapor transport is not significant except for extremely small overall fluxes, as vapor fluxes are generally on the order of 10^{-4} mm/yr, with spikes in fluxes at interfaces on the order of 10^{-3} mm/yr to as much as 10^{-2} mm/yr. Only the low-flow cases are much impacted by this amount of vapor flux.

The simulations were generated using **$ODE/run_ODE_sets.m**, which calls a hierarchy of additional files located in the same directory. Solutions are saved as *Matlab* **mat** files. Plotting is done using **$ODE/fancy_ODE_plots.m**. A description of outputs is found in Table 13-1.
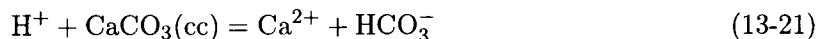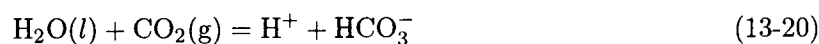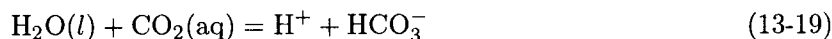
Table 13-1: File Description (12/30/95)

File Name	Description
ODE_gT0.mat	Liquid and vapor outputs assuming isothermal temperature of 20 °C. Variables subscripted with 1, 2, 3, 4, 5, and 6 refer to inposed downward fluxes of 10^{-3}, 10^{-2}, 10^{-1}, 10^0, 10^1, and 10^2 mm/yr, respectively.
ODE_gTref.mat	Same as **ODE_gT0.mat**, except assuming temperature gradient of 0.0177 °C/m, increasing downwards.

Carbon-system chemistry

Murphy et al. (1996) consider the impact of near-field thermal loading on ^{14}C transport. The geochemical model of the carbon system assumes local chemical equilibrium, and mass and

charge conservation. Closely following Murphy et al. (1996), the chemical reactions are:

$$H^+ + OH^- = H_2O(l) \tag{13-17}$$

$$H^+ + CO_3^{2-} = HCO_3^- \tag{13-18}$$

$$H_2O(l) + CO_2(aq) = H^+ + HCO_3^- \tag{13-19}$$

$$H_2O(l) + CO_2(g) = H^+ + HCO_3^- \tag{13-20}$$

$$H^+ + CaCO_3(cc) = Ca^{2+} + HCO_3^- \tag{13-21}$$

and the corresponding mass-action relations are:

$$K_1 = \frac{a_{H_2O(l)}}{a_{H^+} a_{OH^-}} \tag{13-22}$$

$$K_2 = \frac{a_{HCO_3^-}}{a_{H^+} a_{CO_3^{2-}}} \tag{13-23}$$

$$K_3 = \frac{a_{H^+} a_{HCO_3^-}}{a_{H_2O(l)} a_{CO_2(aq)}} \tag{13-24}$$

$$K_4 = \frac{a_{H^+} a_{HCO_3^-}}{(f_{CO_2(g)}/f^o_{CO_2(g)}) a_{H_2O(l)}} \tag{13-25}$$

$$K_5 = \frac{a_{Ca^{2+}} a_{HCO_3^-}}{a_{H^+} a_{CaCO_3(cc)}} \tag{13-26}$$

where (l), (aq), (g), and (cc) refer to liquid, aqueous, gas, and calcite phases, respectively; a_i denotes the thermodynamic activity of species i, $f_{CO_2(g)}$ denotes the fugacity of $CO_2(g)$, and $f^o_{CO_2(g)}$ is the reference fugacity of $CO_2(g)$ (1 bar). In addition to the species in reactions 13-17 to 13-21, Na^+ is included to represent other basic aqueous cations.

Local charge balance in the aqueous phase is represented by

$$m_{H^+} + m_{Na^+} + 2m_{Ca^{2+}} = m_{HCO_3^-} + 2m_{CO_3^{2-}} + m_{OH^-}, \tag{13-27}$$

where m_i is the molality (number of moles per kg of solvent) of species i. Local mass conservation for carbon is expressed by

$$n_{CO_2(g)} + n_{CO_2(aq)} + n_{CO_3^{2-}} + n_{HCO_3^-} + n_{CaCO_3(cc)} = n_C, \tag{13-28}$$

where n_i is the number of moles of species i. Similarly, local mass conservation for calcium is expressed by

$$n_{Ca^{2+}} + n_{CaCO_3(cc)} = n_{Ca}. \tag{13-29}$$

Sodium is conserved in the aqueous phase. The mass of H_2O is conserved in the hydrologic model, and the equilibrium distribution between gas and liquid phases is also calculated in the hydrologic

model. The system is completely oxidized, so there are no oxidation-reduction reactions relevant to the system.

Thermodynamic activities in the mass action relations 13-22 to 13-26 are related to the number of moles and to molalities by

$$a_i = m_i \gamma_i = \frac{n_i \gamma_i}{W_{H_2O}}, \tag{13-30}$$

where γ_i is the activity coefficient of aqueous species i and W_{H_2O} is the mass of $H_2O(l)$ in the representative volume. Activity coefficients are calculated according to

$$\log \gamma_i = -Az_i^2 \sqrt{I}/(1 + \dot{a}_i B \sqrt{I}) + \dot{B} I, \tag{13-31}$$

$$I = \frac{1}{2} \sum_{i=1}^{N_{spec}} m_i z_i^2, \tag{13-32}$$

where I is the ionic strength and z_i is the electrical charge of species i (Helgeson, 1969), and A, $\dot{a}_i$, B, and $\dot{B}$ are empirical coefficients.

Assuming Dalton's law is valid for the low pressure gas phase, the $CO_2(g)$ fugacity is related to the number of moles of gaseous CO_2 by the ideal gas law,

$$f_{CO_2(g)} = P_{CO_2(g)} = n_{CO_2(g)} RT/\epsilon_g, \tag{13-33}$$

where $P_{CO_2(g)}$ is the partial pressure of CO_2.

1/1/96 More Theory.

Energy balance

Following the Stothoff (1995) documentation, energy balance is defined by

$$\frac{\partial}{\partial t}(\epsilon_\alpha \rho_\alpha \chi_\alpha^i U_\alpha^i) + \nabla \cdot (\epsilon_\alpha \rho_\alpha \chi_\alpha^i U_\alpha^i \mathbf{v}_\alpha) + \nabla \cdot \epsilon_\alpha (\mathbf{q}_e + \mathbf{t} \cdot \mathbf{v})_\alpha^i - S_{e\alpha}^i - \epsilon_\alpha \rho_\alpha \chi_\alpha^i R_{e\alpha}^i = 0, \tag{13-34}$$

where

$\quad U \quad$ is internal energy per unit mass,

$\quad \mathbf{q}_e \quad$ is the heat flux,

$\quad \mathbf{t} \quad$ is the stress tensor,

$\quad S_{e\alpha}^i \quad$ is the exchange of energy from other species and other phases,

$\quad R_{e\alpha}^i \quad$ is the supply of energy from external sources.

Note that there is a change in energy when a species changes phase (i.e., latent heat) or when a species reacts (i.e., radioactive decay, endothermal reactions, exothermal reactions).

Summing over all species in each phase,

$$\frac{\partial}{\partial t}(\epsilon_\alpha \rho_\alpha U_\alpha) + \nabla \cdot (\epsilon_\alpha \rho_\alpha H_\alpha \mathbf{v}_\alpha) + \nabla \cdot (\epsilon_\alpha \mathbf{q}_{e\alpha}) - S_{e\alpha} - \epsilon_\alpha \rho_\alpha R_{e\alpha} = 0. \qquad (13\text{-}35)$$

The global energy balance equation results from summing over all phases, thereby cancelling out the $S_{e\alpha}$ terms (since they must sum to zero).

Bird et al. (1960) give an excellent description of mass and energy fluxes for multiple components within a single phase. The following section summarizes the Bird et al. (1960) results.

The total energy flux relative to the mass average velocity, $\mathbf{q}_{erel}$, is given by

$$\mathbf{q}_{erel} = \mathbf{q}^{(c)} + \mathbf{q}^{(d)} + \mathbf{q}^{(x)}, \qquad (13\text{-}36)$$

where

  $\mathbf{q}^{(c)}$ is the conductive energy flux,

  $\mathbf{q}^{(d)}$ is the energy flux caused by interdiffusion, and

  $\mathbf{q}^{(x)}$ is the Dufour flux, or flux caused by mechanical driving forces.

In summary,

$$\mathbf{q}^{(c)} = -k\nabla T, \qquad (13\text{-}37)$$

where k is the instantaneous local thermal conductivity,

$$\mathbf{q}^{(d)} = \sum_{i=1}^{N_{\text{spec}}} \frac{\bar{H}_i}{M_i} \mathbf{j}_i, \qquad (13\text{-}38)$$

where $\bar{H}_i$ is the partial molal enthalpy of species i, and M_i is the molecular weight of species i. Bird et al. (1960) term $\mathbf{q}^{(x)}$ complex and usually of minor importance.

In terms of the energy flux with respect to stationary coordinates, $\mathbf{q}_{etot}$,

$$\mathbf{q}_{etot} = \mathbf{q}_{erel} + [\boldsymbol{\pi} \cdot \mathbf{v}] + \rho(\hat{U} + \frac{1}{2}\mathbf{v}^2)\mathbf{v}, \qquad (13\text{-}39)$$

where $\boldsymbol{\pi}$ is the pressure tensor $(\mathbf{t} + P\boldsymbol{\delta})$. When $\mathbf{q}^{(x)}$, $[\mathbf{t} \cdot \mathbf{v}]$, and $(\frac{1}{2}\rho\mathbf{v}^2)\mathbf{v}$ are of negligible importance (which occurs for most porous medium situations, parenthetically), $\mathbf{q}_{etot}$ can be approximated by

$$\mathbf{q}_{etot} = -k\nabla T + \sum_{i=1}^{N_{\text{spec}}} \frac{\bar{H}_i}{M_i}\rho\chi_i \mathbf{q}_i. \qquad (13\text{-}40)$$

Definition of non-advective fluxes

Again following Bird et al. (1960), nonadvective fluxes within a phase are broken into four components: (i) ordinary diffusion $\mathbf{j}^{(x)}$, (ii) pressure diffusion $\mathbf{j}^{(p)}$, (iii) forced diffusion $\mathbf{j}^{(g)}$, and (iv) thermal diffusion $\mathbf{j}^{(T)}$. These are defined by

$$\mathbf{j}_i^{(x)} = \frac{c^2}{\rho RT} \sum_{j=1}^{N_{\text{spec}}} M_i M_j D_{ij} \left[\chi_j \sum_{\substack{k=1 \\ k \neq j}}^{N_{\text{spec}}} \left(\frac{\partial \bar{G}_j}{\partial \chi_k} \right)_{\substack{T,P,\chi_s \\ s \neq j,k}} \nabla \chi_k \right], \tag{13-41}$$

$$\mathbf{j}_i^{(p)} = \frac{c^2}{\rho RT} \sum_{j=1}^{N_{\text{spec}}} M_i M_j D_{ij} \left[\chi_j M_j \left(\frac{\bar{V}_j}{M_j} - \frac{1}{\rho} \right) \nabla P \right], \tag{13-42}$$

$$\mathbf{j}_i^{(g)} = \frac{c^2}{\rho RT} \sum_{j=1}^{N_{\text{spec}}} M_i M_j D_{ij} \left[\chi_j M_j \left(\mathbf{b}_j - \sum_{k=1}^{N_{\text{spec}}} \frac{\rho_k}{\rho} \mathbf{b}_k \right) \right], \tag{13-43}$$

$$\mathbf{j}_i^{(T)} = -D_i^T \nabla \ln T, \tag{13-44}$$

where

$\quad c$ is the molar density of the solution [mole L^{-3}],

$\quad \chi_i$ is the mole fraction of species i ($\chi_i = c_i/c$),

$\quad D_{ij}$ is the multicomponent diffusion coefficient,

$\quad \mathbf{b}$ is the external force,

$\quad \bar{G}$ is the partial molal free enthalpy (Gibbs free energy) [J/M], and

$\quad \bar{V}$ is the partial molal volume.

The D_{ij} and D_i^T have the following properties:

$$0 = D_{ii}, \tag{13-45}$$

$$0 = \sum_{i=1}^{N_{\text{spec}}} D_i^T, \tag{13-46}$$

$$0 = \sum_{i=1}^{N_{\text{spec}}} (M_i M_j D_{ij} - M_i M_k D_{ik}). \tag{13-47}$$

Note that when $N_{\text{spec}} > 2$ the quantities D_{ij} and D_{ji} are not in general equal, and may in fact be negative.

Bird et al. (1960) comment on these quantities as following. There may be net movement of the species in a mixture through pressure diffusion if there is a pressure gradient on the system, but this term is very small unless centrifuging is occurring. The forced diffusion term is primarily

important in ionic systems, in which the external force on an ion is equal to the product of the ionic charge and the local electric field strength, thus each ionic species may be under the influence of a different force. Gravity acts on each species equal and $j_i^{(g)} = 0$. The thermal diffusion term is quite small unless very steep temperature gradients are imposed.

When considering a binary mixture, the relationship $(d\bar{G}_A)_{TP} = RTd\ln a_A$ can be used to define an alternate form of $j_i^{(x)}$,

$$j_A^{(x)} = -j_B^{(x)} = \frac{c^2}{\rho} M_A M_B D_{AB} \left(\frac{\partial \ln a_A}{\partial \ln \chi_A} \right)_{T,P} \nabla \chi_A. \tag{13-48}$$

In natural waters in a porous medium, pressure diffusion and thermal diffusion are negligible. Generally dissolved species are so dilute that nonadvective mass flux is adequately described with binary ordinary diffusion, each species with liquid water.

When considering ordinary diffusion in multicomponent gases at low density (i.e., atmospheric pressures), the ordinary diffusion equation becomes

$$j_i^{(x)} = \frac{c^2}{\rho} \sum_{j=1}^{N_{\text{spec}}} M_i M_j D_{ij} \nabla \chi_j \tag{13-49}$$

The D_{ij} coefficients depend on concentration.

Definition of ODE treatment of chemistry

In the spirit of the ODE treatment of water fluxes, the fluxes of the elements in the system are assumed to be spatially invariant, since the system is assumed to be at steady state. Thus, q_C, q_{Ca}, and q_{Na} are assumed to be constants. An approach for specifying these values is by assuming that the flux at the top boundary for each element is completely advective. Given the concentration at the top and the liquid flux, the mass flux for each element is completely specified throughout the domain.

Chemistry is specified based on the mass balance equation for carbon and the charge balance equation (Equations 13-28 and 13-27). The mass action equations and thermodynamic relationships are substituted into the balance equations, yielding a pair of equations in two unknowns, $a_{HCO_3^-}$ and a_H. Note that the balance equations are functions of activity coefficients, which are functions of temperature and composition.

1/4/96 Data.

Since the geochemistry is a function of temperature, thermal properties of the YM stratigraphy are necessary. Thermal properties from Table C-1 in Sandia National Laboratories (1994) is copied in Table 13-2.

Table 13-2: Thermal properties from TSPA–1993.

Unit	Upper Contact (m)	Lower Contact (m)	Thermal Conductivity (W/mK)	Heat Capacitance		
				$T \leq 94°C$	$94°C < T \leq 114°C$	$114°C < T$
TCw	0	36.0	1.65	2.0313	9.3748	2.0979
PTn	36.0	74.1	0.85	2.2286	29.3110	1.5236
TSw1	74.1	204.2	1.60	2.0775	12.2655	2.0219
TSw2	204.2	383.5	2.10	2.1414	10.4768	2.1839
TSw3	393.5	409.3	1.28	2.0530	4.5193	2.5535
CHn1v	409.3	414.5	1.20	2.5651	35.3680	1.6702
CHn1z	414.5	518.5	1.28	2.6709	35.3854	2.2835
CHn2	518.5	535.2	1.30	2.5512	22.3349	1.9599

1/16/96 Results and close-out of project.

Due to the reorganization of projects at the CNWRA, the Performance Assessment Research Project is being closed out. Accordingly, this entry serves to close out the contribution under the current organizational structure. It is anticipated that the geochemistry work may continue under the new KTI for Ambient Flow, and some of the hydrology work may as well. Today's entry identifies the conclusions from the work thus far.

The simulations run to date have assumed one of two thermal conditions: (i) isothermal, with no thermal gradient, and (ii) linear thermal gradient, with no consideration of thermal properties or energy transport. For the second case, it is assumed that thermal conduction far outweighs energy redistribution through advective means (liquid and vapor fluxes). The data in Table 13-2 indicates that thermal conductivity is relatively uniform, with somewhat lower conductivity in the PTn unit and almost twice as high in the TSw2 unit, so the linear assumption shouldn't be too bad.

The set of simulations are described in the entry for 12/30/95. The plots were finalized today from the previous simulations. Plots of resulting distributions from the isothermal case are shown in Figures 13-1 and 13-2; corresponding plots of the linear-thermal-gradient case are shown in Figures 13-3 and 13-4. In general, increasing flux rates yield increasing moisture content, saturation, and pressure. The color schemes for the lines are consistent through all plots. Gaps in fracture distributions occur in several nonwelded units, where it was assumed that no fractures exist.

Based on the Figures 13-1 through 13-4, the geothermal gradient at Yucca Mountain should result in vapor fluxes less than 10^{-3} mm/yr, except for spikes at interfaces between highly contrasting material properties. Accordingly, it can be concluded that whenever overall fluxes are greater than 1 mm/yr, vapor fluxes are completely insignificant and can be neglected. As a consequence, it can be concluded that the impact of the geothermal gradient on water fluxes is not large at YM unless extremely low fluxes exist. On the other hand, there may be some (presumably relatively small) impact on the geochemistry; this issue remains to be examined under the new KTI.

1/20/97 Final entry.

This project has been closed out due to reorganization. The work is being continued under the Unsaturated and Saturated Flow in Isothermal Conditions KTI. This will be the final entry for this project in this notebook and the project will not show up in subsequent printouts.
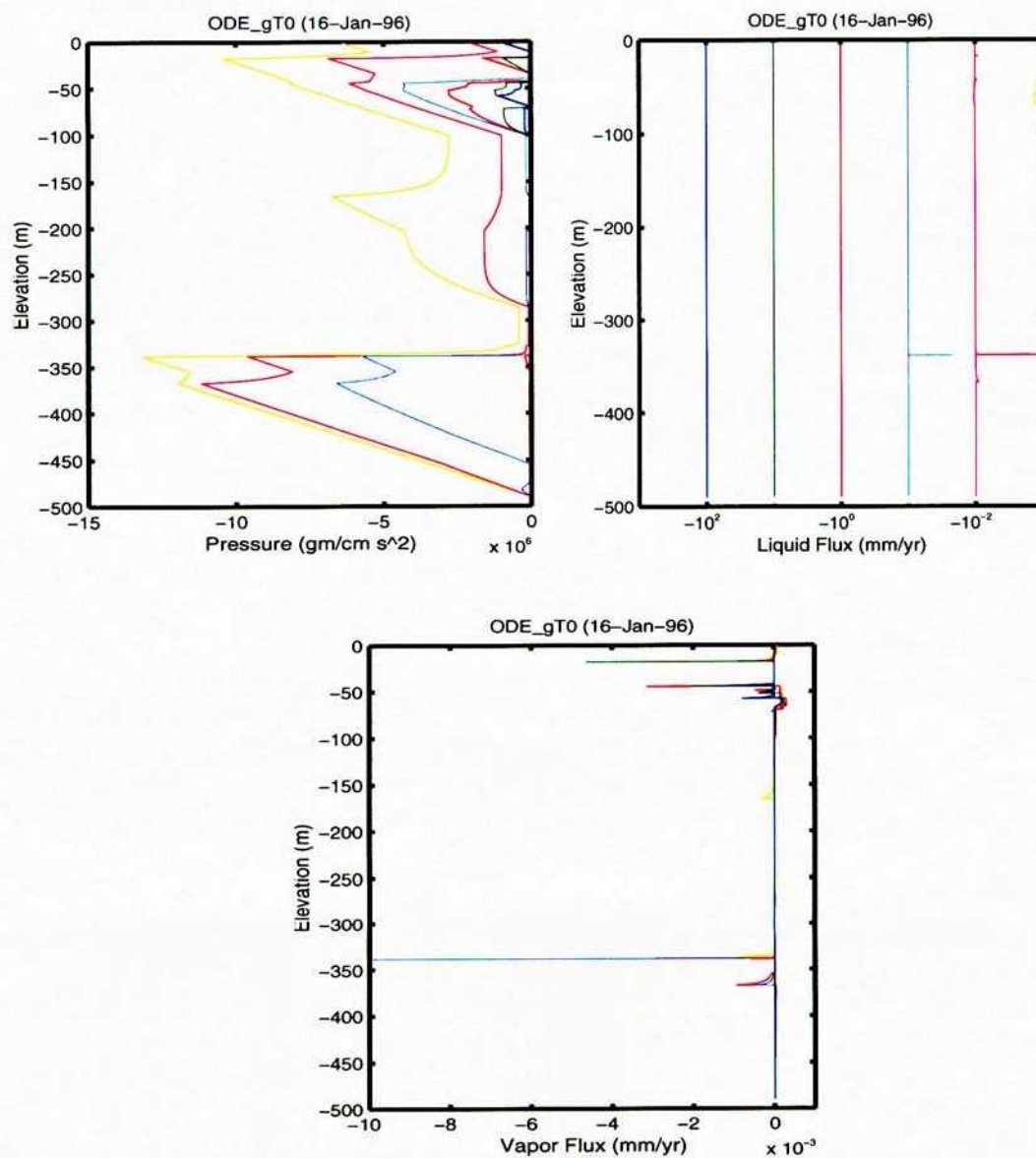
Figure 13-1: Vertical distribution of (a) pressure, (b) liquid flux, and (c) vapor flux for the zero-thermal-gradient case. UZ-16 material properties are used. Zero elevation represents ground surface, and the bottom is an assumed water table.

Figure 13-2: Vertical distribution of (a) moisture content in the matrix, (b) moisture content in the fracture, (c) matrix saturation, and (d) fracture saturation for the zero-thermal-gradient case.

Figure 13-3: Vertical distribution of (a) pressure, (b) liquid flux, and (c) vapor flux for the linear-thermal-gradient case. UZ-16 material properties are used. Zero elevation represents ground surface, and the bottom is an assumed water table.
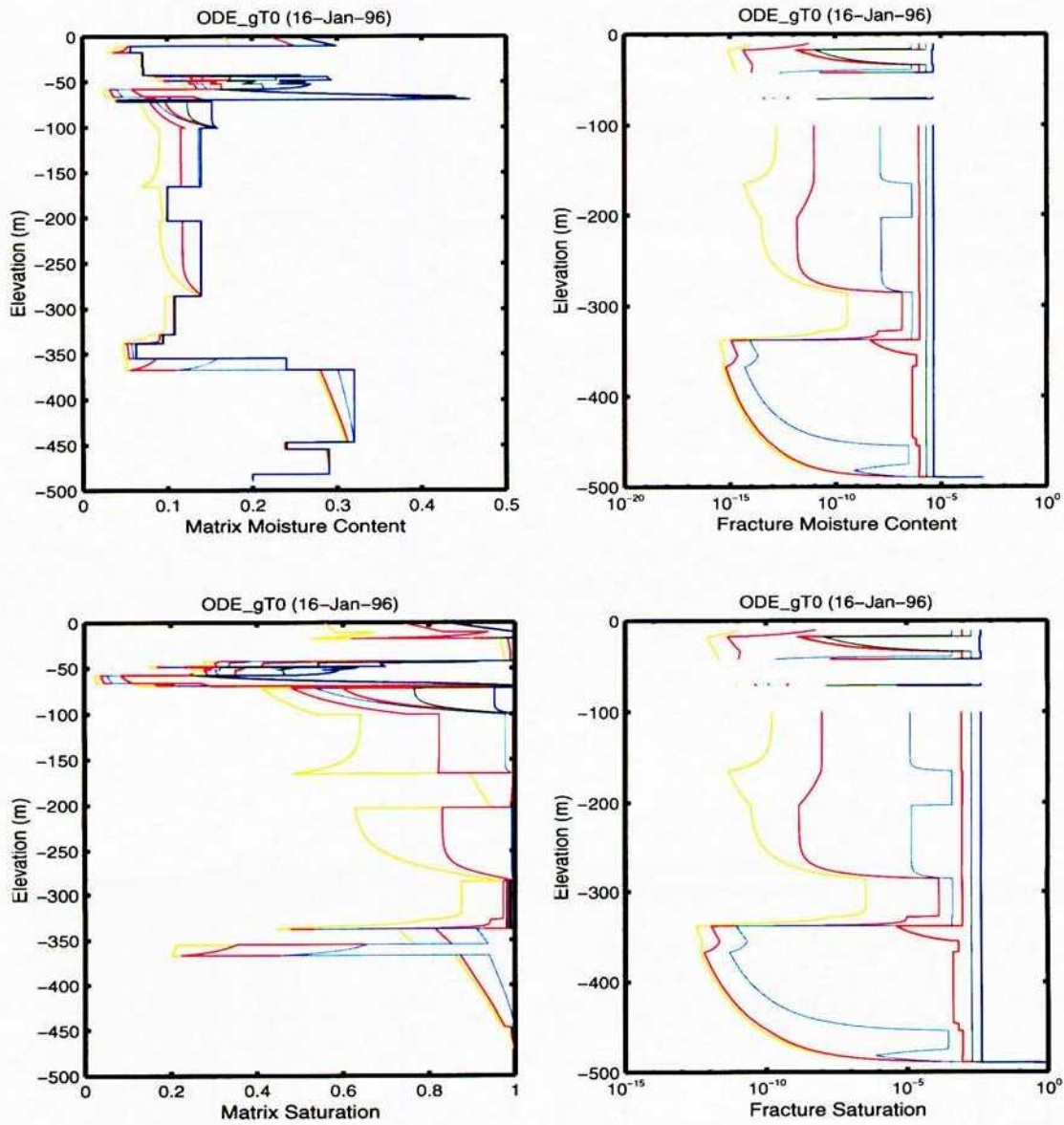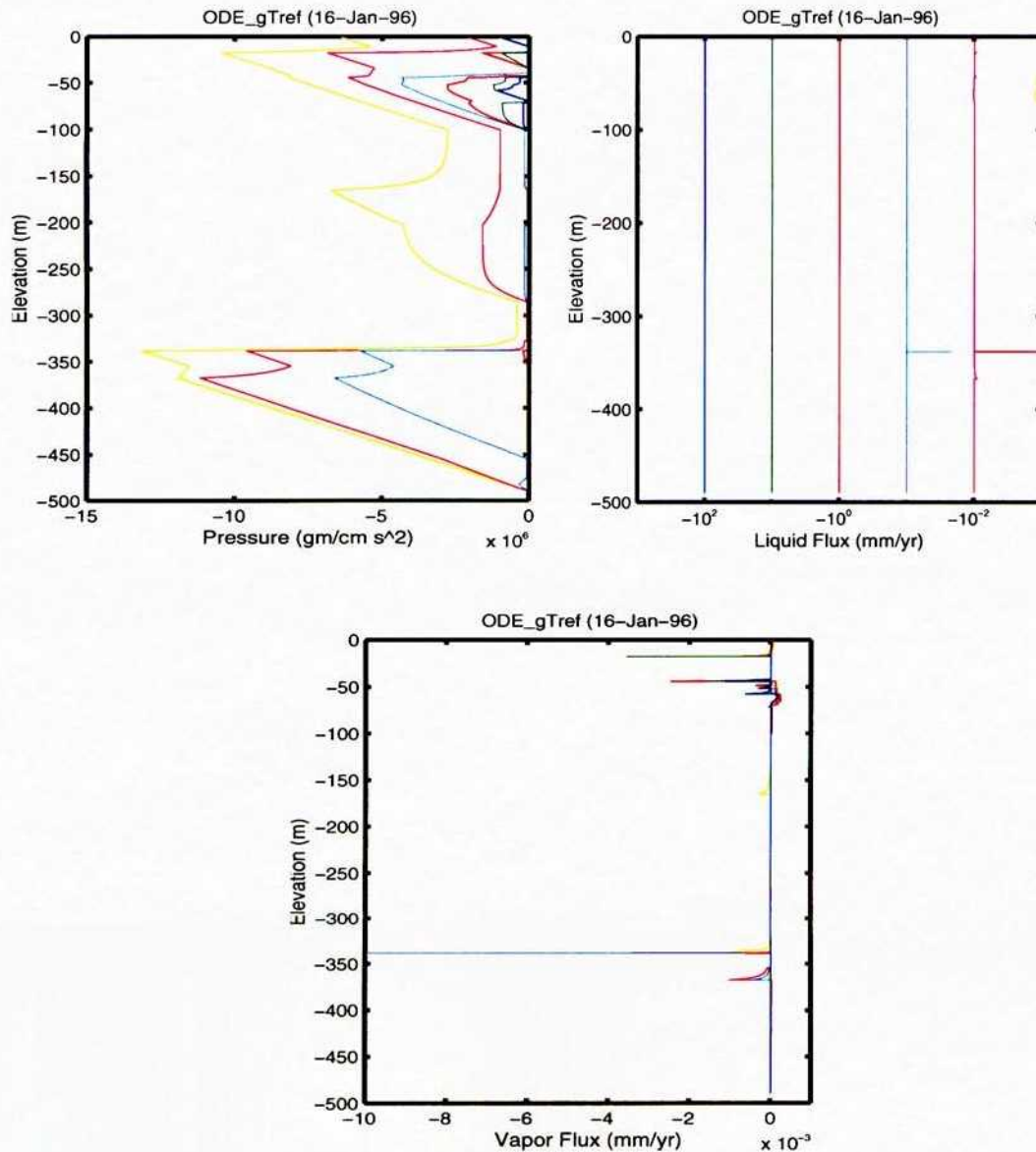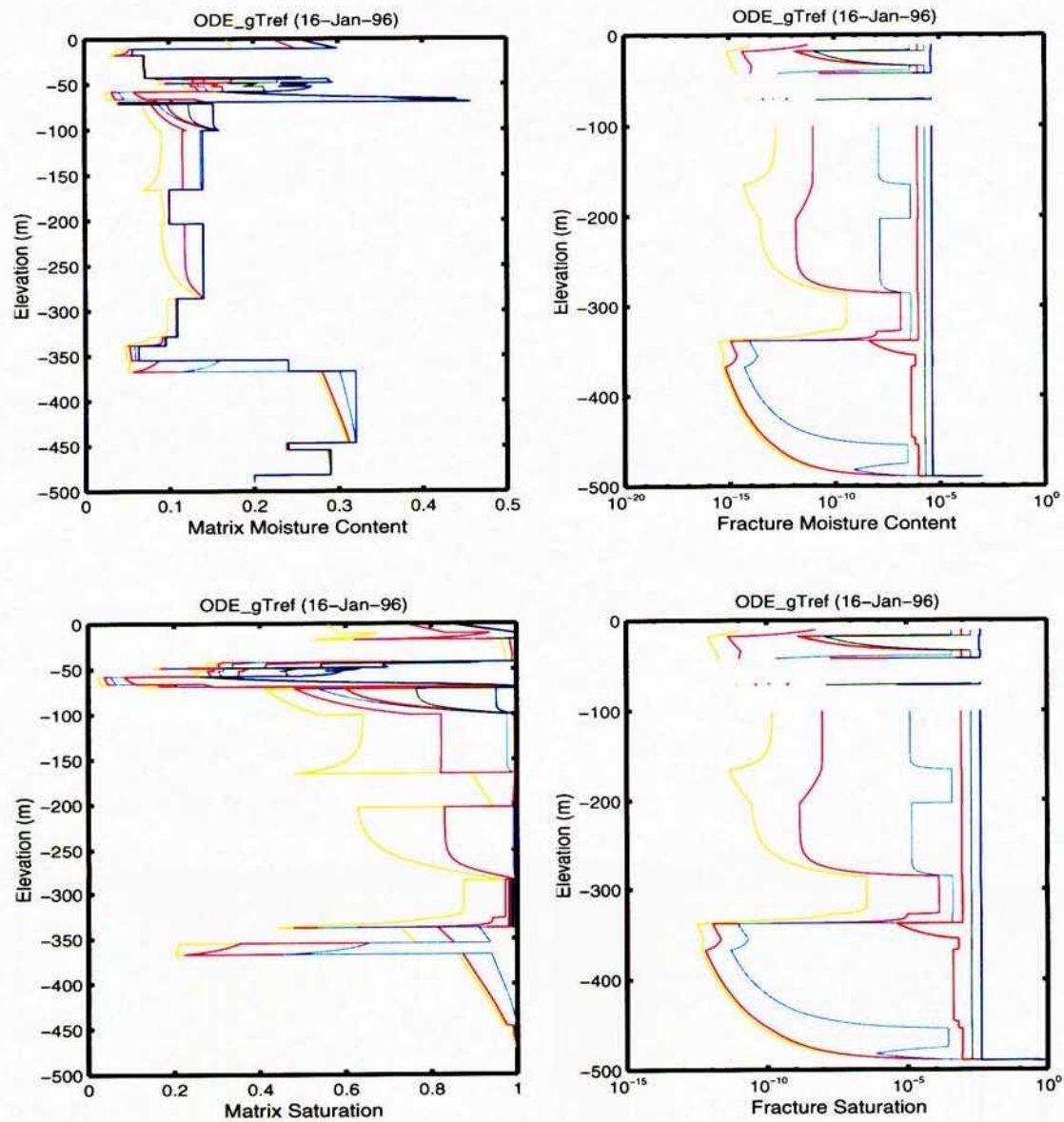
Figure 13-4: Vertical distribution of (a) moisture content in the matrix, (b) moisture content in the fracture, (c) matrix saturation, and (d) fracture saturation for the linear-thermal-gradient case.

References

Baca, R. G., R. D. Manteufel, S. Mohanty, S. A. Stothoff, and G. W. Wittmeyer. 1994. Performance Assessment Research. In B. Sagar (Ed.), *NRC High-Level Radioactive Waste Research at CNWRA, July–December 1993*, Volume CNWRA 93-02S, San Antonio, TX, pp. 7–1–7–29. Center for Nuclear Waste Regulatory Analyses.

Bird, R. B., W. E. Stewart, and E. N. Lightfoot. 1960. *Transport Phenomena*. New York, NY: John Wiley & Sons.

Helgeson, H. C. 1969. Thermodynamics of Hydrothermal Systems at Elevated Temperatures and Pressures. *American Journal of Science 267*, 729–804.

Murphy, W. M. 1995. Contributions of thermodynamic and mass transport modeling to evaluation of groundwater flow and groundwater travel time at Yucca Mountain, Nevada. *Material Research Society Symposium Proceedings 353*, 419–426.

Murphy, W. M., C. J. Freitas, and P. C. Lichtner. 1996. A Numerical Model for the Evolution of the Carbon System Geochemistry at the Proposed Nuclear Waste Repository at Yucca Mountain, Nevada, USA. *TBD*.

Sandia National Laboratories. 1994. *Total-System Performance Assessment for Yucca Mountain–SNL Second Iteration (TSPA-1993)*. SAND93-2675, Sandia National Laboratories, Albuquerque, NM.

Stothoff, S. A. 1995. *BREATH Version 1.1–Coupled Flow and Energy Transport in Porous Media: Simulator Description and User Guide*. NUREG/CR 6333, Nuclear Regulatory Commission, Washington, DC.

14   Ambient KTI – Vertical ODE Solver

Account Number: **20-5708-861**

Collaborators: **Sitakanta Mohanty, Gordon Wittmeyer**

Directories: **$HOME2/Matlab/ODE → $ODE**

Objective: This work is a continuation of work started under the Performance Assessment Research Project. Due to reorganization of the CNWRA projects, the previous task was discontinued. Goals of the previous task are being followed here.

2/6/96 Development of 3D ODE solver.

An idea had occurred to me when the ODE project was first presented, which is to use the Runge-Kutta integration for a heterogeneous steady-state 3D flow domain. As a brief recap, the 1D solver using the ODE formalism integrates in the z direction the steady-state flow equation in the form

$$\mathbf{q}_v = K(P)(\frac{\partial P}{\partial x} + \rho g \frac{\partial z}{\partial x}) = \text{constant}, \tag{14-1}$$

where thermal and vapor effects are neglected for simplicity. The subscripts v and h in the following refer to vertical and horizontal, respectively. This is actually a simplification of the full statement,

$$\nabla \cdot \mathbf{q} = 0, \tag{14-2}$$

subject to appropriate boundary conditions.

Due to the essentially 1D nature of flow in the unsaturated zone at YM, it may be possible to extend the procedure to 3D in a computationally profitable manner. By assuming gravity drainage along a top or bottom boundary with a known boundary flux distribution (presumably top offers advantages since flux information is specified from shallow conditions), the equations can be integrated in one direction, yielding

$$\mathbf{q}_v + \int_{z_0}^{z} \nabla_h \cdot \mathbf{q}_h \, dz = 0 \tag{14-3}$$

for each of several columns. There is an associated total-vertical-flux conservation equation,

$$\mathbf{q}_{tot} = \sum_{i=1}^{N} \mathbf{q}_i = \text{constant}, \tag{14-4}$$

which can be used to normalize horizontal fluxes calculated between adjacent columns. The practical case uses perfectly horizontal layers to hold information required for the integrations. It will be necessary to carry along cumulative lateral fluxes. A purely 1D solution using the generic matlab ode23 routine requires many thousands of vertical steps; however, this might be improved by taking into account stratigraphy.

2/18/96 3D ODE solver code development outline. $\boxed{S\!A\!S}$

The idea is to develop a simple steady-state flow solver suitable for handling 1D, 2D, and 3D test cases. The immediate presentation need is for a paper due in 10 days. There are two YM applications that such a solver would be very useful for, examining PTn shedding and providing initial conditions in a heterogeneous medium. Future extensions to the geothermal regime and perhaps to geochemistry are possible as well.

The application is firmly in the method of lines (MOL) camp, which treats all but one of the coordinate directions in a differential equation uniformly and integrates the remaining direction in a different way. Most MOL applications integrate time as the odd direction. The twist here is that one of the space directions is the odd direction, as time is not a factor. In 1D, the idea is nothing new. I haven't run across the idea in higher dimensions, which is not to say that other applications have never been made. There are related ideas that have been used, in formally vertically averaging strongly horizontal situations. In porous-media flow simulations, Phillips (1991) discusses applications where the lateral pressure gradient is essentially constant over the vertical. Jeff Laible and I discussed a shallow-water application where the pressure equation is vertically integrated, but the vertical integration is done numerically. We also discussed this in regard to the Princeton Transport Code. I sent him email today requesting a reference on this idea if he has it.

As with boundary elements, compatible pressures and normal fluxes are required along all boundaries. In 1D, if a pressure and a flux condition are specified, and there are no sources or sinks, the problem is fully specified by integrating from the known-pressure boundary to the other boundary. In any other case, an interative (shooting) procedure is required, where successive values of boundary fluxes are tried until compatibility is achieved. I believe that the higher-dimensional solver should use a staged approach, where first a 1D solution is obtained by using equivalent material properties to get approximate solutions, then subdividing columns to get successively more refined solutions. It may be possible to subdivide one column at a time.

The formalism for the approach is as follows. Starting with a steady-state mass balance

equation,

$$\nabla \cdot \mathbf{q} + Q = 0, \tag{14-5}$$

integrating vertically,

$$\int_{z_1}^{z_2} [\nabla \cdot \mathbf{q} + Q] \, dz = 0,$$

$$[\mathbf{q}_v]_{z_1}^{z_2} + \int_{z_1}^{z_2} [\nabla_h \cdot \mathbf{q}_h + Q] \, dz = 0, \tag{14-6}$$

and integrating horizontally,

$$\int_{\Omega(z)} \left\{ [\mathbf{q}_v]_{z_1}^{z_2} + \int_{z_1}^{z_2} [\nabla_h \cdot \mathbf{q}_h + Q] \, dz \right\} \, d\Omega = 0, \tag{14-7}$$

the formal set of equations are developed,

$$\int_{\Omega(z)} \mathbf{q}_v(z_2) \, d\Omega = \int_{\Omega(z)} \mathbf{q}_v(z_1) \, d\Omega - \int_{\Omega(z)} \int_{z_1}^{z_2} [\nabla_h \cdot \mathbf{q}_h + Q] \, dz \, d\Omega,$$

$$= \int_{\Omega(z)} \mathbf{q}_v(z_1) \, d\Omega - \int_{z_1}^{z_2} \int_{\Omega(z)} (\nabla_h \cdot \mathbf{q}_h + Q) \, d\Omega \, dz. \tag{14-8}$$

Note that Q includes internal sources and lateral boundary conditions. Also note that the procedure can accommodate variable horizontal cross sections $[\Omega = \Omega(z)]$, such as might occur if the top and bottom boundaries slope.

Another way to look at the problem is on the differential level, creating a system of ordinary diffential equations. Starting with the steady-state mass balance equation,

$$\nabla \cdot \mathbf{q} + Q = \frac{\partial \mathbf{q}_v}{\partial z} + [\nabla_h \cdot \mathbf{q}_h + Q] = 0, \tag{14-9}$$

and if $Y_1 = P$, $Y_2 = \mathbf{q}_z$, and $(\cdot)'$ refers to $\partial(\cdot)/\partial z$, two equations are obtained:

$$Y_2 = -K(Y_1)[Y_1' + \rho g z'] \quad \Rightarrow \quad Y_1' = -[Y_2/K(Y_1)] - \rho g z', \tag{14-10}$$

$$Y_2' = -[\nabla_h \cdot \mathbf{q}_h + Q]. \tag{14-11}$$

Assuming that $\nabla_h \cdot \mathbf{q}_h$ is constant within a column yields the integral form for divergence,

$$\int_\Omega \nabla_h \cdot \mathbf{q}_h \, d\Omega = \nabla_h \cdot \mathbf{q}_h \int_\Omega d\Omega = \int_\sigma \mathbf{n} \cdot \mathbf{q}_h \, d\sigma,$$

$$\nabla_h \cdot \mathbf{q}_h = \frac{\int_\sigma \mathbf{n} \cdot \mathbf{q}_h \, d\sigma}{\int_\Omega d\Omega} = \frac{\int_\sigma \mathbf{n} \cdot \mathbf{q}_h \, d\sigma}{A}. \tag{14-12}$$

The first cut prototype to check out the idea will be located in *$HOME2/Matlab/MoL*. The program design assumes that a number of vertical columns are specified at the finest horizontal scale desired. The horizontal equations will be solved using finite-volume ideas as a quick first cut, so that lateral fluxes will be handled with a set of connection arrays, including pointers to columns and physical variables. Of course, finite element or finite difference ideas could be applied.

For each column, running values of P and $\partial P/\partial z$ are maintained by the ODE solver. In addition, there will need to be a running total of $\mathbf{q}_v(z)$. For the differential approach, this is also maintained by the ODE solver.

In general, one would be able to integrate either bottom up or top down. For the first cut, bottom up will be assumed. Thus, the integration steps that must be followed by the program include: (i) given the current-level pressure, calculate lateral fluxes and vertical conductivity; (ii) update the vertical fluxes; (iii) calculate the vertical pressure gradient; (iv) let the ODE solver predict the next level for pressure. Wrapped around the vertical integration procedure is a boundary-condition compatibility update procedure. This will need to be discussed with Gordon; today only the vertical integration will be worked on.

The representation of system geometry and material heterogeneity is a critical step. One option is to use a finite-difference or finite-element representation, which is particularly appropriate if the solution is required for initial conditions. If the method is to be used as a standalone procedure, it is better to use the actual layering geometry due to the very high vertical resolution that will end up being used. For the PTn layering, the second approach is better; to test against other methods, the first approach is better. I suppose that I should test it first. Sigh.

A few test problems occur to me. The simplest is a deep homogeneous domain with a strip source and gravity drainage or a water table at the bottom. The next simplest is a homogeneous domain with boundary conditions so that flow turns a corner. Adding layers is next, then holes in the layers. Robustness might be checked at a first cut with a lateral-flow problem.

2/19/96 Boundary condition issues.

I discussed the issue of boundary condition matching with Gordon today. A difficulty with the approach is that boundary conditions are typically specified for pressure, normal flux, or a linear combination of pressure and normal flux along all boundaries in the domain. The difficulties arise where the columns terminate (i.e., the top and bottom of the domain). The MOL approach discussed above requires that both pressure and normal flux are specified at one boundary and both are integrated to reach the other *with no impact from the other boundary condition*. Accordingly, the MOL approach requires an excess of information at the first end and a deficit at the other. To remedy this problem, the over-specified boundary condition at the bottom must be adjusted so that the specified boundary condition at the top is exactly specified. A shooting method will be used for this purpose.

Using the notation $\mathbf{y}$ for the boundary condition vector at the underspecified end and ξ for the over-specified boundary condition, an update to the current ξ value is found using Newton's method, which is a steepest-descent method. The process is summarized by

$$\left[\frac{\partial \mathbf{y}}{\partial \xi}\right] \left\{\Delta\xi\right\} = \left\{\mathbf{y} - \hat{\mathbf{y}}(\xi)\right\}, \tag{14-13}$$

$$\xi^{k+1} = \xi^k + \Delta\xi, \tag{14-14}$$

where $\hat{\mathbf{y}}$ refers to the predicted value at iteration k and $\mathbf{y}$ is the required value. The Jacobian matrix (matrix of gradients) will be evaluated using numerical perturbation; some testing will be necessary to evaluate the perturbation size. It may be desirable to use the Newton step as a descent direction and do some line-searching, since each entry in the Jacobian matrix requires a simulation.

2/22/96 Interim results and perturbation theory.

A prototype for the quasi-1D approach was coded using *Matlab* files **rifleman.m**, **generic_rifleman_prime.m**, and **problem1.m**, all in directory *$HOME2/Matlab/MoL*. These files respectively represent a somewhat generic shooting algorithm, a shell for the matlab ODE solver, and a collection of code bits implementing a simple problem all packaged into one file. Additional problems could be examined by copying the **problem1.m** file and modifying the problem-dependent bits.

The problem of interest is a rectangular domain with a bottom water table boundary condition, no-flow sides, and a strip mass source across part of the top and no flow for the remainder.

Purely unsaturated conditions were examined, with only liquid considered. The nominal dimensions were 100 cm $\times$ 100 cm, with saturated conductivity of 10^{-8} cm/sec, van Genuchten m of 0.2, and bubbling pressure of 10^4 gm/cm-s^2. Ranges of source strengths, width-to-height ratios, and conductivity anisotropy ratios were examined. Also, low-permeability inclusions were considered.

In general, once obvious bugs were removed it was found that the procedure only works well if there is minimal divergence of flow. Such situations occurred when the lateral dimension is much greater than the vertical dimension or when the horizontal conductivity is much smaller than the vertical conductivity (!). Even sneaking up on more stringent problems by gradually relaxing the constraining parameter did not seem to work. In general, conditions where the non-1D approach work are rare, leading to doubts as to the method's utility. Still, the 1D solver is very powerful, so additional work is warranted.

Problems popped up in two ways. Occasionally the ODE solver was presented with bottom conditions that were incompatible with a solution, and at least one column formed a dessication singularity. Even when the integration was successful, the shooting method was not guaranteed to work, as the Jacobian matrix can become extraordinarily poorly scaled. Poor scaling occurs when the top and bottom boundary conditions are not connected strongly, such as occurs when a zone of gravity drainage exists to sever the linkage.

Several ideas are still percolating:

- Integrate in the other direction.

- Do some sort of vertically averaged horizontal solution in conjunction with the vertical sweep.

- Create intermediate unknowns close enough together to maintain connection and solve a coupled set of shooting problems.

- Use perturbation ideas to build up a set of solutions.

I have doubts about the first idea, simply because conservation of difficulty pops up. The second and third ideas might be left for future work, since they would take some time to work out.

The perturbation approach would start by doing a true 1D solution, properly averaging all lateral heterogeneities and accommodating lateral boundary conditions and sources. The next step is to build a system of equations that represents perturbation due to lateral behavior. The system would presumably be built up by halving each column. In the following, unperturbed variables

are denoted by overbars and perturbed variables are denoded by carets (hats). The unperturbed equations are written:

$$\nabla \cdot \bar{\mathbf{q}} + \bar{Q} = \frac{\partial \bar{\mathbf{q}}_v}{\partial z} + [\nabla_h \cdot \bar{\mathbf{q}}_h + \bar{Q}] = 0, \tag{14-15}$$

and if $Y_1 = \bar{P}$, $Y_2 = \bar{\mathbf{q}}_z$, and $(\cdot)'$ refers to $\partial(\cdot)/\partial z$, two equations are obtained:

$$Y_2 = -K(Y_1)[Y_1' + \rho g z'] \quad \Rightarrow \quad Y_1' = -[Y_2/K(Y_1)] - \rho g z', \tag{14-16}$$

$$Y_2' = -[\nabla_h \cdot \bar{\mathbf{q}}_h + \bar{Q}]. \tag{14-17}$$

Subtracting the unperturbed solution from the overall system, the perturbed system is written

$$\frac{\partial \hat{\mathbf{q}}_v}{\partial z} + [\nabla_h \cdot \hat{\mathbf{q}}_h + \hat{Q}] = 0, \tag{14-18}$$

$$\bar{Y}_2 + \hat{Y}_2 = -K(P)[\bar{Y}_1' + \hat{Y}_1' + \rho g z']$$

yielding

$$\hat{Y}_1' = -\left[\frac{\bar{Y}_2 + \hat{Y}_2}{K(P)} + \rho g z' + \bar{Y}_1' \right]$$

$$= -\left[\frac{\bar{Y}_2 + \hat{Y}_2}{K(P)} + \rho g z' - \frac{\bar{Y}_2}{K(\bar{Y}_1)} - \rho g z' \right]$$

$$= -\left[\frac{\hat{Y}_2}{K(P)} + \bar{Y}_2 \left(\frac{1}{K(P)} - \frac{1}{K(\bar{Y}_1)} \right) \right], \tag{14-19}$$

$$\hat{Y}_2' = -[\nabla_h \cdot \hat{\mathbf{q}}_h + \hat{Q}]. \tag{14-20}$$

2/24/96 More interim results and perturbation theory.

The perturbed solution technique was coded up in *Matlab*, in **problem2.m**, which is basically the same problem that was looked at in **problem1.m**. Indeed the perturbation technique seems to be more robust than the direct technique and should be kept as the preferred option.

Several insights are coming forth on the procedure. It is obvious that the impact of variation in top and bottom boundary conditions damps out at some distance from the boundary. The result of this observation is that small perturbations from the 1D solution grow with integration distance, sooner or later causing a singularity in the perturbation solution. The stronger the ability for

horizontal flux, the sooner the singularity arises. Thus, as anisotropy becomes strongly preferential to the horizontal, the 1D assumption becomes better. In the two limiting cases of anisotropy, then, strongly horizontal *or* strongly vertical, 1D approaches become appropriate, as a series or in parallel. Not coincidentally, these are just the cases that are found to work best using the ODE approach. Note that doing streamtube analysis, apportioning fluxes transverse to the flow direction strictly due to conductivity, is most appropriate in these two limiting cases. Winding high-permeability zones provide the worst case.

In a homogeneous domain, it appears that if a gravity drainage (zero pressure gradient) zone occurs, there is no lateral flow and the zones above and below the gravity drainage zone are decoupled. A practical implication of this observation is that the 1D solution can be determined for a column, then the column can be partitioned into zones of gravity drainage and zones with lateral flow. Each lateral-flow zone bounded by gravity-drainage zones must be solved independently. Gravity-drainage zones can be identified by integrating a perturbation from a boundary or a discontinuity until the deviation is large, say a few of orders of magnitude; this distance is the practical distance for constructing a Jacobian and should be equivalent to gravity drainage.

It seems that higher overall fluxes shorten the distance to singularity. One might predict that heterogeneity would shorten the elevation required to reach gravity drainage, due to locally higher fluxes.

An algorithm for performing layer identification for sloping layers was coded in **layer_seg-regate.m**. Using the UZ-16 data, PTn shedding will be examined for an example in the CMWR paper Gordon and I are contemplating. The PTn problem may necessitate doing 2D anisotropy for layering.

2/25/96 Tilting anisotropy.

In order to handle sloping layers, cases where the principal directions are not aligned with the gravity vector must be considered. Darcy's law is written

$$\mathbf{q} = -\mathbf{K} \cdot (\nabla P + \rho g \nabla z). \tag{14-21}$$

In 2D component form, this corresponds to

$$\mathbf{q}_x = -K_{xx}\frac{\partial P}{\partial x} - K_{xz}\left(\frac{\partial P}{\partial z} + \rho g \frac{\partial z}{\partial z}\right), \tag{14-22}$$

$$\mathbf{q}_z = -K_{zx}\frac{\partial P}{\partial x} - K_{zz}\left(\frac{\partial P}{\partial z} + \rho g \frac{\partial z}{\partial z}\right). \tag{14-23}$$

In ODE form, with the z coordinate vertically upward,

$$Y_2 = -K_{zx}\frac{\partial Y_1}{\partial x} - K_{zz}\left(Y_1' + \rho g\right),$$

$$Y_1' = -\frac{Y_2}{K_{zz}(Y_1)} - \rho g - \frac{K_{zx}}{K_{zz}}\frac{\partial Y_1}{\partial x}, \tag{14-24}$$

$$\mathbf{q}_x = -K_{xx}\frac{\partial Y_1}{\partial x} - K_{xz}\left(Y_1' + \rho g\right). \tag{14-25}$$

The perturbation equations become

$$\frac{\partial \hat{\mathbf{q}}_z}{\partial z} + [\nabla_x \cdot \hat{\mathbf{q}}_x + \hat{Q}] = \frac{\partial \mathbf{q}_x}{\partial z} + [\nabla_x \cdot \mathbf{q}_x + Q] - \frac{\partial \bar{\mathbf{q}}_z}{\partial z} - [\nabla_x \cdot \bar{\mathbf{q}}_x + \bar{Q}] = 0, \tag{14-26}$$

$$\bar{Y}_2 + \hat{Y}_2 = -K_{zz}(P)[\bar{Y}_1' + \hat{Y}_1' + \rho g] - K_{zx}(P)\frac{\partial}{\partial x}(\bar{Y}_1 + \hat{Y}_1)$$

yielding for the pressure perturbation

$$\hat{Y}_1' = -\left[\frac{\bar{Y}_2 + \hat{Y}_2}{K_{zz}(P)} + \rho g + \frac{K_{zx}(P)}{K_{zz}(P)}\frac{\partial}{\partial x}(\bar{Y}_1 + \hat{Y}_1) + \bar{Y}_1'\right]$$

$$= -\left[\frac{\bar{Y}_2 + \hat{Y}_2}{K_{zz}(P)} + \rho g + \frac{K_{zx}(P)}{K_{zz}(P)}\frac{\partial}{\partial x}(\bar{Y}_1 + \hat{Y}_1) - \frac{\bar{Y}_2}{K_{zz}(\bar{Y}_1)} - \rho g - \frac{K_{zx}(\bar{Y}_1)}{K_{zz}(\bar{Y}_1)}\frac{\partial \bar{Y}_1}{\partial x}\right]$$

$$= -\left[\frac{\hat{Y}_2}{K_{zz}(P)} + \frac{K_{zx}(P)}{K_{zz}(P)}\frac{\partial \hat{Y}_1}{\partial x} + \left[\frac{\bar{Y}_2}{K_{zz}(p)} + \frac{\partial \bar{Y}_1}{\partial x}\frac{K_{zx}(p)}{K_{zz}(p)}\right]_{p=\bar{Y}_1}^{p=\bar{Y}_1+\hat{Y}_1}\right], \tag{14-27}$$

and yielding for the flux perturbation

$$\hat{Y}_2' = -[\nabla_x \cdot (\mathbf{q}_x - \bar{\mathbf{q}}_x) + \hat{Q}]$$

$$= -\frac{\partial}{\partial x}\left\{\left[-K_{xx}(P)\frac{\partial}{\partial x}(\bar{Y}_1 + \hat{Y}_1) - K_{xz}(P)\left(\bar{Y}_1' + \hat{Y}_1' + \rho g\right)\right]\right.$$

$$\left. - \left[-K_{xx}(\bar{Y}_1)\frac{\partial \bar{Y}_1}{\partial x} - K_{xz}(\bar{Y}_1)\left(\bar{Y}_1' + \rho g\right)\right]\right\} - \hat{Q},$$

$$= -\frac{\partial}{\partial x}\left\{-K_{xx}(P)\frac{\partial \hat{Y}_1}{\partial x} - K_{xz}(P)\hat{Y}_1' - \left[K_{xx}(P) - K_{xx}(\bar{Y}_1)\right]\frac{\partial \bar{Y}_1}{\partial x}\right.$$

$$\left. - \left[K_{xz}(P) - K_{xz}(\bar{Y}_1)\right]\left(\bar{Y}_1' + \rho g\right)\right\} - \hat{Q}. \tag{14-28}$$

3/5/96 Update. $\boxed{\mathcal{S\!A\!S}}$

Over the last few days, I tried several methods for calculating multiple columns, spawning a series of *Matlab* files entitled **problem1.m**, **problem2.m**, etc., through **problem5.m**. The key seems

to have been found in **problem5.m**, which goes back to the original non-incremental approach and gets minus signs in the right places. With **problem5.m**, I am able to solve some several-layer problems with permeability ten times greater in the direction tangential to the layering, with the layers tilted six degrees and infiltration clustered in one quarter of the domain. Gravity-drainage boundary conditions are imposed on the bottom and down-dip sides. Using the UZ-16 data between 35 m and 80 m, this problem converges for four columns and comes close for eight. I notice that the total lateral diversion is pretty close for the one-column, two-column, and four-column cases, even though the individual columns do not have the average values, suggesting that 1D simulations may be sufficient to give a good idea of the final conclusions.

In the process of testing this problem, I tried some three-layer problems using "representative" layers for the PTn and the adjacent layers. I noticed that in some cases I get almost total lateral diversion in the layer above the PTn (as much as 99.8 percent), and in other cases less than 15 percent, for surface infiltration of 10 mm/yr over a 500-m domain. After some experimentation, it turns out that the TC hackly layer is the key lateral-diversion layer; without it, generally no more than 15 percent is diverted in the PTn zone, no matter how detailed the stratigraphy. It doesn't seem to matter whether another (lower-permeability) welded tuff unit is below (presumably forming a permeability barrier) or a higher-permeability non-welded tuff is below, presumably forming a capillary barrier. If indeed infiltration ranges up to an average of 30 mm/yr as the Flints say, this could be the layer that allows the rather low deep percolation rates that are inferred from other evidence. Where does this layer go? Is it breached by washes? What about faults? Some followup studies are in order!

3/13/96 Verification work. | $S\!A\!S$ |

Over the last few days, Gordon, Ross, and Goodluck have become involved in verification exercises. Gordon has coded up a point-source (Warrick and Loman, 1977) and a strip-source analytic solution by Warrick faxed to Rachid Ababou June 4, 1992. Both steady-state analytic solutions require exponential permeabilities. Goodluck is using Multiflo, and Ross is using Bigflow. We have settled on one comparison problem, based on the domain used in the Bigflow documentation. The domain is 64 cm horizontally, 1 m vertically, with no-flow side boundary conditions, a water table bottom boundary condition, and the strip source top condition. In order to have comparable van Genuchten and Gardner relative permeabilities, the Tiva Canyon hackly unit was selected for a comparison, as the two relative permeability distributions are very similar. However, the alpha parameter causes problems for the analytic solution, so the parameter was increased by a factor of ten. Exercises to date have used an infiltration rate of 1 mm/yr, which is about 1/24 of the saturated hydraulic

conductivity.

In general, the analytic solution is the fastest when it works, while Bigflow and Multiflo are the slowest. The method-of-lines approach works well for this domain with up to 8 columns, but 16 columns give it fits. No direct comparisons have been made yet, but the analytic and method-of-lines seem to be in qualitative agreement.

3/18/96 Analytic perturbation evaluation. $\boxed{\mathcal{SAS}}$

The evaluation exercises pointed out a few coding problems in the method-of-lines routines. Properly evaluating conductivity values was one problem, so that all 2D results to date are suspect. After fixing these problems, only 4 columns can be solved using numerical evaluation for perturbations on the relatively easy comparison problem. It appears that the analytic solution and the Bigflow solution are very close, while the Multiflow solution and the MOL solution are reasonably close but suffer from lack of horizontal resolution. When 8 columns were tried, problems became evident: (i) inability to integrate forward solutions, due to bad bottom conditions; (ii) highly variable perturbations required to numerically evaluate gradients of top boundary conditions with respect to the bottom overspecified condition; and (iii) nonexistent convergence to a solution.

As inaccurate evaluation of the boundary-condition gradients can pollute the solution process, direct evaluation of the gradients is highly desirable. The initial-value equations do allow a direct gradient solution, by differentiating the equations with respect to pressure and imposing a boundary-condition perturbation at the bottom.

Starting with the direct equations in 2D,

$$\frac{\partial P}{\partial y} = -\frac{q_y}{K_{yy}} - \frac{K_{yx}}{K_{yy}}\left(\frac{\partial P}{\partial x} + \rho g\frac{\partial z}{\partial x}\right) - \rho g\frac{\partial z}{\partial y}, \tag{14-29}$$

$$\frac{\partial q_y}{\partial y} = \frac{\partial}{\partial x}\left[K_{xx}\left(\frac{\partial P}{\partial x} + \rho g\frac{\partial z}{\partial x}\right) + K_{xy}\left(\frac{\partial P}{\partial y} + \rho g\frac{\partial z}{\partial y}\right)\right], \tag{14-30}$$

letting $\psi = dP/dY$ and $\theta = dq_y/dY$, where Y is the boundary condition variable being differentiated, the new differential equations are written

$$
\begin{aligned}
\frac{\partial \psi}{\partial y} &= -\frac{\theta}{K_{yy}} - \mathbf{q}_y \frac{d(1/K_{yy})}{dP}\psi - \frac{K_{yx}}{K_{yy}}\frac{\partial \psi}{\partial x} - \frac{d(K_{xx}/K_{yy})}{dP}\psi\left(\frac{\partial P}{\partial x} + \rho g \frac{\partial z}{\partial x}\right) \\
&= -\frac{\theta}{K_{yy}} + \frac{\psi}{K_{yy}^2}\left[\mathbf{q}_y K'_{yy} - (K_{yy}K'_{yx} - K_{yx}K'_{yy})\left(\frac{\partial P}{\partial x} + \rho g \frac{\partial z}{\partial x}\right)\right] - \frac{K_{yx}}{K_{yy}}\frac{\partial \psi}{\partial x}, \quad (14\text{-}31)
\end{aligned}
$$

$$
\begin{aligned}
\frac{\partial \theta}{\partial y} &= \frac{\partial}{\partial x}\left[K_{xx}\frac{\partial \psi}{\partial x} + \frac{dK_{xx}}{dP}\psi\left(\frac{\partial P}{\partial x} + \rho g \frac{\partial z}{\partial x}\right) + K_{xy}\frac{\partial \psi}{\partial y} + \frac{dK_{xy}}{dP}\psi\left(\frac{\partial P}{\partial y} + \rho g \frac{\partial z}{\partial y}\right)\right] \\
&= \frac{\partial}{\partial x}\left[K_{xx}\frac{\partial \psi}{\partial x} + K_{xy}\frac{\partial \psi}{\partial y} + \psi\left[K'_{xx}\left(\frac{\partial P}{\partial x} + \rho g \frac{\partial z}{\partial x}\right) + K'_{xy}\left(\frac{\partial P}{\partial y} + \rho g \frac{\partial z}{\partial y}\right)\right]\right]. \quad (14\text{-}32)
\end{aligned}
$$

The prime ($'$) in the above equations denotes differentiation with respect to P, and differentials of fractions are expanded using the formula

$$
\frac{d}{dx}\left(\frac{f}{g}\right) = \frac{1}{g^2}\left(g\frac{df}{dx} - f\frac{dg}{dx}\right). \quad (14\text{-}33)
$$

The same quarter-strip-source test problem that was examined against the analytic solution was retried using the new approach. *Matlab* files **rifleman_ap.m**, **rifle_prime_base.m**, **rifle_prime_grad.m**, **evalGradCoef.m**, **baseEval.m**, and **gradEval.m** were created to handle the analytic perturbation approach and **cmwr11_prob_2.m** defined the problem. Amazingly enough, the new approach worked the first time all obvious coding mistakes *Matlab* complained about were removed, both for the no-flow lateral boundaries and for a tilted domain with gravity drainage lateral boundary conditions. The new approach definitely worked better than the numerical differentiation approach, particularly in the elimination of guesswork in selecting perturbation increments and to some extent in providing higher-quality Jacobian entries. The method did not, however, allow more columns to be solved for than the numerical perturbation approach.

By varying the length of the domain and the number of columns, it became clear that cases that allow a unit perturbation to grew to more than about 10^{16} do not converge while cases with perturbations growing to less than about 10^{13} do converge. For the same domain, as the number of columns increases, the perturbation growth increases dramatically (e.g., four columns may yield 10^{12} while eight columns might yield 10^{17}). When convergence does occur, it usually takes no more than three Newton steps for the few cases run (which are barely nonlinear due to the choice of material properties).

Insofar as the approach so far uses highly accurate integration approaches but is still limited by integration path length, it appears that subdividing the integration path and introducing intermediate unknowns may be the solution to the difficulty. An intermediate level might be introduced at a point where a perturbation grows to 10^{12}, for example.

One method for attacking the subdivision approach is to use piecewise sensitivities to boot-strap up one level at a time. Over some intermediate interval, changes in the unknowns can be propagated by requiring that the change in an unknown at the upper end of the interval is caused by the change in the unknowns at the lower end of the interval, or

$$\sum_{i=1}^{N} \frac{du_j^{n+1}}{du_i^n} \Delta u_i^n = \Delta u_j^{n+1}. \tag{14-34}$$

At the bottom boundary ($i = 1$), an additional set of equations appear requiring that $\Delta u_i^1 = 0$ for specified-pressure or specified-flux conditions, or $\Delta u_i^1 = \Delta u_i^1(\Delta u_j^1)$ for gravity-drainage conditions. At the top boundary, a set of equations similar to the previous formulation is applied, enforcing the requirement that the top boundary condition is satisfied. The matrix form of the problem is

$$\begin{bmatrix} \mathbf{J}_N(red) & & & & \\ -\mathbf{I} & \mathbf{J}_{N-1,N-2} & & & \\ & \ddots & \ddots & & \\ & & -\mathbf{I}\,\mathbf{J}_{n,n-1} & & \\ & & & \ddots & \ddots \\ & & & & -\mathbf{I}\,\mathbf{J}_{2,1} \end{bmatrix} \left\{ \begin{array}{c} \Delta\mathbf{u}^{N-1} \\ \vdots \\ \Delta\mathbf{u}^{n-1} \\ \vdots \\ \Delta\mathbf{u}^1 \end{array} \right\} = \left\{ \begin{array}{c} \mathbf{Y}_{BC} - \hat{\mathbf{Y}}_{BC} \\ \vdots \\ 0 \\ \vdots \\ 0 \end{array} \right\}, \tag{14-35}$$

where $\mathbf{I}$ is the identity matrix, $\mathbf{J}_{n,n-1}$ is the Jacobian of level-n unknowns with respect to level-$(n-1)$ unknowns, $\mathbf{J}_N(red)$ is the reduced Jacobian, or Jacobian of top boundary conditions with respect to the level-$(N-1)$ unknowns, and $\mathbf{Y}_{BC} - \hat{\mathbf{Y}}_{BC}$ represents the difference between the top boundary conditions and the desired values. The specified-boundary-condition part of the lower boundary values reduces the number of bottom equations by the number of specified conditions. The number of equations balances the number of unknowns when there are the same number of over-specified bottom conditions as there are under-specified top conditions.

References

Phillips, O. M. 1991. *Flow and Reactions in Permeable Rocks.* Cambridge, England: Cambridge University Press.

Warrick, A. W. and D. O. Loman. 1977. Flow From a Line Source Above a Shallow Water Table. *Soil Science Society of America Journal 41*, 849–852.